# Durham E-Theses

## *Flow-vegetation interactions at the plant-scale: the importance of volumetric canopy morphology on flow field dynamics*

BOOTHROYD, RICHARD,JAMES

**How to cite:**

**Use policy**

# Flow-vegetation interactions at the plant-scale:
# the importance of volumetric canopy morphology
# on flow field dynamics

## Richard James Boothroyd

Department of Geography

Durham University

A thesis submitted in partial fulfilment of the requirements for the University of Durham for the degree of Doctor of Philosophy

June 2017

# Flow-vegetation interactions at the plant-scale: the importance of volumetric canopy morphology on flow field dynamics

## Richard James Boothroyd

## Abstract

Vegetation is abundant in rivers, and has a significant influence on their hydraulic, geomorphological, and ecological functioning. However, past modelling of the influence of vegetation has generally neglected the complexity of natural plants. This thesis develops a novel numerical representation of flow through and around floodplain and riparian vegetation, focusing on flow-vegetation interactions at the plant-scale. The plant volumetric canopy morphology, which comprises the distribution of vegetal elements over the three-dimensional plant structure, is accurately captured at the millimetre scale spatial resolution using Terrestrial Laser Scanning (TLS), and incorporated into a Computational Fluid Dynamics (CFD) model used to predict flow. Numerical modelling, with vegetation conceptualised as a porous blockage, is used to improve the process-understanding of flow-vegetation interactions. Model predictions are validated against flume experiments, with plant motion dynamics investigated, and analysis extended to consider turbulent flow structures and the plant drag response.

Results demonstrate the spatially heterogeneous velocity fields associated with plant volumetric canopy morphology. The presence of leaves, in addition to the posture and aspect of the plant, significantly modifies flow field dynamics. New insights into flow-vegetation interactions include the control of plant porosity, influencing 'bleed-flow' through the plant body. As the porosity of the plant reduces, and bleed-flow is prevented, the volume of flow acceleration increases by up to ~150%, with more sub-canopy flow diverted beneath the impermeable plant blockage. Species-dependent drag coefficients are quantified; these are shown to be dynamic as the plant reconfigures, differing from the commonly assigned value of unity, and for the species' investigated in this thesis range between 0.95 and 2.92. The newly quantified drag coefficients are used to re-evaluate vegetative flow resistance, and the physically-determined Manning's $n$ values calculated are highly applicable to conveyance estimators and industry standard hydraulic models used in the management of the river corridor.

# List of Contents

# List of Figures

# List of Tables

# List of Notation

| Notation | Description | Units |
|:---:|:---:|:---:|
| $CSA$ | Cross-sectional area | (m²) |
| $a_c$ | Neighbour links | - |
| $A$ | Reference area | (m²) |
| $A_c$ | Cell face area | (m²) |
| $Ap$ | Frontal area | (m²) |
| $a$ | Frontal area per canopy volume | (m⁻¹) |
| $b$ | Value at cell centre | - |
| $B^{SA}$ | Proportion of the plan surface area containing vegetation | (%) |
| $B^{V}$ | Proportion of the volume containing vegetation | (%) |
| $B^{X}$ | Proportion of a cross-section containing vegetation | (%) |
| $c$ | Value at neighbouring cell centre | - |
| $c'_{\mu}$ | Empirical coefficient | - |
| $C$ | Chezy resistance coefficient | (m$^{1/2}$ s⁻¹) |
| $C_d$ | Drag coefficient | - |
| $C_{ij}$ | Convective transport | - |
| $CL$ | Canopy length | (m) |
| $C_s$ | Smagorinsky constant | - |
| $d$ | Stem diameter | (m) |
| $d_V$ | Visual distance | - |
| $D$ | Diffusion term | - |
| $D_{ij}$ | Diffusive transport | - |
| $E$ | Elastic modulus | (N m⁻²) |
| $f$ | Variable of interest | - |
| $f_D$ | Darcy-Weisbach friction coefficient | - |
| $f_{KH}$ | Frequency of Kelvin-Helmholtz instability | (Hz) |
| $F_d$ | Drag force | (N m²) |
| $F_i$ | Source term | - |
| $F_p$ | Pressure drag | (Pa) |
| $Fr$ | Froude number | - |
| $F_s$ | Skin friction | (N m²) |
| $g$ | Gravitational acceleration | (m s⁻²) |
| $F_{safety}$ | Factor of safety | - |

| | | |
|---|---|---|
| $h$ | Plant height, or $h_{tot}$. | (m) |
| $h_{norm}$ | Normalised plant height | (-) |
| $hs$ | Grid spacing | (m) |
| $h_{slab}$ | Slab height | (m) |
| $H$ | Flow depth | (m) |
| $I$ | Second moment of area | (m$^4$) |
| $I_t$ | Turbulence intensity | (%) |
| $J$ | Flexural rigidity | (N m$^2$) |
| $k$ | Turbulent kinetic energy | (m$^2$ s$^2$) |
| $k_s$ | Length scale of the roughness element | (m) |
| $l$ | Mixing length | (m) |
| $len$ | Length scale | (m) |
| $l_t$ | Turbulent length scale | (m) |
| $L_{ij}$ | Local change in time | (-) |
| $m$ | Degree of meandering | - |
| $n$ | Manning's resistance coefficient | (m$^{1/3}$ s$^{-1}$) |
| $n_0$ | Manning's boundary-roughness coefficient | (m$^{1/3}$ s$^{-1}$) |
| $n_1$ | Resistance from surface roughness | (m$^{1/3}$ s$^{-1}$) |
| $n_2$ | Resistance from variation in channel cross section | (m$^{1/3}$ s$^{-1}$) |
| $n_3$ | Resistance from the presence of obstructions | (m$^{1/3}$ s$^{-1}$) |
| $n_4$ | Resistance from vegetation | (m$^{1/3}$ s$^{-1}$) |
| $NX$ | Number of cells in downstream direction | - |
| $NY$ | Number of cells in cross-stream direction | - |
| $NZ$ | Number of cells in vertical direction | - |
| $p$ | Pressure | (Pa) |
| $p_o$ | Order of convergence | - |
| $P$ | Cell porosity | (%) |
| $P_C$ | Cylindrical porosity | (%) |
| $P_{ij}$ | Production of mean flow deformation | - |
| $P_{RC}$ | Rectangular cuboid porosity | (%) |
| $P_{SF\_RC}$ | Plant solid volume fraction, rectangular cuboid | (%) |
| $P_{SF\_C}$ | Plant solid volume fraction, cylindrical | (%) |
| $r$ | Grid refinement ratio | - |
| $R$ | Hydraulic radius | (m) |
| $Re$ | Reynolds number | - |
| $Re_k$ | Roughness Reynolds number | - |

| | | |
|---|---|---|
| $Re_s$ | Stem Reynolds number | - |
| $S$ | Mean strain rate | - |
| $S_0$ | Channel slope | - |
| $SC$ | Number of scan positions | - |
| $S_{ij}$ | Deformation tensor | - |
| $S_l$ | Linear source coefficient | - |
| $Sp$ | Spacing between elements | (m) |
| $t$ | Time | (s) |
| $T$ | Transient term | - |
| $u$ | Characteristic velocity | (m s$^{-1}$) |
| $u$- | Downstream velocity | (m s$^{-1}$) |
| $u_*$ | Shear velocity | (m s$^{-1}$) |
| $\tilde{u}$ | Unresolved component of velocity | (m s$^{-1}$) |
| $\langle u \rangle$ | Resolved component of velocity | (m s$^{-1}$) |
| $\bar{u}_i$ | Time averaged instantaneous velocity | (m s$^{-1}$) |
| $u'_i$ | Time-varying component of velocity | (m s$^{-1}$) |
| $u_i$ | Instantaneous velocity component | (m s$^{-1}$) |
| $u_m$ | Free-stream velocity | (m s$^{-1}$) |
| $u_t$ | Turbulent velocity scale | (m s$^{-1}$) |
| $U$ | Flow velocity | (m s$^{-1}$) |
| $U_{norm}$ | Velocity normal to inlet | (m s$^{-1}$) |
| $v$ | Kinematic viscosity | (m$^2$ s$^{-1}$) |
| $v$- | Spanwise velocity | (m s$^{-1}$) |
| $\tilde{v}$ | Viscosity like variable | - |
| $V_C$ | Cylindrical volume | (m$^3$) |
| $V_P$ | Total plant volume | (m$^3$) |
| $V_{RC}$ | Rectangular cuboid volume | (m$^3$) |
| $w$- | Vertical velocity | (m s$^{-1}$) |
| $W_{\max\_x}$ | Plant width on the $x$-axis | (m) |
| $W_{\max\_y}$ | Plant width on the $y$-axis | (m) |
| $x_i$ | Direction | - |
| $z$ | Distance from wall | (m) |
| | | |
| $\psi$ | Vogel exponent | - |
| $v_t$ | Eddy viscosity | (m$^2$ s$^{-1}$) |
| $\delta_{ij}$ | Kronecker delta function | - |

| | | |
|---|---|---|
| $\varepsilon_{12}$ | Absolute error between grids | - |
| $\varepsilon_{23}$ | Absolute error between grids | - |
| $\varepsilon_{ij}$ | Viscous dissipation tensor | - |
| $\eta_0$ | Fixed point for homogeneously strained turbulent flows | - |
| $\theta_m$ | Momentum thickness | (m) |
| $\tau_{ij}$ | Reynolds stress | $((\text{m s}^{-1})^2)$ |
| $\beta$ | von Karman constant, or $K$ | - |
| $\delta(i,j)$ | Minimum Euclidean distance | (m) |
| $\varepsilon$ | Viscous energy dissipation | $(\text{m}^2\ \text{s}^{-3})$ |
| $\mu$ | Dynamic viscosity | $(\text{Kg m}^{-1}\ \text{s}^{-1})$ |
| $\rho$ | Fluid density | $(\text{kg m}^{-3})$ |
| $\omega$ | Specific dissipation rate | $(\text{m}^2\ \text{s}^{-3})$ |
| | | |
| $\phi$ | Cell face porosity | (%) |
| $\phi_{ij}$ | Stress redistribution tensor due to pressure strain | - |
| $\partial$ | Partial differential | - |
| $\Delta$ | Finite difference | - |

# List of abbreviations

| | |
|---|---|
| aDcp | acoustic Doppler current profiler |
| aDv | acoustic Doppler velocimeter |
| ALS | Airborne Laser Scanning |
| AUC | Area Under Curve |
| BFC | Boundary Fitted Coordinate |
| CANUPO | CAractérisation de NUages de POints |
| CFD | Computational Fluid Dynamics |
| DBH | Diameter at Breast Height |
| DNS | Direct Numerical Simulation |
| GCI | Grid Convergence Index |
| GPS | Global Positioning System |
| IMU | Inertial Measurement Unit |
| LAI | Leaf Area Index |
| LES | Large Eddy Simulation |
| LiDAR | Light Detecting And Ranging |
| LoD | Level of Detail |
| MAE | Mean Absolute Error |
| MFSA | Mass Flux Scaling Algorithm |
| MLS | Mobile Laser Scanning |
| PLS | Personal Laser Scanning |
| QSM | Quantitative Structure Models |
| RANS | Reynolds-Averaged Navier Stokes |
| RMA | Reduced Major Axis |
| RMSE | Root-Mean-Square-Error |
| RNG | Renormalization Group Theory |
| RSM | Reynolds Stress Models |
| SfM-MVS | Structure from Motion with Multi-View Stereo |
| SGS | Sub-Grid Scale |
| SOR | Statistical Outlier Removal |
| TKE | Turbulent Kinetic Energy |
| TLS | Terrestrial Laser Scanning |
| UAV | Unmanned Aerial Vehicle |

# Statement of Copyright

The copyright of this thesis rests with the author. No quotation from it should be published without the author's prior written consent and information derived from it should be acknowledged.

## Acknowledgments

Firstly, I would like to thank Rich Hardy and Jeff Warburton for their supervision, guidance, advice, and enthusiasm. I can't thank them enough for a great four years working on the PhD. I would also like to thank Tim Marjoribanks for his help and expertise, and for always being on hand to answer PHOENICS related questions.

I would like to extend thanks to the academic, technical, and support staff in the Department of Geography who made Durham University an excellent place to study; and friends who made Durham an even better place to live.

I am also grateful to Brendan Murphy, Mark Anderson, Daniel Parsons, and Stuart McLelland for access to the flume at the University of Hull, and for assistance during the experiments. Thanks also to Rob Thomas for help with processing the aDv data.

Finally, I would like to say a huge thank you to my parents for their support, and to Ruth for her encouragement along the way.

## Dissemination

The following papers have been published from this thesis:

- Boothroyd RJ, Hardy RJ, Warburton J, Marjoribanks TI. 2016. The importance of accurately representing submerged vegetation morphology in the numerical prediction of complex river flow. *Earth Surface Processes and Landforms* **41**: 567-576.

- Boothroyd RJ, Hardy RJ, Warburton J, Marjoribanks TI. 2016. Modelling vegetation-flow interactions: the importance of accurately representing plant morphology. In *11th International Symposium on Ecohydraulics* Melbourne, Australia.

- Boothroyd RJ, Hardy RJ, Warburton J, Marjoribanks TI. 2017. Modeling complex flow structures and drag around a submerged plant of varied posture. *Water Resources Research* **53**: 2877-2901.

# Chapter 1

# Introduction

## 1.1     Background and rationale

Vegetation is abundant in rivers, and has a significant influence on their hydraulic, geomorphological, and ecological functioning.   Influencing multiple spatial and temporal scales, vegetation can control river form and morphodynamics (Gurnell, 2014), flow conveyance (Järvelä, 2002b), mean and turbulent flow fields (Nepf, 2012a), and sediment dynamics (Sand-Jensen *et al.*, 1989).   In doing so, vegetation provides habitat, alters light availability and temperature, and regulates concentrations of oxygen, carbon, and nutrients (Carpenter and Lodge, 1986).   Vegetation is therefore critically important in controlling the hydrodynamics of aquatic ecosystems (Nikora, 2010).

Based on the position in the river system, in this thesis vegetation is characterised into one of three different types; in-channel vegetation, floodplain vegetation, and riparian vegetation (Figure 1.1).   The different vegetation types interact with the river as the water level rises and falls, with vegetation therefore influential for channel and floodplain flows across a variety of spatial and temporal scales.   This interaction is dynamic, as flood events can disturb and uproot vegetation, modifying the spatial distribution (Crouzy *et al.*, 2013).   An additional temporal dynamic is introduced by seasonal changes, with the spatial distribution of vegetation modified during periods of growth and recession (Coon, 1998).
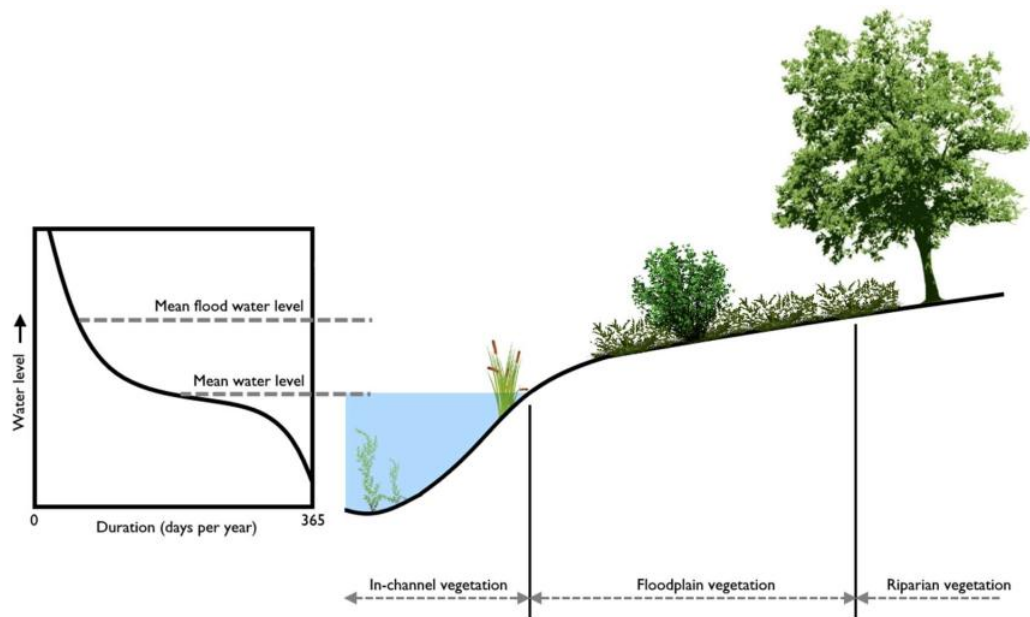
*Figure 1.1 Contextual diagram of the vegetation types within river systems.*

The influence of vegetation on hydraulic processes in river systems has often been evaluated through the contribution of vegetation towards flow resistance (Curran and Hession, 2013). In terms of river flow, vegetation adds an additional local and boundary flow resistance, and in doing so, strongly reduces the channel conveyance and flow velocity (Kouwen *et al.*, 1969; Nepf *et al.*, 2007b). This is because vegetation extracts energy from open channel flows through the process of drag. The total drag force acting on vegetation is the sum of skin friction exerted over the vegetation surface, and form (pressure) drag resulting from flow separation, associated with the generation of turbulence (Bakry *et al.*, 1992; Siniscalchi and Nikora, 2012). With the reach-scale functionally defined as a stretch of river composed of largely homogeneous geomorphic units (Eyquem, 2007; Parker *et al.*, 2012), flow resistance is the sum of the component parts, including the contribution made by vegetation (Cowan, 1956; Kadlec, 1990).

Flow resistance is therefore influenced by a combination of factors, not limited to flow characteristics, but also vegetation factors that are primarily a function of the vegetation species, influencing the distribution and growth form of individual plants (Large and Prach, 1999). In confined channels, increased flow resistance produces higher water levels per unit discharge due to continuity constraints (conservation of mass) (Petryk and Bosmajian, 1975), and this can increase the risk of flooding and pose management issues for vegetated watercourses (Environment Agency, 2014). A correct understanding of the influence of vegetation is therefore essential in correctly estimating conveyance, which is typically predicted either by applying a one-dimensional hydrodynamic model

(e.g. ISIS, MIKE11, HEC-RAS), or using a Conveyance Estimation System (Wallingford, 2004). However, the representation of vegetation is one of the largest sources of uncertainty in one-dimensional hydrodynamic models, where a number of effects are represented through lumped hydraulic resistance terms (Lane *et al.*, 2005). A clear need is therefore identified to develop our understanding of how vegetation partitions discharge between changes in velocity, width, and depth; and how this impacts upon conveyance.

An understanding of the influence of vegetation and its potential contribution to flood risk is especially relevant to discussions of flooding in the United Kingdom. In England alone, over 5 million people and over 2.4 million properties are at risk of flooding from rivers or the sea (Environment Agency, 2009b). Following the 2007 UK summer flooding, the UK's largest peacetime emergency since World War II with an economic cost of over £ 3 billion, a number of recommendations for river corridor management were published in the Pitt Review (Pitt, 2008). The Pitt Review was commissioned to provide a comprehensive analysis of the lessons to be learned in managing future flood risk. A key observation from the Pitt Review was that management processes such as dredging and vegetation clearance were no longer being performed as frequently, and instead the management focus had shifted towards flood control as an integrated part of river restoration and ecological integrity (Pitt, 2008). The presence of in-channel, floodplain, and riparian vegetation has therefore increased, acting to slow the passage of the flood wave through the river corridor by increasing the hydraulic resistance and reducing the conveyance. Furthermore, it has been suggested that in recent decades the frequency of high magnitude river flows have increased (Wheater, 2006), occurring alongside a 'flood-rich' period in the hydrological record (Lane, 2008; Pattison and Lane, 2012). Combined, these effects heighten the likelihood of flooding, and this increases the relevance of vegetation in rivers.

Historically, removal of vegetation was implemented to accelerate the passage of flow (Nepf *et al.*, 2007a); although this can increase flood frequency downstream, can negatively impact upon ecology, and may provide only a short-term solution (Trepel *et al.*, 2003). In the late 1990s, these practices were phased out having been shown to be uneconomical and environmentally damaging in many cases (Thorne, 2014). Under the Water Framework Directive (WFD), which promotes the maintenance and improvement of the ecological status of watercourses, such damaging practices are restricted with maintenance works completed with due regard for watercourse ecology (Environment

Agency, 2009a). Dredging and vegetation clearance should not therefore be viewed as the only solution to flooding (CIWEM, 2014).

Issues surrounding dredging and vegetation clearance re-emerged following the severe winter flooding in the United Kingdom in early 2014. In terms of event magnitude, figures released by the Association of British Insurers estimate a cost of £ 1.1 billion in flood insurance claims for the period 23$^{rd}$ December 2013 to 28$^{th}$ February 2014. Some of the worst affected areas included the Somerset Levels and the River Thames, where a lack of river maintenance was blamed for the inland flooding (Thorne, 2014). However, these claims were countered by Bates (2014), citing the complexity of the problem, and warning against deciding on long-term flood mitigation strategy in light of the event. The public debate which ensued, as to whether flooding had been exacerbated due to inadequate dredging and vegetation clearance practices, enabled local political activists to capitalise on national and local political sensitivities to promote a solution which involved a substantial change in Environment Agency policy, culminating in the introduction of a 20-year flood plan that involved dredging (Smith *et al.*, 2016a). Combined with the 2007 floods, the winter 2014 floods highlighted the public and flood victim perception that flooding may occur due to, or be exacerbated by, a lack of river maintenance associated with vegetation clearance practices (Evans *et al.*, 2009). With vegetation viewed as a significant driver of flood risk, this raises important questions of how best it should be managed.

Given the importance of vegetation in river corridor management, especially during periods where the likelihood of flooding is heightened, an improved process-understanding of flow-vegetation interactions is necessary. This understanding is central to help improve the prediction of conveyance, which presently relies on lumped hydraulic resistance terms in one-dimensional hydrodynamic models or Conveyance Estimation Systems, and so does not explicitly account for the influence of vegetation. Hydraulic resistance terms are typically based upon the Manning's equation, which parameterises and/or calibrates all frictional resistance at the reach-scale; therefore, these values have only a limited physical meaning. To improve upon this, a new quantification of vegetative resistance is needed, based on physically-determined drag terms, developed alongside a full process-understanding of flow-vegetation interactions. For this, it is necessary to develop a numerical representation of vegetation in response to river flow.

In vegetated flows, the canopy is defined as the above ground part of the plant stand consisting of all branches, stems, leaves, and stipes (Paul *et al.*, 2014). Flow through and around canopies of morphologically simple, single stemmed (or analogue) plants have been extensively studied in both field and flume settings (Finnigan, 2000; Sukhodolov and Sukhodolova, 2010b; Nepf, 2012a). Therefore, the three-dimensional mean and turbulent flow, plant motion, and drag are quite well understood (Ackerman and Okubo, 1993; Ghisalberti and Nepf, 2002; Ortiz *et al.*, 2013), and can be predicted using validated numerical models (Tanino and Nepf, 2008; Stoesser *et al.*, 2010; Kim and Stoesser, 2011; Marjoribanks *et al.*, 2015). However, canopies exhibit a wide range of morphologies and plant densities (Valiela *et al.*, 1978; Leonard and Luther, 1995; Lightbody and Nepf, 2006), and in natural settings, therefore, a considerable range of plant morphologies exist.

This is especially important at the scale of individual plants; relevant to the vegetation types that intermittently interact with floods (O'Hare *et al.*, 2016), including the perennial woody plant species often located on riverbanks, floodplains, or mid-channel bars (Gurnell, 2014), shown as floodplain and riparian vegetation in Figure 1.1. At the plant-scale, the understanding of flow-vegetation interactions is challenging given the multitude of stem and leaf scales involved with vegetal elements (de Langre, 2008; Albayrak *et al.*, 2012; Luhar and Nepf, 2013), the variation in plant morphology (Wilson *et al.*, 2003), and the reconfiguration of plants to minimise drag during hydrodynamic loading (Vogel, 1994). Although the drag response is well understood for simple geometric shapes (such as cylinders), it is less well understood for the complex geometries associated with natural vegetation (Marjoribanks *et al.*, 2014a). Different plant species are therefore expected to have different effects on the flow and drag responses (Watts, 1990). Together, these dynamic morphological factors add significant complexity to the problem of quantifying vegetative flow resistance (Kouwen and Unny, 1973; Aberle and Järvelä, 2013), and currently therefore, no validated numerical models exist to predict three-dimensional mean and turbulent flow at the plant-scale.

Vegetation has previously been conceptualised as a porous blockage to flow (Lane and Hardy, 2002; Ghisalberti and Nepf, 2009; Marjoribanks *et al.*, 2014a). This is because although individual vegetal elements represent a mass blockage (stems and leaves, for example), within a controlled volume flow can pass through the plant body, with flow restricted but not fully prevented. As the porosity of the blockage increases, penetration of fluid through the canopy increases, and this influences the three-dimensional mean

and turbulent flow (Schnauder and Moggridge, 2009). To this, additional morphological complexity must be considered, as the spatial structure of the plant will control flow routing (Tempest *et al.*, 2015). Therefore, both the porosity and morphology of the porous blockage are influential in determining the response to flow. Further complexity is added as the porous blockage is dynamic, in that it interacts with flow forcing during reconfiguration. Under hydrodynamic loading, therefore, a plant can be conceptualised as a dynamically moving porous blockage. Because of this, natural plants do not behave as a traditional blockage to flow (Schnauder *et al.*, 2007), and this has important implications for three-dimensional mean and turbulent flow, drag, and vegetative resistance.

## 1.2     Thesis aim

The goal of this thesis is to develop a numerical representation of floodplain and riparian vegetation in response to river flow.  This will be achieved by focusing on flow-vegetation interactions at the plant-scale.  The thesis will investigate three-dimensional mean and turbulent flow around morphologically complex, submerged, natural plants, to improve the process-understanding of flow-vegetation interactions.  This improved process-understanding will be used to inform the quantification of vegetative resistance, providing physically-determined values that can be readily applied to the systems used to estimate conveyance.  Following the methodological developments outlined in subsequent chapters:

***The aim of this research is to investigate how plant volumetric canopy morphology influences three-dimensional mean and turbulent flow, drag, and vegetative resistance at the plant-scale.***

At this point it is important to introduce and explain the term *plant volumetric canopy morphology*.  As identified in Section 1.1, at the plant-scale both the porosity and morphology of the plant blockage are expected to influence the three-dimensional mean and turbulent flow.  The plant volumetric canopy morphology therefore describes the distribution of vegetal elements over the three-dimensional structure of the plant, and is quantified by the solid volume fraction occupied by the plant in a control volume.  This is dynamic, as the plant volumetric canopy morphology will change as the plant reconfigures under hydrodynamic loading.  The plant volumetric canopy morphology therefore refers to all vegetal elements that contribute towards the structure and form of the plant.

## 1.3    Research Questions

To address the aim, a series of specific Research Questions (RQ) have been developed:

***RQ1 – How can plant volumetric canopy morphology be represented in a high resolution numerical model used to predict river flow?***

This question has been formulated to develop the methodology necessary to address the research aim. It requires the development of a new methodology capable of capturing and representing the full three-dimensionality of plant volumetric canopy morphology, and incorporating this into a high resolution numerical model used to predict flow.

***RQ2 – How well does the numerical model predict measured three-dimensional mean flow?***

This question was formulated to evaluate numerical model predictions against measured validation data; to ensure that the modelling system is capable of accurately predicting three-dimensional mean flow, so then analysis can be extended to investigate turbulent flow structures, drag, and vegetative resistance.

***RQ3 – What are the feedbacks between flow and plant motion dynamics?***

This question involves understanding and quantifying the plant response under hydrodynamic loading. To minimise drag, a plant will reconfigure through changes in the plant volumetric canopy morphology. It is therefore essential to investigate this response by quantifying plant motion dynamics. This understanding will also be used to inform the discretisation of the plant in the high resolution numerical model.

***RQ4 – How important are changes in plant posture and porosity on the three-dimensional mean and turbulent flow?***

Changes in the plant posture and porosity as the plant reconfigures under hydrodynamic loading (RQ3) are hypothesised to influence the three-dimensional mean and turbulent flow. The effect of this must be quantified to provide an improved process-understanding of flow-vegetation interactions, and define the relative importance of each factor.

*RQ5 – How important is plant morphology and 'how the plant looks to flow' on the three-dimensional mean and turbulent flow?*

Specifically focusing on plant morphology and 'how the plant looks to flow', this research question further develops the process-understanding of flow-vegetation interactions. It is important to identify the key plant morphology characteristics that control three-dimensional mean and turbulent flow, and quantify the influence of how vegetal elements are exposed and presented by the plant to the flow.

*RQ6 – What is the dominant factor controlling the drag exerted on submerged natural plants?*

The drag response is poorly understood for natural plants. High resolution process predictions are extended to quantify the drag exerted on plants with a range of volumetric canopy morphologies. Comparisons are made between the newly quantified, physically-determined drag terms, and the predefined and constant drag terms that are commonly used to describe flow-vegetation interactions.

*RQ7 – What are the implications for vegetative resistance?*

Vegetative resistance is not explicitly accounted for in the prediction of conveyance, instead relying on lumped hydraulic resistance terms, and this introduces uncertainty into hydraulic model predictions. Using the physically-determined drag terms and the full process-understanding of flow-vegetation interactions at the plant-scale developed by the previous Research Questions, vegetative resistance is quantified. Comparisons are made between the newly quantified terms and the conventional, lumped hydraulic resistance terms; with implications for upscaling to the reach-scale considered.

# 1.4      Thesis structure

The thesis is divided into eight chapters, and structured to sequentially address each Research Question (Section 1.3). An overview of each of the chapters is shown below.

Chapter 2      Provides a review of the current understanding of flow-vegetation interactions and vegetative resistance across a range of spatial scales, before focusing on the plant-scale. This chapter reports the current knowledge gaps, and building on these develops a series of specific thesis objectives in Section 2.5.

Chapter 3      Provides a synopsis of the current understanding of how plant volumetric canopy morphology can be captured, and develops the methodology relevant to the first part of RQ1. This involves applying Terrestrial Laser Scanning (TLS) to measure plant volumetric canopy morphology at the millimetre scale spatial resolution, and develops the workflow to incorporate this into the numerical model. The chapter demonstrates how plant structure and form is quantified for floodplain and riparian vegetation.

Chapter 4      Concerned with development of the numerical model, initial application, and testing; this chapter provides support for the second part of RQ1. With specific reference to good practice in numerical modelling, an overview of how the plant is represented in the model is provided, and the steps taken during model verification detailed. Justification for the numerical representation of open channel flows selected in this thesis is given, with results from initial applications and testing provided. Flow around a geometrically simple cuboidal blockage and a characteristic section of a natural plant are shown.

Chapter 5      Results from a combined flume and numerical model study of flow around a submerged riparian plant are shown, in support of RQ2, RQ3, and RQ4. This study improves the process-understanding of flow-vegetation interactions, providing a quantification of plant motion dynamics, three-dimensional mean flow, and an evaluation of model predictions against the spatially distributed velocity validation data. Analysis is then extended to investigate turbulent flow structures, to

assess the influence of plant posture and porosity, and directly address RQ4.

Chapter 6    Concerned with understanding the importance of accurately representing plant volumetric canopy morphology in the numerical model, the workflow is applied to a second plant species, which has a different morphology, and is more typical of those distributed on gravel bars. This chapter contributes towards improving the process-understanding by simulating the role of foliage, plant posture, and plant aspect on three-dimensional mean and turbulent flow. The influence of plant structure and form is assessed by modelling flow around three different plants of the same species. In support of RQ4 and RQ5, changes in plant volumetric canopy morphology and 'how the plant looks to flow' are hypothesised to influence flow field dynamics.

Chapter 7    This chapter focuses on quantifying the drag response and vegetative resistance of floodplain and riparian plants, to address RQ6 and RQ7. This chapter further investigates the role of porosity by modelling flow around porous and fully impermeable plants, and provides a new conceptualisation of flow-vegetation interactions at the plant-scale. Implications for the reach-scale are considered, and further applications of the research discussed.

Chapter 8    The final chapter provides an overview of the key findings made throughout this thesis, revisiting each Research Question to address the thesis aim.

# Chapter 2

# Current understanding of flow through vegetation

## 2.1    Introduction

The previous chapter showed the influence of vegetation on hydraulic processes in river systems, and highlighted the importance of vegetation in river corridor management. Specific Research Questions were developed to support the aim of the thesis: *'to investigate how plant volumetric canopy morphology influences three-dimensional mean and turbulent flow, drag, and vegetative resistance at the plant-scale'*.  This chapter further develops the understanding of flow through vegetation, and considers the implications for vegetative resistance.

Flow resistance in open channels is detailed in Section 2.2, introducing the equations used to calculate the drag force and drag coefficient, and providing an overview of resistance coefficients that can be used to quantify vegetative resistance.  Then, the effects and controls of vegetation on flow field dynamics are discussed (Section 2.3), reviewing the turbulent flow regimes associated with vegetation, and the biomechanical and morphological factors that influence flow-vegetation interactions.  This helps inform the process-understanding to be developed in RQ3 – RQ5.  A discussion of how plants are currently represented in laboratory and numerical models follows (Section 2.4), and finally a series of specific thesis objectives are developed based on current knowledge gaps (Section 2.5).

## 2.2         **Flow resistance**

This section will introduce flow resistance, with specific reference to the drag force and drag coefficient associated with flow-body interactions. Flow resistance will be discussed in the context of open channel flows, with specific reference to resistance parameterisation, before focusing on vegetative resistance.

### 2.2.1        **Flow resistance**

External flows are defined as flows over bodies immersed in an unbounded fluid (Pritchard *et al.*, 2010). Where there is relative motion between a viscous fluid and an immersed body, the fluid will exert a force on that body, and this force is termed the drag (Peerless, 1967). With flow around an immersed body, surface stresses are generated. These are composed of tangential stresses from viscous action, and normal stresses from local pressure (Pritchard *et al.*, 2010). Flow resistance results from the interactions of these stresses, acting on and within the fluid to resist motion.

Flow past an immersed body is first introduced through an idealised example, shown in Figure 2.1. According to Kumar (2008), the flow can be split into four main zones (labelled i – iv):

     i.     Velocity reduction and streamline divergence upstream of the object.

     ii.     Boundary layer development over the surface of the body. A boundary layer is defined as a region of flow where the velocity increases rapidly from zero at the surface (the no-slip condition), approaching the free-stream velocity asymptotically (Anderson, 1984). The increasing velocity with distance from the surface indicates the presence of shear stresses (Massey, 2006).

     iii.     Flow separation of the boundary layer at separation points, (labelled S1 and S2 in Figure 2.1).

     iv.     Separation zone behind the immersed body, with the shedding of eddies on the downstream side (orange arrows). The disturbed fluid behind the body is referred to as the wake, the character of which depends on the shape of the body, and varies with flow Reynolds number (Peerless, 1967). The separation of flow has far reaching consequences for the dynamics of the flow (Tritton, 1988), as discussed in subsequent sections.
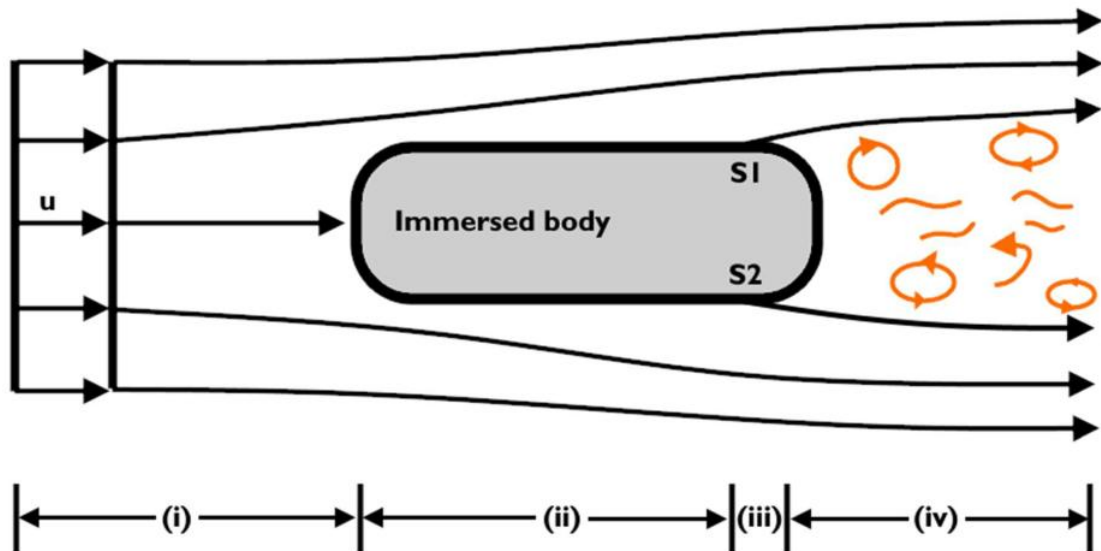
*Figure 2.1 Zones of flow past an immersed body in plan view, redrawn from Kumar (2008). S1 and S2 show separation points of the boundary layer. Orange arrows show disturbed fluid in the wake. The numbered zones are discussed above.*

The forces that generate drag on the immersed body can be categorised into two main types, shear forces and pressure forces (Pritchard *et al.*, 2010) .

Shear forces are a consequence of viscosity, and act tangentially to an objects surface, orientated in the local flow direction. This is termed the skin friction (although sometimes referred to as the viscous drag), and is the product of all resolvable components of tangential forces applied to the objects surface. This is the result of viscous action (Massey, 2006). In Figure 2.1, it is boundary layer development and shear stresses that result in skin friction (occurring in zone ii). Viscous interactions between the fluid and the objects surface produce a shear region, with skin friction proportional to the surface exposed to the flow (Pritchard *et al.*, 2010).

If the object is aligned normal to the flow, drag arises from the resolved components of pressure acting normal to the objects surface. Where the dynamic pressure on the object front is no longer counterbalanced by an equal and opposite dynamic pressure at the rear, an additional drag force results (Tritton, 1988). This additional drag force, termed the pressure drag, depends on the shape of the object (so is sometimes referred to as the form drag). The pressure drag can be calculated from knowledge of the shape and pressure distribution over a body exposed to flow (Peerless, 1967).

Figure 2.2 shows the variation in velocity and pressure around an idealised sphere. As flow approaches the sphere, velocity initially decelerates and then begins to accelerate reaching a maximum at the mid-section of the object. Beyond this, a minimum velocity is reached in the lee of the sphere. Flow subsequently accelerates to recover and retain the free-stream velocity. Pressure variations about the sphere follow the inverse of velocity variations, and it is these variations in pressure that drive changes in velocity. Where the pressure gradient is negative at the upstream end, a net force in the direction of the motion is produced, resulting in flow acceleration. The pressure gradient is said to be favourable (Massey, 2006). At the lee of the obstacle, the opposite is true, with increases in the pressure gradient producing a force that opposes motion. Here, the pressure gradient is adverse, resulting in a reduction of velocity (Massey, 2006). For real flows where viscous forces are present, and flow shears over the boundary, a front-to-back asymmetrical pressure distribution is often generated, and therefore an adverse pressure gradient exists.
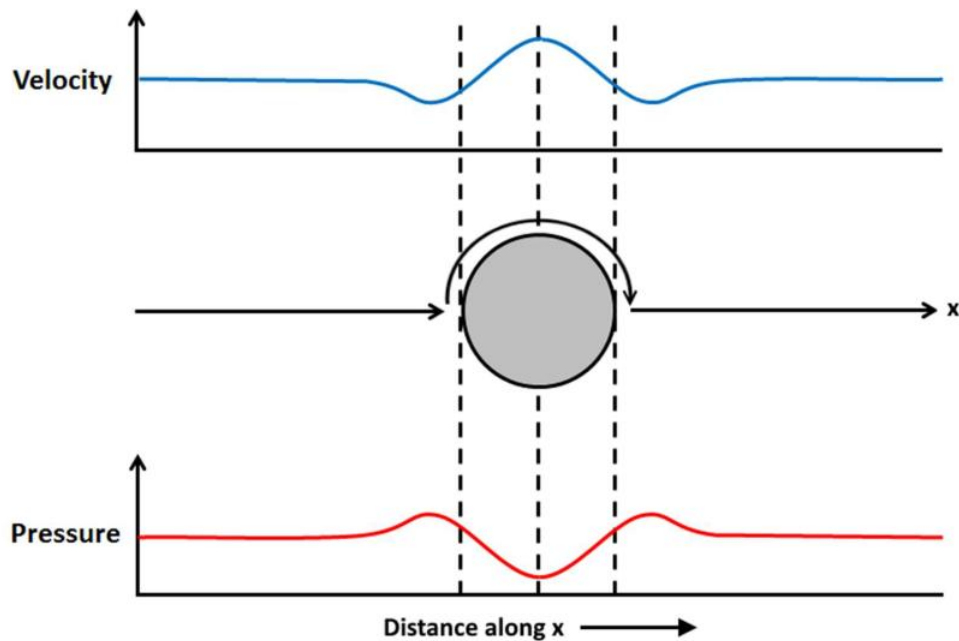


*Figure 2.2 Downstream variation in velocity and pressure along x. Dashed lines indicate the upstream and downstream ends of the sphere (shown in side view); with pressure gradient favourable on the upstream end, and adverse on the downstream end. Adapted from Middleton and Southard (1984).*

Form drag can be enhanced when flow detaches from an objects surface through the process of flow separation, an effect of the pressure gradient. Considering flow over a curved surface (Figure 2.3), initially a negative pressure gradient exists on the upstream side (Massey, 2006). A boundary layer extends from the surface to the free-stream zone due to viscous forces, observing a standard logarithmic profile (profiles a – d). However,

with curvature of the surface the pressure increases, and the forward flow begins to be opposed. Positive pressure results in the formation of an adverse pressure gradient, with this effect most strongly experienced closest to the surface where the momentum is lowest (Massey, 2006). In this region, if the flow is decelerated to zero or reversed (profile e) then the flow will detach from the boundary, no longer following the contour of the surface. The point of detachment is referred to as the separation point, shown as the black dot in Figure 2.3, and can only occur when an adverse pressure gradient exists. The more adverse the pressure gradient, the sooner separation occurs (Massey, 2006). Further along the curved surface, flow is reversed (profiles f and g) and this results in a region of high turbulence dominated by large-scale eddying in the separated region (orange zone, Figure 2.3). The continuous production of eddies causes high rates of energy dissipation, and therefore the separated region exacerbates further the front-to-back asymmetrical pressure distribution, thereby increasing the form drag (Massey, 2006).
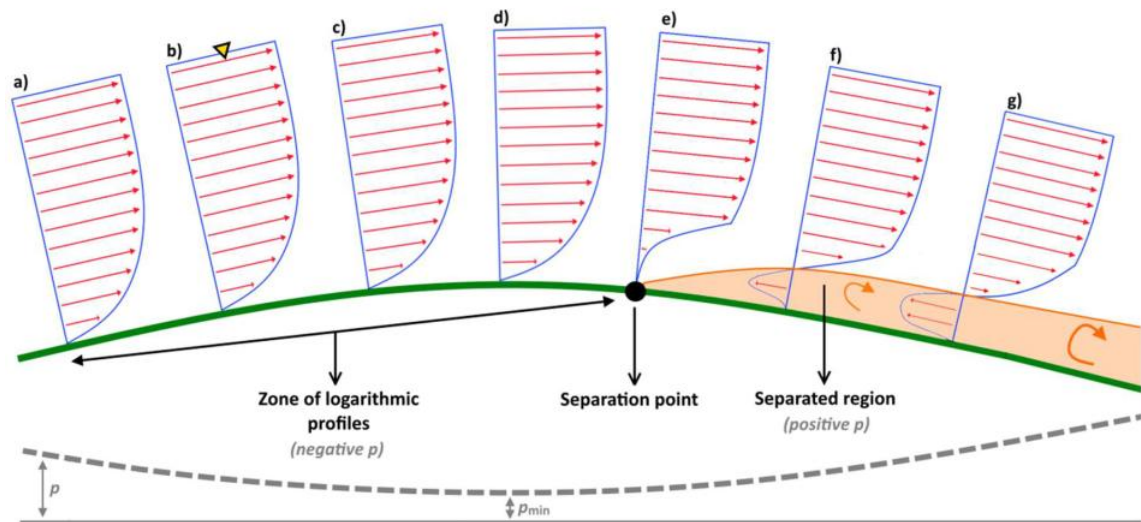


*Figure 2.3 Schematic of flow separation over a curved surface, adapted from Massey (2006). Following the separation point, black dot, standard logarithmic profiles are no longer observed in the separated region, shown by the orange zone. The dashed grey line shows the longitudinal pressure distribution, resulting in a favourable pressure gradient on the upstream side, and an adverse pressure gradient on the leeward side that allows separation.*

The total drag force, $F_d$ (N m$^2$), is the sum of the skin friction drag component, $F_S$ (N m$^2$), and the pressure drag component, $F_P$ (N m$^2$):

$$F_d = F_S + F_P \qquad\qquad (2.1)$$

The relative proportion of the skin and pressure drag towards total drag depends on the objects shape, and the orientation to flow. Bluff and streamlined bodies are the two extremes of object body shapes (Figure 2.4). For bluff bodies (Figure 2.4a), flow separation results in wake development, with pressure drag the dominant contributor to total drag (Massey, 2006). However, the magnitude of the pressure drag depends on the wake size, which varies with the position of the separation point (Figure 2.3). If separation occurs towards the objects front, the resulting wake and pressure drag will be comparably greater, with the flow separated over much of the surface. Conversely, if the point of separation is nearer to the objects rear, the resulting wake and pressure drag will be comparably smaller, meaning that for streamlined bodies (Figure 2.4b), skin friction drag dominates the total drag (Massey, 2006). Whether a body is bluff or streamlined has important implications for the total drag; for example, when comparing a two-dimensional streamlined body to a two-dimensional bluff body with the same thickness, despite the increased surface area of the streamlined body, the drag can be as little as 1/15th that of the bluff body (Tritton, 1988).
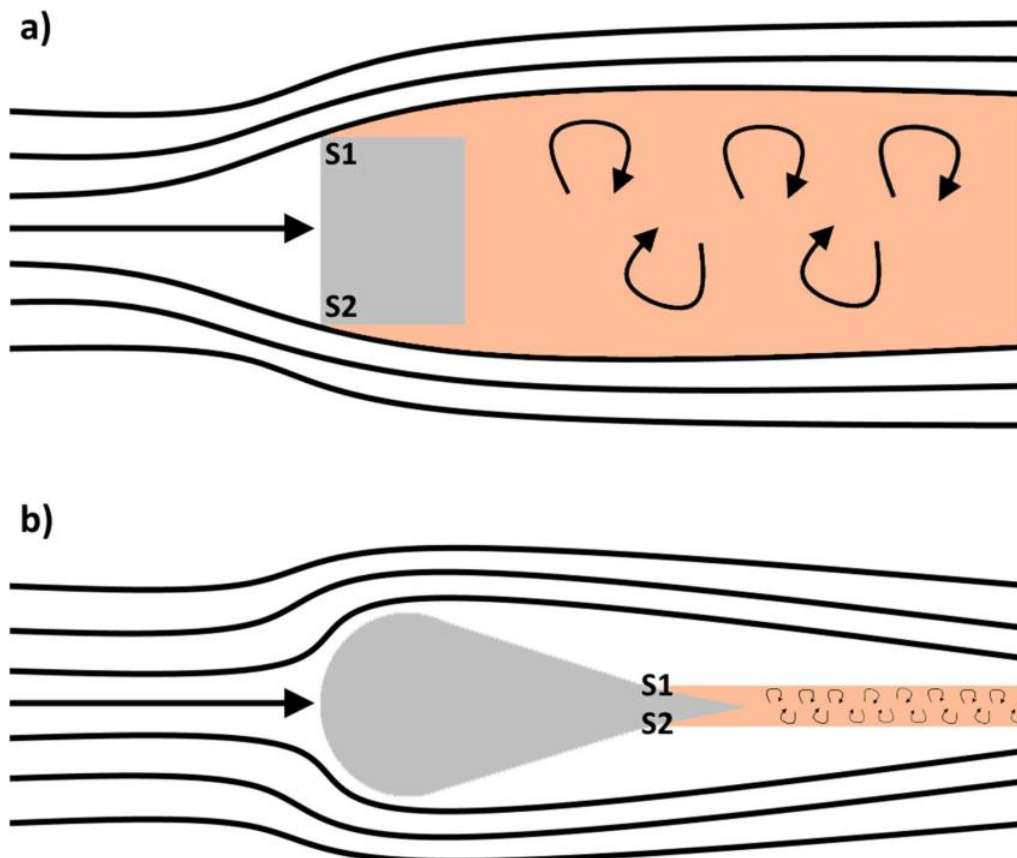


*Figure 2.4 (a) Schematic of streamlines around a bluff body and (b) a streamlined body. Note the differences in position of the separation points (S1 and S2), and the differences in size of the wake (highlighted orange).*

The flow pattern in the wake depends on the Reynolds number (*Re*) of the flow (Massey, 2006). *Re* is the non-dimensional ratio of inertial to viscous forces, and for open channel flows is quantified following:

$$Re = \frac{uR}{v}$$

(2.2)

where $u$ is the characteristic velocity (m s$^{-1}$), $R$ is the hydraulic radius (m), and $v$ is the kinematic viscosity (m$^2$ s$^{-1}$). Flows where $Re < 500$ are classified as laminar, and flows are considered fully turbulent when $Re > 2000$. Flows are classified as transitional between this range (Bridge and Demicco, 2008). For flow through an array of elements, such as the case through stems of vegetation, the stem Reynolds number, $Re_s$, is calculated following:

$$Re_s = \frac{du}{v}$$

(2.3)

where $d$ is the stem diameter (m). A drag-dependency is exhibited with increasing *Re*, with skin friction more significant at lower *Re*, and pressure drag more significant at higher *Re* (Panton, 1984). This is explained with the example of flow around an infinitely long cylinder under increasing *Re*, as shown in Figure 2.5. Points i-v correspond with increases in *Re*, and are adapted from Massey (2006).
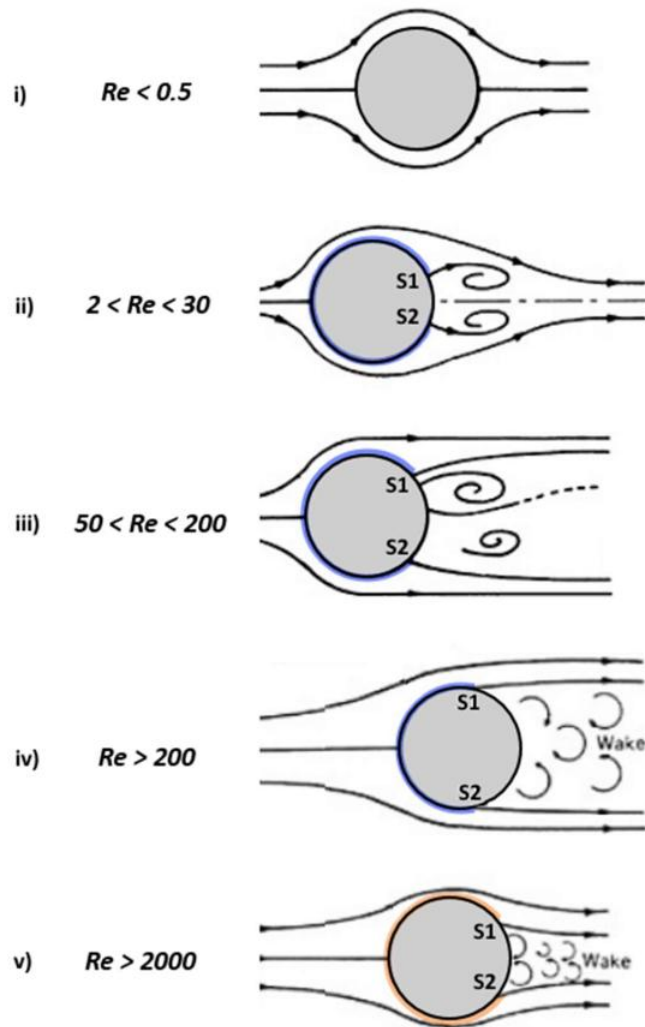
**Figure 2.5 Characteristics of the wake behind an infinitely long cylinder with increasing Re, adapted from Massey (2006). Blue areas indicate a laminar boundary layer, whereas orange areas indicate a turbulent boundary layer. S1 and S2 denote separation points. Flow from left to right.**

i.    Inertial forces are negligible, so drag is almost entirely due to skin friction.

ii.   The laminar boundary layer (blue, Figure 2.5) separates symmetrically from the cylinder at separation point S1 and S2, with the formation of fixed, counter-rotating eddies. The wake length is limited, as the energy of the vortices is maintained.

iii.  Eddies detach from the separation points alternately, forming a von Karman vortex street. As each eddy detaches, the lateral symmetry of the flow pattern is disturbed, therefore altering the pressure distribution. Associated with this, the pressure drag contribution to total drag is increasing, with skin friction less important.

 iv. A turbulent wake has formed behind the cylinder, and pressure drag dominates. In the turbulent wake, mean kinetic energy (MKE) is transformed into turbulent kinetic energy (TKE), and passed along the energy cascade as large-scale eddies generate smaller eddies, which are eventually damped by viscous forces. The largest eddies contain most of the energy, and are most effective in the transfer process along the energy cascade (Rodi, 2017).

 v. As the flow becomes turbulent, the width of the wake narrows as the separation point moves downstream. This is because the turbulent boundary layer (orange, Figure 2.5) can better withstand the adverse pressure gradient, so separation occurs further towards the cylinder rear (Massey, 2006). The structure and type of boundary layer controls the position of the separation point, thereby influencing the extent of energy dissipation in the wake.

For natural open channels flow would be fully turbulent (*Re* > 2000), with wake patterns around an obstacle expected to resemble iii – v.

## 2.2.2  Drag force and drag coefficient

Although the drag force can be determined analytically by integrating the pressure around the surface of the object, this requires a detailed knowledge of the pressure and stress distributions. Consequently, the total drag force, $F_d$ (N m²), is usually determined empirically, following:

$$F_d = \frac{1}{2}\rho C_d A u^2 \tag{2.4}$$

where $\rho$ is the density of the fluid (kg m⁻³), $C_d$ is the drag coefficient (-), $A$ is the reference area of the body (m²), and $u$ is the reference velocity (m s⁻¹). In experiments of flow around cylinders and other obstacles, the reference area is usually taken as the frontal area perpendicular to the flow, $Ap$ (m²), and the reference velocity is taken as the free-stream velocity, commonly denoted by $u_m$ (m s⁻¹).

The drag coefficient is a dimensionless quantity used to describe the combined viscous and pressure effects of an object in the flow. The drag coefficients for various two-dimensional and three-dimensional geometries have been evaluated in wind tunnel and

flume experiments under a range of Reynolds numbers (e.g. Streeter, 1998). The drag coefficient is empirically calculated, following:

$$C_d = \frac{F_d}{\frac{1}{2}\rho u^2 Ap} \tag{2.5}$$

The drag coefficient varies as a function of object geometry and *Re* (Douglas *et al.*, 2005). The values for the drag coefficient are well understood for simple geometric shapes such as cylinders, with a $C_d$ value of unity for *Re* in the range $10^3$ to $3 \times 10^5$ (Panton, 1984; Tritton, 1988). Beyond *Re* $3 \times 10^5$, the drag coefficient drops by a factor of over three, and this is associated with the onset of turbulence in the boundary layer (Tritton, 1988). The law of similitude states that independent of the size of an object, for a given *Re* and object geometry, the drag coefficient will not change. However, for complex geometric shapes, comparably less is known about the drag coefficient.

## 2.2.3 Flow resistance and resistance parameterisation in open channel flows

Considering momentum, flow resistance is the resultant of forces acting on a boundary against flow; considering energy, flow resistance reflects the energy lost inside a control volume or reach (Yen, 1992). For open channel flows, Rouse (1965) classified four components of flow resistance, namely: (i) surface resistance for shear stresses acting on the boundary, (ii) form resistance from drag of obstacles protruding into the flow, (iii) wave resistance from free-surface effects, and (iv) resistance from local acceleration and flow unsteadiness. A range of factors over various spatial and temporal scales contribute towards the total flow resistance in open channels.

At the channel-scale, surface resistance is imposed at the channel boundaries. Variations in channel cross-section and planform geometry introduce flow resistance (Leopold *et al.*, 1960). Therefore, the morphology of the channel, comprising local bank irregularities through to planform sinuosity, exerts an influence on flow resistance. Longitudinal changes in bed-elevation can also introduce alterations to the water-surface slope and energy gradients.

Roughness at the channel perimeter also contributes to flow resistance, with hydraulically smooth and hydraulically rough flows defined by the roughness Reynolds number, $Re_k$, following:

$$Re_k = \frac{k_s u_*}{v} \tag{2.6}$$

where $k_s$ is the length scale of the roughness element (m) and $u_*$ is the shear velocity (m s$^{-1}$). Flow is defined as hydraulically smooth when $Re_k < \sim 5$, transitional when $5 < Re_k < 70$, and hydraulically rough when $Re_k > 70$ (Nikuradse, 1933). Protrusion of roughness elements into the flow therefore influences resistance in open channel flows.

Flow separation about large-scale roughness elements acts to dissipate energy (Best, 2005). These large-scale roughness elements introduce macro-scale turbulent structures into the flow field, with resistance depending on their size, shape, spacing, and distribution (Bathurst, 1978; Furbish, 1987). In gravel-bed and boulder-bed rivers, the arrangement of coarse clasts extracts energy through turbulence generation (Lacey and Roy, 2007). In step-pool rivers, flow resistance is generated by the form drag of step-forming roughness features (Wilcox and Wohl, 2006).

The temporal dynamics of flow resistance need also be considered. Energy can be extracted from the flow with the movement and interactions of sediment (Bergeron and Carbonneau, 1999). Furthermore, the variations in flow depth, which influence the channel morphology, are also important. In flood, channels are composed of a main channel conveying the primary flow, and a floodplain/flood storage area with a smaller conveyance capacity (Figure 2.6a). When coupled, these elements constitute a compound channel, and generate complex, turbulent flow between the high-velocity main channel flow, and low-velocity floodplain flow (Sellin, 1964). Knight and Shiono (1990) observed that with transverse variation in channel depth, strong lateral shear was induced within an experimental compound channel. During overbank flows, the lateral momentum exchange is complicated by lateral shear interactions which transfer energy from the mean flow to large eddies (Figure 2.6b). This momentum transfer reduces the overall discharge capacity of the channel system, and encourages the ridging of water overbank (Figure 2.6b). Plan form eddies, with enhanced lateral momentum, force the flow towards the floodplain, resulting in a net reduction in the discharge capacity through the 'kinematic effect' (Zheleznyakov, 1965; Zheleznyakov, 1971). Such

interactions introduce a temporally dynamic energy loss, additional to that imposed by the static boundary conditions.
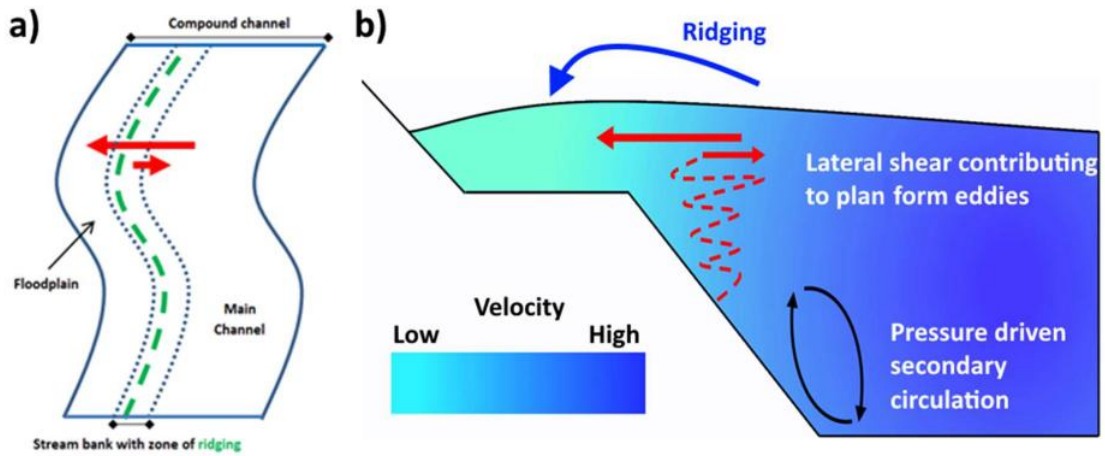


*Figure 2.6 (a) Plan view and (b) transverse view demonstrating 'ridging' where plan form eddies (red arrows) enhance lateral momentum transfer, reducing the main channel discharge capacity*

External factors can introduce further complexities to the flow resistance. A ubiquitous and fundamental feature of many lowland river ecosystems is vegetation (Clarke, 2002; Franklin *et al.*, 2008), and this is associated with an additional flow resistance in open channel flows (Section 1.1). Vegetative resistance, imposed by in-channel, floodplain, or riparian vegetation (Green, 2005c), or by woody debris (Buffington and Montgomery, 1999; Manga and Kirchner, 2000) is significant for energy losses. These energy losses result from skin friction and pressure drag (Section 2.2.1), the magnitude of which depends on a range of plant properties, including: age, seasonality, foliage, volumetric and areal porosities, density, and patchiness (Shields *et al.*, 2017).

Flow resistance is often expressed as a resistance coefficient. Semi-empirical formulae have been proposed that relate open channel flow velocity to resistance coefficients (Yen, 1992). The most commonly used formula is the Manning's equation, following:

$$u = \frac{1}{n}R^{\frac{2}{3}}S_0^{\frac{1}{2}} \tag{2.7}$$

where $R$ is the hydraulic radius (m), $S_0$ is the channel slope (-), and $n$ is the Manning's coefficient ($m^{1/3}$ $s^{-1}$) (Manning, 1891). Other resistance coefficients such as Chezy $C$ and Darcy-Weisbach $f_D$ can be related to Manning's $n$, with no theoretical advantage of one resistance coefficient over the others (Yen, 2002). However, Manning's $n$ is dominant in

practical river management applications (Järvelä, 2002b), and is the default resistance term in hydrodynamic models (e.g. DELFT, HEC-RAS, ISIS, LISFLOOD, MIKE, and TELEMAC). Manning's *n* will therefore be the resistance coefficient referred to in this thesis.

Although most treatments link the resistance coefficients to channel boundary roughness, resistance coefficients can be used to represent many sources of flow resistance, including that of vegetative resistance (Shields *et al.*, 2017). Resistance coefficients can be given as the sum of their individual components. This means that resistance can be parameterised for the different components that contribute towards total flow resistance. Einstein and Banks (1950) combined the friction factors of the different components using linear superposition to estimate total resistance. Cowan (1956) then introduced a superposition method to estimate composite Manning's *n*, additively treating the different scales of resistance, following:

$$n = (n_0 + n_1 + n_2 + n_3 + n_4)m \tag{2.8}$$

where $n$ is the Manning's coefficient; $n_0$ is the Manning's boundary-roughness coefficient; $n_1$ is resistance from surface roughness; $n_2$ is resistance from variation in channel cross section; $n_3$ is resistance from the presence of obstructions; $n_4$ is resistance from vegetation; and $m$ is the degree of meandering.

Resistance coefficient values are primarily selected from reference tables with correction/adjustment factors, empirical equations, and photographs for 'visual comparison' (e.g. Chow, 1959; Barnes, 1967; Acrement and Schneider, 1989; Hicks and Mason, 1991; Coon, 1998). These values are inputted into hydraulic models, and used to calibrate all frictional resistance and produce the correct relationship between flow and water level. Summation approaches have been criticised for over-predicting total conveyance (Garbrecht and Brown, 1991; Knight and Shiono, 1996). However, the method provides a framework to isolate and understand the relative contribution of the different components that contribute towards flow resistance.

This is especially important for the quantification of vegetative resistance, which as discussed here and in Section 1.1, is poorly understood and not explicitly accounted for in predictions of flow conveyance, therefore introducing uncertainty into hydraulic model predictions. Finding the $n_4$ term in Equation (2.8) therefore requires determination of

vegetation drag coefficients and frontal areas (Shields *et al.*, 2017). The goal of this thesis is to develop a numerical representation of floodplain and riparian vegetation in response to river flow, improving the process-understanding of flow-vegetation interactions at the plant-scale. The methodological developments outlined in the subsequent chapters make this possible, thereby meeting the research aim and allowing vegetative resistance to be quantified.

## 2.3    The effects and controls of vegetation on flow field dynamics

This section describes the effects of vegetation on flow field dynamics over a range of spatial scales. First, to reduce ambiguity when describing vegetation, a clear and consistent set of terminologies are outlined, and these are expressed through a common spatial framework (Section 2.3.1). Next, the role of hydrodynamics in flow through vegetation are discussed (Section 2.3.2), and following this, the scales of turbulent regimes summarised (Section 2.3.3). Finally, the biomechanical and morphological controls that influence flow field dynamics and vegetative resistance, specifically focusing on the plant-scale, are outlined (Section 2.3.4).

### 2.3.1    Spatial framework to describe vegetation

Corresponding with the botanic literature, Paul *et al.* (2014) introduces a range of terminologies to describe vegetation. A stand refers to an entire vegetated area. As shown in Figure 2.7, meadow-building species tend to have their biomass distributed evenly along their vertical height. In contrast, crown-building species tend to have their biomass distributed towards the upper part of their vertical height. The canopy is part of the above-ground plant stand including all stems, stipes, and leaves. In vascular plants, the stem is the structural axis, further subdivided into nodes and internodes. The nodes hold leaves, and are linked together by the internode regions. A stipe refers to stalks that are sometimes present and support some other part of the plant structure, like flowers. Leaves tend to have a flattened, blade-like structure, and are the most significant organ for photosynthesis and transpiration. In certain species, the process of abscission leads to the shedding of leaves, therefore the level of plant foliage varies temporally.
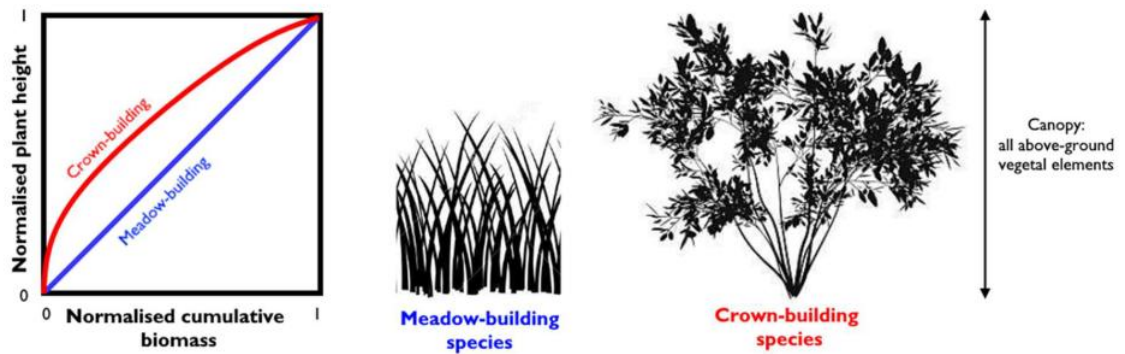
*Figure 2.7 Comparison of the vertical distribution of normalised cumulative biomass over the normalised plant height, between crown-building and meadow-building species.*

A framework is required to describe the different spatial scales relevant to the flow-vegetation interactions investigated in this thesis. Six spatial scales have been identified (Figure 2.8), namely: the leaf-, stem-, plant-, patch-, canopy- and reach-scales:

- Logical distinctions are made between the leaf-, stem-, and plant-scales, with the plant-scale representing individual plants.
- The patch-scale consists of a discontinuous collection of individual plants.
- The canopy-scale is a contiguous unit of plants, where the length of the canopy, *CL,* is greater than the plant height, *h*.
- The reach-scale consists of functional geomorphological units, encompassing the previous spatial scales in the framework.

An important distinction is made where the patch-, canopy-, and reach-scales can be composed of heterogeneous plant communities, and within these three scales, differing plant species with a range of biomechanical and morphological properties will be found.
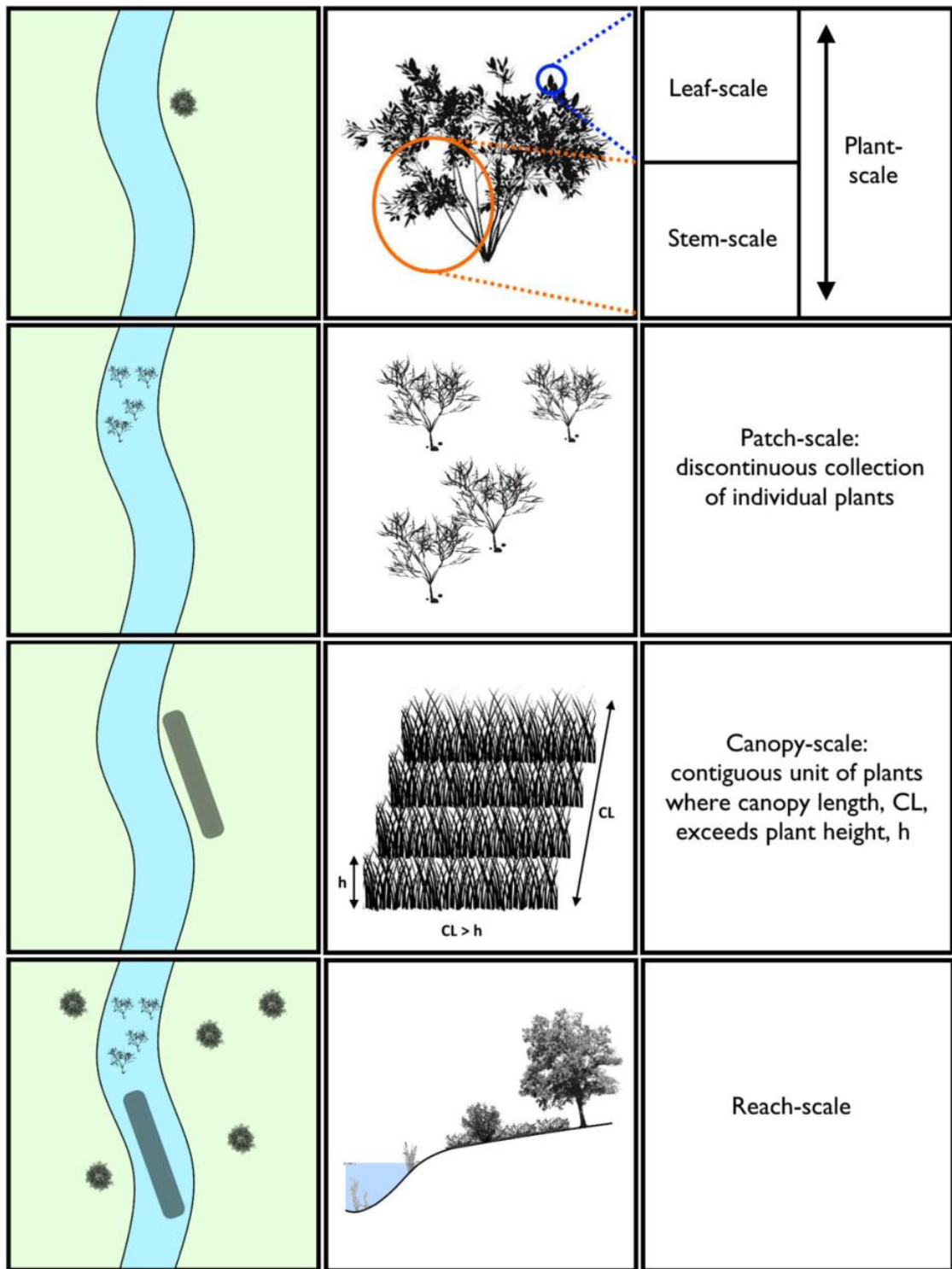
*Figure 2.8 Spatial framework comprising the leaf-, stem-, plant-, patch-, canopy-, and reach-scales.*

## 2.3.2    Role of hydrodynamics in flow through vegetation

Hydrodynamic factors contribute towards flow through vegetation and vegetative resistance. Bölscher *et al.* (2005) categorise three hydrodynamic states relevant to the plant-scale, namely: submerged, submerged with canopy and bottom flow, and

emergent; as represented in Figure 2.9. The hydrodynamic state depends on factors such as the flow depth, *H* (m), and plant characteristics such as the plant height, *h* (m).
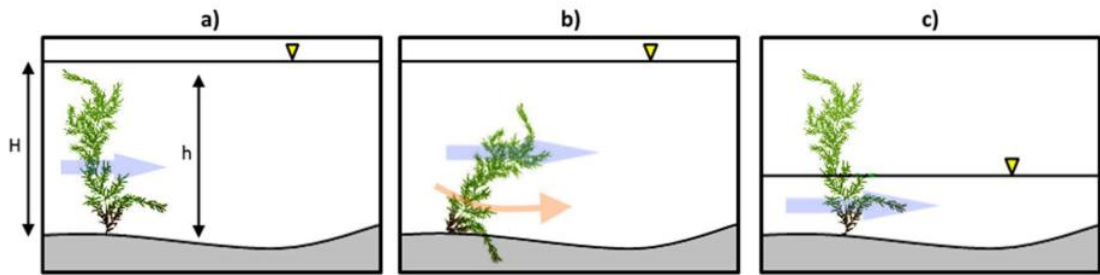


***Figure 2.9 Role of hydrodynamics in flow through vegetation, comparing: (a) submerged plants, (b) submerged plants with canopy flow and bottom flow, and (c) emergent plants. Canopy flow is shown by the blue arrows, whereas bottom flow is shown by orange arrows.***

Under the submerged hydrodynamic state (Figure 2.9a), the velocity and the driving forces within a submerged plant have a range of behaviours depending on the relative depth of submergence (Nepf and Vivoni, 2000), defined as the ratio of flow depth, *H*, to plant height, *h*. In lowland river systems, most submerged aquatic canopies occur in the range of shallow submergence *H*/*h* < 5 (e.g., Chambers and Kaiff, 1985; Duarte, 1991), for which both turbulent stress and potential pressure gradients are important in driving flow over the canopy. Furthermore, the effectiveness of a plant or canopy to attenuate waves is higher with lower submergence ratios (Koch, 2001). A submerged hydrodynamic state with canopy and bottom flow (Figure 2.9b), can be achieved following plant reconfiguration, often associated with increases downstream velocity (Bölscher *et al.*, 2005).

Under the emergent hydrodynamic state (Figure 2.9c), whereby *H*/*h* < 1 and so the plant penetrates the free water surface, subcritical flow is driven by the potential pressure gradients, and the effectiveness for wave attenuation is even greater (Knutson *et al.*, 1982). These conditions are often met in tidal marshes, kelp forests, and seagrass meadows during low tide periods, and because of this, plants often have more rigid biomechanical properties, with rounded stems (Nepf, 2012a). Interactions between the plant, wind sheltering effects, and water surface effects add further complexity to the balance of forces acting on plants in emergent hydrodynamic states (Nepf, 1999).

During flood events, changes in the flow depth mean the extent to which a plant remains submerged or emergent can vary through time. This is especially important for crown-building species, where more biomass is held in the upper part of the plant. Once the

crown becomes submerged, a greater proportion of the vegetation begins to interact with the flow. For these reasons, research concerned with assessing the dampening performance of mangroves in tsunami events have applied different submerged volume ratios to each vertical segment of the forest, such as roots, trunk and canopies (Mazda *et al.*, 1997). A link therefore exits between hydrodynamics and the vertical structure of vegetation.

### 2.3.3        Scales of turbulent regimes in flows through vegetation

Several turbulent length scales are conceptualised for flows through vegetation. Focusing on the canopy and the patch mosaic scales (the latter comparable with the patch-scale outlined in the spatial framework used in this thesis, Section 2.3.1), Nikora *et al.* (2012) conceptualise and hypothesise nine turbulent length scales. Although not definitive, the turbulent length scales provide a good overview of flow through vegetation, with each scale shown in Figure 2.10 categorised into the turbulent regimes of boundary layers (blue, 1-3), mixing layers (magenta, 4-6), and wakes (orange, 7-9). It is the superposition and interaction of these different turbulent regimes over varying scales that give rise to the highly complex flow fields associated with flow through vegetation. An overview for each of the numbered turbulent regimes is provided below (from Nikora (2010) and Nikora *et al.* (2012)), before a more complete description for each of the turbulent length scales is provided in the following sections (Sections 2.3.3.1 – 2.3.3.3).
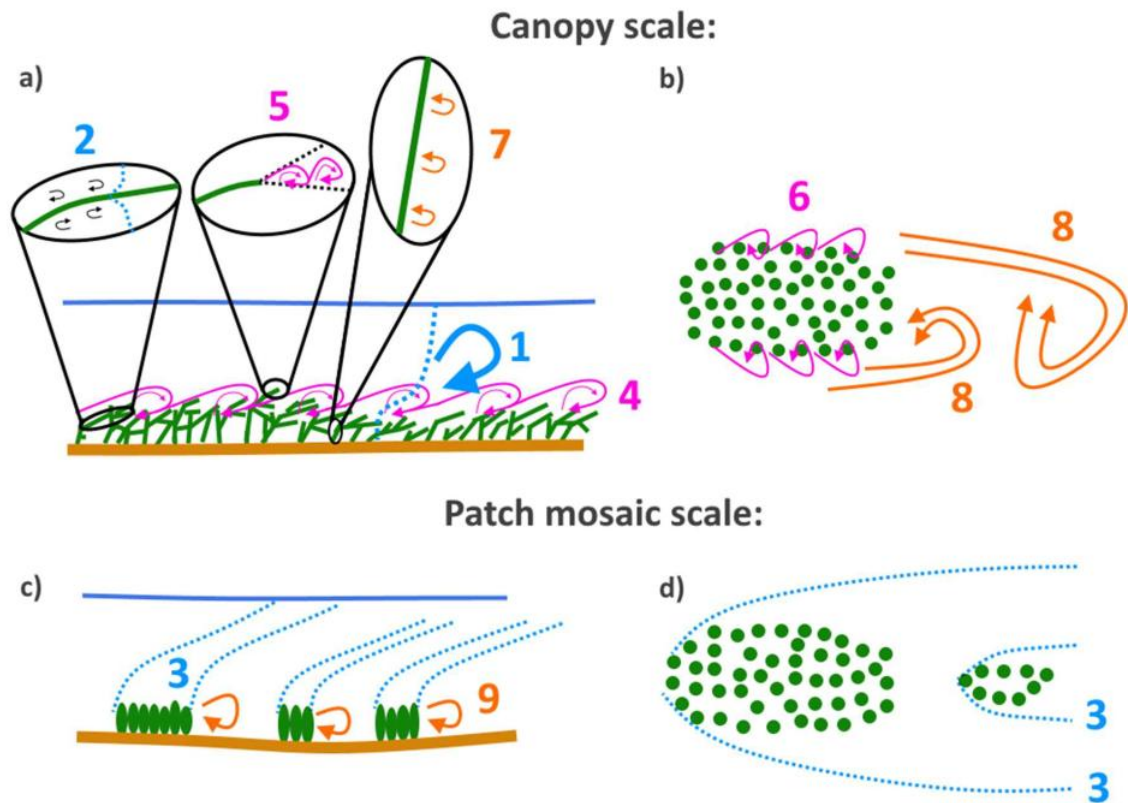
*Figure 2.10 Scales of turbulence associated with: (a and b) the canopy and (c and d) patch mosaic scales in side view (column 1) and plan view (column 2). Blue regions show boundary layers (1-3), magenta arrows show mixing layers (4-6), and orange arrows show wakes (7-9). Adapted from Nikora et al. (2012).*

1.  Depth-scale, shear-generated turbulence within a boundary layer formed between the vegetated bed and the free-surface.
2.  Leaf-scale boundary layer turbulence associated with the surfaces of individual leaves.
3.  Interacting vertical and horizontal internal boundary layers forming at the patch mosaic scale.
4.  Canopy-scale mixing layer turbulence, arising as a result of the inflected or S-shaped velocity profile at the canopy top, where Kelvin–Helmholtz instabilities develop.
5.  Leaf-scale mixing layer turbulence, forming from the different surface roughness on opposing sides of the leaf, which acts as a splitter plane, enabling mixing layer development.
6.  Boundary layer and mixing layer turbulence at the sides of the canopy, aligned in the direction of flow. Such mixing layer turbulence is also likely to be present at the patch mosaic scale, although was not included in Nikora *et al.* (2012).
7.  Stem-scale wake turbulence associated with flow separation about individual stems, and the formation of von Karman vortices.

8. Canopy-scale wake turbulence associated with flow separation about the canopy, and the formation of von Karman vortices.

9. Patch-scale wake turbulence associated with flow separation about individual patches, and the formation of von Karman vortices.

### 2.3.3.1 Boundary layers

An initial level of turbulence complexity is first introduced by the boundary layers generated across the numerous boundaries present in flows through vegetation (1-3, Figure 2.10). Nikora (2010) defines a canonical boundary layer as a flow region where velocity is zero at the boundary, and increases towards the free-stream velocity with distance from the surface.

Boundary layers can be associated with vegetal elements at finest spatial scales, associated with the surface boundaries at leaf- and stem-scales, but will also form at the patch- and canopy-scales. At the scale of individual blades and leaves (2, Figure 2.10) the hydrodynamic response is dominated by viscous boundary layer formation at the leading edge of the surface, with transition along the blade toward a turbulent boundary layer (Nepf, 2012b). However, blade or leaf motion adds complexity to the idealised boundary layer, with the replacement of fluid next to the surface from outside the boundary layer (Nepf, 2012b). Further complexity is added by irregularities of leaf shape, such as corrugations, undulations, stipes, and bulbs (Stevens and Hurd, 1997). At the leaf-scale, boundary layers are important for the drag response, but also for substance transfer and uptake by the leaves (Albayrak *et al.*, 2012).

At the patch- and canopy- scales, depth-limitation (Section 2.3.2) plays an important role in boundary layer development. Because of this depth-limitation, key differences emerge between flows through terrestrial and aquatic plant canopies. In the terrestrial environment, plant height is small in comparison to the boundary layer height ($H/h > \infty$), enabling unrestricted boundary layer development in these unconfined settings. In the aquatic environment, however, flows are generally depth-limited, and this can restrict boundary layer development (Marjoribanks *et al.*, 2017). This is because vegetation growth is limited by light availability, with vegetation unlikely to be present at the flow depths required for unrestricted boundary layer development in open channel flows (Marion *et al.*, 2014). Because of the low ratio of flow depth to roughness height, depth-limited boundary layers through vegetation cannot usually be described

using a logarithmic velocity profile (Nikora, 2010), complicating whether flow through vegetation can be treated simply as bed roughness.

Furthermore, when considering patch- and canopy-scale boundary layers, the density of vegetation is an important characteristic controlling boundary layer development. This is defined by assuming that if the canopy elements have a characteristic diameter, $d$, and an average spacing between elements of $\Delta S$, then the frontal area per canopy volume is $a = d/\Delta Sp^2$. This is the leaf area index (Kaimal and Finnigan, 1994) and when integrated over the plant height, $h$, the canopy density is predicted from the frontal area per bed area, also known as the roughness density (Wooding *et al.*, 1973). For low roughness densities (sparse canopies), element-scale turbulence dominates, and this can result in the formation of a depth-limited turbulent boundary layer. In this case, canopy-drag is small compared with bed drag, and so treatment of vegetation as bed roughness is appropriate. As the density of the patch or canopy increases, however, mixing layer processes begin to dominate, and the canopy-drag contribution from this interaction increases. This is demonstrated in Figure 2.12, in the following section.

### 2.3.3.2 Mixing layers

A mixing layer is defined by Raupach *et al.* (1996) as the region of mixing between two co-flowing streams of different velocities. For flows through vegetation, turbulence is generated as a result of the discrepancy in drag magnitudes between the vegetated and non-vegetated flow regimes (Marjoribanks *et al.*, 2014a), and this usually results in a velocity profile that no longer follows the universal logarithmic law, instead tending towards an inflected profile that is S-shaped (Nepf, 1999). Unlike for the boundary layer regime, the drag introduced by vegetation is often greater than the drag introduced by the bed, and therefore vegetation can no longer be treated simply as bed roughness. Instead, it is complicated by the generation of a region of shear resembling a free shear layer (Nepf, 2012a). Although mixing layers at the canopy-scale are the focus of many studies (4, Figure 2.10), mixing layers are present at several spatial scales in flows through vegetation (5-6, Figure 2.10).

Focusing on the structure of mixing layers, although previously identified in terrestrial canopies, Ikeda and Kanazawa (1996) quantified the inflected velocity profiles associated with aquatic canopies. Subsequently, Nezu and Sanjou (2008) developed a phenomenological model which subdivided the inflected velocity profile into three distinct regions, defining an emergent zone, a mixing layer zone, and a log-law zone

(Figure 2.11).  The emergent zone (i) lies closest to the bed within the canopy, where flow is pressure driven, and velocities are relatively low and quiescent owing to the combined influence of stem wake effects (Nezu and Sanjou, 2008).  Nepf and Vivoni (2000) identify this as the 'longitudinal exchange zone', given the negligible vertical transport of momentum.  Above this, a mixing layer zone (ii) located at the canopy top is characterised by an inflection point of the velocity profile, triggering the generation of coherent flow structures through a Kelvin–Helmholtz instability (Raupach *et al.*, 1996). Kelvin–Helmholtz and Görtler-type vortices are generated through shear instability (Nezu and Onitsuka, 2001), and evolve with distance downstream.  This zone is of critical importance for turbulence generation, with mixing layer vortices accounting for up to 80% of longitudinal exchange between the canopy and the open flow (Ghisalberti and Nepf, 2009), and mixing layer turbulence dominating the turbulent kinetic energy (TKE) budget (Raupach *et al.*, 1996).  Considering the downstream evolution of mixing layer vortices at the canopy-scale, in the downstream direction the height of the vortex centre progressively increases due to canopy drag, and also expands with distance and time (Ghisalberti and Nepf, 2002).  However, vortex growth appears to stop when turbulent energy production is equal to dissipation, meaning a fixed scale and penetration depth are reached (Ghisalberti and Nepf, 2004).  Above this zone, the log-law zone (iii) describes the region where the profile is logarithmic.
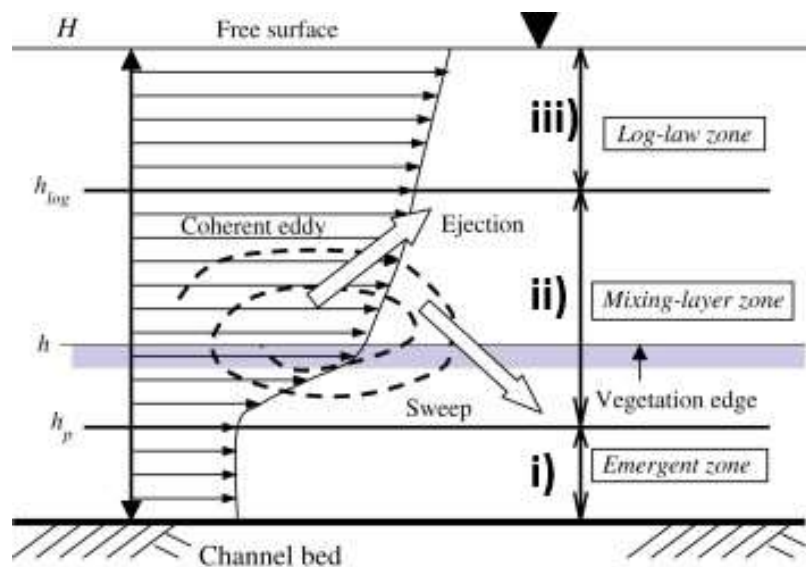


***Figure 2.11 Schematised phenomenological flow model at the canopy scale (from Nezu and Sanjou 2008).***

In reality, however, the phenomenological flow model for canopy flow is modified with changes in submergence ratio, and with characteristics of the canopy.  In depth-limited

flows, the log-law zone may not be fully developed, and in some cases may disappear completely. As the submergence ratio decreases, the thickness of the log-law zone decreases until a critical zero value is attained around 1.5 - 2 $H/h$ (Nezu and Sanjou, 2008). Beyond this, the mixing layer zone will extend to the free-surface. The coherent flow structures generated due to shear instability are significantly influenced by changes in submergence.

Vegetation characteristics not only influence turbulent boundary layer development, but also modify the attributes of the mixing layer zone, thereby altering the turbulence regime. The shear region present in patch or canopy flows is the product of a bulk drag discontinuity (Nepf *et al.*, 2007a), with the scale of the discontinuity quantified by the term $C_Dah$ (bringing together the drag coefficient, frontal area per canopy volume, and canopy height); thereby accounting for canopy form (size and shape) and density. As shown in Figure 2.12a, for sparse canopies ($C_Dah < 0.04$) the velocity profile follows a boundary layer form. In a transitional canopy where $C_Dah > 0.10$, an inflection point and mixing layer develops (Figure 2.12b), and this generates a region of shear at the top of the canopy (Nepf, 2012a). However, for dense canopies shown in Figure 2.12c where $C_Dah > 0.30$, the mixing layer is unable to penetrate the canopy, and so is attenuated (Nepf and Ghisalberti, 2008). Vegetation characteristics therefore play an important role in controlling the development of different types of turbulent regime, especially in influencing whether a boundary layer or mixing layer will be present.
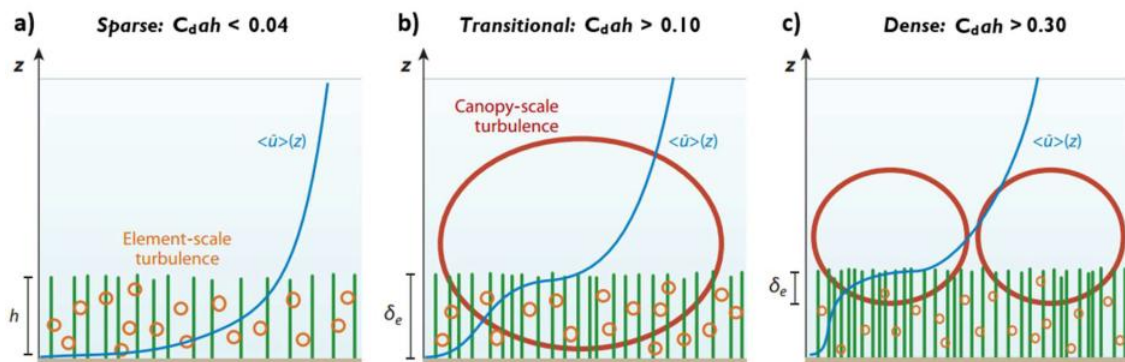


*Figure 2.12 Hypothetical profiles of downstream velocity from Nepf (2012a) for: (a) sparse canopies, (b) transitional canopies, and (c) dense canopies. A boundary layer develops in the sparse canopy. Mixing layers and a region of strong shear at the canopy top generates canopy-scale turbulence in the transitional and dense canopies.*

Mixing layers are equally important for finite-sized patches of vegetation. In these, flow complexity increases due to the 'bleed-like' flow through the patch, as well as interactions between the patch edges and the surrounding open water region (Koken

and Constantinescu, 2016). Analogous to the vertical mixing layers observed at the canopy-scale, lateral mixing layers can develop due to the formation of shear layers as a result of the sharp velocity gradient between the vegetated region and the adjacent free-stream region, providing the necessary conditions for production of coherent vortex structures (Yang *et al.*, 2007). Therefore, for submerged finite-size patches, both horizontal and vertical interfaces and their associated shear layers exist. Lateral mixing has previously been shown at the edge of shallow vegetated floodplain flows (Nezu and Onitsuka, 2001). For an emergent porous blockage, Rominger and Nepf (2011) demonstrated the development of shear layers along both flow-parallel edges of a rectangular patch of varying porosities (Figure 2.13a and b), with the coherent flow structures shed out of phase on either side. Shear layer growth and development occurs downstream of a region of interior adjustment (Figure 2.13c). Similarly, where only one streamwise interface is present at the edge of a porous patch, White and Nepf (2007) report the drag differential to create an instability characterised by regular coherent vortices, with the periodic coherent fluctuations indicative of Kelvin–Helmholtz type vortices. These vortices dominate mass and momentum exchange between the vegetation and the adjacent open channel flow (Zong and Nepf, 2010).
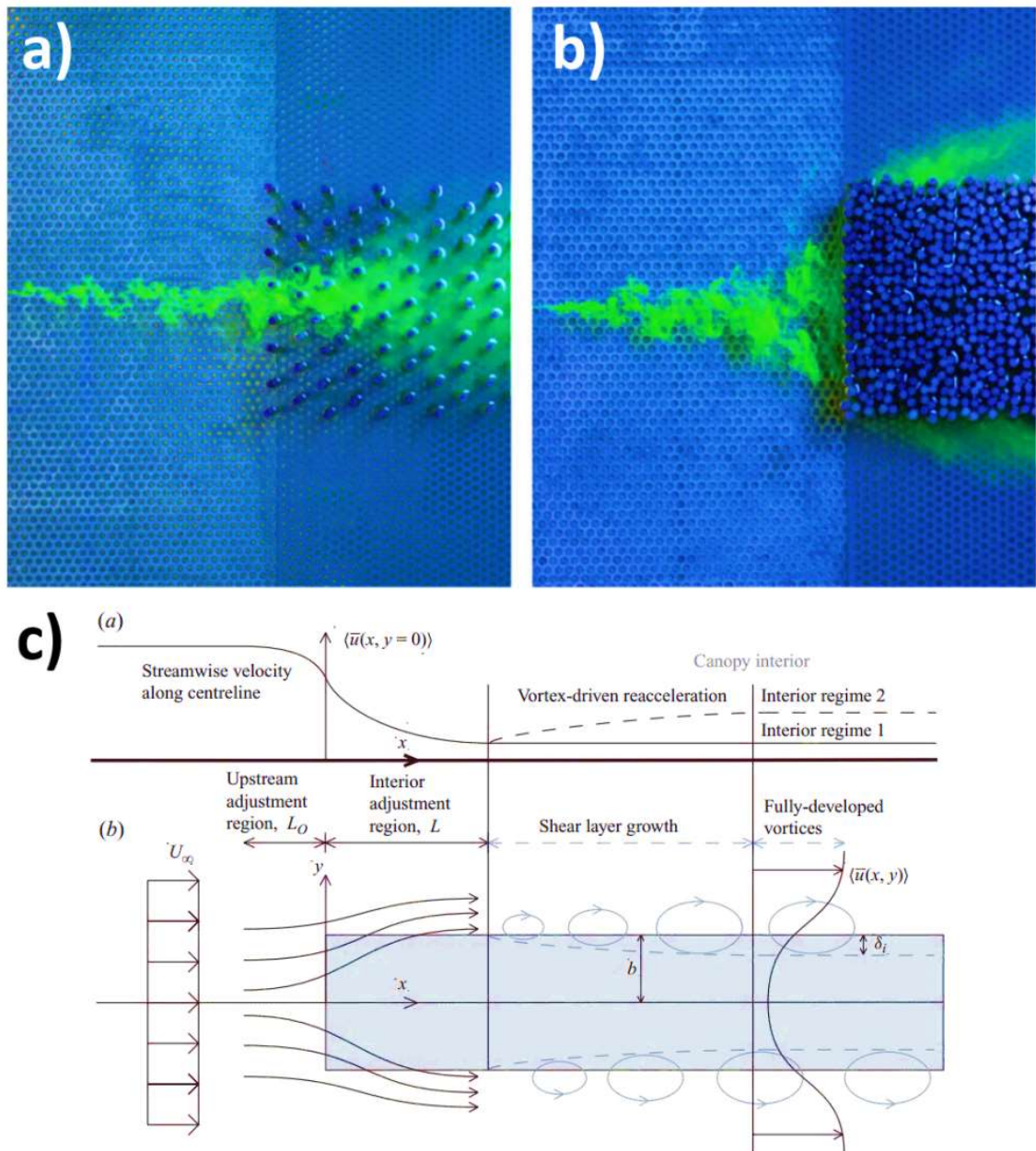
*Figure 2.13 Dye tracer experiments showing flow at the leading edge of: (a) an emergent sparse and (b) dense patch of finite-length. Conceptualisation of flow adjustment about the lateral edge of the patch, showing (c - upper) downstream velocity along the centreline and (c – lower) plan view illustrating shear layer formation. Taken from Rominger and Nepf (2011).*

At the plant-scale, less is known about vertical and horizontal mixing layer development. At the vertical interface between vegetation and flow, Cameron *et al.* (2013) report shear layer development above a single *Ranunculus penicillatus* plant, and find this significantly contributes towards the TKE budget (Figure 2.14). Schoelynck *et al.* (2013) quantify a sharp downstream velocity gradient behind an isolated *Callitriche platycarpa* plant, with a 50-70% reduction of downstream velocity in the low-velocity zone behind the plant indicative of shear layer development. However, very little is known about the potential for a lateral mixing layer to form at the horizontal interfaces between

vegetation and flow at the plant-scale. Finally, a leaf-scale mixing layer is hypothesised to be present where individual leaves can act as splitter planes (5, Figure 2.12), produced by a contrasting surface roughness on opposing leaf sides (Nikora, 2010).
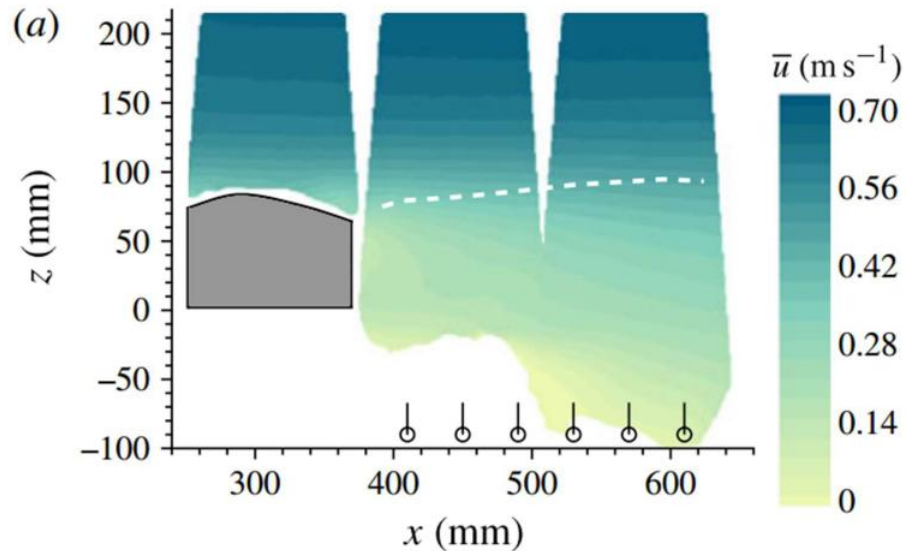


*Figure 2.14 Time-averaged downstream velocity about an individual Ranunculus penicillatus plant (shown by grey area), with shear layer development (dashed line) above the plant, taken from Cameron et al. (2013).*

Mixing layers are therefore present in depth-limited vegetated flows over a range of spatial scales. Such mixing layers are hydraulically and ecologically important, controlling vertical and horizontal transport of mass and momentum and therefore scalar fluxes of flow (Ghisalberti and Nepf, 2002; Zong and Nepf, 2010). Mixing is therefore one of the principal mechanisms of delivery for nutrients, sediment, and heavy metal pollutants to the bed, thereby influencing flushing and trapping behaviours in vegetated beds (Ghisalberti and Nepf, 2005).

### 2.3.3.3    Wakes

The wake is defined as a region of disturbed fluid downstream of a body, where momentum transport is reduced, and therefore a momentum deficit exists (Nikora, 2010). Wake flows are characterised by steep velocity gradients, following flow separation about the separation point, associated with the form drag mechanism (Section 2.2.1). At the lee side of the body, recirculation of flow results in velocity and stress reductions (Schnauder and Moggridge, 2009). Resulting from flow separation and separated shear layer development, wake structures can contribute towards the formation of von Karman vortices through the roll up of shear layers, and this can occur

across a number of spatial scales. Wakes can therefore develop simultaneously at the stem-, plant- and patch-scales.

At the stem-scale, the length scale of vortices are defined by stem or branch diameter, *d*, and the average spacing between these elements, *ΔS*. Spatial heterogeneity exists in the flow field, and this is enhanced by the overlapping and interacting nature of wakes (Figure 2.15). The recirculation zone is positioned directly behind the stem, and beyond this is the wake zone where downstream velocities are diminished relative to the inlet velocity. Where stem-scale wakes overlap, the velocity deficit is the linear sum of individual wake deficits (Nepf *et al.*, 2007a). This spatial heterogeneity in the stem-scale flow field was shown through a series of experiments by Nepf *et al.* (2007a). By measuring the trajectory of particles, the interaction and recirculation with numerous stem-scale wakes results in longitudinal dispersal, as shown in Figure 2.15. Stem-scale wakes therefore have important implications for particle transport.
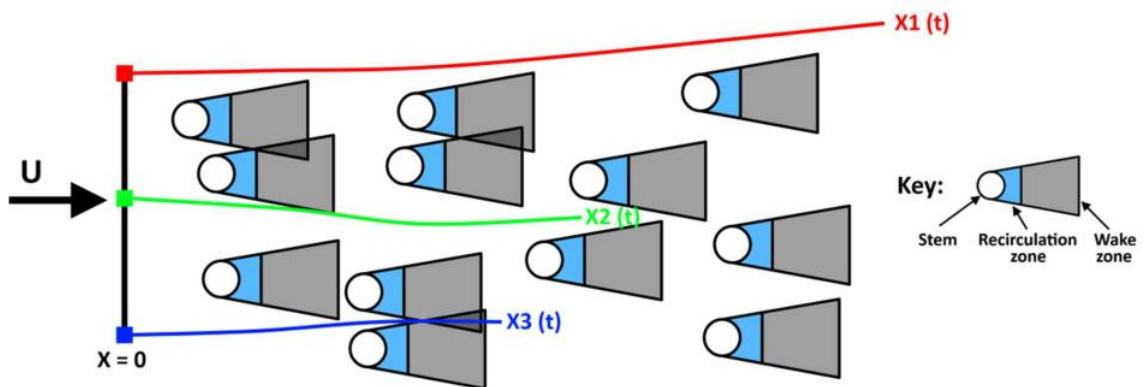


*Figure 2.15 Plan view of overlapping stem-scale wakes and the effect on the longitudinal dispersion of particles 1, 2 and 3, released together at X = 0, t = 0. Particle 3 has a particle length half that of particle 1, due to the interaction with multiple stem-scale wakes. Redrawn from Nepf et al. (2007a).*

The average spacing between stems acts as a first order control on the development of flow structures, by controlling the overlap and interaction between individual wakes. Takemura and Tanaka (2007) show that for an emergent case when the spacing between individual stems is small, individual wakes interact and overlap, coalescing to form a large-scale von Karman vortex street (Figure 2.16a). As the average spacing increases, individual wakes become isolated, with the smaller recirculation zones unable to interact. Here, a primitive von Karman vortex street forms (Figure 2.16b). Similar flow structures are shown to form under submerged conditions (Tanaka and Yagisawa, 2010).
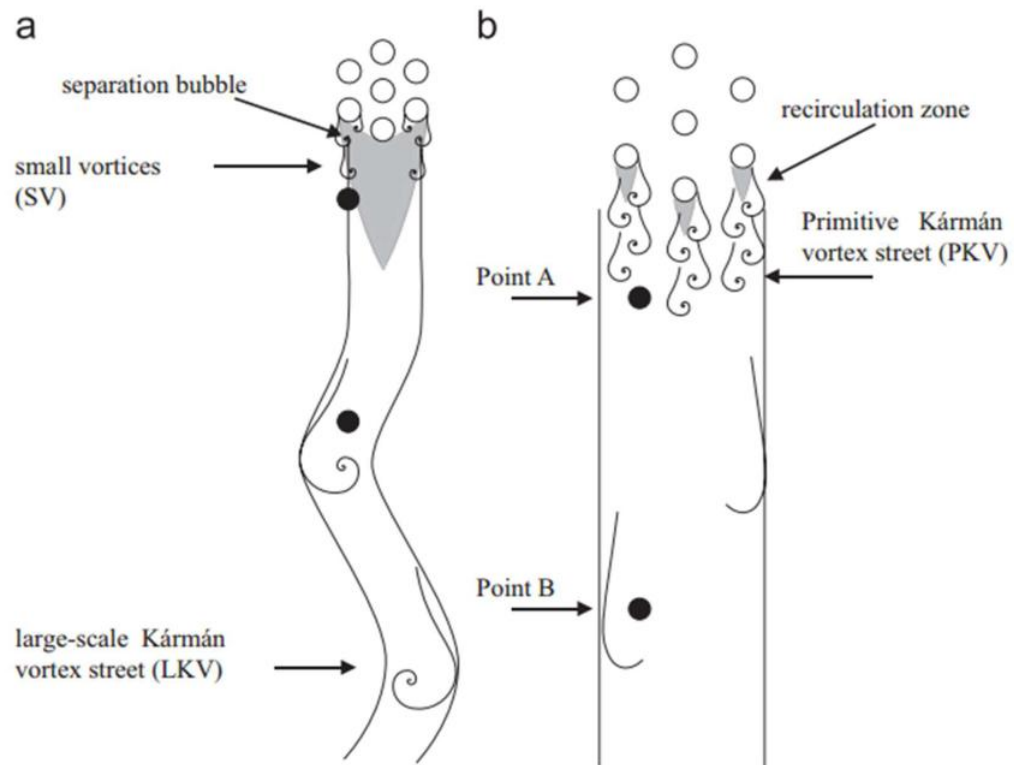
*Figure 2.16 Flow structures behind idealised stems of different average spacing taken from Takemura and Tanaka (2007).*

The field observations of Naden *et al.* (2006) illustrate the significant contribution of stem-scale structures to the overall TKE, with high turbulence intensities in the lower third of velocity profiles associated with stem-scale, wake generated turbulence. In laboratory experiments, wake induced stem-scale turbulence production has been shown to be comparable, or greater than, the turbulence produced by bed shear alone (Nepf *et al.*, 1997; López and García, 1998). Stem-scale wake turbulence is therefore an influential element, with implications for sediment transport, elevating the vertical diffusivity to maintain sediment suspension (López and García, 1998). Increases in turbulence intensity due to stem-scale turbulence can also augment nutrient uptake and gas exchange (Anderson and Charters, 1982).

At the plant-scale, the volumetric canopy morphology of the plant exerts a major control on the wake response. Plant volumetric canopy morphology was previously defined in Section 1.2, as the distribution of vegetal elements over the three-dimensional structure of the plant, quantified as the solid volume fraction occupied by the plant in a control volume. For low porosity plants that act as a solid impermeable bluff body, idealised flow patterns are expected to resemble wake flow with classic vortex regimes at sufficiently high Reynolds numbers (Figure 2.17). This is exemplified and idealised by

flow around a solid cylinder, whereby on the upstream end the downwards deflection and rotation of the incident flow initiates development of large scale turbulent structures in a horseshoe vortex system (Baker, 1980). Flow separation has occurred under the adverse pressure gradient, with the separated shear layer rolled up to form a spiral vortex stretching around the base of the cylinder, trailing off downstream. The horseshoe vortex system has been shown to heighten local scouring processes (Breusers *et al.*, 1977). On the leeward side of the cylinder, flow recirculation and velocity reduction occurs in the wake zone, with alternating roller-type vortices shed from the separation points, forming von Karman vortex streets. Three-dimensional turbulent structures on the scale of the shear layer vortices are expected to develop in this region (Wei and Smith, 1986; Williamson *et al.*, 1995) as well as further flow three-dimensionality on the scale of the von Karman vortices (Williamson, 1996).
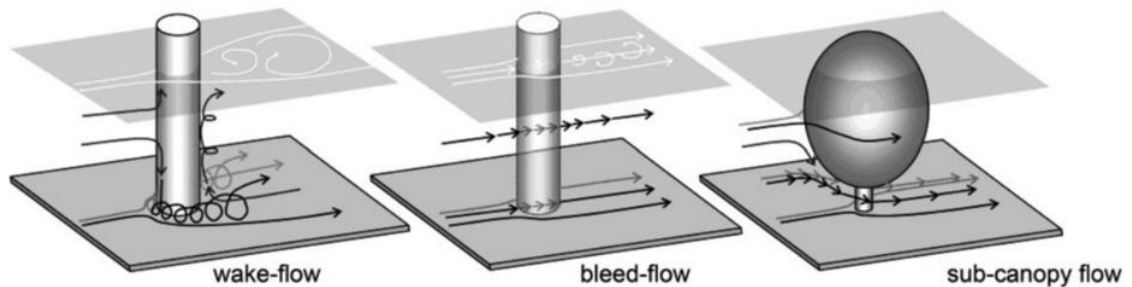


*Figure 2.17 Schematisation of the three main types of flow around a single plant, from Schnauder and Moggridge (2009).*

Plants with higher porosities act as permeable bluff bodies, and no longer behave as a traditional blockages to flow (Schnauder *et al.*, 2007), instead tending towards porous media flows (Yagci *et al.*, 2010), with penetration of fluid through the canopy resembling 'bleed-flow' (Raine and Stevenson, 1977). This has important implications for the plant-scale wake structures. As porosity increases, the bleed-flow zone extends downstream due to the downstream advection of low-velocity fluid through the canopy (Raine and Stevenson, 1977; Schnauder *et al.*, 2007). This can reduce velocity gradients, deflections of flow paths, turbulence levels, and the size of coherent flow structures (Schnauder and Moggridge, 2009).

Chang and Constantinescu (2015) define two distinct flow regimes based on porosity. At low porosities, wake billows with alternate directions of rotation are shed in the wake of a porous cylinder, resembling the von Karman vortex streets of a solid cylinder. For higher porosities, however, no equivalent von Karman vortex streets are present, with

weaker billows located further downstream from the back of the porous cylinder due to the extension of the bleed-flow zone.

The plant volumetric canopy morphology further complicates flow patterns and wake generated turbulence at the plant-scale. Variations in the size, shape, and density of plant elements have a vertical and horizontal dependence, which contribute towards the overall plant shape (Wilson *et al.*, 2005). Differences in volume between the foliated body of a plant, and the main branching region beneath, can generate a strong sub-canopy jet (Yagci and Kabdasli, 2008), which can induce significant bed scouring (Yagci *et al.*, 2016). Plant structure and form, in particular the volumetric canopy morphology, can therefore control flow through, over, and around vegetation layers (Tempest *et al.*, 2015). Similar observations have been made in air flow around a fir tree windbreak and have revealed large scale recirculation caused by an upwelling vortex immediately behind the trees, sustained by this sub-canopy acceleration (Lee and Lee, 2012), while in open channel applications, Freeman *et al.* (2000) reported flow diversion and acceleration beneath the plant canopy. A phenomenon Bölscher *et al.* (2005) quantified in the field with velocity profiles. Yagci *et al.* (2010) showed this sub-canopy jet to extend beyond the immediate vicinity of the plant, shifting the position of the wake, and leading to extended momentum exchange. In each case, these accelerations increase near bed shear stress (Gross, 1987), and therefore have implications for the morphodynamics of the river bed.

At the patch-scale, the collection of individual plants that make up the patch can be likened to the distribution of individual roughness elements, whereby each element's wake has the potential to interact with neighbouring and downstream elements, as conceptualised by Morris (1955). Three flow regimes were identified: (i) skimming flow, when elements were so tightly packed that wakes cannot form between gaps, with flow instead partitioned to skim as overflow above the roughness element, (ii) wake interference flow, when wakes for individual elements interact significantly with neighbouring and downstream elements, and (iii) isolated roughness flow, when there is no interaction between wakes and roughness elements. Applying this conceptualisation to stands of flexible vegetation, Folkard (2011) defines a further flow regime, through-flow, for when no separation exists but the flow entering gaps between downstream patches comes through the upstream patch. As such, this resembles the bleed-flow through individual permeable plants. In this flow regime, because flow through the

canopy is sufficiently strong, and the overflow is sufficiently weak, no recirculation forms in the gap between patches (Folkard, 2016).

### 2.3.3.4 Importance of turbulent regimes in flows through vegetation for sediment and biota

The turbulent regimes about vegetal elements have important implications for sediment and biota. The distribution of vegetation elements influences flow and sediment transport pathways (McBride *et al.*, 2007). Furthermore, the wakes about vegetal elements determine the 'hydro-climate' of downstream regions (Folkard, 2016). In-channel vegetation are used by freshwater fish for shelter and refuge, as a food source (either directly or indirectly), and as spawning, nesting, and nursey sites (Petr, 2000). Several indigenous European fish species inhabit macrophytes as adults, including eels (*Anguilla anguilla)*, pike (*Esox lucius*), rudd (*Scardinius erythrophthalmus*), and tench (*Tinca tinca*), which provide feeding habitats (Petr, 2000). The structure and form of the vegetation is important, as invertebrate biomass is greater around macrophytes with more structural complexity (Hargeby *et al.*, 1994), as these plants offer more efficient shelter against predation from fish (Diehl and Kornijów, 1998).

## 2.3.4 Biomechanical and morphological controls influencing flow through vegetation

The ability of a hydrodynamically loaded plant to reconfigure and minimise drag is crucial, because the forces acting on a flexible bluff body are significantly different from those acting on a rigid bluff body (Chapman *et al.*, 2015). Biomechanical and morphological factors control the response of vegetation under hydrodynamic loading, and therefore are responsible for the controlling the drag response and vegetative resistance. Crucially, the biomechanical and morphological factors influence how vegetation can change its geometry under flow. In this section, the key biomechanical factors and mechanisms (stiffness and flexural rigidity, buoyancy, and the ability to reconfigure) and morphological factors are discussed, with specific focus on the effects for drag and vegetative resistance at the plant-scale.

### 2.3.4.1 Biomechanical factors

Plant biomechanical factors exert a first order control on the response under hydrodynamic loading. However, it is common for these factors to vary spatially over the plant body.

### 2.3.4.1.1  Stiffness and flexural rigidity

A key biomechanical factor in determining the plant response under hydrodynamic loading is the flexural rigidity.  Flexural rigidity, sometimes referred to as the flexural stiffness, measures the ability of an object to resist bending.  The material moduli of the object dictates the stress and strain relation for any level of stress, therefore the magnitude of bending is dependent on both material modulus and shape (Niklas, 1992).  Flexural rigidity counteracts the drag force acting on the plant, and is especially important as aquatic plants can experience drag forces up to 25 times greater than terrestrial plants for the same velocity (Denny and Gaylord, 2002).  Flexural rigidity, $J$ (N $m^2$), is the product of the elastic modulus, $E$ (N $m^{-2}$), and the second moment of area, $I$ ($m^4$), as shown below:

$$J = EI \tag{2.9}$$

$E$ depends on the stem anatomy, including cell wall properties, whereas $I$ is morphologically controlled, relating to stem size (Niklas, 1992).  Stone *et al.* (2013) report the value of $E$ to vary for several floodplain and riparian type plants, with *Tamarix spp.* having significantly lower $E$ values than *Populus spp.* and *Salix spp.*  Marked variation of $E$ between and within plant species is shown.

With the pronounced variation in plant biomechanical properties, values of flexural rigidity vary by seven orders of magnitude for the species shown in Table 2.1.  However, this range comprises a wide range of plant types, ranging from kelp species to floodplain species.  Given the range of flexural rigidities, Nikora (2010) classifies two extreme plant types: 'tensile' plants, which are associated with very low flexural rigidities and therefore passively follow the flow, and 'bending' plants, which have comparatively higher flexural rigidities, are more upright in the water column, and are more able to resist flow.  For tensile plants, including many macrophytes, flow resistance is mainly generated by skin friction drag (Miler *et al.*, 2012).  For bending plants, including many floodplain and riparian plant species, form drag dominates over the skin friction drag component (Nikora, 2010; Västilä and Järvelä, 2014) and can account for 90-97% of the total drag in turbulent flows (Lilly, 1967; Vogel, 1994; Stoesser *et al.*, 2010).

For tensile plants with low flexural rigidities (Table 2.1), the proclivity for deformation can introduce dynamic behaviours into the flow, including regular and chaotic flapping

(Connell and Yue, 2007) as well as high inertial forces (Denny *et al.*, 1998). Tensile plant types have flexural rigidities that can be measured more readily, and have been the focus of much research (e.g. Patterson *et al.*, 2001; Davies *et al.*, 2007).

Flexural rigidities for bending plant types are less well documented. For composite objects such as branches or stems, which consist of materials with different elastic moduli, the flexural rigidity can be evaluated as the sum of individual structural elements, stem tissues, or cell types (Niklas and Spatz, 2012). In natural vegetation, a non-constant thickness along the stem/branch, in addition to the variable age of material, adds further complexity (Whittaker *et al.*, 2013). Furthermore, different parts of the plant have different flexural rigidities, and bending may be concentrated at specific points (Green, 2005b). Moreover, when stems are exposed to loading from unidirectional flows, the stem can become preferentially stiffer in one direction (Paul *et al.*, 2014). For full-scale trees, these variations and complexities are even more pronounced (Chen and Chen, 2016). For bending type plants in general, however, Albayrak *et al.* (2012) demonstrate that stems with the lowest flexural rigidities experience the least drag force per length, while those with the highest flexural rigidities experience the highest drag force per length.

### 2.3.4.1.2    Buoyancy

A key distinction between terrestrial and aquatic vegetation is made where aquatic plants contain elements that can be positively buoyant (Luhar and Nepf, 2011). This has direct implications for the plant posture, and like flexural rigidity, provides resistance against hydrodynamic drag (Paul *et al.*, 2014). Generally, it is the tensile plants that are found to have greater buoyancy (Mendez and Losada, 2004). However, Luhar and Nepf (2011) show buoyancy effects to be dependent on velocity, as well as the spatial distribution of buoyant vegetal elements along the plant.

With increases in velocity, the plant response in restoring plant posture is shown to transition from buoyancy-dominated to stiffness-dominated, where the drag force exceeds the plant buoyancy. Additional complexity is introduced where the buoyant elements are concentrated near the ends of stems, and therefore not evenly distributed along the plant. The control of buoyancy is further complicated by temporal variability, with variations in buoyancy over diurnal and seasonal cycles (Haslam, 1978; Powell, 1978). The extent to which buoyancy controls plant posture varies as a function of species. For tensile species such as *Zostera marina* (eelgrass), the laboratory experiments

of Abdelrhman (2007) show that buoyancy is the most important factor in restoring deflected blades to a vertical posture. For bending plants, the structural rigidity and spatial density of the plant become more important factors in restoring plant posture under hydrodynamic loading (Dijkstra, 2012).

### 2.3.4.1.3    Plant reconfiguration and the Vogel exponent

In response to hydrodynamic loading, up to six modes of plant motion are relevant to morphologically complex plants with branches, stems, and leaves (Gourlay, 1970; Pitlo and Dawson, 1990; Green, 2005c). These are similar to the modes used to describe morphologically simple plants (bracketed terms, Nepf and Vivoni, 2000).

1) At the lowest flow velocities, the plant is barely deflected and remains stationary (*erect*).

2) Stems and leaves become orientated in the downstream flow direction (*gently swaying*).

3) Vibration of stiffest branches, with bending and strong coherent swaying of stems (*monami*).

4) Stiffest branches and stems become inclined, submerged leaves become more strongly orientated, dead parts of the plant removed.

5) The entire plant becomes highly prone, with a marked shift in plant posture (*prone*).

6) Damage and loss of plant parts, risk of uprooting.

Total drag can be minimised through two interacting mechanisms: (i) a reduction in the effective plant surface area, and/or (ii) shape reconfiguration that makes the plant streamlined to minimise the drag coefficient (Usherwood *et al.*, 1997; Nikora, 2010). Combined, the mechanisms allow the skin friction and pressure drag to be minimised. Termed reconfiguration, this effectively reduces the stress induced by an external flow (Harder *et al.*, 2004).

Static reconfiguration refers to the streamlining and reduction of effective plant surface area in response to imposed variations of flow velocity, attained through the folding of leaves or streamlining of the plant body (Sand-Jensen, 2003; O'Hare *et al.*, 2007; Albayrak *et al.*, 2012). This results in a shift in the time-averaged plant posture. The hydrodynamic response of leaves under flow are shown to vary as a function of leaf shape, serration, roughness, and flexural rigidity (Albayrak *et al.*, 2012). Plant body

streamlining reaches a critical maximum point where the rate of change in the frontal area with increasing velocity is zero (Freeman *et al.*, 2000). This form of reconfiguration can reduce the blockage effect of vegetation in natural streams, resulting in a pressure drag reduction (Cooper *et al.*, 2007).

In addition to this, dynamic reconfiguration refers to non-linear interactions that produce flutter or dynamic movement, even under a fixed velocity (Usherwood *et al.*, 1997; Nikora, 2010), and this relates to the time-dynamic plant motion. Siniscalchi and Nikora (2013) show that the trailing end of aquatic plants experience greatest motion under flow; with instantaneous motions closely related to the passage of large scale eddies that interact with the entire plant (Siniscalchi and Nikora, 2012). Coherent plant motions have been shown to be coupled to strong oscillations in flow velocity, associated with the monami phenomenon (Ghisalberti and Nepf, 2006; Okamoto and Nezu, 2009; Okamoto *et al.*, 2016). This time-dynamic plant motion can help absorb momentum from the flow, thereby regulating turbulence (Okamoto and Nezu, 2009).

Siniscalchi and Nikora (2013) view total reconfiguration as the sum of the static reconfiguration and the dynamic reconfiguration components, introduced by local flow-vegetation interactions across multiple spatial scales, ranging from flow separation about individual stems, to macroscale turbulent flow structures associated with individual patch-scales (Siniscalchi and Nikora, 2013). For both components of reconfiguration, plant morphology and the biomechanical properties will influence plant motion dynamics (Hurd, 2000).

Reconfiguration of flexible bodies has important implications for the drag response. Drag on a rigid bluff body scales proportionally with velocity squared, resulting in a quadratic relationship:

$$F_D \propto U^2 \tag{2.10}$$

For non-rigid objects, however, the dependence of drag on velocity is modified. Relevant to vegetation, by reconfiguring their flexible structural elements under hydrodynamic loading, frontal areas are reduced, and the body becomes more streamlined (Vogel, 1994). As a result, the drag load is no longer proportional to the square of velocity, and instead it scales more gradually. This drag reduction is quantified through the Vogel exponent, $\psi$, as an addend in the power function (Vogel, 1984), such that:

$$F_D \propto U^{2+\psi} \tag{2.11}$$

$\psi$ therefore modifies the power to which velocity is raised. The more negative the value of $\psi$, the smaller the increase in drag for an increasing velocity. This is exemplified through the leaf of a tulip tree by Vogel (1989), which rolls up into a conical shape under increasing wind speed as a function of streamlining, where $\psi$ = -1 and so returns a linear force-velocity relation; by contrast if the leaf were rigid ($\psi$ = 0), it would follow the classical squared relation (Cullen, 2005; Whittaker *et al.*, 2013).

Measurements of reconfiguration and the scaling of drag with velocity exist for both terrestrial and aquatic plant species (or by using similar prototypes/analogues) in wind tunnels and water flumes, at scales ranging from individual leaves to entire trees (Table 2.2). Individual and small clusters of leaves tend to give $\psi$ only slightly above those calculated for multi-leafed branches or entire trees (Vogel, 2009). The generally accepted range of $\psi$ for flexible plants is -0.2 to -1.2 (Harder *et al.*, 2004; Vollsinger *et al.*, 2005; de Langre *et al.*, 2012), although from Table 2.2 it is evident that $\psi$ ranges with plant species. The positive values of $\psi$ reported in Ferreira *et al.* (2015) are attributed to the relatively small range of velocities over which reconfiguration was investigated.

Focusing on water flume studies that involve entire trees, $\psi$ is commonly related to flexural rigidity. Oplatka (1998) show that $\psi$ = 0 for entirely stiff trees, $\psi$ = -0.36 when partially stiffened, and $\psi$ = -1 when fully flexible. However, Whittaker *et al.* (2013) report a more complex relationship for their towing-tank experiment results. For specimens of *Alnus spp.*, for which the flexural rigidity was lowest, $\psi$ averaged -0.73 when foliated, and $\psi$ = -0.57 when defoliated. This contrasts with specimens of *Populus spp.* which had a higher flexural rigidity, $\psi$ averaged -0.83 when foliated, and $\psi$ = -0.78 when defoliated. The more negative values of $\psi$ associated with *Populus spp.* indicate a smaller increase in drag with increasing velocity; appearing contradictory given that biomechanical analysis showed this species to be least flexible. The discrepancy is attributed to the role of branch morphology, different modes of reconfiguration, and the non-linear distribution of the flexural rigidity over the entire tree (Whittaker *et al.*, 2013). Both the ability of the plant to reconfigure, and the plant morphology, therefore controls the drag response under hydrodynamic loading.

*Table 2.1 Mean flexural rigidity values for a range of tensile and bending plants, ranging over seven orders of magnitude.*

| Plant type | Species | Flexural rigidity ($N\ m^2$) | Comments | Reference |
|---|---|---|---|---|
| Tensile | *Egeria densa* | $3.2 \times 10^{-6} - 3.2 \times 10^{-6}$ | Submerged macrophyte common throughout lowland rivers (Champion and Tanner, 2000) | Schoelynck *et al.* (2015) |
| Tensile | *Macrocystis pyrifera* | $2.0 \times 10^{-5} - 7.1 \times 10^{-5}$ | Submerged kelp with blade-like morphology (Hurd and Pilditch, 2011). | Hurd and Pilditch (2011) Rominger and Nepf (2014) |
| Tensile | *Myriophyllum alterniflorum* | $2.2 \times 10^{-2}$ | Macrophyte distributed across lakes, ponds and rivers (Preston and Croft, 2001). | Miler *et al.* (2012) |
| Tensile | *Ranunculus Penicillatus* | $2.5 \times 10^{-2}$ | Most common submerged macrophyte in UK rivers (O'Hare *et al.*, 2010). | Miler *et al.* (2012) |
| Bending | *Glyceria fluitans* | $6.7 \times 10^{-1}$ | Marginal plant in rivers and lakes (Preston and Croft, 2001). | Miler *et al.* (2012) |
| Bending | *Salix spp.* | $3.2 \times 10^{1}$ | Bush-like morphology with slender stems, distributed on floodplain/riparian zone. | Stone et al. (2013) |
| Bending | *Populus spp.* | $4.7 \times 10^{1}$ | Clear trunk, spreading limbs, broad crown, distributed on floodplain/riparian zone. | Stone et al. (2013) |
| Bending | *Tamarix spp.* | $5.7 \times 10^{1}$ | Bush-like morphology with slender stems, distributed on floodplain/riparian zone. | Stone et al. (2013) |

*Table 2.2 Vogel exponent, ψ, for a range of real and prototype plants.*

| Real or prototype | Species | Vogel exponent | Comments | Reference |
|---|---|---|---|---|
| Prototype | *N/A* | -0.66 | Flexible fibres immersed in a flowing soap film in the velocity range $0.5 - 3.0\ m\ s^{-1}$. | Alben *et al.* (2002) |
| Prototype | *Poplar spp.* | - 0.68 to -1.02 | Section of artificial plants in a range of spatial configurations, submerged in a water flume, with velocities of up to $0.92\ m\ s^{-1}$. | Jalonen *et al.* (2012) |
| Real and Prototype | *(i) Poplar spp.* *(ii) Salix spp.* | -0.63 to -0.66 -0.85 to -1.09 | Section of artificial and real plants submerged in a water flume, with velocities of up to $0.92\ m\ s^{-1}$. | Schoneboom *et al.* (2010) Aberle and Dittrich (2012) |
| Real | *Salix spp.* | 0 to -1 | Full-scale trees (1.8 – 4.5 m) submerged at flow velocities in the range $1.0 - 4.0\ m\ s^{-1}$. | Oplatka (1998) |
| Real | *Arundo dona* | (i) -0.12 (ii) -0.71 | Giant reed grass, subjected to wind velocities: (i) up to $1\ m\ s^{-1}$ and (ii) and $> 1.5\ m\ s^{-1}$. | Harder *et al.* (2004) |
| Real | *Durvillaea willana* | -0.52 | Intertidal seaweed, submerged in flume and exposed to velocities in the range $0.5 - 2.8\ m\ s^{-1}$. | Harder *et al.* (2004) |
| Real | *Poplar spp.* | -1.03 | Real plant submerged in a water flume, with velocities of up to $0.92\ m\ s^{-1}$. | Västilä *et al.* (2013) |
| Real | (i) *Alnus spp.* (ii) *Poplar spp.* | (i) -0.57 to -0.73 (ii) -0.78 to -0.83 | Full-scale trees submerged in a water towing tank at flow velocities in the range 0.125 – $6\ m\ s^{-1}$, for both defoliated and foliated states. | Whittaker *et al.* (2013) |
| Real | (i) Buxus spp. (ii) Euonymus spp. | (i) 0.83 to 0.85 (ii) 0.15 to 0.37 | Woody shrubs submerged in a water flume at flow velocities up to $0.45\ m\ s^{-1}$, defoliated and foliated. | Ferreira *et al.* (2015) |

### 2.3.4.2 Morphological factors

Morphological factors such as the plant structure and form are influential in determining the resistance of individual plants or vegetation patches, where Neumeier (2007) show that the roughness length of vegetation is not statistically related to the flow depth or velocity, but instead varies as a result of plant form. Aquatic canopies exhibit a wide range of morphologies and densities (Valiela *et al.*, 1978; Leonard and Luther, 1995; Lightbody and Nepf, 2006), with stiffer plants tending to have rounded stems, and submerged grasses tending to have a more blade-like geometry (Nepf, 2012a). Furthermore, variations in the size, shape, and density of plant elements can have a vertical dependence, which contribute towards the overall plant shape (Wilson *et al.*, 2005). This distribution was shown for crown-building species in Figure 2.7; and is especially relevant for floodplain and riparian plant types. In natural settings, therefore, a considerable range of plant morphologies exist.

When comparing simple flexible rods to simple flexible rods with fronds, Wilson *et al.* (2003) report a 50% greater velocity reduction when fronds are present. This difference is attributed to the additional momentum absorbing area of the fronds, reducing mean velocities, and extending the influence over the entire flow-depth boundary layer. Experiments such as these demonstrate the significant role that frond or leaf elements can impart on the flow. Differences are therefore expected in flow field dynamics with changes in the level of foliage. When branches and leaves add to the total surface area, a greater obstacle to flow is created than the plant stem alone (Leonard and Luther, 1995). Flow is forced around each branch or leaf so that the velocity field is spatially heterogeneous at the scale of these elements (Section 2.3.3.3). Vegetation structure, in particular the vertical and horizontal distribution of biomass, will therefore control flow through, over, and around vegetation (Tempest *et al.*, 2015). In aquatic canopies with a significant foliage component, this can inhibit momentum exchange between the canopy and the free-stream zone above, resulting in differences in the shear layer characteristics and turbulent processes (Marjoribanks *et al.*, 2017). Morphological factors can therefore influence the mean three-dimensional and turbulent flow.

## 2.4 Current derivation of flow through vegetation

Much of the theoretical understanding of flow through vegetation, and vegetative resistance, is based on results from laboratory experiments and/or numerical modelling studies, with relatively few field-based studies forming the basis of this understanding. The representation of vegetation in laboratory and numerical modelling studies should therefore be critically assessed.

### 2.4.1 Methods for representing vegetation in laboratory experiments

Laboratory experiments have been extensively used to provide a process-based understanding of flow through vegetation, and especially the drag processes that contribute towards the development of mixing layers (Nepf, 2012b). The representation of the vegetation in these laboratory experiments is crucial, with vegetation generally represented by: (i) artificial plants and surrogates, (ii) scaled plants, and (iii) natural plants (Frostick *et al.*, 2011).

At the simplest level, discrete, rigid cylindrical elements arranged in varying spatial configurations have been used to represent specific attributes such as stem density in stiff, emergent plants (Nepf, 1999). In the most basic form, wooden dowel rods are used to represent floodplain vegetation (e.g. McBride *et al.*, 2007), to assess near bank turbulence (Figure 2.18). Conversely, polyethylene strips have been used to represent the flexibility and reconfiguration observed in shallowly submerged species, such as *Posidonia oceanica* (Folkard, 2005; Folkard, 2011). To replicate realistic structural distributions of natural plants, artificial surrogates with an explicit parameterisation of the structural components have more been recently used (Schoneboom *et al.*, 2010). Often, however, artificial representations of vegetation neglect the variation in plant structure and biomechanics that are observed in the natural prototype habitat, which can lead to the incorrect predictions of flow at the plant- and canopy-scales. Questions therefore remain as to whether these simplified artificial plants or surrogates can adequately represent complex flow-vegetation interactions.

*Figure 2.18 Example of dowel rods used to represent floodplain vegetation from McBride et al. (2007).*

Where natural vegetation has been used (e.g. Järvelä, 2002b; Sand-Jensen, 2003) samples can rapidly deteriorate under laboratory conditions, meaning that biomechanical factors may vary over the duration of the experiment, and may not capture the variety of characteristics observed in nature (Frostick *et al.*, 2011). A further difficulty when using real vegetation is providing a full description of flow both through and around the plant/canopy, with velocity measurements commonly recorded along only a single plane, usually at the flume midline (Yagci *et al.*, 2010). Misrepresentation of vegetation morphology, whether artificial or real would be translated into the flow field, and this will compromise the representativeness of results. Alterations to the velocity and pressure fields have primary implications for the calculation of vegetative flow resistance.

## 2.4.2 Methods for representing vegetation in numerical models

Most numerical modelling has been implemented using Computational Fluid Dynamics (CFD) simulations, solving flow using the Navier-Stokes equations (see Chapter 4). In high dimensional numerical modelling studies, vegetation has been represented by adding a drag-related bulk source and sink term into the continuity equation (Fischer-Antze *et al.*, 2001; López and García, 2001), thereby treating vegetation as a sub-grid scale effect. The drag force term is based on plant density and an assumed rigid, cylindrical representation for vegetation, with a drag coefficient value of unity, applicable to rigid cylinders with Reynolds numbers between $1 \times 10^3$ to $3 \times 10^5$ (Panton,

1984; Cheng, 2013). These models reproduce mean and turbulent flow, although they do not effectively predict the quantitative detail of turbulence, namely shear and wake scales (Defina and Bixio, 2005).

To represent stem-scale processes at a greater spatial resolution, Stoesser *et al.* (2009) included an array of individually represented rigid cylinders using Large Eddy Simulation (LES), and by using a fine grid ensured that drag was directly accounted for, removing the need for empirical drag coefficients. Numerical results were validated with experimental measurements, replicating the classical vortex structures expected for the flow regime. This has been extended to predict the influence of vegetation density on the instantaneous and turbulent flow field, with increases in vegetation density altering the wake turbulence patterns (Figure 2.19). The most promising approaches therefore model plant patches or canopies as porous blockages (Marjoribanks *et al.*, 2014a). The porosity comes from the fact that within a controlled volume, flow can pass through the individual plant elements. Such experiments have been extended to represent circular patches of vegetation, with the porosity of the patch modified using different configurations of rigid cylinders, thereby achieving different solid volume fractions (Chang and Constantinescu, 2015).
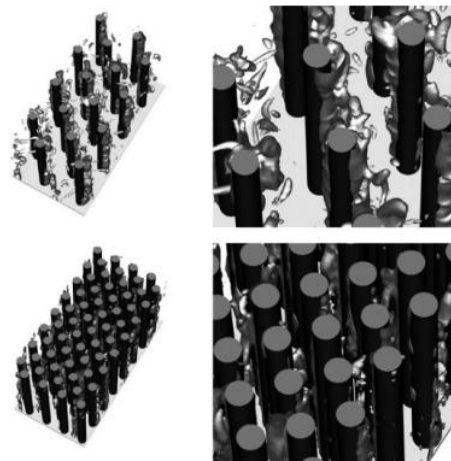


*Figure 2.19 High dimensional numerical modelling of instantaneous and turbulent flow around varying vegetation densities, representing plant stems as rigid cylinders in an LES framework from Stoesser et al. (2010).*

Several studies have sought to incorporate flexible vegetation canopies. Ikeda and Kanazawa (1996) developed a biomechanical plant model based upon the dynamic Euler–Bernoulli cantilever beam equation within a two-dimensional LES framework. Marjoribanks *et al.* (2014c) developed a similar model within a three-dimensional LES framework to look at arrays of semi-rigid stems within flows. This combined

biomechanical-LES model enabled the simultaneous prediction of flow-vegetation interactions at high spatial and temporal scales, and again has been validated with experimental results (Marjoribanks *et al.*, 2015). Similar approaches have been developed for highly flexible vegetation types by applying the N-pendula equation (Abdelrhman, 2007; Dijkstra and Uittenbogaard, 2010).

In all the above numerical modelling studies, stems/plants are represented as homogeneous and uniformly distributed elements within the modelling domain. However, natural plants are highly three-dimensional, discontinuous, and heterogeneous over varying spatial scales, meaning that the physical description of vegetation in many models must be questioned. Currently, therefore most numerical modelling studies fail to adequately represent the morphological complexity inherent to natural vegetation, and this could lead to the incorrect prediction of flow.

At the plant-scale, Endalew *et al.* (2006) were the first to attempt to model wind flows around a more realistic plant. Using a plant-growth simulation model to generate branch architecture, prediction of the three-dimensional airflow through and around discrete branches was achieved in a CFD model (Figure 2.20). Endalew *et al.* (2009) and Endalew *et al.* (2011) then modelled air flow around realistic plant reconstructions (see Section 3.2.2.2.3), for the purpose of improving the design of air-assisted orchard sprayers relevant to pesticide spraying. By incorporating a realistic three-dimensional branch architecture model into a CFD model, and applying a sub-porous domain around the branches to represent the foliage, wake velocities and flow pathways through the branches were visualised. However, adequate validation of the numerical predictions was not provided. A comparable approach has not yet been applied to model flow through and around vegetation in open channel applications.
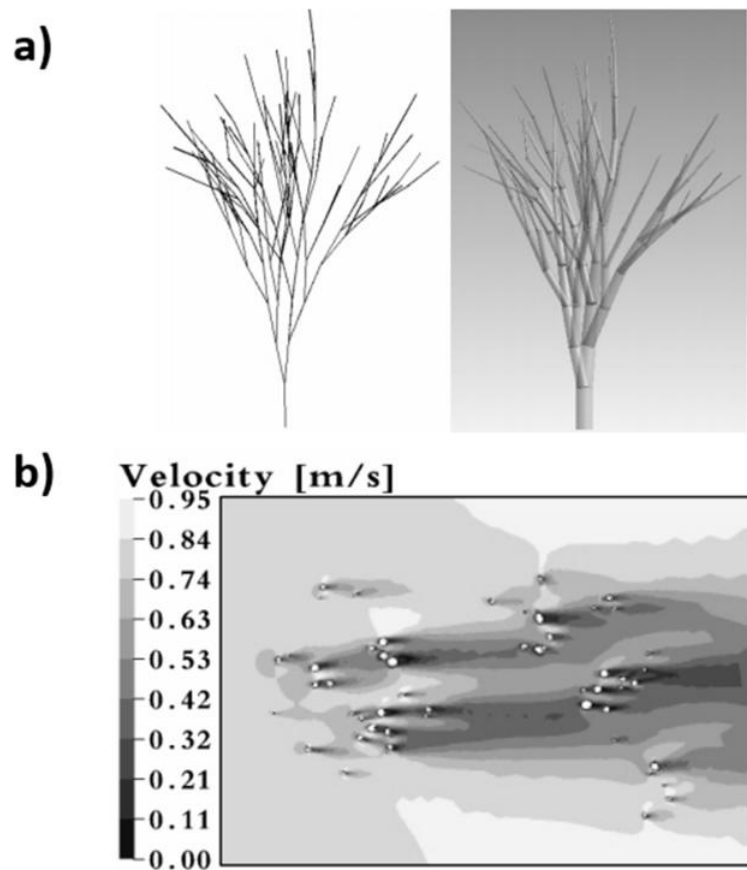
*Figure 2.20 (a) Discrete branches incorporated into a CFD scheme and (b) the predicted three-dimensional airflow expressed as a velocity contour on a horizontal plane at 1.75 m from Endalew et al. (2006).*

To begin to account for heterogeneity at the patch-scale, Marjoribanks *et al.* (2016) modelled flow around realistically distributed, static patches of submerged *Ranunculus penicillatus* in a vegetated channel (Figure 2.21). Vegetation patches were represented in the model as a mass blockage to flow, which accounted for the solid volume fraction measured in the field. The model successfully reproduced the complex spatial flow heterogeneity observed in the field, although the grid resolutions of 0.2, 0.1, and 0.05 m do not allow for the finest flow structures to be resolved. Furthermore, the drag coefficient was assigned a value of unity, with the estimation of more accurate plant drag coefficients needed (Fischer-Antze *et al.*, 2001; Kim and Stoesser, 2011; Marjoribanks *et al.*, 2016). This is because the drag coefficient deviates significantly for more complex vegetation as it is a function of both vegetation density and stem Reynolds number (Tanino and Nepf, 2008). For instance, in sparsely configured leafy shrub communities, laboratory experiments of Hui *et al.* (2010) report drag coefficients of up to four.
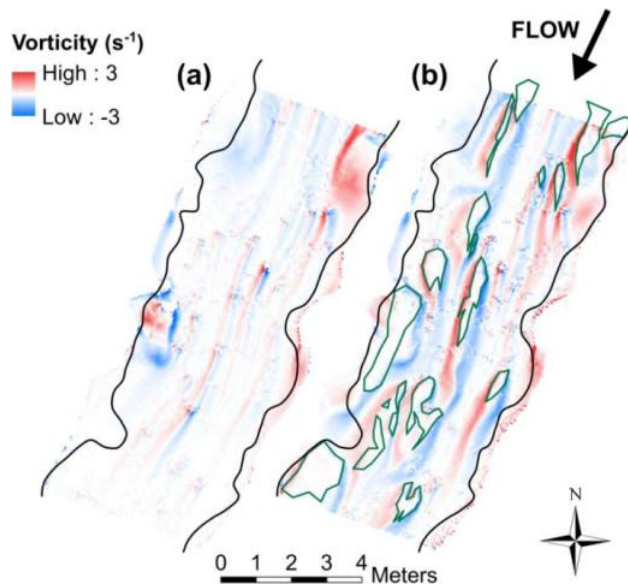
***Figure 2.21 Vorticity plots for (a) unvegetated and (b) vegetated channel scenarios, where green areas indicate patch locations, and black lines denote the measured extent of the river edge (measurements beyond this zone were not possible due to the presence of vegetation on the river bank, although predictions of vorticity were made). From Marjoribanks et al. (2016).***

## 2.4.3 Understanding of flow-vegetation interactions from field studies

Field studies add further to the understanding of flow through vegetation and vegetative resistance. This includes measurement of three-dimensional velocity fields around large woody debris (Daniels and Rhoads, 2003), and isolated patches of submerged macrophytes (Schoelynck *et al.*, 2013). Furthermore, the turbulence structure has been investigated around heterogeneous patches of submerged macrophytes (Sukhodolov and Sukhodolova, 2010a), and tree-centred emergent bars (Sukhodolov and Sukhodolova, 2014). Although these studies provide detail of the flow field, an adequate quantification of the biomechanics and morphology of the vegetation prove difficult in the field environment.

However efforts have been made to understand the spatial distribution of in-channel vegetation in field settings, highly relevant to the quantification of vegetative resistance. Green (2005a) quantifies the proportion of river cross sections occupied by macrophytes, termed the blockage factor, and Green (2006) suggests the relation between the blockage factor and vegetative resistance is non-linear. More recently, the spatial structure and depth-estimates of submerged aquatic vegetation has been made possible by considering the spectral signatures of optical data (Visser *et al.*, 2015), and infrared photography (Thomas *et al.*, 2016).

## 2.5    Identification of knowledge gaps

Flow through and around canopies of biomechanically and morphologically simple, single stemmed (or analogue) plants have been extensively studied in both field and flume settings (Finnigan, 2000; Sukhodolov and Sukhodolova, 2010a; Nepf, 2012a). Therefore, the three-dimensional mean and turbulent flow, plant motion, and to a lesser extent drag are all quite well understood (Ackerman and Okubo, 1993; Ghisalberti and Nepf, 2002; Ortiz *et al.*, 2013), and can be predicted using validated numerical models (Tanino and Nepf, 2008; Stoesser *et al.*, 2010; Kim and Stoesser, 2011; Marjoribanks *et al.*, 2015). For such canopies, vegetation representation using geometrically simple morphologies is justified.

For isolated plant stands that are biomechanically and morphologically complex, however, comparably little is known. The understanding of flow through and around individual plants is challenging given the multitude of stem- and leaf-scales involved with vegetal elements (de Langre, 2008; Albayrak *et al.*, 2012; Luhar and Nepf, 2013), the variation in plant morphology (Wilson *et al.*, 2003), and the reconfiguration to minimise drag during hydrodynamic loading (Vogel, 1994). This dynamic plant volumetric canopy morphology adds significant complexity to understanding flow field dynamics, and presents challenges when quantifying vegetative flow resistance (Kouwen and Unny, 1973; Aberle and Järvelä, 2013).

To improve the process-understanding of flow-vegetation interactions at the plant-scale, several thesis objectives are highlighted:

i.   *To develop a method capable of capturing plant volumetric canopy morphology, and quantifying plant structure and form.* This chapter has demonstrated the heterogeneous vertical and horizontal distribution of biomass in natural plants, which is shown to influence the mean and turbulent regime in flows through vegetation. Aligned with RQ1, a methodology must be developed to capture and represent the full three-dimensionality of plant morphology and porosity. The method must be repeatable, and must accurately represent the plant morphology and porosity at a high spatial resolution, thereby representing spatial scales finer than the smallest vegetal elements of the plant. Given the important role of wake generation in bending type plants, it is crucial to explicitly represent the stem and leaf elements that contribute towards pressure drag, with a millimetre scale

spatial resolution representation therefore required. This representation will be used to quantify the plant structure and form, to better understand the three-dimensional spatial distribution of vegetal elements at the plant-scale.

ii.  *To incorporate the representation of plant volumetric canopy morphology into a high dimension numerical model, capable of accurately predicting three-dimensional mean and turbulent flow.* Following capture of the plant volumetric canopy morphology, the next step is to discretise this into a high dimension numerical model. Computational Fluid Dynamics (CFD) modelling offers the opportunity to simulate flow that is of practical importance, but notoriously difficult to measure (Hardy *et al.*, 2003). Discretisation methods that treat the plant as a porous blockage using numerical porosity are most suitable for this purpose (Marjoribanks *et al.*, 2014a), moving beyond the highly idealised and simplified plant representations that have previously been used. The plant volumetric canopy morphology will therefore act as boundary conditions in the model, enabling high resolution predictions of flow to be made.

iii. *Experimentally quantify plant motion dynamics under hydrodynamic loading for a range of depth-limited flows.* To minimise drag, a plant will reconfigure through time-averaged and time-dynamic plant motion (Siniscalchi and Nikora, 2012). Six modes of plant motion are outlined in this chapter, but whether the entire plant responds to flow in the same way, or whether specific sections of the plant behave differently, remains unclear. Quantification of time-averaged and time-dynamic postural changes (RQ3) are therefore necessary for an improved process-understanding flow-vegetation interactions at the plant-scale.

iv.  *Experimentally and numerically quantify the three-dimensional mean and turbulent flow around natural plants.* For solid, impermeable bluff bodies, flow is quite well understood and can be predicted, however, it is not clear whether this understanding can be applied and extended to natural plants. This is because plants have complex morphologies and porosities, and reconfigure under hydrodynamic loading. This will mean the flow regime is more complex (Schnauder and Moggridge, 2009). It is therefore essential to provide a validated quantification of the effects of plant posture, porosity, morphology, and 'how the plant looks to flow' (RQ2, RQ4, and RQ5), to improve the process-understanding.

v. *Extend the improved process-understanding of flow-vegetation interactions at the plant-scale to quantify vegetative flow resistance.* The high resolution process-understandings are used to quantify vegetative flow resistance. By using the modelled pressure fields, the influence of plant volumetric canopy morphology on vegetative resistance is assessed, through calculation of the physically determined drag response, the Vogel exponent, and Manning's *n* (RQ6 and RQ7). Given the importance of vegetation in river corridor management, the numerical scheme has potential application for understanding how natural vegetation partitions discharge between changes in velocity and depth, and how this impacts the conveyance. This will enable improvements to be made in the reach-scale management of river systems.

## 2.6      Chapter conclusions

This chapter has demonstrated the current understanding of flow through vegetation. Flow resistance in open channel flows, with a specific focus on vegetative resistance, has been described.  The effects and controls of vegetation on flow field dynamics were then discussed, reviewing the turbulent flow regimes associated with vegetation, and the biomechanical and morphological factors that influence flow-vegetation interactions under hydrodynamic loading.   The chapter has shown how plants are currently represented in laboratory and numerical models, and has identified knowledge gaps in the literature.  These have been used to inform a series of specific thesis objectives that enable the development of a numerical representation of floodplain and riparian plant response to river flow.

Corresponding with RQ1, the next chapter is concerned with development of a method capable of quantifying and resolving plant volumetric canopy morphology, that can be incorporated into the high dimension numerical model.  For this, a three-dimensional representation of the plant is required.

<div align="right">

# Chapter 3

</div>

# Using terrestrial laser scanning (TLS) to capture plant volumetric canopy morphology

## 3.1      Introduction

Chapters 1 and 2 have shown that the plant volumetric canopy morphology is an important factor influencing flow through vegetation. Often, however, this has been overlooked in numerical modelling and flume experiments, with vegetation represented by highly simplified structures or idealised surrogates. Such an approach lacks physical representativeness, as it is suggested the plant representation will have a significant influence on flow field dynamics. Corresponding with thesis objective (i), a method should be developed to capture floodplain and riparian plant morphology and porosity. This will be incorporated into a high resolution model used to predict river flow (Chapter 4), in support of RQ1. The plant representation must be able to accurately resolve the full three-dimensionality of the plant, and explicitly represent all vegetal elements, meaning that a millimetre scale spatial resolution is required. The focus of this chapter is therefore how better to capture, represent, and characterise plant volumetric canopy morphology.

First, the range of techniques available to do this will be reviewed (Section 3.2). Selecting the most appropriate technique against outlined criteria, the workflow to derive the plant representation is presented (Section 3.3). This is important to support RQ1 and thesis objectives (i) and (ii). The plant structure and form will then be quantified (Section 3.4), and the quality of the plant representation assessed (Section 3.5).

## 3.2 Capturing vegetation structure and form

Methodological developments are needed to address the Research Questions outlined in Chapter 1. To assess the range of techniques available to capture, represent, and characterise plant volumetric canopy morphology, it necessary to define a set of criteria that the measurement technique must meet. An appropriate technique must provide:

1. A repeatable methodology that can be applied to floodplain and riparian plant species with a range of morphologies, including crown-building species that have non-linear distribution of biomass over their vertical and horizontal extents (Section 2.3.1).

2. A fully three-dimensional representation of the plant at a millimetre scale spatial resolution; thereby resolving the finest vegetal elements, including leaf- and stem-scales that were shown to influence the turbulent flow regime in (Section 2.3.3),

3. The ability to penetrate inside the plant canopy, thereby resolving the internal plant morphology, to allow quantification of plant porosity.

4. A spatially explicit plant representation, from which areal and volumetric distributions can be derived, and quantify plant structure and form.

5. Data in a format that can be readily incorporated into the CFD model, in a regular Cartesian gridded structure.

6. A non-destructive approach, that allows laboratory flume experiments with the same plant specimens.

Direct physical measurements are unlikely to meet the criteria, so an alternative approach is needed. Remote sensing allows the collection of data by detecting the reflected energy from the surface of an object, from a distant platform with no direct physical contact. Remote sensing techniques have previously been applied to capture vegetation structure and form in several forestry, land management, geomorphology, and hydraulic applications (Hyyppä *et al.,* 2004; Straatsma *et al.,* 2008; Antonarakis *et al.,* 2010). Often, however, these have been concerned with the filtering and removal of vegetation, since it can introduce vegetation-induced elevation errors into digital elevation models (Pirotti *et al.,* 2013). In this application, the vegetation is the prime interest, and remote sensing will be used to capture, represent, and characterise plant volumetric canopy morphology.

An overview of applicable remote sensing techniques, and assessment according to the criteria, are shown in Section 3.2.1.

## 3.2.1 Overview of relevant remote sensing techniques

Light Detection And Ranging (LiDAR) is an active remote sensing technique, whereby a sensor records the back-scattered radiation signal from emitted laser pulses, having been reflected by an object. This signal is used to compute ranges, or distances, to objects from the sensor. LiDAR is an established method for collecting elevation data with high accuracy and density, and can therefore be used to generate precise and directly georeferenced point clouds containing spatial information about an object or surface. As such, LiDAR is the preferred tool for compiling remotely sensed three-dimensional measurements of vegetation (Vierling *et al.*, 2008). In LiDAR applications, the position of the sensor influences the density of point clouds, with airborne laser scanning (ALS) enabling metric to decimetric resolution, whereas with ground-based terrestrial laser scanning (TLS), centimetric to millimetric resolution is possible (Petrie and Toth, 2008). With sensor miniaturisation, TLS has been deployed to smaller, mobile platforms, through Mobile Laser Scanning (MLS) and Personal Laser Scanning (PLS).

In addition to LiDAR, advances in photogrammetric measurement techniques, another form of active remote sensing, are also relevant for capturing high resolution, spatially georeferenced point clouds. More specifically, recent developments in Structure from Motion (SfM) with Multi-View Stereo (MVS), the image-based surface restitution method that relies on automated image-to-image registration methods (Carrivick *et al.*, 2016; Smith *et al.*, 2016b), means that the technique has potential for characterising vegetation at a resolution comparable to TLS (Fonstad *et al.*, 2013).

In this section, a brief overview of each remote sensing technique (ALS, TLS, MLS, PLS, and SfM-MVS) is provided, with specific examples of the applications where point clouds have been used to capture vegetation form and structure. Finally, a summary for each remote sensing technique is provided in Table 3.1, with a critical appraisal against the criteria outlined in Section 3.2.

### 3.2.1.1 Airborne Laser Scanning (ALS)

Airborne laser scanning (ALS) is an active remote sensing technique that uses LiDAR. Typical ALS systems operate from fixed-wing planes or helicopters. The laser illuminates

the surface with an elliptical or circular footprint, and the size of the footprint affects the spatial resolution of the objects that can be detected. Because the emitted laser energy typically has a narrow beam divergence angle, the resulting footprints are usually small, in the range of 0.3 – 1 m with flying altitudes of about 1 000 m (Wehr, 2008). Measurement densities of up to 30 points per $m^2$ can be gained from helicopter platforms, although typically, measurement density is considerably lower than this (~1 point per $m^2$). The standard accuracy of the elevation data in the range 0.05 – 0.20 m (Beraldin *et al.*, 2010).

ALS has been revolutionary at the forest stand scale, in providing the rapid acquisition of tree characteristics for forest area-based inventories (Næsset, 2002; Hyyppä *et al.*, 2012). The data is usually ground referenced with manual field measurements using dendrometry techniques, or used in combination with additional remotely sensed data to train the ALS data (Liang *et al.*, 2016). The objectives of these studies include the mapping and characterisation of trees in forest stands (Hyyppä *et al.,* 2012), classification of urban trees (Rutzinger *et al.*, 2008), and the estimation of above- and below-ground biomass (Næsset and Gobakken, 2008).

Relevant to hydraulic applications, ALS point cloud data has been used for land cover classification, necessary for land cover mapping and vegetation classification in hydrodynamic models, when vertical vegetation structure is used for the parameterisation of Manning's *n* (Straatsma and Baptist, 2008; Antonarakis *et al.*, 2009; Vetter *et al.*, 2012). However, discrete waveform ALS has been shown to perform poorly in describing the canopy understorey, which is important for roughness parametrisation. The degree of detail and structure resolved in the canopy is therefore less than that made possible by other remote sensing techniques (Vauhkonen *et al.*, 2016).

An alternative approach is the application of full-waveform ALS, which can better measure this canopy detail (Anderson *et al.*, 2016). Full-waveform ALS has the potential to offer much richer spatial information about canopy characteristics, in three-dimensions, at a higher point density (Koenig and Höfle, 2016). This is because multiple discrete returns from within the canopy are recorded (Danson *et al.*, 2014). Currently, however, full waveform ALS is not widely available.

### 3.2.1.2    Terrestrial Laser Scanning (TLS)

Terrestrial laser scanning (TLS) is the ground-based implementation of LiDAR. The fundamental principles of TLS are similar to ALS, although differences exist due to the shorter ranges to which TLS is applied, the fixed nature of scan positions, the oblique perspective of scans, and a point density several orders of magnitude greater than ALS (Smith, 2015). This therefore allows millimetre scale point clouds to be captured (Smith, 2015). A wide range of TLS systems are available, recording either single or multiple returns, with distance measurement using reflections from the surface of scanned objects, applying either time-of-flight or continuous-wave (phase-difference) ranging (Wehr and Lohr, 1999; Liang *et al.*, 2016). Time-of-flight ranging uses precise timing, and has the capacity to operate over distances of up to several kilometres. Continuous-wave ranging makes use of continuous laser illumination and amplitude modulation of the beam to discern the range at a higher frequency, although these systems are limited to applications over shorter operating ranges (Beraldin *et al.*, 2010). Scanners typically record the intensity of the returned signal, and are coupled with high resolution digital cameras to record RGB values, producing photo-realistic three-dimensional renderings (Brasington *et al.*, 2012).

A key challenge when applying TLS is the issue of occlusion, especially when scanning uneven or complex surfaces (Rosser *et al.*, 2005). Occlusion occurs when an objects surface is hidden from the laser beam by an obstacle, leading to gaps in the point cloud. In most cases multiple scans are collected from different perspectives (multiple scan positions), with the individual scans then co-registered. This offers a possible solution to the problem associated with occlusion effects, whereby objects occluded in one scan are most likely captured by other scans (Liang and Hyyppä, 2013). Further limitations of TLS include the prohibitive cost and bulk of the instrument (Smith, 2015), and the reduced instrumental accuracy under unfavourable conditions, including poorly reflecting surfaces, parallel incident angles, and moist weather conditions (Jaboyedoff *et al.*, 2012).

TLS has been applied to a large number of geomorphological applications, and taking the sub-discipline of fluvial morphology as an example, the spatial scales of applications have ranged from individual grains and sediment patches over $10^0 - 10^1$ m$^2$ (Hodge *et al.*, 2009), to river banks of $10^1 - 10^2$ m$^2$ (Leyland *et al.*, 2015), through to river reaches at the landscape scale $10^2 - 10^4$ m$^2$ (Brasington *et al.*, 2012). The approach has recently been developed to enable patch-scale topographical measurements to be made through

shallow water, with mean error of less than 0.005 m in < 0.2 m flow depths under favourable clear water conditions (Smith *et al.*, 2012).

### 3.2.1.3      Mobile Laser Scanning (MLS) and Personal Laser Scanning (PLS)

The deployment of TLS to mobile platforms has enhanced the spatial extent of data coverage possible (Williams *et al.*, 2014).  MLS is a multi-sensor system operating from a kinematic platform, integrating the TLS with a GPS and Inertial Measurement Unit (IMU) on board a moving vehicle.  MLS has been deployed from a range of moving vehicles, including amphibious all-terrain vehicles for the measurement of braided river systems (Williams *et al.*, 2014), and boats to map and monitor riverine vegetation through time (Saarinen *et al.*, 2013).  However, the point accuracy of MLS is generally at the centimetre scale rather than millimetre scale that is achieved through TLS (Liang *et al.*, 2016).

Personal Laser Scanning (PLS) has been made possible due to continued sensor miniaturisation, with positioning and scanning instruments worn or carried by the user. As shown in Figure 3.1, however, PLS derived point clouds show more surface noise than TLS derived point clouds (Ryding *et al.*, 2015).
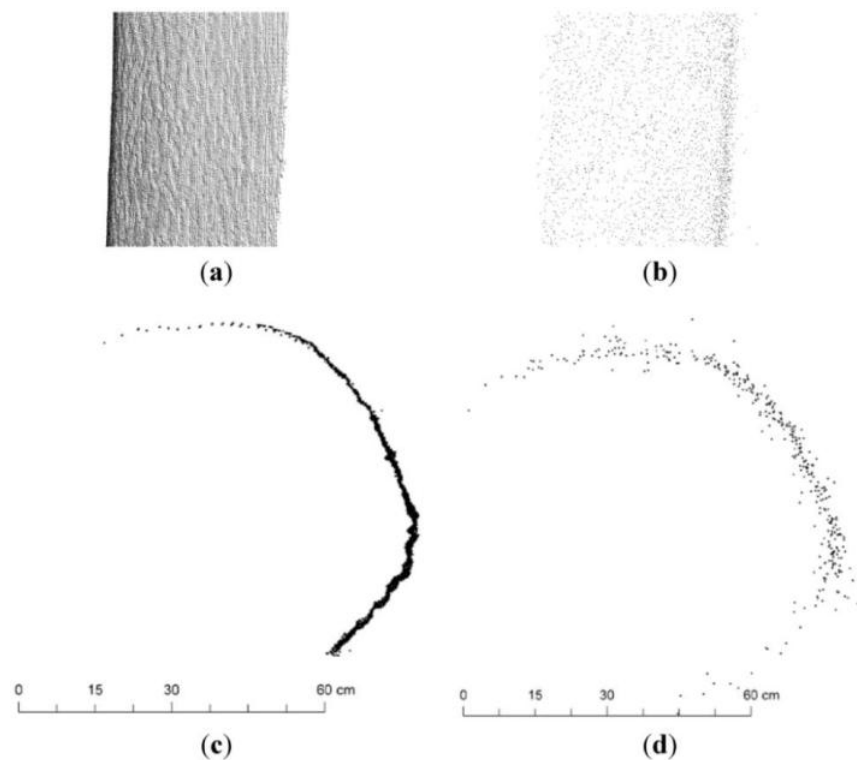


*Figure 3.1 (a and b) Side view and (c and d) plane view showing point cloud comparisons of tree trunks derived from (a and c) TLS and (b and d) PLS.  From Ryding et al. (2015).*

### 3.2.1.4        Structure from Motion (SfM) with Multi-View Stereo (MVS)

In recent years, Structure from Motion (SfM) with Multi-View Stereo (MVS) has been applied to a wide range of environmental problems having been shown to offer rapid three-dimensional point cloud acquisition for minimal expense (Smith *et al.*, 2016b). SfM relies on substantially overlapping photographs from multiple viewpoints as is typical in photogrammetric approaches, but SfM determines the internal camera geometry and camera position/orientation semi-automatically, without the need for ground control points to build a sparse three-dimensional reconstruction (Westoby *et al.*, 2012). The 'motion' term in SfM relates to the image capture from different locations, and when these images are viewed sequentially this creates a sense of movement (Snavely *et al.*, 2008). MVS refers to the building of the dense three-dimensional reconstruction, whereby photogrammetry algorithms are applied to increase the point density by several orders of magnitude. Similar point densities to TLS derived point clouds are achievable with SfM-MVS, although the precision is generally less than in TLS derived point clouds (Smith and Vericat, 2015). Although occlusion is still an issue in SfM-MVS, the issue is comparably smaller than in TLS applications, due to the greater number of viewpoints that can be integrated into the point cloud (Smith *et al.*, 2016b).

When applying SfM-MVS to capture dense point clouds of individual plants, Quan *et al.* (2006) used 30-45 multi-view images to successfully reconstruct three-dimensional plant canopies for leafy plant species. Application of a false high contrast background is found to aid plant segmentation issues (Kumar *et al.*, 2012), although this may not be feasible in field settings. Miller *et al.* (2015) apply a more systematic approach to image acquisition (Figure 3.2), with photo points at regular intervals along three concentric circular paths around the tree perimeter, ensuring at least 50% image overlap, and providing considerably more images than earlier studies (150-180 per tree). Manual field measurement techniques were used to validate tree models, finding root-mean-square-error (RMSE) as low as 4% for metrics such as tree height, and a 19% underestimation for total tree volume. When SfM-MVS has been used to calculate the total volumes of highly complex root segments, Koeser *et al.* (2016) report an RMSE of 12% compared against water displacement measured volumes. Relevant to applications in this thesis, volume underestimation is therefore an issue of SfM-MVS.
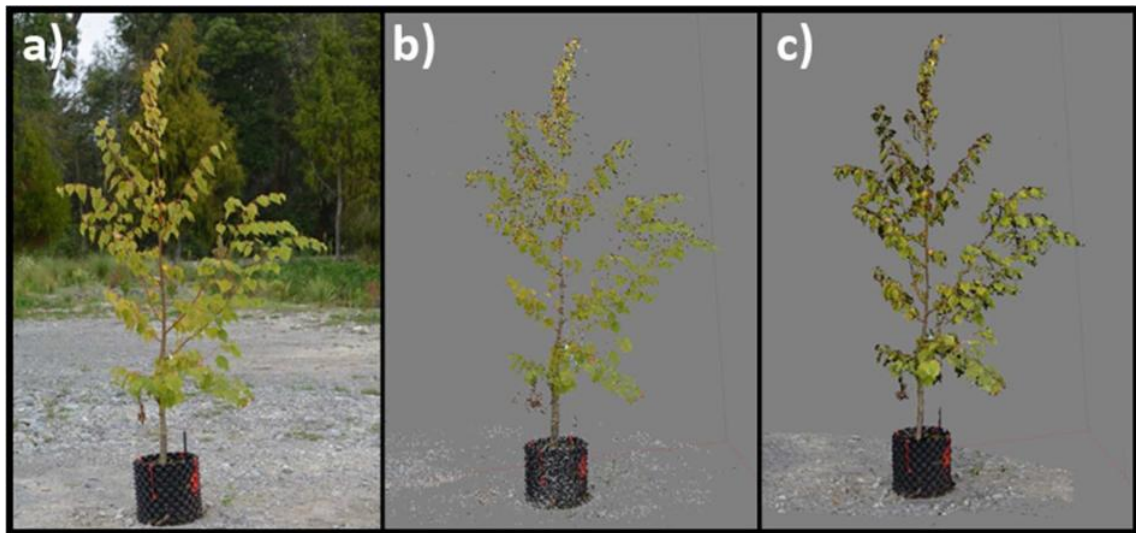
***Figure 3.2 Stages of SfM-MVS for individual tree modelling: (a) The original photograph, (b) the sparse point cloud tree model following SfM, and (c) the dense point cloud following MVS (c). Adapted from Miller et al. (2015).***

In natural scenes, Liénard *et al.* (2016) use SfM-MVS to derive a three-dimensional point cloud of mangrove roots, and are able to resolve the complex morphologies of barnacle-encrusted pneumatophores. They confirm that 90% of diameters obtained by photogrammetry fell between the minimum and maximum values estimated from manual field measurements using a caliper. Over a 250 m x 250 m forest site, Dandois and Ellis (2013) acquired digital photographs from a small Unmanned Aerial Vehicle (sUAV) to generate three-dimensional point clouds through SfM-MVS, attaining point densities of 30-67 points per $m^2$. This enabled canopy height models to be generated, that produced strong correlations between predicted and measured tree heights ($R^2$ = 0.82-0.84), well within the typical range of ALS derived canopy height models.

However, several limitations to the SfM-MVS approach exist. Although estimates of the total tree volume tend to be good, thinner branches are poorly resolved. Relevant to structure, relatively few points are only scattered along thinner branches (Figure 3.3), meaning that morphological detail can be lost. This impacts on volume estimates, where Miller *et al.* (2015) calculate RMSE of 12% for the larger main branches, compared to 48% on the thinner branches. In both cases, volume is consistently underestimated by applying SfM-MVS. Furthermore, changes in the ambient lighting can alter model quality (Gienko and Terry, 2014), with regions of shadow shown to reduce surface detail on tree models (Miller *et al.*, 2015). The effects of shadowing will further diminish the repeatability of the method.
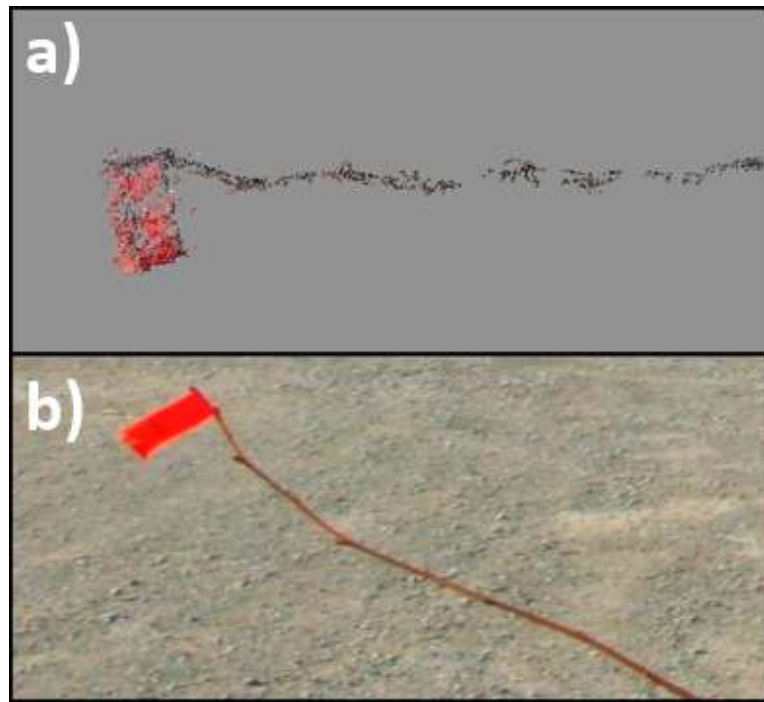
*Figure 3.3 (a) Scattering of points along thin branches, compared against (b) the initial photograph, demonstrating that the finest morphological detail might not be adequately resolved in SfM-MVS derived point clouds.  Adapted from Miller et al. (2015).*

### 3.2.1.5        Selection of the most appropriate remote sensing technique

A comparison of each of the above remote sensing techniques is provided in Table 3.1, assessed against the criteria introduced in Section 3.2.  TLS meets each of the criteria, and therefore for capturing plant volumetric canopy morphology is deemed most appropriate.   TLS has been viewed as the 'gold standard' for three-dimensional measurements (Chandler and Buckley, 2016), providing point clouds that offer an unprecedented spatial resolution, with millimetre scale accuracy.   Although recent advances in each of the other techniques offer much promise and potential, the spatial resolution and repeatability of TLS means that this is the most appropriate technique for this thesis.

*Table 3.1 Comparison of the measurement techniques used to capture plant form and structure. The extent to which each criteria is met is reported and colour coded (criteria defined in Section 3.2).*

| Assessment criteria | Airborne Laser Scanning (ALS) | Terrestrial Laser Scanning (TLS) | Mobile Laser Scanning (MLS) | Personal Laser Scanning (PLS) | Structure from Motion (SfM) with Multi-View Stereo (MVS) |
|---|---|---|---|---|---|
| Typical spatial accuracy (m) | 0.05 – 0.2 (Beraldin *et al.*, 2010) | 0.002 (Liang *et al.*, 2016) | 0.01 (Liang *et al.*, 2016) | 0.01 (Liang *et al.*, 2016) | 0.01 – 0.015 (Smith *et al.*, 2016b) |
| Criteria 1: Repeatable and applicable to range of plant species | Partially | Yes | Partially | Partially | Partially |
| Criteria 2: Fully three-dimensional representation, at the millimetre scale resolution | Limited | Yes | Yes | Yes | Partially |
| Criteria 3: Able to resolve internal plant morphology | No | Yes | Yes | Yes | Yes |
| Criteria 4: Able to derive areal and volumetric distributions | Limited | Yes | Yes | Yes | Yes |
| Criteria 5: Data readily incorporated into CFD model | Limited | Yes | Yes | Yes | Yes |
| Criteria 6: Non-destructive | Yes | Yes | Yes | Yes | Yes |

## 3.2.2     Practical applications using TLS derived point clouds

Given that TLS is the most appropriate method for capturing plant volumetric canopy morphology, literature examples and field data are used in this section to demonstrate:

i. How vegetation can be classified and extracted from complex point cloud scenes, to isolate individual plants.

ii. How plant structure and form can be quantified.

### 3.2.2.1     Vegetation classification and plant extraction

A complex point cloud scene, as derived from TLS, usually contains multiple elements. In these complex scenes it is often necessary to classify and extract individual elements.

The individual elements could be manually segmented, although this is time-consuming and prone to error, especially for large datasets containing numerous elements. Classification attempts using RGB values are limited by shadowing effects and differences in light exposure (Brodu and Lague, 2012). The complex light illumination conditions within point clouds often means that the colour information is difficult to use to separate photosynthetic from non-photosynthetic canopy components, even when correct exposure settings are applied (Ma *et al.*, 2016).

Attempts have also been made to classify complex point cloud scenes using the laser return intensity (Franceschi *et al.*, 2009), although difficulties emerge when correcting for the distance away from the scanner as the laser signal is weakened (Kaasalainen *et al.*, 2011; Eitel *et al.*, 2014). Furthermore, influences such as surface humidity, micro-roughness, and physico-chemical characteristics of the scanned material can further complicate the response of laser return intensity (Lichti, 2005; Nield *et al.*, 2011).

As an alternative, classification of complex point cloud scenes can be achieved following the semi-automated, multi-scale CAractérisation de NUages de POints (CANUPO) approach developed by Brodu and Lague (2012). Discrimination and classification of different elements in the point cloud (Figure 3.4a) is based on the dimensional signature of each element (Figure 3.4b). For each point in the scene, a dimensional signature is compared over multiple spatial scales, thereby providing a dimensionality value and a probabilistic confidence value in the classification result (Brodu and Lague, 2012). For the salt marsh scene in Figure 3.4a, vegetation points are classified and isolated from ground points. As the spatial scale, or interrogation window, increases (Figure 3.4b), vegetation points aggregate along the two-dimensional to three-dimensional axis. In contrast, the ground points remain distributed along the one-dimensional to two-dimensional axis. The different elements therefore have different dimensional signatures across multiple spatial scales. By training classifiers on each of the elements in a complex scene, it is possible to classify and extract specific elements of interest.
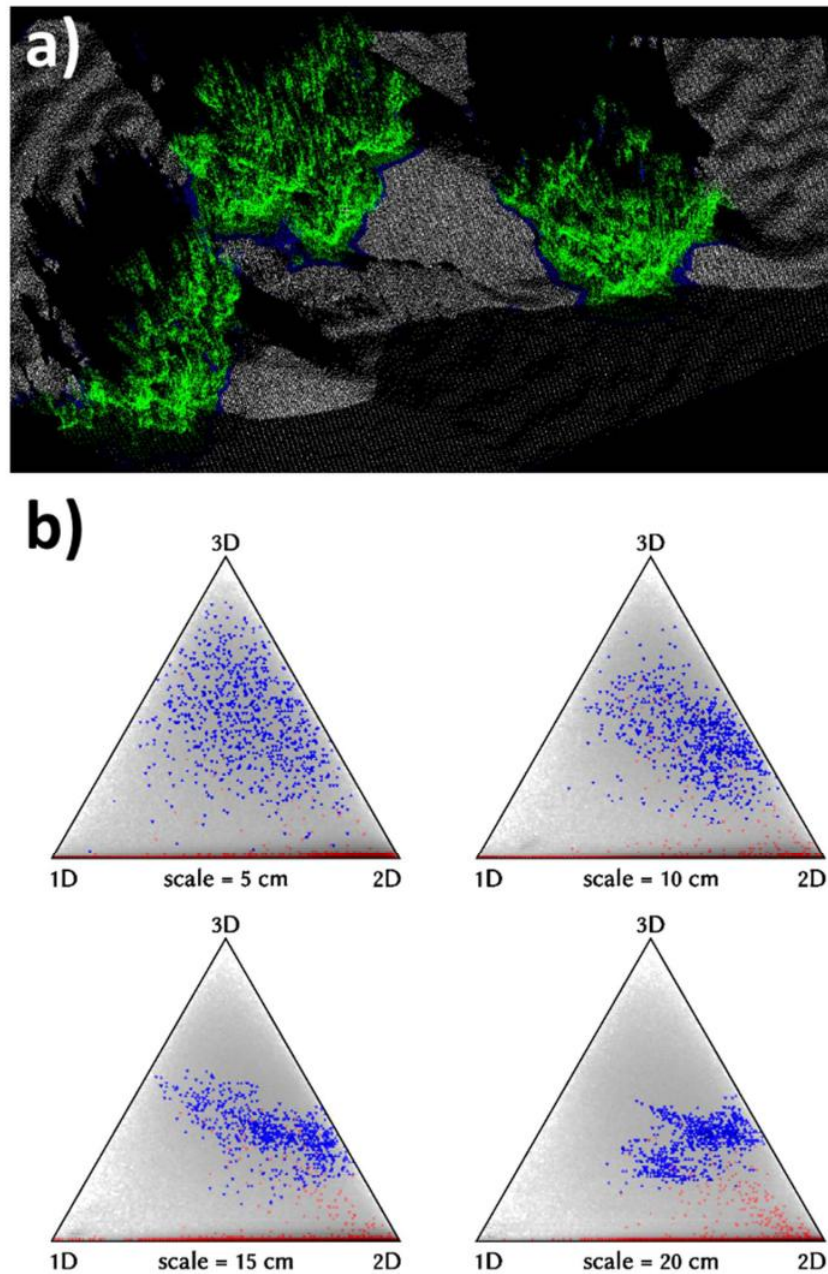
*Figure 3.4 (a) Classified point cloud from Mont Saint-Michel bay salt marshes, where green points are vegetation, white points are ground, and blue points fall below the 80% confidence interval. (b) Dimensional signature for a single vegetation patch at increasing spatial scales from 0.05 – 0.20 m, where blue points indicate vegetation points, and red points indicate ground. As the spatial scale increases, clustering along two-dimensional to three-dimensional axis enables the classification of vegetation). Taken from Brodu and Lague (2012).*

Application of the CANUPO approach is extended to a riparian scene (Figure 3.5), where individual plants have been classified and extracted. Once classified and extracted, the structure and form of individual plants can then be quantified. Although CANUPO was initially designed for the removal of vegetation, here the process is reversed, allowing individual plants to be isolated from complex scenes.
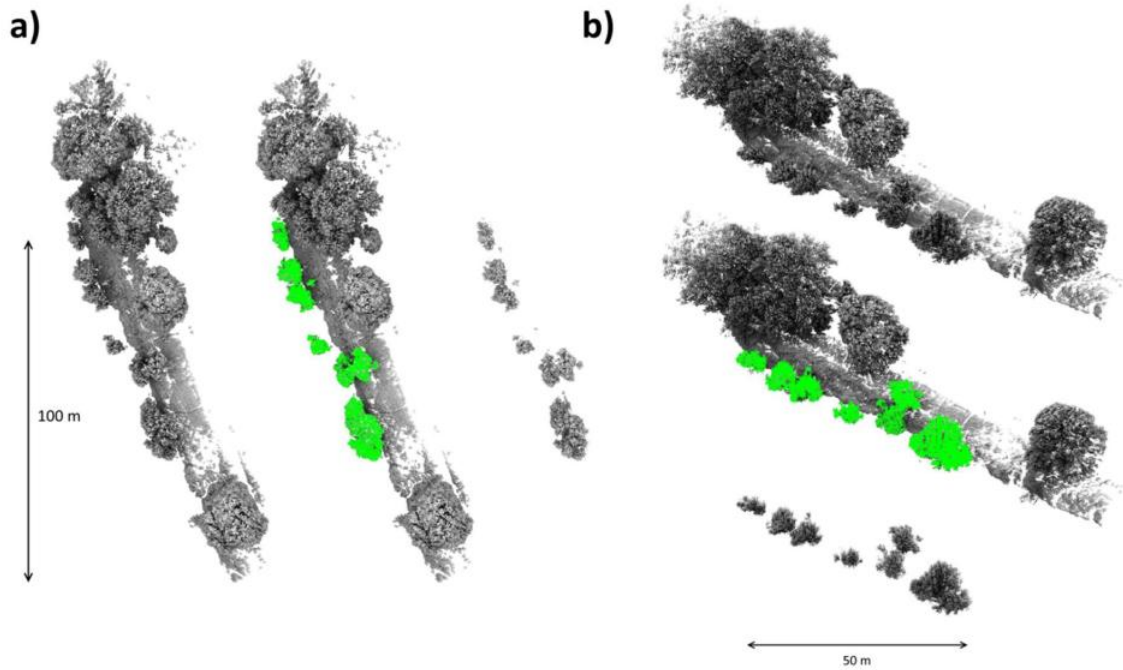
*Figure 3.5 (a) Plan view and (b) oblique view of a natural riverbank scene at the River Wear, Durham, United Kingdom; captured using TLS.  The CANUPO classifier was used to classify and extract individual riparian plants (green).*

### 3.2.2.2　　Quantification of plant structure and form

Following classification and extraction of vegetation elements from a complex point cloud (Figure 3.4), and the isolation of individual plants (Figure 3.5), the spatial information (*xyz*-coordinate data) can be directly used to derive spatially explicit horizontal and vertical plant attributes (termed point cloud based approaches). Alternatively, the isolated plant point cloud can be registered in a three-dimensional voxel space, allowing volumetric characteristics to be identified (termed voxel based approaches).　Furthermore, isolated plant point clouds can be used for the reconstruction of plant models (termed reconstruction).

#### 3.2.2.2.1　　Point cloud based approaches

Hopkinson *et al.* (2004) were one of the first to use TLS derived point clouds, captured at a 0.015 m resolution, for tree metric analysis in a complex forest setting (Figure 3.6a). The point cloud was used to collect objective measurements of tree location, tree height, diameter at breast height (DBH) and stem density, all of which are necessary for timber volume estimation.  The tree metrics were comparable with results from manual field measurements, for example when considering DBH, accuracies were typically < 0.02 m. Watt and Donoghue (2005) measured tree diameter and density using TLS derived point clouds which would be otherwise inaccessible using ALS, and point cloud based

approaches have been extended to automatically detect profiles along tree stems and calculate tree heights (Bienert *et al.*, 2006). Where complex canopies are present, occlusion lowers the rates of tree detection (Antonarakis, 2010), and therefore multiple scan positions are necessary (Kankare *et al.*, 2013). In these challenging settings, an 8% error on tree height is shown by Kankare *et al.* (2013), although in scenes where the canopy complexity is reduced, and trees are almost isolated, performance improves, and tree height errors are less than 0.01 m (Eitel *et al.*, 2013). Watt and Donoghue (2005) therefore suggest TLS may be best suited to analysis at the individual tree level, rather than the plot-scale level.

Rosell *et al.* (2009) use TLS derived point clouds for the quantification of geometric parameters in fruit orchards and vineyards, with correlation coefficients as high as 0.97 for plant volume estimates compared against measured volumes (Figure 3.6b). For TLS derived point clouds of olive trees, Moorthy *et al.* (2011) cut individual plants into hundreds of cross sections, allowing data points to be evaluated in the horizontal perspective with distance into the crown, and in the vertical perspective with distance away from the ground. Using this point cloud based approach, a spatially explicit distribution of geometric parameters including tree height, canopy width/height, and canopy volume are defined. For the approach to be successful, however, the plant must have an open framework that allows the laser to penetrate the canopy interior, to fully quantify the canopy morphology. Because of this challenge, TLS may have a limited applicability when attempting to derive the internal canopy morphology of especially dense plant species, and this is discussed in more detail when selecting the plant species used in subsequent sections of this chapter.
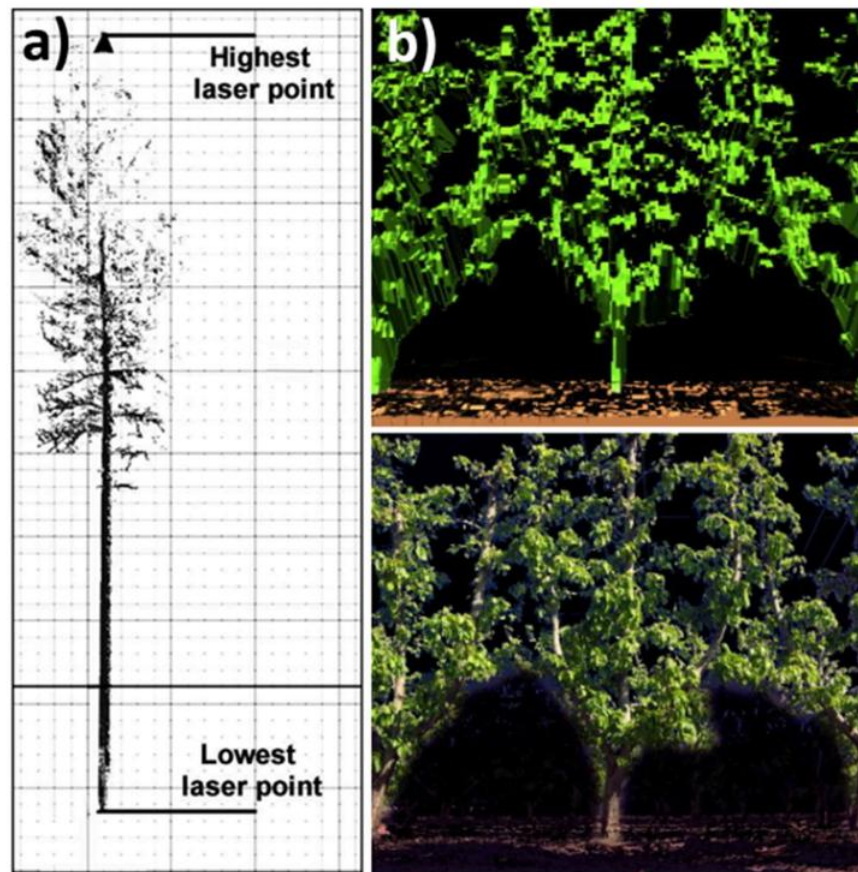
*Figure 3.6 (a) Derivation of geometric parameters including tree height using point cloud based approaches from Hopkinson et al. (2004); and (b) the similarity in plant volume estimates from point clouds and digital photographs from Rosell et al. (2009)*

### 3.2.2.2.2    Voxel based approaches

Geometric information can also be derived by registering the point cloud in a three-dimensional voxel space. A voxel is defined as a volume element in a three-dimensional array, otherwise known as a volumetric pixel (Hosoi and Omasa, 2006; Béland *et al.*, 2011). The spatial information is therefore systematically decomposed into a regular set of volumetric elements, and a value assigned to each of these voxels. At the simplest level, the value assigned can be a binary occupied/unoccupied status, with occupied voxels assigned a value of 1, and unoccupied voxels assigned a value of 0. This results in a binary three-dimensional array, consisting of object and background voxels (Gorte and Winterhalder, 2004). This can be further extended to represent more information from the point cloud, including a count of the number of points in the voxel (enabling point density to be quantified), and colour or laser return intensity for classification purposes.

Geometric information of vegetation have previously been established using either a cubic voxel grid (e.g. Jalonen *et al.*, 2015) or a cylindrical polar voxel grid (e.g. Manners *et al.*, 2013), as shown in Figure 3.7. A cubic voxel grid allows for a common framework

between measurements taken with the instrument positioned at different locations (Béland *et al.*, 2014b). However, in a cubic grid the path lengths of the laser return vary non-uniformly across the voxel (Béland *et al.*, 2014b), and therefore a cylindrical polar grid may be preferred under circumstances where only one scan position is necessary/possible. However, a major advantage of using a cubic voxel grid is that the volume of the voxel remains constant with distance from the scanner, whereas this is variable in space when a cylindrical polar grid is used.
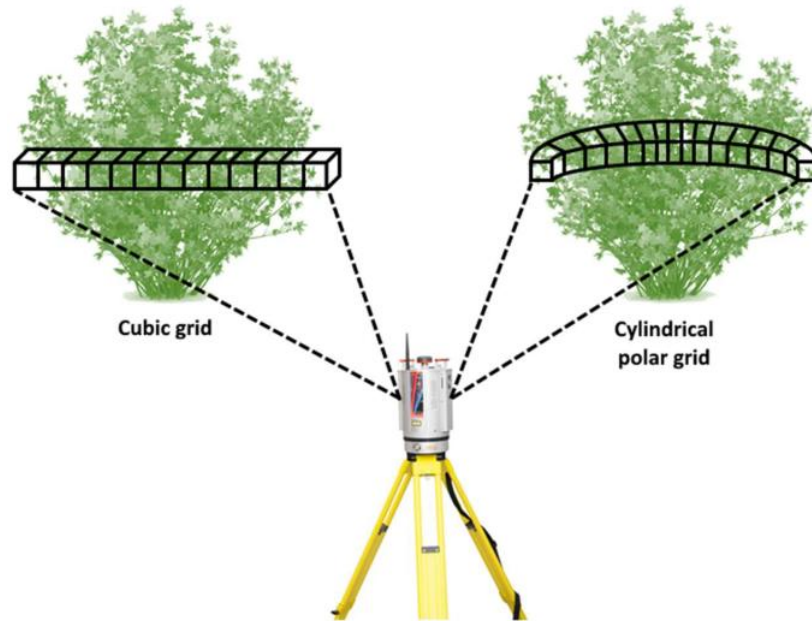


*Figure 3.7 Comparison between cubic and cylindrical polar grid, with the volume of voxels in the cylindrical polar grid not constant.*

For volume estimation, the total plant volume is calculated by the summation of voxel volumes over occupied voxels (Bienert *et al.*, 2014). However, where point cloud data usually only contain points from the surface of an object, unoccupied voxels can potentially be defined within the interior of large diameter trunks or branches, and therefore morphological closing operations to fill these hollows are required where false unoccupied voxels are present (Gorte and Winterhalder, 2004). Without such closing operations, a substantial underestimation of total volume can occur (Gorte and Winterhalder, 2004; Hosoi *et al.*, 2013).

Determination of an appropriate voxel size also influences the accuracy of volume estimates. Too fine of a voxel size, especially without application of a morphological closing operation, will underestimate volumes because of missing structural information, whereas too coarse of a voxel size will overestimate volume due to the additional

artificial structures around the object surface (Hess *et al.*, 2015). Hosoi *et al.* (2013) therefore suggest selecting voxel size on the diameter of the smallest branches, and the volume of one voxel will therefore be the same as the volume of the portion of branch represented (Figure 3.8). At the plant-scale, this often results in a voxel size of approximately 0.005 – 0.01 m (Hess *et al.*, 2015; Jalonen *et al.*, 2015). When these guidelines are followed, voxel based approaches are shown to produce accurate estimates of plant volume, regardless of the architectural complexity of the plant (Hess *et al.*, 2015).
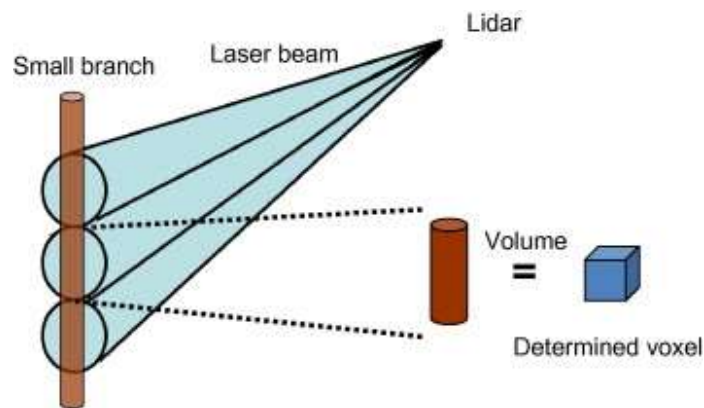


**Figure 3.8 Determination of an appropriate voxel size from Hosoi et al. (2013), with voxel size based on the smallest branches in the point cloud.**

An alternative to the voxel based approach for volume estimation involves fitting a convex three-dimensional hull around the outermost set of points in the point cloud (Barber *et al.*, 1996). This reproduces the smallest area or volume that contain the point set (Graham, 1972). A global convex hull can be calculated when the outer points are used as boundaries, with inner gaps filled to produce a solid object (Figure 3.9b). To improve the spatial representation and include morphological differences over the vertical extent, the convex hull can be applied to individual vertical slices of the object (e.g. 0.05 m vertical slices into the canopy crown, Figure 3.9c). Volume estimation using a convex hull by slices is shown to minimise the volume overestimation of using a global convex hull (Fernández-Sarría *et al.*, 2013), but the voxel based approach best approximated crown shape and volume (Figure 3.9d). When applied to 91 sagebush (*Artemisia tridentate*) specimens sampled in Spring and Autumn, Olsoy *et al.* (2014) found that the global convex hull approach estimated the total biomass more accurately ($R^2 = 0.92$) than the voxel based method ($R^2 = 0.86$).
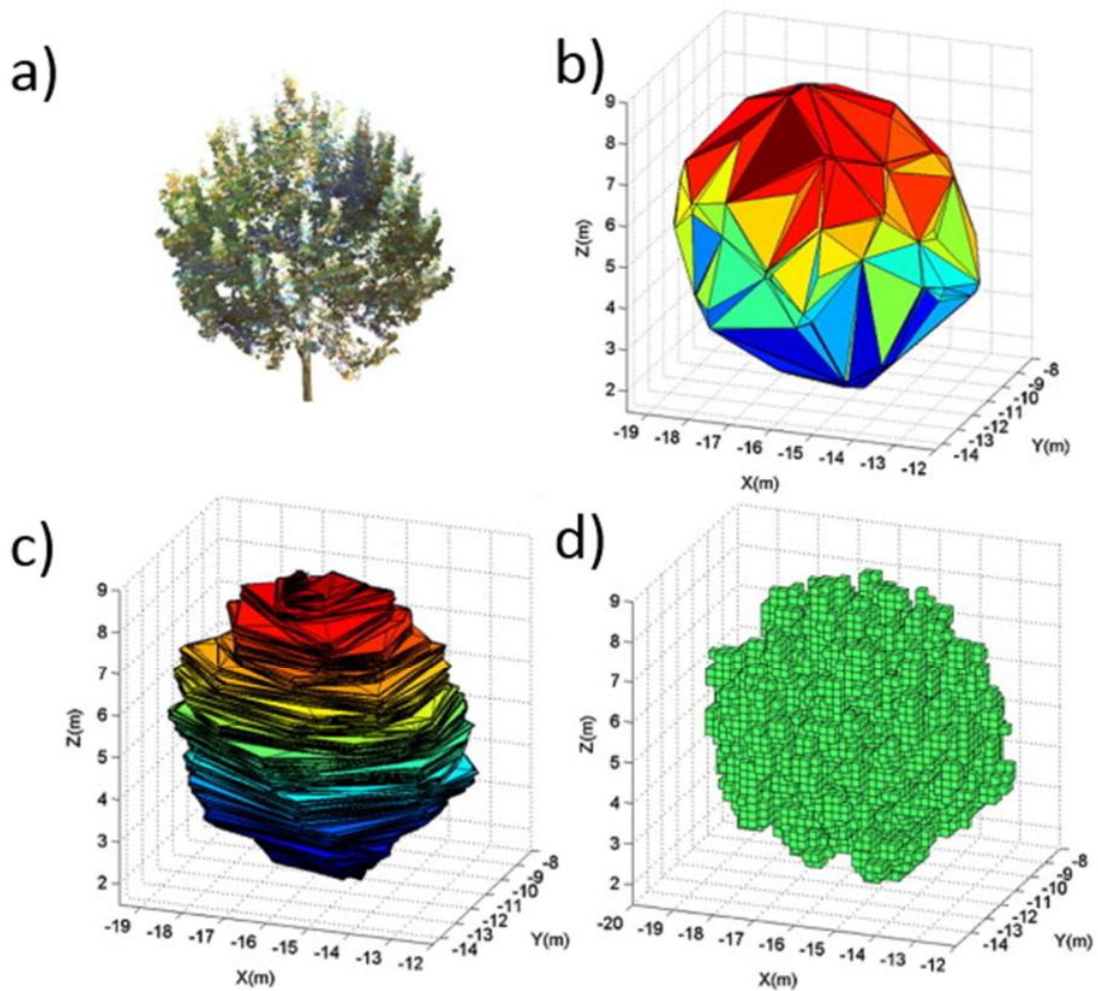
*Figure 3.9 Comparison between convex three-dimensional hull and voxel based approaches adapted from Fernández-Sarría et al. (2013): (a) the initial point cloud, (b) fitted with a global convex hull, (c) fitted with a convex hull by slices, and (d) fitted with a voxel based approach.*

Consequently, the global convex hull approach is most applicable when the laser is unable to penetrate the canopy, and so is especially relevant to closed framework plants, where the canopy interior cannot be resolved. However, for species with extensive gaps in the canopy into which the laser can penetrate, application of the convex hull approach will overestimate plant volume. A voxel based approach is therefore more suitable in these instances, where the distribution of voxels in three-dimensional space allow plant porosity to be defined. Consideration of the plant framework is therefore necessary when selecting an appropriate technique to assess plant volume.

Using a voxel based-approach, Antonarakis *et al.* (2009) attempted to quantify the leafless roughness of full scale riparian trees. In an approach similar to that applied and developed in this thesis, TLS was used to capture point clouds for six forest land cover types, scanned from three perspectives at a 0.02 m spatial resolution. Voxelisation of leafless individual trees, at a 0.05 m voxel size, enabled frontal areas and stage-

dependent frontal areas to be quantified. These areas were then used for the back-calculation of the drag coefficient and Manning's *n*. It is the spatially explicit characterisation of the frontal area that makes this possible. The approach has been further extended to include the leaf elements of vegetation, by calculating the leaf area index (LAI) using the gap fraction method (Straatsma *et al.*, 2008; Antonarakis *et al.*, 2010).

As previously noted, however, determination of an appropriate voxel size can influence areal and volumetric estimates, and therefore the 0.05 m voxel size may be too coarse of a representation. This would likely overestimate the frontal area, with implications for the vegetative resistance values calculated. Similarly, Manners *et al.* (2013) use the vertical frontal area on a cylindrical polar voxel grid to evaluate the structure of *Tamarix spp.* stands (Figure 3.10), which were subsequently used to discretise stem-maps of cylindrical elements in a two-dimensional hydraulic flow model, to calculate stage dependent flow resistance. In this application, however, only a single scan perspective was captured, and therefore the full three-dimensionality of plant structure and form was unlikely represented.
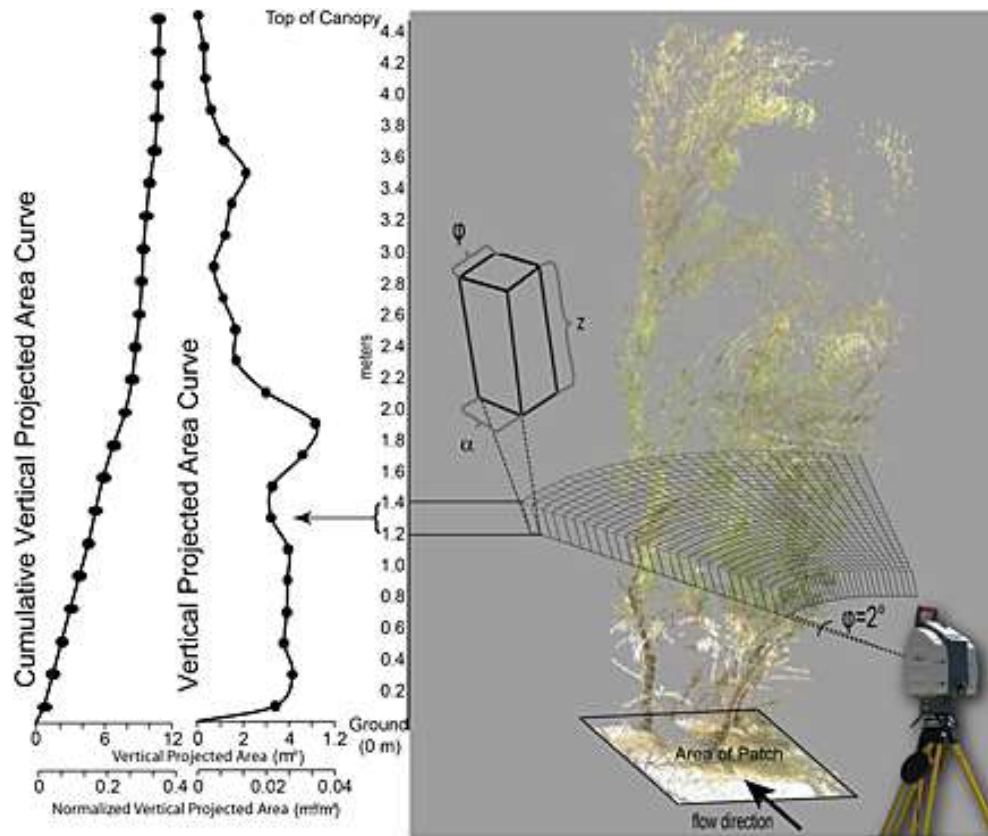
**Figure 3.10 Quantification of vertical frontal area profiles using a cylindrical polar voxel grid, from Manners et al. (2013).**

Extending beyond the plant-scale, Jalonen *et al.* (2014) apply TLS to gather a point cloud for a vegetated floodplain along a 200 m reach of a compound channel in Sipoo, southern Finland. Results indicate that a spatial resolution of at least 0.01 m is required to derive geometric parameters of floodplain vegetation, including vegetation height and volumetric distribution, and it is important to consider both vegetation and ground returns in the complex scene. Similarly, Jalonen *et al.* (2015) apply a voxel based approach to TLS point clouds of both woody and herbaceous vegetation to determine total plant area. For herbaceous vegetation, mean heights from the digital surface model of the point cloud can be used to adequately describe the total plant area, and therefore a linear distribution can be assumed. For woody vegetation, however, the vertical distribution of total plant area is non-linear, and this was also shown in studies of cumulative frontal area for riparian plant species (Aberle and Järvelä, 2013). These findings add further evidence to suggest that morphologically simple plant representations, that are commonly used in flume experiments and numerical modelling studies (Section 2.4), do not adequately represent the complexity of natural plants found on floodplains and in riparian zones.

In addition to total plant area distributions, voxel based approaches have been applied to estimate leaf area distributions. Within each voxel, light transmission statistics are calculated to describe the spatial distribution of the foliage area, therefore providing a spatially explicit measure of leaf area, rather than a spatially representative leaf area estimate (Béland *et al.*, 2014b). Where point clouds are collected in both leaf-off and leaf-on conditions, distinctions can be made between the laser pulses returning from wood and foliage to determine the foliage zone (Béland *et al.*, 2011). Seasonal changes therefore influence the morphology at the individual plant-scale. Béland *et al.* (2014a) recommend a voxel size with linear dimensions approximately 10 times that of the leaf size, to ensure the statistical assumptions of the approach used to estimate LAI. The spatially explicit measure of leaf area can then be displayed over the three-dimensional extent of the tree, as shown in Figure 3.11.



*Figure 3.11 Application of a voxel based approach to TLS data, displaying the spatially explicit measure of leaf area distribution. Colours indicate leaf area estimates per voxel, from red (highest density) to green (lowest density). A 0.15 m voxel size is used to describe the distribution of leaf area, from Béland et al. (2014a).*

Voxel based approaches are extremely useful when determining a range of spatially explicit geometrical parameters. When using a cubic voxel grid, the approach is highly advantageous to the work undertaken in this thesis, by providing data in a regular

Cartesian gridded structure (criteria 5, Section 3.2). This is especially useful for the estimation of plant volume when equally sized voxels are used, and for assessing the spatial distribution of vegetal elements. The spatially explicit characterisation of volume thereby allows plant porosity to be defined, a requisite of RQ1 and thesis aim (i). Furthermore, voxel based approaches can be readily extended to analyse temporal differences in plant structure and form, for instance where growth and decay can be detected, or where seasonal changes result in differences between leaf-on and leaf-off morphology.

### 3.2.2.2.3    Reconstruction of vegetation models

Point clouds are used as the source of data for the reconstruction of simplified vegetation models. Reconstruction is usually achieved by fitting a skeleton to the point cloud, using geometric primitives such as cylinders or circles to represent the structure (Liang *et al.*, 2016), to produce quantitative structure models (QSM). Full scale plants and trees are represented through hierarchical collections of primitives, and can provide the volume approximations necessary to estimate factors such as above ground biomass. Examples of tree models include Raumonen *et al.* (2013) and Hackenberg *et al.* (2015), where vegetation is initially segmented into branches, and then reconstructed as a collection of cylinders, as shown in Figure 3.12.
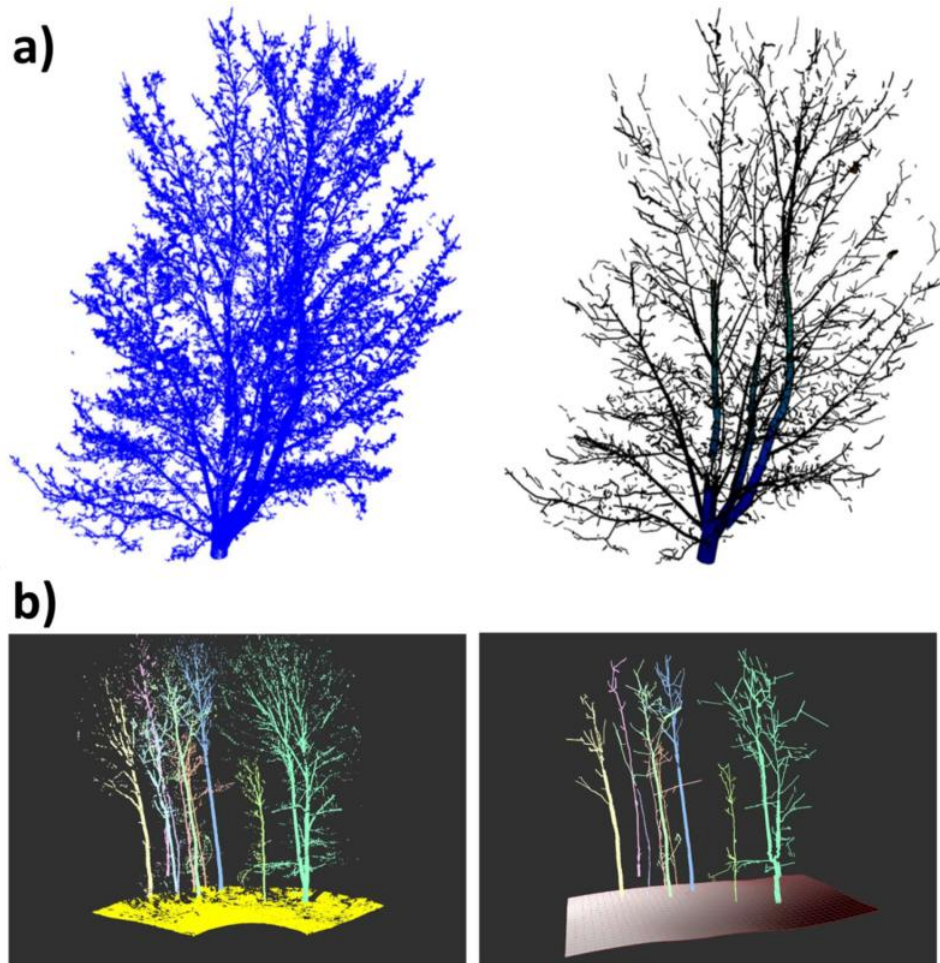
***Figure 3.12 Tree reconstruction using a hierarchical collection of cylinders. In both cases, point clouds are shown on the left, and the tree model on the right. (a) Fast Automatic Precision Tree Models from Raumonen et al. (2013) and (b) SimpleTree algorithm from Hackenberg et al. (2015). Although scale not provided in either publication, reconstructions are at the scale of entire trees (2 – 10 m).***

Vegetation model reconstructions allow the simplification and representation of defoliated elements, and so the approach is most applicable to studies concerned with quantifying defoliated plant architecture. Liang *et al.* (2016) categorise tree models based on their level of detail (LoD), and include the richness of the tree attributes (for example, whether 2nd and 3rd order branches are represented). To reach the highest level (5th LoD), foliage needs to be incorporated within the reconstructions, and this poses a major problem. In previous reconstruction models, foliage has either been completely ignored, or represented as a porous sub-domain around the solid branches (Endalew *et al.*, 2011), as shown in Figure 3.13. However, by doing this, additional uncertainty is introduced into the three-dimensional representation of plant, as the foliage component is not explicitly represented.
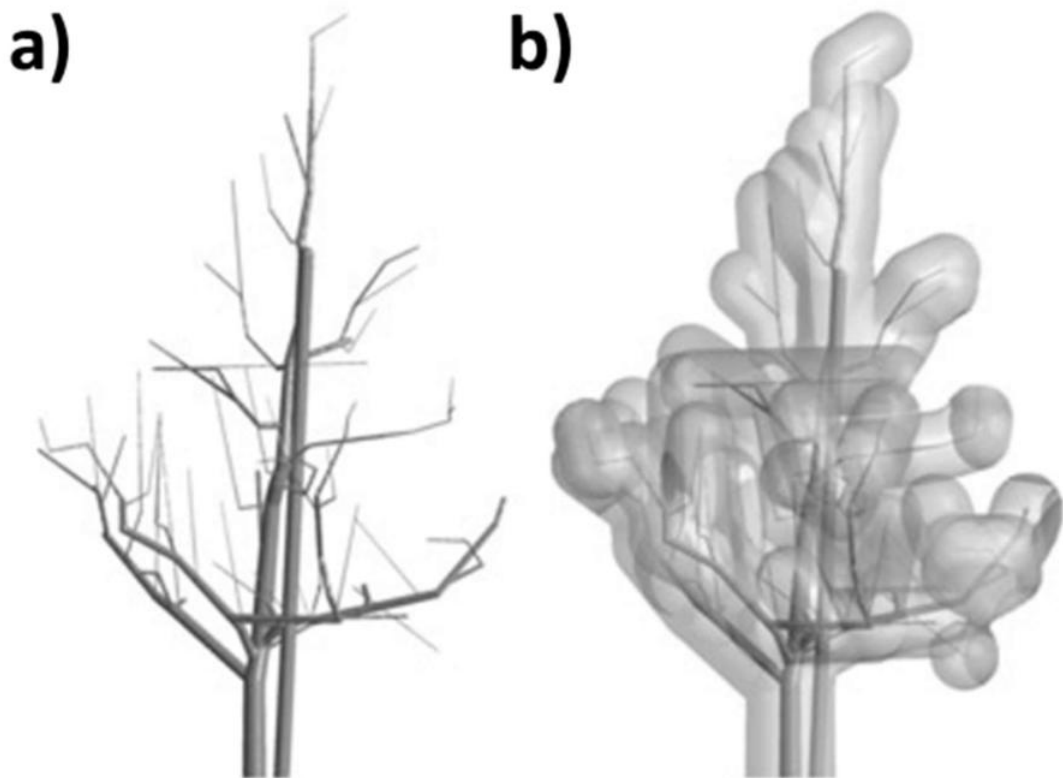
***Figure 3.13 Representation of foliage in a reconstructed tree model. (a) Defoliated tree model represents branch architecture. (b) Foliage simulated through application of a porous sub-domain around the defoliated branches, and therefore is not explicitly represented in the model reconstruction. From Endalew et al. (2011).***

### 3.2.2.2.4          Summary

For the purposes of this thesis, a combined point cloud and voxel based approach is most suitable for quantifying plant structure and form using high resolution point clouds derived from TLS. Vegetation reconstruction does not adequately represent the foliated components of natural plants. Thesis objective (i) requires all vegetal elements including leaf- and stem-scales to be fully resolved in the quantification of plant volumetric canopy morphology, and vegetation reconstruction methods do not currently allow this. Point cloud based approaches have been shown to determine plant geometric parameters with high accuracy, and voxel based approaches enable a spatially explicit characterisation of plant volume. Combined, these approaches allow plant volumetric canopy morphology to captured, as required to address RQ1.

## 3.3    Workflow for capturing plant volumetric canopy morphology

Relevant to RQ1 and thesis objective (i), there is a need to develop a new methodology capable of capturing and representing the full three-dimensionality of floodplain and riparian plant volumetric canopy morphology. This is needed to develop a numerical representation of vegetation response to river flow, as the plant representation is subsequently incorporated into the CFD model. This section therefore provides the workflow used to capture plant volumetric canopy morphology, and is also reported in Boothroyd *et al.* (2016a).

First, the best practice in survey design when applying TLS to characterise vegetation is discussed, detailing the TLS set-up and survey considerations. This is followed by an overview of how the high resolution, three-dimensional point cloud was post-processed to remove erroneous data points, before finally detailing the voxelisation procedure to simplify and reduce the number of data points, ready for incorporation of the plant representation into the CFD model (Chapter 4).

### 3.3.1    Description of the plant used to develop the workflow

In this section, a *Prunus laurocerasus* shrub (measuring 1.48 m x 0.86 m x 0.78 m) was used to develop the workflow, with this species selected for practical and ecological reasons. Practically, the woody shrub had an open framework (Section 3.2.2.2.2), allowing the laser to fully penetrate the plant interior, and accurately quantify the canopy morphology with limited occlusion effects. However, the *Prunus laurocerasus* specimen had a complex branch and leaf structure, with the locally dense collections of leaves providing a challenging test of the workflow. The evergreen shrub can reach heights of 6 m, with large (0.05–0.18 m) oblong-acute, glossy, dark-green leaves and pale green woody branches (Polunin and Everard, 1969; Stace, 2010). Ecologically, the woody shrub shares morphological similarities to woody riverine vegetation species such as *Populus nigra*, which is typically found on floodplains and gravel bars (O'Hare *et al.*, 2016). Scans using TLS were completed with the plant foliated and defoliated, following manual removal of leaves (n = 432), as this allows the volumetric canopy morphology to be quantified under contrasting levels of foliage.

## 3.3.2    Best practice: application of TLS to capture a high resolution point cloud

A RIEGL VZ-1000 scanner was used to collect the high resolution point cloud. The scanner has a beam divergence of 0.3 mrad, a field of view 100° x 360° and an effective measurement rate of up to 122 000 measurements per second. Scans were collected at a distance of 3 m from the plant, with $\pi$ and $\theta$ increments set to 0.012 degrees, controlling the horizontal and vertical alignment respectively. Riegl (2015a) report that at a 10 m distance, the scanner has a range accuracy of 8 mm, and a precision of 5 mm. At the 3 m scanning distance, the mean distance between neighbouring points in the registered point cloud was 0.0018 m. The scanner recorded multiple discrete returns from a single emitted pulse, improving the interrogation of vegetation elements (Pirotti *et al.*, 2013), thereby heightening point density.

To resolve issues of occlusion and improve coverage, scans were acquired from four different perspectives (Figure 3.14), with the scanner set to the same height above the ground at each of the four locations (2 m). Four scanning positions have previously been shown to provide the necessary overlap to capture the three-dimensionality of the plant morphology (Moorthy *et al.*, 2008). By increasing the number of scan perspectives, the point density is heightened, thereby increasing the accuracy when capturing the structure and form (Pueschel *et al.*, 2013; Hess *et al.*, 2015). For each scan location, the instrument was mounted above the surface being scanned to enable greater laser pulse penetration (Heritage and Hetherington, 2007). Reflective targets were placed around the plant, always visible to the scanner (Figure 3.14). Individual point clouds were registered using the georeferenced reflective targets in RiSCAN PRO software 64 bit v2.1.1 (Riegl, 2017), supplemented by multi-station adjustment. Scans were captured in a controlled laboratory setting to minimise the effects of any wind disturbance. In field settings, single tree scans have revealed up to 0.2 m of stem movement in the upper parts when exposed to 9 m s$^{-1}$ winds (Vaaja *et al.*, 2016), and therefore for the workflow developed here, wind effects were removed.
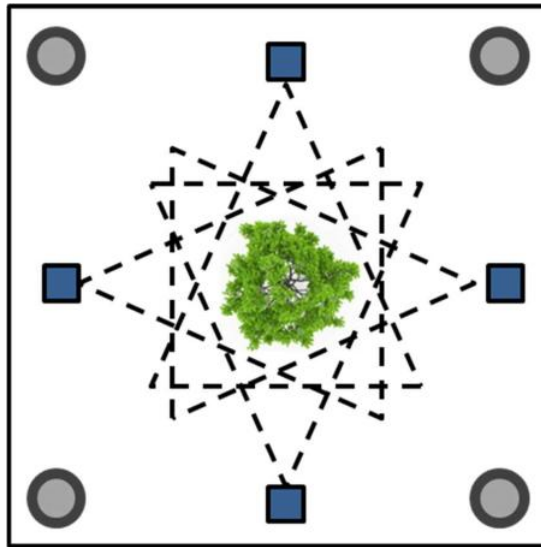
*Figure 3.14 Schematic diagram to show the scan set-up to minimise occlusion in scans. Blue squares indicate scanner position, with grey circles indicating position of reflective targets.*

### 3.3.3 Post-processing the registered point cloud

Following point cloud capture and registration, post-processing was completed using CloudCompare software 64 bit v2.7.0 (CloudCompare, 2017), with the first step involving manual delineation of the area of interest. When applying any filtering or post-processing technique, Hess *et al.* (2015) stress the importance of ensuring only points relating to noise are removed, where removal of correct points (for instance, small sections of branch) can lead to volumetric or morphological inaccuracies.

Erroneous data points were filtered using a statistical outlier removal (SOR) tool. The distance-weighted filter removes isolated points (highlighted orange in Figure 3.15) from the plant surface, specifically those off-centre hits caused by the position and size of the laser pulse footprint relative to the feature being scanned (Béland *et al.*, 2014a). By calculating the mean distance between each point in the initial point cloud and a neighbourhood of its nearest points, and assuming a Gaussian distribution, those points which fall outside of a defined standard deviation threshold are regarded as outliers and removed (Rusu *et al.*, 2008).

In determining the parameter set for the SOR, Jalonen *et al.* (2015) suggest using 100 points as the neighbourhood (*nb*), and applying a standard deviation threshold (σ) of 1. However, for the point clouds processed here, single application with the suggested parameter set does not adequately remove all isolated points (Figure 3.16). To improve post-processing, the SOR tool is twice-applied. With each successive pass of the SOR

tool, ~20% of points are removed when the plant was defoliated, and ~15% when foliated (Table 3.2). However, no real benefit is observed with a third pass of the SOR tool, as non-noise points begin to be removed from the edges of the plant (Figure 3.17). A final overview of post-processed point clouds for the *Prunus laurocerasus* plant when defoliated and foliated are provided in Figure 3.18, shaded by PCV illumination (portion of visible sky), to improve visibility of the point cloud.
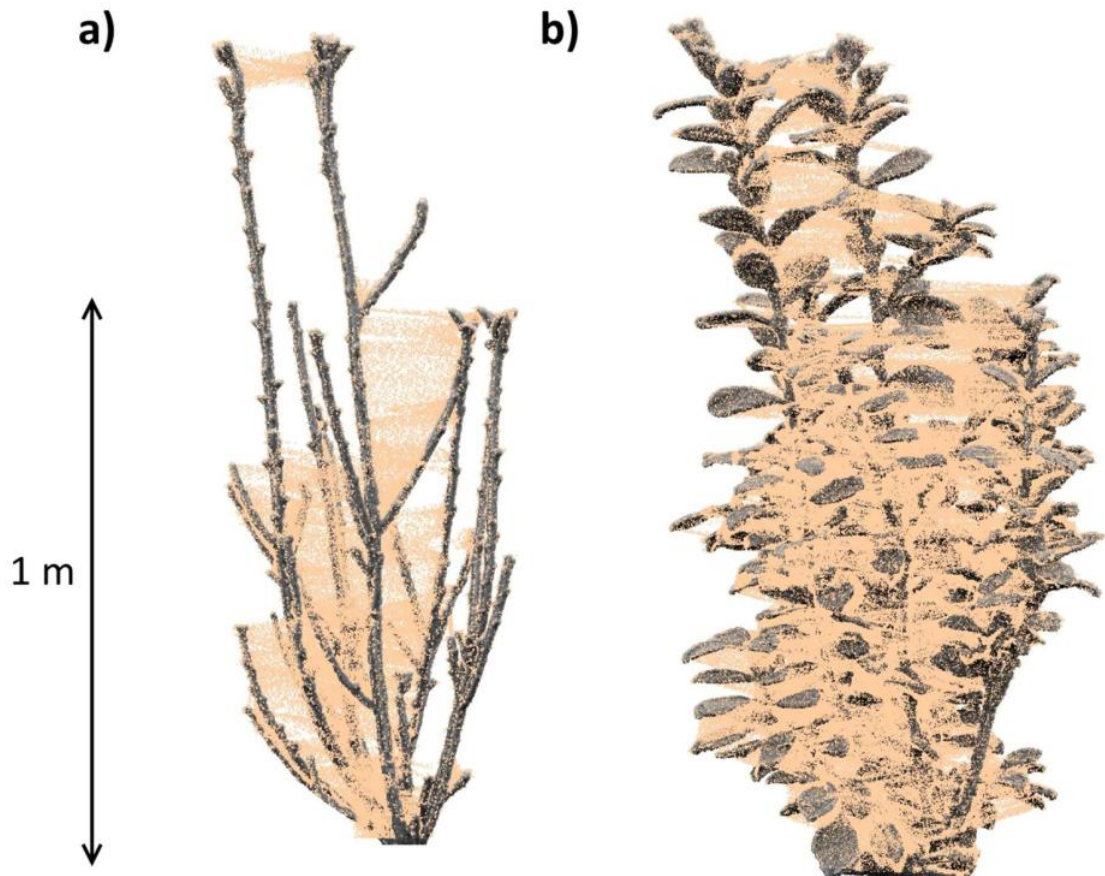


*Figure 3.15 Example of the twice-applied statistical outlier removal (SOR) tool to the (a) defoliated and (b) foliated Prunus laurocerasus plant, following manual removal of 432 leaves. Orange points are those removed by the SOR, where nb = 100 and σ = 1.*
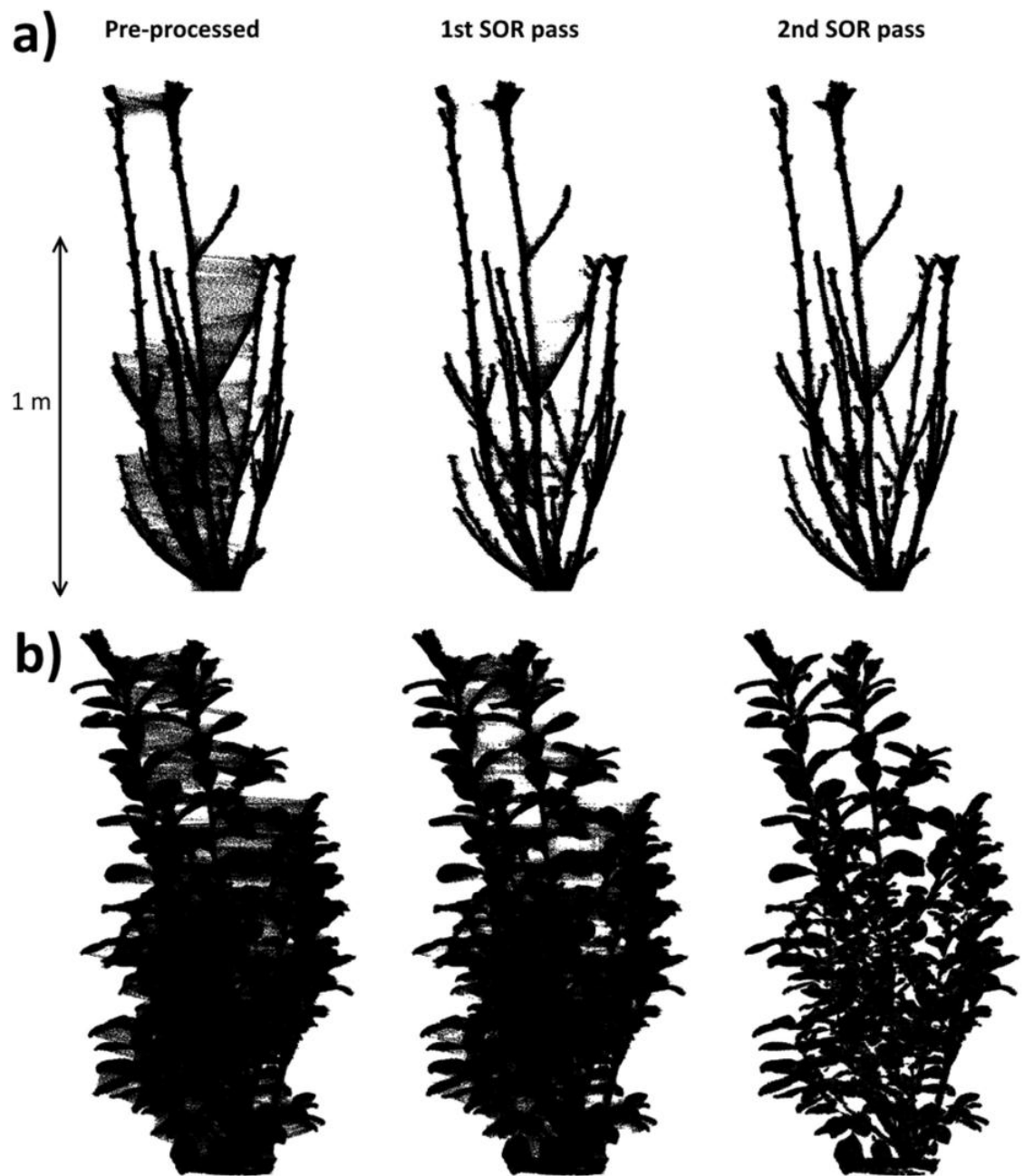
***Figure 3.16 Effect of twice passing the statistical outlier removal (SOR) tool on the (a) defoliated and (b) foliated plant representations.***

*Table 3.2 Removal of isolated points with successive passes of the statistical outlier removal (SOR) tool. Approximately 20% of points are removed when defoliated, 15% when foliated with each pass.*

|  | Defoliated | Foliated |
|---|---|---|
| Pre-processed point cloud number of points | 1 441 340 | 4 363 436 |
| 1st pass of SOR (number of points) | 1 222 895 | 3 821 048 |
| Reduction in number of points pass (%) | 17.9 | 14.2 |
| 2nd pass of SOR (number of points) | 1 032 526 | 3 354 715 |
| Reduction in number of points with 2nd pass of SOR (%) | 18.4 | 13.9 |
| 3rd pass of SOR (number of points) | 875 468 | 2 940 860 |
| Reduction in number of points with 3rd pass of SOR (%) | 18.0 | 14.1 |
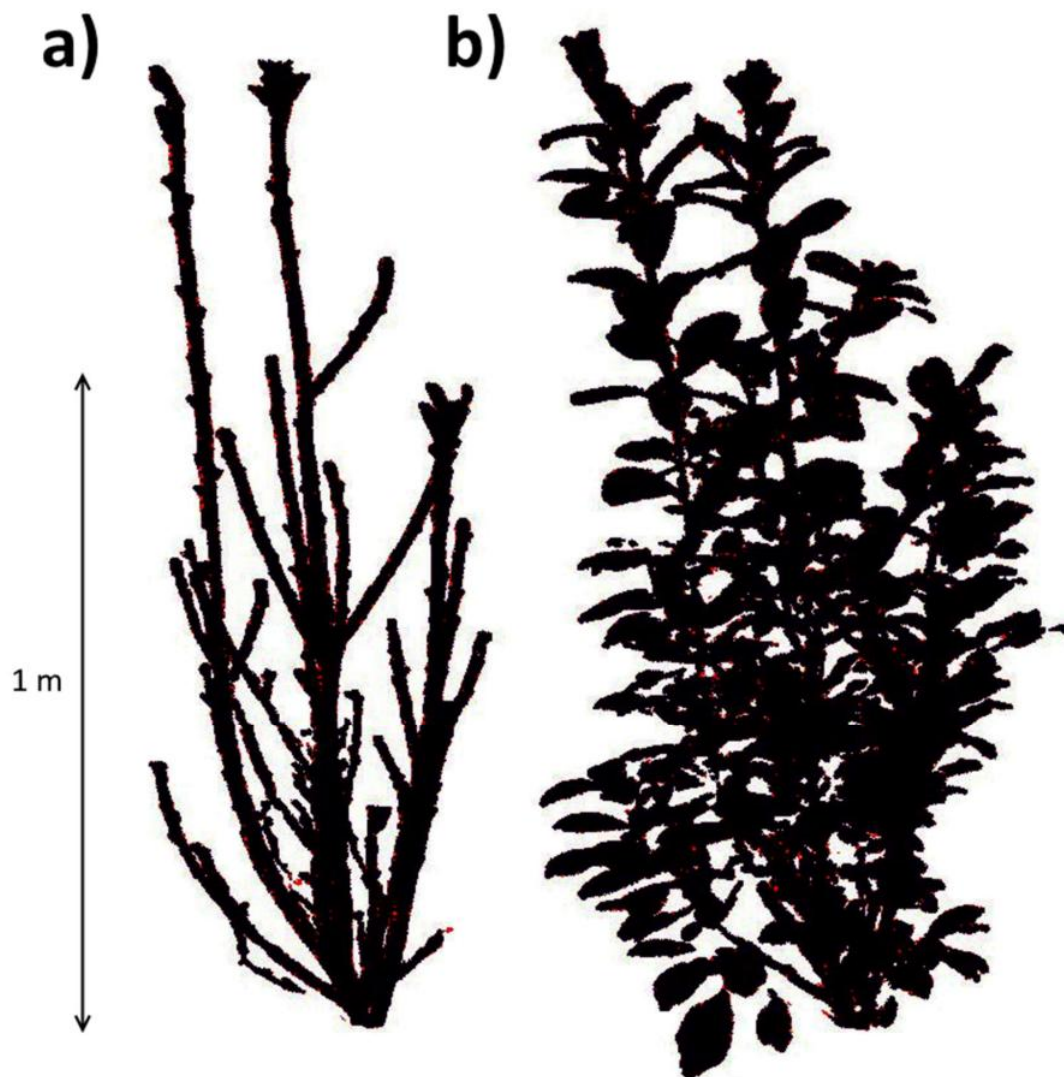


*Figure 3.17 Comparison between 2nd and 3rd pass of the SOR tool, differences are minimal and shown as red points on (a) defoliated and (b) foliated Prunus laurocerasus plant.*
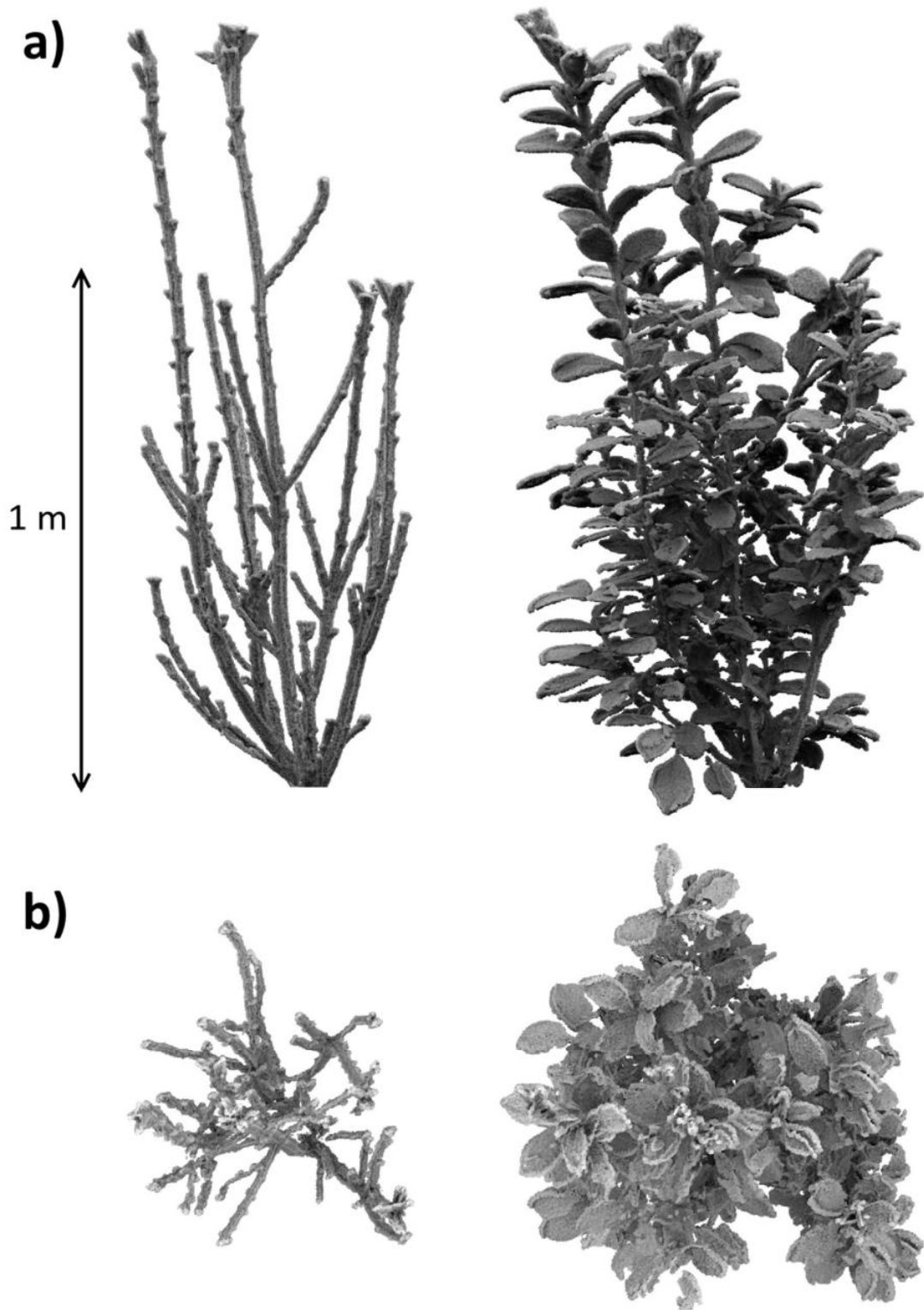
*Figure 3.18 Post-processed point clouds of defoliated and foliated Prunus laurocerasus plant, viewed from (a) the front and (b) above.*

The post-processed point clouds with the twice passed SOR tool are shown to visually match the actual plant morphology (Figure 3.19), containing ~1 000 000 points when defoliated, and ~3 500 000 points when foliated. The average point spacing when defoliated is 0.0026 m, and similar when foliated (0.0023 m). In the subsequent

chapters of this thesis, characteristic sub-subsections of the *Prunus laurocerasus* plant (highlighted in Figure 3.19), are used to investigate flow-vegetation interactions. This is because characteristic sub-sections share the same morphological characteristics (branch thickness, leaf density) as the remainder of the plant, but having a smaller volume allow flow to be solved at a higher spatial resolution. The orange sub-section (0.28 x 0.28 x 0.23 m) is used in Chapter 4 for model development, initial application, and testing. The purple highlighted sub-section (0.92 x 0.45 x 0.29 m) is used in Chapter 6 for testing the importance of plant volumetric canopy morphology.
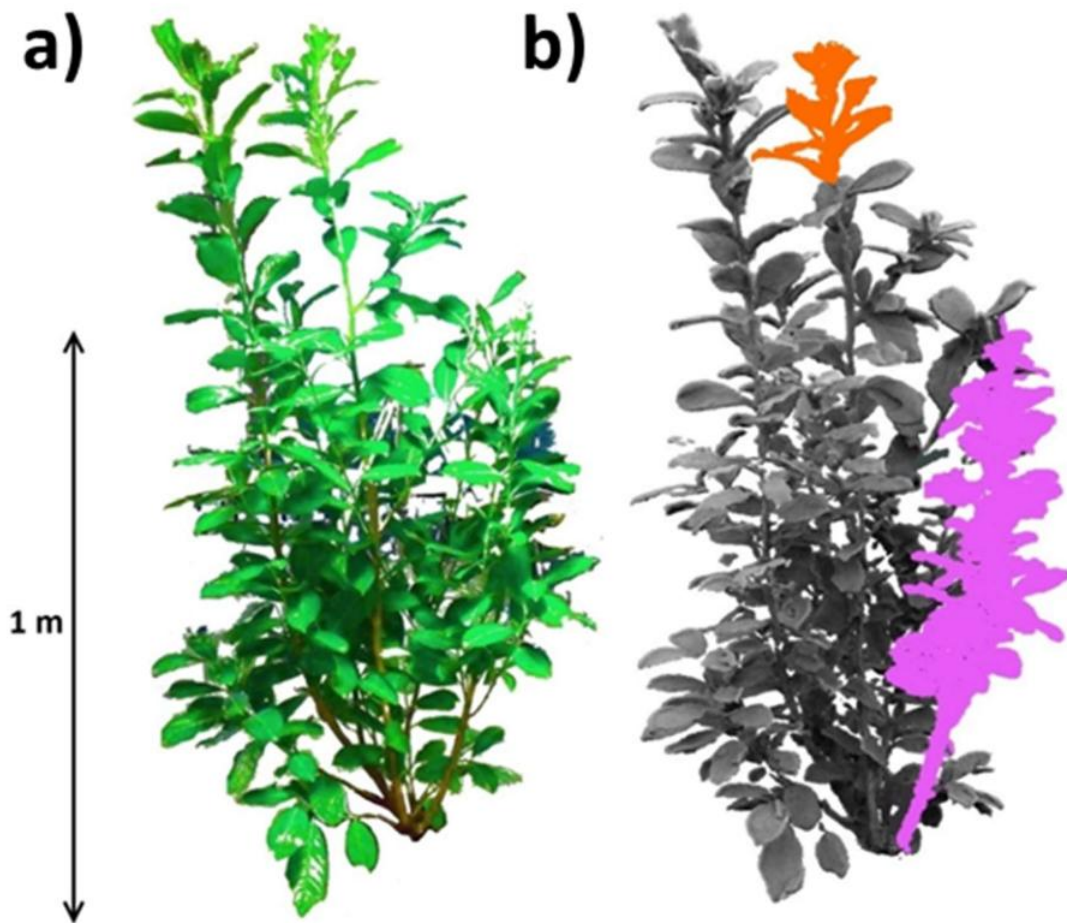


*Figure 3.19 (a) The Prunus laurocerasus plant and (b) point cloud with orange highlighted section for voxel size sensitivity analysis and purple highlighted section for modelling.*

### 3.3.4    Voxelisation procedure

The millimetre scale spatial resolution of the post-processed point cloud far exceeds what can feasibly be discretised within the CFD model, owing to the computational expense associated with solving flow at such high spatial resolutions (Hardy *et al.*, 2003). A simplification procedure following the gap fraction method of Straatsma *et al.* (2008)

is applied, with subdivision of the scan into individual voxels. Given the Cartesian grid structure of the CFD domain (Chapter 4), a regular cubic voxel grid is most applicable to this application, with the added advantage that all voxels have an equal volume.

Voxelisation involves the fitting of an octree structure with a user-defined maximum cell size around the post-processed point clouds, with the *xyz*-coordinate centroids extracted and read directly into the numerical scheme (Figure 3.20). Removal of isolated and erroneous data points (as described in Section 3.3.3) prior to voxelisation was important, given that voxels occupied by noise or measurement errors would lead to morphological errors and volumetric overestimation of the plant representation once voxelised (Bienert *et al.*, 2014). Selection of an appropriate user-defined maximum cell size, or voxel size, is crucial to retain the morphological complexity of the plant (see Section 3.2.2.2.2).
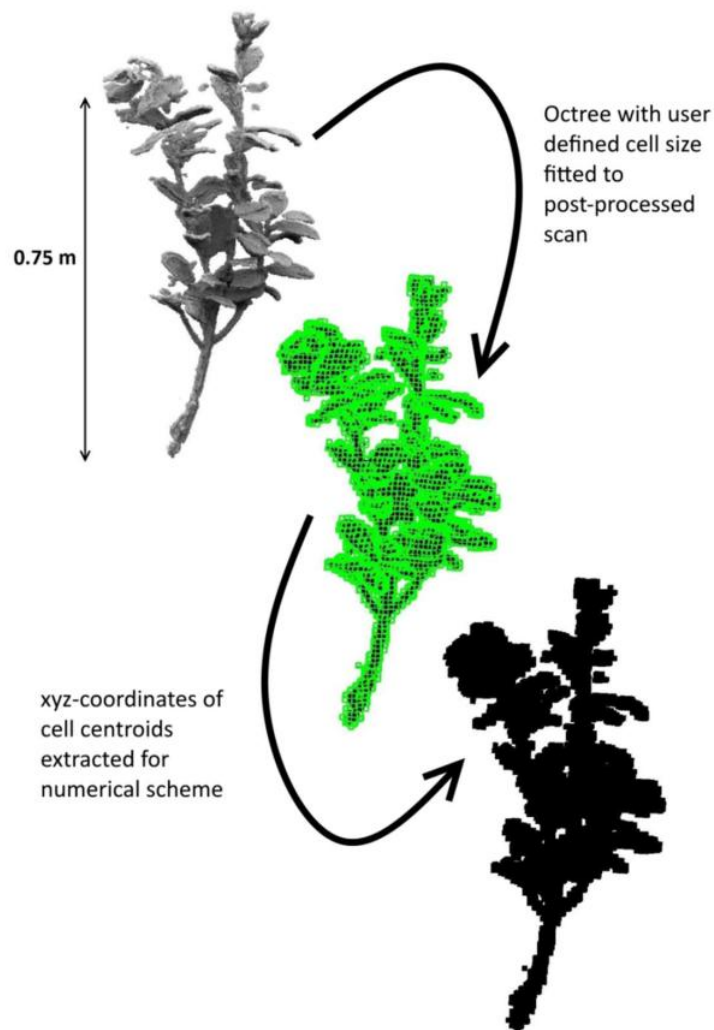


*Figure 3.20 Procedure for voxelisation, with the fitting of an octree structure around the post-processed point cloud, and extraction of xyz-coordinates in a regular Cartesian grid.*

The effect of refining the voxel size on the plant representation is shown in Table 3.3 and Figure 3.21. By reducing the voxel size, additional morphological detail from the post-processed scan can be resolved. However, a halving of the voxel size results in at least a four-fold increase in the number of cells required to represent the plant, and this would require much greater computational expense in the CFD model. A trade-off therefore exits between capturing and representing the requisite detail of plant morphology and porosity, whilst enabling the representation to be efficiently incorporated into the numerical scheme. Extraneous detail must therefore be avoided. Figure 3.21 clearly demonstrates similarities in plant shape over the range of voxel sizes, with the greatest difference observed between 0.02 and 0.01 m voxel sizes. Visually, a 0.01 m voxel size would adequately describe the plant morphology. This follows Hosoi *et al.* (2013), who suggest that the voxel size should be based on the smallest branch diameter (~0.01 m). Therefore the 0.01 m voxel size closely approximated the finest morphological element needing to be represented. In this application, a morphological closing operation was not deemed necessary, as no noticeable holes were found in the voxelised representation.

*Table 3.3 Volumetric properties of the voxelised Prunus laurocerasus plant with voxel sizes in the range 0.0025 – 0.02 m.*

| Voxel size (m) | Defoliated | | | | Foliated | | | |
|---|---|---|---|---|---|---|---|---|
| | 0.02 | 0.01 | 0.005 | 0.0025 | 0.02 | 0.01 | 0.005 | 0.0025 |
| Number of cells | 412 | 1167 | 6982 | 34942 | 1778 | 4968 | 30187 | 133024 |
| Total plant volume (m³) | 0.0033 | 0.0012 | 0.0009 | 0.0005 | 0.0142 | 0.0050 | 0.0038 | 0.0021 |
| Reduction in plant volume associated with decreasing voxel size (%) | - | 175 | 33 | 80 | - | 184 | 32 | 81 |
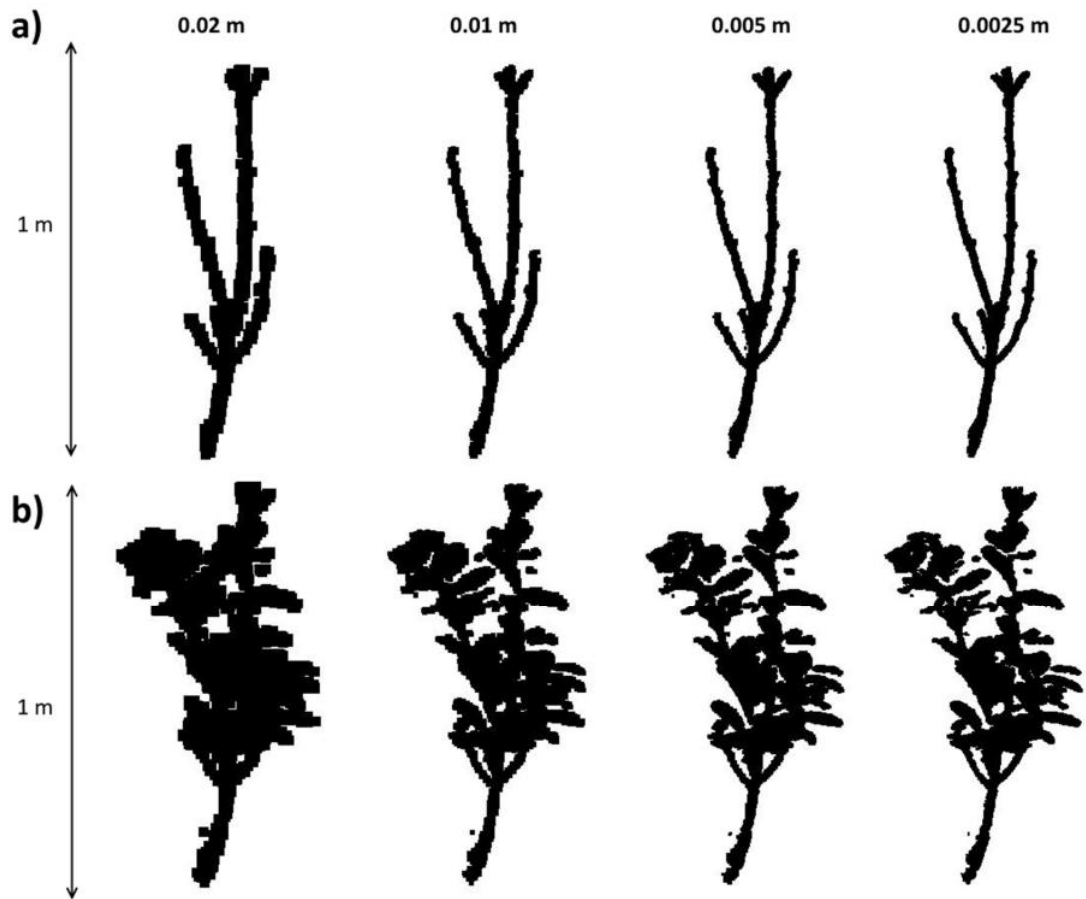
*Figure 3.21 Effect of refining the voxel size on the (a) defoliated and (b) foliated Prunus laurocerasus plant.*

Although the plant representations visually appear similar when refining the voxel size, the total plant volume ($V_P$) is sensitive to these changes (Table 3.3 and Figure 3.22). A finer voxel size results in the estimation of a smaller total plant volume. Between 0.02 and 0.01 m voxel sizes, the reduction in total plant volume associated with the decrease in voxel size is largest (~175% when defoliated and ~185% when foliated). Beyond this point, however, the reduction in total plant volume with further decreases in voxel size becomes smaller. However, changes to the total plant volume will have important implications for the blockage volume represented in the CFD model, in addition to the frontal area in a plane normal to the flow. This topic will be further addressed in Chapter 4, whereby sensitivity analysis is undertaken to assess the effect of voxel size on the modelled flow field response.
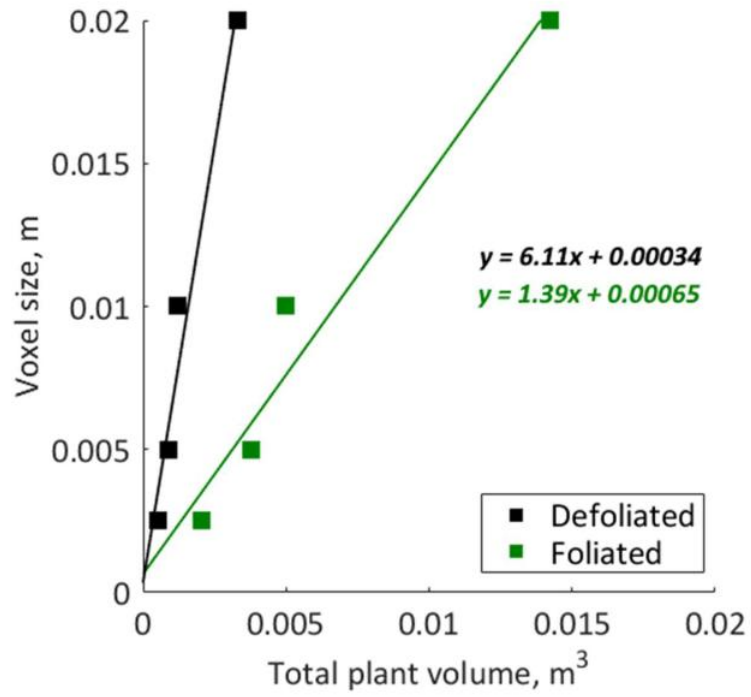
*Figure 3.22 Influence of voxel size on the total plant volume, plotted with a linear trendline. $R^2 = 0.96$ defoliated and $R^2 = 0.95$ foliated.*

### 3.3.5 Workflow summary

The summary of the workflow developed in this chapter is shown below in Figure 3.23.
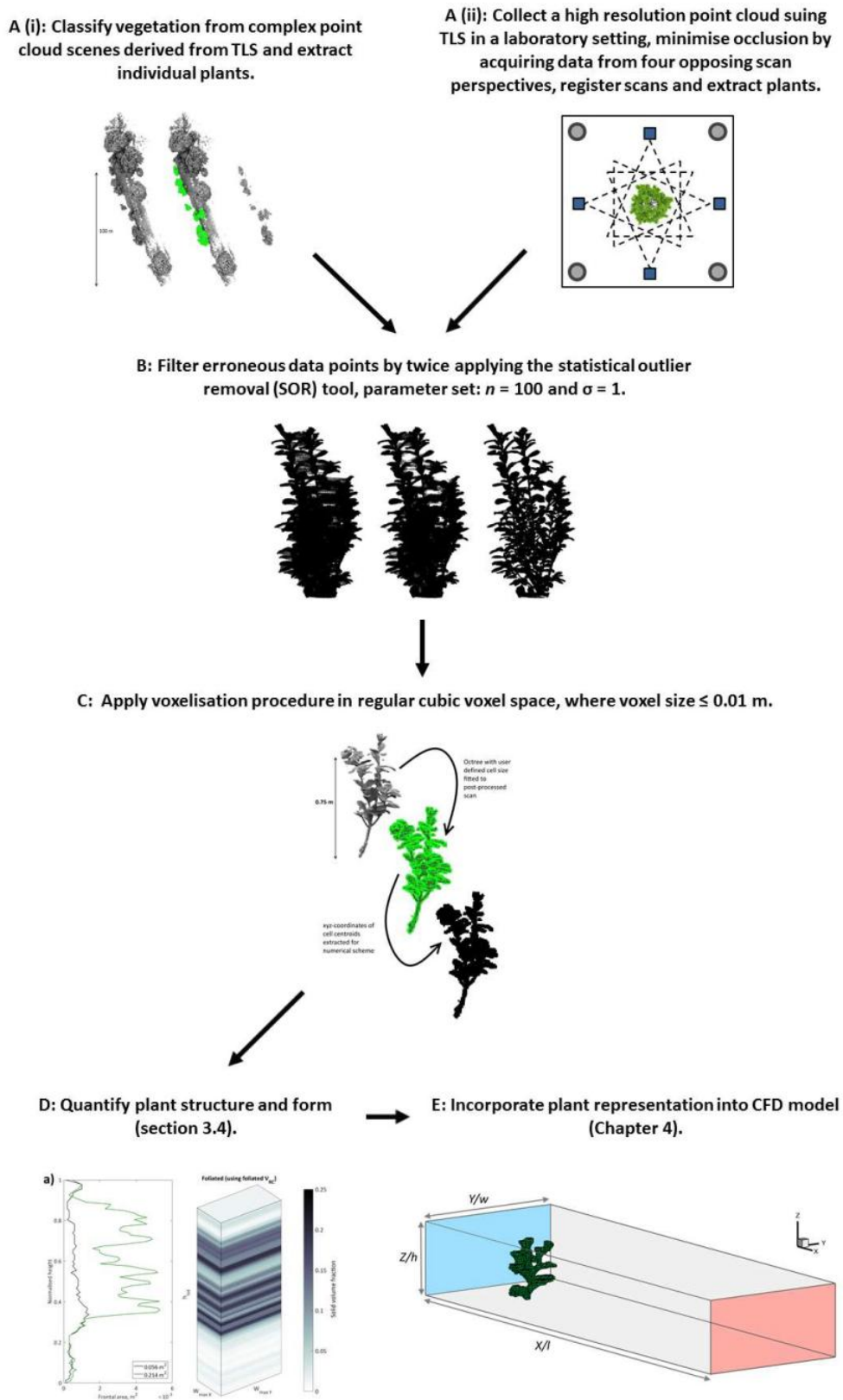


**Figure 3.23 Summary of the workflow used to capture plant volumetric canopy morphology.**

## 3.4 Quantification of plant structure and form using voxelised plant representations

The complex structure and form of plants can be characterised in several different ways. Godin and Caraglio (1998) define plant structure as the organisation of all plant constituents, referring to all vegetal elements including roots, branches, stems, and leaves. This plant structure term can be further subdivided into the spatial structure, geometrical structure, and topological structure. Spatial structure refers to the distribution of all vegetal elements in three-dimensional space. The geometrical structure is defined by morphological features of vegetal elements, referring to the form, size, and shape of these. The topological structure refers to the decomposition and connections between each of the vegetal elements (Sinoquet *et al.*, 1997; Godin and Caraglio, 1998). This involves subdivision into axes and segments, with application of a hierarchical ordering scheme to count and order these elements. A scheme based on stream ordering by Strahler (1957) has been applied to characterise the topological structure of plants in hydraulic applications (Järvelä, 2004; Wilson *et al.*, 2006; Antonarakis *et al.*, 2009). When considering plant structure, it is important to note that the organisation of vegetal elements in space can change through time (Godin *et al.*, 1999).

In support of RQ1, the spatial and geometric subdivisions of plant structure are more important than the topological structure. Using the defoliated and foliated voxelised plant representations at a 0.01 m voxel size, the spatial resolution which was shown to adequately represent complex plant morphology in Figure 3.21, spatial and geometric plant structure is characterised, helping to quantify plant volumetric canopy morphology. For both the defoliated and foliated plants, results are shown for crown width, frontal area and hypsometry, vertical distribution of plant volume, and the blockage volume. In each case, results are normalised over the vertical extent of plant height ($h_{norm}$).

### 3.4.1.1 Crown width

Using the voxelised representations, dimensional properties of the plant are first assessed through the vertical variation in crown width. The crown width, calculated as the maximum width of all branch and leaf elements, is displayed over $h_{norm}$ in Figure 3.24. The mean crown width in the defoliated plant (0.10 m) is less than the foliated

plant (0.17 m), and this is due to the additional contribution from the leaf body. However, this contribution is not equal over the entire vertical extent of the plant, and therefore crown width varies vertically between the defoliated and foliated plants. Similarity is shown until approximately 0.33 $h_{norm}$, where the main branching point of the plant is reached, and the leaf body emerges. In the region $0 - 0.33\ h_{norm}$, the average crown width is 0.06 m for defoliated and foliated plants. Beyond this region, however, marked changes exist. In the defoliated plant, the crown width remains approximately equal in the range $0.33 - 0.80\ h_{norm}$ (mean average width 0.15 m, standard deviation 0.02m). For the foliated plant in the range $0.33 - 0.88\ h_{norm}$, the mean width is greater (0.27 m), but there is greater variability (standard deviation 0.05 m). This variability in crown width is associated with individual leaf elements within the foliated body, accounting for the spikes in crown width. Dimensional properties of the plant differ beyond the main branching point due to the foliated body.
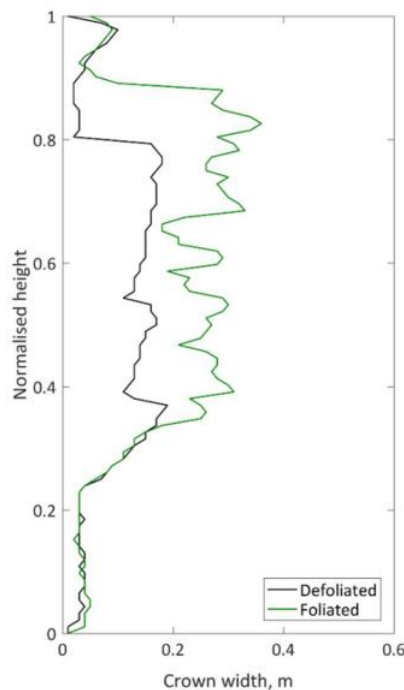


*Figure 3.24 Vertical distribution of crown width for the defoliated and foliated voxelised plant representations.*

### 3.4.1.2 Frontal area and hypsometry

The voxelised plant representations allow the estimation of the location-based total area of the plant, and it is important that this measure is accurate, as all leaves and branches contribute towards hydraulic resistance (Jalonen *et al.*, 2013; Jalonen *et al.*, 2015). Compared with digital photogrammetry techniques, which can overestimate the area of the features closest to the camera in an image frame because of the effects of central

projection (Sagnes, 2010), TLS derived measurements are advantageous as the central projection issue does not exist. TLS therefore allows a fully three-dimensional and spatially distributed understanding of plant area (Straatsma *et al.*, 2008).

By considering only the area of the plant projected on a plane normal to the flow, the frontal area is defined. In this example, the total frontal area of the defoliated plant is approximately four times smaller than the foliated plant (Figure 3.25a), demonstrating the important contribution of foliage in modifying plant frontal area. For both the defoliated and foliated plants, the vertical distribution of frontal area follows a pattern like the vertical distribution of crown width (Figure 3.24). Similar differences emerge beyond the main branching point of the plant. In the defoliated plant beyond the main branching point, the frontal area decreases slightly with $h_{norm}$, representative of along-branch thinning. For the foliated plant, greater variation in the frontal area corresponds with the region of the leaf body, associated with alternating regions of relatively sparse and dense leaf collections.

These differences in frontal area are also visualised through hypsometric relationships, plotting the cumulative area against normalised height (Figure 3.26a). For both plants, three notable changes in slope of the hypsometric curve are apparent, and therefore it possible to subdivide the curve into three distinct zones (Zone 1: base, Zone 2: second order branches/foliated body, and Zone 3: tip, Figure 3.26a), with each zone approximated by a linear fit. The overall relationship of the entire curve is not linear, but individual zones are. This zonation of hypsometry is similar to Wilson *et al.* (2006), who denoted three distinct zones for a foliated *Salix fragilis* specimen. They found the greatest increase in cumulative area with height to be distributed in the base region (Zone 1), although for the example here the greatest increase is found in Zone 2, associated with the second order branches/foliated body. For the *Salix fragilis* specimen investigated by Wilson *et al.* (2006), the contribution from the base of the tree to the total frontal area is greater than the *Prunus laurocerasus* specimen investigated here, where the contribution of second order branches/foliated body is more important. This pattern is similar for the defoliated voxelised representation. These findings correspond with results from Järvelä (2002b), in that the frontal area as a function of flow depth increases linearly if the base and tip regions of a plant is ignored. Hypsometric curves provide an effective means of comparing the vertical plant structure, allowing comparisons within and between different plant species.

For comparison to other species, Weissteiner *et al.* (2015) produced hypsometric curves of 20 plant specimens harvested from a wetland in Finland. The specimens strongly differed in terms of morphology and height (0.8 – 3.3 m). They found smaller specimens (< 2 m in height) to show an almost linear hypsometric curve, whereas taller specimens showed a more pronounced increase of cumulative area over height. This size dependency was not reflected in the measurements of Righetti (2008), who found the hypsometry to be similar for 0.7 m tall bushes as for 1.5 – 3.5 m tall willows. Differences in hypsometry between plant species are therefore expected, and can be explained by differences in the natural habitat of species. For instance, Weissteiner *et al.* (2015) show that because *Salix caprea* is positioned close to riverbanks, and therefore is inundated by frequent flooding, it has adapted its branch architecture by reducing the frontal area at the tree base, modifying the bending response under hydrodynamic loading.

### 3.4.1.3      Vertical distribution of plant volume

The voxelised representation also allows for the characterisation of the vertical distribution of plant volume, thereby helping provide an understanding of the volumetric canopy morphology (Figure 3.25b). The total plant volume ($V_P$) is more than four times greater in the foliated than defoliated plant. Unsurprisingly, for both plants the vertical dependence of volume follows a similar pattern to crown height and frontal area. Again, beyond the main branching point, along-branch thinning results in a reduction in volume with normalised height for the defoliated plant. For the foliated plant, marked vertical variation in volume is noted over the region of the leaf body, again showing the alternating regions of relatively sparse and dense collections of leaf elements, although here this is averaged over three dimensions.

As before, the normalised cumulative volume is expressed against $h_{norm}$ (Figure 3.26b), and this follows a very similar pattern to the previous hypsometric relations (Figure 3.26a). For both the defoliated and foliated plants, the overall curve is again subdivided into three distinct, almost linear zones. However, for Zone 2 associated with second order branches and the foliated body, a greater number of undulations are present on this section of the curve, with deviations from the linear trend especially detected in the defoliated plant. Volume is therefore less linearly distributed over the normalised plant height than frontal area, and this has important implications for the volumetric blockage factor of the plant.
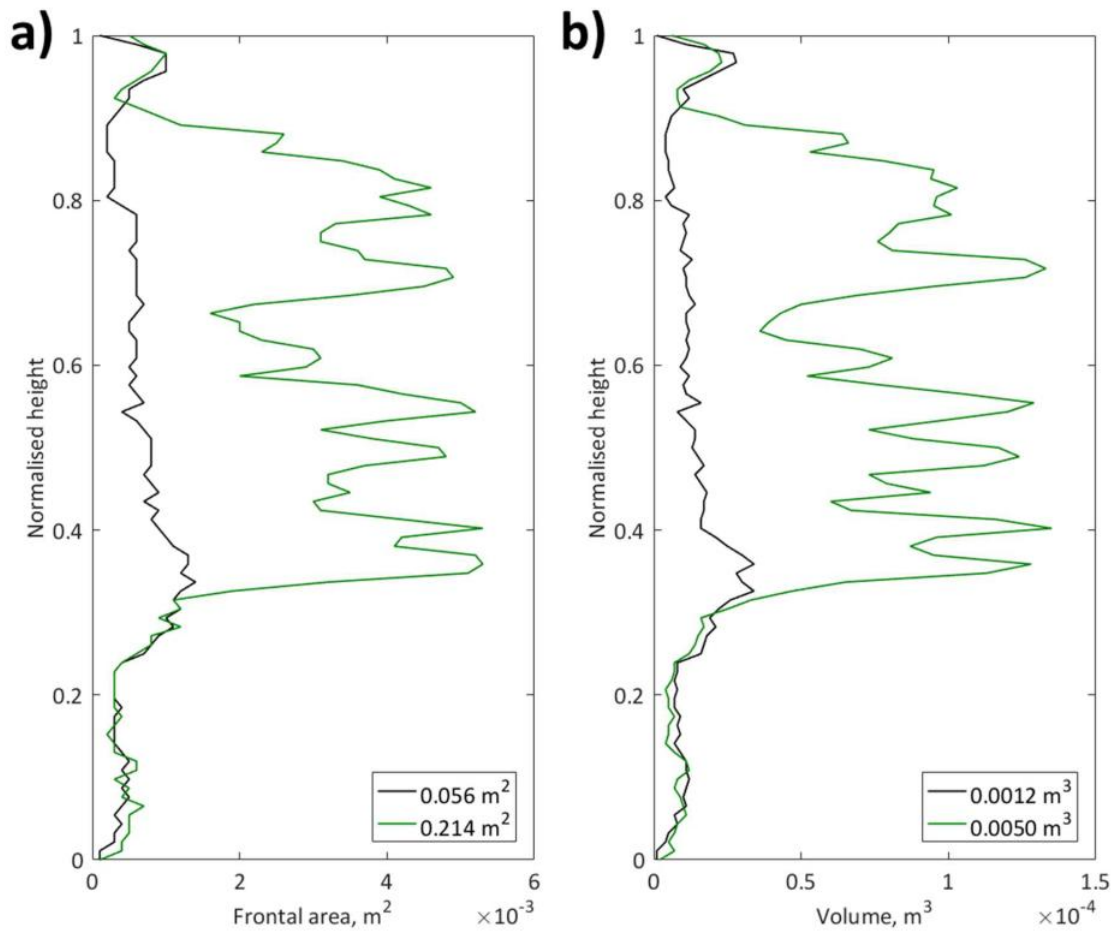
***Figure 3.25** Vertical distribution of (a) frontal area and (b) volume for the defoliated and foliated voxelised representations. Total plant areas and volumes are shown in each of the legends.*
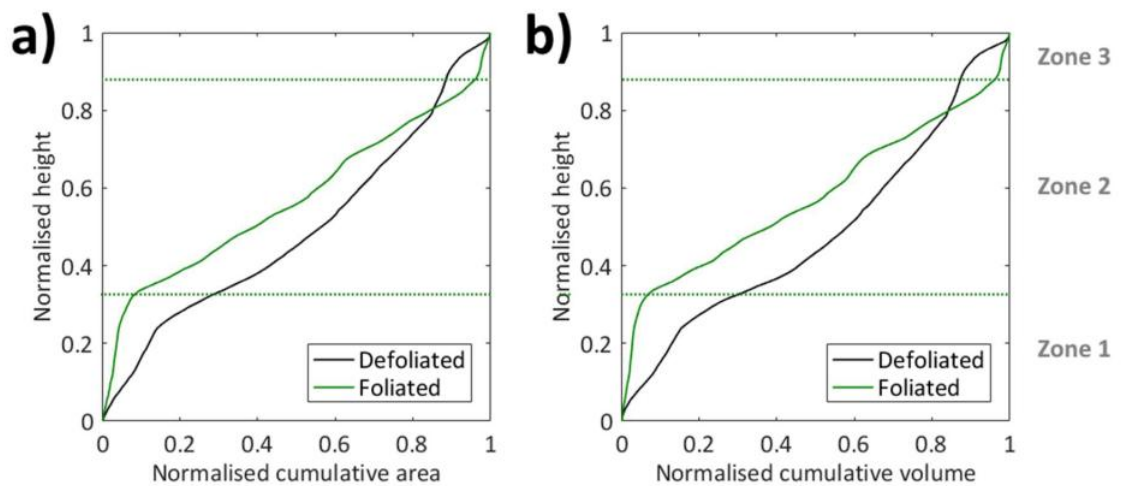


***Figure 3.26** (a) Normalised cumulative area and (b) volume plotted against normalised height for the defoliated and foliated voxelised plant representations. Annotated zones are shown for the foliated plant only.*

### 3.4.1.4          Volumetric blockage factor and plant solid volume fraction

Relevant to open channel flows where vegetation is present, the blockage factor has been defined in several ways, including the proportion of the plan surface area containing vegetation, $B^{SA}$, the proportion of a cross-section containing vegetation, $B^X$, or most relevant to this application, the proportion of the volume containing vegetation, $B^V$ (Fisher, 1992).  A blockage factor is useful because it can be applied to a range of spatial scales to account for patchiness and spatial variability of vegetation, and has been used to predict vegetative resistance from field measurements (Green, 2005a).  Using a TLS-derived point cloud of a vegetated floodplain, Jalonen *et al.* (2014) estimate the volumetric blockage factor for different water levels, and relate this back to Manning's *n*, with results dependent on the spatial resolution of the point clouds.  Because of this sensitivity to the spatial resolution of the point cloud, for hydraulic studies at the plant-scale, Jalonen *et al.* (2014) recommend methods other than the volumetric blockage factor, namely: applying leaf area index (Antonarakis *et al.*, 2010), or additional methods that use estimates of vegetation density from the proportion of intercepted returns from the laser pulse (Straatsma *et al.*, 2008).  With correct data capture, however, here it is shown that volumetric blockage factor concept can be a useful tool for characterising the spatial structure of plants.  This is especially relevant where an improved description of plant architecture is required in three-dimensional hydraulic modelling studies (Weissteiner *et al.*, 2013).

The volumetric blockage factor concept is extended and used to calculate the solid volume fraction of the plant for each of the voxelised representations.  Following Weissteiner *et al.* (2013), porosity can be defined by fitting a reference volume (bounding box) around the plant as shown in Figure 3.27a.  First, this reference volume can be defined as a rectangular cuboid volume occupied by the plant ($V_{RC}$), following:

$$V_{RC} = h_{tot}\, W_{\text{max}\_x}\, W_{\text{max}\_y} \tag{3.1}$$

where $h_{tot}$ is the total height of the plant (m), $W_{\text{max}\_x}$ is the plant width on the *x*-axis (m), and $W_{\text{max}\_y}$ is the plant width on the *y*-axis (m).  Using the total plant volume ($V_P$), the porosity ($P_{RC}$) is defined as:

$$P_{RC} = \left(\frac{V_{RC} - V_P}{V_{RC}}\right) \tag{3.2}$$

Secondly, the reference volume can be defined as a cylindrical volume occupied by the plant ($V_C$), following:

$$V_C = \left( \frac{1}{2} \left( \frac{1}{2} \left( W_{\text{max}\_x} + W_{\text{max}\_y} \right) \right) \right)^2 \pi\, h_{tot}$$

(3.3)

with the porosity ($P_C$) then defined as:

$$P_C = 1 - \left( \frac{V_C - V_P}{V_C} \right)$$

(3.4)

In each case, the plant solid volume fraction ($P_{SF\_RC}$ or $P_{SF\_C}$) is calculated following:

$$P_{SF\_RC} = 1 - P_{RC}$$

(3.5)

$$P_{SF\_C} = 1 - P_C$$

(3.6)
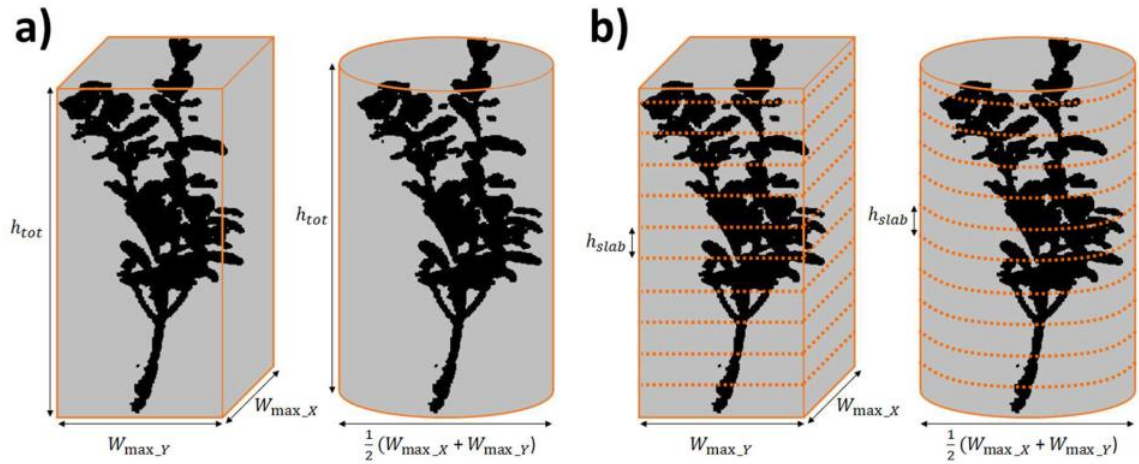


**Figure 3.27 (a) Fitting of reference volumes around the plant, defined as rectangular cuboid or cylinder and (b) slab reference volumes.**

Relevant to the plant-scale (Figure 3.27a), solid fraction volumes are shown in Table 3.4. As shown here, and noted by Weissteiner *et al.* (2013), plant solid volume fractions are similar using both the rectangular cuboid and cylinder reference volumes. When using reference volumes specific to the defoliated and foliated plants, the defoliated plant is shown to have a larger solid volume fraction than the foliated plant, although the foliated plant is more than four times greater volumetrically. This difference in solid volume fraction is attributed to differences in the total reference volumes, caused by

approximately two times greater $W_{\max\_x}$ and $W_{\max\_y}$ values when foliated. To account for these differences in $W_{\max\_x}$ and $W_{\max\_y}$, we use the foliated reference volume to calculate the defoliated plant solid volume fraction, enabling a more useful comparison. In doing so, the defoliated plant is shown to have a solid volume fraction four times smaller than the foliated plant.

**Table 3.4 Comparison of plant solid volume fractions.**

|  | Defoliated (using defoliated $V_{RC}$ and $V_c$) | Defoliated (using foliated $V_{RC}$ and $V_c$) | Foliated (using foliated $V_{RC}$ and $V_c$) |
|---|---|---|---|
| $P_{SF\_RC}$ | 0.110 | 0.018 | 0.078 |
| $P_{SF\_C}$ | 0.102 | 0.021 | 0.090 |

To relate this back to the concept of the volumetric blockage factor, and begin to account for patchiness and spatial variations over the plant height, a spatially distributed plant solid volume fraction is defined. By incrementally splitting the reference volume into smaller slabs of equal height (Figure 3.27b), this allows the calculation of slab reference volumes, that are used to calculate individual slab porosities. By stacking the slabs together, the method allows the spatially distributed plant solid fraction volume to be quantified, useful for the visualisation and identification of changes with plant height (Figure 3.28). In this case, $h_{slab}$ is equal to 0.01 m.
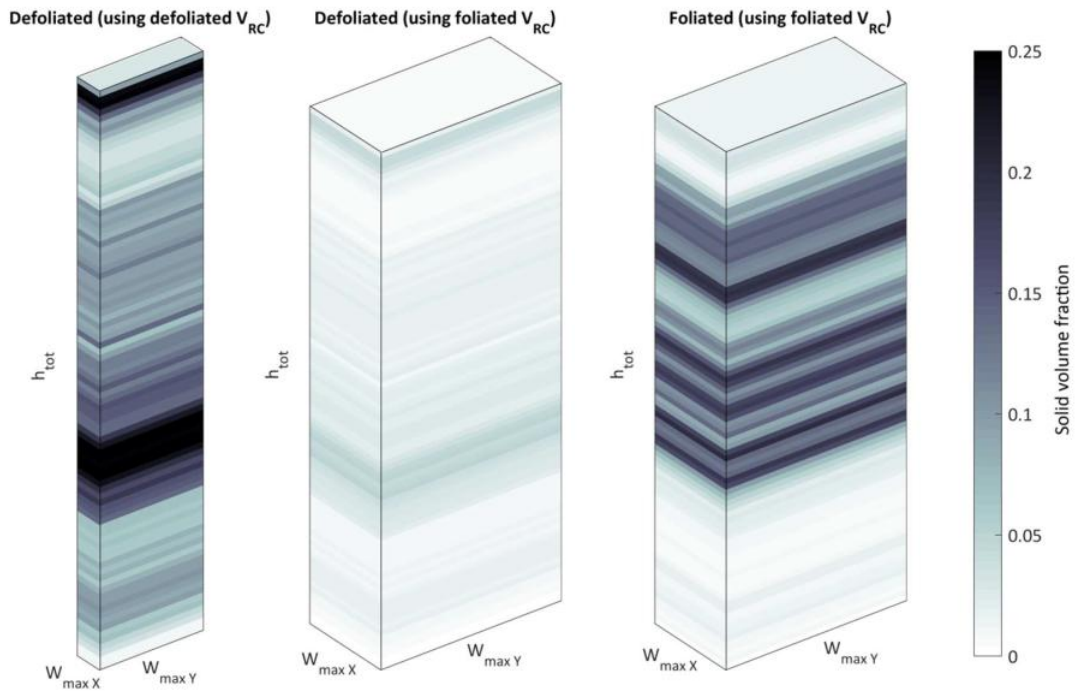
**Figure 3.28 Spatially distributed plant solid volume fraction for the defoliated and foliated plants, where h$_{slab}$ is equal to 0.01m.**

Comparing the spatially distributed solid volume fractions for the defoliated plant using the different reference volumes, defoliated $V_{RC}$ and the foliated $V_{RC}$, the plant clearly has a far smaller solid volume fraction when the reference volume is increased. Only a band of relatively high solid volume fraction (> 0.1) persists around the main branching point, and a second smaller band at the plant tip. The reference volume is therefore crucial when comparing plant solid volume fractions. For the foliated plant, the solid volume fraction differs, with several relatively high (> 0.1) bands distributed throughout the leaf body. Interestingly, the spatially distributed solid volume fraction shows a lack of volume in the near bed region in for both the defoliated and foliated plants, and this may have implications for the partitioning of flow. Righetti (2008) suggests that the plant porosity values, and by extension plant solid volume fraction, remain almost constant over plant height. However, for the *Prunus laurocerasus* plant species analysed here when defoliated and foliated, and for the specimens investigated by Weissteiner *et al.* (2013) and Weissteiner *et al.* (2015); variable porosity and plant solid volume fraction is shown over the plant height. Consequently, plant volumetric canopy morphology will vary between and within plant species, and this will have implications for flow-vegetation interactions.

### 3.4.1.5  Summary

This section has shown how plant structure and form can be characterised from a TLS derived point cloud of an individual *Prunus laurocerasus* plant. It is shown that even when the plant is defoliated, a complex plant structure exists, as demonstrated through the spatially distributed crown width, frontal area, volume, and plant solid volume fraction. With the addition of the leaf body, further complexity in plant structure is shown, due to the contribution from vegetal elements such as stems, branches, and leaves (Aberle and Järvelä, 2015).

Results show that spatial structure of the natural plant differs significantly from the highly idealised or simplified plant structures that are used in flume experiments and numerical models to understand flow-vegetation interactions (Section 2.4). This complex plant volumetric canopy morphology is expected to have major implications for flow-vegetation interactions, as investigated in the subsequent chapters of this thesis.

# 3.5    Quality assurance of the plant representation

The workflow proposed here is mainly applicable to those plants with an open framework, especially those species with visible gaps in the canopy, so that the laser can penetrate the canopy interior to provide a fully three-dimensional representation of volumetric canopy morphology. To assess the extent to which the laser has penetrated the interior of the canopy, and assure the quality of the plant representation, the relative point density is quantified for two plant species with different morphologies. The first species, *Prunus laurocerasus*, has an upright woody structure, as introduced in Section 3.3.1. The second species, *Hebe odora*, is a riparian shrub with a more rounded structure, as detailed in Section 5.2.1.1. The *Hebe odora* shrub is subsequently used in flume experiments in the thesis (Chapter 5).

### 3.5.1.1    *Prunus laurocerasus* relative point density

A relative point density is calculated by using the voxelised representation, combined with the post-processed plant representation. This is achieved by counting the number of points to fall in each of the individual voxels, and dividing the number of points by the maximum number of points contained in any one voxel over the entire post-processed scan. This returns a relative point density per voxel, with a value between 0 and 1. Using the voxelised representation at a 0.01 m voxel size, which was previously shown adequately represent plant morphology, Figure 3.29 demonstrates the spatial distribution of the relative point density over the three-dimensional extent of the defoliated and foliated plant.
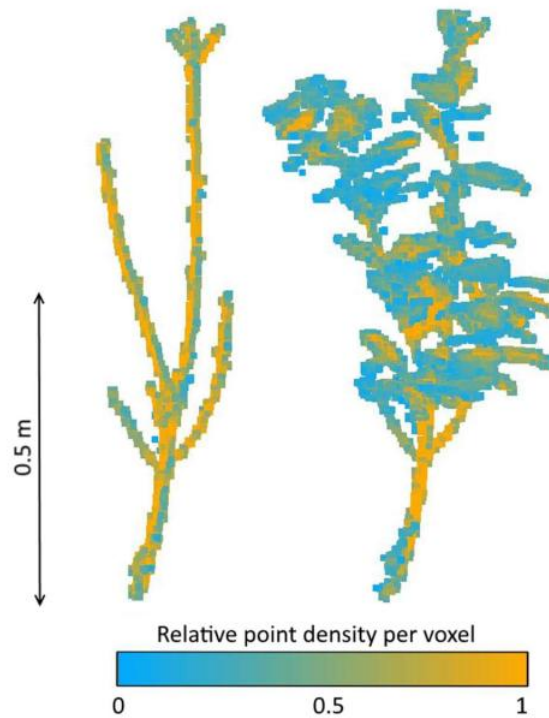
**Figure 3.29 Relative point densities over the defoliated and foliated Prunus laurocerasus plants.**

When defoliated, the centres of individual branches have higher relative point densities. This is to be expected given that branch edges result in fewer point returns due to the size of the laser footprint relative to the feature scanned (Liang *et al.*, 2016), and so a lower relative point density is recorded. When foliated, a more complex spatial pattern in the relative point density is shown, with lower relative point densities recorded on leaf elements, and higher values at the centre of branches, specifically around the main branching point. For the defoliated and foliated plants, the occlusion effects are shown to be minimal. Applying the workflow developed in this thesis, the open framework of the *Prunus laurocerasus* plant lends itself to a full three-dimensional representation.

### 3.5.1.2 *Hebe odora* relative point density

To further test the quality assurance, the same method is applied to a different plant species. The rounded *Hebe odora* shrub has a different morphology than the upright, woody *Prunus laurocerasus* plant. The *Hebe odora* shrub is smaller, with a height of 0.22 m, a diameter of 0.20 m, and a denser leaf structure consisting of small glossy leaves (< 0.02 m) that are distributed in uniform whorls along complex stems (Figure 3.30a). The *Hebe odora* shrub therefore has a less open framework than the *Prunus laurocerasus* plant, providing more challenging conditions to apply the workflow.
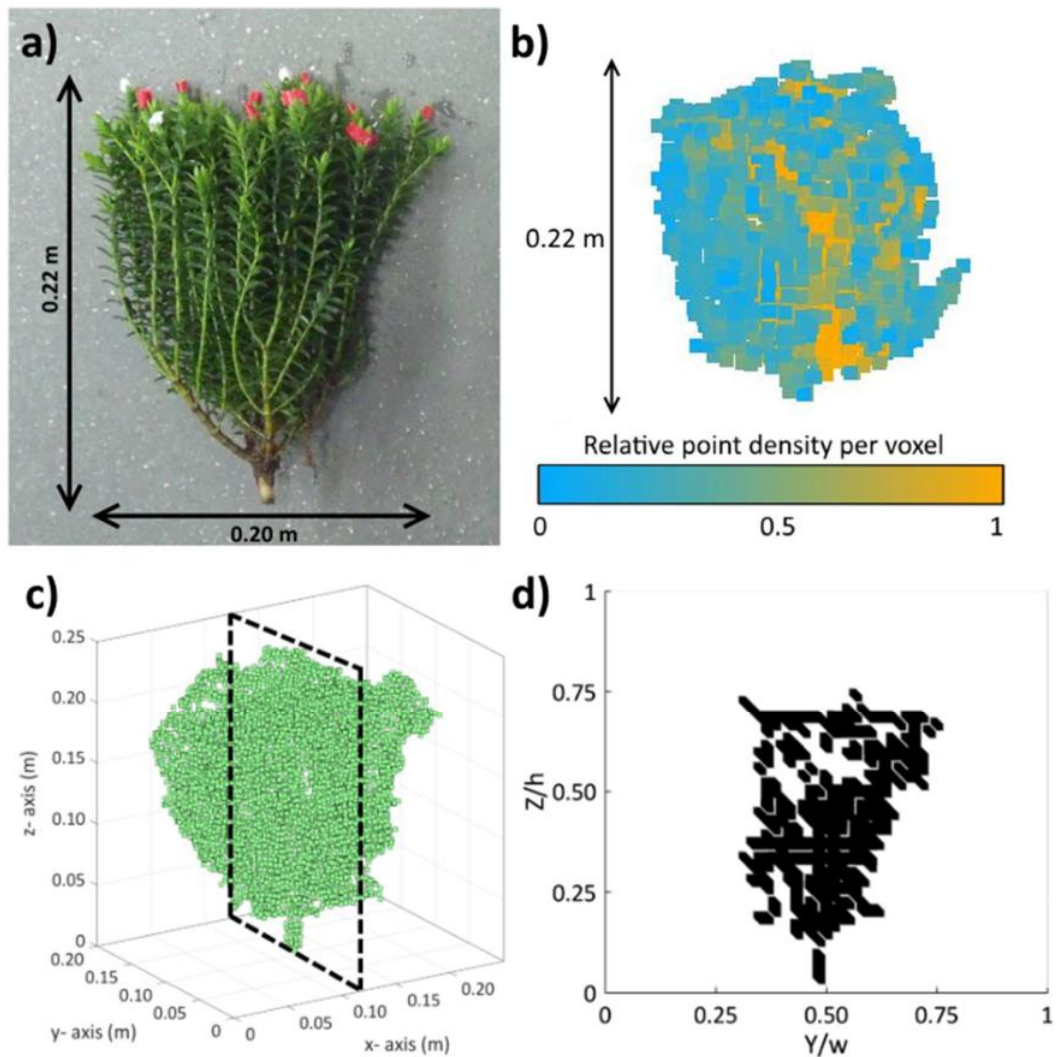
*Figure 3.30 (a) Photograph of the Hebe odora plant, (b) the relative point density, (c) three-dimensional overview of the voxelised representation with the dashed box indicting the position of slice (d), a section through the centre of the plant, showing the internal structure resolved.*

Despite these challenges, however, a similar pattern in the relative point density to the *Prunus laurocerasus* is recorded (Figure 3.30b). The interior of the plant is still characterised by high relative point densities (> 0.5). It therefore appears that occlusion is minimal, even for a smaller, rounded shrub with denser foliage, as the internal structure remains well represented (Figure 3.30c and Figure 3.30d).

For the two specimens shown here, *Prunus laurocerasus* (an upright, woody plant with an open framework) and *Hebe odora* (a rounded riparian shrub with denser foliage), a complete three-dimensional representation can be resolved. By following the best practice in applying TLS to capture plant volumetric canopy morphology and applying the workflow developed throughout this chapter, a quality plant representation is collected, and this can be readily incorporated into the CFD model.

## 3.6      Chapter summary and conclusions

Based on a literature review, this chapter has established that Terrestrial Laser Scanning (TLS) can be used to capture three-dimensional measurements of plant structure and form at an unprecedented resolution, with millimetre scale spatial accuracy. Relevant to the specific requirements of this thesis, TLS satisfies the criteria outlined in Table 3.1, and therefore it is suggested to be the most appropriate measurement technique. With application of the workflow developed in this chapter (Figure 3.23), quantification of plant volumetric canopy morphology is made possible, to address RQ1 and thesis objective (i).

The workflow developed in this chapter takes a high resolution, three-dimensional point cloud of a single plant containing millions of individual data points, post-processes this to remove erroneous data points, and then simplifies it whilst retaining the morphological structure of the plant through a voxelisation procedure. This voxelised representation can then be readily incorporated into a CFD model scheme, as discussed in Chapter 4.

The final section of this chapter has shown how plant structure is quantified from the voxelised plant representations, to derive a spatially explicit distribution of vegetal elements. This ranges from relatively simple metrics such as crown width, through to more complex metrics including the plant solid volume fraction. The spatial distribution of these metrics indicate that spatial structure of natural plants is complex, and differs significantly from the highly idealised or simplified plant structures that are frequently used in flume experiments and numerical models, used to gain the current understanding flow-vegetation interactions (Section 2.4). Complex plant volumetric morphologies are therefore expected to have major implications for flow field dynamics.

To assess this influence, the next chapter describes how the plant volumetric canopy morphology is incorporated in the CFD model, to further support RQ1 and address thesis objective (ii). Following this, by combining flume experiments and numerical modelling, flow-vegetation interactions are investigated for the *Hebe odora* shrub in Chapter 5, and the *Prunus laurocerasus* plant in Chapter 6, in support of RQ2 – RQ5, and thesis objectives (iii and iv).

# Chapter 4

# Model development, initial application, and testing

## 4.1      Introduction

The previous chapters have discussed the importance of flow-vegetation interactions at the plant-scale (Chapter 1 and Chapter 2), and the ability to capture, represent, and characterise the volumetric canopy morphology of floodplain and riparian plants using TLS (Chapter 3).   Bringing these elements together, the focus of this chapter is the development, initial application, and testing of a high resolution numerical model that incorporates realistic plant representations, and can accurately predict three-dimensional mean and turbulent flow.  This supports RQ2 and thesis objective (ii).  The chapter will show how the voxelised plant representations that were produced in Section 3.3 are discretised in a Computational Fluid Dynamics (CFD) model, enabling full flow field predictions to be made.

Here, a commercially available, three-dimensional CFD package called Parabolic, Hyperbolic Or Elliptic Numerical Integration Code Series (PHOENICS) is used to model flow-vegetation interactions at the plant-scale.  PHOENICS (64 bit software, from CHAM, 2013) has the advantage over other CFD packages in allowing bespoke code to be developed and applied (as described in Section 4.3.4.2), and this helps to investigate specific problems.  The software has previously been used to simulate complex open channel flows at the sub-reach scale in fluvial geomorphology applications, including confluences (Bradbrook *et al.*, 1998), meander bends (Ferguson *et al.*, 2003), and flows over heterogeneous gravel surfaces (Hardy *et al.*, 2007).

Although initially applied to fluvial systems, the complexity of the application has been increased to consider ecohydraulics, with CFD models used to investigate the dynamics of fish locomotion (Borazjani and Sotiropoulos, 2009), the effective design of spoiler baffle geometries that aid fish passage through circular culverts (Feurich *et al.*, 2012),

turbulent structures over clusters of mussels (Constantinescu *et al.*, 2013), and to describe fish passage at confluences (Andersson *et al.*, 2016). Highly relevant to this thesis, high resolution flow-vegetation interactions at the patch- and canopy-scale have also been investigated using PHOENICS (Marjoribanks *et al.*, 2014c; Marjoribanks *et al.*, 2016).

Application of CFD to understand flow-vegetation interactions is useful for two main reasons. Firstly, CFD can be used to provide flow field predictions for a range of plant morphologies and hydraulic boundary conditions, thereby improving the process-understanding. The spatial richness and coverage of the predicted flow field far exceed what is feasibly obtainable from flume and field studies, and this aids the insight and understanding of complex flows (Bates, 2005). Secondly, these flow field predictions are useful when considering the drag response and vegetative flow resistance, which are notoriously difficult to quantify (Marjoribanks *et al.*, 2016). Application of CFD allows physically determined, species-specific, plant drag terms to be converted back into resistance coefficients that are commonly applied to conveyance estimation systems and industry standard hydraulic models. High resolution CFD predictions of flow-vegetation interactions can therefore be used to inform an improved process representation in lower resolution models, useful to a range of practitioners.

Section 4.2 first provides an overview of the numerical representation of open channel flows. This involves solving the Navier-Stokes equations, and with decreasing levels of complexity, discusses time-dependent and time-averaged (or Reynolds-averaged) solutions. A justification for the numerical representation of open channel flow is then outlined. Following this, initial application is undertaken in Section 4.3. Model specifications are provided, including flow solver mechanics, spatial discretisation, boundary conditions, and a detailed description of how the plant is conceptualised and discretised into the model. A discussion of good modelling practice, with a specific focus on model verification and validation follows. In Section 4.4, sensitivity analysis to the hydraulic boundary conditions is undertaken. Finally, a description of the method used to calculate drag and vegetative resistance is given (Section 4.5).

## 4.2 Numerical representation of open channel flows

### 4.2.1 Properties of open channel flows

Water modelled in open channel flows is an incompressible, Newtonian fluid, meaning that the shear stress is proportional to the velocity gradient (Anderson, 1995). At the scale of interest relevant to this thesis, the density and viscosity of water are assumed constant, as is expected under the temperature limits of a natural channel.

The governing equations for open channel flows are based on the assumption that the density of the fluid can be approximated as a continuum (Tritton, 1988), relating the molecular structure to the overall flow characteristics (Lane, 1998). Eulerian transformation of the Newtonian laws is used to describe fluid motion, treated as an arbitrary volume that moves through time and space (Versteeg and Malalasekera, 1995; Pope, 2000). Important flow variables such as velocity, pressure, temperature, and density can therefore be defined for each point of the fluid, in their time/space derivative (Blazek, 2005).

In shallow open channel flows, where the ratio of roughness height to flow is typically less than 10, the effects of topography extend throughout the flow depth (Lane *et al.*, 2005). Topography exerts friction at the channel boundaries through a no-slip condition, with a zero-velocity at the fluid-channel interface (Anderson, 1984). Additionally, this topography acts as a physical blockage to flow, over a variety of spatial scales (Section 2.3.1); this results in flow separation and the generation of turbulence, relevant for momentum loss in these systems. Here it is hypothesised that vegetation can be viewed as an extension of topography, exerting friction and acting as a physical blockage to the flow (see detailed description in Section 4.3.4).

Turbulence is a complex fluid motion concerned with the transfer of energy to smaller spatial scales. The turbulent nature of flow is characterised through the Reynolds (*Re*) number, as the non-dimensional ratio of inertial to viscous forces, shown in Equation 2.2 in Chapter 2. When *Re* > 2000, flow is considered turbulent (Graf and Yulistiyanto, 1998). Markatos (1986) characterises a fluid motion as turbulent "if it is three-dimensional, rotational, intermittent, highly disordered, diffusive and dissipative". Turbulent flows have been characterised by their spatially and temporally chaotic nature, having a very complex structure (Devaney, 1989). Turbulent motion consists of a wide

range of eddy sizes, with kinetic energy passed along the energy cascade as large-scale eddies generate smaller eddies, which are eventually damped by viscous forces (Figure 4.1). The largest eddies contain most of the energy, and are most effective in the transfer process along the cascade (Rodi, 2017).
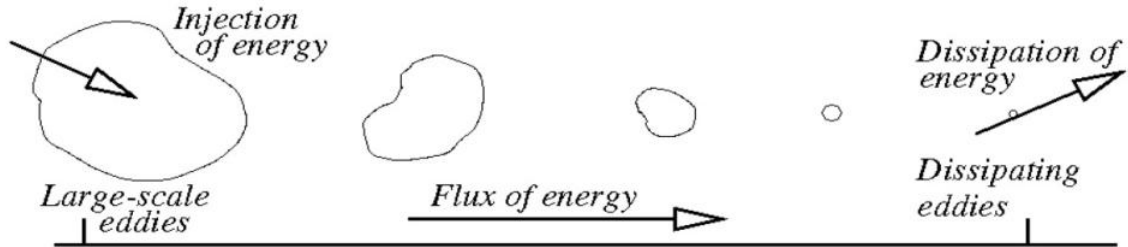


**Figure 4.1 The energy cascade of turbulent motion, fllux of energy from left to right, taken from Bakker (2008).**

## 4.2.2    The Navier-Stokes equations (NS)

The Navier-Stokes equations are a fundamental set of partial differential equations that are used to describe the motion of incompressible fluids in three dimensions. The equations are composed of a momentum equation (4.1) and a mass or continuity equation (4.2) for Newtonian fluids (Lane, 1998). The equations must satisfy the fundamental conservation laws of physics, namely the conservation of mass, momentum, and energy. Although the Navier-Stokes equations can be written in several different forms; here the Einstein summation convention is used:

$$\rho \left( \frac{\partial u_i}{\partial t} + u_j \frac{\partial u_i}{\partial x_j} \right) = -\frac{\partial p}{\partial x_i} + \mu \left( \frac{\partial^2 u_i}{\partial x_j x_j} \right) + F_i \qquad (4.1)$$

$$\frac{\partial u_i}{\partial x_i} = 0 \qquad (4.2)$$

where $\rho$ is the fluid density (kg m$^{-3}$), $\mu$ is the dynamic viscosity (Kg m$^{-1}$ s$^{-1}$), $p$ is the pressure (Pa), $t$ is time (s), $u_i$ is the instantaneous velocity component (m s$^{-1}$) in the $x_i$ direction (m), and $F_i$ represents additional forces on the flow, also known as the source term. Because it is rarely possible to solve the Navier-Stokes equations analytically at the *Re* numbers associated with natural river systems, numerical methods must be applied (Ferziger and Perić, 2002). The numerical methods are subdivided into time-averaged (or Reynolds-averaged) and time-dependent solutions.

The Navier-Stokes equations can be semi-empirically analysed to assess the effects of turbulent motions on the mean properties of the flow (Rodi, 1993; Lane, 1998). Turbulence fluctuations in the velocity signal are described as an instantaneous variation about a time-average, through Reynolds-decomposition (Reynolds, 1895):

$$u_i = \bar{u}_i + u'_i \qquad (4.3)$$

where $u_i$ represents the instantaneous value of velocity (m s$^{-1}$), $\bar{u}_i$ represents the time-averaged value (m s$^{-1}$), and $u'_i$ is the time-variant or fluctuating component (m s$^{-1}$). The Reynolds-decomposition can then be substituted back into the time-averaged Navier-Stokes equations. Reynolds-averaging of the Navier-Stokes equations (RANS) therefore removes the time-dependent terms, but in doing this, extra terms appear (called Reynolds stresses) and these need to be linked to properties of the time-averaged flow using turbulence models (Versteeg and Malalasekera, 1995; Keylock *et al.*, 2005). This is further discussed in Section 4.2.4. RANS methods are routinely applied in practical hydraulic flow calculations, providing a quantification of the average flow (Rodi, 2017).

Solving the time-dependent Navier-Stokes equations, Direct Numerical Simulation (DNS) resolves all scales of turbulent motions (Rodi, 2017). However, the computational expense is enormous and not possible at the *Re* numbers of interest to this thesis. Computationally less expensive, but still capable of solving the time-dependent Navier-Stokes equations, Large Eddy Simulation (LES) resolves only the larger turbulent motions that contain most of the energy, accepting that smaller scales of turbulence can be represented by a sub-grid scale model (Versteeg and Malalasekera, 1995). LES therefore involves space-filtering of the time-dependent Navier-Stokes equations, and is viewed as an intermediate form of turbulence calculation between DNS and RANS.

Numerical predictions are not always improved by using more complex models (Lane, 1998), and therefore when selecting a numerical representation of open channel flow, it is necessary to make a choice of the processes that need to be represented. In many cases, it is unnecessary to resolve the details of the instantaneous turbulence fluctuations, with information about the time-averaged properties of the flow (e.g. mean velocity and mean pressure) often sufficient (Versteeg and Malalasekera, 1995).

Over the next sections, the different approaches for solving the Navier-Stokes equations are shown. These are ordered by complexity, starting with the most complex time-dependent solutions, moving through to Reynolds-averaged solutions. Having reviewed the available approaches, justification for the numerical representation of open channel flow that is used in this thesis is provided (Section 4.2.5).

## 4.2.3 Time-dependent solutions

### 4.2.3.1 Dynamic numerical simulation (DNS)

Theoretically, the most fundamental method for solving the Navier-Stokes equations involves resolving all spatial and temporal scales of turbulence, and is referred to as direct numerical simulation (DNS). As a result, the turbulence resolved would range in spatial and temporal scale from large, low frequency turbulent eddies associated with momentum exchange; through to the smallest, high frequency eddies involved with dissipation and molecular heat transfer, as controlled by viscous forces (Sotiropoulos, 2005). DNS therefore differs from most other approaches in removing the need for sub-grid scale turbulence models that are often based upon approximations, resolving all scales of turbulence (Figure 4.1). Using DNS, the time-dependent Navier-Stokes equations are numerically solved using spectral and pseudospectral techniques (Ingham and Ma, 2005). In resolving the smallest scales of turbulence for all points in space, at all points in time, a very large number of grid cells are required.

DNS approaches therefore tend to be limited in application to simple yet fundamental flow problems. These include the investigation of near wall turbulence in channel flows (Kim *et al.*, 1987; Moser *et al.*, 1999; Hoyas and Jiménez, 2006), and have been extensively applied to flows with turbulent boundary layers (Spalart, 1988; Schlatter and Örlü, 2010; Sillero *et al.*, 2011). DNS has also been used to model flow around bluff body objects, including flow past a fixed cylinder (Braza *et al.*, 1986; Braza *et al.*, 1990; Ma *et al.*, 2000), rigidly-oscillating cylinders (Mittal and Tezduyar, 1992), flexible cylinders (Evangelinos and Karniadakis, 1999), and pairs of cylinders (Papaioannou *et al.*, 2006).

However, difficulties are experienced when applying DNS to geometrically complex topographies, and high Reynolds number flows. Complex topography requires explicit representation in the model, which requires a finer grid size to capture the smallest turbulence scales (Ingham and Ma, 2005). In addition to topographic complexity, a higher Reynolds number flow also requires a finer grid size (Rogallo and Moin, 1984;

Argyropoulos and Markatos, 2014).  As the Reynolds number increases, the range of eddies with significant turbulence dissipation also increases (Keylock *et al.*, 2005).  For topographically complex and/or high Reynolds number flows, the computational expense required for the fine cell treatment can prove prohibitive (Rodi, 2017).  This means that it is rarely possible to apply DNS in practical applications.

### 4.2.3.2 Large Eddy Simulation (LES)

A modelling approach that promises greater accuracy than RANS, yet reduced computational expense than DNS, is referred to as Large Eddy Simulation (LES).  Unlike RANS approaches, LES retains a time derivative, and can therefore be employed to give time-dependent solutions (Keylock *et al.*, 2005).   LES enables analysis of the instantaneous flow field, and investigation of unsteady flow structures.   RANS approaches may not fully describe, or can misinterpret, these flow structures due to temporal averaging (Lane *et al.*, 1999), and therefore LES can provide improved descriptions of complex turbulent flow structures.

The premise of LES is to fully and explicitly resolve large eddies, whilst smaller eddies are implicitly accounted for by a sub-grid scale (SGS) model (Versteeg and Malalasekera, 1995).  Where the large scale anisotropic eddies are generally associated with greater energy, and are therefore more effective transporters of the conserved properties than the smaller, isotropic counterparts; it follows that larger eddies should be more exactly treated (Ferziger and Perić, 2002).  Additionally, these large scale eddies are associated with greater variation and momentum, whereas smaller eddies are assumed to be more universal (Rogallo and Moin, 1984).  To separate the resolved from the unresolved component, a filtering process is required.  Therefore, unlike RANS modelling which involves decomposing the velocity signal into a mean and fluctuating term, LES is concerned with separating the velocity signal into a resolved and unresolved component, following:

$$u = \langle u \rangle + \tilde{u} \qquad (4.4)$$

where $\langle u \rangle$ is the resolved component (m s$^{-1}$), and $\tilde{u}$ is the unresolved component (m s$^{-1}$) which require sub-grid scale treatment, and are implicitly modelled.  A range of different filters can be applied to perform this separation (Pope, 2000).  Once separated, SGS models approximate energy exchange between the grid and the sub-grid scales (Rogallo

and Moin, 1984). Commonly applied SGS models include the eddy-viscosity based Smagorinsky (1963) model, the Scale Similarity model proposed by Bardina *et al.* (1980), and the Wall Adapting Local Eddy Viscosity model proposed by Nicoud and Ducros (1999).

Each model has its own strengths and weaknesses (see Keylock *et al.* (2005) and Keylock *et al.* (2012) for reviews), however, an underlying limitation exists throughout all SGS models, in that SGS model accuracy is highly dependent on the relationship between scales of turbulence present, and the grid size used to solve the flow. Computational constraints in LES, especially from the complex boundaries that are associated with natural river systems, often mean that coarser grids are required. This raises the importance of SGS model performance (Rodi *et al.*, 1997), and if the SGS model miscalculates the energy exchange, numerical diffusion errors can exceed the sub-grid stresses in magnitude, casting doubt on the legitimacy of LES simulations (Bernard and Wallace, 2002). Grid resolution and selection of an appropriate SGS model can directly impact upon the solution. Furthermore, grid resolution is shown to be especially important for the correct temporal reproduction of flow structures. Grids of different resolutions produce only small differences in the flow structures in time-averaged simulations, but substantial differences when time-dependent structures are considered (Hardy *et al.*, 2003). LES is therefore not always the most suitable approach.

## 4.2.4　　　Reynolds-averaged solutions

The Navier-Stokes equations can be semi-empirically analysed to assess the effects of turbulent motions on the mean properties of the flow (Lane, 1998). The Reynolds-decomposition (4.3) can be substituted back into the Navier-Stokes equations, and after applying ensemble averaging, results in the momentum (4.5) and mass or continuity (4.6) equations:

$$\frac{\partial \bar{u}_i}{\partial t} + \bar{u}_j \frac{\partial \bar{u}_i}{\partial x_j} = -\frac{1}{\rho}\frac{\partial \bar{p}}{\partial x_i} + \frac{1}{\rho}\frac{\partial}{\partial x_j}\left(\mu \frac{\partial \bar{u}_i}{\partial x_j} - \rho \overline{u'_i u'_j}\right) \tag{4.5}$$

$$\frac{\partial \bar{u}_i}{\partial x_i} = 0 \tag{4.6}$$

However, following Reynolds-decomposition of the Navier-Stokes equations, convective

acceleration terms associated with the products of $u'_i$ result in the production of extra terms (Rodi, 1993). These additional unknown terms are no longer balanced, and therefore the Reynolds-averaged Navier-Stokes equations are not fully closed (Olson and Wright, 1990). The need for closure originates from the number of unknown quantities (pressure, velocity in three dimensions, and six stresses) being greater than the number of available equations (Argyropoulos and Markatos, 2014). This unknown term is called the Reynolds stress, $\tau_{ij}$ ((m s$^{-1}$)$^2$):

$$\tau_{ij} = u'_i u'_j \tag{4.7}$$

and represents the transport momentum that can attributed to turbulence, is symmetric, and has six stress components (Ingham and Ma, 2005). This cannot be directly calculated, and therefore to solve the mean flow, an approximation is required. Closure can be achieved where models relate the Reynolds stress to the global properties of the fluid in a physically consistent manner (Ingham and Ma, 2005). This frequently involves linking the Reynolds stresses to the time-averaged flow properties (Keylock *et al.*, 2005), using the Boussinesq (1877) approximation.

Using this approach, Reynolds stress is proportional to the mean rate of strain, following the eddy viscosity principle. For this, turbulent eddies are visualised as parcels of fluid that exchange momentum. However, the analogy is limited where in reality turbulent eddies are highly complex and can be spatially inconsistent (Devaney, 1989). Acknowledging these limitations, the eddy viscosity concept has worked well in practice, and therefore is frequently used in turbulence models, where the relationship is formulated as:

$$-\overline{u'_i u'_j} = v_t \left( \frac{\partial \bar{u}_i}{\partial x_j} + \frac{\partial \bar{u}_j}{\partial x_i} \right) - \frac{1}{3} k \delta_{ij} \tag{4.8}$$

where $v_t$ is the eddy viscosity (m$^2$ s$^{-1}$), a proportionality coefficient between the Reynolds stresses and the mean velocity gradients that is dependent on the local degree of turbulence, $k$ is the turbulent kinetic energy (TKE, m$^2$ s$^2$), and $\delta_{ij}$ is the Kronecker delta function (-) which ensures the equation is valid for normal tension. The instantaneous turbulent kinetic energy, $k$ (m$^2$ s$^{2)}$, is calculated following:

$$k = \frac{1}{2}(u'^2 + v'^2 + w'^2) \tag{4.9}$$

It is the different methods for calculating eddy viscosity, the product of turbulent length scale, $l_t$ (m), and turbulent velocity scale, $u_t$ (m s$^{-1}$), that define the different turbulent closure models. In such models, the eddy viscosity is assumed to be an isotropic scalar quantity, which is incorrectly assumed in areas of anisotropic turbulence. Moreover, where the local degree of turbulence varies throughout flow depth, it is important to recognise that eddy viscosity will also vary, where Rodi (1993) suggests open channel flows show a parabolic shaped eddy viscosity distribution. In reality, therefore, the distribution of eddy viscosity will be complex, and linked to the local flow conditions (Bradbrook, 2000). The different methods for calculating eddy viscosity, the basis of different turbulence closure models, are discussed in the following sections.

### 4.2.4.1    Reynolds stress models

The turbulence closure model with the highest level of complexity is associated with Reynolds stress models (RSMs, otherwise known as differential second-moment or algebraic stress models). These schemes offer the most physically complete closure model, where history, transport, and anisotropy of the turbulence are all explicitly accounted for (Ingham and Ma, 2005). Notably, the recognition of anisotropic turbulence contrasts with simpler one- and two-equation models whereby turbulence is assumed isotropic following the eddy viscosity principal. Therefore, instead of approximating Reynolds stress, this scheme explicitly employs transport equations for the individual Reynolds stresses (Launder *et al.*, 1975). The superiority of RMSs over eddy-viscosity methods has been demonstrated for curved, swirling, and recirculating flows (Leschziner, 1990; Hanjalić, 1994), where the transport equation of $-\overline{u'_i u'_j}$ can be qualified as:

$$L_{ij} + C_{ij} = P_{ij} + \phi_{ij} + D_{ij} - \varepsilon_{ij} \tag{4.10}$$

where $L_{ij}$ is the local change in time (-), $C_{ij}$ is the convective transport (-), $P_{ij}$ is the production of mean flow deformation (-), $\phi_{ij}$ is the stress redistribution tensor due to pressure strain (-), $D_{ij}$ is the diffusive transport (-), and $\varepsilon_{ij}$ is the viscous dissipation tensor (-) (Ingham and Ma, 2005).

However, owing to the complex nature of the second-order closure model, implementation and numerical convergence can be difficult to achieve (Ingham and Ma, 2005). RSMs can suffer from convergence problems because of issues coupling the mean flow and turbulent stress fields through source terms (Versteeg and Malalasekera, 1995). A further consideration is the computational cost associated with these schemes, where Hanjalić (2004) estimates the computational demands of RSM to be approximately twice that of less complex two-equation models (Section 4.2.4.2).

### 4.2.4.2        Two-equation models

Two-equation models involve solving transport equations to derive a transportable mixing length scale (Versteeg and Malalasekera, 1995). This means transport processes can be treated in a similar way to the velocity scale (Rodi, 1993). These additional transport equations account for the spatial variation of the length scale, necessary where the characteristic eddy size would vary downstream due processes in the energy cascade (Rodi, 1993). Namely, eddy dissipation which acts to destroy small eddies, thus increasing the characteristic eddy size, and vortex shedding which acts to effectively reduce the characteristic eddy size. Unlike simpler one-equation (Section 4.2.4.3) and zero-equation models (Section 4.2.4.4), the characteristic length and timescales of turbulence are determined directly from the flow, rather than *a priori*. This is especially important where topography dominates the turbulence response over near-wall turbulence, as is the case for shallow open channel flows. To date, the most commonly used models are the $k-\omega$ and $k-\varepsilon$ models. The transport equations are written for the turbulent kinetic energy, $k$, and either the viscous energy dissipation, $\varepsilon$ (m$^2$ s$^{-3}$), or the specific dissipation rate, $\omega$ (m$^2$ s$^{-3}$), where $\omega = k/\varepsilon$.

### 4.2.4.2.1        k − ω model

The $k-\omega$ model is analogous to the $k-\varepsilon$ model in many respects, although a key difference exists where the transport equations are based on the specific dissipation rate, $\omega$, conceptualised as the ratio of $k$ to $\varepsilon$; rather than the viscous dissipation rate, $\varepsilon$, alone. The $k-\omega$ model also includes a low Reynolds number extension for the near wall turbulence, so does not require any additional approximations for wall functions (Ingham and Ma, 2005). This means that the $k-\omega$ model can be integrated over the viscous sublayer, without the application of additional damping functions (Wilcox,

2006). The eddy viscosity, $v_t$ (m$^2$ s$^{-1}$), turbulent kinetic energy, and specific dissipation rate equations can be written following:

$$v_t = \frac{k}{\omega}$$ (4.11)

where the velocity scale becomes $u_t = \sqrt{k}$ and the length scale becomes $l_t = \sqrt{k}/\omega$. Although the $k - \omega$ model produces accurate flow predictions for fully turbulent flows and boundary layers with adverse pressure gradients, weaknesses exist for predicting the flow of free-stream boundaries, where a build-up of turbulent viscosity proximal to stagnation points has been found (Ingham and Ma, 2005).

### 4.2.4.2.2    k − ε model

The standard $k - \varepsilon$ model was first proposed by Launder and Spaulding (1972) and is the most frequently used of all two-equation models in geomorphological applications. Eddy viscosity is specified following:

$$v_t = \frac{k^2}{\varepsilon}$$ (4.12)

where the velocity scale becomes $u_t = \sqrt{k}$ and the length scale becomes $l_t = k^{2/3}/\varepsilon$. This can be substituted into the turbulence kinetic energy and turbulence dissipation rate equations, with the typically assumed values of the constants provided in Table 4.1.

$$\frac{\partial k}{\partial t} + \bar{u}_j \frac{\partial k}{\partial x_j} = \frac{\partial}{\partial x_j} \left[ \frac{(v + v_t)}{\sigma_k} \frac{\partial k}{\partial x_j} \right] - \varepsilon + \tau_{ij} \frac{\partial \bar{u}_i}{\partial x_j}$$ (4.13)

$$\frac{\partial \varepsilon}{\partial t} + \bar{u}_j \frac{\partial \varepsilon}{\partial x_j} = \frac{\partial}{\partial x_j} \left[ \frac{(v + v_t)}{\sigma_\varepsilon} \frac{\partial \varepsilon}{\partial x_j} \right] + C_{\varepsilon 1} \frac{\varepsilon}{k} \tau_{ij} \frac{\partial \bar{u}_i}{\partial x_j} - C_{\varepsilon 2} \frac{\varepsilon^2}{k}$$ (4.14)

where $\sigma_k$ and $\sigma_\varepsilon$ are the Prandtl numbers for $k$ and $\varepsilon$, respectively. The model is shown to perform well for the prediction of turbulent shear flows, although inaccuracies are noted in turbulent flows with adverse pressure gradients, separation and additional strains; including swirling, curved, or rotating flows (Hanjalić, 2004; Wilcox, 2006).

These inaccuracies result from an underlying assumption of isotropy in the turbulence fluctuations, which result in a large turbulent viscosity (Ingham and Ma, 2005). As a result, for flows with significant mean strain (i.e. separation zones), an under-prediction of separation zone length is produced when applying the $k - \varepsilon$ model (Lien and Leschziner, 1994).

### 4.2.4.2.3 Renormalization Group $k - \varepsilon$ model

Following identification of the weaknesses in the $k - \varepsilon$ model under certain turbulence scenarios, Yakhot and Orszag (1986) developed a variation of the $k - \varepsilon$ model based on the Renormalization Group Theory (RNG). Application of the RNG $k - \varepsilon$ model is better suited to flows with a large degree of fluid strain. The RNG $k - \varepsilon$ model is similar to the standard $k - \varepsilon$ model, but uses different values for the constants (Table 4.1), and an additional production term for $\varepsilon$ (Yakhot and Smith, 1992). Importantly, the RNG $k - \varepsilon$ model calculates diffusion across the spectrum of scales, whereas the standard $k - \varepsilon$ model only accounts for diffusion at a single scale (Yakhot and Orszag, 1986). The modified coefficient, $C_{\varepsilon 2}$, in the RNG $k - \varepsilon$ model are represented through:

$$C_{\varepsilon 2} \equiv C_{\varepsilon 2} + \frac{C_\mu \eta^3 \left(1 - \frac{\eta}{\eta_0}\right)}{1 + \beta_1 \eta^3} \tag{4.15}$$

where $\beta$ is evaluated to give a von Karman constant of 0.4 and $\eta_0$ is the fixed point for homogeneously strained turbulent flows:

$$\eta = S \frac{k}{\varepsilon} \tag{4.16}$$

where $S$ is the mean strain rate:

$$S = \sqrt{S_{ij} S_{ij}} \tag{4.17}$$

where $S_{ij}$ is the deformation tensor:

$$S_{ij} = 0.5 \left( \frac{\partial \bar{u}_i}{\partial x_j} + \frac{\partial \bar{u}_j}{\partial x_j} \right) \tag{4.18}$$

Fundamental to the RNG $k - \varepsilon$ model is the role of mean strain rate. Where the mean strain rate is weak, the effect of the additional production term for $\varepsilon$ is small. In contrast, when the mean strain rate is strong, the effect of the additional production term for $\varepsilon$ is greater, thus increasing turbulent dissipation, decreasing the eddy viscosity, and increasing momentum extraction from the mean flow (Bradbrook, 2000). Effectively, this increases the length of the separation zone in model predictions, that may be under-predicted when applying the standard $k - \varepsilon$ model.

**Table 4.1 General constants applied to two-equation models.**

|  | $c'_\mu$ | $\sigma_k$ | $\sigma_\varepsilon$ | $c_{\varepsilon 1}$ | $c_{\varepsilon 2}$ |
|---|---|---|---|---|---|
| $k - \varepsilon$ model | 0.09 | 1.0 | 1.3 | 1.44 | 1.92 |
| RNG $k - \varepsilon$ model | 0.0845 | 0.7194 | 0.7194 | 1.42 | 1.68 |

It should be noted that the constants used in the RNG $k - \varepsilon$ model are obtained theoretically, whereas the constants in the standard $k - \varepsilon$ model have been determined experimentally (Ingham and Ma, 2005). In terms of weaknesses, studies have shown that the RNG $k - \varepsilon$ model fails to predict flows with considerable acceleration (Hanjalić, 2004). However, the RNG $k - \varepsilon$ model is theoretically and empirically superior to the standard $k - \varepsilon$ model in flows with significant mean strain, and Rodi (1993) saw no real benefit of employing more complex RSMs over RNG $k - \varepsilon$ models. Because of these factors, the RNG $k - \varepsilon$ model has become widely adopted in geomorphological CFD applications, and is especially applicable where shearing flow is present in natural rivers (Ferguson *et al.*, 2003; Hardy *et al.*, 2011b).

### 4.2.4.3 One-equation models

At a reduced level of complexity, one-equation models solve only one turbulent transport equation for eddy viscosity. Such models account for the production, transport, and dissipation of a single determinant of eddy viscosity. This additional transport equation is frequently solved using the turbulent kinetic energy per unit mass, $k$. Rodi (1993) states that the most physically meaningful way of characterising velocity fluctuations is through $\sqrt{k}$, a velocity scale that approximates the fluctuating velocity.

This can be related to eddy viscosity using a number of different methods including the Kolmogorov-Prandtl expression (Kolmogorov, 1942; Prandtl, 1945):

$$v_t = c'_\mu \sqrt{kl} \qquad (4.19)$$

where $c'_\mu$ is an empirical constant. More frequently, however, the Spalart-Allmaras model is applied (Spalart and Allmaras, 1994):

$$v_t = \tilde{v} f_{v1} \qquad (4.20)$$

where $\tilde{v}$ is a viscosity-like variable, and $f_{v1}$ is a function of $\tilde{v}$ as well as additional flow properties and a range of empirical coefficients (Deck *et al.*, 2002).

However, the models exaggerate numerical diffusion (Hankin *et al.*, 2001), especially in three-dimensional vortical flows (Gatski and Rumsey, 2002). Much like zero-equation models, the application of one-equation models is limited where the length scales are prescribed from empirical data. Therefore, this is only an *a priori* designation of the characteristic length and timescales of turbulence, and is problematic where the values are highly variable under complex and different flow conditions. Such weaknesses are exaggerated in the case of flows with separation or recirculation, and therefore one-equation models have only a limited applicability in high resolution, process studies; however, one-equation models are often used as the base models in more complex schemes (Koken and Constantinescu, 2016).

### 4.2.4.4 Zero-equation models

Zero-equation, or algebraic models, provide the most basic form of turbulence closure, by specifying both the turbulent length and velocity scales through a single algebraic expression (Sotiropoulos, 2005). A significant disadvantage of zero-equation models compared to one- and two-equation models is that they do not attempt to account for convective and diffusive transport of the velocity scale (Lane, 1998). Partial differential equations are used for modelling the mean fields, and algebraic expressions for turbulence quantities. In a boundary layer flow, according to Prandtl (1925), eddy viscosity is given by the mixing length model:

$$v_t = 2l_t^2 \left| \frac{\partial u_1}{\partial x_2} \right| \tag{4.21}$$

Where $v_t$ is the eddy viscosity, and for isotropic turbulent eddies it follows that velocity scale is proportional to the length scale multiplied by the velocity gradient:

$$\left( u_t = l_t \left| \frac{\partial u_1}{\partial x_2} \right| \right) \tag{4.22}$$

where $u_t$ is the velocity scale. The Prandtl (1925) method therefore assumes eddy viscosity depends on the mixing length and an average fluctuating velocity. Here, the mixing length can be defined by a simple empirical formula, e.g. $l = \kappa z$ (Schlichting, 1955), where $\kappa$ is the von Karman constant, and $z$ is the distance from the nearest wall. It follows that turbulent eddies must be compressed nearer to the wall. Zero-equation models assume that turbulence is dissipated where it is generated (Rodi, 1993), so does not account for turbulence transport. However, zero-equation models have seen widespread application in geomorphology, as it is the basis for law-of-the-wall (Lane, 1998).

### 4.2.5      Justification for the numerical representation used in this thesis

The above sections have reviewed the main methods for the numerical representation of open channel flows. For the purposes of this thesis, the numerical representation must meet the criteria outlined in RQ2 and thesis objective (ii), in that the model should be capable of accurately predicting and reproducing three-dimensional mean and turbulent flow at the plant-scale.

The computational expense associated with DNS is unfeasible, and the method is discounted. Viable alternatives are LES and RANS models, both of which have been applied previously to model flows through vegetation (Section 2.4.2). A key difference between RANS and LES models are the scales of turbulent motions resolved. For RANS, the turbulence closure scheme is necessary to simulate the effects of all contributions to turbulent motion, with all aspects of turbulence modelled, thereby enhancing numerical

efficiency at the expense of a strong model dependency (Rodi, 1997; Lübcke *et al.*, 2001). For LES, the large-scale unsteady motions that make up a major portion of the turbulence spectrum are resolved, with a SGS model applied to model the remainder of small-scale, unresolvable turbulent motions (Rodi, 1997; Lübcke *et al.*, 2001). RANS models have been shown to reach their limits when large-scale turbulent structures dominate, and when turbulence is strongly anisotropic, with LES superior in such circumstances (Rodi, 2017). However, in resolving a greater portion of the turbulence spectrum, significantly more computational effort is required by LES in comparison with RANS.

RANS models have been shown to accurately represent the time-averaged flow field especially with the application of more sophisticated turbulence closure schemes (Lien and Leschziner, 1994). These models enable time-averaged flow quantities to be evaluated, but not the time-dependent fluctuations in velocity (Keylock *et al.*, 2005). As it is the mean three-dimensional and turbulent flow that is of interest in this thesis, application of a RANS model with a sophisticated turbulence closure scheme is suitable for this purpose. Although LES would provide the instantaneous flow field through a time-dependent solution, the temporal element of flow is not necessary at this stage. Furthermore, the computational expense associated with LES would limit the number of simulations feasible. To understand the influence of plant volumetric canopy morphology on flow field dynamics (RQ4 and RQ5), many simulations are required, and this would not be realistically achievable using an LES model.

In selection of the most suitable RANS model, two-equation models are most appropriate for this specific application (Section 4.2.4.2). Two-equation models have been frequently applied, and are well validated, showing good results across a range of hydraulic flow applications (Versteeg and Malalasekera, 1995). The $k - \varepsilon$ turbulence model, modified using Renormalization Group Theory, is used as the turbulence closure scheme (Yakhot and Orszag, 1986). This model has been shown to outperform the standard $k - \varepsilon$ turbulence model in regions of high strain, flow separation, and reattachment (Yakhot and Orszag, 1986; Lien and Leschziner, 1994; Hodskinson and Ferguson, 1998; Bradbrook *et al.*, 2000), particularly relevant to flows with shear in natural channels, and therefore has been widely adopted in geomorphological CFD applications (Marjoribanks *et al.*, 2016). The model has been shown to be numerically stable (Hardy *et al.*, 2005), and is most suitable given the expected effects of shearing flow through vegetation.

# 4.3 Initial application

In this section, initial application work is shown to demonstrate the numerical model using the turbulence closure scheme specified previously. A detailed description and justification for each of the boundary conditions are provided, with a focus on maintaining good modelling practice.

## 4.3.1 Flow solver mechanics

PHOENICS solves the full three-dimensional Navier-Stokes equations discretised with a finite-volume method, solving the mass and momentum equations in a semi-coupled manner through the SIMPLEST algorithm (CHAM, 2005). This is a variant of the SIMPLE algorithm (Patankar and Spalding, 1972), with convective and diffusive terms treated separately in the finite-volume equation (Spalding, 1980), producing convergence more smoothly (CHAM, 2005). The mass and momentum equations are semi-coupled by applying the SIMPLEST algorithm, where the velocity field is solved using the momentum equation (4.5), followed by a pressure correction to solve the mass or continuity equation (4.6), ensuring a divergence-free velocity field. The process is iteratively repeated until convergence is achieved, with continuity and momentum errors acceptably small (CHAM, 2005). The convergence criterion was set such that the residuals of mass and momentum flux were reduced to 0.1% of the inlet flux, as has been accepted in previous work (Ferguson *et al.,* 2003; Lane *et al.,* 2004; Marjoribanks *et al.,* 2016).

The differencing scheme used was hybrid-upwind, where upwind differences are used in high convection areas (Peclet number > 2) and central differences are used where diffusion dominates (Peclet number < 2). Weak linear relaxation was used for the pressure correction, while false time step relaxation was used for the other variables. The hybrid-upwind differencing scheme is numerically robust, so avoids the introduction of spurious oscillations associated with some higher-order numerical schemes (Hardy *et al.,* 2003).

## 4.3.2 Spatial discretisation

In this application, the grid was designed with a regular structure, using a Cartesian coordinate system. This was selected given the regular grid spacing of the plant

representation derived from the voxelisation procedure (Section 3.3). For this initial application, a hypothetical domain was created 2.25 m long, 0.70 m wide, and 0.35 m high. Three independent meshes were defined, with the number of grid cells in the computational domain defining the grid resolution, here set to 0.005, 0.01, and 0.02 m (Figure 4.2, Table 4.2). Taking the initial grid resolution as 0.01 m, refinement of the grid corresponds to a doubling and halving of the grid resolution, and this is especially relevant for the assessment of grid independence (Section 4.3.7.2).
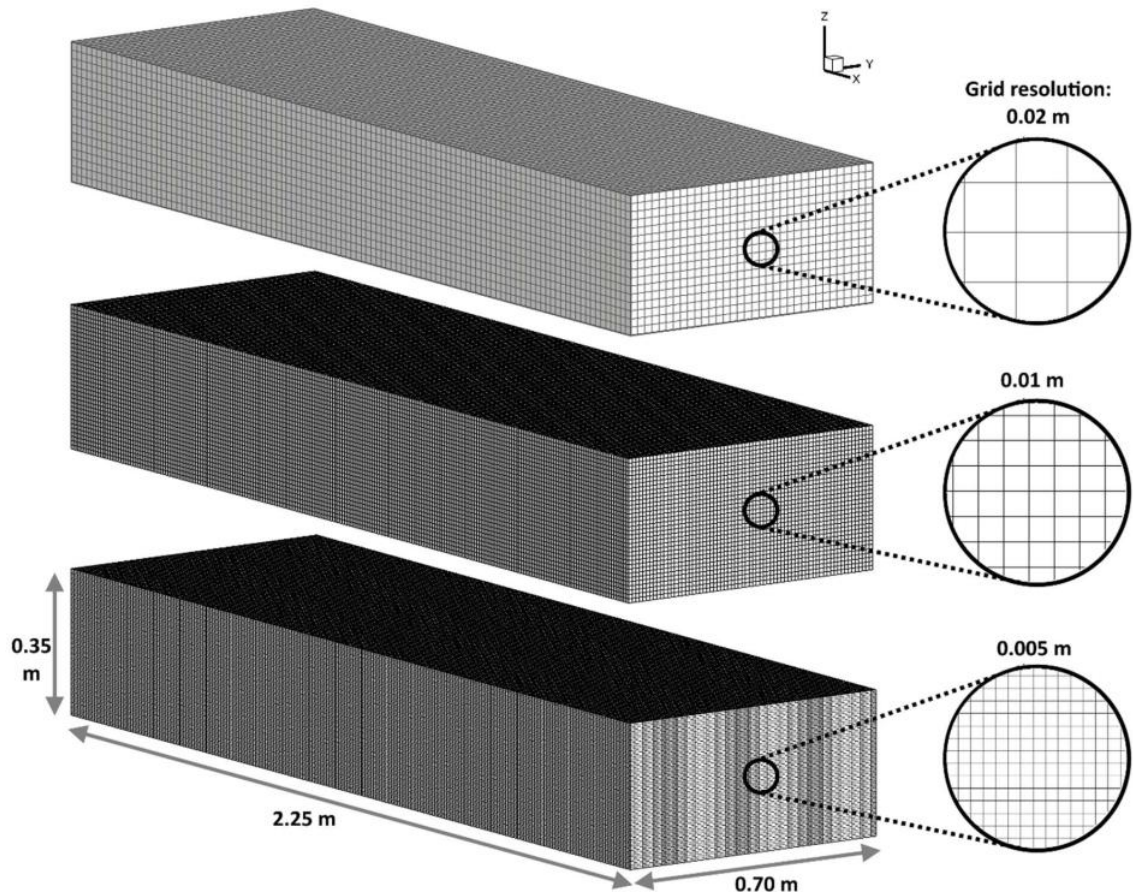


*Figure 4.2 Range of grid resolutions tested during the model development stage (0.005 – 0.02 m).*

*Table 4.2 The grid resolutions used in proof of concept work. NX is the number of cells in the downstream direction, NY in the cross-stream direction, NZ in the vertical direction.*

| Grid | NX | NY | NZ | Grid resolution (m) | Number of grid cells |
|------|-----|-----|-----|---------------------|----------------------|
| 3 | 113 | 35 | 18 | 0.02 | 71 190 |
| 2 | 225 | 70 | 35 | 0.01 | 551 250 |
| 1 | 450 | 140 | 70 | 0.005 | 4 410 000 |

### 4.3.3       **Free-surface treatment**

The boundary at the air-water interface offers a significant degree of freedom for open channels, and through super-elevation or depression, the water surface elevation can vary spatially and temporally. Ferreira *et al.* (2017) has recently detected small scale water surface disturbances in the wake of vegetation, with these disturbances being progressively dissipated downstream, and non-normally distributed in the plant vicinity. However, the magnitude of these disturbances for different plants under different hydrodynamic conditions remains unclear. Relevant to the CFD model used, a number of free-surface treatments exist.

The most simplistic scheme available to treat the free-surface is with a rigid lid approximation, with the water surface specified as a fixed, planar solid boundary, across which all normal velocity resolutes are set to zero (Bradbrook *et al.*, 2000). The pressure at the surface is non-zero, and varies to reflect the effective free-surface as if the lid was not fixed (Meselhe and Odgaard, 1998). Introduction of a pressure correction term in the momentum equations therefore accounts for surface deviations (Leschziner and Rodi, 1979), but no correction is made for the effects of non-zero pressure on the mass or continuity equation. This has the potential for the over-prediction of velocity in areas of super-elevation, and under-prediction in areas of depression (Weerakoon and Tamai, 1989; Bradbrook *et al.*, 1998; Bradbrook *et al.*, 2000). Despite this limitation, the rigid lid approximation has been favoured in similar flow-vegetation modelling applications (Marjoribanks *et al.*, 2014c; Marjoribanks *et al.*, 2016), owing to the relatively small variations in water-surface elevation anticipated under the hydrodynamic conditions.

An alternative approach involves treatment of the free-surface layer by numerical porosity (Bradbrook *et al.*, 1998). In this way, areas of surface depression are assigned porosities of less than 1, and areas of surface super-elevation are assigned porosities greater than 1 (Spalding, 1985). This porosity based correction is applied to the mass continuity equation by altering the effective discharge through the cells, and ensures there is no distortion to the downstream velocity. The approach has been successfully applied to a number of geomorphological CFD applications including river meanders (e.g. Ferguson *et al.,* 2003), and is most relevant to applications where variation of water surface elevation is considerable. A numerical porosity approach for the free-surface has not yet been applied and validated in the case of flow-vegetation interactions.

Throughout this thesis, where vegetation always remains fully submerged and variations in water surface elevation are expected to be minimal, a rigid lid approximation is deemed most suitable, with the additional complexity introduced by numerical porosity treatment unnecessary, especially as this has the potential to introduce numerical instability issues.

## 4.3.4 Vegetation conceptualisation, representation, and incorporation into the CFD model

A characteristic section of the *Prunus laurocerasus* plant first introduced in Section 3.3 is selected for initial testing (Figure 4.3). In this 0.28 m high section, the branch diameter is typically ~0.02 m, and leaves typically measure ~0.08 m. This section of plant is used throughout the remainder of the chapter.
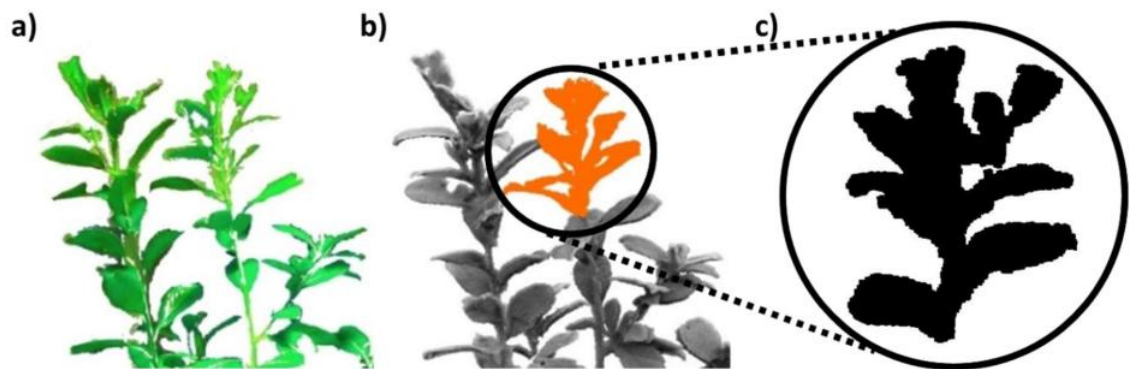


*Figure 4.3 Characteristic section (0.28 m high) of Prunus laurocerasus: (a) photograph, (b) point cloud with characteristic section highlighted orange, and (c) voxelised representation.*

### 4.3.4.1 Vegetation conceptualisation

Following the voxelisation procedure (Section 3.3), the volumetric canopy morphology of the plant is described by regularly structured, binary occupied/unoccupied cells in the voxel space. Selection of an appropriately fine voxel size, relative to the feature scanned, has been shown to be crucial for the accurate representation of plant morphology (Section 3.3). By using this approach, the volumetric blockage of the vegetation is readily quantified, given the volume of each voxel is user-defined and remains the same throughout the voxelised representation. The plant is therefore represented as a three-dimensional model, on a regular, Cartesian digital framework. This is highly advantageous, given the Cartesian grid coordinate system used in the CFD model, thereby enabling direct discretisation.

The approach applied here assumes that vegetation is a dynamically moving porous blockage (Lane and Hardy, 2002). Its porosity comes from the fact that within a controlled volume, flow is able to pass through individual vegetal elements. The detailed morphological representation ensures that gaps and conduits in the internal plant structure are resolved, thus enabling the passage of flow. Previously, vegetation has been represented as a porous medium with a permeability (Papke and Battiato, 2013; Battiato and Rubol, 2014; Rubol *et al.*, 2016). Here, vegetation is represented as a grid-scale blockage, and therefore a permeability is not required. The plant volume is conceptualised to be dynamic, in that it interacts with flow-forcing. As the flow strength increases, the plant will reconfigure and as such the plant volume will decrease, thus pushing the vegetal elements (such as branches, stems, and leaves) closer together, thereby decreasing the porosity.

The initial volumetric canopy morphology, under unstressed conditions (no flow-forcing), is provided by the voxelised representation derived from TLS (Section 3.3). However, to represent the volumetric canopy morphology under stressed conditions (flow-forced), an explicit knowledge of plant motion under flow is required. This is determined experimentally, with results shown in Chapter 5, providing an understanding of the time-dynamic and time-averaged plant motions. For stressed plant representations, the time-averaged plant posture is used as boundary conditions to inform the spatial discretisation of the plant (Section 5.2.2). However, for both the unstressed and stressed plant representations, the plant is read into the numerical model in the same way, using a mass flux scaling algorithm, as described below.

### 4.3.4.2    Mass Flux Scaling Algorithm (MFSA)

The voxelised plant can be viewed as complex topography having complex boundaries, and this needs to be incorporated into the computational domain. However, one of the most problematic factors in applying CFD to geomorphological applications is the incorporation of complex topography in the spatial discretisation. In the past, complex topography has been represented by the fitting of structured numerical grids, called boundary-fitted coordinate (BFC) grids, to the complex boundaries (Figure 4.4a). However, Lane *et al.* (2002) showed that BFC grids are unsatisfactory for four main reasons: (1) the resulting numerical meshes can be strongly skewed (see Figure 4.4a), thus introducing issues of numerical diffusion and numerical instability; (2) an inability

to achieve grid independence; (3) the need to re-mesh following any topographic change, and; (4) the need for equal grid cells when applying spatial filtering techniques associated with turbulence modelling in an LES framework. The extent of grid skewing and distortion depends on the grid resolution (as shown in Figure 4.4b), and this is the fundamental reason as to why it is difficult to achieve a grid independent solution (Lane *et al.*, 2002). To resolve these issues, an alternative treatment of complex topography in the spatial discretisation is therefore required, and this can be achieved using numerical porosity.

A numerical porosity based approach for representing complex topography was first suggested by (Olsen and Stokseth, 1995). In principal, the topography is specified using cell porosities, where $P = 1$ for cells that are unoccupied and so are completely unblocked, $P = 0$ for cells that are occupied and so are completely blocked, and $0 < P < 1$ for partly blocked cells. This numerical porosity based approach was subsequently developed to include the relevant drag terms in the momentum equations and termed the mass flux scaling algorithm (Lane *et al.*, 2002; Lane *et al.*, 2004). An additional drag treatment to the momentum equations was applied by Hardy *et al.* (2005) to permit changes in porosity between cells. For blocked cells where $P = 0$, the cell is completely blocked using a volume approach, and no scaling of drag is required. For partly blocked cells which interface between topography and water, the cell volumes and faces are modified to reduce the flux that can pass through the cell, and a drag coefficient scaling based upon the equivalent surface area is applied (Lane *et al.*, 2002; Hardy *et al.*, 2007). This is shown in Figure 4.4c, with the portion of each cell shaded reflecting the mass flux.
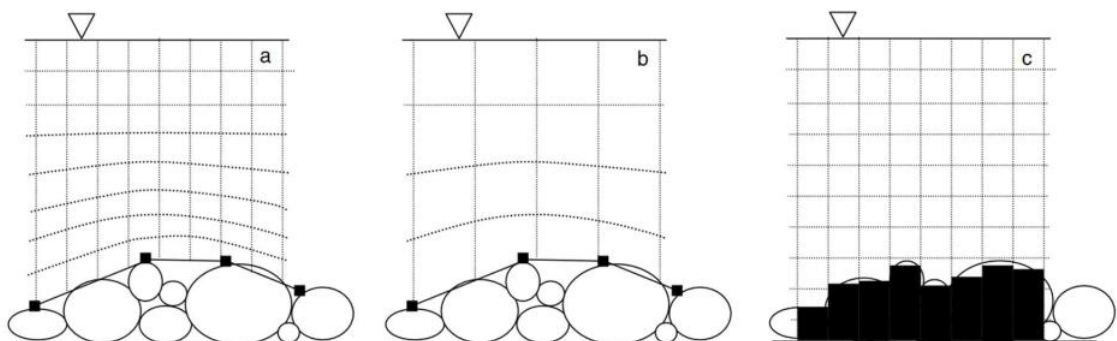


*Figure 4.4 Examples of different methods for discretising complex bed topography in Y/w view, (a) using boundary-fitted coordinates, (b) with a lower grid resolution, and (c) with a porosity treatment using a mass flux scaling algorithm. Taken from Lane et al. (2002)*

In geomorphological CFD applications, the MFSA has previously been used over various spatial scales to represent complex gravel surfaces (Lane and Hardy, 2002; Hardy *et al.*, 2007) and three-dimensional dunes (Hardy *et al.*, 2014), through to river reaches approximately 1 km in length (Sandbach *et al.*, 2012).  Relevant to flow-vegetation interactions, Marjoribanks *et al.* (2014c) applied a MFSA to represent flexible, cylindrical, single stemmed, vegetation elements.  More recently, Marjoribanks *et al.* (2016) applied a modified MFSA to represent submerged vegetation patches, with the porosity related to the solid volume fraction to account for patch distributions (Section 2.4.2).

The main advantages of a MFSA is that complex topography can be included in a stable Cartesian discretisation.  By using this regular, blocked, structured grid, the issues associated with numerical diffusion and instability are therefore removed.  Clearly, the MFSA approach closely corresponds with the unoccupied/occupied voxelisation procedure previously described in Section 3.3, used to represent plant volumetric canopy morphology.  By conceptualising vegetation as a porous blockage, application of a MFSA is an extremely valuable tool for modelling flow-vegetation interactions.

Taking a schematic plant in *Z/h* view, Figure 4.5 demonstrates how the plant can be represented using the different methods of discretisation.  If boundary-fitted coordinates were used, substantial grid distortion and an incomplete representation of plant morphology is expected (Figure 4.5a).  With application of a MFSA on the same grid resolution, Figure 4.5b, the issues of distortion are removed, and greater morphological detail of the plant is represented.  Finally, with application of a MFSA to an even finer grid, more morphological detail can be resolved in the plant representation.  The implications for changing the grid resolution, both in terms of the grid used in the computational domain, and in the resolution of the cells used to describe the plant, are discussed in Section 4.3.7.2.
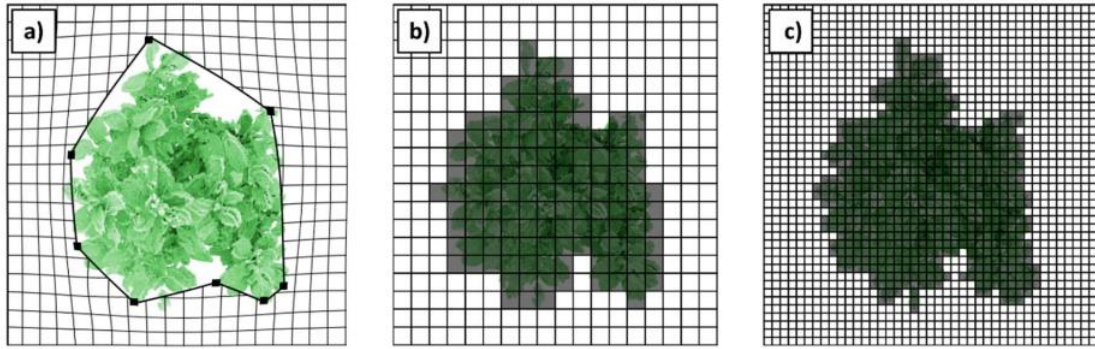
**Figure 4.5 Examples of different methods for discretising a plant in Z/h view: (a) using boundary-fitted coordinates, (b) with the mass flux scaling algorithm on a coarse mesh, and (c) with the mass flux scaling algorithm on a finer mesh.**

As discussed in Section 4.3.4.1, vegetation is conceptualised as a dynamically moving, porous blockage. The internal structure of the plant, and notable gaps and in the canopy, will influence flow through and around the plant. Application of a MFSA therefore enables this morphological detail to be fully resolved, which would otherwise be lost using a BFC method.

The MFSA accounts for the volumetric blockage created by the vegetation. As such, the finite-volume continuity equation takes the form:

$$f_p = \frac{\sum_c a_c f_c}{a_b + S_l} \tag{4.23}$$

where $f$ is the variable of interest $(u,v)$, $b$ represents the value at the cell centre, the index $c$ represents the values at neighbouring cell centres and the previous time-step, and $S_l$ is the linear source coefficient. The neighbour links $(a_c)$ then have the form:

$$a_c = A_c \phi \rho u + D + T \tag{4.24}$$

Where, $A_c$ is the cell-face area, $\phi$ is the cell-face porosity, $\rho$ is the fluid density, $u$ is the local velocity perpendicular to the face, $D$ is the diffusion term, and $T$ is the transient term. To introduce the MFSA, the value of $\phi$ is calculated for each face according to the presence of vegetation. The numerical grid was defined with vertices that are exactly collocated with the voxelised representation, meaning that the voxelised plant maps directly onto the grid cells (having equal density), and therefore a binary

blocked/unblocked porosity treatment follows (Lane *et al.*, 2004). This means that all permeability through the plant is explicitly represented through the grid-scale blockage.

In previous applications, an additional drag force term has been implemented as a momentum sink term in the Navier-Stokes equations (e.g. Wilson and Shaw (1977); Fischer-Antze *et al.* (2001); López and García (2001)). However, because of the binary porosity treatment used here, no additional drag force term is needed, as the wall condition is automatically set at the edge of each cell. In summary, the voxelised plant is represented as a grid-scale blockage in the computational domain, treated using numerical porosity, by application of a mass flux scaling algorithm (MFSA).

### 4.3.5        Wall treatment

At the solid boundary interface it is important to specify boundary conditions. No modification has been applied to the turbulence model for either bed and domain side walls, which were treated as a no-slip boundary, and the non-equilibrium wall function applied which assumes local equilibrium of turbulence ($y^+ = 47$) (Launder and Spaulding, 1974). No-slip treatment of the boundary at the bed and domain side walls was selected so as to prevent wall effects dominating the flow. At the interface of the plant blockage, the non-equilibrium wall function is automatically set at the edge of each cell, and this has been shown to provide a more realistic approximation of wall conditions in separated flows (Launder and Spaulding, 1974).

### 4.3.6        Inlet and outlet boundary conditions

The specification of inlet and outlet conditions are key boundary conditions in CFD applications (Figure 4.6). In PHOENICS, the *u-*, *v-*, and *w-* velocities at the inlet are specified by the user, in addition to the turbulence intensity. Velocities can be held constant over the spatial extent of the inlet, or can be set to follow a predetermined boundary layer (e.g. logarithmic velocity profile).
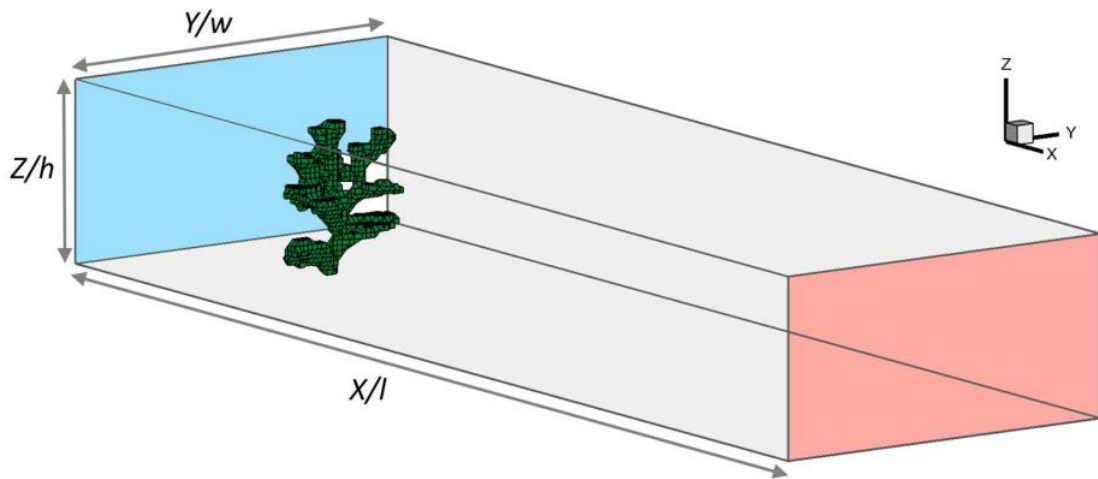
***Figure 4.6 Locations of inlet (blue) and outlet (red) for the domain. Flow is from left to right.***

In this thesis, *u-* velocity is held constant over the spatial extent of the inlet, with inlet velocities assessed over the range 0.125 – 1 m s$^{-1}$ (Section 4.4.1). The *v-* and *w-* velocities were constantly set to 0 m s$^{-1}$. Inlet turbulence intensity was assessed over the range 5 – 25% of the inlet velocity (Section 4.4.2). Thus, the flow was assumed to be fully turbulent and subcritical. For initialisation, the *u-* velocity of all cells in the computational domain were set equal to the inlet velocity. The outlet was defined using a fixed-pressure boundary condition, where mass can enter and leave the domain.

The approach significantly differs from that of Marjoribanks *et al.* (2014c) where cyclic inlet and outlet boundary conditions were used to effectively recirculate the flow, to evaluate flow-vegetation interactions over an extended canopy. This thesis is focused on the individual plant-scale, so is concerned with the effect of an individual plant on flow. If a series of plants were to be considered, then cyclic boundary conditions could be introduced.

### 4.3.7      Good practice in numerical modelling

The previous sections have outlined and justified the design and boundary conditions used in the CFD model. However, for results to be valid, good modelling practice should be followed, and this requires model verification and validation. Verification refers to obtaining the correct solution to the equations applied, whilst validation refers to assessing the extent to which the real system is simulated (Oberkampf and Trucano, 2002), and therefore solves the correct equations (Roache, 1997).

### 4.3.7.1    CFD verification

Verification involves the assessment and minimisation of coding, discretisation, and numerical solution errors (Hardy *et al.*, 2003). PHOENICS, the CFD model applied in this thesis, solves the full three-dimensional Navier-Stokes equations using a finite-volume method, and it should be assumed that the developers, CHAM, have verified the codes to provide an accurate simulation of fluid flow. Within finite-volume schemes, as the grid spacing, *hs*, tends towards zero, the code should converge on the correct mathematical solution, with the discrete solution tending towards the exact solution at $hs = 0$. However, computational cost increases as *h* reduces, and therefore the necessary grid spacing is often unfeasible. This means that complete convergence is rarely attained, and instead a threshold for convergence is needed, so that when the solution falls within an acceptable range of the exact solution, the model is assumed to be suitably accurate. Verification in this context is therefore concerned with spatial discretisation and numerical solution errors.

Although few frameworks for the systematic assessment of verification in open channel applications exist, the American Society of Mechanical Engineers (ASME, 1993) published an editorial statement regarding the importance of verification, with holistic validation viewed as optional and not a substitute for thorough verification. Lane *et al.* (2005) provide an updated critique of the AMSE guidelines, relevant to numerical models used in fluvial geomorphology applications. With reference to both of these guidelines, good modelling practice is discussed below.

   *i.      Level of solution accuracy in space*

ASME guidelines suggest that the numerical method must be at least formally second-order accurate in space. However, second-order methods have known difficulties in obtaining converged solutions with complex geometries (Shaw, 1992), and therefore a hybrid scheme offers a practical compromise that is necessary for such geometries (Lane *et al.*, 2005). The hybrid-upwind differencing scheme used in this thesis is therefore justified (Section 4.3.1), although an acknowledgement that first-order methods may be inaccurate if diffusive terms are dominant over convective terms is necessary (Lane *et al.*, 2005).

## ii.     *Grid independence testing*

ASME guidelines suggest that solutions over a range of significantly different grid resolutions should be presented, to demonstrate grid independence and convergence of the solution.  This is essential as the solution should be insensitive to, and independent of, the grid resolution selected; meaning that simulations should be performed over successively refined grids (see Section 4.3.7.2).  For complex geometries, however, the spatial discretisation over refined grids is a recurring problem (Lane *et al.*, 2005).  However, the effects of the grid resolution can be quantitatively assessed through the Grid Convergence Index (GCI) (Roache, 1994), and this is comprehensively addressed in Section 4.3.7.2.  For the variables of interest, namely downstream velocity and pressure, the GCI is calculated.  These variables are of greatest physical importance to this thesis, and therefore explicitly reported.

## iii.     *Determination of solution convergence*

ASME guidelines suggest that the stopping criteria for iterative calculations be precisely reported and explained.  Convergence has occurred for a variable of interest when the sum of the absolute values of the residuals fall below a pre-specified tolerance (Lane *et al.*, 2005).  Here, the convergence criteria was defined where the residuals of mass and momentum flux were reduced to 0.1% of the inlet flux, following previous applications.  However, in high resolution applications where complex geometry introduce flow complexity, the convergence criteria is not always met (Lane *et al.*, 2005).  In these cases, convergence spot values were observed, with convergence defined when all variables had flat-lined.  In practice, approximately 1500 iterations were necessary for the convergence criteria to be met.  Convergence was aided as the inlet velocity was used to initialise the entire flow field, providing a more accurate starting value.  Furthermore, relaxation is systematically applied to increase the convergence rate (Lane *et al.*, 2005), as specified in Section 4.3.1.

## iv.     *Specification of boundary conditions*

Boundary conditions include the free-surface treatment, representation of topography, wall treatment, inlets and outlets, and a range of hydraulic factors.  The sensitivities to a range of hydraulic boundary conditions are reported in Section 4.4.

### 4.3.7.2 Grid independence

For a CFD simulation to be credible, the code should be verified, and good modelling practice dictates that solutions over a range of significantly different grid resolutions should be presented, to demonstrate grid-independent results (ASME, 1993; Hardy *et al.*, 2003). In this thesis, the spatial discretisation of the plant blockage is crucial, i.e. how the plant is represented in the computational domain (see Section 4.3.4), and this is especially important because of the spatial variation in flow properties across a range of spatial scales (Hardy *et al.*, 2003). Selection of a grid resolution that appropriately discretises the plant, and is appropriate for the scale of analysis conducted, is therefore the key source of spatial discretisation uncertainty and this requires quantification. As such, grid independence needs to be assessed on two levels: the traditional effect of the discretisation of the grid on the flow, but linked to this, how the discretisation of the grid influences the volume of the plant represented. The grid discretisation therefore has implications for the plant discretisation, which will influence the flow field.

The Grid Convergence Index (GCI) was originally proposed by Roache (1994; 1997; 1998) as a method for reporting the sensitivity of model solutions to numerical discretisation. GCI uses the generalised Richardson extrapolation to obtain a higher-order estimate of the value at zero grid spacing. As such, it is based on comparisons of the solution at different grid resolutions, and provides an index of the solution uncertainty for a particular grid resolution.

Here, GCI is tested for three grid resolutions, with grid size incrementally increasing from 0.005 – 0.02 m (see Section 4.3.7.2). The grids are labelled from 1 (finest) to 3 (coarsest), with the properties of each grid shown in Table 4.2. The flow variable of interest, $f$, corresponds with the numbered grid (i.e. $f_1$ = finest solution, $f_3$ = coarsest solution).

The grid refinement ratio, $r$, is calculated following:

$$r_{12} = \left(\frac{hs_1}{hs_2}\right) \qquad r_{23} = \left(\frac{hs_2}{hs_3}\right) \tag{4.25}$$

where $hs$ is the grid spacing. In this application, $r$ is equal in each coordinate direction, and $r_{12} \approx r_{23}$. When applying GCI, the value of $r$ should be greater than 1.1, to ensure

that discretisation error is differentiated from the noise from other influences such as convergence and rounding errors (Roache, 1994).

The order of convergence, $p_o$, is then calculated using the solutions at each grid resolution, following:

$$p_o = \frac{\ln\left(\frac{\varepsilon_{23}}{\varepsilon_{12}}\right)}{\ln(r)} \tag{4.26}$$

where $\varepsilon_{23}$ and $\varepsilon_{12}$ are the absolute numerical error between the grids:

$$\varepsilon_{12} = (f_1 - f_2) \qquad \varepsilon_{13} = f_1 - f_3 \qquad \varepsilon_{23} = f_2 - f_3 \tag{4.27}$$

The order of convergence, $p_o$, is then used in the Richardson extrapolation to estimate the true value of the solution at $hs = 0$, following:

$$f_{hs=0} = f_1 + \left(\frac{f_1 - f_2}{r^p - 1}\right) \tag{4.28}$$

Finally, the grid convergence index, $GCI$, is calculated following:

$$GCI_{12} = \frac{F_{safety}\,|\varepsilon_{12}}{(r^p - 1)} \qquad GCI_{13} = \frac{F_{safety}\,|\varepsilon_{13}}{(r^p - 1)} \qquad GCI_{23} = \frac{F_{safety}\,|\varepsilon_{23}}{(r^p - 1)} \tag{4.29}$$

where $F_{safety}$ is a safety order, $F_{safety} = 1$ provides the median error, whereas $F_{safety} = 3$ provides a conservative upper limit analogous to the statistical confidence interval (Hardy *et al.*, 2003), $F_{safety} = 3$ is used herein. The $GCI$ is expressed as an absolute percentage, and can be calculated for a single point, a cross-section, or the entire extent of the computational domain.

It is also necessary to check that the grid convergence is within the asymptomatic range of convergence, and for the three grids is calculated following:

$$\frac{GCI_{23}}{r^p|GCI_{12}} \cong 1 \tag{4.30}$$

For the grid resolutions outlined in Table 4.2, analysis of grid convergence through the GCI is completed for two contrasting scenarios. In the first scenario, a geometrically simple, cuboidal blockage is incorporated into the domain by application of the MFSA (Section 4.3.7.2.1). The volume of the blockage is conserved between the different grid resolutions, and therefore any differences in the flow variables of interest can be attributed to changes in the grid resolution. Both the global GCI, and the cross-section GCI are calculated. This is because it is useful to plot the spatial distribution of GCI at cross-sections of the computational domain to identify spatial patterns of convergence, as the global GCI could potentially average out regions of low and high error when reported as a single statistic (Hardy *et al.*, 2003). In each case, common geo-located data points between the different grid resolutions must be compared, and this involves repeating elements in the three-dimensional arrays of grids 2 and 3 to match those of grid 1.

In the second scenario, the characteristic plant blockage is incorporated into the domain, again by application of the MFSA (Section 4.3.7.2.2). However, this scenario differs from the first in that the volume of the plant blockage is not conserved between the different grid resolutions, as an artefact of the relationship between the voxelisation procedure and the grid resolution. The volume and morphological representation of the plant will vary between different grid resolutions, and this will introduce an additional uncertainty into the flow variables of interest. This occurs because the binary numerical porosity treatment used to spatially discretise the plant does not translate naturally between the different grid resolutions, introducing the additional uncertainty.

Finally, to address the additional uncertainty caused by the spatial discretisation and volumetric blockage of the plant, the finest grid resolution (0.005 m) is selected, but the voxel size used to discretise the plant is increased incrementally from 0.005 to 0.04 m, with the sensitivity of the flow variables of interest quantified (Section 4.3.7.2.3). As such, sensitivity to the voxel size used to represent the plant is quantified.

### 4.3.7.2.1 Grid convergence of a geometrically simple cuboidal blockage

For the first test of grid convergence, a geometrically simple cuboidal blockage with a volume of 0.0015 m$^3$ is incorporated into the computational domain at 0.22 *X/l*, and centred at the midline (0.5 *Y/w*). Between the different grid resolutions, the volume of

the cuboidal blockage is conserved, and the spatial discretisation remains the same. The only factor changing is the grid resolution (Table 4.2). First, the downstream velocity and pressure fields are compared, before showing the spatial distribution of GCI at cross-sections, and calculating the global GCI.

Figure 4.7 shows similarity in the spatial patterns of the downstream velocity field at 0.5 *Y/w* for the three grid resolutions. This cross-section was selected to be representative of the flow region containing the most complex flow structures, and therefore likely to be most sensitive of grid design. In all cases, a general agreement is shown in the magnitude and position of the low velocity zone immediately behind the blockage, the presence of a zone of faster flow above this, and a region of shear separating these zones. The most notable difference present is that as the grid resolution coarsens from 0.005 to 0.02 m, the modelled zone of reduced velocity increases in length.
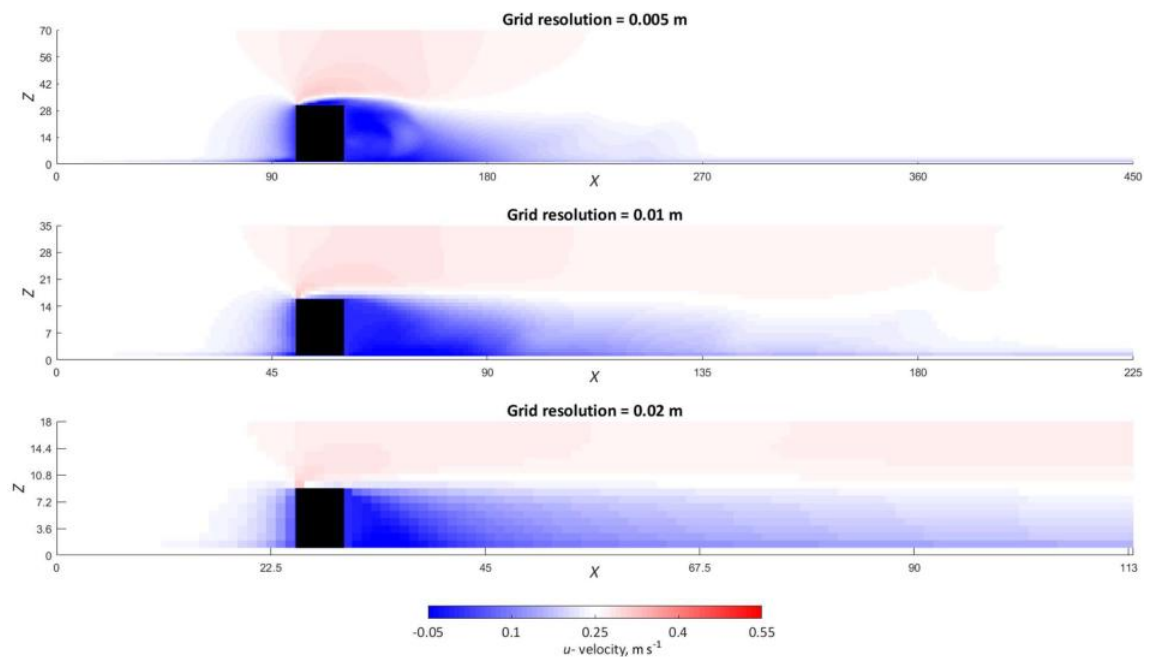


**Figure 4.7 Downstream velocity at 0.5 Y/w with coarsening grid resolution (top to bottom). X and Z refer to the number of cells. Black pixels represent the cuboidal blockage (volume = 0.0015 m³).**

This agreement is further examined by comparing downstream velocity profiles at increasing distances downstream and cross-stream (Figure 4.8). Immediately upstream of the blockage (0.2 *X/l*, 0.5 *Y/w*), the velocity profiles between the three grid resolutions appear very similar, with the magnitude of the velocity reduction marginally greater for the 0.02 m grid resolution. Immediately behind the blockage at 0.3 *X/l*, 0.5 *Y/w,* the velocity profiles become more heterogeneous as velocity is reduced and a shear zone is present, but again the shape of the profile remains similar between the different grid

resolutions. The position of the shear zone is particularly similar for grid resolutions of 0.005 and 0.01 m. Downstream of this (0.35 – 0.50 *X/l*), flow begins to recover more quickly for the 0.005 m grid resolution, reverting towards the inlet velocity profile. It is in this region that the greatest difference in velocity is shown between grid resolutions, with the reduced velocity zone extending further downstream for grid resolutions of 0.01 and 0.02 m. For the downstream velocity profiles at 0.33 and 0.66 *Y/w,* the 0.02 m grid resolution fails to adequately capture the heterogeneity displayed by the 0.005 and 0.01 m profiles. The downstream velocity profiles reveal greater similarities between the 0.005 and 0.01 m grid resolutions, with the 0.02 m grid resolution consistently unable to adequately reproduce the profile heterogeneity.
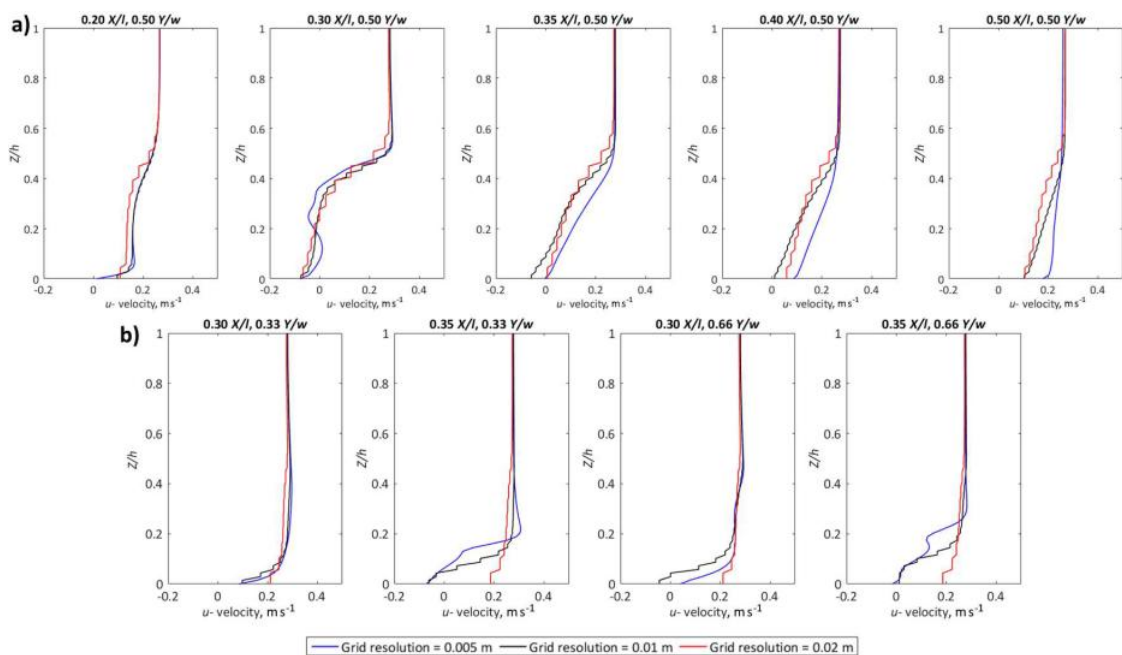


*Figure 4.8 (a) Downstream velocity profiles for the different grid resolutions at increasing distances downstream at 0.5 Y/w and (b) at 0.33 and 0.66 Y/w.*

The pressure field shows even greater similarities between the different grid resolutions. For each grid resolution, Figure 4.9 shows the magnitude and spatial distribution of pressure about the cuboidal blockage is very similar for cross-sections at 0.5 *Y/w* and 0.5 *Z/h*. A similarly shaped region of high pressure is shown on the upstream end of each blockage, with a comparably larger region of low pressure curved around the downstream end. Regardless of grid resolution, the spatial distribution of the pressure field therefore remains similar throughout.
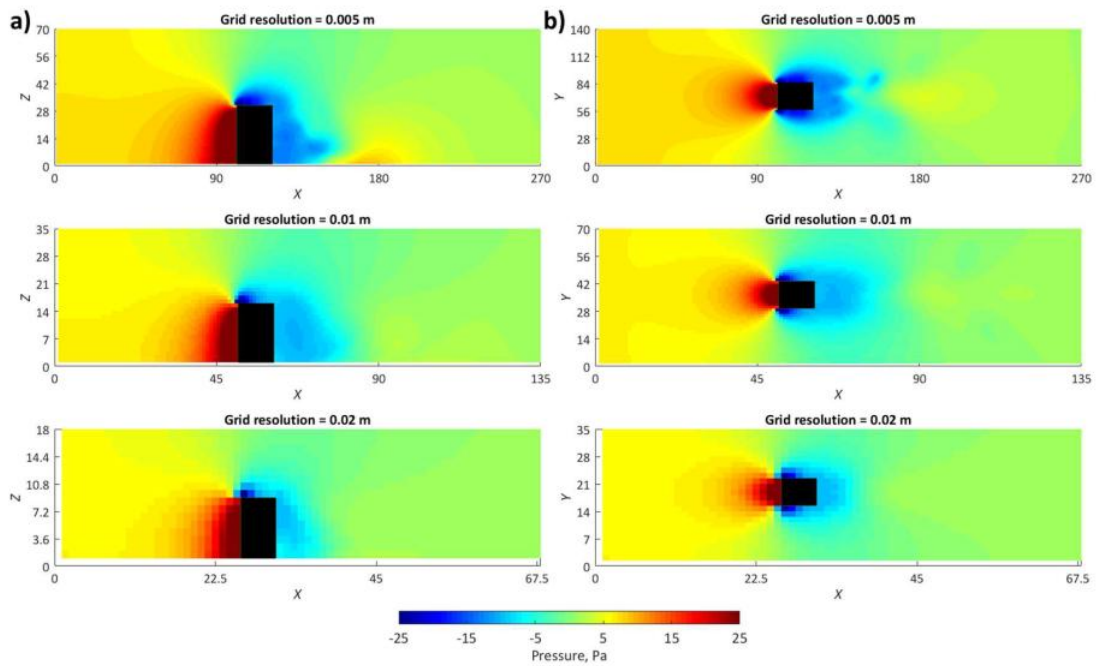
**Figure 4.9 (a) Pressure fields at 0.5 Y/w and (b) 0.5 Z/h for coarsening grid resolutions (top to bottom). X and Z refer to the number of cells.**

For the downstream velocity field, the cross-section GCI is calculated at 0.5 $Y/w$ (Table 4.3) and the spatial distribution shown in Figure 4.10. Between grids 1 and 2 the average cross-section GCI is ~1.5%, with a higher value of ~4% calculated between grids 1 and 3. Considering the spatial patterns of GCI, the region of greatest difference persists in the zone of reduced velocity immediately behind the cuboidal blockage in both grid comparisons. However, the position of the shear layer appears to be well resolved throughout. Considering the entire computational domain, the global GCI is calculated to be ~0.5% between grids 1 and 2, and ~1.3% between grids 1 and 3. The uncertainty is therefore small between the grids, demonstrating grid independence for the downstream velocity field.
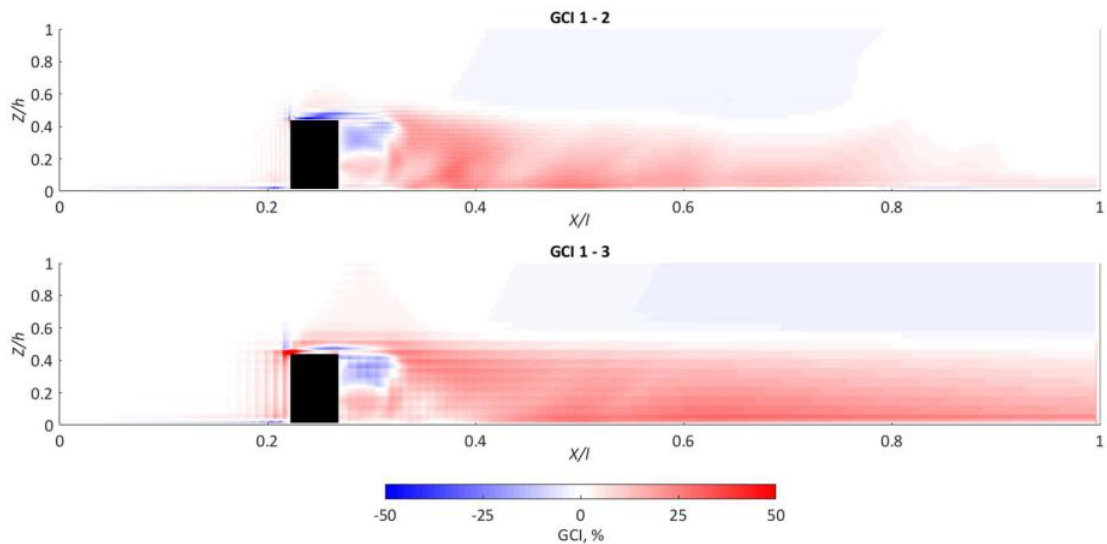
*Figure 4.10 Cross-section GCI at 0.5 Y/w for downstream velocity.*

For the pressure field, the cross-section GCI is again calculated at 0.5 *Y/w* (Table 4.3), and the spatial distribution shown in Figure 4.11.  Averaged over the cross-section, GCI is higher for grids 1 and 3 (~1.2%), than grids 1 and 2 (~0.8%).  The spatial distribution of the error is less obvious than for the downstream velocity field, with the largest magnitude of uncertainties distributed on the upstream edge of the cuboidal blockage, especially in grids 1 and 3.  A global GCI value of ~0.4% is calculated between grids 1 and 2, and ~0.5% between grids 1 and 3.  The GCI values are smaller than for the downstream velocity field, and this is to be expected given the mechanics of the flow solver, in that the velocity field is solved based on an estimated initial pressure field (Patankar and Spalding, 1972).  Grid independence for the pressure field is therefore demonstrated.
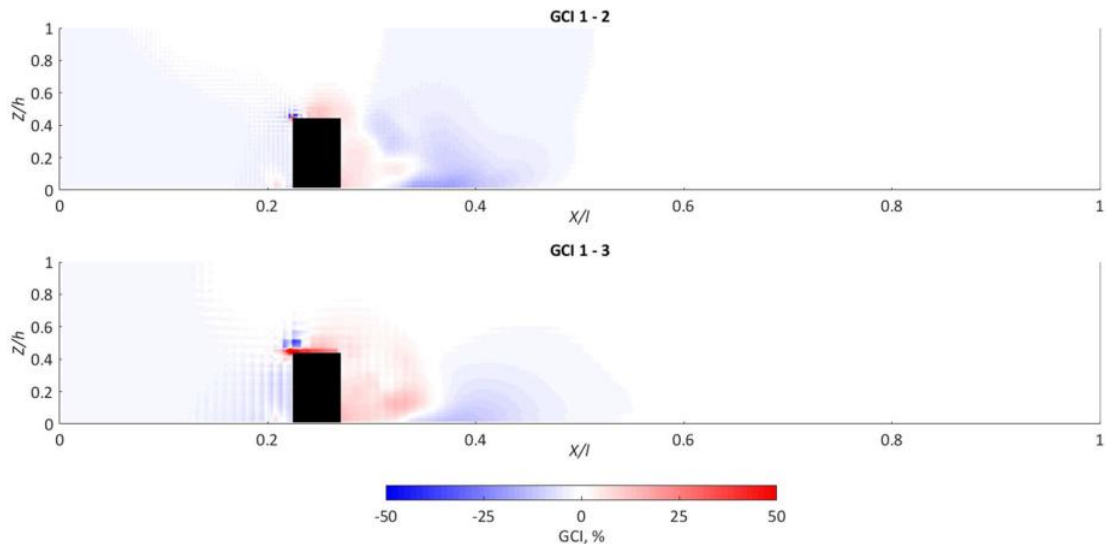
**Figure 4.11 Cross-section GCI at 0.5 Y/w for pressure.**

**Table 4.3 Cross-sectional and global GCI for the cuboidal blockage.**

| Variable | Cross-section GCI (%) | | Global GCI (%) | |
|---|---|---|---|---|
| | GCI 1 – 2 | GCI 1 – 3 | GCI 1 – 2 | GCI 1 – 3 |
| *u*- velocity | 1.57 | 3.97 | 0.62 | 1.31 |
| Pressure | 0.82 | 1.23 | 0.38 | 0.54 |

It is shown that grid independence has been achieved for the downstream velocity and pressure fields, particularly between grids 1 and 2 where the GCI values remain lower than those of grids 1 and 3. Where GCI is analogous to a 99.9% statistical confidence interval, the uncertainty quantified around a conserved blockage volume suggests that the numerical schemes are of an acceptable numerical accuracy to be used in predictive terms (Hardy *et al.*, 2003).

### 4.3.7.2.2    Grid convergence of a characteristic plant blockage

For the second test of grid independence, the characteristic plant blockage is incorporated into the computational domain at 0.15 *X/l*, 0.5 *Y/w*. Blockage volume is not conserved between different the grid resolutions (an artefact of the voxelisation procedure and the grid-scale volumetric blockage from the MFSA), and this introduces an additional unknown into the assessment of grid independence. A voxel size of 0.02 m was selected, given the coarsest grid resolution of 0.02 m. The plant blockage volume increases with changes in grid resolution; at a grid resolution of 0.005 m the plant blockage volume is 0.0032 m$^3$, at 0.01 m is 0.0038 m$^3$, and at 0.02 m is 0.0057 m$^3$. The

plant blockage volume therefore increases by ~20% between grid resolutions of 0.005 and 0.01 m, and ~80% between grid resolutions of 0.005 and 0.02 m. The plant blockage therefore accounts for 0.58% of the domain at a grid resolution of 0.005 m, 0.68% at 0.01 m, and 1.0% at 0.02 m.

For the downstream velocity field at 0.5 $Y/w$ (Figure 4.12), considerable differences are apparent with changes to the grid resolution and the spatial discretisation of the characteristic plant blockage. For a 0.005 m grid resolution, the velocity reduction introduced immediately behind the plant is small, with the magnitude of the velocity reduction, and the length of this zone, greater at grid resolutions of 0.01 and 0.02 m. To further quantify this difference, the downstream velocity profiles in Figure 4.13 show that flow has fully recovered by 0.25 $X/l$ for a grid resolution of 0.005 m, but does not fully recover until 0.35 $X/l$ for a grid resolution of 0.01 m, and is not completely recovered until 0.50 $X/l$ for a grid resolution of 0.02 m. For the downstream velocity profiles at 0.33 and 0.66 $Y/w$, similarity is shown between grid resolutions of 0.005 and 0.01 m, but not the 0.02 m grid resolution, due to the presence of a large region of reduced velocity associated with the larger volumetric blockage. With the volume of the characteristic plant blockage not conserved, differences in the downstream velocity field between grid resolutions therefore exist.
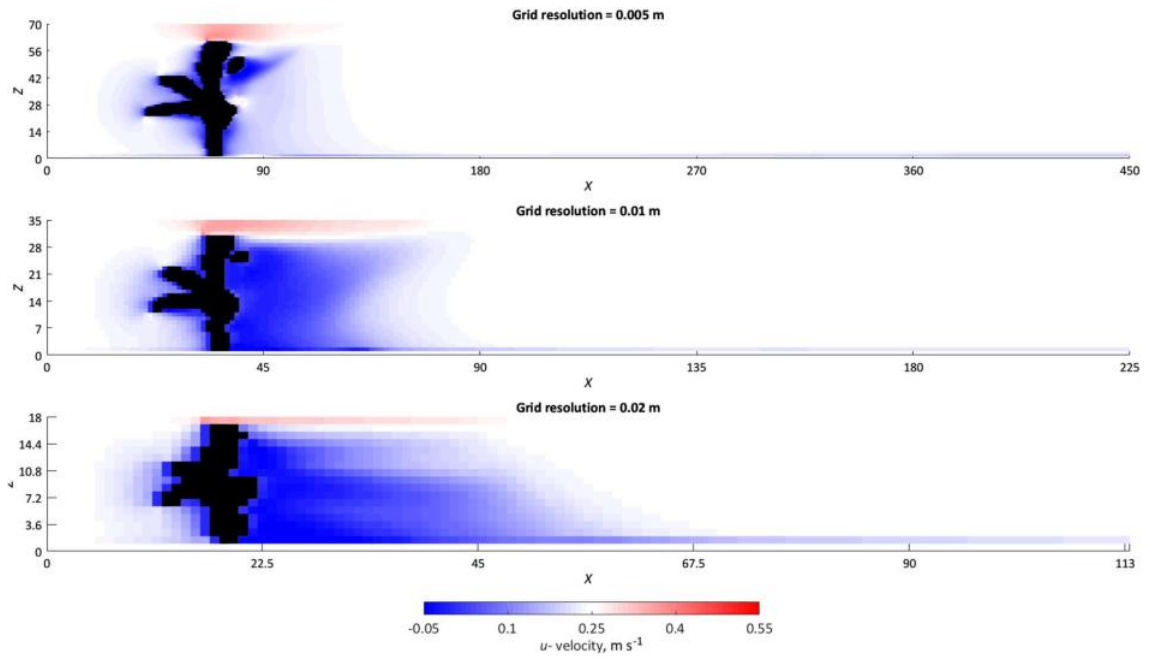
**Figure 4.12 Downstream velocity at 0.5 Y/w with coarsening grid resolution (top to bottom). Black pixels indicate plant blockage, the volume of which is not conserved between different grid resolutions, and increases by ~20% and ~80% relative to the 0.005 m grid resolution. X and Z refer to the number of cells.**



**Figure 4.13 (a) Downstream velocity profiles for the different grid resolutions at increasing distances downstream at 0.5 Y/w and (b) at 0.33 and 0.66 Y/w.**

The pressure field and therefore the drag appears less sensitive to changes in grid resolution and the associated changes in blockage volume than the downstream velocity field, as shown in Figure 4.14. For a coarsening grid resolution, the spatial distribution

and magnitude of pressure remains similar over the lateral extent of the plant, with only a slight exaggeration of the high and low pressure zones a function of increasing grid size and volumetric blockage.
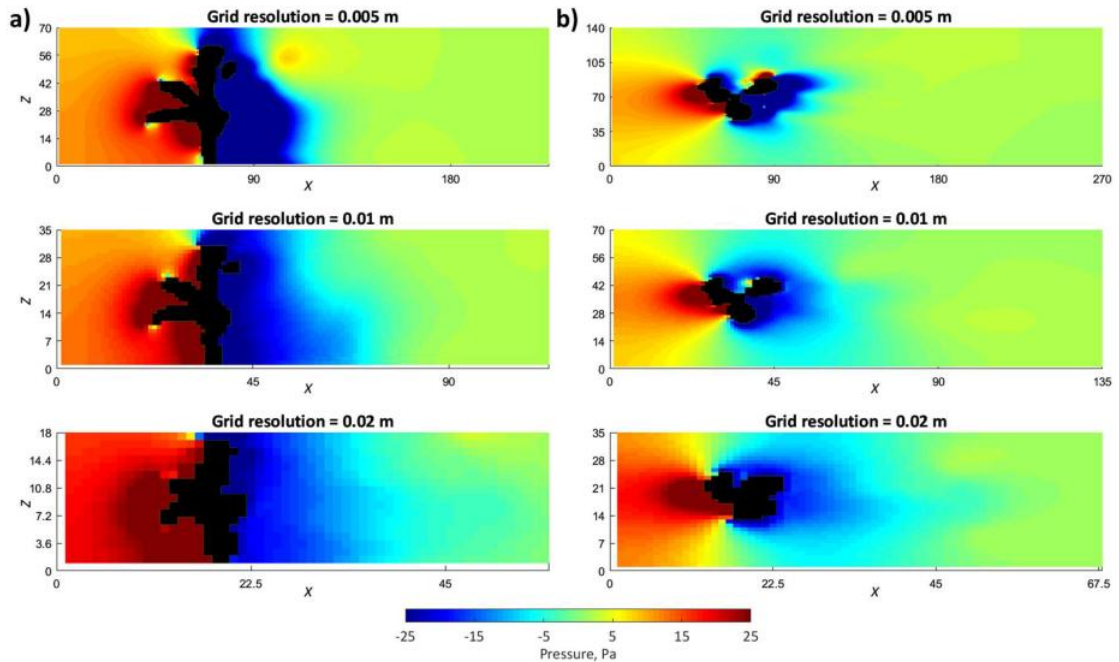


*Figure 4.14 (a) Pressure fields at 0.5 Y/w, and (b) 0.5 Z/h for coarsening grid resolutions (top to bottom). X and Z refer to the number of cells.*

For the downstream velocity field, the cross-section GCI is calculated at 0.5 *Y/w* (Table 4.4) and the spatial distribution shown in Figure 4.15. Between grids 1 and 2 the average cross-section GCI is ~20%, with a higher value of ~35% calculated between grids 1 and 3. Owing to the differences in blockage volume, cross-section GCI is higher than for the conserved cuboidal blockage volume (Section 4.3.7.2.1). Differences in the length of the reduced velocity zone result in marked uncertainty between the different grid resolutions, although the position of the shear layer remains similar throughout. The global GCI is quantified as ~10% between grids 1 and 2, and ~20% between grids 1 and 3, so again is higher than for the conserved cuboidal blockage volume.
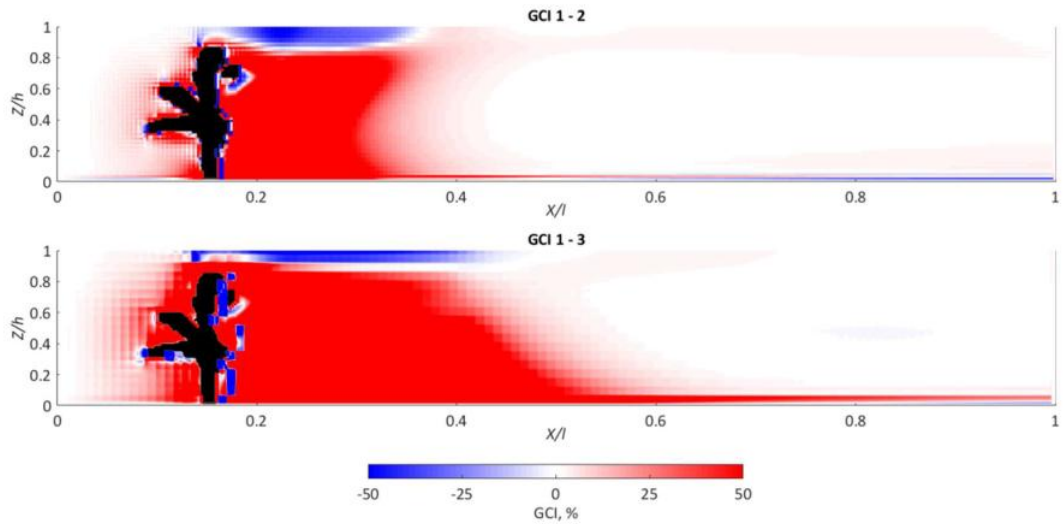
***Figure 4.15 Cross-section GCI at 0.5 Y/w for downstream velocity.***

For the pressure field, the cross-section GCI is calculated at 0.5 *Y/w* (Table 4.4) and the spatial distribution shown in Figure 4.16. Between grids 1 and 2 the average cross-section GCI is ~3.2%, with a higher value of ~4.4% calculated between grids 1 and 3. Highest GCI values are distributed immediately behind the plant blockage in the low pressure zone, and this is consistent for both grids. For the zone of high pressure on the upstream end, comparably low GCI values are quantified. For the global GCI, a value of ~1.4% is calculated for grids 1 and 2, and ~2.3% between grids 1 and 3. This is higher than for the conserved cuboidal blockage volume.
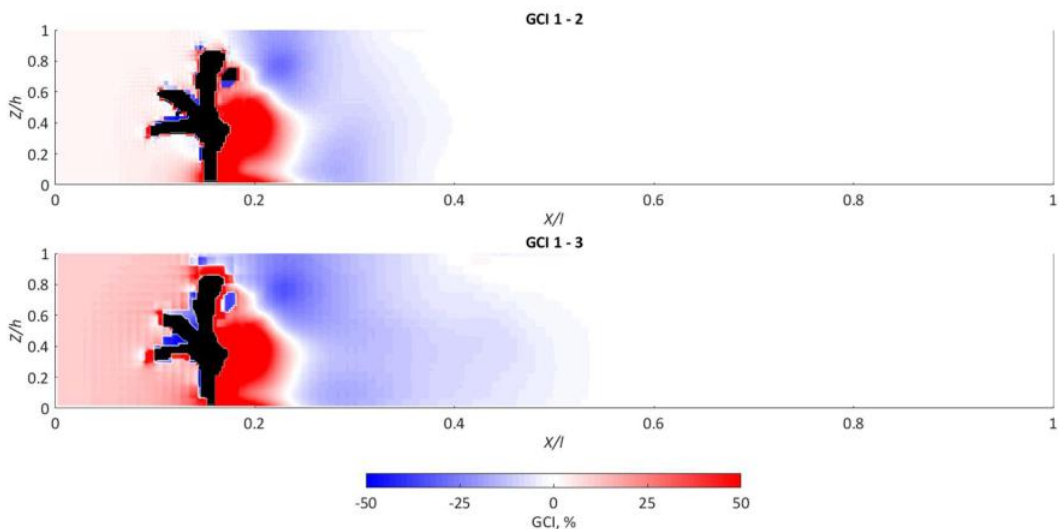


***Figure 4.16 Cross-section GCI at 0.5 Y/w for pressure.***

*Table 4.4 Cross-sectional and global GCI for the characteristic plant blockage.*

| Variable | Cross-section GCI (%) | | Global GCI (%) | |
|---|---|---|---|---|
| | GCI 1 – 2 | GCI 1 – 3 | GCI 1 – 2 | GCI 1 – 3 |
| *u-* velocity | 17.78 | 33.94 | 8.21 | 19.37 |
| Pressure | 3.19 | 4.40 | 1.41 | 2.29 |

With the volume of the characteristic plant blockage not conserved between the different grid resolutions, cross-section and global GCI is shown to be substantially higher than for the conserved cuboidal volume. Additional uncertainty arises when attempting to represent complex geometry in the numerical domain, an artefact of the relationship between the voxelisation procedure and the grid resolution, and because the numerical grid was defined with vertices that are exactly collocated with the voxelised representation. When the plant is explicitly represented through a grid-scale, volumetric blockage that changes with grid resolution, the uncertainty associated with grid independence is higher.

### 4.3.7.2.3    Sensitivity to the voxel size used to discretise the plant

Following Boothroyd *et al.* (2016b), to test the sensitivity of the voxel size used to discretise the plant, the characteristic plant blockage for defoliated and foliated plants are incorporated into the computational domain at 0.15 *X/l*, 0.5 *Y/w,* using voxel sizes of 0.005, 0.01, 0.02, and 0.04 m. The grid resolution is held constant at 0.005 m, and therefore only the voxel size and volumetric plant blockage are changing.

For the defoliated plant, the volume of the plant blockage is 0.0003 $m^3$ at a 0.005 m voxel size, 0.0005 $m^3$ at a 0.01 m voxel size, 0.001 $m^3$ at a 0.02 m voxel size, and 0.0025 $m^3$ at a 0.04 m voxel size. The volume of the blockage therefore varies by almost an order of magnitude, with percentage increases in volume relative to the 0.005 m voxel size of ~80, ~280, and ~820% respectively. The volume of the plant blockages represents only 0.05 – 0.45% of the entire model domain. In plan view at 0.5 *Z/h* (Figure 4.17), an increasing voxel size is shown to substantially alter the visual representation of the branches, and this has consequences for the modelled flow field. At voxel sizes < 0.04 m, individual branches are resolved, whereas at a voxel size of 0.04 m the gaps between branches cannot be discerned. When incorporated into the computational domain, faster flow is shown in the gaps between branches at the finest voxel sizes. Furthermore, faster flow is shown around the outer edge of branches, and with increasing voxel size the magnitude of this faster flow increases. At the 0.04 m

voxel size, this results in a pronounced zone of flow acceleration, with downstream velocities of > 0.35 m s$^{-1}$ around the outer edge of the leftmost branch. An increasing voxel size therefore controls fine-scale patterns of flow.
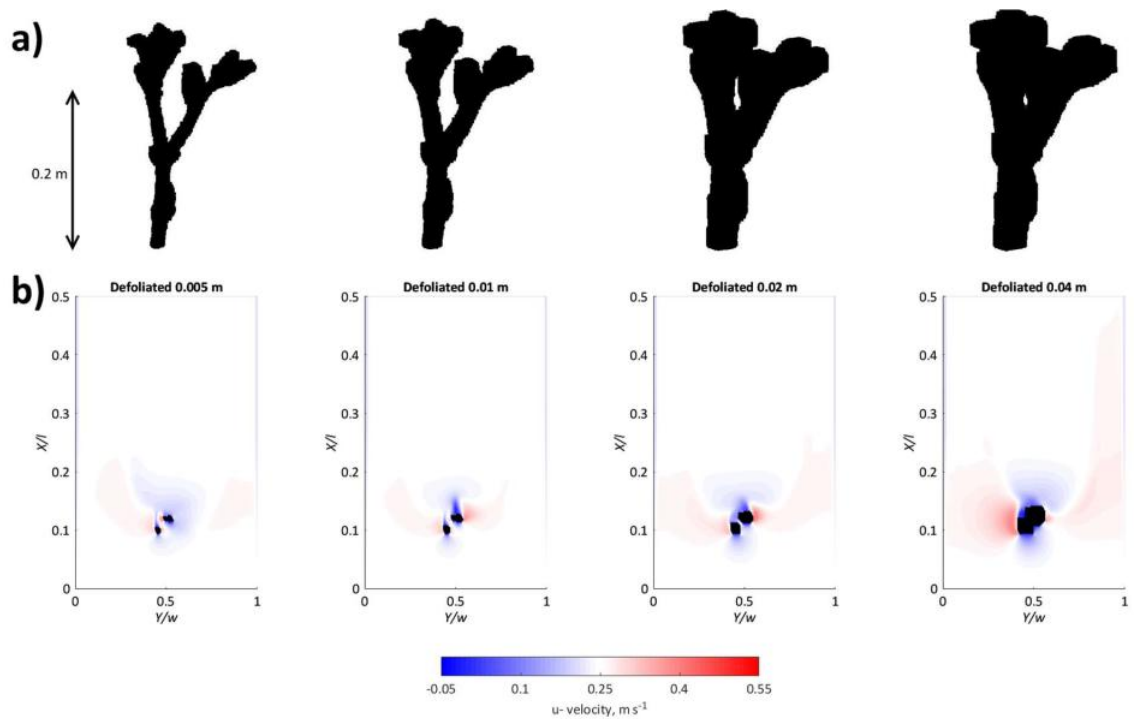


**Figure 4.17 (a) Voxelised defoliated plant at voxel sizes of 0.005 m, 0.01 m, 0.02 m and 0.04 m. Blockage volume increases by 81%, 280%, and 819% relative to the 0.005 m voxel size representation. (b) Downstream velocity field at 0.5 Z/h.**

For the downstream velocity field at 0.5 *Y/w* (Figure 4.18), with increasing voxel size, the zone of reduced velocity immediately downstream of the branch is shown to increase in magnitude and size. The greatest similarity is present between voxel sizes of 0.005 and 0.01 m (associated with an ~80% difference in blockage volume). As the voxel size increases to 0.02 and 0.04 m, more pronounced flow reduction on both the upstream and downstream ends of the blockage is shown. Furthermore, faster flow over the top of the voxelised blockage is shown at voxel sizes of 0.02 and 0.04 m.
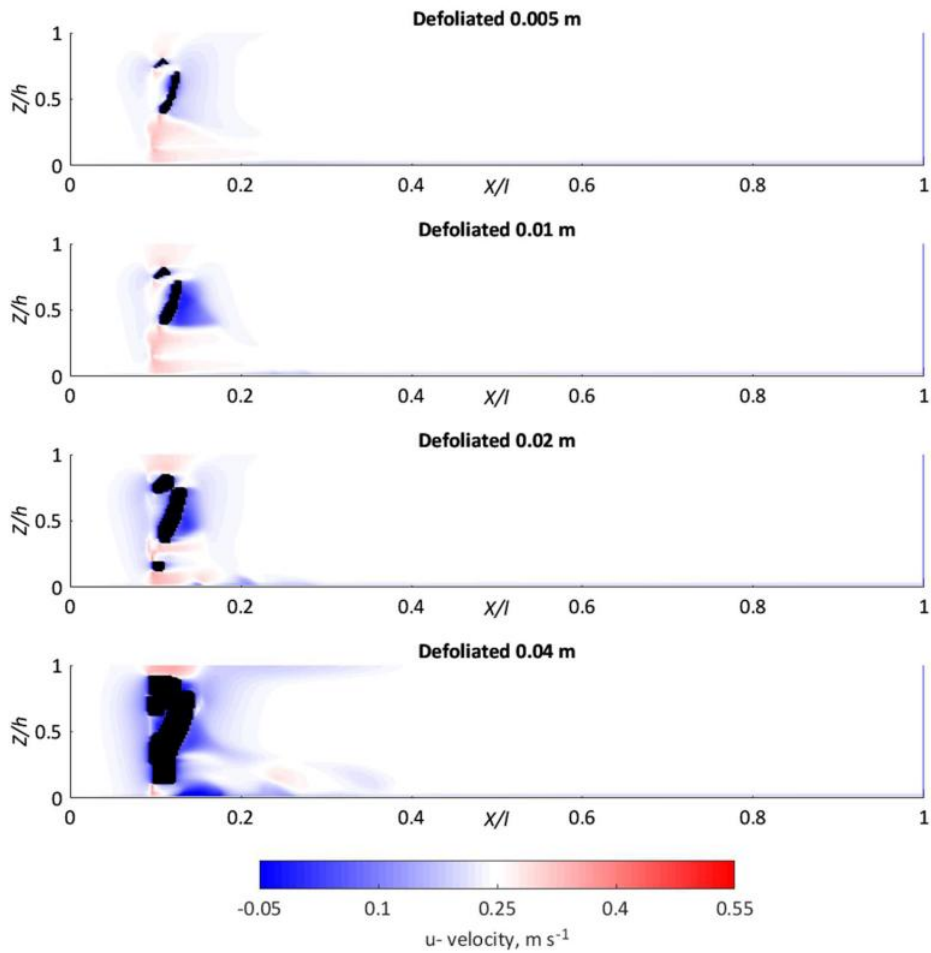
**Figure 4.18 Downstream velocity field at 0.5 Y/w for increasing voxel sizes.**

With increasing voxel size, velocity patterns are further investigated by comparing velocity profiles at pre-defined distances downstream and cross-stream (Figure 4.19), and the mean downstream velocities calculated (Table 4.5). With an increasing voxel size, downstream velocity tends to be reduced. The velocity profiles for 0.005 and 0.01 m voxel sizes most closely match, with a mean difference of -0.01% calculated over the six velocity profiles. For voxel sizes of 0.02 and 0.04 m, mean differences of -0.9 and -1.8% exist relative to the 0.005 m voxel size. Closer to the defoliated plant blockage, these differences are exaggerated, with up to a ~10% velocity reduction at the 0.04 m voxel size, explained by the greater volumetric blockage posed. By 0.4 *X/l*, the flow has recovered, and therefore velocity profiles and mean values closely match.
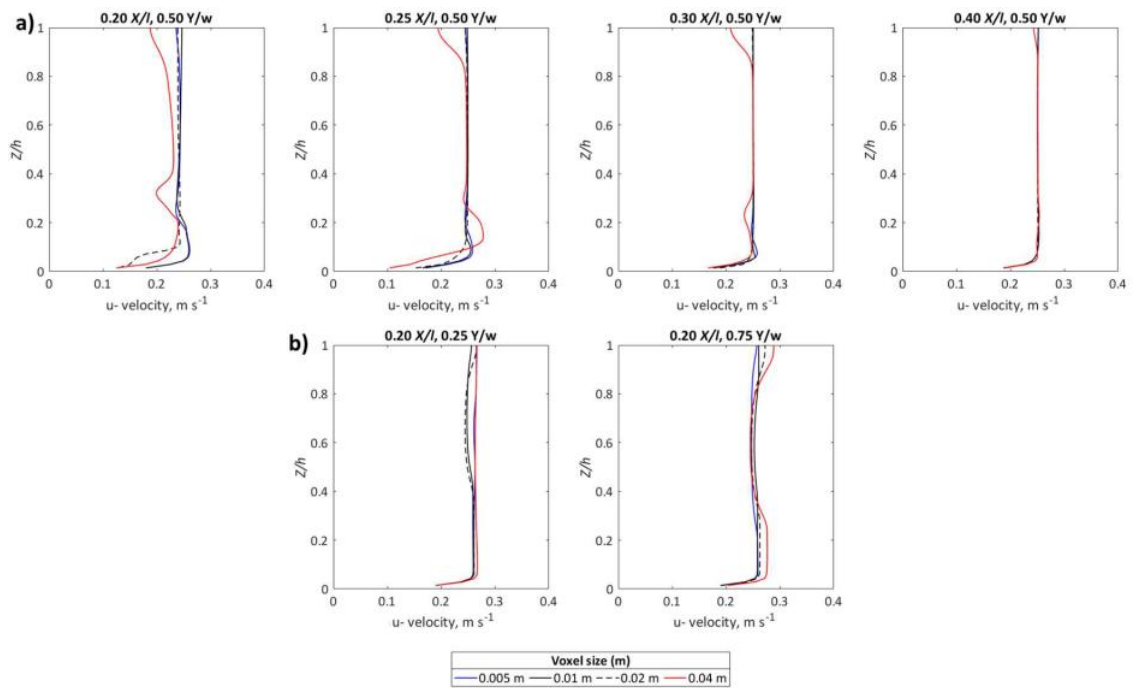
**Figure 4.19 (a) Velocity profiles extracted at predefined intervals downstream and (b) cross-stream from the defoliated representation, for the increasing voxel sizes.**

**Table 4.5 Mean downstream velocities around the defoliated plant at each of the velocity profiles from Figure 4.19.**

| | Mean downstream velocity, m s⁻¹ | | | | | |
|---|---|---|---|---|---|---|
| Voxel size (m) | 0.20 *X/l* 0.5 *Y/w* | 0.25 *X/l* 0.5 *Y/w* | 0.30 *X/l* 0.5 *Y/w* | 0.40 *X/l* 0.5 *Y/w* | 0.20 *X/l* 0.25 *Y/w* | 0.20 *X/l* 0.75 *Y/w* |
| **0.005** | 0.242 | 0.247 | 0.249 | 0.250 | 0.261 | 0.251 |
| **0.01** | 0.244 | 0.247 | 0.249 | 0.250 | 0.253 | 0.256 |
| **0.02** | 0.234 | 0.245 | 0.249 | 0.249 | 0.253 | 0.256 |
| **0.04** | 0.219 | 0.239 | 0.242 | 0.249 | 0.263 | 0.261 |

For the foliated plant, the volume of the plant blockage is 0.0008 m³ at a 0.005 m voxel size, 0.0016 m³ at a 0.01 m voxel size, 0.0032 m³ at a 0.02 m voxel size, and 0.0071 m³ at a 0.04 m voxel size. Again, the volume of the blockage therefore varies by almost an order of magnitude, with percentage increases in volume relative to the 0.005 m voxel size of ~90, ~280, and ~750% respectively. The volume of the plant blockages represents only 0.15 – 1.29% of the entire model domain. As before, morphological detail is lost with a coarsening voxel size (Figure 4.20), and in plan view at 0.5 *Z/h*, an increasing voxel size and volumetric blockage is shown to substantially alter the observed flow patterns. At voxel sizes of 0.005 and 0.01 m, individual stems and leaves produce flow separation and reattachment with the formation of narrow downstream wakes of reduced velocity, interspersed by regions of faster flow. Flow is forced within and between the gaps in the blockage. As the voxel size increases to 0.02 and 0.04 m, individual wakes have coalesced behind the volumetrically greater blockages. As a

result, pronounced low velocities are observed directly behind the blockages which are almost an order of magnitude greater in volume, with the internal flow structure unable to be distinguished. Furthermore, faster flow around the edges of the blockages are noted, especially for the 0.02 and 0.04 m voxel sizes.
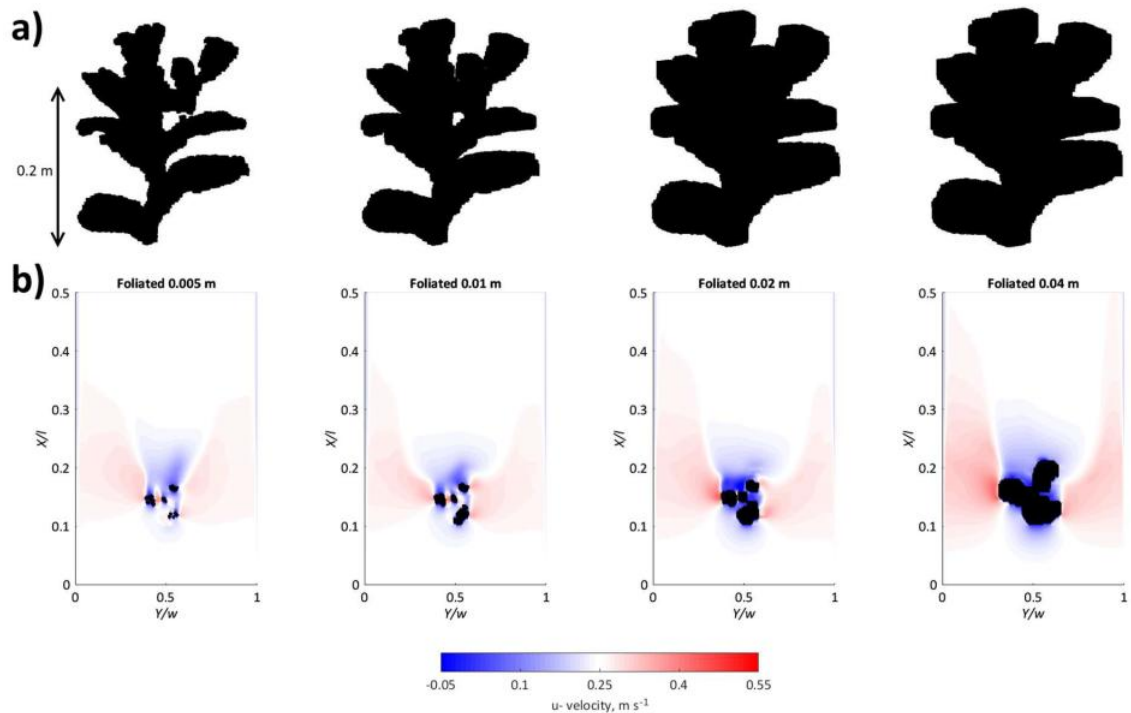


*Figure 4.20 (a) Voxelised foliated plant at voxel sizes of 0.005 m, 0.01 m, 0.02 m and 0.04 m. Blockage volume increases by 87%, 284%, and 751% relative to the 0.005 m voxel size representation. (b) Downstream velocity field at 0.5 Z/h (bottom).*

For the downstream velocity field at 0.5 *Y/w* (Figure 4.21), with increasing voxel size, the zone of reduced velocity immediately downstream of the foliated body is shown to increase in magnitude and size. As was the case for the defoliated plant, the greatest similarity is shown between the 0.005 and 0.01 m voxel sizes (associated with a ~90% difference in blockage volume). As the voxel size and blockage volume increases further, differences become more marked, with the reduced velocity zone becoming larger, and the zone of faster flow above the plant blockage becoming more pronounced.
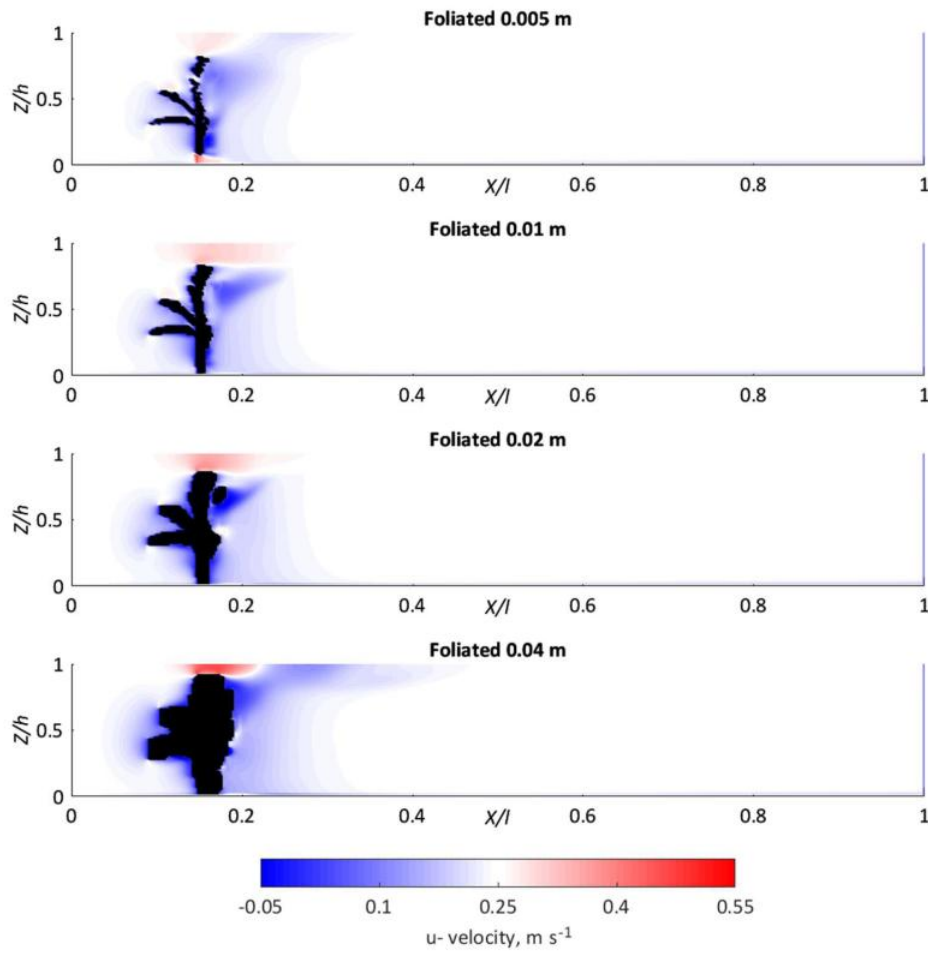
**Figure 4.21 Downstream velocity field at 0.5 Y/w for increasing voxel sizes.**

Velocity profiles at pre-defined distances downstream and cross-stream (Figure 4.22), and the mean downstream velocities (Table 4.6) are calculated with increasing voxel size. Immediately downstream of the blockage (0.2 $X/l$), the velocity profile for the 0.01 m voxel size most closely matches the shape of the profile for the 0.005 m voxel size. In contrast, the 0.04 m profile appears very different, with an inflection exaggerated towards lower velocities around 0.75 $Z/h$. Relative to the 0.005 m profile at 0.2 $X/l$, the mean average velocity is ~3% lower for 0.01 m, ~6% lower for 0.02 m, and ~30% lower for 0.04 m voxel sizes. The evolution, development, and reattachment of the wake is demonstrated by incremental velocity profiles downstream, and again demonstrates the important role of blockage volume in controlling the flow patterns observed.

As for the defoliated representation, velocity profiles indicate that the flow has almost fully recovered by 0.4 $X/l$, and this is consistent for all voxel sizes. Towards the left blockage edge (0.25 $Y/w$), increases in voxel size correspond with increased flow acceleration, with the mean velocity of the 0.04 m voxel size profile ~12% greater than

that for the 0.005 m voxel size.  On the right blockage edge (0.75 *Y/w*), flow disturbance appears more minimal across all voxel sizes, with magnitudes of mean difference less than ~3%.  This difference is suggested to be caused by the asymmetry in plant morphology.  Over the six velocity profiles, mean differences of -0.6, -1.0 and -7.5% for voxel sizes of 0.01, 0.02, and 0.04 m are calculated relative to the 0.005 m voxel size.
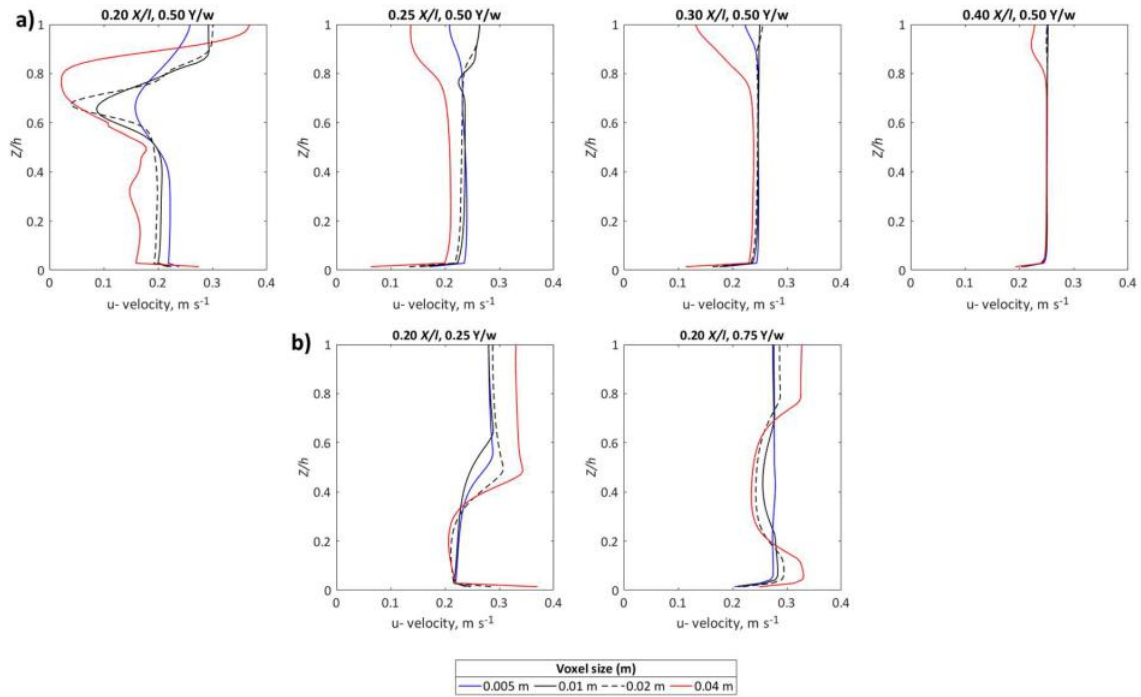


**Figure 4.22 (a) Velocity profiles extracted at predefined intervals downstream and (b) cross-stream, for the foliated representation, for the increasing voxel sizes.**

**Table 4.6 Mean downstream velocities around the foliated plant at each of the velocity profiles from Figure 4.22.**

| | Mean downstream velocity (m s⁻¹) | | | | | |
|---|---|---|---|---|---|---|
| **Voxel size (m)** | 0.20 *X/l* 0.5 *Y/w* | 0.25 *X/l* 0.5 *Y/w* | 0.30 *X/l* 0.5 *Y/w* | 0.40 *X/l* 0.5 *Y/w* | 0.20 *X/l* 0.25 *Y/w* | 0.20 *X/l* 0.75 *Y/w* |
| **0.005** | 0.208 | 0.232 | 0.245 | 0.250 | 0.259 | 0.274 |
| **0.01** | 0.202 | 0.237 | 0.246 | 0.250 | 0.254 | 0.270 |
| **0.02** | 0.197 | 0.233 | 0.244 | 0.250 | 0.266 | 0.267 |
| **0.04** | 0.149 | 0.191 | 0.220 | 0.244 | 0.289 | 0.280 |

Differences in downstream velocity are investigated by subtracting the 0.005 m downstream velocity field from the downstream velocity fields incorporating plant representations with 0.01, 0.02, and 0.04 m voxel sizes (Figure 4.23 shows horizontal slices along the midline (0.5 *Y/w*)).  As the voxel size increases, the magnitude of the velocity difference becomes greater.  Velocity differences between the 0.005 and 0.01 m representations are minimal (generally less than ± 0.05 m s⁻¹), and located in close

proximity to the plant blockage. In contrast, between the 0.005 and 0.04 m representations, more marked velocity differences cover a greater area, with differences exceeding ± 0.20 m s$^{-1}$. This indicates a more significant flow disturbance introduced when the voxel size, and blockage volume, is greater.
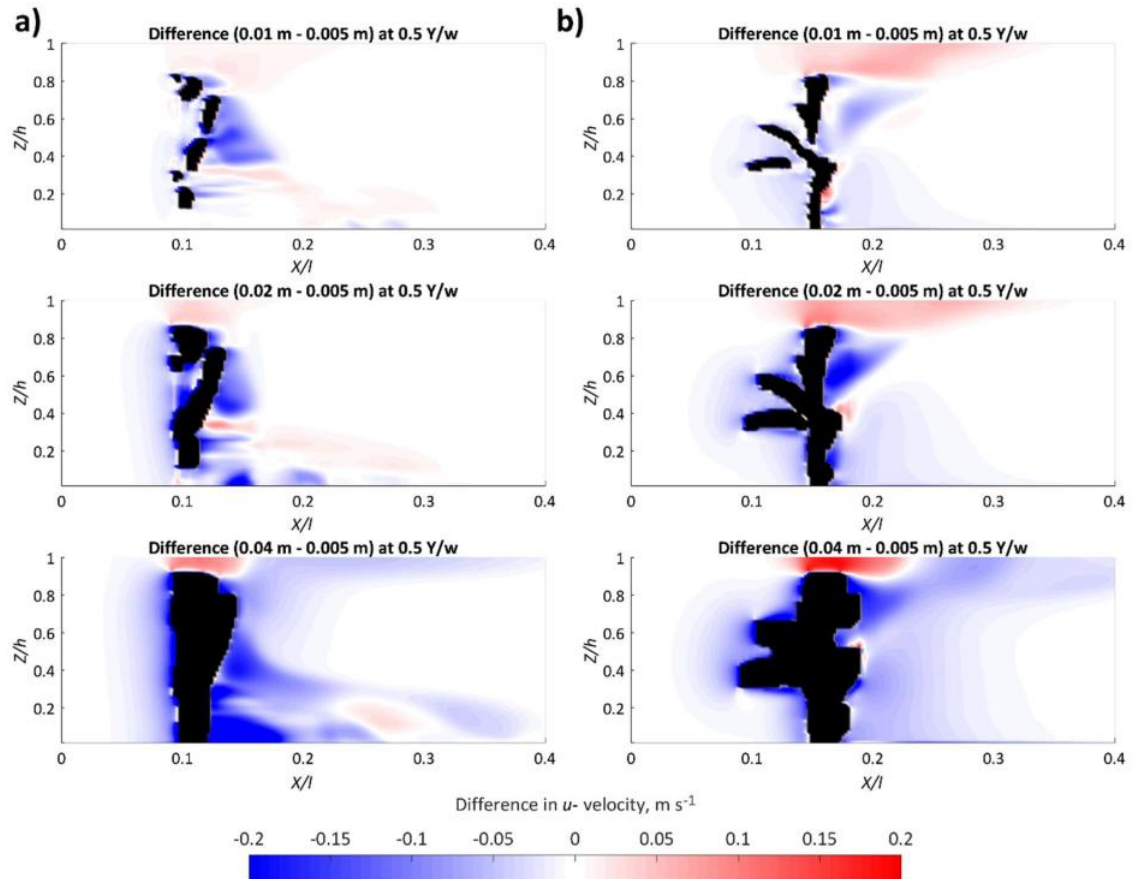


*Figure 4.23 (a) Differences in the downstream velocity with increasing voxel size, calculated by subtracting the 0.005 m velocity field, from the 0.01 m, 0.02 m, and 0.04 m velocity fields at the midline (0.5 Y/w) for the defoliated plant and (b) the foliated plant.*

An understanding of the effect voxel size has on the pressure field is also necessary. The effect of voxel size on the pressure field is shown to be even more significant than on the downstream velocity field (Figure 4.24). At 0.005 and 0.01 m voxel sizes, small individual zones of high pressure are apparent on the upstream side of each branch/leaf, with individual low pressure zones almost reflected on the downstream side. As voxel size increases, and the volume of the blockage increases, these zones become larger through coalescence, becoming exaggerated on the downstream side. This increases the pressure gradient, and would increase the drag. Beyond a voxel size of 0.01 m, the definition of individual high/low pressure regions upstream and downstream of the plant cannot be distinguished. Proximal to the blockage edges, pressure values are at their greatest (> ± 50 Pa), and this diminishes with distance from away the plant.
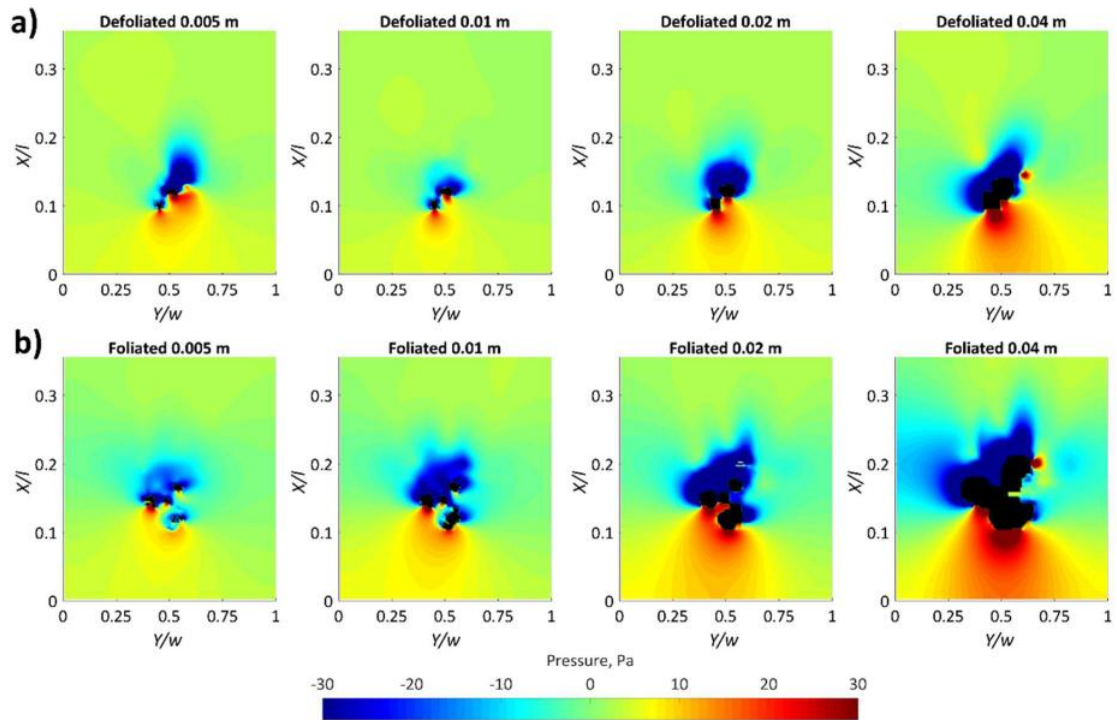
***Figure 4.24 (a) Pressure fields about the defoliated plant and (b) foliated plant section at 0.5 Z/h. With increasing voxel size, high pressure zones on the upstream edge, and low pressure zones on the downstream edge become more pronounced.***

With increasing voxel size, the magnitude of the pressure gradient, defined as the difference in pressure upstream/downstream of the blockage, is shown to increase (Figure 4.25). In this figure, the sum of the pressure gradient for each vertical increment (0.005 m) over the vertical extent of the flow depth containing defoliated and foliated blockages are displayed. By calculating the mean average of the sum of pressure gradients at each vertical increment (Table 4.7), average pressure gradients can be compared.

Most notably, with increasing voxel size from 0.005 – 0.04 m, the pressure gradient increases by over an order of magnitude for both defoliated and foliated plants. This is to be expected given the order of magnitude increase in blockage volume. Therefore, by altering the voxel size, significant changes in the magnitude of the pressure response are calculated. Beyond this, similarities in the shape of the pressure gradient profiles exist between the different voxel sizes, with peaks of pressure gradient almost corresponding with one another, and caused by similar morphological features of the plant representations, albeit with different volumes.

However, spatial lags in the peaks are most clearly evident in the defoliated plant, with peaks displaced higher in the vertical extent at coarser voxel sizes. Cross-correlation is

used to estimate the delay in pressure gradient between the 0.005 m voxel size and the 0.01, 0.02 and 0.04 m voxel sizes, with a delay of 1, 2 and 7 vertical increments (0.005, 0.01 and 0.035 m) quantified for the defoliated plant. For the foliated plant, no appreciable delay is found. Therefore, changes in voxel size and volume of the blockage are shown to modify the spatial distribution of the pressure field over the plant extent, as well as the magnitude of the pressure gradient.
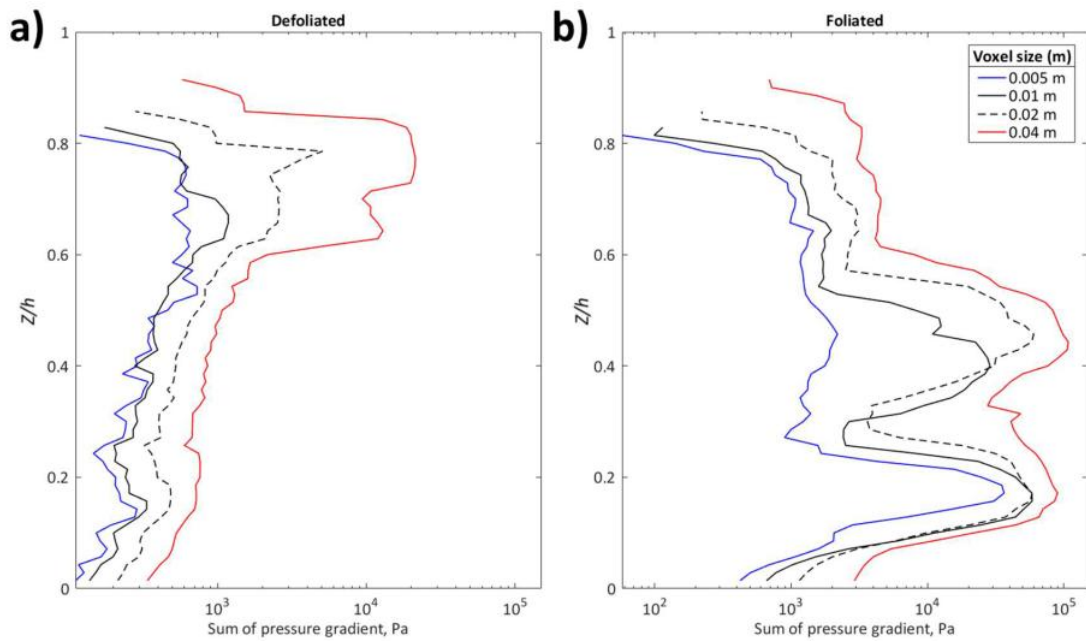


*Figure 4.25 (a) Sum of pressure gradients at each vertical increment in flow depth for defoliated plant and (b) foliated plant.*

*Table 4.7 Mean pressure gradient over the entire vertical extent of flow depth with defoliated and foliated blockages.*

| | | Voxel size (m) | | | |
|---|---|---|---|---|---|
| | | 0.005 | 0.01 | 0.02 | 0.04 |
| **Mean pressure gradient (Pa)** | Defoliated | 296 | 365 | 866 | 4295 |
| | Foliated | 3303 | 10123 | 14815 | 31839 |

#### 4.3.7.2.4    Grid independence summary

For a geometrically simple, cuboidal blockage where the volume is conserved between different grid resolutions, grid independence has been shown, with cross-section GCI values for downstream velocity and pressure quantified to be ~1%, and global GCI values quantified to be ~0.5% between grid resolutions of 0.005 and 0.01 m. Grid independence for the hydraulics at the grid resolutions analysed is demonstrated. When incorporating a geometrically complex, characteristic plant blockage into the same grid

design, the volume of the blockage is not conserved between the different grid resolutions, and additional uncertainty arises. Cross-section and global GCI is shown to be substantially higher. This is caused by the volumetric increase in the plant blockage, an artefact of the voxelisation procedure, resulting from the spatial discretisation of the plant. This is also expected to alter the morphology of the blockage, further altering the flow field. Finally, the sensitivity to the voxel size has been quantified for the characteristic plant blockage under contrasting levels of foliage (defoliated and foliated). Again, volume was not conserved between the different voxel sizes, but grid resolution was held constant. These results show the similarity in the downstream velocity and pressure fields between voxel sizes of 0.005 and 0.01 m, but at voxel sizes coarser than this, the results are shown to diverge.

These results demonstrate the importance of selecting a grid resolution and voxel size appropriate to the scale of analysis to be undertaken. Previously, it has been shown that a 0.01 m voxel size closely approximated the finest morphological elements of the plant (Section 3.3.4), and this follows Hosoi *et al.* (2013), who suggest that the voxel size should be based on the smallest branch diameter. Were the branch diameter smaller, a finer voxel size would therefore be necessary. However, it is important to acknowledge the additional computational expense associated with solving flow at the finest grid resolutions, and therefore a trade-off exists between computational expense and the detail required. Grid independence is shown between grid resolutions of 0.005 and 0.01 m, and therefore with appropriate selection of the voxel size used to describe the specific plant, the numerical solution should be credible. The grid resolution must therefore be appropriate for the discretisation of the plant, and for the scale of analysis conducted.

### 4.3.7.3 CFD validation

Comparison with reliable experimental results, the traditional form of model validation, is only an optional criterion in the ASME guidelines. However, in application of CFD to open channel flow problems, some evaluation of the practical utility of the CFD model through model assessment is often required (Lane and Richards, 2001; Hardy *et al.*, 2003; Lane *et al.*, 2005). Validation conventionally relies upon the comparison of predictions with empirical measurements, considering the goodness of fit, precision, and accuracy (Lane and Richards, 2001). However, it is important to be critical about the validation data. The data used to validate the model should reflect what the model is attempting to predict (Lane *et al.*, 2005), and any errors in the data should be

recognised, e.g. the spatial structure of the validation data error field (Bradbrook *et al.*, 1998). Error can exist in both the measured and modelled data, and this has important implications for the selection of appropriate statistical methods (Lane *et al.*, 2005). Where possible it is important to consider the entire flow field, rather than selected points over a small sample of model predictions, with the optimal assessment usually through some form of regression (Lane *et al.*, 2005). By following such an approach, the levels of precision and accuracy can be defined, and a judgement provided as to which aspects of the model are being reproduced sufficiently for practical interpretation (Lane *et al.*, 2005). In this thesis, a complementary flume study of depth-limited flow around an isolated, submerged riparian plant at three different flow Reynolds numbers provides the validation data, and additional boundary conditions, required for the CFD model (Chapter 5).

### 4.3.7.4 Good modelling practice summary

This section has shown the criteria used to demonstrate good modelling practice, focusing on model verification and validation, with specific reference to the guidelines outlined by ASME (1993) and Lane *et al.* (2005) for CFD applied to open channel flows. Considerable attention has been paid to the spatial discretisation of the plant in the CFD model (Section 4.3.7.2), with discussion and justification for selection of the grid resolution appropriate for the scale of analysis. In the subsequent section (Section 4.4), model sensitivity to a range of hydraulic boundary conditions is assessed, focusing on the inlet velocity (Section 4.4.1), inlet turbulence intensity (Section 4.4.2), and submergence (Section 4.4.3).

## 4.4        Model sensitivity to hydraulic boundary conditions

Taking the characteristic section of the plant outlined previously (Section 4.3.4), and designing a grid with a resolution of 0.01 m, and an equal voxel size of 0.01 m to represent the plant, the sensitivity to a range of hydraulic boundary conditions are tested. Unless otherwise indicated, inlet velocity was set to 0.25 m s$^{-1}$, an inlet turbulence intensity of 5% was specified, and flow was fully turbulent and subcritical. In all cases, the plant blockage remained fully submerged and the plant was positioned fully upright to flow in an unstressed posture.

### 4.4.1        Inlet velocity

The first hydraulic boundary condition tested for sensitivity is the downstream inlet velocity. The inlet velocity is defined at the domain inlet, and here is set uniform over the spatial extent of the inlet. The sensitivity to downstream inlet velocities of 0.125, 0.25, 0.5, and 1 m s$^{-1}$ are tested, with the *v*- and *w*- components of velocity set to 0 m s$^{-1}$. To enable comparisons of the spatial distribution of downstream velocity over the entire inlet velocity range, downstream velocities are normalised by inlet velocity (Figure 4.26, Figure 4.27, and Figure 4.28). Firstly, the distribution of normalised downstream velocity for a slice at 0.5 Y/w is shown in Figure 4.26, and from this the spatial distribution of normalised downstream velocity clearly remains similar throughout the range of inlet velocities tested. For each inlet velocity, a zone of reduced downstream velocity is observed in the immediate upstream vicinity of the plant blockage. Similarly, a consistent zone of flow acceleration is shown above each plant blockage, the magnitude of which remains very similar throughout (~1.25 of normalised velocity). On the downstream side of the plant blockage, a pronounced zone of reduced normalised velocity exists. Generally, the shape and extent of this reduced velocity zone remains similar throughout the inlet velocities tested, although a slight lengthening of the zone is shown for inlet velocities of 0.5 and 1 m s$^{-1}$, and therefore the flow takes longer to fully recover in these cases. However, for a midline slice of the domain the normalised downstream velocity remains remarkably consistent, and therefore appears insensitive to the range of inlet velocities tested.
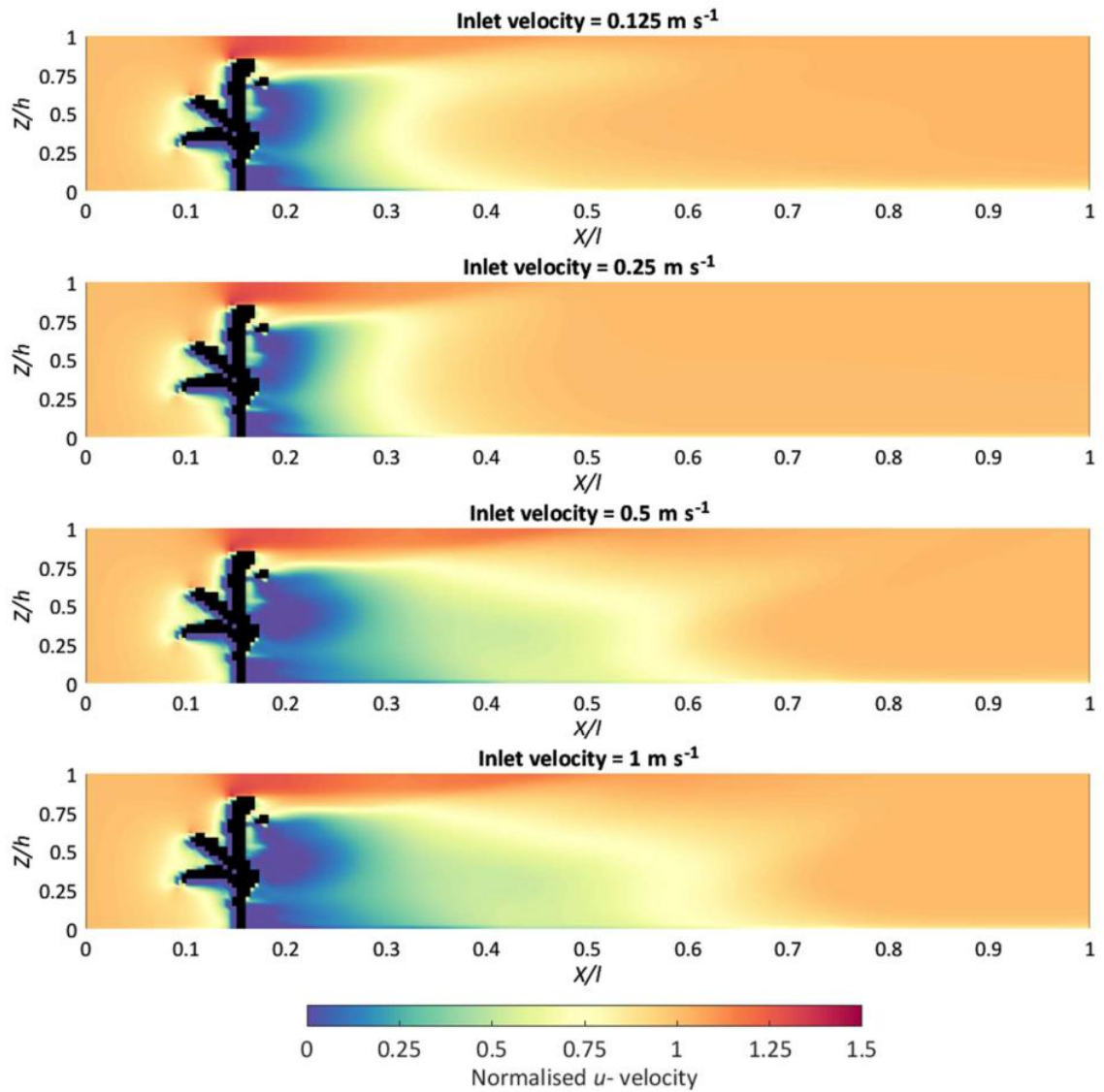
*Figure 4.26 Normalised downstream velocity with increasing inlet velocities (top to bottom) at 0.5 Y/w.*

This similarity is further emphasised in Figure 4.27, showing the distribution of normalised downstream velocity for a slice at 0.5 *Z/h*. Again, the spatial distribution of normalised downstream velocity appears insensitive to the inlet velocity. Zones of flow acceleration around the outer edges of the plant blockage (distributed at ~0.3 and ~0.7 *Y/w*) appear consistent in shape and magnitude throughout the range of inlet velocities. However, as shown in Figure 4.26, again a slight downstream lengthening of the reduced velocity zone is noted for inlet velocities of 0.5 and 1 m s⁻¹. It is suggested that the zone becomes more intense, with a greater gradient. The shape of the zone has slightly changed, with an increased 'waviness' at higher inlet velocities. This is further investigated by analysing normalised downstream velocity profiles at incremental distances down the domain.
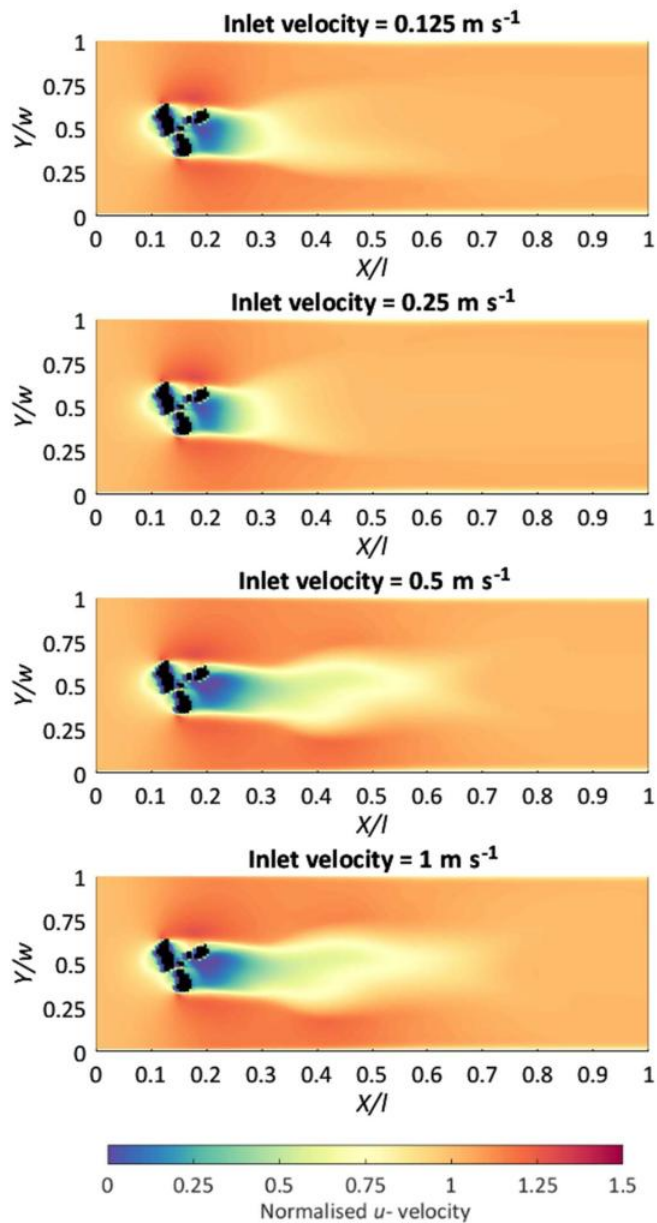
**Figure 4.27 Normalised downstream velocity with increasing inlet velocities (bottom to top) at 0.5 Z/h.**

Normalised downstream velocity profiles are extracted for each of the inlet velocities at increasing distances downstream at the midline (0.5 *Y/w*), and at 0.33 and 0.66 *Y/w* of the domain (Figure 4.28). Within closest proximity to the plant blockage, the shape of the velocity profiles under the range of inlet velocities are most similar (e.g. 0.20 *X/l*, 0.50 *Y/w*), especially in the zone of flow acceleration above the plant blockage. At the midline, with increasing distance downstream the shape of normalised velocity profiles at inlet velocities of 0.125 and 0.25 m s$^{-1}$ become separated from those with inlet velocities of 0.5 and 1 m s$^{-1}$. The magnitude of the velocity reduction is greatest at higher inlet velocities in this downstream region, as the flow begins to recover more quickly for the lower inlet velocities (as shown at 0.3 *X/l*, 0.5 *Y/w*). At 0.33 and 0.66 *Y/w*, the shape and magnitude of the velocity profiles remain very similar throughout the inlet velocities

tested. At 0.25 *X/l*, 0.66 *Y/w,* normalised downstream velocities greater than 1 indicate flow acceleration throughout much of the flow depth, consistent across the range of inlet velocities. Although the normalised downstream velocity profiles have shown that the reduced velocity zone extends further under higher inlet velocities, the overall spatial distribution is shown to be very similar (Figure 4.26 and Figure 4.27), and therefore the spatial patterns of downstream velocity around the plant blockage appear almost insensitive to the inlet velocity.



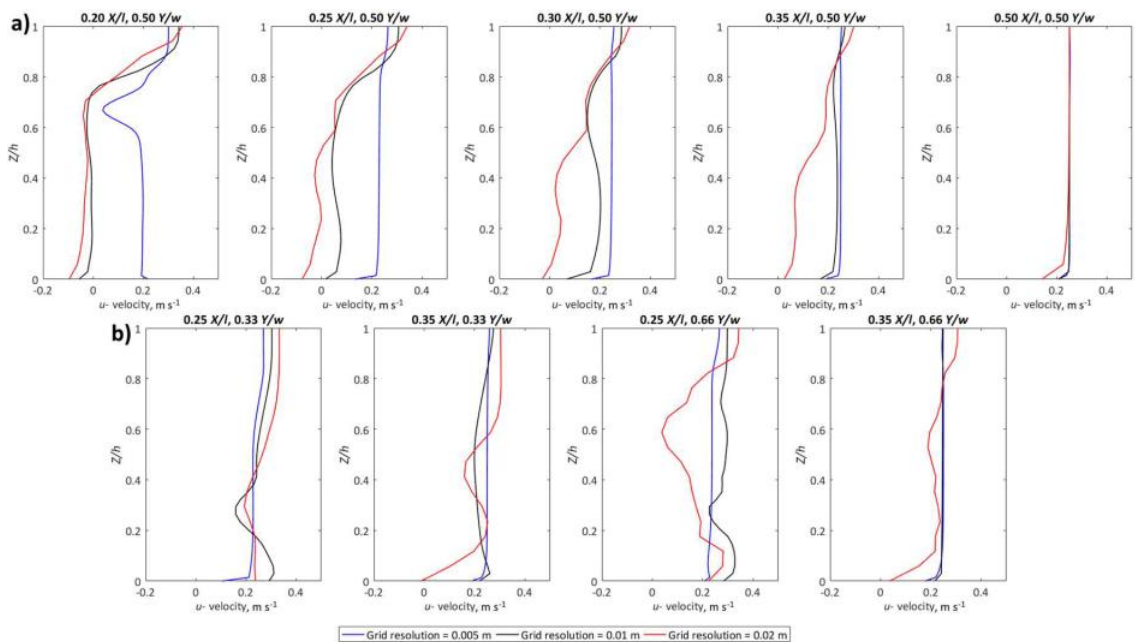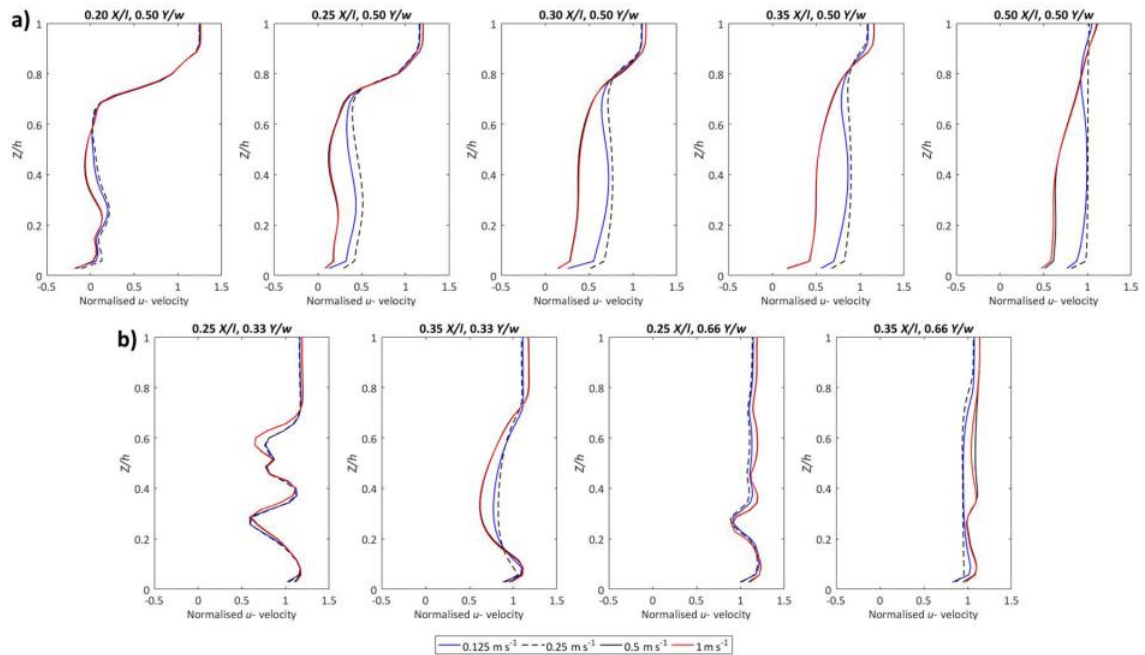*Figure 4.28 (a) Normalised downstream velocity profiles for the different inlet velocities at increasing distances downstream at 0.5 Y/w and (b) at 0.33 and 0.66 Y/w.*

In addition to the effects of inlet velocity on the normalised downstream velocity field, the effects on the spatial distribution of the pressure field are also considered. It is important to note the differences in scale between the different inlet velocities in Figure 4.29, but similar pressure distributions are apparent. In each case, highest pressures are located on the upstream end of the plant, with lowest pressure recorded on the downstream end. With increasing inlet velocity, the magnitude of the high and low pressure zones increase, which will increase the drag, but the spatial distributions remain the same, as shown by highest pressures recorded in the zone between individual leaves on the upstream end. Combined, the similarity in downstream velocity and pressure fields at different inlet velocities justifies running simulations for a single velocity.
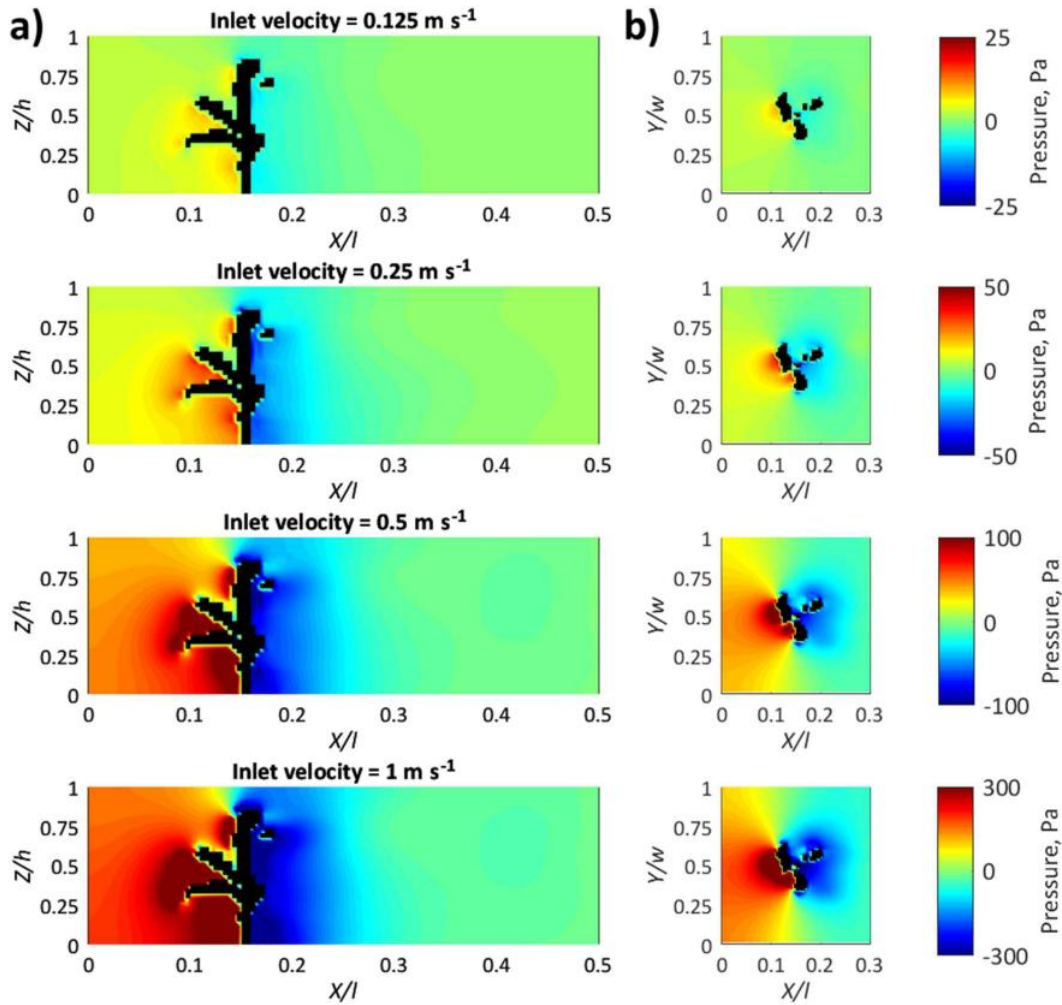
***Figure 4.29 (a) Pressure fields at 0.5 Y/w, (b) and 0.5 Z/h for increasing inlet velocities (top to bottom). Note the differences in scale for the pressure fields.***

## 4.4.2      Inlet turbulence intensity

The effect of modifying the inlet turbulence intensity on downstream velocity and pressure fields are also quantified. In PHOENICS, the turbulence quantities at the inlet can be specified by the user. The inlet values of $k$ and $\varepsilon$ are calculated following:

$$k_{in} = (0.01\, I_t\, U_{norm})^2 \qquad (4.31)$$

$$\varepsilon_{in} = (C_\mu C_d)^{3/4} k_{in}^{\,3/2}(0.1\, len) \qquad (4.32)$$

where $I_t$ is the inlet turbulence intensity (%), $U_{norm}$ is the velocity normal to the inlet (m s⁻¹) and *len* is the length scale, taken as the hydraulic radius of the inlet (m). The constants in the turbulence model $C_\mu$ and $C_d$, are defaulted to values of 0.5478 and 0.1643 (CHAM, 2007). In a previous study, various inlet turbulence intensities between

5 and 20% resulted in a graphically indistinguishable influence on the velocity field over an upland urban river (Ma *et al.*, 2002), and therefore a 10% inlet turbulence intensity was assumed to account for the non-uniform bed topography. In Ma *et al.* (2002) inlet velocities varied over the spatial extent of the inlet (using aDcp data as inlet conditions), whereas here the inlet velocity is set to be uniform over flow depth. The inlet turbulence intensity should be set sufficiently high to initiate turbulence in the domain, but in the absence of inlet profile data, Nallasamy (1987) suggest a careful and judicious choice of inlet turbulence intensity for a physically meaningful prediction. In this application, the sensitivity to inlet turbulence intensities of 5 and 25% are tested.

Figure 4.30 demonstrates the differences in downstream velocity along the midline (0.5 *Y/w*) with inlet turbulent intensities set to 5 and 25%. In both cases, a velocity reduction exists immediately upstream of the plant, with flow acceleration shown above the top of the plant. For the 25% inlet turbulence intensity, this zone of flow acceleration extends further downstream (~0.6 *X/l*) than for the 5% case (~0.4 *X/l*). This trend is repeated for the zone of reduced velocity downstream of the plant, extending to ~0.45 *X/l* at the 5% turbulent intensity, compared with ~0.75 *X/l* when the turbulent intensity is set to 25%. Immediately behind the plant, however, the distribution and magnitude of the velocity reduction appear similar between the inlet turbulent intensities (e.g. at 0.2 *X/l*). With distance downstream, flow is shown to recover more quickly in the 5% inlet turbulence intensity case, owing to the introduction of less turbulence. Another subtle difference exists in the shape of the shear layer separating the flow acceleration zone from the reduced velocity zone, with the 5% inlet turbulence intensity case inclined upwards, whereas the shear layer for the 25% inlet turbulence intensity is flatter.
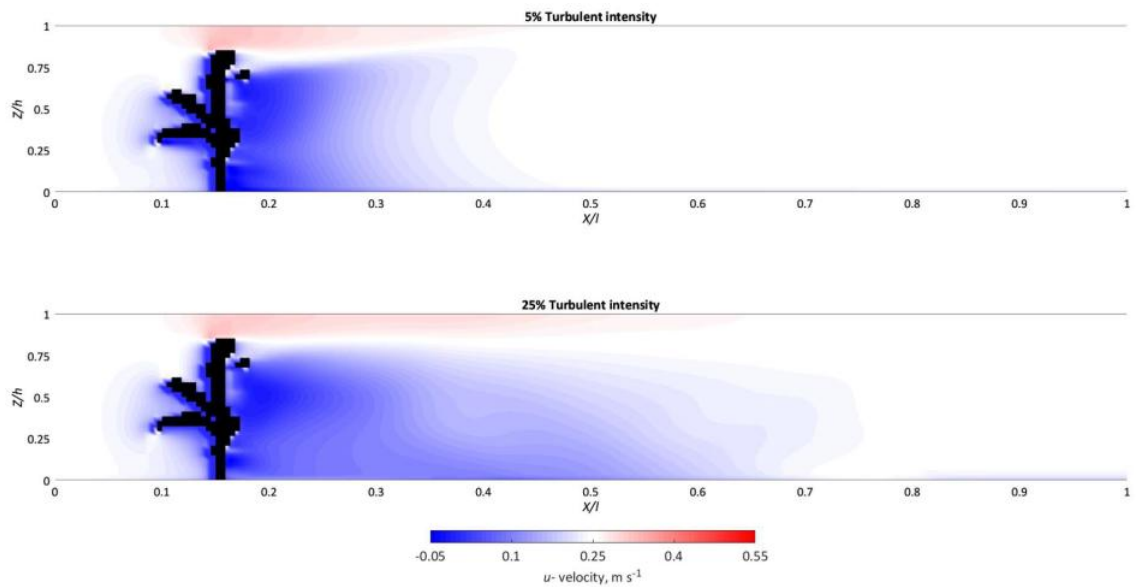
*Figure 4.30 Downstream velocity at 0.5 Y/w for the 5% inlet turbulence intensity and 25% inlet turbulence intensity.*

Further differences are quantified by considering downstream velocity at 0.5 $Z/h$ (Figure 4.30). For the 5% inlet turbulence intensity, the zones of greatest flow acceleration are shown around the outer edge of the plant blockage (~0.15 $X/l$), whereas for the 25% inlet turbulence intensity, an additional zone of flow acceleration is present around 0.4 – 0.5 $X/l$, far beyond the extent of the plant blockage. This additional zone of flow acceleration appears not to be physically realistic. In both cases, the zone of reduced velocity is approximately constrained by the width of plant blockage, and again the zone of reduced velocity extends further downstream at the 25% inlet turbulence intensity, as was shown in Figure 4.30.

**5% Turbulent intensity**

**25% Turbulent intensity**

$u$- velocity, m s$^{-1}$
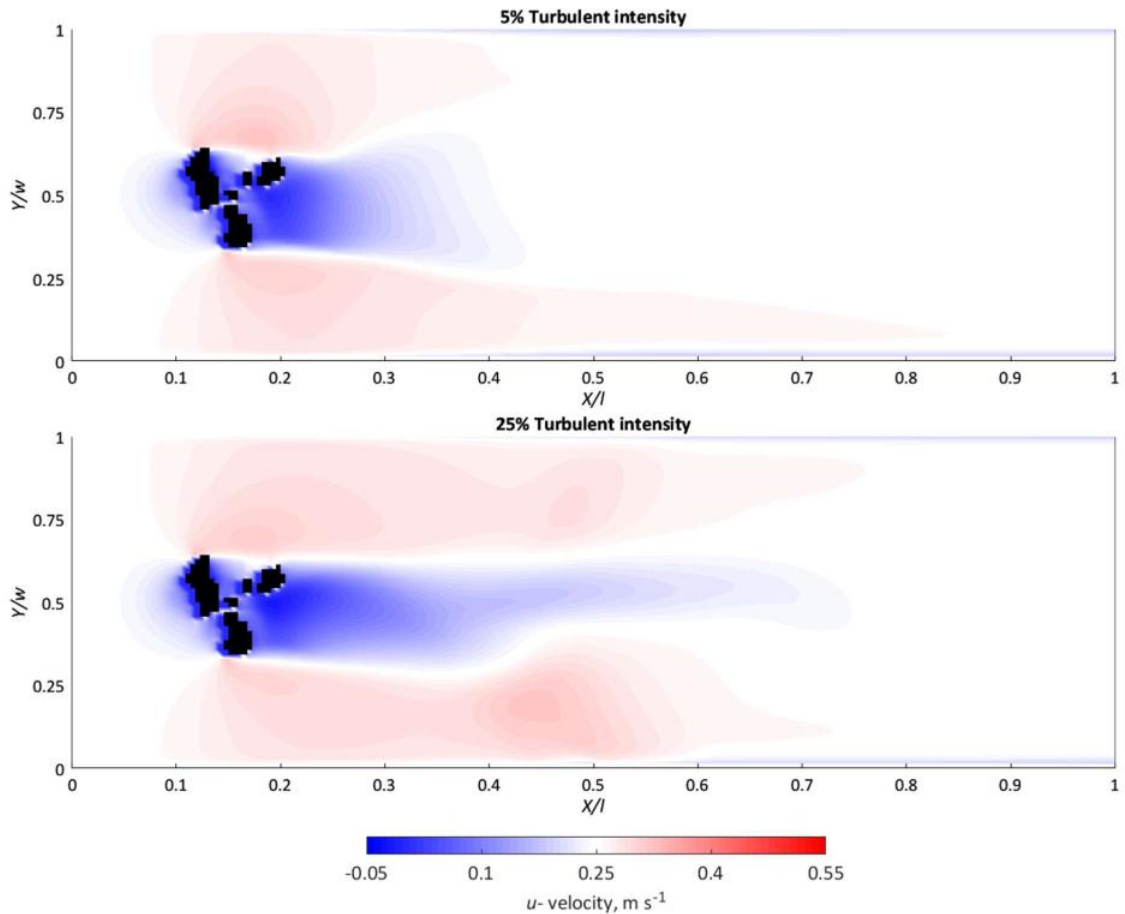
*Figure 4.31 Downstream velocity at 0.5 Z/h for the 5% inlet turbulence intensity and 25% inlet turbulence intensity case.*

Downstream velocity profiles are extracted for the different inlet turbulence intensities at increasing distances downstream at the midline (0.5 *Y/w*), and at 0.33 and 0.66 *Y/w* of the domain (Figure 4.32). Although broadly the profiles show a similar shape, a number of differences exist. At the midline (0.5 *Y/w*), flow has recovered more quickly for the 5% inlet turbulence intensity. Furthermore, the velocity profiles most proximal to the plant blockage differ, where flow heterogeneity is expected to be highest in this region. For the 5% inlet turbulence intensity, this heterogeneity is well predicted, whereas for the 25% inlet turbulence intensity, a lack of heterogeneity is present. Profiles proximal to the blockage appear unnaturally smooth at the 25% turbulence intensity. For these reasons, it is suggested that the 5% inlet turbulence better predicts the expected patterns of downstream velocity.
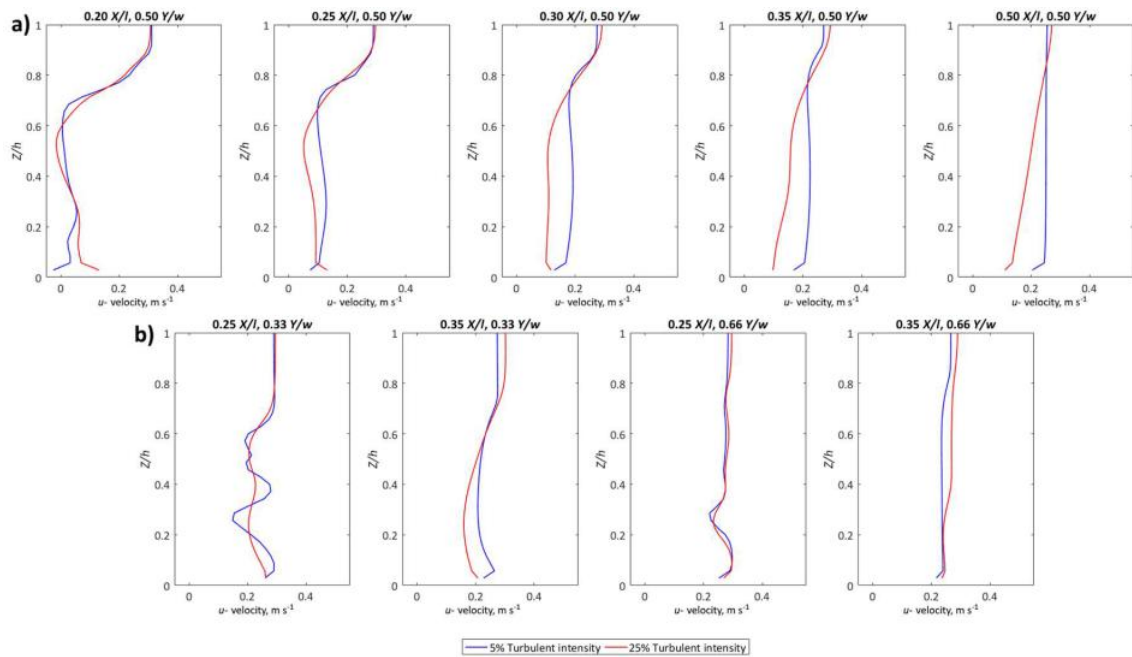
*Figure 4.32 (a) Downstream velocity profiles for the two inlet turbulence intensities at increasing distances downstream at 0.5 Y/w and (b) at 0.33 and 0.66 Y/w.*

In terms of the sensitivity of the pressure field to differences in the inlet turbulence intensity, Figure 4.33 demonstrates that the low pressure zone downstream of the plant blockage extends further downstream under the 5% inlet turbulence intensity. This results in a more rapid return of pressure back towards the ambient pressure for the 25% inlet turbulence intensity. Subtle differences in the spatial distributions of the pressure field therefore exist with differences in the inlet turbulence intensity. However, by quantifying the pressure gradient (difference in pressure immediately upstream and immediately downstream of the plant blockage, Figure 4.34), the overall effect of these spatial differences are minimal. The overall pressure gradient is only 3% higher for the 25% inlet turbulence intensity, and therefore the effect on pressure gradient is only negligible.
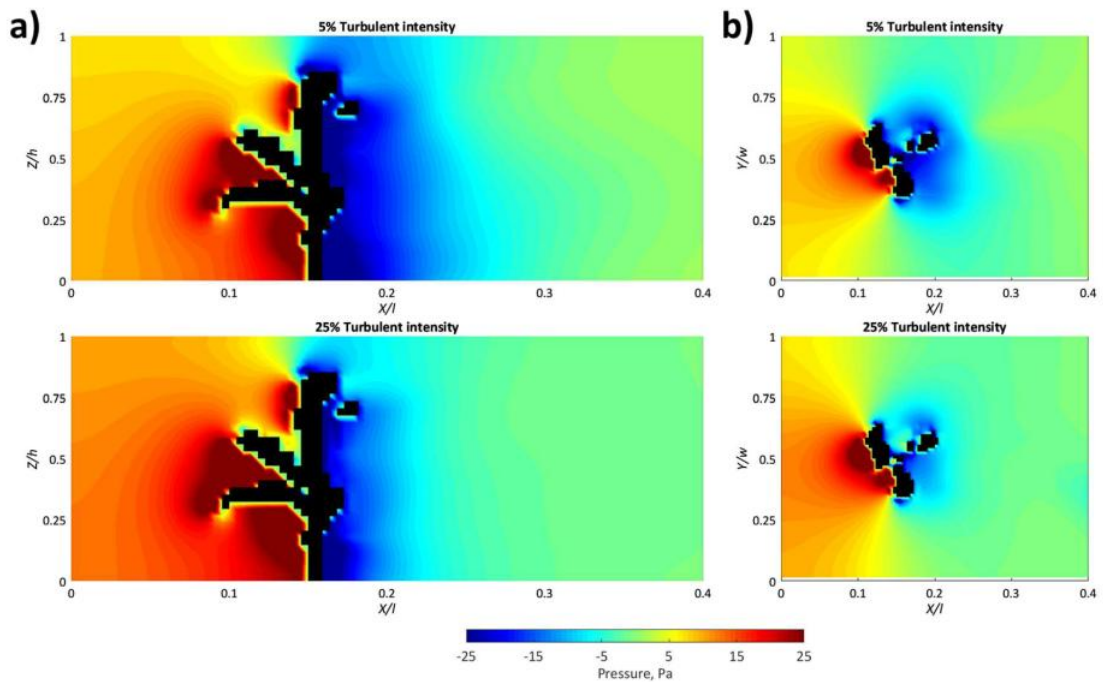
*Figure 4.33 (a) Pressure fields at 0.5 Y/w and (b) 0.5 Z/h for inlet turbulence intensities of 5% and 25%.*
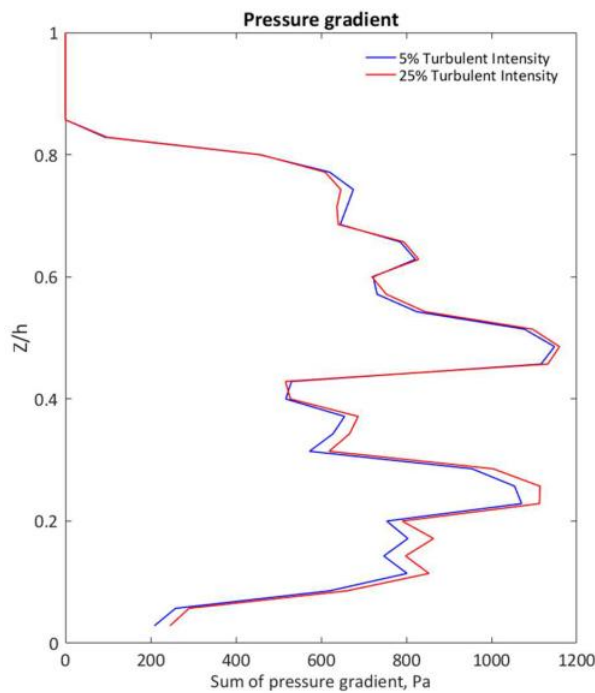


*Figure 4.34 Pressure gradients across the lateral plant extent.*

Finally, the sensitivity of the inlet turbulence intensity on the turbulent kinetic energy (TKE) is quantified. The instantaneous TKE calculation is shown in (4.9), and for the time-averaged TKE follows the same equation, only overbars are placed on the *u-*, *v-*, and *w-* components of velocity to denote time-averaging. As expected, Figure 4.35 demonstrates that additional turbulence is introduced by the 25% inlet turbulence

intensity, resulting in a downstream lengthening of regions of high TKE (> 0.05 m² s²). In close proximity to the plant blockage, patterns of TKE appear very similar between the different inlet turbulence intensities, but with distance downstream the regions introduced by the 25% inlet turbulence intensity are more prominent, whereas for the 5% inlet turbulence intensity, these have dissipated.
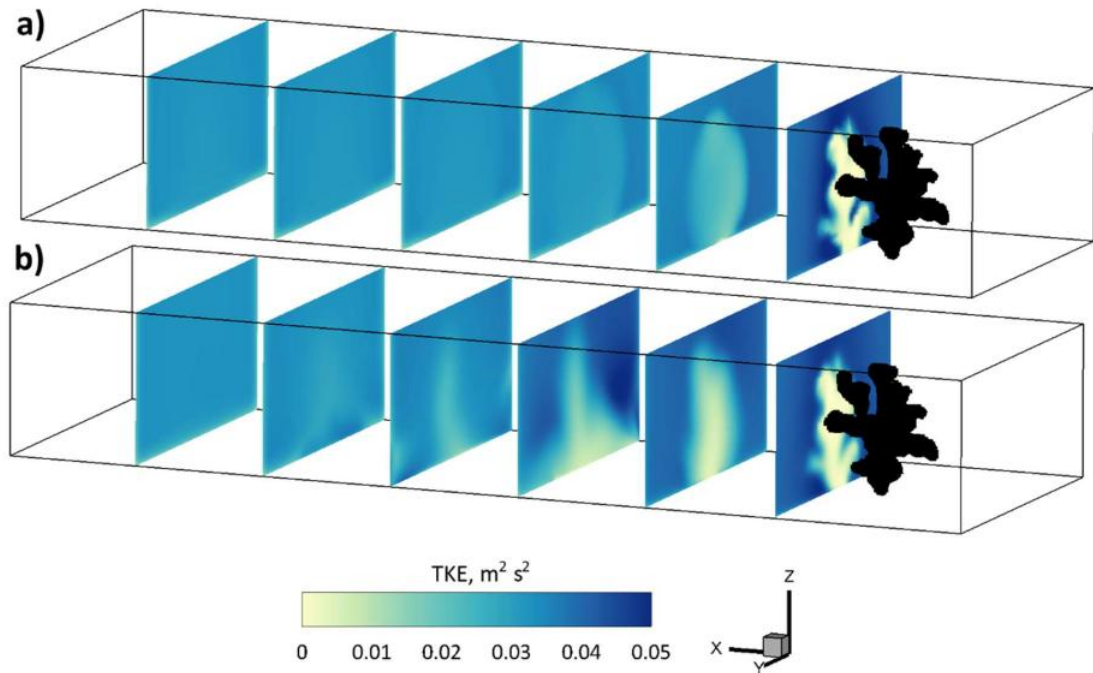


*Figure 4.35 (a) TKE comparison at regular increments downstream for the 5% inlet turbulence intensity and (b) 25% inlet turbulence intensity.*

Distinguishable differences on the velocity, pressure, and TKE fields indicate sensitivity to the inlet turbulence intensity. However, the physical meaningfulness of some of the predictions from the 25% inlet turbulence intensity are lacking, and therefore a 5% inlet turbulence intensity is most appropriate for this application. This is less than the 10% inlet turbulence intensity used by Ma *et al.* (2002), but understandable given no additional complex bed topography is incorporated. An inlet turbulence intensity of 5% has been used in a comparable study by Sandbach *et al.* (2012), which also treated topography with a MFSA.

### 4.4.3     Submergence

Section 2.3.2 has previously shown that the velocity and pressure around submerged vegetation can have a range of behaviours depending on the relative depth of submergence. To test the sensitivity of these factors to the flow hydrodynamics, the

vertical limit of the computational domain is extended by 50% and 100%, with the domains termed 1, 1.5, and 2 *Z/h* (Figure 4.36). The grid resolution and all boundary conditions remain the same for each of the domains, and therefore submergence is the only factor changing.
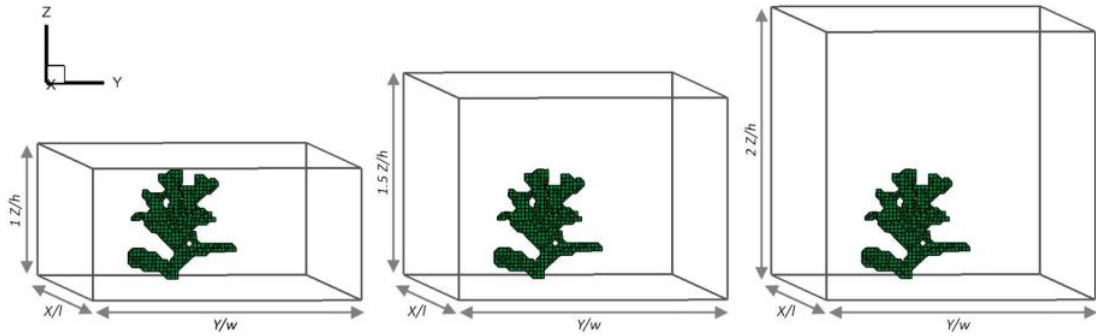


**Figure 4.36 Schematic of the computational domains used to represent increasing submergence. The vertical limit of the domain is extended, meaning that at 1 Z/h = 551 250 cells, 1.5 Z/h = 834 750 cells, and 2 Z/h = 1 102 500 cells.**

The downstream velocity field at 0.5 Z/h and at 0.5 *h* (Figure 4.37) indicates a visual similarity in spatial distribution of downstream velocities under the different submergences, suggesting an insensitivity to submergence over the range assessed. This is further confirmed by assessing downstream velocity profiles over the comparable range 0 – 1 *Z/h* (Figure 4.38), with only very minor differences shown between the velocity profiles. The shape and magnitude of the velocity profiles are very similar, with only slight deviations for 1 *Z/h*. In the region of faster flow above the plant blockage (0.75 – 1 *Z/h*), the downstream velocity is slightly faster for 1 *Z/h*. Furthermore, in the reduced velocity zone behind the plant, the downstream velocity is slightly less than for 1.5 and 2 *Z/h*. However, these differences are only negligible, and can be attributed to the fixed lid used to treat the free-surface (Section 4.3.3). At 1 Z/h, flow is slightly squeezed towards the surface, and due to continuity constraints, this negligibly influences the zone of reduced velocity behind the characteristic plant blockage. Overall, however, downstream velocity appears insensitive to changes in submergence.
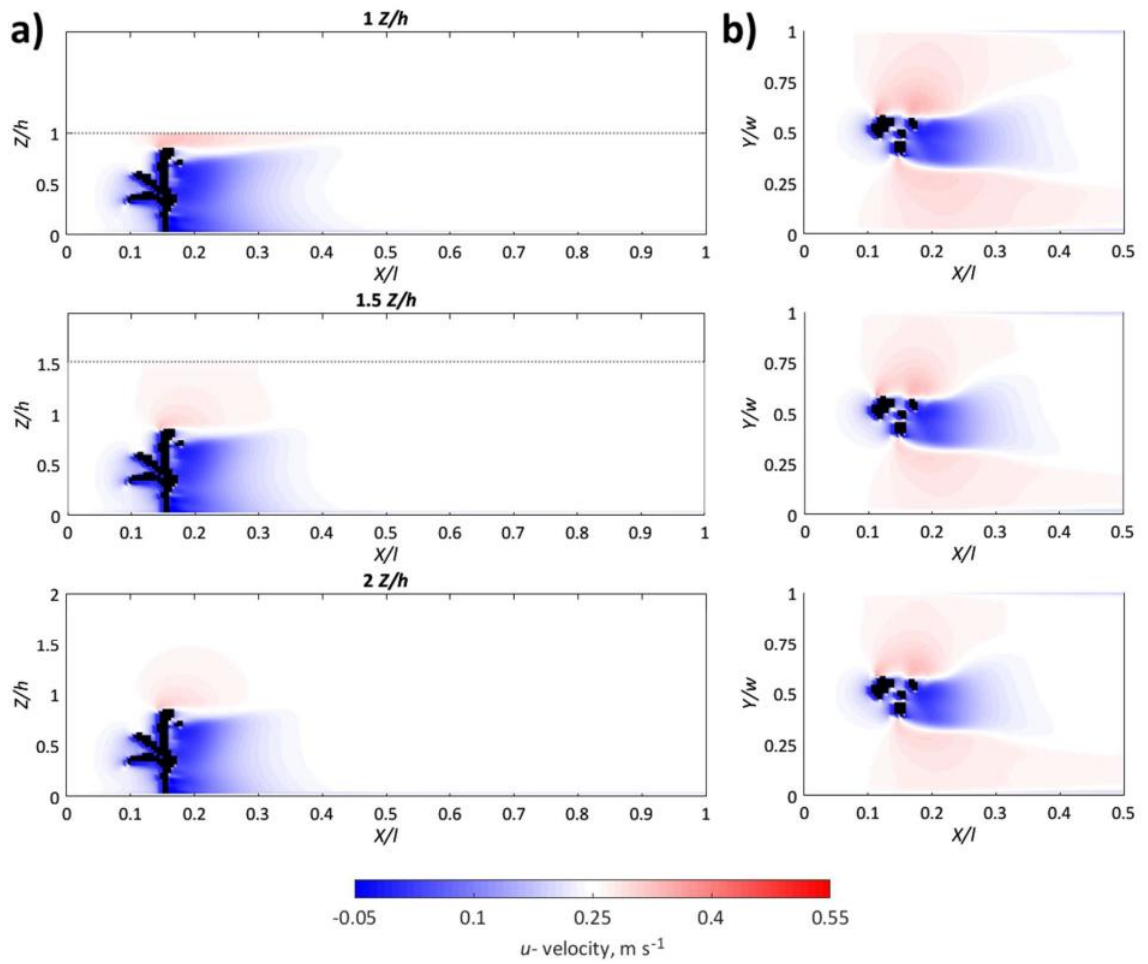
*Figure 4.37 (a) Downstream velocity at 0.5 Y/w and (b) 0.5 h, for increasing plant submergences (top to bottom). The dotted line is the lid of the domain.*
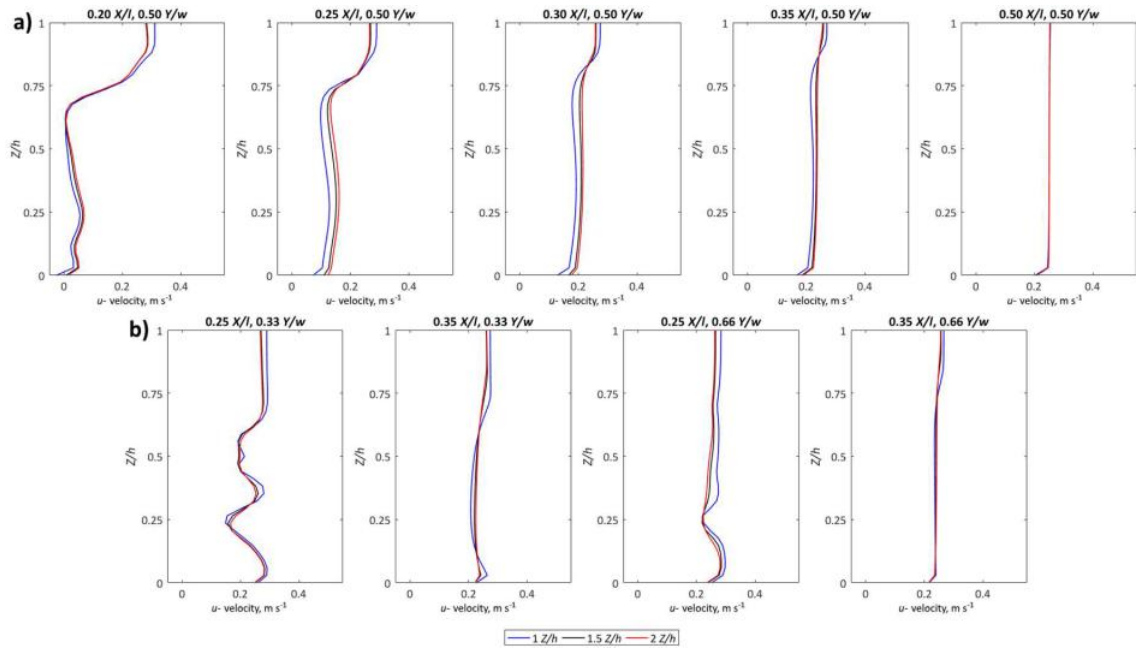
***Figure 4.38 Downstream velocity profiles at increasing plant submergences (compared over the region 0 – 1 Z/h), at incremental distances downstream at 0.5 Y/w (a) and at 0.33 and 0.66 Y/w (b).***

For the pressure field, Figure 4.39 demonstrates a similar insensitivity to submergence as shown by downstream velocity. At 0.5 *Y/w* and 0.5 *h*, the spatial distribution of the pressure field appears to be negligibly influenced by changes in submergence. Combined, these results suggest that it is only necessary to run simulations for a single submergence, as the spatial distribution of downstream velocity and pressure remain unchanged throughout the range assessed.
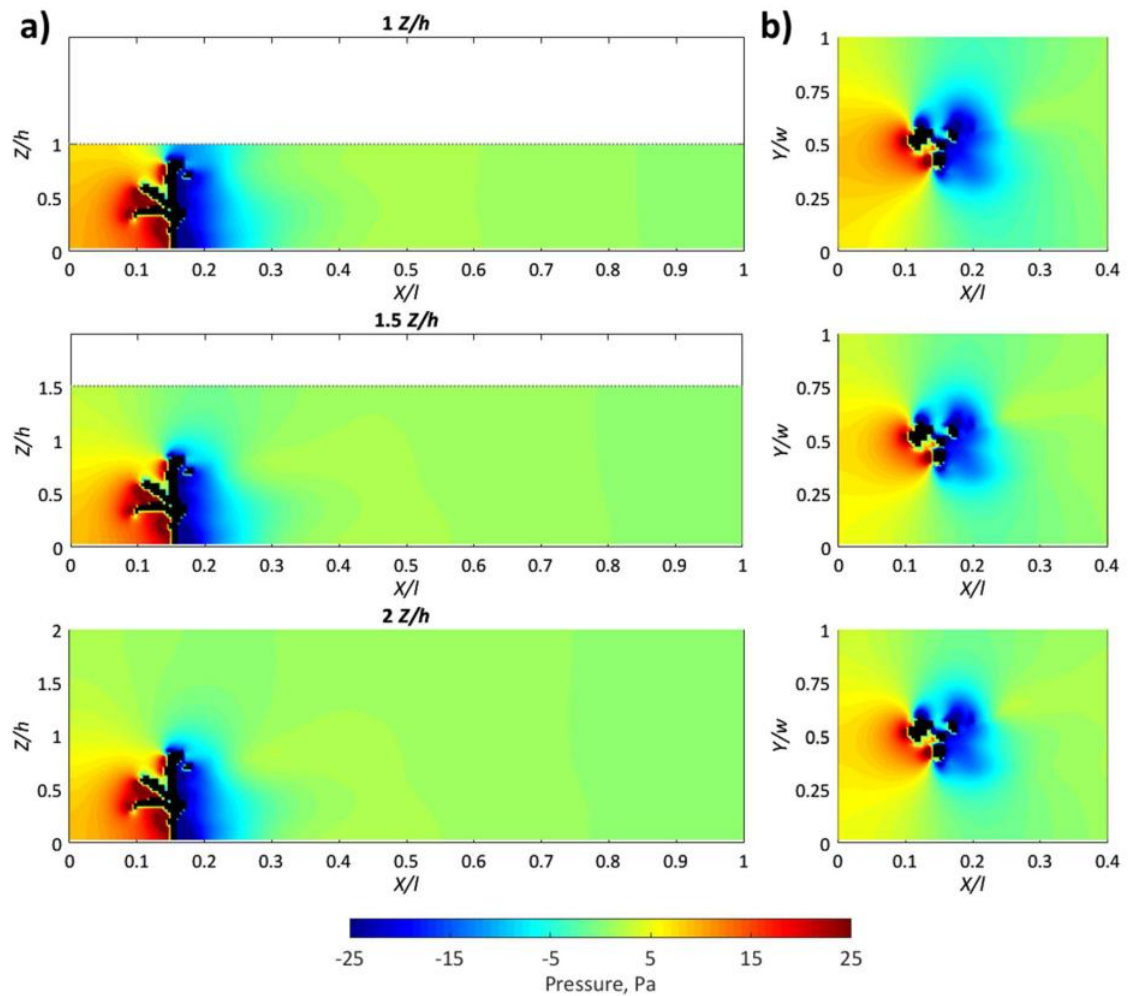
*Figure 4.39 (a) Pressure at 0.5 Y/w and (b) 0.5 h (right), for increasing plant submergences (top to bottom). The dotted line is the lid of the domain.*

### 4.4.4  Summary of sensitivity to hydraulic boundary conditions

This section has demonstrated insensitivity to the range of inlet velocities and submergences assessed, and therefore future chapters will focus on a single inlet velocity and submergence unless otherwise stated. Sensitivity was shown to the inlet turbulence intensity, although justification for the 5% turbulence intensity has been provided, and this will be used in future chapters.

## 4.5      Calculation of drag and vegetative flow resistance

The high resolution predictions of the flow field are useful when calculating drag and vegetative flow resistance, necessary to support RQ6 and RQ7. CFD models offer the advantage of readily accessible velocity and pressure fields, and these can be used to directly calculate form drag (Stoesser *et al.*, 2009; Stoesser *et al.*, 2010). Relevant to vegetative flow resistance, this offers the opportunity to remove the need to rely on predefined constants for the drag coefficient, and instead calculate species-dependent values, which can subsequently be used in the quantification of bulk resistance parameters such as Manning's *n*. It therefore follows that high resolution model results are used to inform improved process representation in lower resolution models, which can be practically applied to reach-scale studies.

Drag coefficients are well understood for simple geometric shapes such as cylinders, but are less well understood for the complex geometries associated with natural vegetation (Marjoribanks *et al.*, 2014a). Modelling studies typically assign a drag coefficient value of unity for vegetation, however this is only applicable to the simplest reed and grass type plants. This is true for a single cylinder between *Re* $10^3$ to $3 \times 10^5$ (Panton, 1984; Tritton, 1988), but deviates significantly for other plants as it is a function of both vegetation density and stem Reynolds number (Tanino and Nepf, 2008). For sparsely configured leafy shrub communities, the flume experiments of Hui *et al.* (2010) report drag coefficients of up to 4. The wide range of plant morphologies associated with natural vegetation, and the effects of their foliage contribution, will further act to modify the drag coefficient (Wilson *et al.*, 2003). Furthermore, temporal changes in drag coefficient are expected with changes in plant posture associated with reconfiguration, and these are further complicated by variation in the drag coefficient along individual stems (Marjoribanks *et al.*, 2014b). Relevant to vegetation canopies, drag is also expected to vary depending on the spatial location within the canopy. A temporally and spatially complex drag coefficient distribution is therefore expected to exist. In practical applications dealing with vegetation, however, a predefined and constant drag coefficient of 1.0 or 1.2 is most often assumed (Dittrich *et al.*, 2012), and this clearly does not account for plant volumetric canopy morphology.

## 4.5.1        Pressure coefficient approach for calculation of drag

The drag force is calculated by integrating the difference in the pressure field acting normal to the vegetation surface over the entire lateral extent of the plant, and involves summing the difference in pressure from immediately upstream and downstream of the vegetation blockage.   In this thesis, it is achieved by applying a mask to the three-dimensional vegetation extent, and extracting pressure values in the immediate proximity, from one cell upstream and one cell downstream of the mask (Figure 4.40).



*Figure 4.40 Schematic of pressure values extracted from one cell immediately upstream (M-1) and downstream (M+1) of the plant blockage (M), used in the calculation of drag forces.*

Calculation of the drag force therefore follows the standard method in aerodynamics for calculating drag from pressure (Anderson, 1984), with the drag force calculated following:

$$F_d = \int_A (p_f - p_b)dA_p \qquad (4.33)$$

where $F_d$ is the drag force (N m$^2$), $p_f$ is the pressure at the blockage front (Pa), $p_b$ is the pressure at the blockage back (Pa), and $A_p$ is the frontal area (m$^2$).  To calculate the plant frontal area, the number of cells at the blockage front are counted, and multiplied by the cell area.  The pressure coefficient approach readily quantifies the net downstream force exerted on the plant, can be applied to any plant morphology, and can be extended to configurations of multiple plants, by considering discrete plant masks and their pressure fields independently.  Plant drag forces (4.33) are used to calculate the drag coefficient, following (2.5).

The pressure coefficient approach, applied to the high resolution predictions of flow from the CFD model, and the accurate quantification of plant geometry from the voxelisation of the TLS scan, thereby provide an efficient means for calculating drag forces and drag coefficients for individual plant species.

## 4.5.2 Vogel exponent

The Vogel exponent, $\psi$, quantifies the drag reduction by reconfiguration of a flexible body through a power law dependence with flow velocity (Vogel, 1984). Using the $F_d$ – U relationship:

$$F_D \propto U^{2+\psi} \tag{4.34}$$

$\psi$ has previously been found to typically range from -0.2 to -1.2 for natural vegetation (de Langre *et al.*, 2012), with the Vogel exponent relating to the flexibility of the plant (Aberle and Dittrich, 2012). Typical values were previously tabulated (Table 2.2).

For a rigid plant, $\psi = 0$, (4.34) returns the classical squared relation, while for a flexible plant, $\psi = -1$, (4.34) returns a linear force-velocity relation (Cullen, 2005; Whittaker *et al.*, 2013). It is important to remember the $F_d$ – U relationship is representative only of the velocity range investigated. Furthermore, although providing an empirical relationship, the Vogel exponent is not dimensionally correct, and cannot be used to calculate the drag force and subsequent energy loss within vegetated rivers (Marjoribanks *et al.*, 2014a). However, the $\psi$ has been widely used to quantify flexibility in plants (Dittrich *et al.*, 2012), and therefore is a standard approach in ecological and hydraulic literature.

Using $\psi$, a number of authors have characterised bulk vegetative resistance terms including parameterisation of plant biomechanical and plant geometry components, with inclusion of separate foliage and stem contributions (Västilä and Järvelä, 2014), and species-dependent drag coefficients (Järvelä, 2004; Aberle and Järvelä, 2013) to improve process representation in such equations (Marjoribanks *et al.*, 2014a). In this thesis, the potential to use the high resolution process understanding to back-calculate the Vogel exponent is assessed, providing an indication of the species-dependent plant flexibility.

### 4.5.3        Manning's n

The species-dependent drag coefficient is also linked back to Manning's *n*.  In cases of submerged vegetation, the presence of a turbulent mixing layer between the vegetated low velocity and free-stream zones adds complexity to derivations of vegetative resistance (Shucksmith *et al.*, 2011), and therefore an equation applicable to submerged vegetation is required. For submerged grasses, (Wilson and Horritt, 2002) consider the momentum absorbing plant area for the calculation of Manning's *n* (m$^{1/3}$ s$^{-1}$), following:

$$n = \left( \frac{1}{2g} R^{1/3} C_d \frac{A_p}{a} \right)^{1/2} \qquad (4.35)$$

where *g* is gravitational acceleration (m s$^{-2}$), R is the hydraulic radius (m), $A_p$ is the momentum absorbing area or frontal area calculated from the voxelised plant representation (m$^2$), and a is the cross-sectional flow area (m$^2$).  Species-dependent Manning's *n* values can therefore be calculated, applying the drag coefficient term from Section 4.5.1.  Established texts, such as with Chow (1959), suggest a Manning's *n* value of 0.035 – 0.070 for floodplains with scattered brush and heavy weeds.  The look-up table values, however, represent the resistance to flows over large spatial areas in channel and floodplains, whereas the calculated values presented in this thesis are reflective of a single vegetation element in the computational domain.

### 4.5.4        Drag and vegetative resistance summary

High resolution predictions of flow are used for the calculation of species-dependent drag forces and drag coefficients following the pressure coefficient approach (Section 4.5.1).  To help answer RQ6, the drag response and Vogel exponents are calculated for a range of plant volumetric canopy morphologies in Section 7.5, with the physically-determined drag coefficients used in the quantification of Manning's *n* (Section 7.6), thereby addressing RQ7.  The high resolution model results are used to inform an improved process-representation in lower resolution models, which can be practically applied to reach-scale studies.

## 4.6        Chapter conclusions

This chapter has described and justified the numerical methods that will be applied in Chapters 5, 6, and 7, and has provided detail of model development, initial application, and testing. Justification for the numerical representation of open channel flow and the turbulence closure scheme has been provided, with the necessary boundary conditions specified. The chapter has shown the methodological developments required for incorporating realistic plant representations into the CFD model, to address RQ2 and thesis objective (ii), and therefore it should now be possible to predict three-dimensional mean and turbulent flow around plants of various volumetric canopy morphologies.

A comprehensive discussion of how the plant is spatially discretised in the CFD model, and how this relates to the grid resolution has been provided; with a consideration of good modelling practice, specifically focusing on model verification. Finally, the model sensitivity to a range of hydraulic boundary conditions have been demonstrated. By completing this comprehensive work, the next step is to incorporate entire plants in the CFD model, and evaluate numerical model predictions.

<div align="right">**Chapter 5**</div>

# Flume experiments and numerical model validation

## 5.1 Introduction

Chapter 4 outlined the method for incorporating realistic plant representations into the CFD model, enabling the prediction of three-dimensional mean and turbulent flow around floodplain and riparian plants of various morphologies and postures. However, good practice in numerical modelling requires the model to be validated (Lane *et al.*, 2005), with flume experiments therefore necessary to provide the requisite spatially distributed velocity validation data. Flume experiments allow an assessment of whether the model can accurately predict measured flow, but also provide a second approach for understanding flow-vegetation interactions, contributing to the improved process-understanding.

This chapter reports on a combined flume and numerical model study of depth-limited flow around a submerged riparian plant at three different flow Reynolds (*Re*) numbers (Boothroyd *et al.*, 2017). The chapter provides an examination of the feedbacks between flow and vegetation dynamics, addressing RQ4 and RQ5 in three key ways, through;

i. an understanding of time-dynamic and time-averaged plant motion characteristics;
ii. quantification of the three-dimensional mean and turbulent flow, and;
iii. an evaluation of how accurately the numerical model can predict measured flow.

In Section 5.2, the methodologies of the flume and numerical experiments are described. For the flume experiments, the steps taken in measuring flow velocities and plant motion dynamics are detailed and justified (Section 5.2.1). For the numerical experiments (Section 5.2.2), the methods used for evaluation against the validation data

are shown (Section 5.2.3). Results of plant motion dynamics, reporting the time-dynamic plant motion and time-averaged plant posture, are shown in Section 5.3. Results from the evaluation of numerical predictions are then given in Section 5.4, followed by an investigation of the pressure field (Section 5.5). Finally, the analysis is extended to investigate turbulent flow structures (Section 5.6). For the last two sections, however, the data are not constrained by direct empirical comparisons.

## 5.2        Methodology

The methodology workflow used in this chapter is shown in Figure 5.1. First, the three-dimensional plant volumetric canopy morphology was captured using TLS, following the voxelisation procedure outlined in Section 3.3. This provides an unstressed representation of the plant, with no flow-forcing (Figure 5.1a). Next, flume experiments were undertaken to quantify and record plant motion dynamics using high-definition video imagery, and this provides a stressed representation of the plant with flow-forcing (Figure 5.1b), a necessary boundary condition in the numerical model. Acoustic Doppler velocimeters (aDv's) were used to measure velocity profiles, providing spatially distributed velocity validation data. The unstressed and stressed plant representations were subsequently incorporated into the CFD model (Figure 5.1c), enabling an evaluation of model predictions against the validation data (Figure 5.1d), with the CFD model then extended to predict turbulent flow structures (Figure 5.1e).
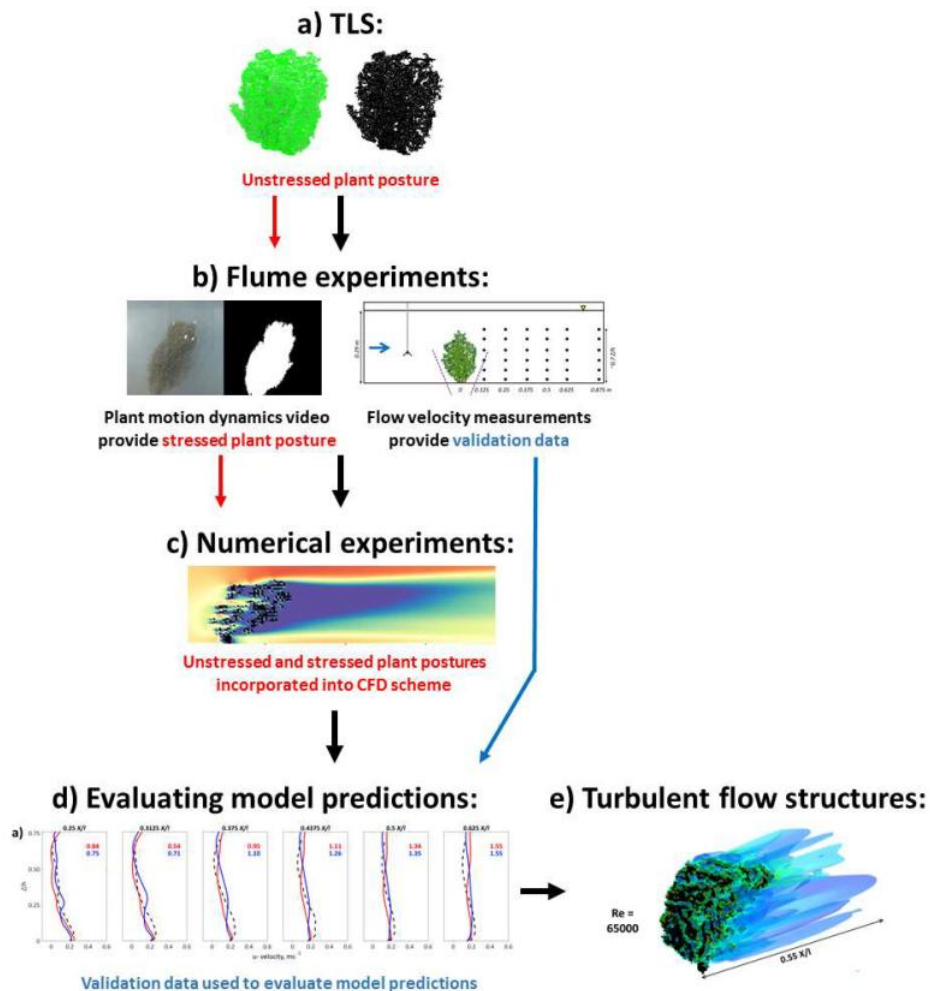


*Figure 5.1 (a-e) Methodology workflow providing an overview of the different steps in this chapter.*

## 5.2.1    Flume experiments

Flume experiments were undertaken in an Armfield S6 MKII glass-sided tilting recirculatory flume with a 0.3 m wide cross-section, and a length of 12 m (Figure 5.2). The working section was the central 2 m, unaffected by inlet or outlet flows.  The slope of the flume was adjusted to achieve constant local flow depth (0.29 ± 0.005 m) in the central working section (with uniform flow conditions).  The influence of *Re* number was investigated by increasing the mean flow velocity whilst keeping flow depth constant. Experimental conditions are shown in Table 5.1.  At these width-to-depth ratios, there is the potential for wall-induced secondary circulation, although secondary flow of this nature is typically less than a few percent of the average flow velocity (Colombini, 1993). Furthermore, blockage ratio effects will also exist, as the plant width is of the same order as the flume width, and this has previously been shown to influence drag acting on submerged macrophytes (Cooper *et al.*, 2007).

Velocity was controlled by a water pump, with the pump speed incrementally increased, providing measured inlet velocities at 0.4 *Z/h* of 0.22, 0.30, and 0.37 m s$^{-1}$.  In all experiments flow was fully developed after the entrance region, turbulent (*Re* 65 000, 89 000, and 110 000) and subcritical (*Fr* = 0.13, 0.18, and 0.22).  The flume bed was fabricated stainless steel, with a 1 m length of additional Perspex (0.01 m thickness, smooth surface) fixed on to the bed to attach the plant.  The bed therefore provided a non-deformable, no-slip condition.  The plant was positioned at the midline of the flume (0.5 *Y/w*), attached using a small cable gland (0.024 x 0.024 x 0.017 m) milled into the Perspex sheet, to minimise any local disturbance to the flow field.

*Figure 5.2 The flume experiments conducted at the Department of Geography, Environment and Earth Sciences, University of Hull (completed March 2016).*

*Table 5.1 Experimental conditions for each flume experiment.  Upstream velocity reported as mean average and standard deviation over duration of experiments.*

| Experimental conditions | Experiment number | | |
|---|---|---|---|
| | 1 | 2 | 3 |
| Upstream velocity (m s$^{-1}$) | 0.22 ± 0.016 | 0.30 ± 0.022 | 0.37 ± 0.027 |
| Water depth (m) | 0.29 ± 0.005 | 0.29 ± 0.005 | 0.29 ± 0.005 |
| Reynolds number | 65 000 | 89 000 | 110 000 |
| Froude number | 0.13 | 0.18 | 0.22 |

### 5.2.1.1   Plant characteristics

The plant used in these experiments was the waxy-leaved, evergreen shrub *Hebe odora* (Figure 5.3a), selected to represent a typical riparian plant.  *Hebe odora* was chosen for both ecological and practical reasons.  Ecologically, Cockayne (1958) reports *Hebe odora* to be distributed across many river beds or near to streams flowing through tussock-grass-land or fell-field sites.  The species is particularly widespread throughout New Zealand, especially on flushed ground and stream banks (Wardle, 1991).  Practically, the shrub had a measured height of 0.22 m and a diameter of 0.20 m, therefore enabling complete submergence in the flume.  The open framework, and internal structure of stems/leaves that were not especially dense, allowed the laser to penetrate into the plant

interior and fully quantify the plant volumetric canopy morphology in the unstressed state (Figure 5.3b and c). Furthermore, the ability of the plant not to deteriorate in a laboratory environment for the duration of the measurement period (48 hours), and the stable root ball which could be firmly attached to the base of the flume, were further reasons for selection of this particular species.
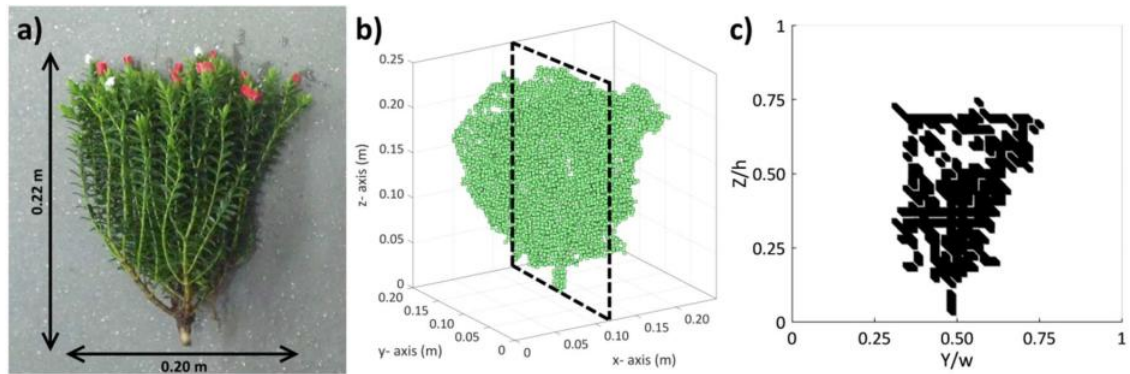


*Figure 5.3 (a) The Hebe odora plant used in the experiments, the white and red coloured tips are targets used for tracking plant tip motion (Figure 5.8b, Figure 5.15), (b) the voxelised plant representation as discretised in the unstressed CFD model, with the dashed box indicating the position of the slice; and (c) a section through the centre of the plant, showing the internal structure and porous blockage this presents to flow.*

### 5.2.1.2 Measuring flow velocity

Velocity measurements were taken to obtain inlet boundary conditions upstream of the plant that would be replicated by the inlet boundary conditions in the modelling domain, and to collect spatially distributed velocity validation data downstream of the plant. Velocities were measured using acoustic Doppler velocimeters (aDv's) in three orthogonal directions that correspond to the streamwise ($u$-), spanwise ($v$-), and vertical ($w$-) velocity components.

For inlet boundary conditions, a Sontek 16-MHZ Micro aDv was mounted 1 m upstream from the plant, at 0.5 $Y/w$, 0.4 $Z/h$. The Sontek Micro aDv collected velocity measurements at 50 Hz with a 0.05 m (nominal) fixed distance to the remote sampling volume (< 0.01 m$^3$). The aDv has a reported accuracy of 0.0025 m s$^{-1}$ ± 1% of the measured velocity (Sontek, 1999). Inflow measurements were made for the entire ~2.5 hour duration of the experimental runs.

Downstream of the plant, a Nortek Vectrino-II Profiler aDv was mounted on a moveable carriage and used to collect velocity profiles centred at 0.5 $Y/w$. Each velocity profile was composed of six overlapping 0.035 m-high sub-profiles (black dots, Figure 5.4). The

sub-profiles overlapped by 10%. Within each 0.035 m-high sub-profile, velocity was recorded in 0.001 m-high cells (giving 35 cells for each sub-profile, corresponding with the 0.035 m height of the measurement volume). The point spacing between each cell where velocity measurements were made was 0.001 m. A streamwise spacing of 0.125 m was selected for the first five profiles, and 0.25 m thereafter, so that the wake zone was fully measured. This gave six velocity profiles in total (Figure 5.4). The measurement volume of the Vectrino-II is displaced 0.04 m below the transceiver (covering the range 0.04 – 0.075 m). This meant that sampling was limited to within ~0.06 m of the water surface; and therefore velocity profiles capture ~0.7 *Z/h*. The Vectrino-II has a reported accuracy of 0.001 m s$^{-1}$ ± 0.5% of the measured velocity (Nortek, 2012). The aDv measurement frequency 100 Hz. Flume experiment design is shown in Figure 5.4.
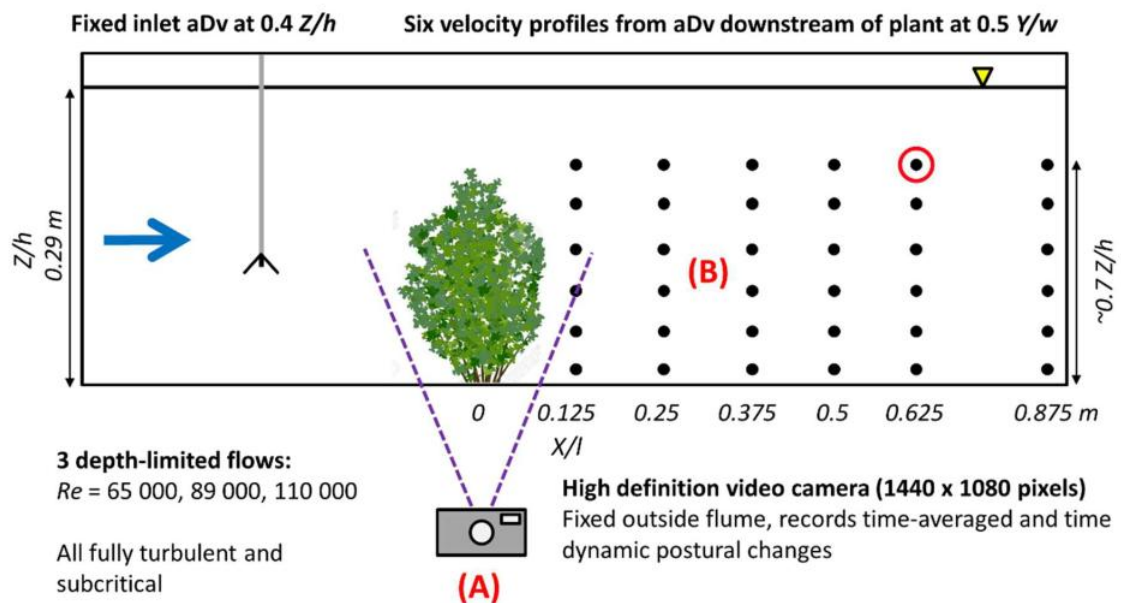


*Figure 5.4 Flume experiment design, with (A) and (B) used as boundary conditions and validation data. The red circle highlights the sub-profile used in Figure 5.6.*

The cumulative variance associated with different time-averaging windows in the velocity time-series was used to test for stationarity in the velocity signal (Sukhodolov and Rhoads, 2001). This was tested for a range of positions in the measurement region, with a typical example taken 0.625 m downstream of the plant shown in Figure 5.5. A measurement period of 120 seconds (dashed vertical line in Figure 5.5), consistently showed stationarity in the cumulative average and cumulative variance of *u-* velocity for each *Re*.
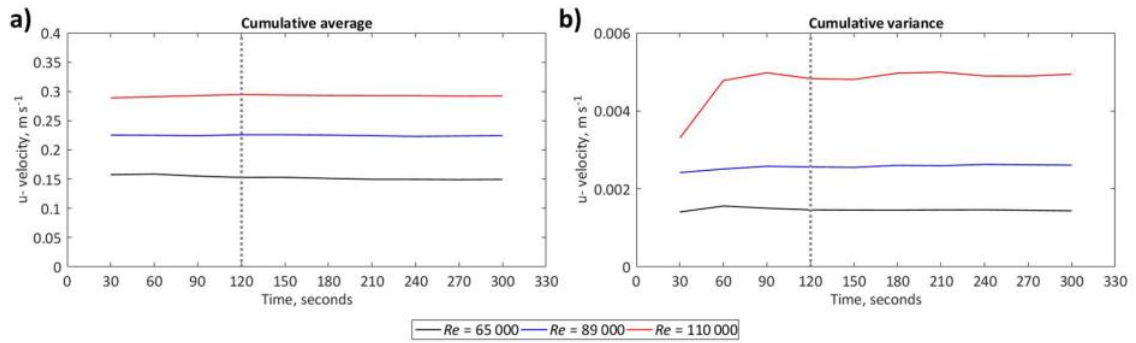
*Figure 5.5 (a) Cumulative average and (b) cumulative variance of downstream velocity from a velocity profile taken 0.625 m downstream of the plant. Stationarity consistently shown by 120 seconds (dashed vertical line), determining measurement length.*

Post processing of the aDv data followed the recommendation of Thomas and McLelland (2015). Initially, two-dimensional phase unwrapping or de-aliasing was undertaken applying the two-step non-continuous quality-guided path (TSNCQUAL) algorithm (Parkhurst *et al.*, 2011). Next, the phase-space filter of Wahl (2003) was applied to reduce the number of spikes resulting from Doppler noise or phase difference ambiguities (McLelland and Nicholas, 2000). Finally, a noise analysis threshold of Zedel and Hay (2010) was applied, with the threshold set as a confidence interval of 99.9%. The time-averaged velocities presented herein were computed using only the data retained after de-aliasing and filtering.

The effect of post-processing is best shown through an example. The uppermost sub-profile for the velocity profile 0.625 m downstream of the plant is selected for this purpose (red circle, Figure 5.4). For the uppermost 0.001 m cell of the 0.035 m sub-profile, a raw 30 second $u$- velocity time-series at *Re* 110 000 is shown in Figure 5.6a. In Figure 5.6b, spikes are shown to be removed from the post-processed time-series, with erroneous negative velocities visibly removed. By comparing the raw and post-processed $u$- velocity time-series values within a tolerance of 1% (to account for rounding errors following post-processing), 5.8% of the time-series is amended following post-processing. In terms of flow statistics, the mean $u$- velocity increases from 0.234 m s$^{-1}$ to 0.241 m s$^{-1}$ (~3% increase) having applied the post-processing steps.

Next, the effect of post-processing is shown for the full sub-profile. The red arrow indicates the position of the 0.001 m cell shown in Figure 5.6a and b. The effect of post-processing for the same 30 second time-series is shown in Figure 5.6c, with the amendment of discontinuous negative $u$- velocity spikes from the time-series clear. In total, 6.2% of the values are amended following post-processing, with a ~4% increase in

the mean *u*- velocity over the entire sub-profile (0.234 m s$^{-1}$ when raw, 0.243 m s$^{-1}$ when post-processed).
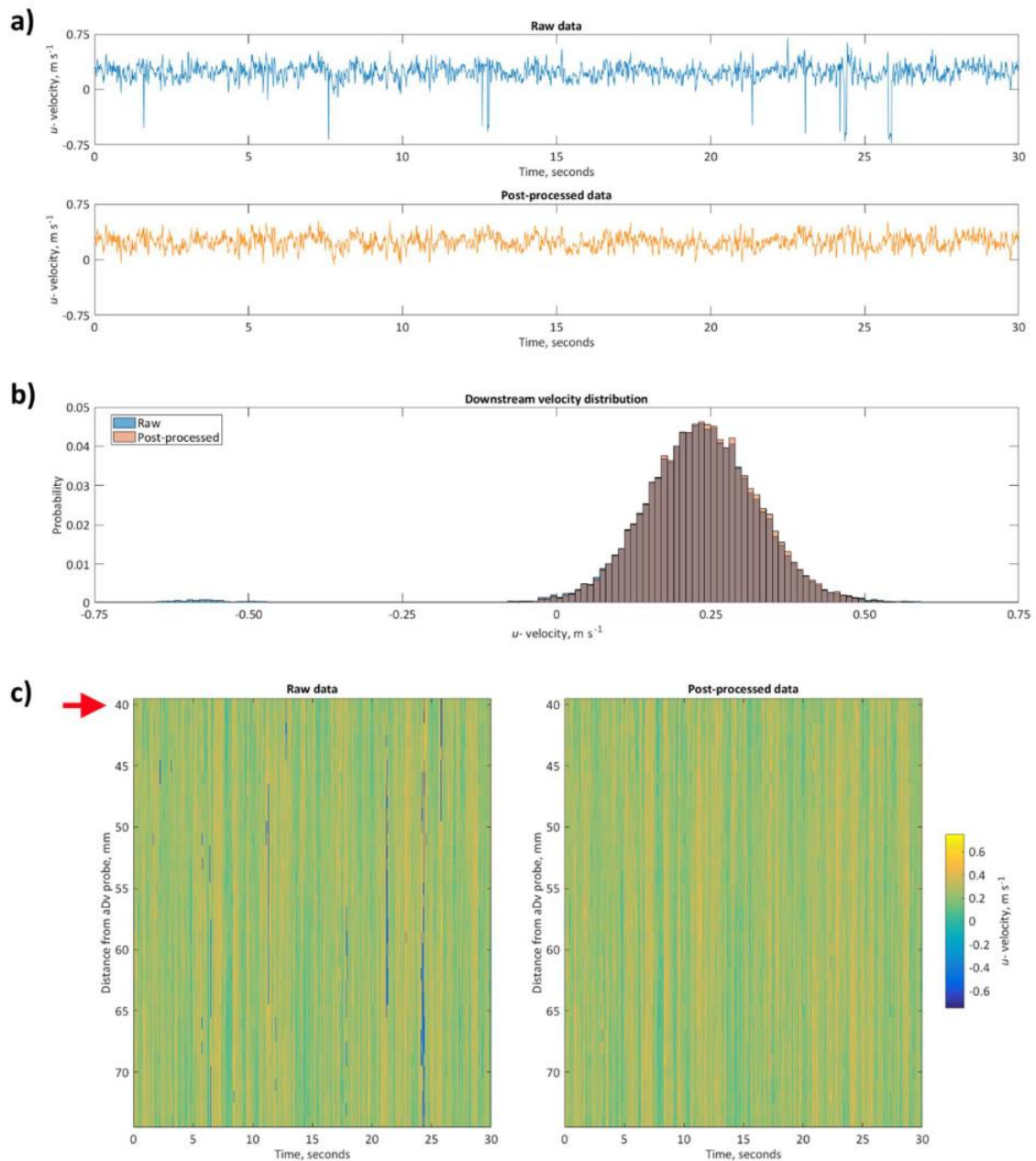


***Figure 5.6** Raw and post-processed 30 second u- velocity time-series taken 0.625 m downstream from the plant at Re 110 000, for the uppermost 0.001 m cell of the 0.035 m sub-profile (a) and (b), and (c) the 0.035 m sub profile (circled red in Figure 5.4). The red arrow denotes the position of (a) and (b) in (c). In each case, spike removal primarily at erroneous negative values are clearly visible, with 5.8% of values changed in (a) and (b), and 6.2% of values changed in (c).*

A weakness of the Nortek Vectrino-II aDv is that the signal to noise ratio (SNR) is not constant over the 0.035 m measurement volume. In some cases this can lead to discontinuous velocity profiles when the sub-profiles are placed on top of one another and stacked (MacVicar *et al.*, 2014). Consequently, Brand *et al.* (2016) show mean

velocities from the upper 0.025 m of sub-profiles to be the most reliable, with sensitivity increased when analysing turbulence statistics (MacVicar *et al.*, 2014; Brand *et al.*, 2016). Recently, Thomas *et al.* (2017) showed mean velocity was consistently underestimated in the distal cells, with a 'sweet spot' around 0.01 m in sub-profiles.

The effect of this is tested using the measured data. First, by retaining different fractions of sub-profiles, the shape of *u-* velocity profiles for the near-plant region at *Re* 110 000 is shown in Figure 5.7a. The shape of the velocity profile retaining the uppermost 20% of sub-profiles is compared against the 100% case. For the 100% case, sub-profiles were overlapped by 10%, and the extremities of overlapping sub-profiles averaged to reduce any artefacts introduced at the periphery of the measurement footprint. This is shown to minimise any discontinuous effects on the mean velocity (Figure 5.7a).

For increasing fractions of retained sub-profiles, Figure 5.7b demonstrates the effect on the normalised *u-* velocity when interpolated over the entire measurement region. Overall, modifying the fraction of the sub-profile retained does not substantially alter the magnitude or structure of the flow patterns observed. As the fraction retained increases, however, more detail in the flow is resolved, for example around 0.25 *Z/h* for the 100% retained case. This is because the spatial coverage increases as the fraction retained increases.

For this study it is important to maintain the maximum spatial coverage, which is necessary to resolve fine-scale flow structures, as this enables comparisons with the high resolution CFD predictions. Although, Thomas *et al.* (2017) show that the most reliable velocity data to be collected in upper-section of sub-profiles (between 0.03 – 0.021 m), here full sub-profiles are retained, and used in the following sections.
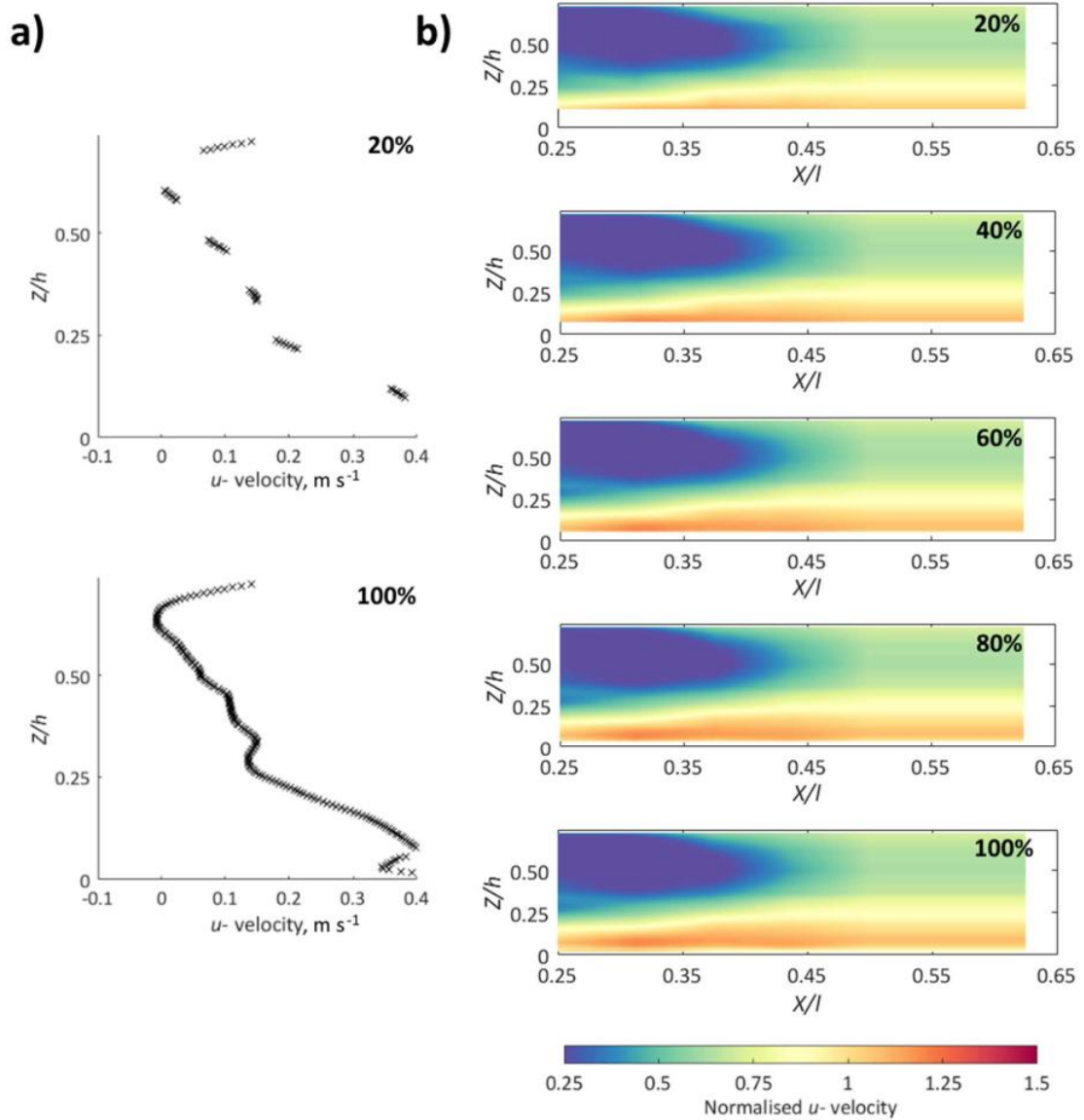
***Figure 5.7 Effect of retaining different fractions of the aDv sub-profiles at Re 110 000. (a) Velocity profiles when retaining the upper 20% and retaining 100% of sub-profiles. (b) Comparison of the normalised u- velocity field, interpolated over the entire measurement region, for increasing retained fractions.***

### 5.2.1.3    Measuring plant motion dynamics

To monitor the time-dynamic and time-averaged plant motion characteristics, a high definition video camera with a 1440 x 1080 pixel resolution was fixed perpendicular to the plant on the outside of the flume (Figure 5.4). The video camera was focused on the plant, and a 0.3 m ruler attached to the outside of the flume for spatial scale. Video was recorded at 25 Hz, which in post processing far exceeded the resolution required to capture the plant motion (see Section 5.3.2). Video was not synchronised with the aDv, and had a different recording rate, although video was recorded for the entire duration of aDv measurements.

Individual image frames from the video were extracted and corrected for distortion (Wackrow *et al.*, 2015). To relate the size of pixels in the image space to measured distances on a photogrammetric target, the image scale factor (ISF) was quantified (Wackrow *et al.*, 2015). This was completed by measuring the pixel distance on a photogrammetric target (a black and white checkerboard, each square 0.02 m in length, total size 0.20 x 0.14 m) in the undistorted image space, and comparing this to the real distance in the object space. As such, pixels in the undistorted image frames were related to measured distances, allowing characteristics such as plant height and length to be determined with ± 0.005 m measurement error.

To distinguish between plant versus water pixels, frames were converted into a binary plant image, by applying the Otsu (1979) image classification algorithm (Figure 5.8). Isolating the blue band of the RGB image space, a standard image processing technique was used to reduce the grayscale image into a binary image, by calculating the global threshold using the method of Otsu (1979). Following Hardy *et al.* (2011a), the binary images were post-processed to remove any isolated, spur or H-connected pixels, with disconnected areas containing less than 50 pixels assumed to be floating flume debris and removed. Similarly, holes in the binary image were filled, with the final binary image for each frame detailing the outer extent of the plant (0 = unoccupied, 1 = occupied, Figure 5.8).
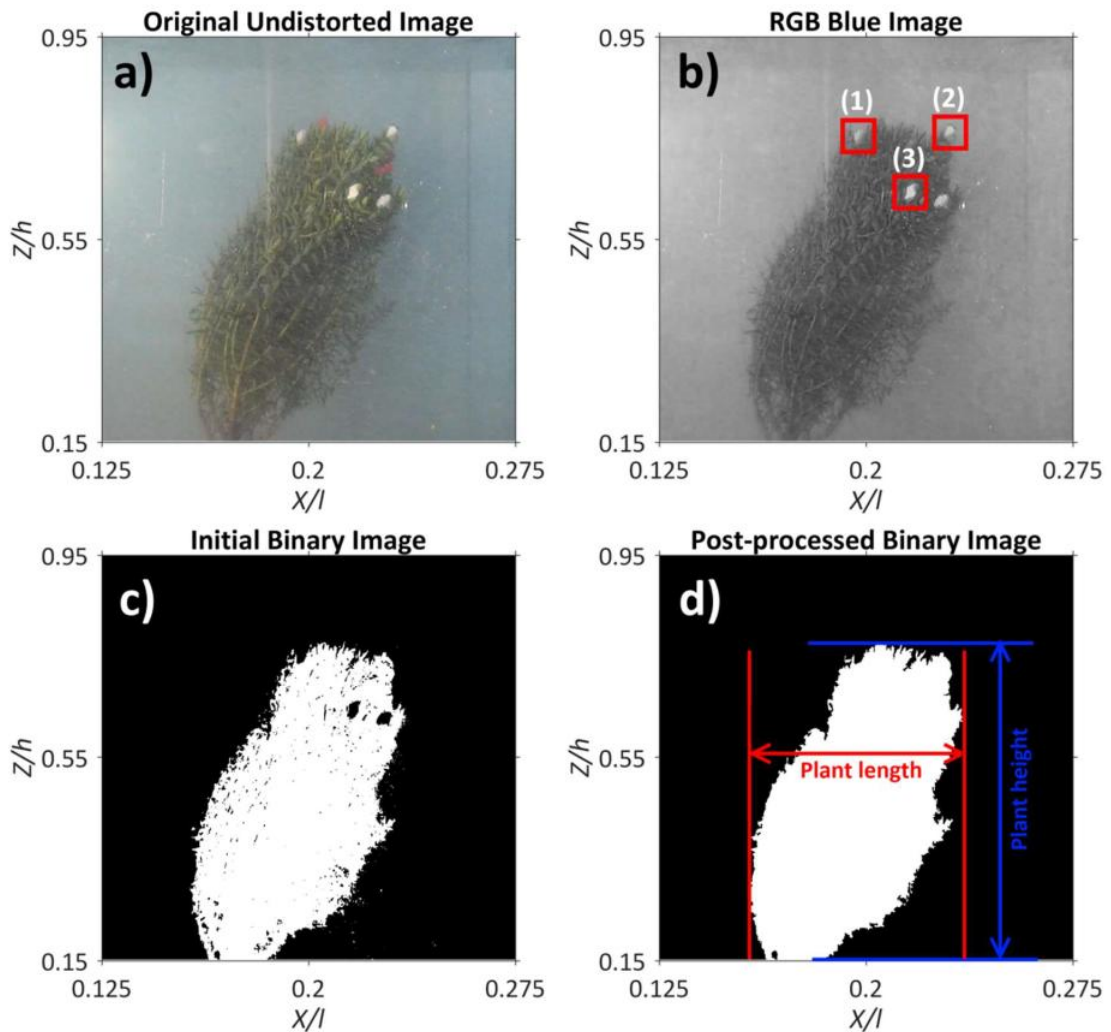
**Figure 5.8 Stages in the workflow developed to automatically generate a binary plant image from: (a) the undistorted image following camera calibration, allowing (b) isolation of the blue component of the RGB colour space, whereby (c) an Otsu (1979) image threshold has been applied, and (d) post-processed. Plant height and plant length are indicated on (d). The white and red coloured tips visible in (a) and (b) were used for time-dynamic plant motion characterisation (Figure 5.15), selected at three distinct locations across the plant body (1 = uppermost front, 2 = uppermost back, 3 = middle).**

When investigating the time-dynamic and time-averaged plant motion characteristics, the full range of plant motion must be represented. Although high-definition video was recorded for the duration of aDv measurements (120 seconds) at 25 Hz, quantification of two-dimensional plant motion for the duration at this high resolution is very challenging. If the same patterns of plant motion are being repeated throughout the time-series, instead it follows to extract and analyse a representative sample of the time-series. With the time-series of plant height extracted (Figure 5.9a) and de-trended from the binary plant images (Figure 5.8d), Fast Fourier transform (FFT) was used to isolate the dominant frequencies of plant motion, shown by the peaks in power spectral density (0.042, 0.058, and 0.147 Hz, in Figure 5.9b - d). The sample length therefore needed to be longer than 0.042 Hz (~24 seconds), with a sample length of 25 seconds representing

the full cycles of plant motion over the range of *Re*. Oscillations of plant height over the 25 second sample length, relative to the 120 second record, are shown in Figure 5.9a. A 25 second sample length is therefore used in the analysis of two-dimensional plant motion dynamics.
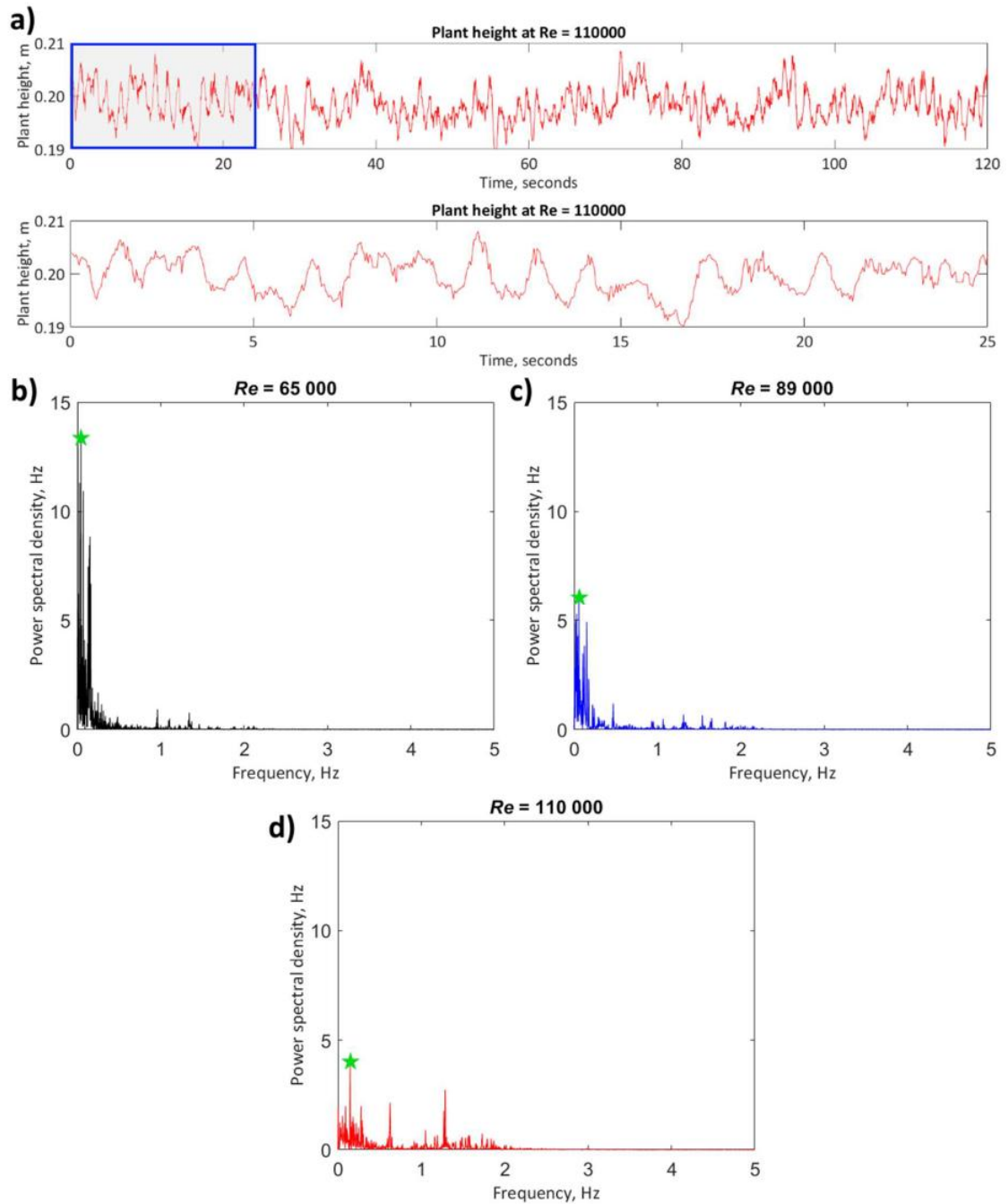


*Figure 5.9 (a) 120 second time-series of plant height at Re 110 000, with the blue boxed section reproduced below over the 25 second time-series. Dominant frequencies of plant motion from the time-series of plant height, calculated at 0.042 Hz, 0.058 Hz, and 0.147 Hz (denoted by green stars) for (b) Re 65 000, (c) 89 000, and (d) 110 000.*

### 5.2.1.3.1    Time-dynamic plant motion

To investigate the time-dynamic plant motion characteristics, tracks of the centroids from isolated plant tips were monitored. Plant tips were selected as these regions would represent the greatest potential for plant motion (Siniscalchi and Nikora, 2013). Trial and error revealed that plant tips were consistently exposed throughout the whole video sequence, whereas if markers were placed further towards the plant body they were intermittently hidden, and this resulted in an incomplete image series, causing problems when tracking plant motion. Furthermore, the markers on the plant tips were more easily detected due to the contrast of the water in the background of image frames. Plant tips were selected at three distinct locations across the plant (1 = uppermost front, 2 = uppermost back, 3 = middle, Figure 5.8b), and are displayed as time-dynamic tracks that represent apparent two-dimensional motion in the downstream and vertical. Time-dynamic plant motion results are shown in Section 5.3.2.

### 5.2.1.3.2    Time-averaged plant posture

The time-averaged plant posture was quantified by calculating the mean position of the plant from the binary images over the representative sample of plant motion. This was displayed as a relative probability, where a probability value of 1 indicates that the pixel was constantly occupied, and a probability of 0 indicates no occupancy. To highlight zones of time-averaged plant motion, a transition frequency matrix was constructed using the sequence of binary values in each pixel. By concentrating on transitions from 0 to 1, or from 1 to 0, it is possible to detect the zones which were intermittently occupied, and therefore represent where motion has occurred. This was displayed as a fraction of the binary time-series where transitions occur, with a greater fraction indicating comparably more plant motion. Time-averaged plant posture results are shown in Chapter 5.3.3.

## 5.2.2    Numerical experiments

Initially, the unstressed (no flow-forcing) three-dimensional morphology of the *Hebe odora* plant was captured using TLS, following the workflow outlined in Section 3.3. Scans were collected from four opposing perspectives at a distance of 5 m, resulting in a mean distance between neighbouring points in the registered point cloud of 0.0024 m. For the voxelisation procedure, a 0.005 m voxel size was defined, as this represents the finest morphological elements (branches/stems) of the *Hebe odora* plant, and as the voxel size is more than double the scan resolution, provides an adequate representation

of the internal plant structure (Figure 5.3b and c). Discretisation of the plant in the numerical model at a 0.005 m voxel size was shown to produce appropriate results in Section 4.3.7.2. TLS was used to capture the plant volumetric canopy morphology, before the same plant was used for the flume experiments.

The model domain was designed to replicate the working section of the flume; 400 cells long, 60 cells wide, and 59 cells high (1 416 000 grid cells) created with a grid resolution of 0.005 m. Inlet velocity was set to match the bulk inlet boundary conditions measured using the inlet aDv (0.22, 0.30, and 0.37 m s$^{-1}$, Table 5.1). The 0.005 m voxel size was equal to that of the 0.005 m grid cell size, following Section 4.3.7.2.3. The plant was incorporated 0.35 m downstream from the inlet (0.175 *X/l*), and centred in the domain (0.5 *Y/w*). The computational domain is shown in Figure 5.10.
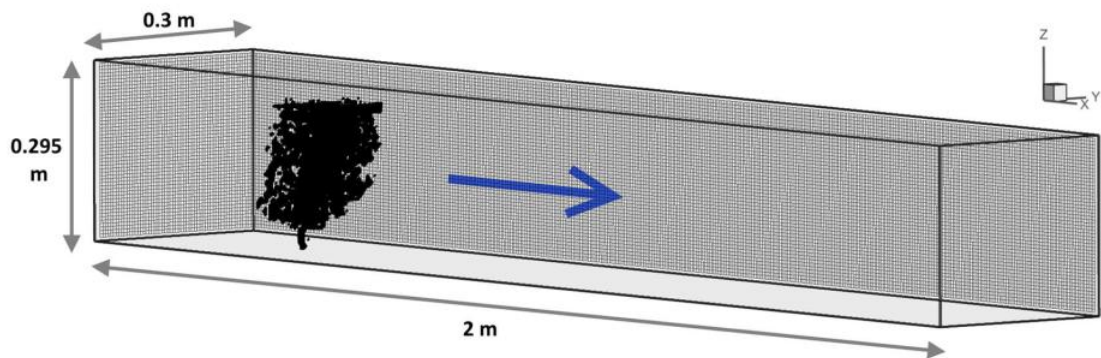


***Figure 5.10 The computational domain, showing the position of the voxelised plant. The blue arrow demonstrates flow direction.***

The unstressed plant representation was discretised directly from the voxelised point cloud, and herein referred to as the unstressed model. For the stressed plant representation, the time-averaged plant postures were used as boundary conditions to inform the discretisation of the plant for the stressed model. To do this, the unstressed voxelised representation was equally sliced at 0.02 m intervals along the vertical axis, and these slices incrementally translated to match the time-averaged plant posture in the model coordinate system, and repeated under increasing *Re*. The location of the centroids for each of the 0.02 m slices are shown in Figure 5.11. No translation occurs in the spanwise direction, with posture only shifted in the vertical and streamwise directions. The approach ensures that the number of voxels remained constant between unstressed and stressed plant representations, therefore conserving the plant volume. With increasing *Re,* porosity is reduced as the plant is vertically compressed, forcing the vegetal elements closer together, and altering the volumetric canopy morphology.
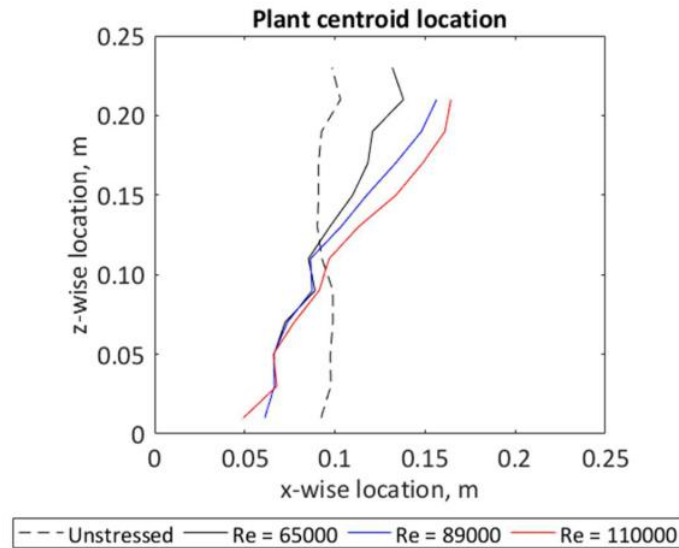
*Figure 5.11 Shifts in the voxelised plant centroid for each 0.02 m slice. A profile is produced as the centroid for each slice is different in the z-wise location. This was used to match time-averaged plant posture.*

In the numerical experiments, two distinct plant representations are therefore modelled. The unstressed posture is derived directly from the three-dimensional volumetric canopy morphology from TLS (no flow-forcing); whereas in the stressed postures, the time-averaged plant posture is used alongside the TLS data, providing the flow-forced plant postures.

## 5.2.3      Validation analysis methods

The general agreement of velocity profiles between measured and modelled data are quantified under the unstressed and stressed plant postures. Velocity profiles were selected to cover the entire downstream range of wake separation and reattachment. Each of the measured velocity profiles consists of 195 points at a 0.001 m spatial resolution, therefore covering ~0.7 $Z/h$ due to sampling constraints near the surface. For the modelled velocity profiles, the 59 points at a 0.005 m spatial resolution were linearly interpolated to the 0.001 m spatial resolution of the measured data, meaning that point densities between the data sets were equal. A number of validation analysis methods are applied to quantify the differences between measured and modelled velocity profiles, as outlined below.

### 5.2.3.1 Reduced major axis (RMA) regression

To quantify the general level of agreement between measured and modelled points on the velocity profiles, it is necessary to consider both the degree of scatter and the degree of bias in the data. This provides an important first step towards model validation, and was analysed using the correlation coefficient ($r$) and the slope ($b$) obtained from reduced major axis (RMA) regression. RMA regression was selected to reflect the expected uncertainty on both the dependent and independent variables (Hardy *et al.*, 2003), as both velocity data has uncertainty, and this is especially relevant given the known data quality issues surrounding the Nortek Vectrino-II Profiler aDv (Section 5.2.1.2). Only points with the same $x$, $y$, and $z$ coordinates were compared, i.e. those directly geo-located. Given the equal point densities between the measured and modelled data following linear interpolation of the modelled data, the maximum offset between points is limited to ± 0.001 m. The approach allows the spatial structure of the error field to be investigated, an important aspect of model validation (Section 4.3.7.3).

Furthermore, the approach lends itself to testing the sensitivity to the position at which velocity profiles were selected in the modelling domain. Although velocity measurements were taken at 0.5 $Y/w$, there is potential error from the aDv being misaligned at the flume centreline, or errors associated with inlet boundary conditions. RMA regression is therefore repeated along $Y/w$ at increments of 0.012 $Y/w$, to see how the agreement between measured and modelled velocity profiles varies.

### 5.2.3.2 Pointwise root-mean-square error (RMSE) and mean absolute error (MAE)

To assess the magnitude of differences between measured and modelled velocities at individual points, the root-mean-square error (RMSE) and mean absolute error (MAE) are calculated. This is an important step towards understanding the magnitude of velocity differences, and was averaged over the six velocity profiles to provide a comparable summary statistic for each flow.

### 5.2.3.3 Visual distance ($d_V$) for looking at velocity profile shape

To assess in detail the agreement between measured and modelled data, a shape-based similarity statistic is used to calculate the visual distance ($d_V$) between velocity profiles. Conventional distance based methods, such as the area between curves, only compute the distance in one direction, and therefore do not truly capture the notion of shape (Minas *et al.*, 2011). The $d_V$ statistic was first proposed by Marron and Tsybakov (1995) in

the context of qualitative smoothing, with the distance measure analogous to that detected by the naked eye. It has since been applied to quantify similarity in gene expression curves through time (Minas *et al.*, 2011), although in this thesis, time is replaced by the location on the velocity profile.

To the author's knowledge, this is the first time that the technique has been applied to velocity profiles. In providing a shape-based similarity statistic, the technique lends itself well for comparing modelled and measured velocity profiles, where the interest lies in the evaluating whether the model can accurately reproduce the shape of measured velocity profiles. The $d_V$ statistic therefore complements RMA regression and pointwise RMSE and MAE, that were concerned with looking at the magnitude of differences between measured and modelled velocities. By combining the approaches, a more complete evaluation of numerical prediction is made possible. The approach is not limited to velocity profiles, and could be of interest to many geomorphological applications that deal with the comparison of curves/profiles.

To calculate differences between two velocity profiles, $\mu^{(i)}$ and $\mu^{(j)}$, first scaling effects are removed by rescaling both axes between 0 and 1, meaning that any difference detected are due to shape. Marron and Tsybakov (1995) show that $d_V$ is then calculated as:

$$d_v\left(\mu^{(i)}, \mu^{(j)}\right) \equiv \left(\int_0^1 \delta(i,j)^2 dx + \int_0^1 \delta(j,i)^2 dx\right)^{0.5} \tag{5.1}$$

where for a given point on the profile, $x$, $\delta(i,j)$ is the minimum Euclidean distance between point $\mu^{(i)}(x)$, and all points on $\mu^{(j)}$, $\delta(j,i)$ is the minimum Euclidean distance between point $\mu^{(j)}(x)$, and all points on $\mu^{(i)}$. The closer the $d_V$ value to zero, the greater the similarity between velocity profiles. The $d_V$ statistic therefore accounts for the minimum Euclidean distances between points in both the horizontal and vertical directions.

This is exemplified for hypothetical velocity profiles in Figure 5.12, comparing profile 1 against three additional profiles (2-4). Profile 2 was designed to have a considerably different shape (with the velocity minima positioned lower in the flow depth), profile 3 to have the same shape but a different magnitude (with the profile shifted towards

higher velocities), and profile 4 to have a similar profile shape to profile 1. After rescaling, the shape of profile 3 is shown to exactly match profile 1 ($d_V = 0$). Profile 4 ($d_V = 0.36$) more closely matches profile 1 than profile 2 ($d_V = 0.77$). The visual distance statistic therefore allows shape comparisons to be made between velocity profiles, and this is especially useful when comparing measured and modelled velocity profiles that are heterogeneous in shape, but could be displaced in space. This is important when evaluating numerical model predictions, as the correct processes may be represented by the model, but they could be offset in space (e.g. between profile 1 and profile 3). By applying the $d_V$ statistic, similarities in shape can be evaluated, which may otherwise be overlooked if only the magnitude of differences were analysed.
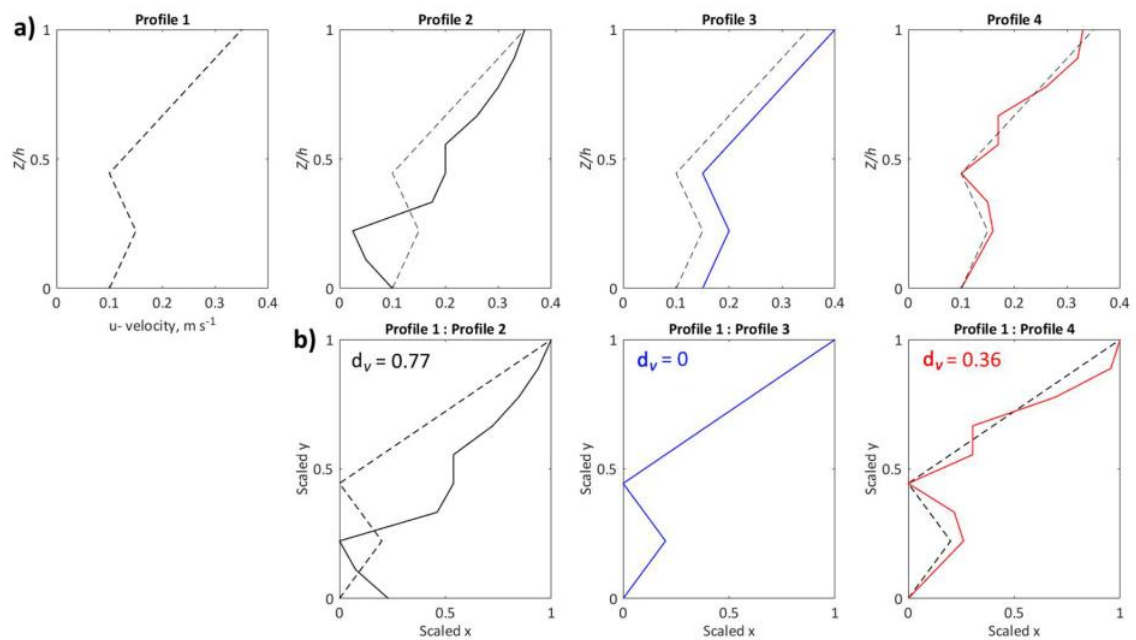


*Figure 5.12 Comparison of hypothetical velocity profiles using the visual distance (d$_v$) statistic. Velocity profiles are unscaled in (a), and scaled on both x and y axis in (b).*

## 5.3        Two-dimensional plant motion dynamics

This section provides results of two-dimensional plant motion dynamics by first assessing changes in plant height and length, before focusing on time-dynamic plant motions, and then the time-averaged plant posture.

### 5.3.1        Plant height and length

For the 25 second time-period representative of plant motion, the time-series of plant height and length are shown for each *Re* in Figure 5.13. For each time-series, variation in plant height and length is displayed as a percentage change from the mean. Over the *Re* range, this variation remains within ± 5% of the mean, however, with increasing *Re*, variation in plant height and length increases. The magnitude of these oscillations in plant height and length are first analysed, before considering the harmonics between the two.

For *Re* 65 000 (Figure 5.13a), the variation in plant height is more marked than the variation in plant length. Although plant length oscillates, it remains approximately consistent about the horizontal 0% line. Separating the positive and negative variations, the mean positive variation in plant height (0.57%) slightly exceeds the mean positive variation in plant length (0.33%). Similarly, the mean negative variation in plant height (-0.45%) exceeds the mean negative variation in plant length (-0.30%). For *Re* 89 000 (Figure 5.13b), similar patterns are shown, with variations in plant height greater than those of plant length. As before, mean positive variation in plant height (0.78%) is greater than the mean positive variation in plant length (0.51%). Again, mean negative variation in plant height (-0.87%) is greater than the mean negative variation in plant length (-0.57%). For *Re* 65 000 to 89 000, oscillations in height are therefore greater than oscillations in length.

For *Re* 110 000 (Figure 5.13c), however, variations in plant height are less than variations in plant length. Mean positive variation in plant height (0.96%) is less than mean positive variation in plant length (1.37%). Mean negative variation in plant height (-1.02%) is less than mean negative variation in plant length (-1.17%). This suggests a transitioning of the motion regime, as oscillations in plant length are have become more pronounced.
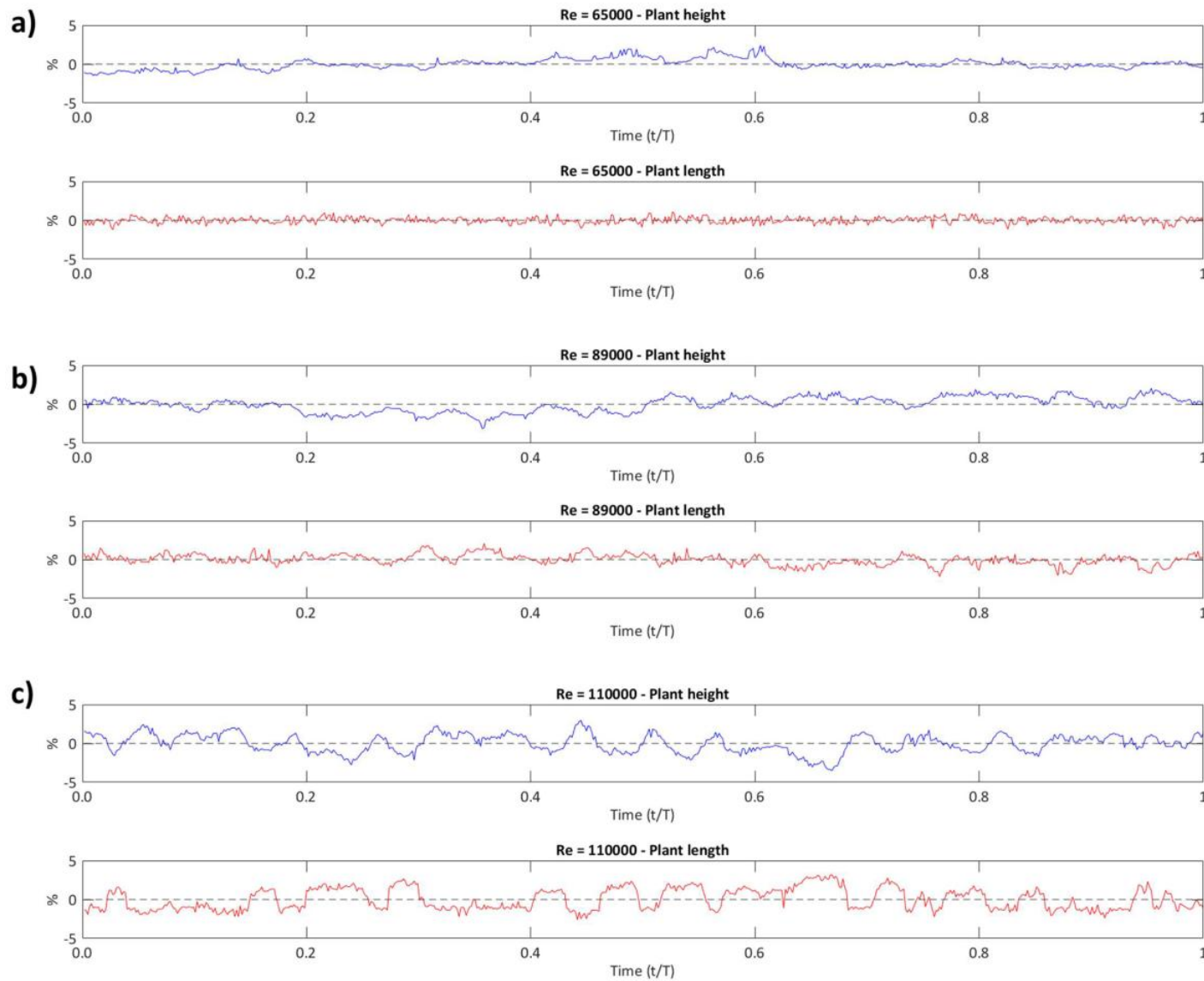
*Figure 5.13 Time series of plant height (top) and length (bottom) for: (a) Re 65 000, (b) Re 89 000, and (c) Re 110 000.*

In addition to quantifying the magnitude of oscillations, the harmonics are also assessed. Taking the plant height and length time series' shown in Figure 5.13, sample cross-correlation is applied to assess whether plant motion is harmonic (Figure 5.14). For *Re* 65 000, no significant cross-correlation is shown. However, for both *Re* 89 000 and 110 000, significant cross-correlation is shown, with no discernible lag between plant height and length. This suggests that plant motion is inversely harmonic, with decreases in plant height occurring simultaneously with increases in plant length at these *Re*. The strength of the cross-correlation is greater for *Re* 110 000, suggesting that the harmonic relationship is stronger and more consistent throughout the time-series.
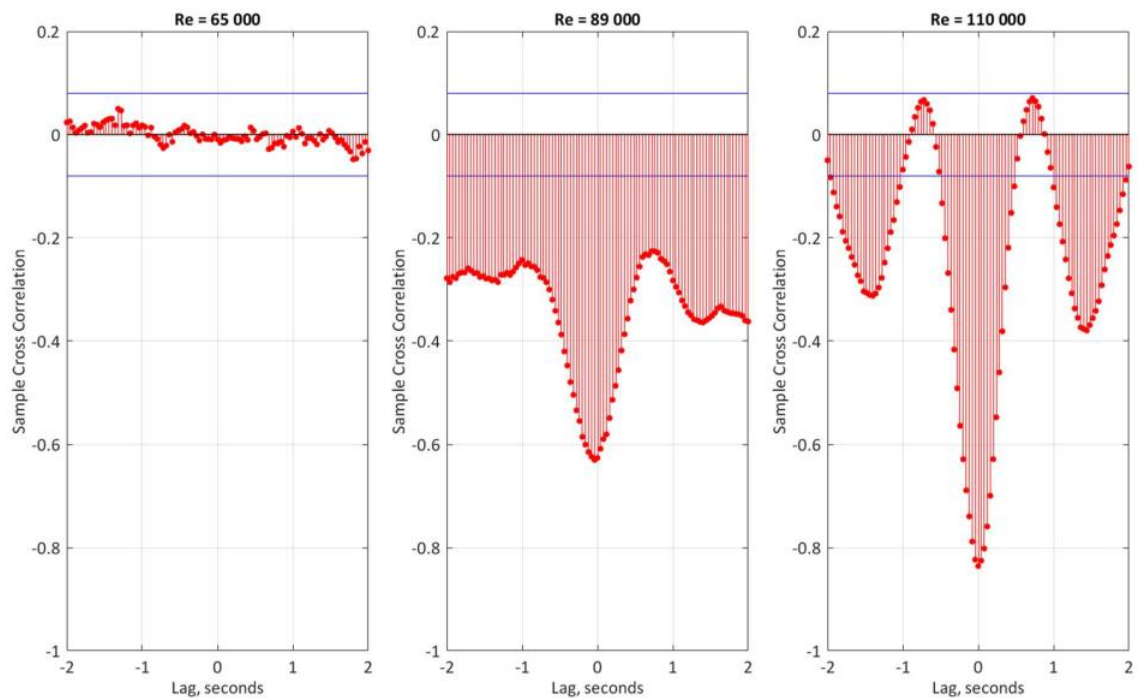


***Figure 5.14 Sample cross-correlation between plant height and length with increasing Re. Blue horizontal line indicates the approximate confidence bounds of the cross-correlation assuming plant height and width are uncorrelated.***

The data might appear to suggest the conservation of plant volume with increasing *Re*, as the magnitude of oscillations between plant height and length are similar, and these motions are harmonic for higher values of *Re*. However, to comment on changes in plant volume under hydrodynamic loading, spanwise motion would also need to be quantified. As plant motion dynamics are quantified only in two-dimensions, at this stage it remains unclear if the spanwise motion contracts the plant (thus decreasing plant volume), or relaxes the plant (conserving or increasing plant volume).

## 5.3.2 Time-dynamic plant motion

To investigate time-dynamic plant motion, the centroid of three isolated plant tips (Figure 5.8b) are tracked through the binary image time-series (Figure 5.15), with the mean position of each tip shown. An approximately linear motion track is detected at each of the plant tips. However, the individual motion tracks at different positions across the plant body show different movement extents and characteristics of motion (note differences between Tip 1 and Tip 2 at *Re* 110 000), suggesting that individual tips are not moving simultaneously, and that this could be a reaction to the flow, and more specifically the local turbulence.

With increasing *Re*, the maximum downstream extent of motion remains similar (~0.01 m), but the maximum extent of vertical motion increases (from ~0.0075 m to ~0.02 m at Tip 2, the uppermost back position). The plant tips therefore begin to follow a more steeply inclined trajectory with increasing *Re*. Divergence from a 1:1 ratio between downstream and vertical movement extents, and the more pronounced variation about the motion tracks at higher *Re*, imply a transition in the oscillation regime as the plant reacts to the increased flow.

Plant tip motion varies across the plant body in reaction to the local flow, and shows a dependence with *Re*. These different movement extents and characteristics of motion result from differences in the internal plant structure and age, including different stem widths, lengths, thicknesses, and flexural rigidities, meaning that drag force will affect each component differently, causing a range of plant responses to the flow. Different exposures/hiding to the flow will further complicate this, with different natural frequencies of movement implied. Some parts of the plant will respond to the flow first, while other parts of the plant will take longer to readjust and reconfigure. In addition, motion in one part of the plant is not independent due to the mechanical connectivity of the plant structure. Although these time-dynamic plant motions are only highlighted for three isolated plant tips, differences in motions are demonstrated across the extent of the plant body, meaning that over the whole plant, the potential range of movement is likely to be large.
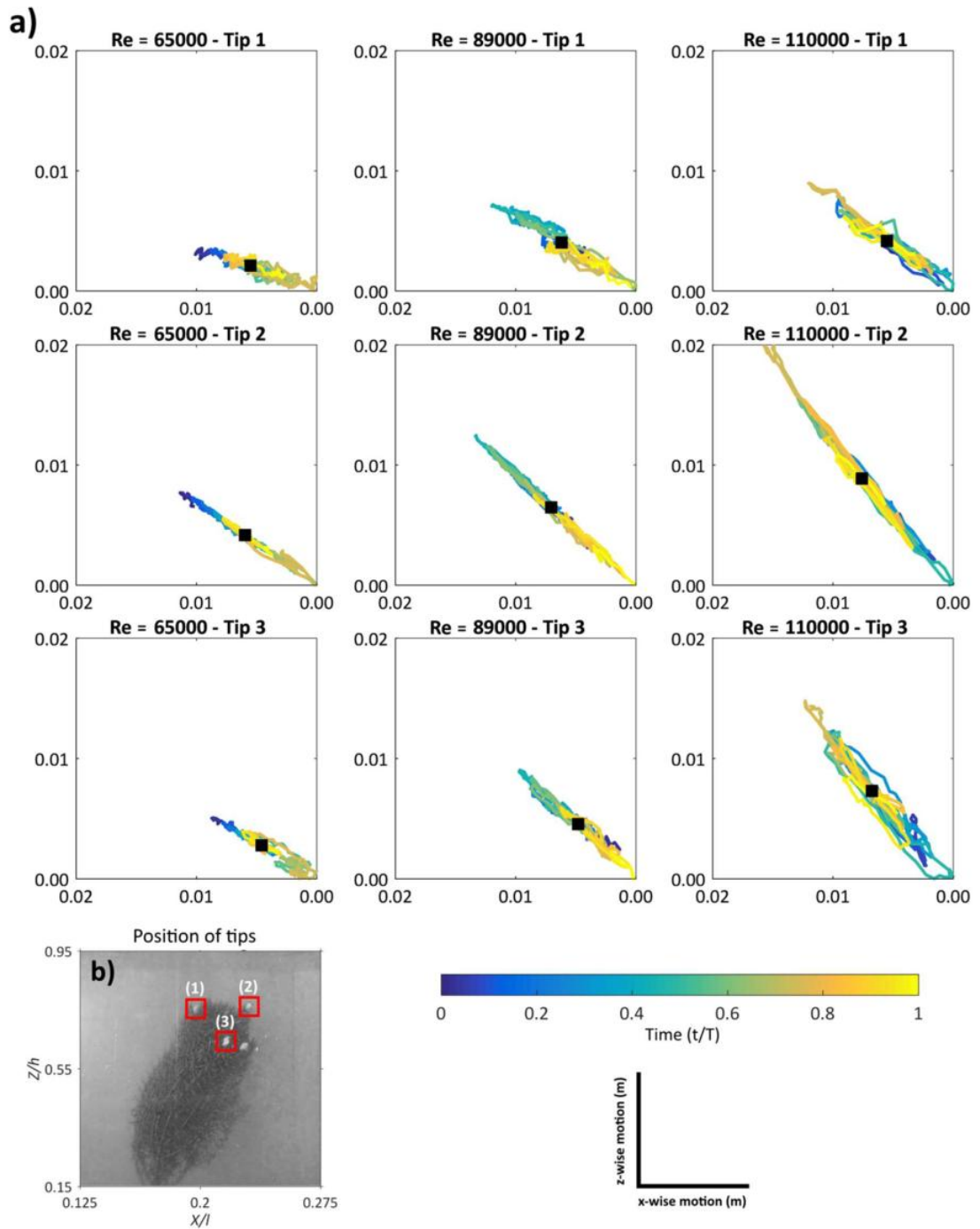
**Figure 5.15 (a) Time-dynamic plant motion characterised by the tracked positions of the plant tips for Re 65 000 (column 1), Re 89 000 (column 2), and Re 110 000 (column 3) for tip 1 (row 1), tip 2 (row 2) and tip 3 (row 3) from Figure 2b. The mean position of each tip over the 25 second time-series plotted as a black square. Time (t) is normalised by the length of the time-series (T). Position of tips shown in (b).**

### 5.3.3     Time-averaged plant posture

Changes in the time-averaged plant posture with increasing *Re* are shown in Figure 5.16, detailing the mean position of the plant (Figure 5.16a), and the zones where greatest plant motion is detected (Figure 5.16b).   The plant is clearly deflected and vertically

compressed when stressed, with the plant positioned lower in the flow depth and shifted further downstream. Compared to the unstressed state, the mean plant height is lowered by 6.4, 11.2, and 17.7% with increasing *Re*. In contrast, the mean plant length increased by 4.8, 9.8, and 14.4%. This demonstrates that as the time-averaged plant posture is shifted under the constant flow, the plant is vertically compressed. This suggests a reduction of the plant volumetric canopy morphology, and a reduction in the plant porosity. The postural changes influence the lead angle at the plant front and lee angle at the plant back, both of which are measured from the upright (Table 5.2). The lead angle is consistently greater than the lee angle (> 3.5°) throughout the *Re* range, and as *Re* increases from 65 000 to 110 000, both lead and lee angles are shown to more than double, again indicating a *Re* dependence.
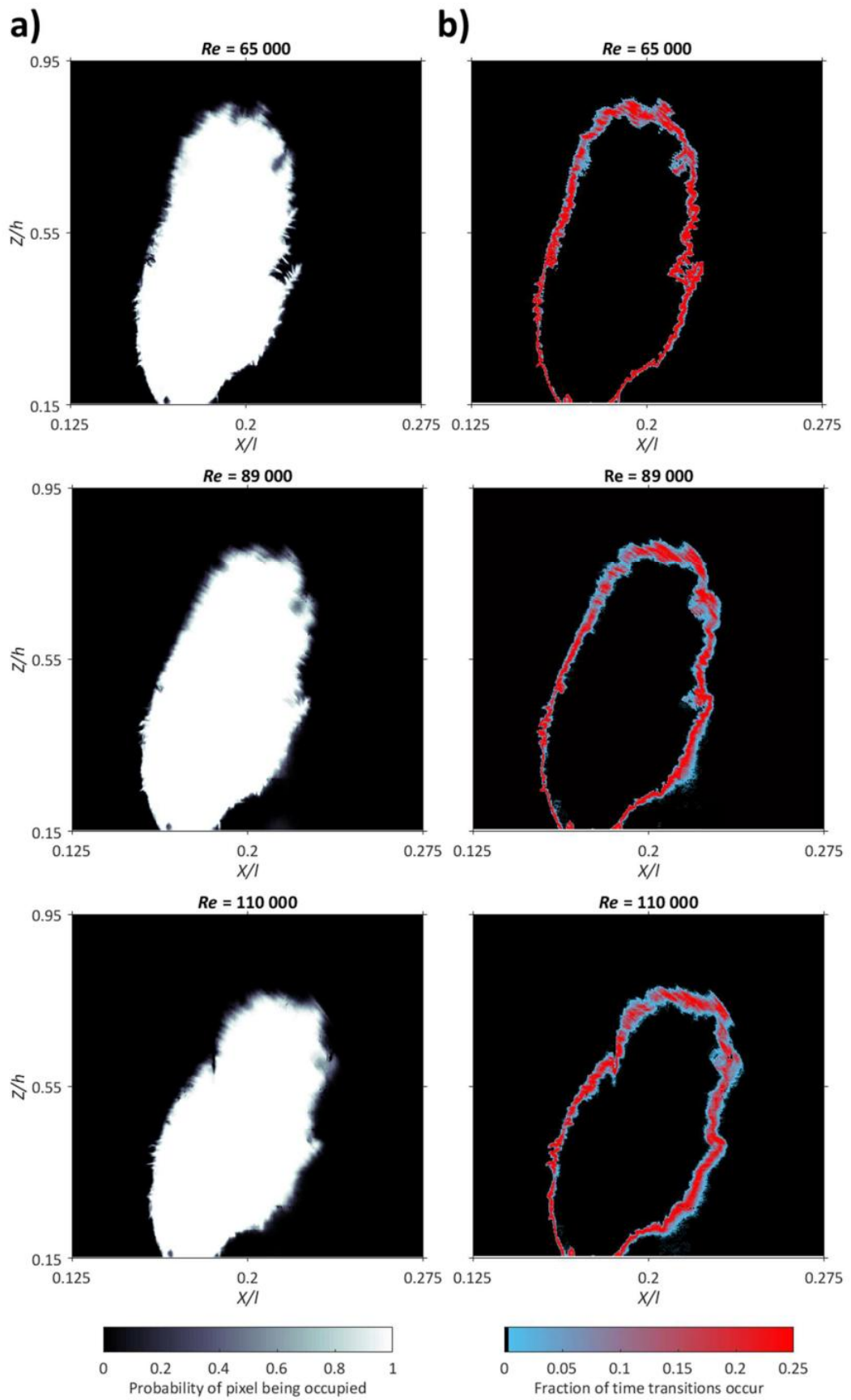
**Figure 5.16 (a) Time-averaged plant position for Re 65 000 (row 1), Re 89 000 (row 2), and Re 110 000 (row 3), showing the probability of individual pixels being occupied through time (column 1), and (b) the fraction of time transitions occur (column 2), highlighting zones of greatest motion on the upper and leeward sides.**

*Table 5.2 Time-averaged plant properties. Note, lead and lee angles not measured for unstressed plant as non-regular plant morphology.*

| Reynolds number | 65 000 | 89 000 | 110 000 | Unstressed (out of flow) |
|---|---|---|---|---|
| Mean plant height (m) | 0.20 | 0.19 | 0.18 | 0.22 |
| Mean plant length (m) | 0.16 | 0.17 | 0.18 | 0.20 |
| Lead angle from upright at plant front (°) | 8.5 | 13.1 | 16.4 | - |
| Lee angle from upright at plant back (°) | 5.0 | 7.3 | 10.3 | - |

Time-averaged plant motion is highlighted through the fraction of time occupied by transitions in the binary time-series image sequence (Figure 5.16b). Regions of greatest motion are shown by thicker zones around the plant extent, and tend to be positioned on the upper and leeward sides of the plant body. As *Re* increases from 65 000 to 89 000, the area of the transition zones increases by 12.7%; with a further 1.4% increase in area as *Re* increases from 89 000 to 110 000. Due to biomechanical constraints, it is expected that there will be an upper limit as to how much the plant can reconfigure without permanent damage, and because of this, the amount of change will be initially large but then decrease with increasing *Re*.

### 5.3.4      Summary of two-dimensional plant motion dynamics

Traditionally, the spectrum of vegetation canopy motion in response to increasing flow speeds can be categorised into four distinct and main regimes (Section 2.3.4.1.3); erect, gently swaying, strong coherent swaying (monami, or vortex-induced vibrations for the case of a single plant), and prone (Nepf and Vivoni, 2000). The entire canopy would therefore fall into one of these regimes. Here, however, the time-dynamic and time-averaged plant motions are shown to vary across the single plant body. Locally, some parts of the plant move more than others. This is because a range of vegetal elements contribute towards plant volumetric canopy morphology (branches, stems, and leaves), each with different properties relating to age (e.g. thicknesses, lengths, flexural rigidities), each exposed differently to the flow, and influencing flow locally. The plant is therefore not a single homogenous unit (Hurd, 2000), and does not respond as such. The effects of this are further discussed in Section 7.3.

With increasing *Re*, an inverse harmonic relationship between plant height and length is shown, with the magnitude of oscillations less than ± 5% of the mean (Section 5.3.1). At plant tips, time-dynamic motions showed a transition from horizontally dominated to vertically dominated movement, and increased movement extents as *Re* increases

(Section 5.3.2). Plant tip motion varies across the plant body in reaction to the local flow, and this shows a dependence with *Re*.

Time-averaged plant motion is associated with shifts in the general plant posture which reconfigures to the mean flow, resulting in up to an 18% reduction in plant height, a 14% increase in plant length, and a doubling of the lead and lee angles of the plant body (Section 5.3.3). Combined, these motions are responsible for vertically compressing the plant in the flow, thereby reducing the volumetric canopy morphology and plant porosity.

Representation of this vertical compression and reduction of plant volumetric canopy morphology, as described in Section 5.2.2, is shown in Figure 5.17. With increasing *Re*, peaks in the solid volume fraction are shifted lower in the flow depth. This reconfiguration under flow reduces the plant porosity, and is explicitly represented by the stressed plant representations in the CFD model.
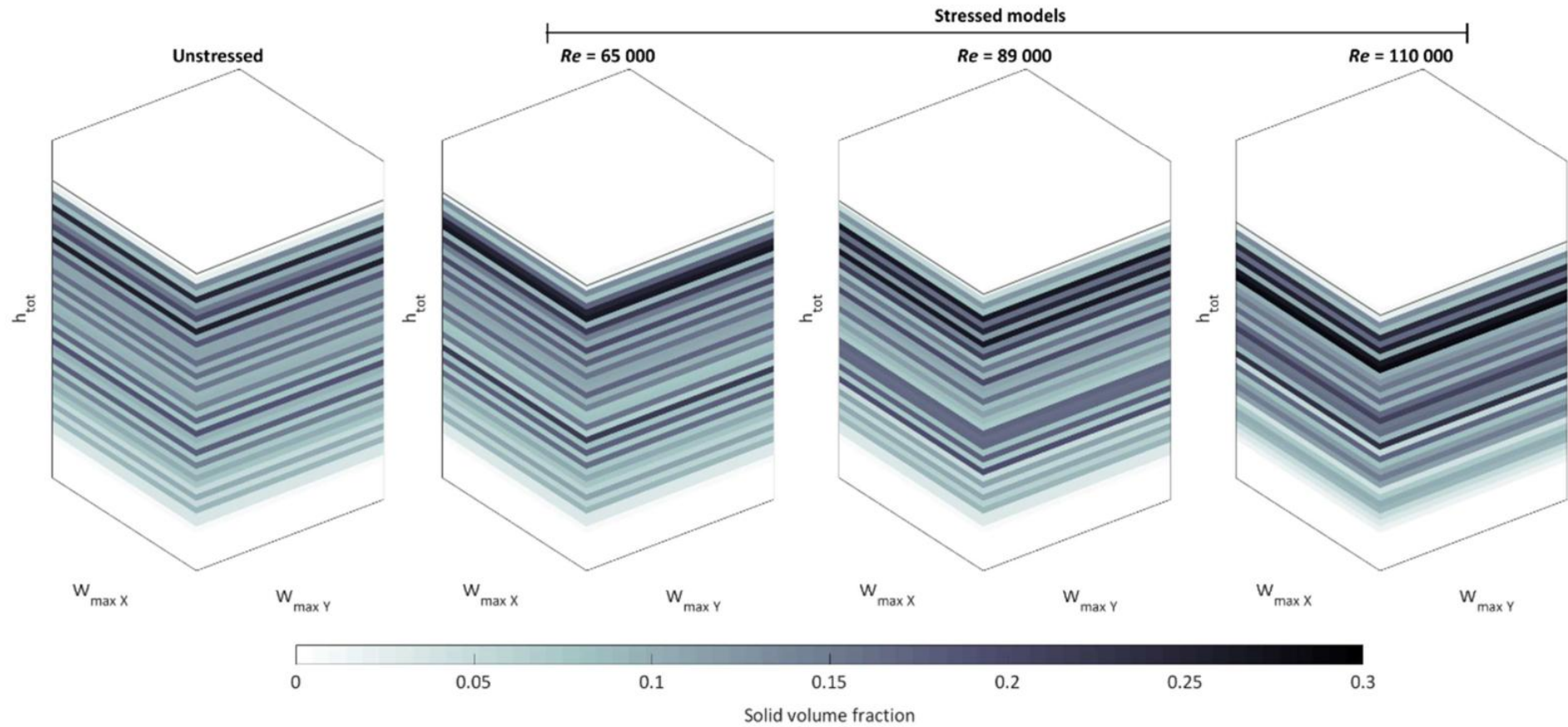
*Figure 5.17 Spatially distributed plant solid volume fraction for the Hebe odora plant used for the unstressed plant model, and the three stressed plant models, derived from TLS and time-averaged plant posture.*

## 5.4 Quantification of the mean flow and evaluation of numerical model predictions

### 5.4.1 Velocity profiles

Measured velocity profiles at 0.5 $Y/w$ are compared against modelled velocity profiles under unstressed and stressed postures for the three flows.

#### 5.4.1.1 Reduced major axis regression (RMA) and differences at 0.5 Y/w

Results from the RMA regression are shown (stressed model in Figure 5.18; correlation coefficient ($r$) and slope ($b$) of unstressed and stressed models in Table 5.3). For $u$-velocity, a good level of agreement is found with the stressed model, showing correlation coefficient values of 0.80, 0.87, and 0.92 with increasing $Re$. These are consistently higher than the correlation coefficient values with the unstressed model. For $v$- and $w$-velocities, the correlation coefficient values are higher with the unstressed model, although the magnitude of these velocities are only small (< 0.05 m s$^{-1}$). The correlation coefficients compare favourably with previous applications of CFD to velocity profiles in open channel flows (Ferguson *et al.*, 2003; Lane *et al.*, 2004; Hardy *et al.*, 2005; Hardy *et al.*, 2011b; Sandbach *et al.*, 2012), and therefore demonstrate a very good general agreement between the measured and modelled data.

The slope of the RMA regression is generally lower than unity for $u$- and $w$- velocity, suggesting an overall model under-prediction for these velocity components (Table 5.3). This could be an error in the inlet boundary conditions, especially as the plant is positioned so close to the inlet in the numerical domain, and is further discussed in Section 5.4.1.2. For $w$- velocity, the unstressed model results in an under-prediction, and the stressed model results in an over-prediction. The stressed plant representation reflects the flow induced shift in time-averaged plant posture, with this vertical compression of the volumetric canopy morphology likely to be responsible for generating a larger $w$- component of flow.
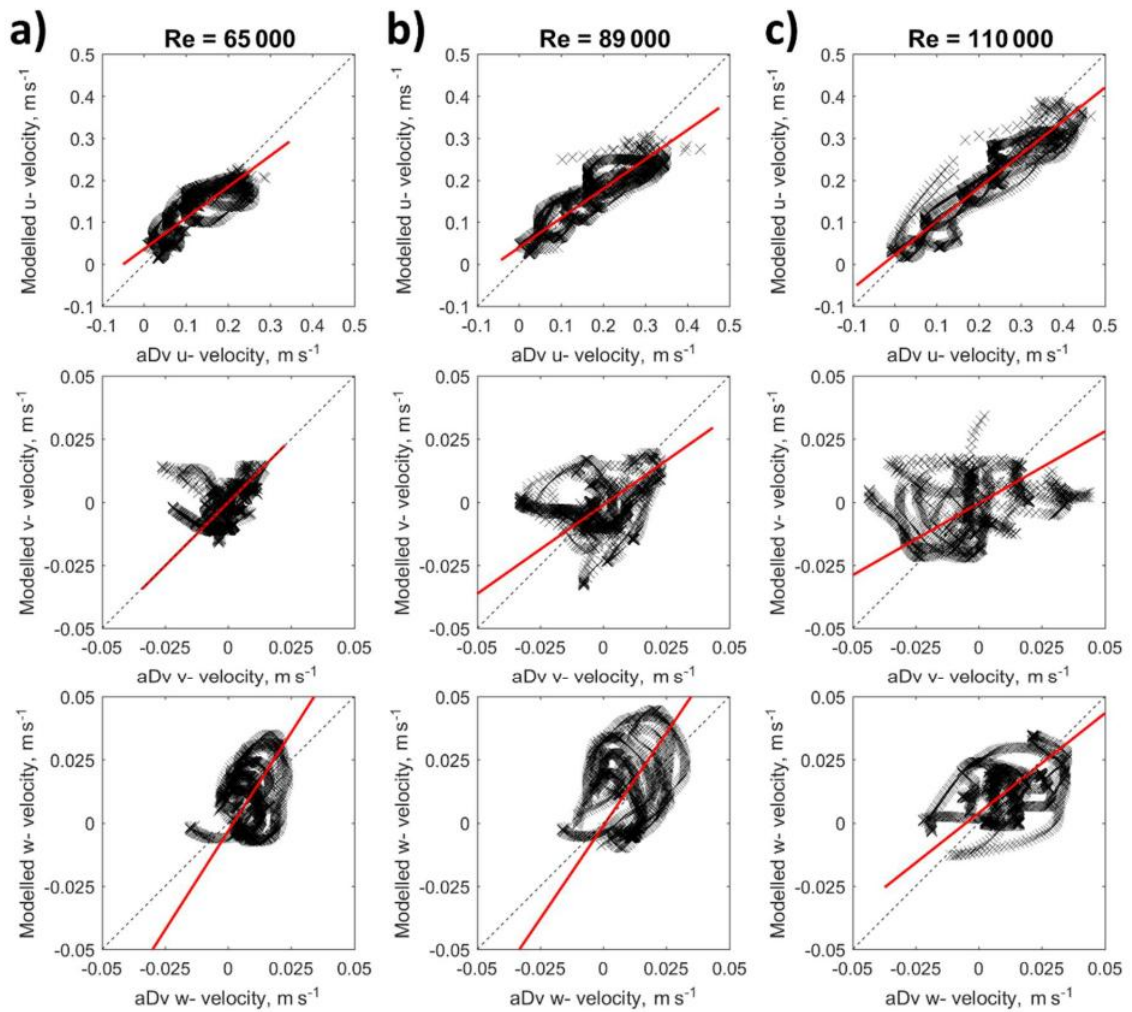
***Figure 5.18 Comparisons between the measured and modelled u-, v-, and w- velocity components for: (a) Re 65 000, (b) Re 89 000 and (c) Re 110 000. The notable spirals, causing a structural difference in the data, are caused by a transition from zones of model under-prediction in the sub-canopy region, to zones of model over-prediction in the wake region (discussed further in Section 5.4.1.3). Dashed line indicates the 1:1 line, red solid line indicates reduced major axis (RMA) regression. Slope (b), and the correlation coefficients (r) are shown in Table 5.3. Note different y-axis scales for the v- and w- velocities.***

***Table 5.3 The reduced major axis (RMA) regression of slope (b), and the correlation coefficients (r) between experimental data and the numerical model predictions for the i) unstressed plant posture and ii) stressed plant posture.***

| Plant Representation | | Velocity Component | Re 65 000 | | Re 89 000 | | Re 110 000 | |
|---|---|---|---|---|---|---|---|---|
| | | | r | RMA (b) | r | RMA (b) | r | RMA (b) |
| | | u- | 0.776 | 0.85 ± 0.02 | 0.843 | 0.90 ± 0.02 | 0.897 | 0.92 ± 0.01 |
| i) | Unstressed | v- | 0.426 | 1.38 ± 0.04 | 0.626 | 0.94 ± 0.02 | 0.631 | 0.80 ± 0.02 |
| | | w- | 0.489 | 0.83 ± 0.02 | 0.518 | 0.79 ± 0.02 | 0.576 | 0.78 ± 0.02 |
| | | u- | 0.797 | 0.74 ± 0.01 | 0.872 | 0.70 ± 0.01 | 0.921 | 0.80 ± 0.01 |
| ii) | Stressed | v- | 0.326 | 1.01 ± 0.03 | 0.203 | 0.71 ± 0.03 | 0.229 | 0.57 ± 0.02 |
| | | w- | 0.225 | 1.56 ± 0.06 | 0.159 | 1.47 ± 0.06 | 0.339 | 0.79 ± 0.03 |

To further quantify the differences between the measured and modelled data, the root-mean-square error (RMSE) and mean absolute error (MAE) are calculated, and the mean average of these errors over the six profiles displayed (Table 5.4). Although both the unstressed and stressed models represent the measured values well, with maximum RMSE of 0.072, 0.020 and 0.017 m s$^{-1}$, and MAE of 0.059, 0.016, and 0.015 m s$^{-1}$ for *u*-, *v*-, and *w*- velocities; errors are consistently lower for *u*- velocity in the stressed CFD model. For *v*- and *w*- velocity, errors remain very small (< 0.02 m s$^{-1}$) for both the unstressed and stressed models. Relating this back to the general agreement of velocity profiles from the RMA regression (Figure 5.18, Table 5.3), these very small errors are associated with low magnitude velocity values (< 0.05 m s$^{-1}$), implying that minor discrepancies between measured and modelled data result in relatively large differences in the correlation coefficient values.

*Table 5.4 The root-mean-square errors (RMSE) and mean absolute errors (MAE) calculated for the experimental data and the numerical model predictions for the u-, v-, and w- components of velocity for the i) unstressed plant posture and ii) stressed plant posture.*

| Velocity component | *Re* 65 000 | | | | *Re* 89 000 | | | | *Re* 110 000 | | | |
|---|---|---|---|---|---|---|---|---|---|---|---|---|
| | i) Unstressed | | ii) Stressed | | i) Unstressed | | ii) Stressed | | i) Unstressed | | ii) Stressed | |
| | RMSE | MAE | RMSE | MAE | RMSE | MAE | RMSE | MAE | RMSE | MAE | RMSE | MAE |
| u- (m s$^{-1}$) | 0.049 | 0.042 | 0.044 | 0.037 | 0.062 | 0.053 | 0.053 | 0.043 | 0.072 | 0.059 | 0.055 | 0.043 |
| v- (m s$^{-1}$) | 0.010 | 0.007 | 0.009 | 0.006 | 0.011 | 0.009 | 0.015 | 0.012 | 0.015 | 0.011 | 0.020 | 0.016 |
| w- (m s$^{-1}$) | 0.009 | 0.008 | 0.012 | 0.011 | 0.012 | 0.010 | 0.017 | 0.015 | 0.013 | 0.011 | 0.013 | 0.011 |

### 5.4.1.2 Testing the sensitivity of model predictions along Y/w

In the previous section, RMA regression was completed between measured and modelled velocity profiles only at 0.5 *Y/w* (the flume centreline). However, there is the potential for the aDv to be misaligned in the flume, in addition to error on the inlet boundary conditions, and it is therefore important to assess the sensitivity of model predictions along *Y/w*. RMA regression is therefore repeated for the modelled velocity profiles incrementally along *Y/w* (at 0.012 *Y/w*), under both the unstressed and stressed plant postures.

Correlation coefficients along *Y/w* for the unstressed plant model are shown in Figure 5.19. Correlation coefficients for *u*- velocity remain consistently higher than *v*- and *w*- velocities over the *Re* range. For *u*- velocity, the *r* values are greatest at < 0.5 *Y/w*, and tend to decrease from 0.40 to 0.60 *Y/w*. The opposite trend is true for *v*- velocity, with *r* values greatest closer to 0.60 *Y/w*. For *w*- velocity, correlation coefficient values are

greatest around 0.5 *Y/w*, and markedly fall away with distance from the centreline. These spatial differences are further investigated by considering the slope of the regression.
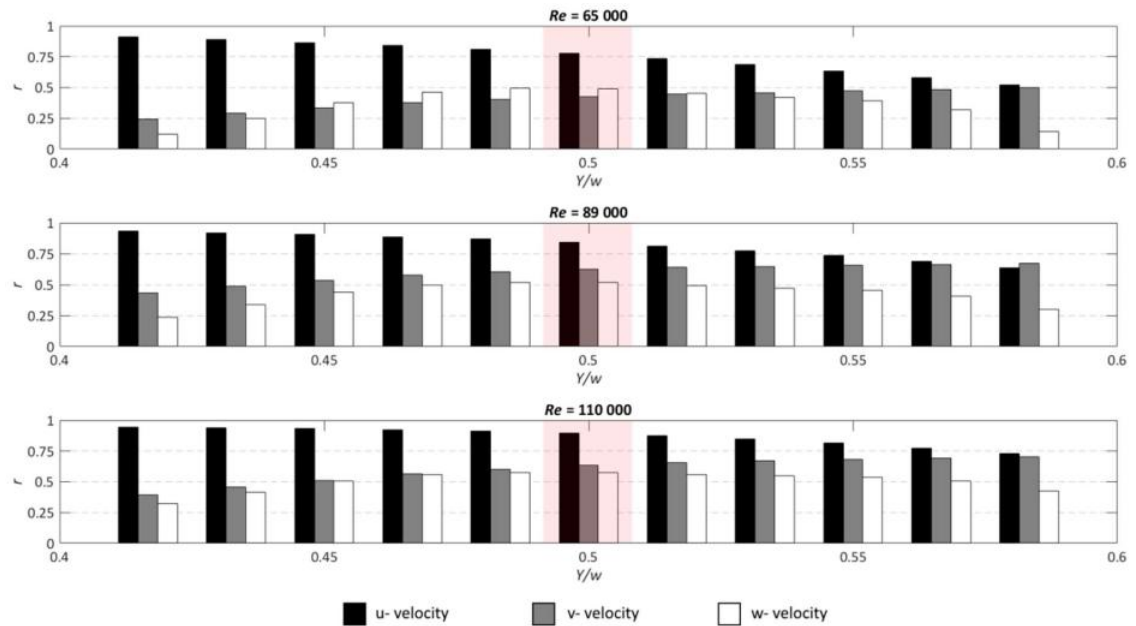


*Figure 5.19 Correlation coefficients (r) from the RMA regression between experimental data and the numerical model predictions in the unstressed posture along Y/w for the three components of velocity.*

The slope of the regression along *Y/w* (Figure 5.20) tends to follow a similar spatial pattern as the correlation coefficient. For *u-* velocity, the slope of the regression generally remains lower than unity throughout the *Re* range, indicating model under-prediction. As with the correlation coefficient, the slope of *u-* velocity is closest to unity at < 0.50 *Y/w*. A more complex pattern is shown for *v-* velocity, with consistent over-prediction at *Re* 65 000, and consistent under-prediction at *Re* 110 000. For *w-* velocity, under-prediction is consistent throughout the *Re* range, with slope closest to unity at 0.5 *Y/w*.
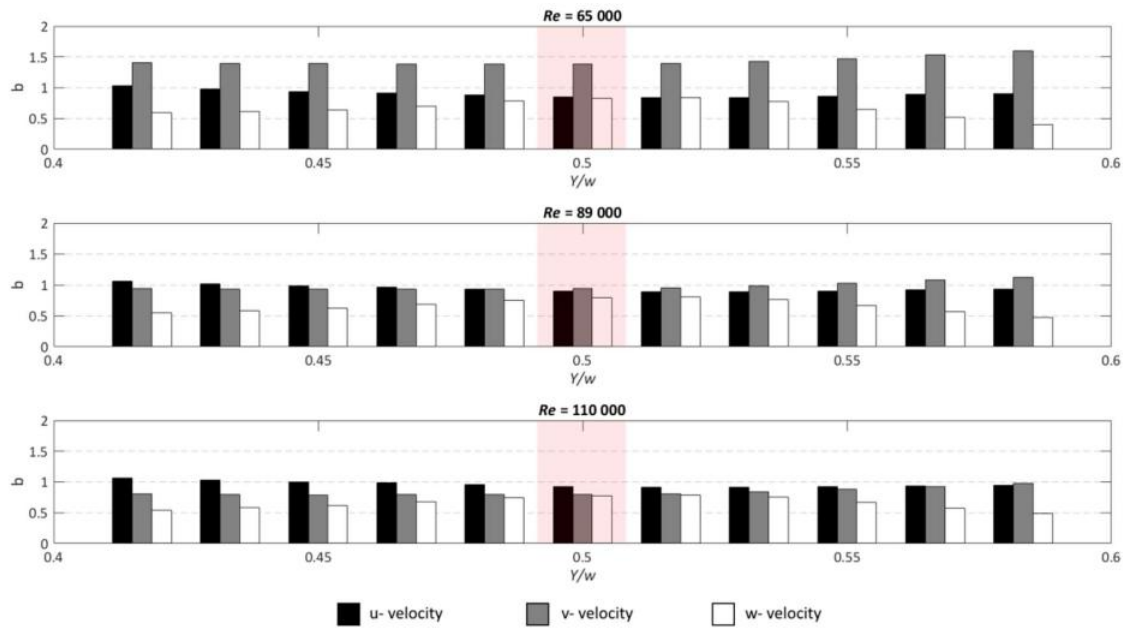
*Figure 5.20 Slope (b) from the RMA regression between experimental data and the numerical model predictions in the unstressed posture along Y/w for the three components of velocity.*

RMA regression across *Y/w* is also completed for the stressed plant postures. The correlation coefficient remains markedly higher for *u-* velocity than *v-* and *w-* velocities (Figure 5.21). As for the unstressed posture, the correlation coefficient of *u-* velocity decreases from 0.40 to 0.60 *Y/w*, whereas the correlation coefficient for *v-* velocity increases over this range. For *w-* velocity, the greatest correlation coefficients are typically found around 0.5 *Y/w*.
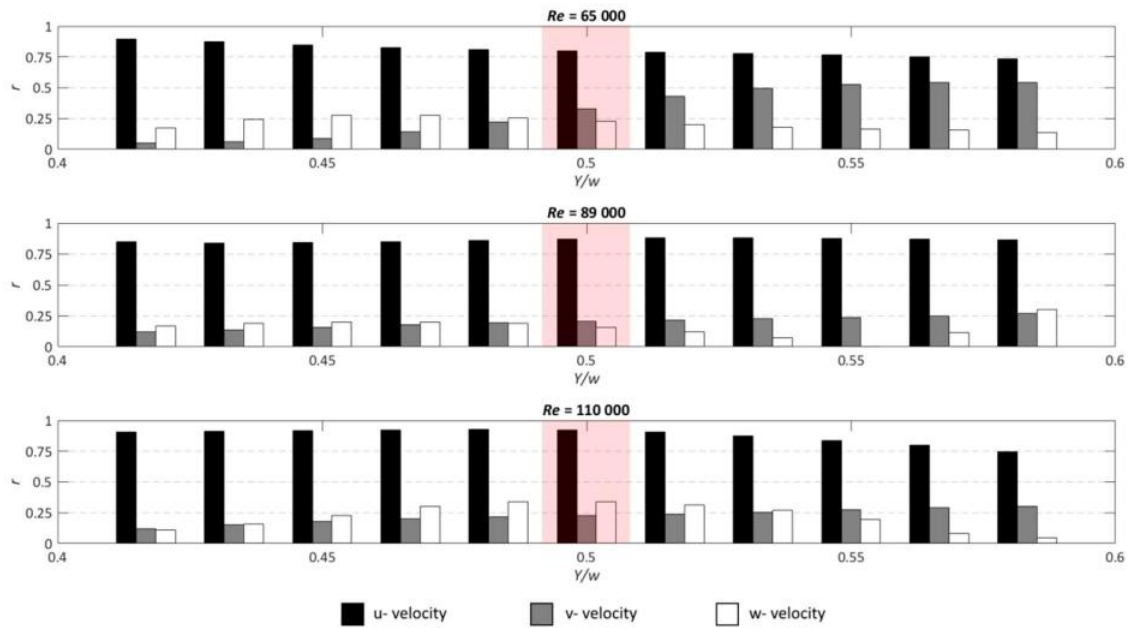
***Figure 5.21 Correlation coefficients (r) from the RMA regression between experimental data and the numerical model predictions in the stressed posture along Y/w for the three components of velocity.***

The slope of the regression along *Y/w* for the stressed posture (Figure 5.22) differs slightly from the unstressed posture. For *u-* velocity, as *Y/w* increases from 0.40 to 0.60, the slope tends to decrease from unity, demonstrating consistent model under-prediction. For *v-* velocity, slope is closest to unity at 0.5 *Y/w* for *Re* 65 000 and *v-* velocity is over-predicted elsewhere. As *Re* increases, the slope is closest to unity away from 0.5 *Y/w*, but *v-* velocity is consistently under-predicted. For *w-* velocity, over-prediction peaks at 0.5 *Y/w* for *Re* between 65 000 and 89 000 (with under-prediction elsewhere), but *w-* velocity is consistently under-predicted for *Re* 110 000.
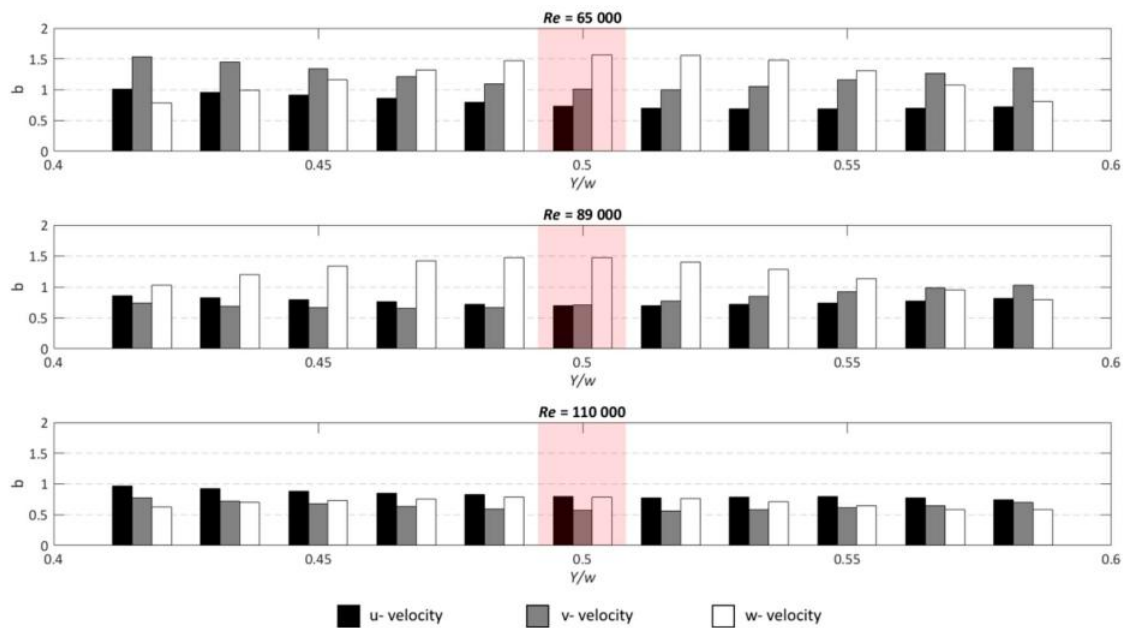
*Figure 5.22 Slope (b) from the RMA regression between experimental data and the numerical model predictions in the stressed posture along Y/w for the three components of velocity.*

For both the unstressed and stressed plant postures, correlation coefficients are not usually the highest, and slope values rarely closest to unity, at 0.5 $Y/w$ for all three components of velocity (highlighted red, Figure 5.19 – Figure 5.22). At this position, however, good overall agreement between measured and modelled velocities is consistently shown.

Higher correlation coefficients and slope values closer to unity, at different positions across $Y/w$, are attributed to the asymmetry in the volumetric canopy morphology of the plant blockages, which likely result in asymmetry of the resultant velocity field. Sensitivity to the position from which modelled velocity profiles are taken along $Y/w$ therefore exists, and although it is important to acknowledge that misalignment errors may exist in aDv measurements, these are likely to be small. Error on the inlet boundary conditions must also be considered. Inlet velocity was measured for single point in the flume at 0.4 $Z/h$, and this was used as the representative value for the inlet boundary conditions over $0 - 1$ $Z/h$ in the numerical model. Above 0.4 $Z/h$, the inlet velocity is likely greater than that measured, and this error is carried into the numerical predictions of flow. Furthermore, error from wall effects must also be considered, as working at these width-to-depth ratios there is the potential for wall-induced secondary circulation, although secondary flow of this nature is typically less than a few percent of the average flow velocity (Colombini, 1993). Accepting these potential errors, but also

acknowledging the good overall agreement between measured and modelled velocities at 0.5 Y/w, the remainder of this chapter continues to deal with comparisons at 0.5 *Y/w*.

### 5.4.1.3    Quantifying differences in measured and modelled velocity profiles

To understand the specifics of *u*- velocity profiles at 0.5 *Y/w*, Figure 5.23 shows measured velocity profiles and modelled velocity profiles (unstressed and stressed) in the downstream region 0.25 – 0.625 *X/l*. An agreement in the overall profile shape between the measured and modelled data is shown. A zone of reduced velocity in the plant wake exists in the range 0.25 – 0.375 *X/l*. For the unstressed model, velocities in this wake zone appear regular and gradually transition from low to high, whereas for the stressed model more velocity fluctuations are shown (Figure 5.23c at 0.25 *X/l*). Velocity minima in the low velocity zone are better represented by the stressed model, with a maximum difference in minima of $\pm$ 0.037 m s$^{-1}$ against the measured profiles over the entire *Re* range, compared to $\pm$ 0.049 m s$^{-1}$ with the unstressed model. Beneath 0.2 *Z/h*, a zone of flow acceleration associated with sub-canopy flow in the near-bed region is measured and modelled, although the model consistently fails to capture the magnitude in the velocity peak. With increasing distance downstream, velocity profiles show signs of recovery, reverting towards a fully developed profile.

To quantify the shape-based similarity between these profiles, the visual distance statistic, $d_V$, is calculated and displayed (Figure 5.23). Proximal to the plant (0.25 – 0.3125 *X/l*) where the velocity profiles are most heterogeneous, when the visual distance statistics are averaged over the entire *Re* range, the shape of the stressed model ($d_V$ = 0.67), are more similar than the unstressed model ($d_V$ = 0.70) to the measured profiles. When all of the visual distance statistics are averaged over the entire *Re* range, the shape of the velocity profiles from the stressed model ($d_V$ = 1.04) are again more similar than the unstressed model ($d_V$ = 1.06), to the six measured profiles. Velocity profile shape is therefore better modelled closer to the plant. Overall, given the closer general agreement and similarity in profile shapes of the stressed CFD model for *u*- velocity, and the smaller quantified errors of *v*- and *w*- velocity, it is argued that the stressed model is more representative and better able to predict three-dimensional mean flow than the unstressed model.
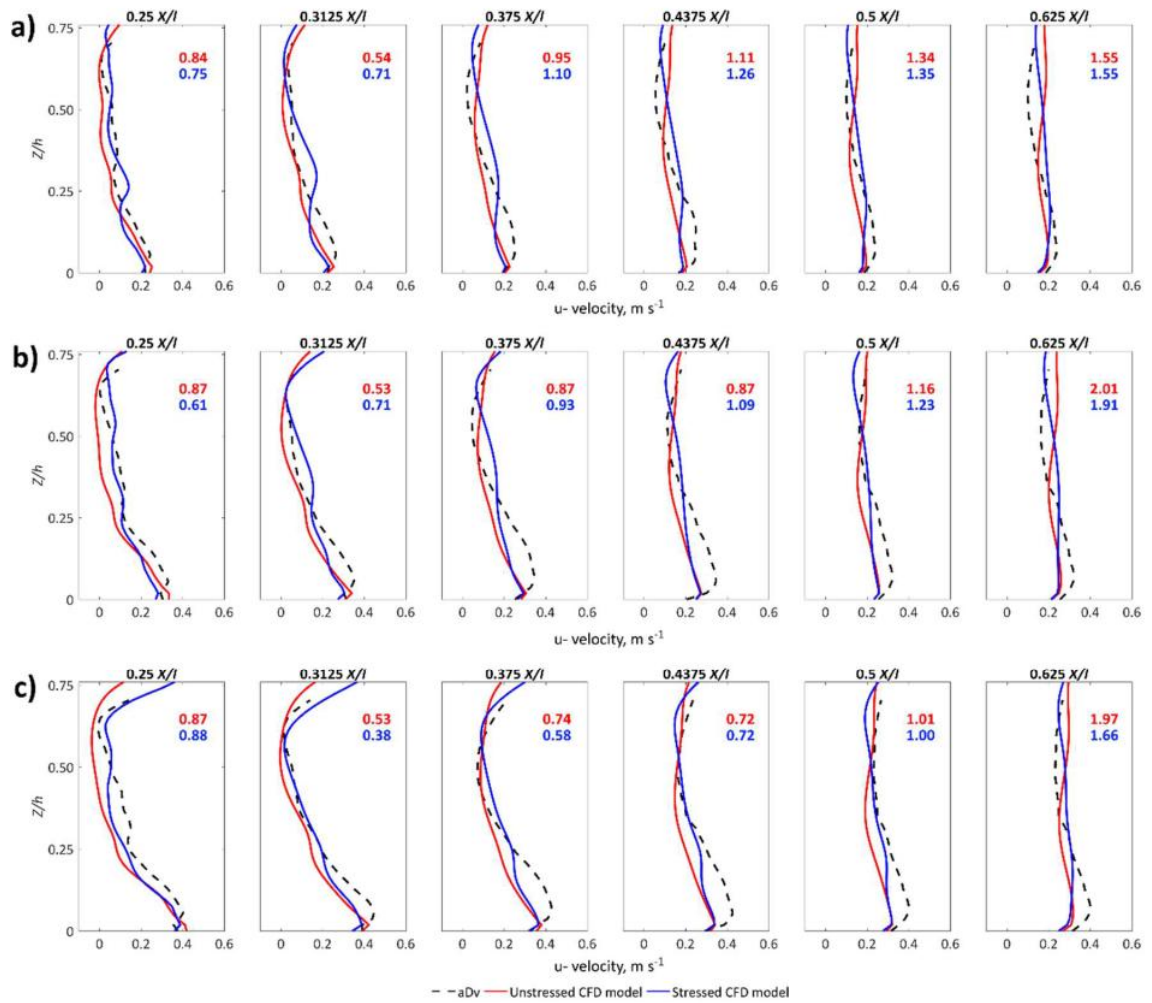
***Figure 5.23 Time-averaged streamwise velocity profiles for (a) Re 65 000, (b) Re 89 000, and (c) Re 110 000 comparing the measured aDv data (black dashed) to the CFD model with the unstressed CFD model (red) and stressed CFD model (blue) for six profiles in the range 0.25 – 0.625 X/l. Velocity profiles have equivalent point densities representing a 0.001 m spatial resolution in the vertical dimension. Red (unstressed plant posture in CFD model) and blue (stressed plant posture in CFD model) values denote the shape-based similarity to the aDv profile, quantified by $d_v$. The values range from ~0.5 to ~2, indicating considerable range in the shape-similarity over the measurement region.***

Next, the spatial patterns of $u$- velocity difference between the measured and stressed modelled data (aDv – CFD), and the cumulative difference over the six profiles, are analysed to investigate areas of model under- and over-prediction (Figure 5.24). In general, measured $u$- velocities exceed modelled $u$- velocities, although this varies with $Re$, and changes with distance downstream and vertically throughout the flow depth. The mean average difference across the six measured profiles increases from -0.002 m s$^{-1}$ at $Re$ 65 000, to 0.025 m s$^{-1}$ at $Re$ 110 000, indicating a slight under-prediction of $u$-velocity by the model at higher $Re$. Proximal to the plant (0.25 – 0.3125 $X/l$) the magnitude of differences are largest, but generally remain < 0.10 m s$^{-1}$. Further downstream as flow recovers, the magnitude of this velocity difference becomes smaller. Over the vertical extent, measured $u$- velocities tend to be greater than modelled $u$-

velocities in the range 0 – 0.3 $Z/h$, suggestive of model under-prediction in the sub-canopy region. This effect is most prominent closest to the plant, before flow recovers. This model under-prediction in the sub-canopy region is present for the entire $Re$ range. Above this zone, model over-prediction is noted in the plant wake region.

These differences between the measured and stressed modelled velocities, and specifically their vertical dependence, explain the systematic variation shown in Figure 5.18. The structural difference is caused by the transition from zones of model under-prediction in the sub-canopy region, to zones of model over-prediction in the wake region. This is attributed to an under-representation of the plant blockage in the model, meaning that the plant representations are more porous than the actual plant in the flume. This could possibly be caused by an insufficient scan resolution (as further discussed in Section 7.7.1), or could be an artefact of not representing the spanwise deformation of the plant during reconfiguration, which would likely further reduce the porosity of the plant, and is a potential limitation of the current approach applied here. This would help account for the limited ability to capture the magnitude of velocity peaks in the sub-canopy region, and over-prediction of velocity in the wake region, whereby penetration of flow through the interior of the plant is responsible for modifying the velocity immediately behind the plant blockage (Figure 5.23 and Figure 5.24). If the plant porosity was further reduced, the magnitude of sub-canopy flow would increase, with reduced velocity expected in the wake region.
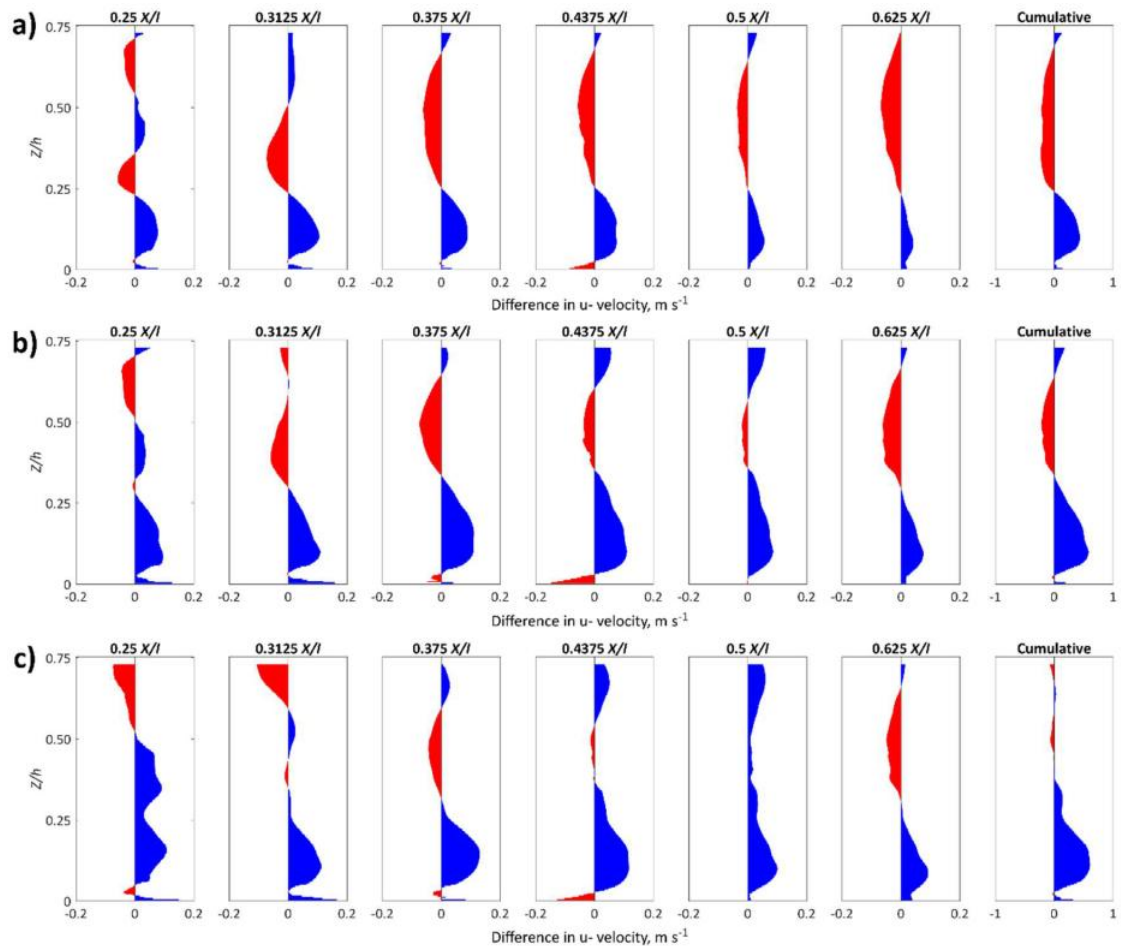
*Figure 5.24 Vertical and downstream differences in u- velocity (aDv – CFD) for: (a) Re 65 000, (b) Re 89 000, and (c) Re 110 000. Blue areas indicate sections of the profile where aDv measured u- velocities exceed those predicted by the stressed plant posture CFD model (model under-prediction), whereas red areas indicate sections of the profile where measured u- velocities are less than those predicted by the stressed plant posture CFD model (model over-prediction).*

## 5.4.2   Streamwise velocity field and wake structure

To further investigate the streamwise velocity field and wake structure, measurements of *u*- velocity have been linearly interpolated to allow for the comparison of the region 0.25 – 0.625 *X/l* against the same region in the stressed model. Time-averaged *u*- velocity was normalised by the inlet velocity (0.22, 0.30, and 0.37 m s$^{-1}$, Figure 5.25), with the difference then calculated (aDv – CFD). Vertical slices of the *u*- velocity flow field along the midline of the model domain were compared (0.5 *Y/w*). Numerous similarities between *u*- velocity fields are clear, most notably in the length and shape characteristics for each of the plant wakes. The calculated differences (Figure 5.25) reflect the zones of model under-/over-prediction identified previously, associated with an under-representation of the plant blockage in the model.
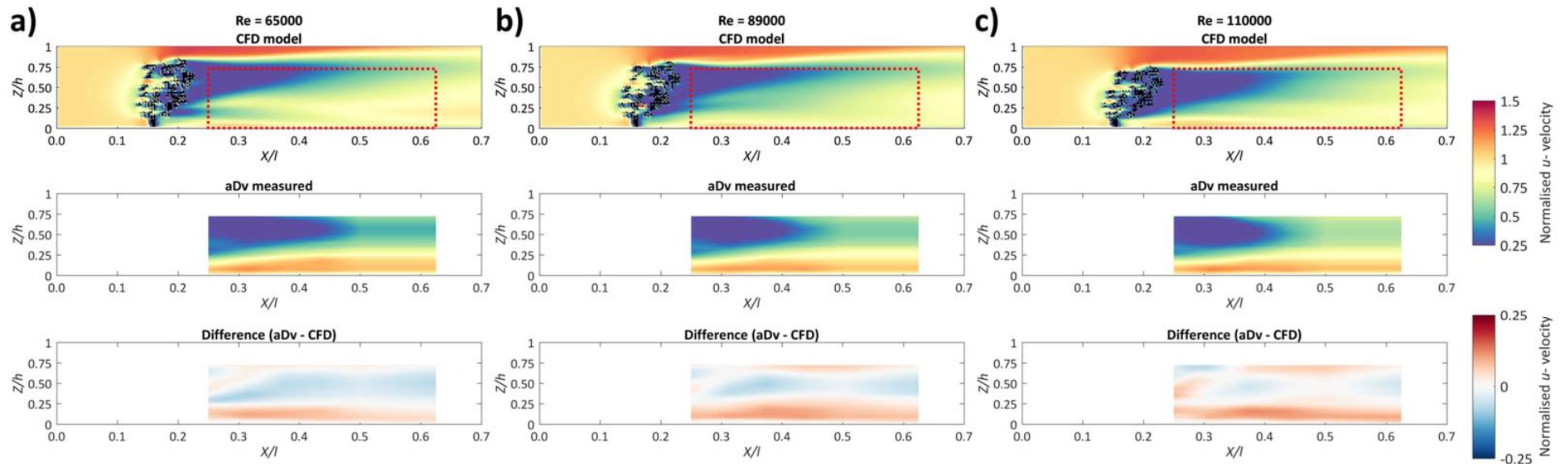
**Figure 5.25 Comparison of the aDv measured and CFD modelled normalised u- velocity field on a plane at 0.5 Y/w for: (a) Re 65 000, (b) Re 89 000, and (c) Re 110 000.**

Flow separation and reattachment results in the formation of a low velocity wake zone behind the plant blockage; here defined as < 0.5 of the streamwise velocity normalised by inlet velocity (Figure 5.26). A number of similarities are evident between the measured and stressed modelled plant wakes. For the stressed modelled data, the wake shape remains approximately constant in the *Re* range 65 000 to 89 000, forming a dual-layered structure, with the larger upper wake inclined slightly upwards. At *Re* 110 000, a single-layered, thicker wake exists, and this is positioned lower in the flow depth. In each case the wake markedly thins in the downstream direction. The modelled wake thickness has decreased by 42, 60, and 41% between 0.25 and 0.4 *X/l* for each *Re*. Also, the modelled wake length decreases from ~3.9 plant lengths at *Re* 65 000, to ~3.3 plant lengths at *Re* 110 000.

In the measured case, a single-layered wake maintains an almost consistent shape throughout the entire *Re* range, although ends more abruptly than in the modelled case. The abrupt ending could be attributed to the interpolation of measurement data, although in general the agreement of wake characteristics between measured and modelled data is good. The measured wake thickness has decreased by 39, 44, and 40% between 0.25 and 0.4 *X/l* for each *Re,* and therefore demonstrates a similar thinning pattern to the modelled wake. The measured wake length is similar to the modelled wake length, showing a decrease with increasing *Re*, from ~3.9 plant lengths at *Re* 65 000, to ~3.1 plant lengths at *Re* 110 000. The trailing edge of the wake, which indicates the downstream wake limit, is progressively shifted towards lower values of *Z/h* with increasing *Re*, and is expected to be associated with the vertical compression of the plant.

Combining Figure 5.25 and Figure 5.26, a rapid gradation in velocity is modelled to occur between the low velocity wake zone and the free-stream zone, with this velocity discontinuity indicative of shear layer formation and the presence of Kelvin-Helmholtz instabilities (Ghisalberti and Nepf, 2002). The frequency of which, $f_{KH}$ (Hz), depend on the characteristics of the shear layer (Ho and Huerre, 1984), following :

$$f_{KH} = 0.032 \frac{\bar{u}}{\theta_m} \tag{5.2}$$

where $\bar{u}$ is the mean velocity (m s$^{-1}$), and $\theta_m$ is the momentum thickness (m), a measure of the thickness of the shear layer. From this, $f_{KH}$ is calculated to be 0.20, 0.23, and 0.30 Hz for the different *Re*.
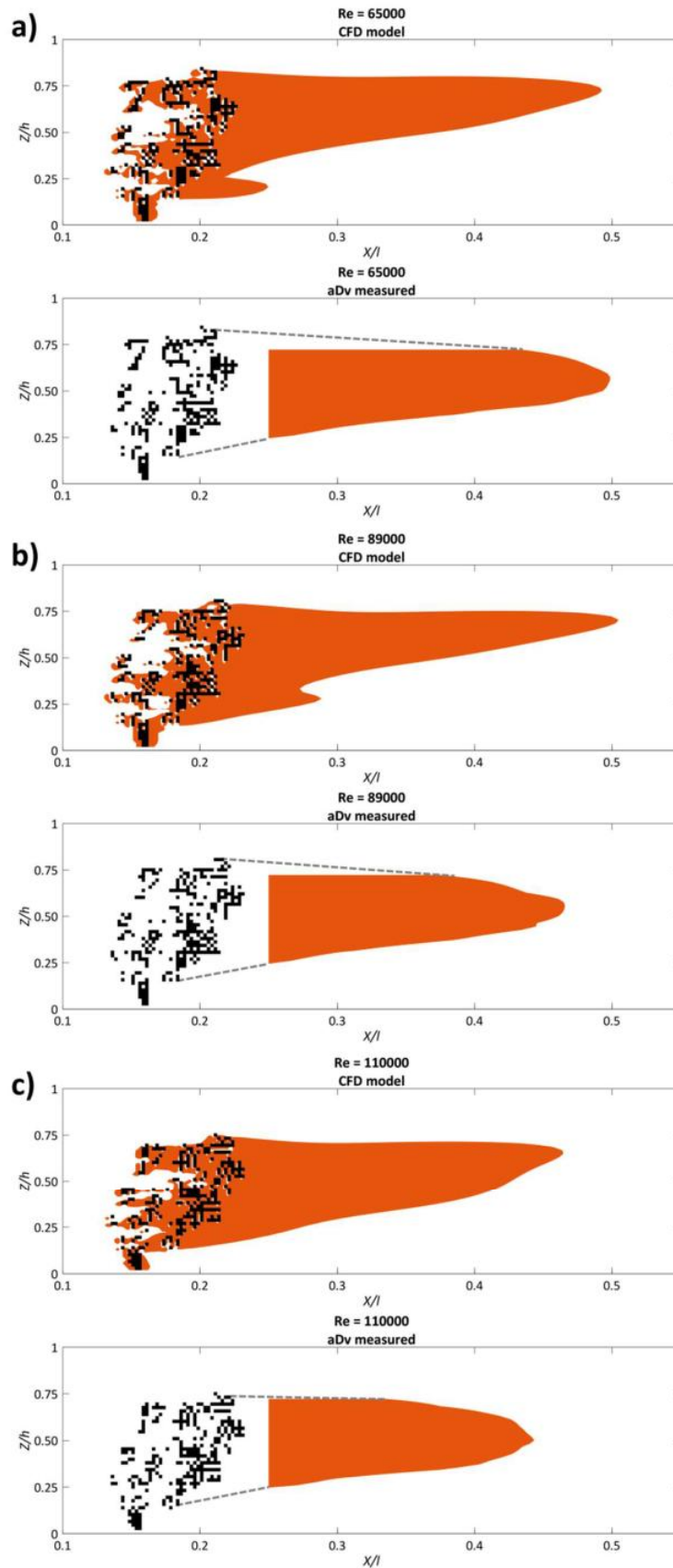
***Figure 5.26 Vertical distribution of the CFD modelled and aDv measured wake zone (orange) defined as < 0.5 of the streamwise velocity normalised by inlet velocity for: (a) Re 65 000, (b) Re 89 000, and (c) Re 110 000. Black pixels denote plant location. Dashed lines indicate the inferred location of the aDv measured wake in the zone where flow measurements were not possible.***

## 5.5        Spatial distribution of the pressure field

The CFD model also provides predictions of the pressure field, which are eventually used to calculate the drag response of the plant (Chapter 7). Although the pressure field is not directly validated, the spatial distribution of pressure is important for improving the process-understanding of flow vegetation interactions.

Figure 5.27 shows the pressure distribution at 0.5 $Z/h$ under increasing $Re$. High pressure zones form on the upstream side of the plant blockage, with low pressure zones on the downstream side. With increasing $Re$, the magnitude of these high and low pressure zones increases; and is most pronounced for $Re$ 110 000, where a considerable high pressure zone has formed on the upstream side. An asymmetric distribution of pressure is consistent for each plant, with highest pressures at 0.5 $Z/h$ in the region > 0.5 $Y/w$. Smaller regions of high and low pressure are also distributed in the interior of the plant. As the plant is vertically compressed under increasing $Re$, reducing the plant volumetric canopy morphology, the magnitude of pressure in these interior regions is also shown to increase.
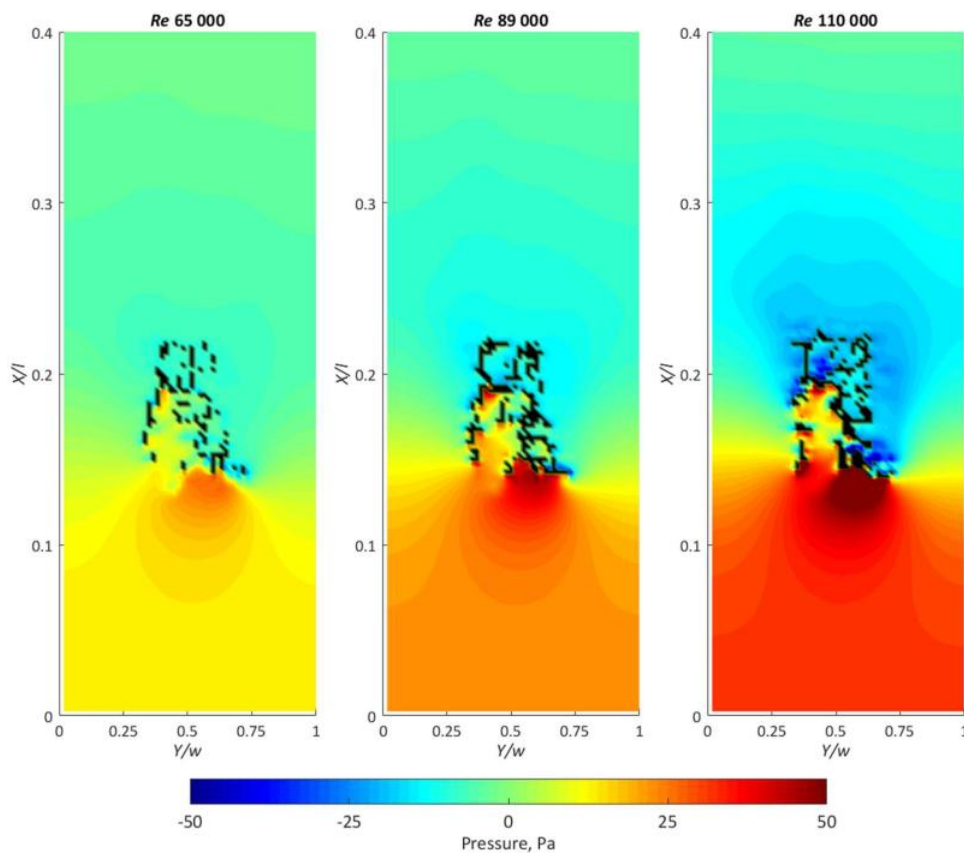


*Figure 5.27 Pressure fields at 0.5 Z/h with increasing Re. Black cells denote the position of the plant.*

To further investigate the spatial distribution of pressure, the pressure field is plotted over the surface of the plant front in Figure 5.28a, and over the surface of the plant back in Figure 5.28b. The distribution of pressure is spatially heterogeneous for both the plant front and the plant back. For each *Re*, zones of high pressure are recorded slightly to the left of the main stem, off-centre in the leaf body. Zones of low pressure are recorded even further from the centre of the plant, distributed towards the outer edge of the plant. Consistent with Figure 5.27, the magnitude of the high and low pressure zones increases with *Re*. This results in the formation of a more adverse pressure gradient with increasing in *Re*, as shown in Figure 5.28c. The total pressure gradient at *Re* 110 000 is more than twice as great as the total pressure gradient at *Re* 65 000. However, the vertical distribution of the pressure gradient appears similar for each *Re*, with the pressure gradient relatively small around the main stem, but then significantly increasing as flow begins to interact with the leaf body. At the top of the plant, the pressure gradient rapidly falls away; this is associated with the relatively planar top to the leaf body (shown in Figure 5.8). If the blockage at the top of the plant was distributed more gradually, the fall away in pressure gradient would likely be less rapid. Changes in the pressure gradient have important implications for the calculation of the drag response, as detailed in Section 7.5.
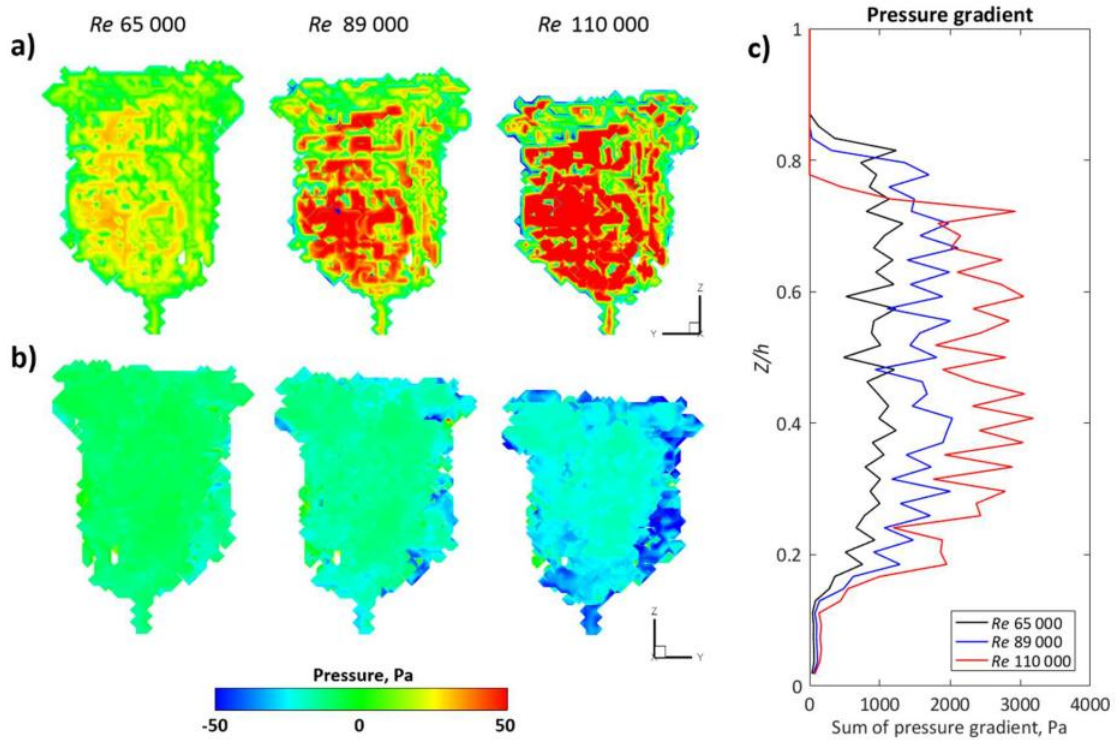
**Figure 5.28 (a) Pressure distribution over the plant front and (b) over the plant back with increasing Re. This shows the spatially heterogeneous pressure field, and differences in magnitude with increasing Re. (c) Pressure gradients over the lateral extent of the plant, with more adverse pressure gradients at higher Re.**

## 5.6      Turbulent flow structures

Section 5.4 has shown that the model can predict the measured time-averaged flow conditions, and therefore analysis is extended to investigate the turbulent structures associated with the submerged plant under increasing *Re*. As with the pressure field (Section 5.5), the data are not constrained by direct empirical comparisons, but are useful to improve the process-understanding. First, regions of high vorticity are identified, to help understand the spatial distribution and underlying cause of any turbulent structures. However, the vorticity field alone is unable to distinguish between vortices and the strain field. In transitional regions where there is a sharp velocity gradient, the strain field is expected to be higher, and this could be reflected through higher vorticity values (Cucitore *et al.*, 1999). Careful interpretation of the vorticity field is therefore required, with analysis also extended to identify vortices using the Q criterion (Hunt *et al.*, 1988), which identifies a vortex to be present if the magnitude of the vorticity tensor is greater than the rate of the strain tensor, with a local pressure minimum present.

The horizontal distribution of *uv-* vorticity in a plane at 0.5 *Z/h* is shown in Figure 5.29, with two-dimensional *uv-* flowlines overlain, to show the modelled flow pathways through and around the plant. The *uv-* vorticity refers to the horizontal lateral vorticity. In each *Re* case, the shedding of counter rotating regions of high vorticity occurs, with the development of a large region of high vorticity at the outer edge of the plant boundary, whose position correspond with deflections to flowlines. Here it is suggested that this plant shear layer turbulence is dominated by Kelvin–Helmholtz and Görtler-type vortices generated through shear instability (Ghisalberti and Nepf, 2002). A horizontal interface therefore exists at the outer edges of the plant boundary, forming between the low velocity wake zone and the faster moving fluid that is forced around the outside of the plant blockage.

Within the plant body, smaller regions of high vorticity are distributed in the central region of the plant, and the flowlines distorted. This demonstrates the internal flow dynamics and the forcing of flow through gaps and conduits in the plant morphology. As *Re* increases, and the volumetric canopy morphology is vertically compressed and its porosity reduced, both the magnitude of the *uv-* vorticity and the length of the high vorticity regions at the outer plant boundary increase. To exemplify this, by taking an arbitrarily defined value of *uv-* vorticities as ± > 1.5 Hz, the maximum length of the high vorticity region increased by ~40% over the entire *Re* range. Changes in the volumetric canopy morphology therefore influence the velocity gradient and regions of vorticity present.
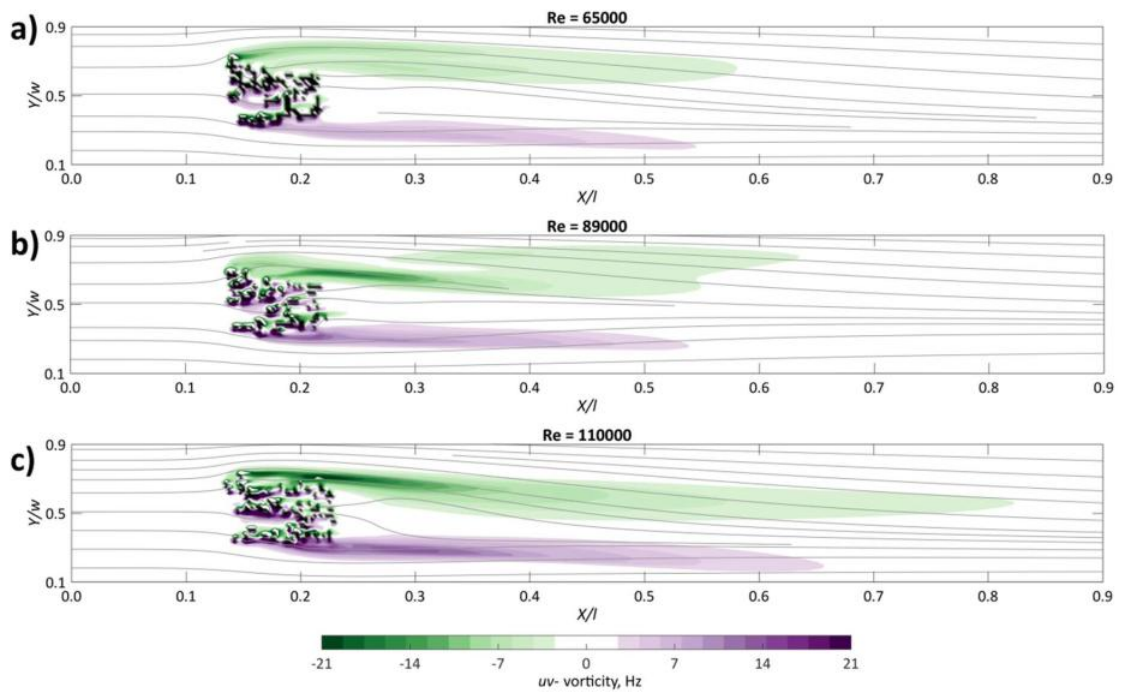
***Figure 5.29 Horizontal distribution of uv- vorticity along a plane at 0.5 Z/h for: (a) Re 65 000, (b) Re 89 000, and (c) Re 110 000, showing clockwise (green) and anticlockwise (purple) regions of high vorticity.***

The vertical distribution of *uw-* vorticity in a plane at 0.5 *Y/w* is shown in Figure 5.30, with two-dimensional *uw-* flowlines overlain to show the modelled flow pathways over and around the plant. The *uw-* vorticity refers to the horizontal vertical vorticity. In each *Re* case, the shedding of counter rotating regions of high vorticity occurs, with the development of the largest region of vorticity located above the plant boundary, corresponding with deflections to the flowlines. Again, this shear layer turbulence appears to be dominated by Kelvin–Helmholtz and Görtler-type vortices generated through shear instability, this time forming at the vertical interfaces. Above the plant, shearing occurs between the low velocity wake zone and the free-stream zone. Beneath the plant, another vertical interface between the low velocity zone and the zone of flow acceleration associated with the sub-canopy flow component is present. The region of high vorticity below the plant blockage is shorter than the corresponding region above the plant, but the magnitude of vorticity is similar.

As with the *uv-* vorticity field, where small regions of high vorticity were distributed within the plant body, the same is true for the *uw-* vorticity field. These are especially prominent towards the upstream end of the plant body, again highlighting the internal flow dynamics. With increasing *Re*, the length of the largest regions of high vorticity increases, again associated with reductions of the volumetric canopy morphology and porosity, and results in the strengthening of the shear layer turbulence. This is clearly

demonstrated above the plant in Figure 5.30c, with highest magnitudes recorded. Taking the arbitrarily defined value of *uw-* vorticities as ± > 1.5 Hz, the maximum length of the high vorticity region increased by ~30% over the entire *Re* range. The interplay between volumetric canopy morphology and velocity gradients is therefore crucial in determining the spatial distribution of vorticity.
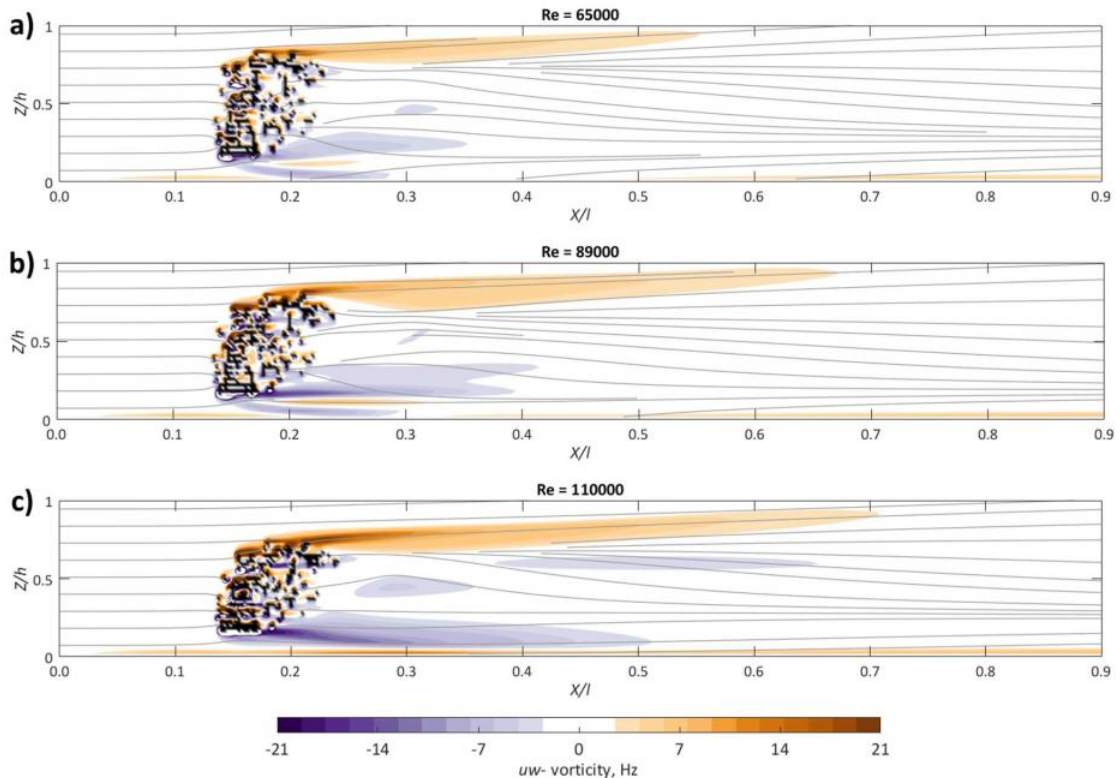


**Figure 5.30 Vertical distribution of uw- vorticity along a plant at 0.5 Y/w for: (a) Re 65 000, (b) Re 89 000, and (c) Re 110 000, showing clockwise (orange) and anticlockwise (purple) regions of high vorticity.**

An impression of the three-dimensional turbulent structures forming around the plant blockage are visualised by plotting isosurfaces of the Q criterion, applying a Q threshold of 3.5 (Hunt *et al.*, 1988) (Figure 5.31). For a physical interpretation of the Q criterion, a vortex is assumed to be present where the vorticity tensor exceeds the rate of the strain tensor, and a local pressure minima exists, forming the vortex envelope. The Q criterion was selected for vortex identification purposes, rather than alternative methods such as the $\lambda_2$, as it has previously been shown to successfully detect canopy-scale vortices around vegetation (Marjoribanks *et al.*, 2017).

With increasing *Re*, vortices extend further downstream, with the maximum vortex length almost doubling over the modelled *Re* range. Vorticity magnitude increases with *Re*, with higher magnitudes distributed towards the upper region of the plant. In the *Re* range 65 000 to 89 000, the vortex appears to be stretched but retains a similar form, although vorticity magnitude increases. For *Re* 110 000, the vortex shape is modified, with a lengthening of the uppermost vortex tail, and this is suggested to be associated with the stronger shear layer instability formed between the low velocity wake zones and the free-stream zone above. Again, this indicates the interplay between the volumetric canopy morphology and regions of high vorticity. Several scales of turbulence are therefore expected to be present, as discussed further in Section 7.4.3.2.
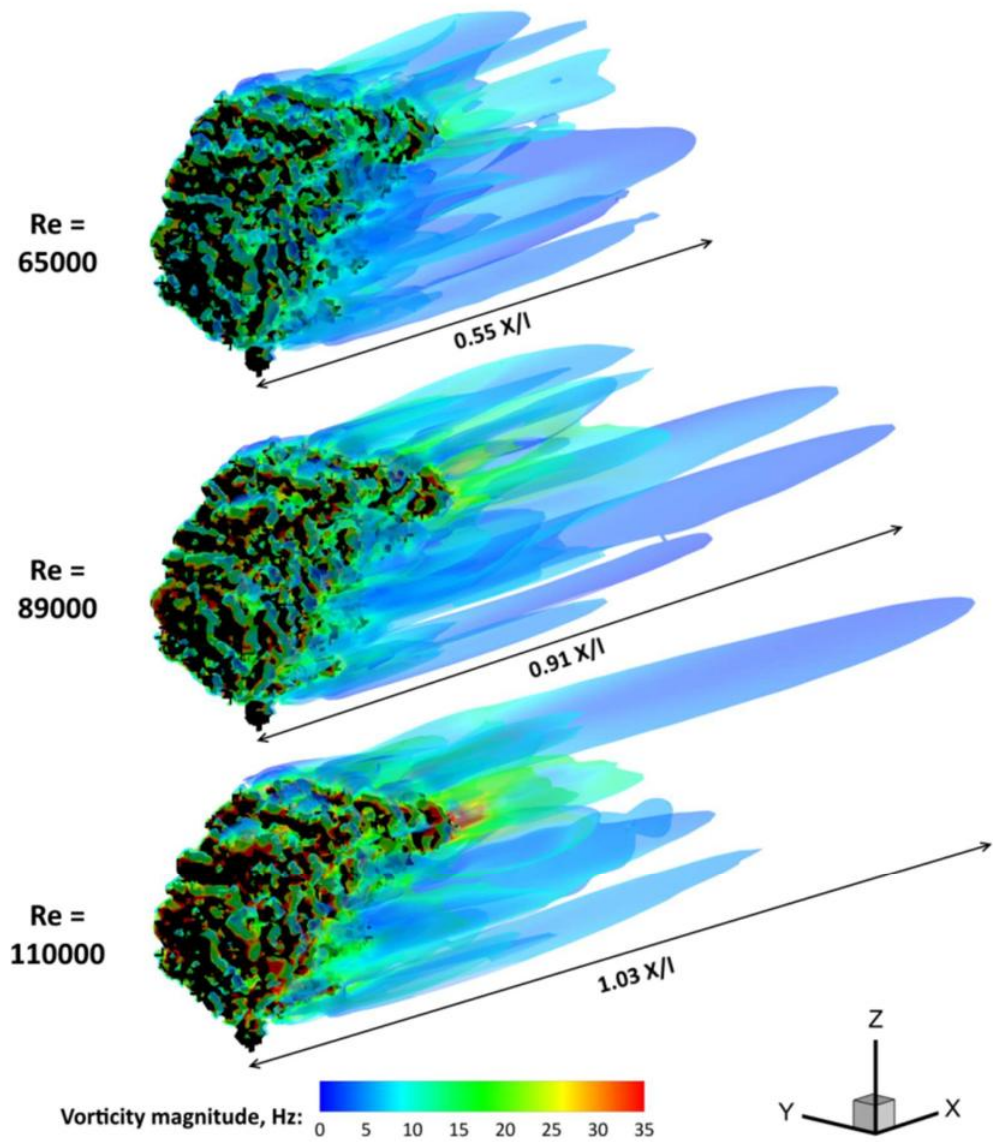
*Figure 5.31 Comparison of three-dimensional structure of turbulence using the Q criterion, applying a Q threshold of 3.5, with the isosurface coloured by vorticity magnitude.*

## 5.7        Chapter conclusions

This chapter has examined the feedbacks between flow and vegetation dynamics, with respect to RQ4 and RQ5, through a combined flume and numerical model study around a submerged *Hebe odora* plant at three different flow Reynolds (*Re*) numbers. Results demonstrate that by incorporating the time-averaged plant posture into a high resolution CFD model, it is possible to accurately predict three-dimensional mean and turbulent flow. The chapter has successfully demonstrated that:

i.    Under hydrodynamic loading, an inverse harmonic relationship between plant height and plant length is shown for *Re* 89 000 and 110 000 (Section 5.3.1). Overall plant motion can be separated into time-dynamic and time-averaged components. Time-dynamic plant motions were investigated by tracking the motion of plant tips (Section 5.3.2), showing a transition from horizontally dominated to vertically dominated movement and increased movement extents as Re increases. Plant tip motion varies across the plant body in reaction to the local flow, and shows a dependence with Re. Time-averaged plant motion (Section 5.3.3) is associated with shifts in the general plant posture which reconfigures to the mean flow, resulting in up to an 18% reduction in plant height, a 14% increase in plant length, and a doubling of the lead and lee angles of the plant body. These motions are responsible for vertically compressing the plant in the flow, thereby reducing the volumetric canopy morphology and plant porosity.

ii.   Velocity profiles illustrate a zone of sub-canopy flow acceleration which interacts with the low velocity wake region behind the plant (Section 5.4.1), and helps generate an upwardly inclined wake structure that thins in the downstream direction. With the wake defined as < 0.5 of *u*- velocity normalised by inlet velocity, with increasing *Re* the wake length decreases from ~3.9 plant lengths to ~3.1 plant lengths (Section 5.4.2). It is suggested that the plant shear layer turbulence is dominated by Kelvin–Helmholtz and Görtler-type vortices generated through shear instability (Ghisalberti and Nepf, 2002), the frequency of which is estimated to be 0.20, 0.23, and 0.30 Hz at *Re* 65 000, 89 000, and 110 000.

iii.    Using the time-averaged plant posture as boundary conditions to discretise the plant in the high resolution CFD model, the modelling system is shown to accurately predict flow measurements (Section 5.4). General agreement is quantified through RMA regression, with $u$- velocity correlation coefficients > 0.8. Furthermore, the visual distance statistic ($d_v$) demonstrates the similarity between aDv measured and CFD modelled velocity profile shapes. Following validation, analysis is extended to investigate the pressure field and turbulent flow structures associated with the plant, where it is shown that the modelled vortices migrate further downstream as the shear instability grows stronger (Section 5.6). Complex three-dimensional structures are therefore present at the plant-scale.

Good practice in numerical modelling requires both CFD verification and validation. Verification was previously demonstrated in Section 4.3.7.1, with validation forming the basis of this chapter. Here it has been shown that an explicit consideration of plant postural changes is essential in the prediction of three-dimensional mean and turbulent flow. To explore this further, the numerical model will be extended to assess the importance of plant volumetric canopy morphology on three-dimensional mean and turbulent flow through further numerical experiments in the next chapter.

<div align="right">

**Chapter 6**

</div>

# The importance of accurately representing plant volumetric canopy morphology in the numerical model

## 6.1 Introduction

This chapter will address the importance of plant volumetric canopy morphology on the three-dimensional mean and turbulent flow in support of RQ4 and RQ5, allowing dominant factors that control flow field dynamics to be identified and quantified. Throughout this chapter, the *Prunus laurocerasus* specimen first outlined in Section 3.3 is analysed, given its complex branch and leaf structure, and similarity to woody riverine vegetation species such as *Populus nigra*, typically found on gravel bars (O'Hare *et al.*, 2016). The previous chapter has shown how plant reconfiguration under hydrodynamic loading reduces the volumetric canopy morphology, and influences the three-dimensional mean and turbulent flow. However, additional factors that contribute towards the plant volumetric canopy morphology such as foliage and the plant structure and form will also exert a control on the flow field dynamics (Chapter 2), which will contribute towards the drag response and vegetative resistance (Chapter 7).

In the first section of the chapter, the effect of modifying the representation of the plant within the CFD model will be quantitatively assessed. The effect of collecting scans from different numbers of positions when using TLS to capture the plant point cloud, prior to applying the voxelisation procedure (Section 3.3), will be quantified. This section therefore quantifies the effect of using different numbers of scan positions, thereby giving different levels of completeness to the plant representations, on the flow field dynamics. This will help inform the best practice when collecting boundary conditions necessary for plant discretisation in the CFD model, useful for future studies concerned with high resolution modelling of flow-vegetation interactions.

Following this, the influence of foliage is investigated by comparing the *Prunus laurocerasus* plant when defoliated and foliated (Section 6.3). To the author's knowledge, this is the time that foliage has been explicitly represented in a CFD model, with the implications for the flow field dynamics discussed. By comparing results from the same plant, the method ensures that any differences are attributable to the leaf body.

Having quantified the influence of foliage, a range of additional factors that contribute to the volumetric canopy morphology relevant to flow-vegetation interactions will be analysed. The section first focuses on simulated changes in plant posture (Section 6.4.1), and then simulated changes in plant aspect (Section 6.4.2). In both cases, changes in 'how the plant looks to flow' are hypothesised to have a response on the flow field.

In the final section of the chapter (Section 6.5), simulations of flow around three different *Prunus laurocerasus* plants are compared. The specimens were selected for their similarity in size, but natural variation in branch and leaf structure, resulting in different plant volumetric canopy morphologies. These differences allow the influence of plant structure and form on flow field dynamics to be isolated.

## 6.2    Sensitivity to the number of scan positions used to capture plant volumetric canopy morphology

In this section, the sensitivity of flow field dynamics to the number of scan positions used to capture plant volumetric canopy morphology will be analysed, focusing on the downstream velocity and pressure fields. This different numbers of scan positions are defined following: a single scan position ($SC_1$), two scan positions ($SC_2$), and four scan positions ($SC_4$). For $SC_2$ and $SC_4$, scan positions are opposing, and this helps to provide a more complete representation of the plant. Having analysed the sensitivity to the voxel size used to describe the plant in Section 4.3.7.2.3, it follows that the number of scan positions used to capture and represent the plant blockage should be quantitatively assessed. This section therefore seeks to assess how plant representations with different levels of completeness influence the flow field dynamics. The different levels of completeness are caused by the effects of occlusion; expected to be higher when fewer scan positions are used (Section 3.3.2). The flow field is predicted around a characteristic subsection of the *Prunus laurocerasus*, highlighted purple in Figure 6.1. As in Section 4.4, model inlet conditions were held constant at 0.25 m s$^{-1}$, and the turbulence intensity was specified at 5%. Flow conditions are fully turbulent and subcritical.
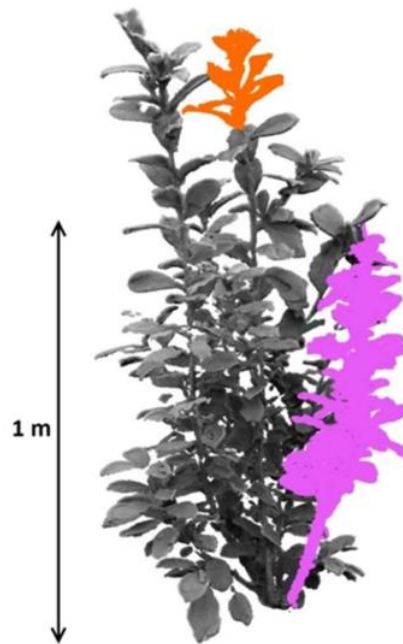
***Figure 6.1 Excerpt from Figure 3.19, the purple section of the Prunus laurocerasus plant was used to assess the sensitivity of flow field dynamics to the number of scan positions used when capturing the plant volumetric canopy morphology.***

## 6.2.1        Comparing plant volumetric canopy morphologies

Post-processed point clouds of the section of the *Prunus laurocerasus* plant for $SC_1$, $SC_2$, and $SC_4$ are shown in Figure 6.2a.  The flow response is simulated around a characteristic subsection of the plant, with the voxelised representations shown in Figure 6.2b at a 0.01 m voxel size.   In total $SC_1$ contains 2693 voxels, $SC_2$ contains 3647 voxels, and $SC_4$ contains 4968 voxels.  Between $SC_1$ and $SC_2$, and between $SC_2$ and $SC_4$, the increase in the number of voxels is ~35%.  Between $SC_1$ and $SC_4$, the number of voxels increases by ~85%.  These differences transfer to the plant volume, as voxel size is held constant at 0.01 m.

By defining $SC_4$ as the 'complete' plant representation, the total volume of $SC_2$ is 73% that of $SC_4$, and the total volume of $SC_1$ is 54% that of $SC_4$.  The distribution of voxels over the vertical extent of the modelling domain are shown in Figure 6.2c, and this represents the vertical distribution of the plant blockage.  General similarities in the distribution of voxels are shown for all the representations, with peaks in the number of voxels around 0.65 – 0.80 $Z/h$.  However, differences in the distribution of voxels are especially clear between $SC_1$ and $SC_4$ in the region< 0.5 $Z/h$, and correspond with visible gaps in the branch and leaf structure in the voxelised representations (Figure 6.2b). Between $SC_2$ and $SC_4$, these gaps are infilled, with $SC_2$ providing a more complete

representation of the plant than $SC_1$. Because the plant volumetric canopy morphology varies between the different representations, primarily through increases in the volume of the blockage with an increasing number of scan positions, it is hypothesised that flow field dynamics will be influenced.
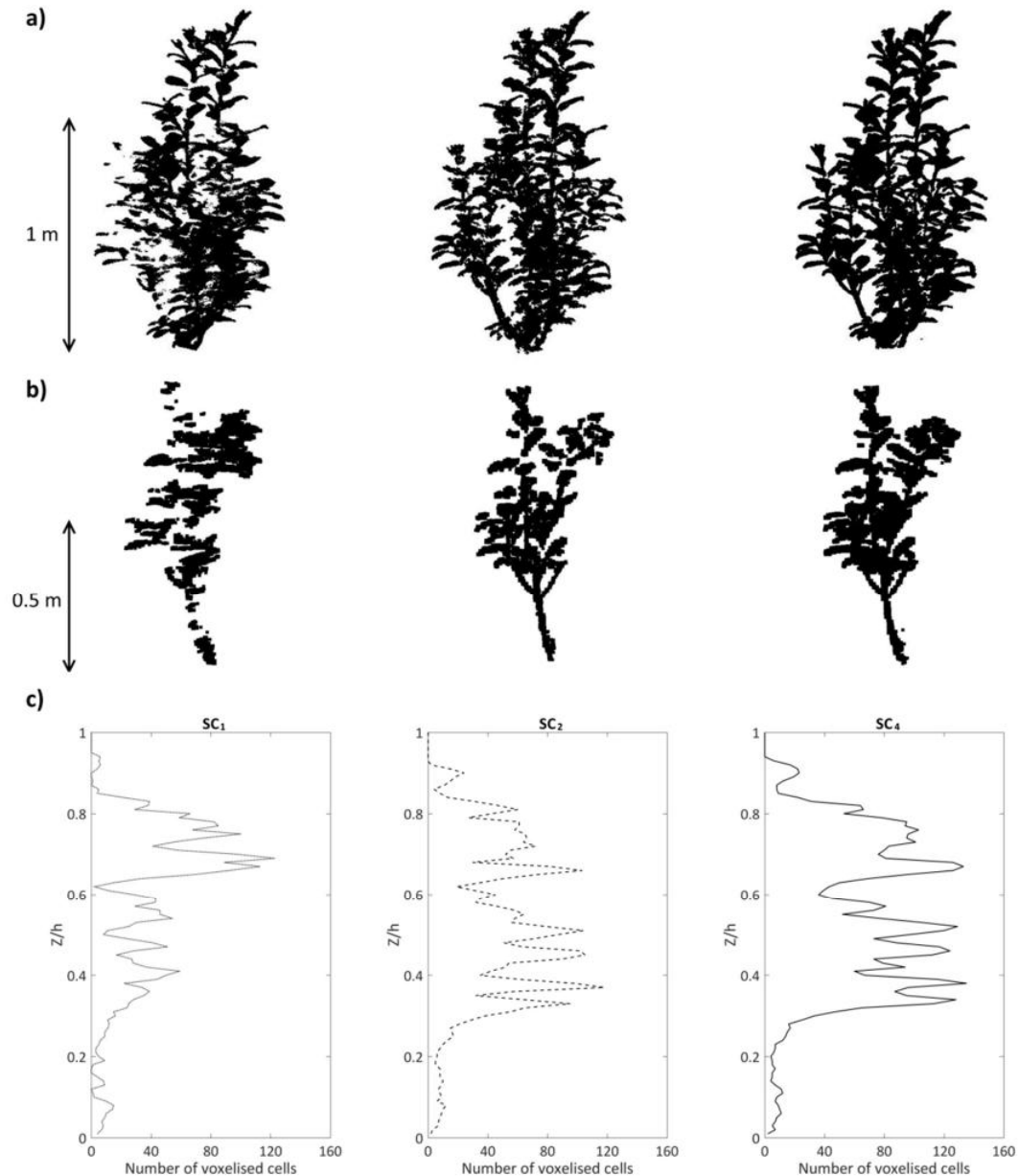


*Figure 6.2 (a) Post-processed point clouds of the foliated Prunus laurocerasus plant for $SC_1$, $SC_2$, and $SC_4$. (b) Voxelised representations at a 0.01 m voxel size. (c) Distributions of voxels over the vertical extent of the modelling domain. The total volume of $SC_2$ is 73% that of $SC_4$, and the total volume of $SC_1$ is 54% that of $SC_4$.*

### 6.2.2 Sensitivity to the number of scan positions on flow field dynamics

The effect of changing the number of scan positions on the downstream velocity field is shown in Figure 6.3, comparing downstream velocity profiles at pre-defined distances downstream (0.25, 0.30, 0.35, and 0.40 $X/l$), along the midline of the domain (0.5 $Y/w$). The shape of velocity profiles change as the number of scan positions increases, although general similarities between the velocity profiles are seen. In the range $0 - 0.2$ $Z/h$, relatively minor flow disturbance corresponds with the region of the main branch. Above this, the flow disturbance is greater and is associated with flow separation about the leaf body of the plant.
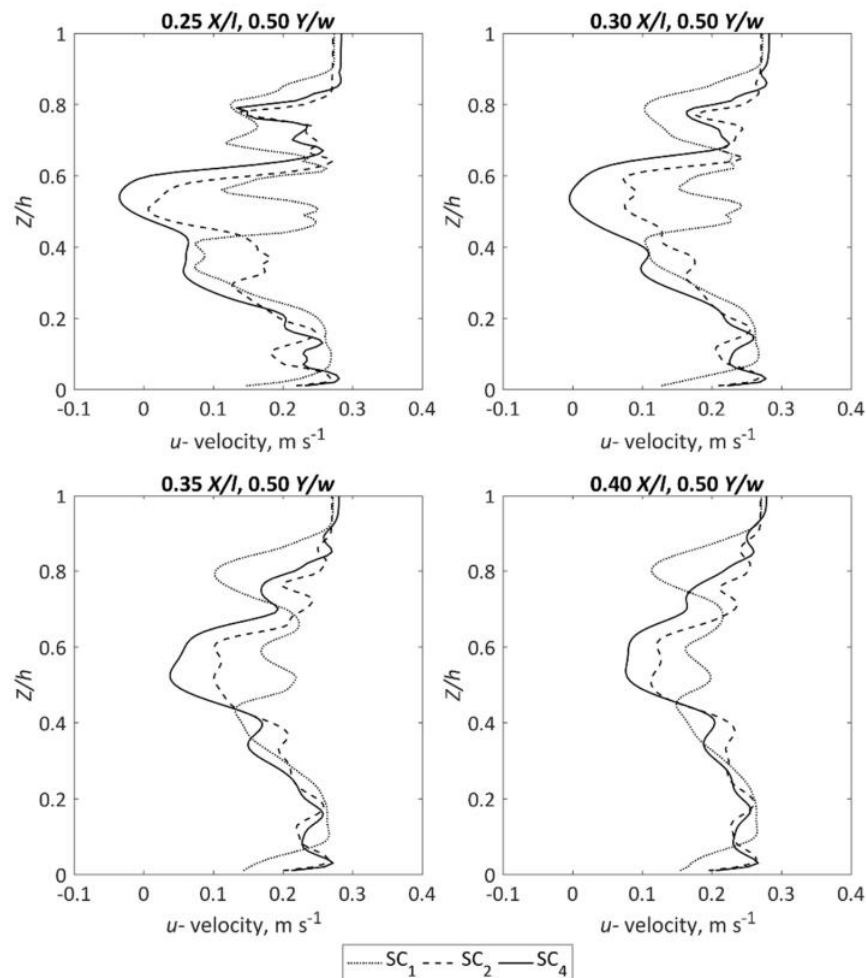
**Figure 6.3 Velocity profiles for the downstream component of flow extracted at predefined intervals downstream from the voxelised plant representation, with an increasing number of scan positions.**

With an increasing number of scan positions, however, differences in velocity profiles emerge. As the number of scan positions increases, the magnitude of the flow disturbance introduced by the plant blockage increases. This is quantified by calculating

the average downstream velocity for each profile, shown in Table 6.1.  For each of the four distances downstream where velocity profiles are extracted, the average downstream velocity is consistently lowest for $SC_4$, but similar between $SC_1$ and $SC_2$, with average downstream velocities over the four profiles ~12% lower for $SC_4$ than both $SC_1$ and $SC_2$.  For the 'complete' plant representation ($SC_4$), which has the largest plant volume, the magnitude of the flow disturbance is greatest.  However, for the two 'incomplete' plant representations ($SC_1$ and $SC_2$), the magnitude of flow disturbance is comparable, although the plant volume is 35% larger in $SC_2$.

*Table 6.1 Mean downstream velocities for each of the profiles shown in Figure 6.3*

| Number of scan positions | Mean downstream velocity, m s$^{-1}$ | | | |
|:---:|:---:|:---:|:---:|:---:|
| | 0.25 *X/l* | 0.30 *X/l* | 0.35 *X/l* | 0.40 *X/l* |
| $SC_1$ | 0.196 | 0.197 | 0.201 | 0.204 |
| $SC_2$ | 0.189 | 0.198 | 0.207 | 0.214 |
| $SC_4$ | 0.161 | 0.168 | 0.184 | 0.195 |

To further quantify the detail of the flow disturbance introduced by the plant blockages with increasing numbers of scan positions, the area under the curve (AUC) for each velocity profile is calculated, with results shown in Table 6.2.  The area under the curve calculates the area of the graph lying beneath a specified value, in this case the inlet velocity, and therefore a larger area is indicative of a greater flow disturbance (Figure 6.4).  At 0.25 *X/l*, the flow disturbance introduced by $SC_4$ is ~60% greater than that of the $SC_1$, and ~50% greater than that of $SC_2$.  Further downstream at 0.4 *X/l*, the flow disturbance introduced by the voxelised representation from $SC_4$ is ~25% greater than that of $SC_1$, and ~50% greater than that of $SC_2$.  For all representations, the area under the curve is reduced in the downstream direction as the separated flow recovers.  Combined with Table 6.1, these results demonstrate that the total flow disturbance is greatest for the most 'complete' plant representation ($SC_4$), which has the greatest plant volume.  For the more 'incomplete' plant representations ($SC_1$ and $SC_2$), the flow disturbance again appears comparable.
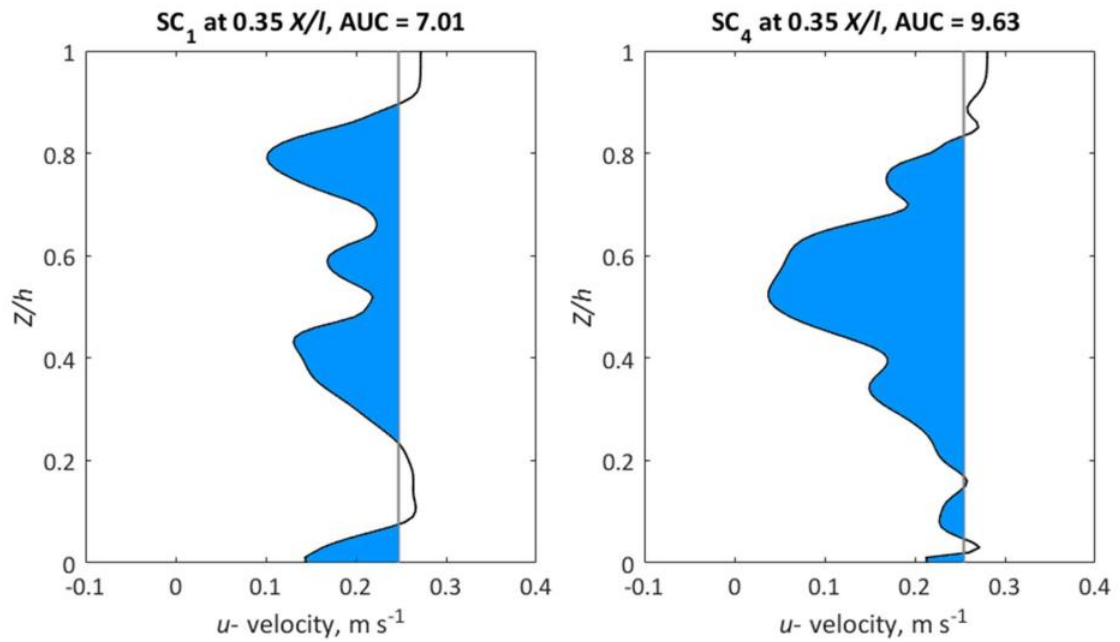
*Figure 6.4 Example of the area under the curve (AUC) for downstream velocity profiles for $SC_1$ and $SC_4$ at 0.35 X/l. The blue area represents the AUC, and falls beneath a specified value, in this case the inlet velocity (0.25 m $s^{-1}$).*

*Table 6.2 Area under the curve for each of downstream velocity profile shown in Figure 6.3*

| Number of scan positions | Area under the curve | | | |
| --- | --- | --- | --- | --- |
| | 0.25 *X/l* | 0.30 *X/l* | 0.35 *X/l* | 0.40 *X/l* |
| $SC_1$ | 7.72 | 7.51 | 7.01 | 6.67 |
| $SC_2$ | 8.22 | 7.25 | 6.33 | 5.53 |
| $SC_4$ | 12.32 | 11.44 | 9.63 | 8.29 |

This flow disturbance introduced by the different plant representations is further investigated by comparing the position of the velocity minima (Figure 6.5a), and the absolute value of the velocity minima (Figure 6.5b). Between $SC_4$ and $SC_2$, the position of the velocity minima remains relatively similar throughout, with the minima positioned between 0.5l – 0.59 *Z/h* in the range 0.25 – 0.4 *X/l*. Between $SC_4$ and $SC_1$, however, the position of the velocity minima varies more markedly, and is associated with discrete peaks in the distribution of the plant blockage outlined in Figure 6.2c. The position of velocity minima is therefore associated with the distribution of the plant blockage, especially for the most 'incomplete' blockage ($SC_1$). On average, the velocity minima for $SC_4$ is 0.055 m $s^{-1}$ lower than $SC_2$, ~20% of the normalised inlet velocity. The velocity minima for $SC_4$ is 0.079 m $s^{-1}$ lower than $SC_2$, ~30% of the normalised inlet velocity. This shows that the greatest reductions in downstream velocity are associated with the most 'complete' and volumetrically largest plant blockage ($SC_4$).
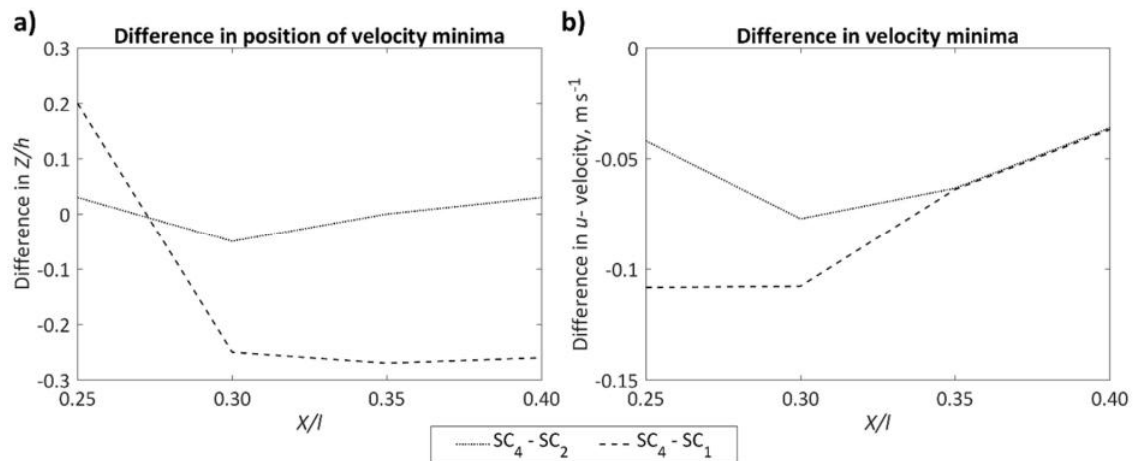
*Figure 6.5 (a) Differences in the position of the velocity minima and (b) differences in the absolute value of the velocity minima (b) with an increasing number of scan positions.*

Differences in downstream velocity profiles are further investigated by subtracting velocity profiles for $SC_1$ from $SC_4$ (Figure 6.6a) and $SC_2$ from $SC_4$ (Figure 6.6b), plotting the cumulative difference across the four downstream velocity profiles.

Between the $SC_4$ and $SC_1$, comparably little difference in downstream velocity profiles are evident in the near bed region between 0 and 0.42 $Z/h$. Above this region, however, key differences begin to emerge. Between 0.43 and 0.67 $Z/h$, where 130% more voxels are present for $SC_4$, this results in a mean velocity reduction of ~0.13 m s$^{-1}$ compared with $SC_1$ (~50% of normalised inlet velocity). Between 0.68 and 0.88 $Z/h$, only 21% more voxels are present in $SC_4$. This results in an unexpected mean velocity increase of ~0.05 m s$^{-1}$ in the region (~20% of normalised inlet velocity). This flow feature is associated with the position of the velocity minima which was previously highlighted in Figure 6.5b, and demonstrates how the distribution of the plant blockage plays an important role in the downstream velocity response.

Between $SC_4$ and $SC_2$, the cumulative differences in Figure 6.6b are similar between 0.3 and 0.8 $Z/h$, showing that the downstream velocity for $SC_4$ is consistently less than $SC_2$. In this region, 41% more voxels are present for $SC_4$, and this results in a mean velocity reduction of ~0.05 m s$^{-1}$ (~20% of normalised inlet velocity). This indicates that the magnitude of the downstream velocity varies with different levels of completeness in the plant representation.
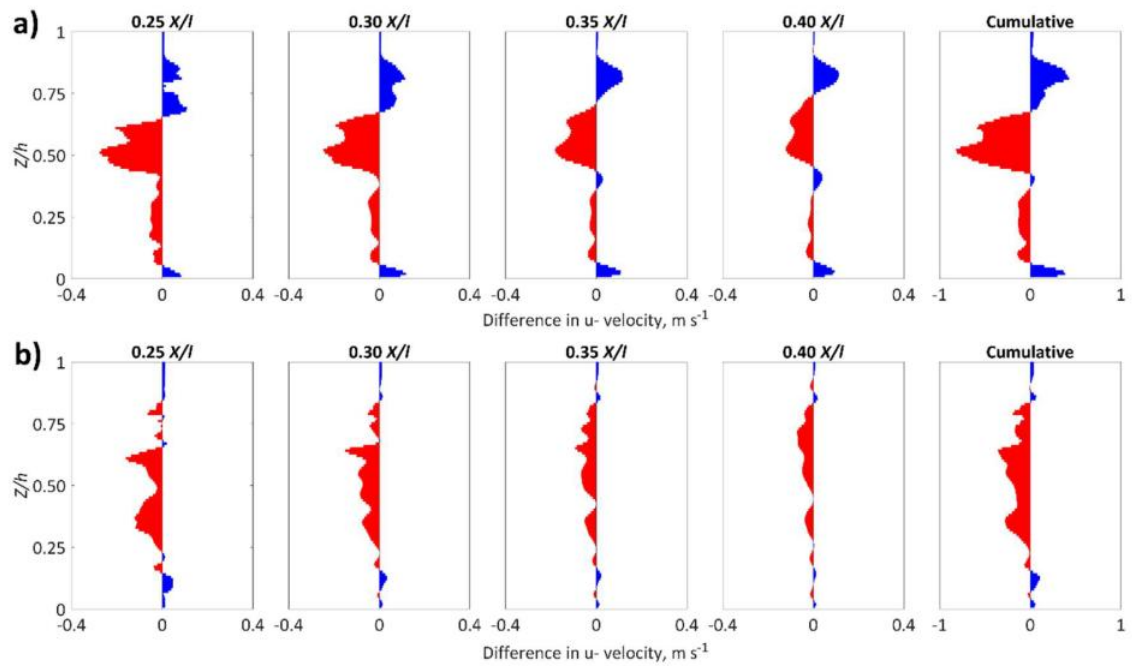
***Figure 6.6 Difference in downstream velocity, for (a) $SC_4 - SC_1$ and (b) $SC_4 - SC_2$. Blue areas indicate sections of the profile where $SC_4$ velocities exceed those of $SC_2$ or $SC_1$, whereas red areas indicate sections of the profile where $SC_4$ velocities are less than those of $SC_2$ or $SC_1$.***

To further investigate a greater extent of the downstream velocity field, rather than downstream velocity at individual profiles, three vertical slices of the downstream velocity field at 0.44, 0.50, and 0.56 $Y/w$ (right to left, Figure 6.7) are displayed. With an increasing number of scan positions, the flow disturbance introduced by the plant representation increases (Figure 6.7, a-c), with reduced velocity wake zones becoming more pronounced. For $SC_1$, isolated low velocity wakes form around collections of the plant blockage. As shown previously, these velocity minima are associated with discrete peaks in the plant blockage (Figure 6.2 and Figure 6.5), and result in relatively small disturbances to the flow field (Table 6.1 and Table 6.2). As visible gaps in the plant blockage begin to be infilled for $SC_2$ and $SC_4$, and the plant volume increases, the isolated wakes coalesce and form more pronounced zones of reduced velocity. Flow disturbance is not limited to velocity reductions, whereby Figure 6.7 demonstrates zones of faster moving fluid positioned above and beneath the voxelised plant representations. This is most clearly visible for $SC_4$ in Figure 6.7c at 0.44 and 0.56 $Y/w$.

To delineate and quantify the zones of flow disturbance (both reduced velocity and flow acceleration), the wake is defined as < 0.5 of inlet velocity, and the flow acceleration zone defined as > 1.1 of inlet velocity (Figure 6.8 and Table 6.3). With an increasing number of scan positions, both wake and flow acceleration zones increase in size. Comparing $SC_4$ and $SC_1$, the wake zone is up to ~850% larger and on average is ~350%

larger for $SC_4$. Comparing $SC_4$ and $SC_2$, the wake zone is up to ~675% larger, and on average is ~270% larger for $SC_4$. The wake zone is largest for $SC_4$ because the flow separation zone is wider, and this attributed to the increased volume of the plant blockage.

Comparing the area of the zones of flow acceleration, $SC_4$ is up to ~330% larger than $SC_1$, and on average ~260% larger. Between $SC_4$ and $SC_2$, the zone of flow acceleration is up to ~350% larger for $SC_4$, and on average ~280% larger. The flow acceleration zone associated with $SC_4$ is therefore considerably larger than $SC_1$ and $SC_2$, which are similar in size. The zone of flow acceleration for $SC_4$ extends ~110% and ~70% further downstream than $SC_2$ and $SC_1$ respectively. This differs from the wake zone which had similar lengths for all three plant representations. Analysis of the area of the wake and flow acceleration zones have revealed the zones for $SC_4$ are considerably larger than $SC_1$ and $SC_2$, which are shown to be approximately similar in size.

*Table 6.3 Area of the wake and flow acceleration zones delineated in Figure 6.8*

| | Area of wake zone (m²) | | | Area of flow acceleration zone (m²) | | |
|---|---|---|---|---|---|---|
| Number of scan positions | 0.44 Y/w | 0.5 Y/w | 0.56 Y/w | 0.44 Y/w | 0.5 Y/w | 0.56 Y/w |
| $SC_1$ | 0.026 | 0.146 | 0.149 | 0.018 | 0.014 | 0.034 |
| $SC_2$ | 0.201 | 0.169 | 0.032 | 0.019 | 0.015 | 0.026 |
| $SC_4$ | 0.252 | 0.335 | 0.249 | 0.078 | 0.042 | 0.118 |

### 6.2.2.1 Recommendations for the number of scan positions used to capture plant volumetric canopy morphology

This section has highlighted the sensitivity to the number of scan positions used to capture the plant volumetric canopy morphology, demonstrating the control on flow field dynamics. With an increasing number of scan positions, e.g. $SC_4$, the 'completeness' and volume of the plant representation increases, thereby providing an adequate representation of plant volumetric canopy morphology. This contrasts with $SC_1$ and $SC_2$, whereby the effects of occlusion result in an 'incomplete' plant representation. Such 'incomplete' plant representations under-represent the plant volume, and omit key parts of the plant morphology that influence flow field dynamics. These under-predict the flow disturbance introduced by the plant. It is therefore recommended that when using TLS to capture plant volumetric canopy morphology for the purposes of modelling flow-vegetation interactions at a high resolution, four scan positions are necessary.
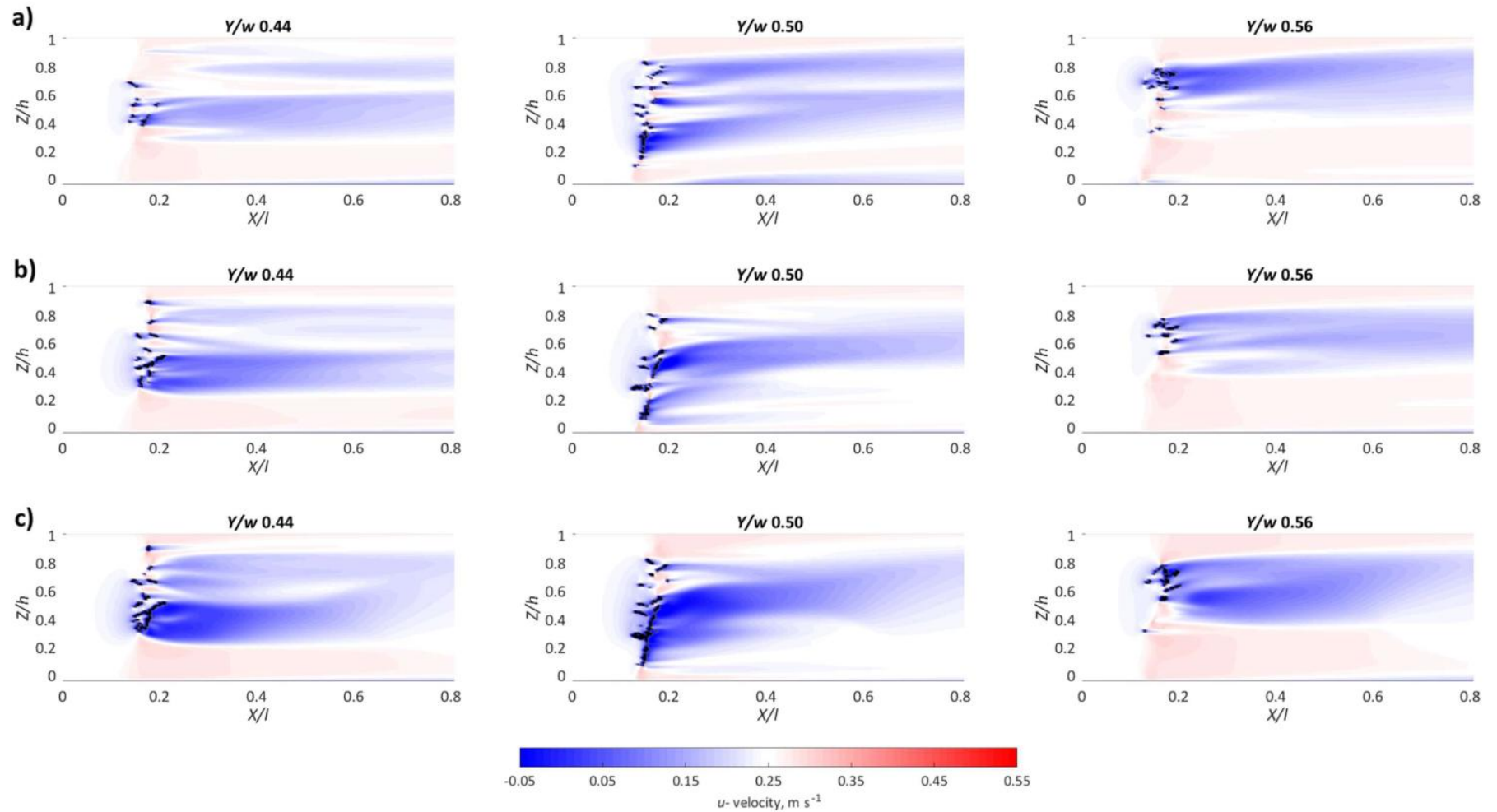
*Figure 6.7 Downstream (u-) velocity field around the Prunus laurocerasus plant the for: (a) SC₁, (b) SC₂, and (c) SC₄. Slices at 0.44, 0.50, and 0.56 Y/w are presented, where black areas indicate the streamwise position of the plant.*
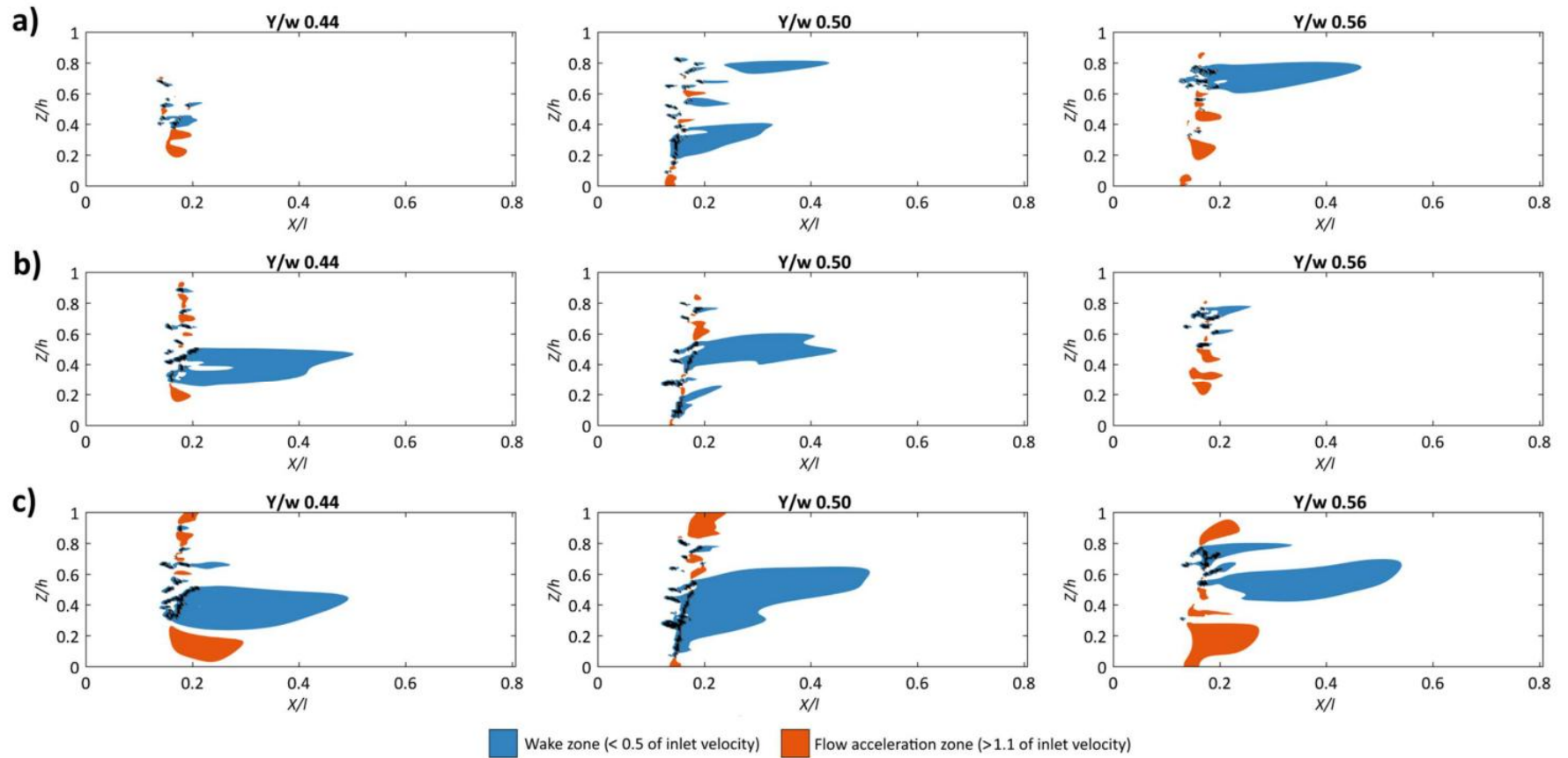
*Figure 6.8 Delineated wake and flow acceleration zones around the Prunus laurocerasus plant for: (a) SC₁ , (b) SC₂, and (c) SC₄. Slices at 0.44, 0.50, and 0.56 Y/w are presented, where black areas indicate the streamwise position of the plant.*

## 6.3       The influence of foliage on flow field dynamics

In this section, the influence of foliage on flow field dynamics for the *Prunus laurocerasus* plant is modelled and quantified. As shown in Section 3.3, scans were captured for defoliated and foliated plants, following the manual removal of leaves (n = 432). These characteristic subsections of the plant (Figure 6.1) are then incorporated into the numerical model. Following the recommendations outlined in Section 6.2, the plant was scanned from four opposing scan positions, and voxelised to a 0.01 m voxel size. The voxelised blockage was incorporated 0.5 m downstream from the inlet (0.14 $X/l$), and centred (0.5 $Y/w$). As before, inlet velocity was held constant at 0.25 m s$^{-1}$, and turbulence intensity set to 5%. Flow conditions are fully turbulent and subcritical.

### 6.3.1       Downstream velocity field

First the downstream velocity field for the defoliated and foliated plants in plan view at 0.4 and 0.6 $Z/h$ are described. When defoliated (Figure 6.9a), individual branches introduce flow separation and reattachment with the formation of narrow wakes of reduced velocity. At 0.4 $Z/h$, coalescence of these wakes is observed. However, this behaviour varies vertically, and at 0.6 $Z/h$, where the branches are spaced further apart, wakes behave independently. Wake coalescence therefore depends on the separation distance between individual branches. When foliated (Figure 6.9b), a single, more pronounced zone of flow separation and reattachment is evident, which is indicative of behaviour by a bluff-style object (Simpson, 1989).

For the foliated plant, the shape of the wake varies over the vertical extent of the plant; a function of the plant volumetric canopy morphology, and more specifically the distribution of the plant blockage, which results in flow asymmetry. For example, at 0.4 $Z/h$ the abundance of leaves at lower $Y/w$ values produce an asymmetrical wake structure that extends further downstream than the corresponding wake when the plant is defoliated. For both the defoliated and foliated plants, similarities can be observed; namely the reduction in downstream velocity immediately upstream of the blockage, with marginal flow acceleration around the blockage edges. Such patterns are indicative of flow in a junction vortex system (Simpson, 2001), although further quantification and evaluation of the turbulent flow structures are needed (Chapter 7).

The wake shape is further illustrated through a vertical slice down the midline (0.5 *Y/w*) (Figure 6.9c and Figure 6.9d). In both cases, wake shape varies considerably with *Z/h*. For the defoliated plant, development of a wake zone at 0.2-0.4 *Z/h* corresponds with the main branching point of the plant (see Figure 3.26), with a concentration of branches. Marginal flow acceleration is evident around the outer edge of the central branch. A more complex wake structure consisting of two discrete layers is shown for the foliated plant. Again, the lower wake corresponds with the branching point at 0.2-0.4 *Z/h*. Above this, a pronounced and thicker wake zone at 0.45-0.65 *Z/h* corresponds with the leaf body, extending further downstream than the lower wake beneath. The dense foliage component of the plant is therefore influential in producing a highly localised velocity response.
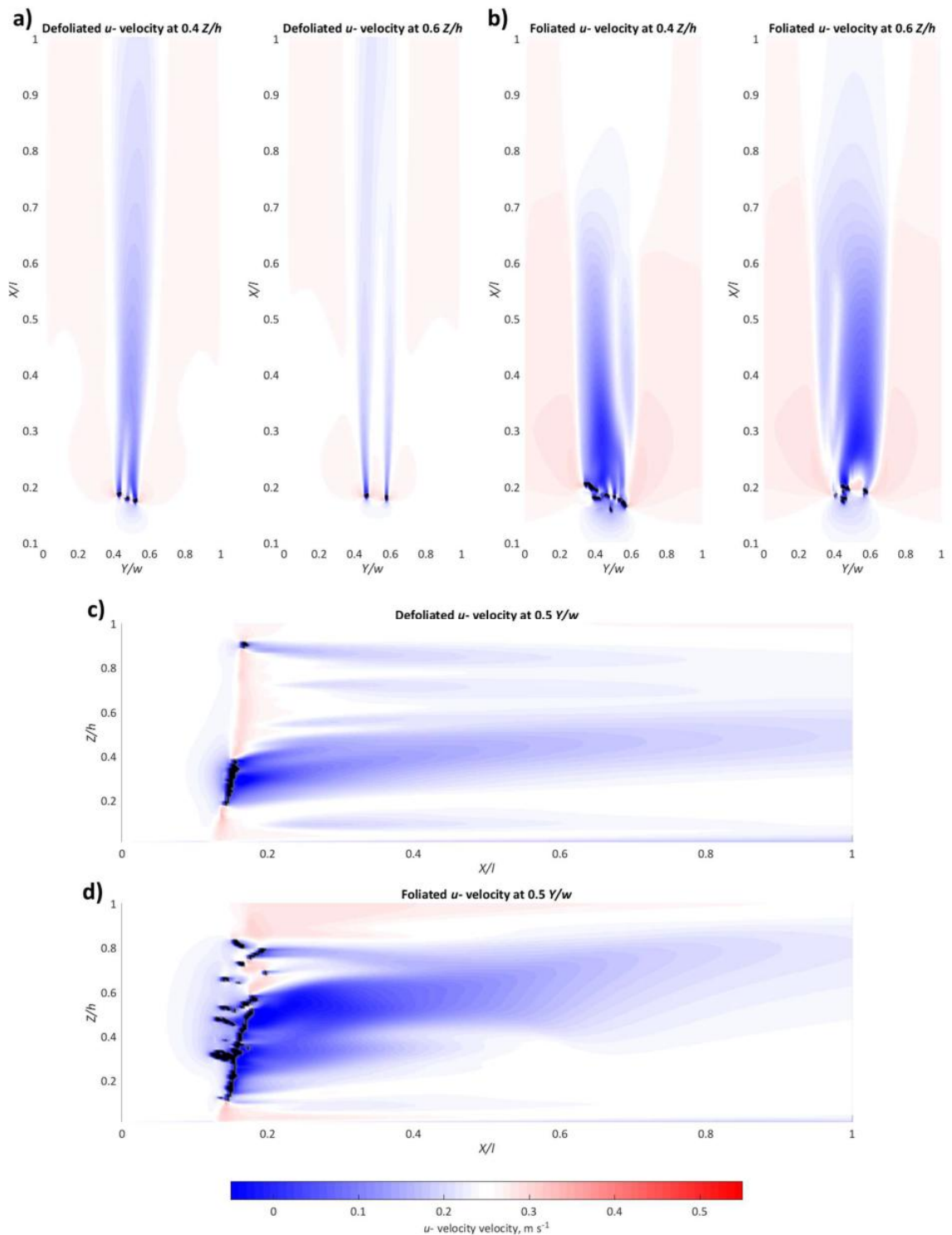
**Figure 6.9 Comparison of downstream velocity field data for the defoliated and foliated Prunus laurocerasus plants. (a) Defoliated slices at 0.4 and 0.6 Z/h where individual wakes can coalesce or act independently from one another, based on the separation distance of individual branches. (b) Foliated slices at slices at 0.4 and 0.6 Z/h showing a single more pronounced zone of flow separation and reattachment, indicative of behaviour by a bluff body object.   (c) Defoliated vertical slice at 0.5 Y/w, showing that the wake zone at 0.2-0.4 Z/h is associated with the main branching point.  (d) Foliated vertical slice at the 0.5 Y/w, shows two discrete wakes (lower wake associated with the main branching point, upper wake at 0.45-0.65 Z/h is more pronounced and corresponds with the bulk of the leafy blockage.**

The complexity of the plant volumetric canopy morphology introduces flow heterogeneity, and therefore velocity profiles begin to deviate from the idealised inflected (or S-shaped) profiles that are associated with canopy flows (Figure 6.10, inset graph). Figure 6.10 shows three distinct velocity zones in the vertical dimension, namely: a zone of relative flow acceleration beneath the bulk of the plant in the near bed region (sub-canopy flow), a zone of flow acceleration above the plant in the free-stream zone, and between these a low velocity zone associated with flow deceleration around the plant blockage. The shape of the vertical velocity profiles clearly differs between the defoliated and foliated plants. When defoliated, the velocity minima is positioned lower in the flow depth, and associated with the point at which the main branch splits into sub-branches. When foliated, however, the velocity minima is positioned higher in the flow depth, and associated with the main leaf body. The magnitude and size of the low velocity zone for the foliated plant is greater than the defoliated plant, showing the important role of the leaf body in modifying the local flow field dynamics.
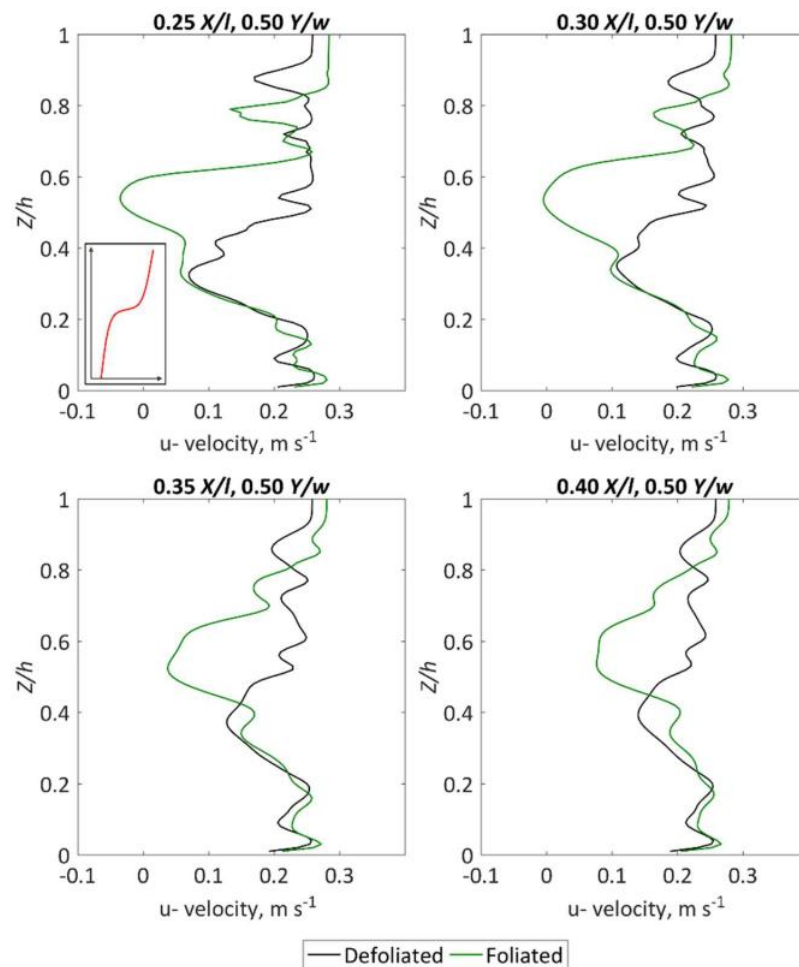


***Figure 6.10** Downstream velocity profiles extracted from the midline (0.5 Y/w) at increasing distances downstream: 0.25, X/l, 0.30 X/l, 0.35 X/l, and 0.40 X/l. The inset graph in illustrates an idealised inflected velocity profile often used to characterise vegetated flows. The velocity profiles illustrate the complex vertical structure in the wake of the flow.*

For the defoliated and foliated plants, sub-canopy flow appears to be similarly sized and shaped, indicating that the distance between the bed and the base of the plant blockage influences the characteristics of this zone. More attention is paid to the sub-canopy flow in the following sections. Overall, it is shown that for the defoliated and foliated plants the plant volumetric canopy morphology, specifically the distribution of the plant blockage, results in a complex downstream velocity field, with spatially heterogeneous velocity profiles. The velocity profiles have greater heterogeneity than the inflected, or S-shaped, profiles that are often used to describe and characterise flows through vegetation.

## 6.3.2 Wake and flow acceleration zones

Following delineation of the wake zone as < 0.5 of inlet velocity, and the flow acceleration zone as > 1.1 of inlet velocity, the spatial extent of these zones are quantified (Figure 6.11). The defoliated wake zone has a volume of 0.023 $m^3$, compared to the foliated wake zone of 0.093 $m^3$, a volume over four times greater. This difference in wake volume is attributed to the additional plant volume introduced by the foliage. In Section 3.4, the total plant volume for the foliated plant was shown to be approximately four times greater than the defoliated plant, and therefore an association between the total volume of the plant blockage, and the volume of the wake zone is evident.

The wake zone extends up to 0.73 m downstream for the defoliated plant, and almost twice as far when the plant is foliated (up to 1.38 m). However, when normalised against the defoliated and foliated plant length, the maximum extent of the wake extends a similar distance of ~4.4 and ~4.8 plant lengths respectively. Plant length is here defined as the maximum length of the plant in the downstream direction. For the defoliated and foliated plants, the wake is inclined slightly upwards, and thins in the downstream direction. The width of the wake is constrained by the plant width, and therefore does not extend beyond the outer limit of the plant. Plant width is here defined as the maximum width of the plant in the cross-stream direction.

For the zone of flow acceleration, the volume for the foliated plant is over an order of magnitude greater than the defoliated plant (0.003 $m^3$ when defoliated, 0.061 $m^3$ when foliated). The zone extends only ~1 plant length when defoliated, but ~2 plant lengths when foliated. More pronounced flow acceleration is therefore observed when the plant

is foliated. Combined, the volumetrically larger wake and flow acceleration zones associated with the foliated plant blockage indicate a more marked flow disturbance.
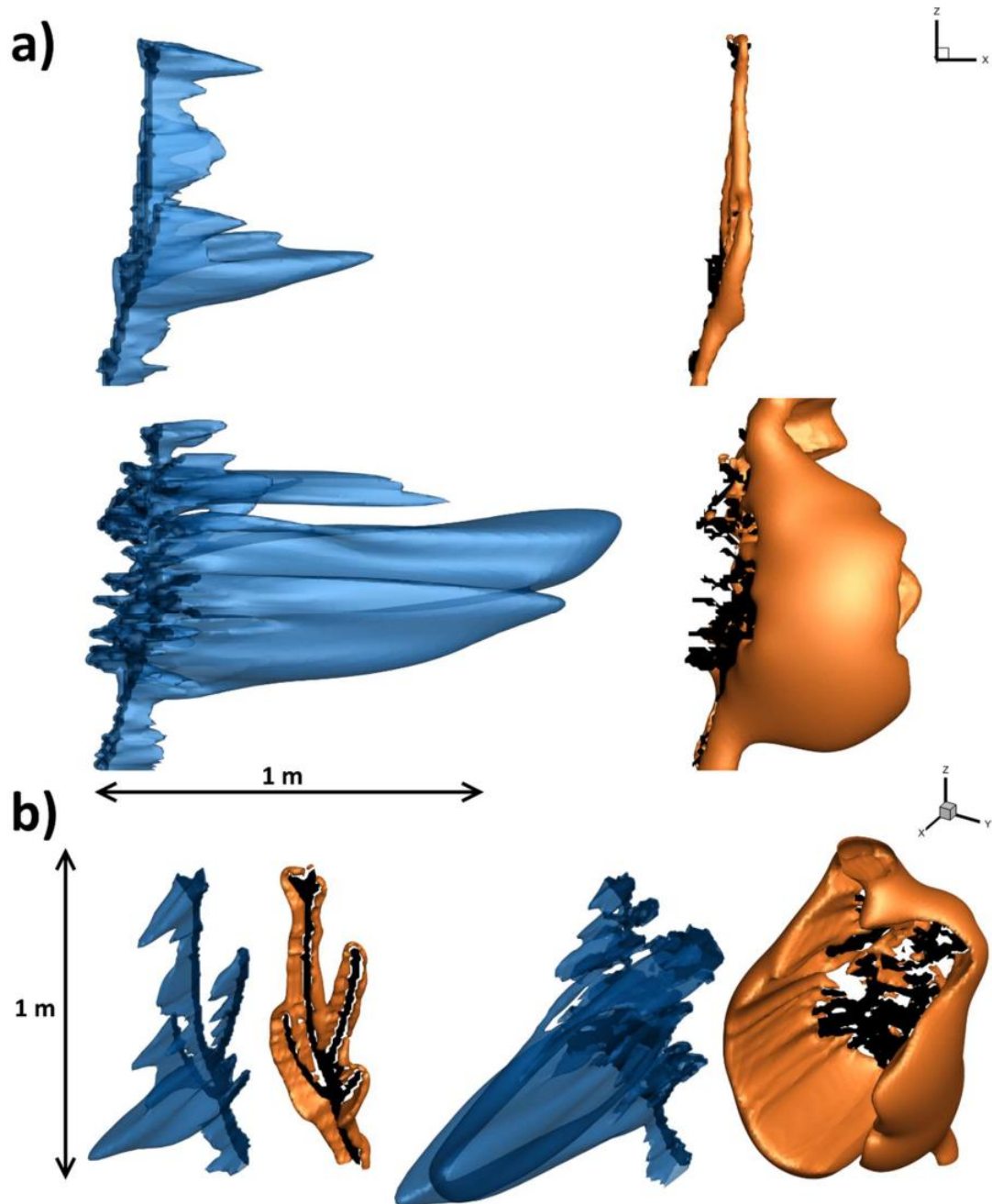


***Figure 6.11 Three-dimensional extent of the wake (< 0.5 of inlet velocity, blue) and flow acceleration (> 1.1 of inlet velocity, orange) zones shown from 2 different perspectives (a-b), note different scale in (a) and (b).***

### 6.3.3 Streamlines

Three-dimensional streamlines for the downstream, $u$-, spanwise, $v$-, and vertical, $w$-, components of the velocity field are used to further investigate differences in the spatial

heterogeneity of the flow field for the defoliated and foliated plants. Figure 6.12 demonstrates the complexity of the streamlines at 0.5 *Y/w* for both plants, as the flow clearly interacts with the plant blockages. For the defoliated plant, a small region of negative *w*- velocity is observed immediately upstream of the plant blockage, indicating a downwards forcing of flow towards the sub-canopy region. For the foliated plant, this upstream region of negative *w*- velocity is larger, with values of a greater magnitude, indicating a more pronounced forcing of flow towards the sub-canopy region. As flow is forced through gaps and conduits in the plant blockage, isolated pockets of high-magnitude *w*- velocity ($\pm$ ~0.08 m s$^{-1}$) are shown, and these are present for both the defoliated and foliated plants. However, these are more numerous when the plant is foliated, associated with individual clusters of vegetal elements in the plant body, responsible for a vertical forcing of flow. This forcing of flow is reflected by the zones of flow acceleration through the plant blockage as shown in Figure 6.11b. Although wake patterns resembled a bluff body object (Figure 6.9a), the plant is not a fully impermeable blockage. Instead, flow is forced through the gaps and conduits in the plant body, therefore resembling a porous bluff body object. This will have implications for whether flow follows a simple junction vortex system (Simpson, 1989).

Immediately behind the plant blockages, the differences become even more marked. For the defoliated plant, a small region of streamline recirculation is noted behind the main branching point (centred ~0.25 *Z/h*), which previously has been shown to correspond with the low velocity wake zone (Figure 6.11a). For the foliated plant, a larger recirculation zone is positioned higher in the flow depth (centred ~0.5 *Z/h*), corresponding with the low velocity wake zone associated with the bulk of the leaf body (Figure 6.11a). The recirculation zone causes pronounced deflections to the streamlines downstream.

Positive *w*- velocities are recorded in the plant wake region for both the defoliated and foliation plants, associated with the upwards deflection of streamlines, and interaction with the sub-canopy region. This corresponds with the inclined upward wake identified in Figure 6.9a and Figure 6.9b. As before, the zone is larger for the foliated plant, with *w*- velocities having a greater magnitude. For the foliated plant, a further region of negative *w*- velocity is identified in the region behind the top of the plant (centred ~0.8 *Z/h*). Here, the downwards deflection of streamlines is associated with flow over the top of the plant, and is not replicated by the defoliated plant. More complex streamlines are associated with the foliated plant, resulting from the downwards deflection at the plant

top, the marked recirculation around the foliated body, and the upwards deflection from the sub-canopy region; this means that streamlines converge and straighten at ~0.65 $Z/h$, demonstrating the interaction of these complex zones.
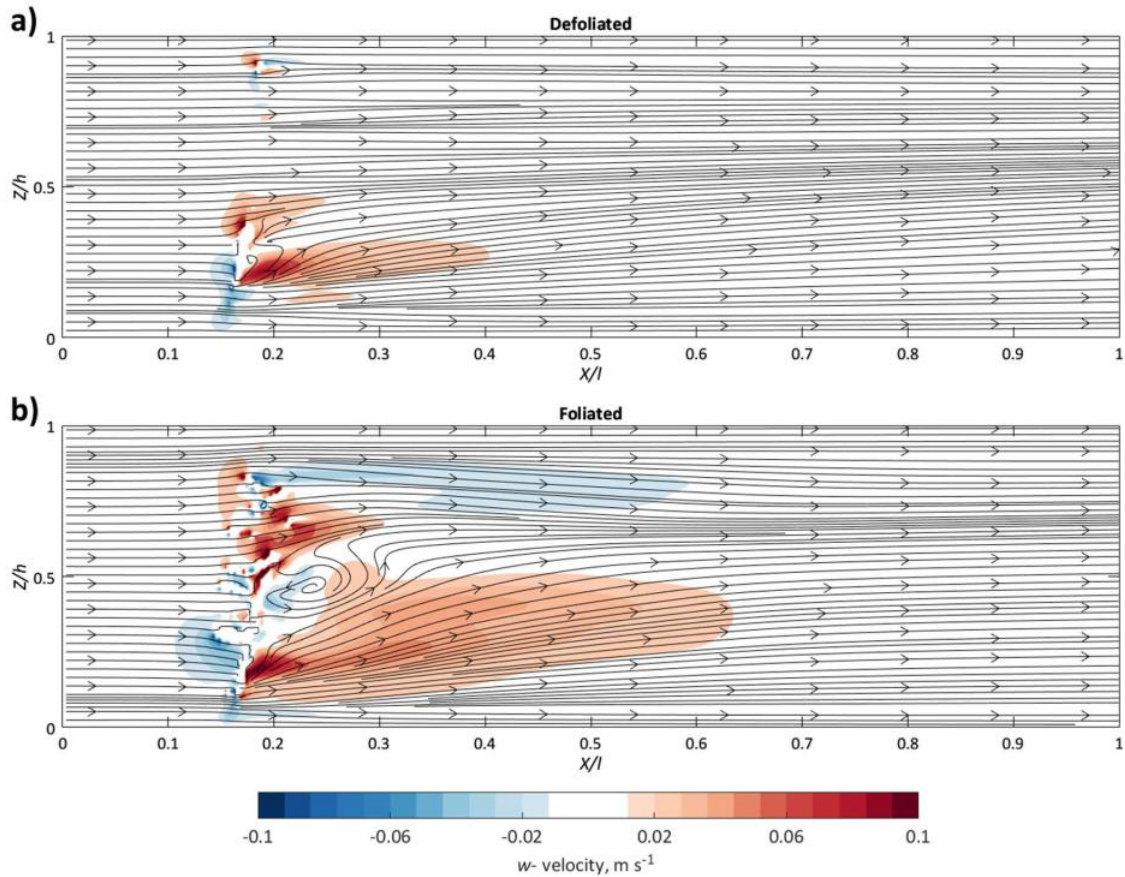


**Figure 6.12 Streamlines equally spaced at 0.035 Z/h intervals, overlain on top of the w- component of velocity for: (a) defoliated and (b) foliated (b) plants at 0.5 Y/w.**

Figure 6.13 shows a plan view of the three-dimensional streamlines at 0.5 Y/w, over the entire flow depth. Similarities and differences in streamlines between the defoliated and foliated plants are shown. For both plants, the lateral deflection does not extend beyond the outer-edge of the plant blockage, as indicated by the dashed lines in Figure 6.13, and therefore the width of deflection is approximately constrained by the width of the plant. This corresponds with the wake width, which as constrained by the plant width (Section 6.3.2). For the defoliated plant, streamlines tend to be deflected to the right of the blockage, further indicating flow asymmetry, and the maximum range of deflection is 0.17 $Y/w$. For the foliated plant, streamlines are deflected over a greater lateral range (0.24 $Y/w$), and this disturbance is introduced more proximal to the blockage, especially around the zone of flow recirculation. As flow is forced through the plant blockage, it immediately spreads laterally resulting in more complex streamlines for the foliated plant.
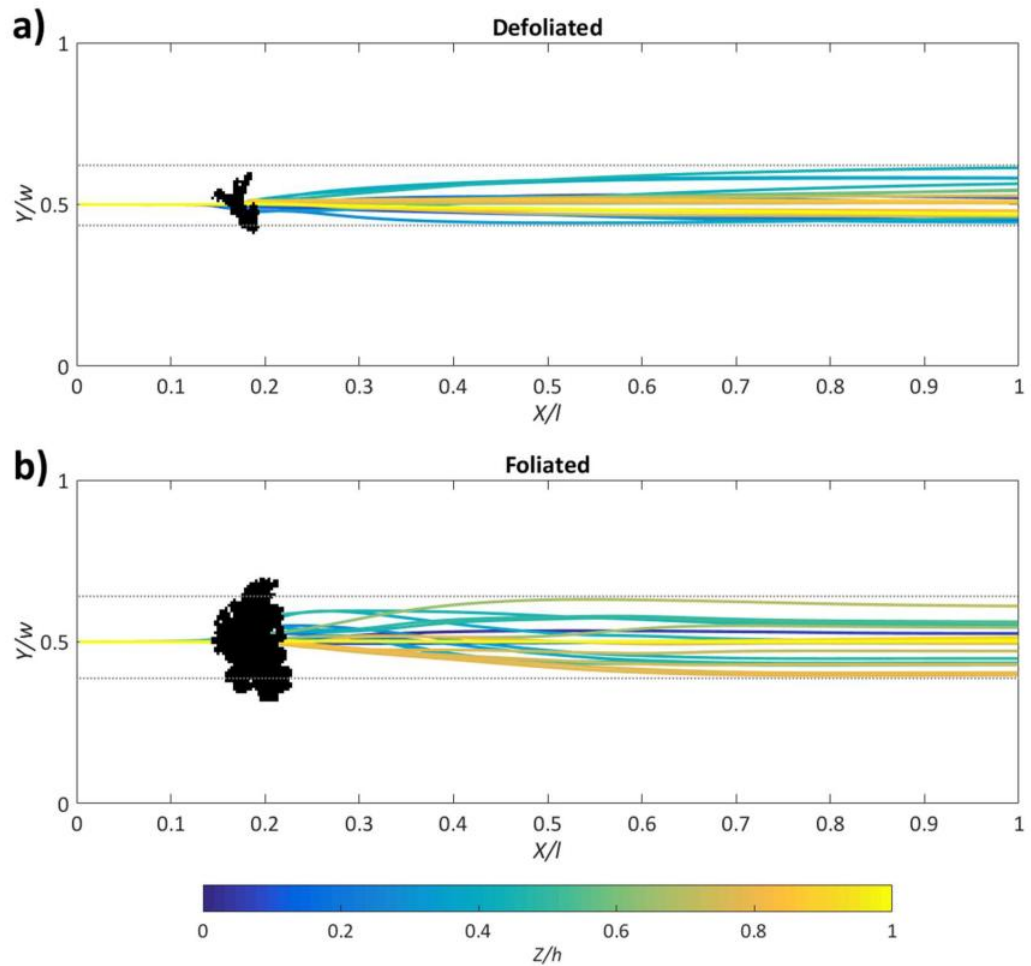
**Figure 6.13 Streamlines with starting points specified at 0.5 Y/w, in the range 0 – 1 Z/h at regular intervals of 0.05 Z/h. Streamlines are coloured by Z/h. A plan view of the (a) defoliated and (b) foliated plants are shown. Dashed lines indicate maximum lateral extent of deflections.**

The complexity of streamlines in the flow recirculation zone behind the foliated plant are further investigated in Figure 6.14 and Figure 6.15. By focusing on streamlines originating from within the foliated body, more detail of the deflections to streamlines are visualised. Figure 6.14 clearly demonstrates significant streamline deflections proximal to the foliated plant blockage, and that this deflection is limited to the immediate downstream vicinity of the plant (before 0.5 *X/l*).

To further illustrate the magnitude of these deflections, Figure 6.15 more clearly demonstrates streamline deflections through the recirculation zone from a different perspective. The convoluted and looping streamlines are significantly deflected both laterally and vertically. With streamlines originating from a very focused zone (0.1 *Y/w*, 0.03 *Z/h*), at 0.5 *X/l* the streamlines are deflected to cover a much greater zone (0.28 Y/w, 0.35 *Z/h*). The foliated body therefore has a major influence on the deflection of

three-dimensional streamlines in the immediate vicinity of the plant, thereby controlling flow pathways through the porous blockage.
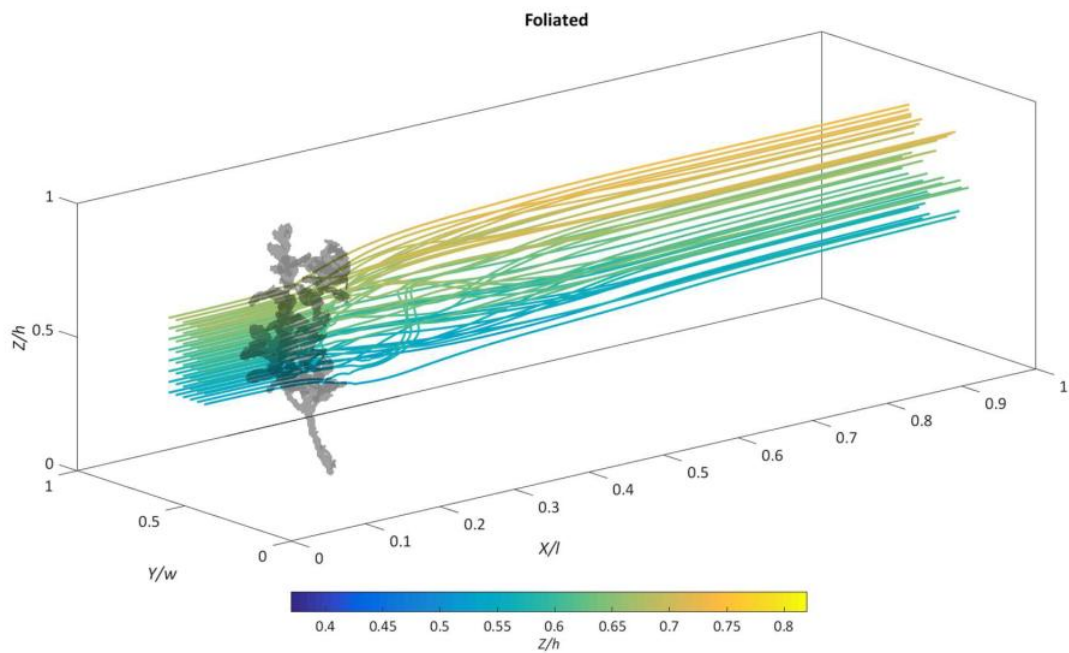


**Figure 6.14 Streamlines with specified starting points in the range 0.42 – 0.58 Y/w, 0.40 – 0.70 Z/h, having equal spacing of 0.04 Z/h.  Streamlines are coloured by Z/h, although the scale differs from Figure 6.13.  A three-dimensional view for the foliated plant is shown.**
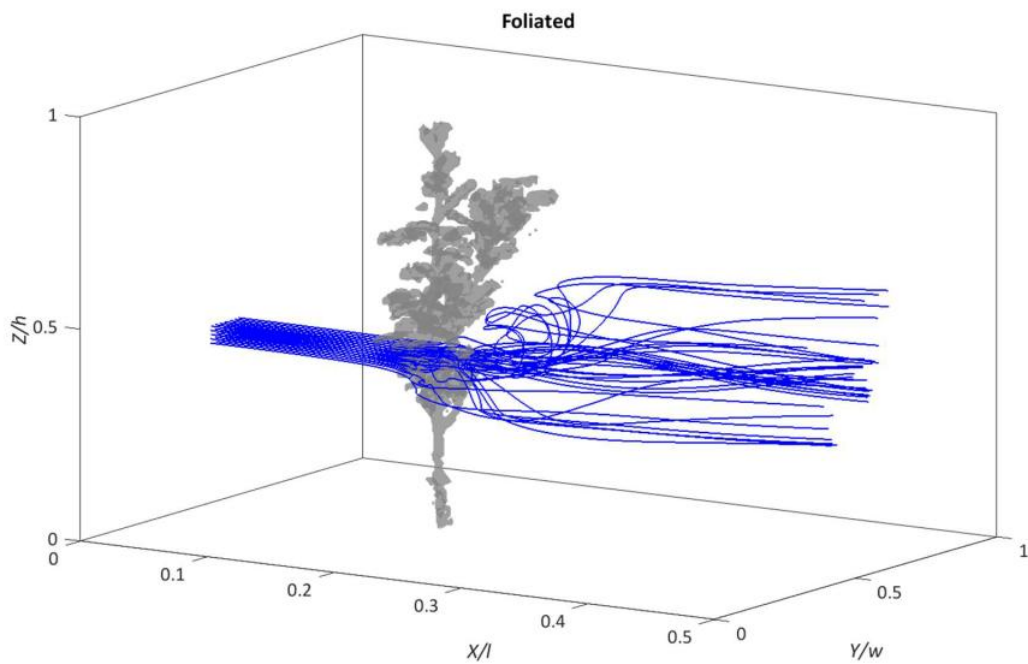


**Figure 6.15 Streamlines with specified starting points in the more focused range 0.45 – 0.55 Y/w, 0.32 – 0.35 Z/h, with a three-dimensional view of the foliated plant.  All streamlines same colour to help identify the zone of recirculation.**

## 6.3.4      **Turbulent flow structures**

To further investigate the role of foliage, the structure of turbulent vortices associated with the defoliated and foliated plants are compared. This involves looking at the stable, Reynolds-averaged regions of vorticity. For the whole domain, the mean vorticity magnitude for the defoliated plant is 0.35 Hz, and for the foliated plant is ~40% higher at 0.48 Hz. The maximum vorticity magnitude is 36.3 Hz for the defoliated plant, and for the foliated plant is ~30% higher at 46.3 Hz. The standard deviation of the vorticity magnitude for the foliated plant is also ~30% greater than the defoliated plant (0.97 Hz when defoliated, 1.25 Hz when foliated). Overall, therefore, vorticity is greater for the foliated plant.

As well as these absolute differences, it is hypothesised that the spatial patterns of vorticity will differ between the defoliated and foliated plants because of the effects of foliage. As noted in Section 5.6, however, the vorticity field alone is unable to distinguish between vortices and the strain field (Cucitore *et al.*, 1999). Again, analysis is therefore extended to identify vortices using the Q criterion (Hunt *et al.*, 1988).

First, the vertical distribution of uw- vorticity in planes at 0.4, 0.5, and 0.6 Y/w are shown in Figure 6.16 with two-dimensional *uw-* flowlines overlain. This provides an understanding of the magnitude and spatial distribution of vorticity in the flow field, and provides an impression of vorticity about the horizontal axis. For the defoliated plant, vorticity regions at the outer extent of the plant (0.4 and 0.6 *Y/w*) are negligible, with only very minor disturbance to the flowlines. This contrasts with the foliated plant, where owing to the distribution of clusters of leaf elements, a larger region of both positive and negative *uw-* vorticity is present. Towards the top of the foliated plant body, positive vorticity values dominate. The positive vorticity region appears spatially coherent in the downstream direction. On the underside of the plant, a region of negative vorticity with a similar magnitude is found, although these appear more spatially discontinuous. Flowlines associated with the foliated plant are visibly more disturbed than for the defoliated plant at 0.4 and 0.6 *Y/w*.

Focusing on 0.5 Y/w, at the plant midline the regions of vorticity between the defoliated and foliated plants are more similar in shape, extending approximately 0.75 m downstream. This is equivalent to ~4.5 plant lengths when defoliated, and ~2.5 plant lengths when foliated. A complex region of positive and negative vorticity is found in

the zone between the top and bottom of the plant blockage. Again, flowlines are disturbed, especially for the foliated plant, with flowlines initially deflected downwards towards the bed immediately behind the plant, before this is reversed towards the surface at the distal end of the wake region. For each plane shown in Figure 6.16, *uw*-vorticity regions are approximately twice as thick for the foliated plant. A greater component of *uw*- vorticity is therefore introduced by the foliated plant, associated with the presence of the leaf body.

The horizontal distribution of uv- vorticity for planes at 0.25, 0.50, and 0.75 Z/h are shown in Figure 6.17, with two-dimensional *uv*- flowlines overlain. This provides an impression of vorticity about the vertical axis. At 0.25 *Z/h*, zones of high vorticity of a similar magnitude and length are present about the defoliated and foliated plants. The *uv*- vorticity response therefore appears similar in the near-bed region.

Differences emerge at 0.5 *Z/h* where for the defoliated plant, counter-rotating regions of *uv*- vorticity are present proximal to one another around individual branches. The maximum extent of the region of high *uv*- vorticity is ~1.05 m downstream, equivalent to ~6.2 plant lengths. For the foliated plant, counter-rotating regions of high vorticity are present on the outer edges of the foliated body, separated by a region of *uv*- vorticity with lower magnitude values, where a large extent of flowline disturbance is seen. The maximum extent of *uv*- vorticity is ~50% further downstream for the foliated plant than the corresponding region for the defoliated plant, and twice as wide as the region associated with the defoliated plant. At 0.75 *Z/h*, smaller counter-rotating regions of *uv*-vorticity are present around the single branch for the defoliated plant. Where the blockage is greater in the foliated state due to the presence of leaf elements, a larger zone of *uv*- vorticity extends more than double the distance downstream (~1.45 m, or ~5 plant lengths). As such, beyond the main branching point of the plant, marked differences in the structure of regions of high vorticity emerge due to the presence of the foliated body.
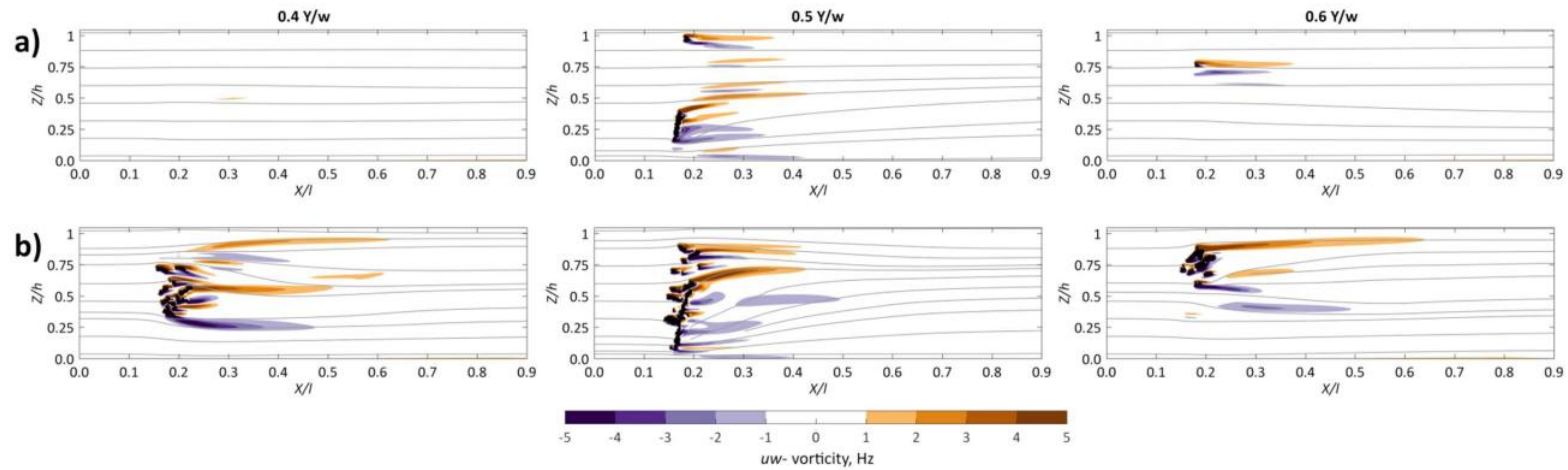
**Figure 6.16** *Distribution of uw-vorticity along horizontal planes at 0.40, 0.50, and 0.60 Y/w. Two-dimensional uw- flowlines overlain with an equal spacing at 0.1 Z/h. (a) Defoliated and (b) foliated.*
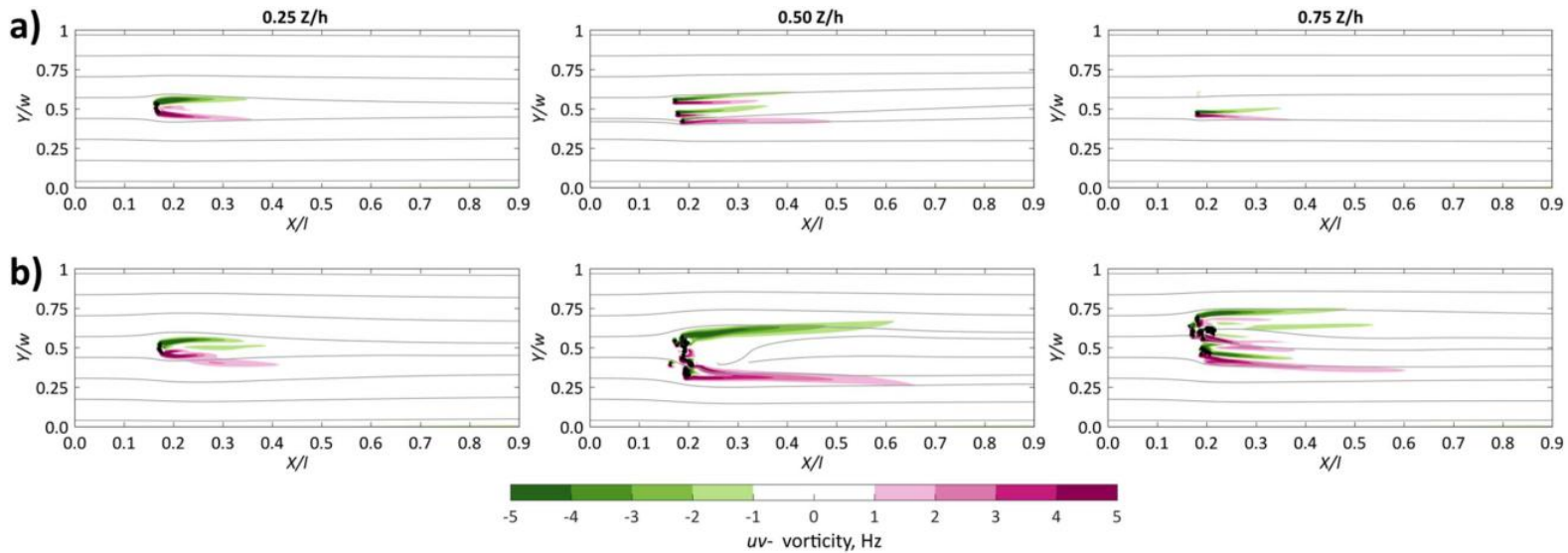


**Figure 6.17** *Distribution of uv- vorticity along vertical planes at 0.25, 0.50, and 0.75 Z/h.  Two-dimensional uv- flowlines overlain with an equal spacing of 0.125 Y/w.  (a) Defoliated and (b) foliated.*

Finally, an impression of the three-dimensional turbulent flow structures forming around each of the plants is visualised by plotting isosurfaces of the Q criterion (Hunt *et al.*, 1988) (Figure 6.18). As in Section 5.6, the Q criterion was thresholded at 3.5, with the Q criterion better able to distinguish individual vortices than the vorticity field alone.

Beneath the main branching point of the plant, turbulent flow structures are similar in length and magnitude. Differences begin to emerge above this region, where although the maximum length of the flow structure remain similar (foliated extends only 20% further downstream than defoliated), the structures are much more densely packed behind the foliated plant. For both the defoliated and foliated plants, several scales of turbulence are present, and therefore the turbulent flow structures are complex and highly three-dimensional. The total volume of detected vortices for the foliated plant ($0.079$ m$^3$) is approximately three times that of the defoliated plant ($0.026$ m$^3$). This volumetric difference is attributed to lengthening, widening, and thickening of vortices that were previously noted (Figure 6.16 and Figure 6.17), associated with the volumetrically larger plant blockage when foliage is present.
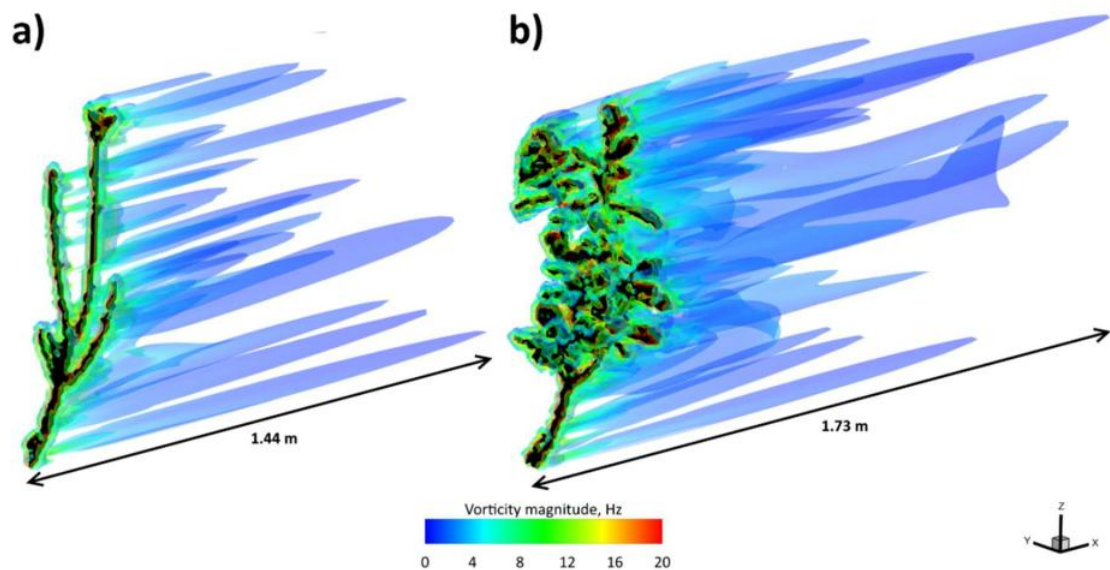


*Figure 6.18 Comparison of the three-dimensional structure of turbulence using the Q criterion, mapping Q values thresholded at 3.5, with the isosurface coloured by vorticity magnitude.*

## 6.3.5 Turbulent kinetic energy (TKE)

At the wake scale, mean kinetic energy is converted into wake-generated turbulent kinetic energy at the scale of the plant stems (Ghisalberti and Nepf, 2002) and therefore analysis of the turbulent kinetic energy (TKE) provides an estimation of the amount of

form drag introduced by the plant (Raupach and Shaw, 1982). Direct comparisons between the defoliated and foliated plants are shown at 0.45 *Z/h* (Figure 6.19). In both cases, zones of high TKE (> 0.04 $m^2$ $s^2$) are observed proximal to the outer edge of the plant, driven by the forcing of flow around the blockage, previously quantified as the zone of flow acceleration (> 1.1 of normalised velocity, Figure 6.11). For the defoliated plant, these high TKE zones are enclosed around individual branches, whereas for the foliated plant, the zone is comparably larger and extends a greater distance downstream from the plant front. Because of the complex, interacting nature of the wakes in the defoliated state, the leeward zone of low TKE (< 0.015 $m^2$ $s^2$) is more fragmented and extends a greater distance downstream than in the foliated state. The larger zone of high TKE therefore indicates a greater form drag contribution from the foliated plant.
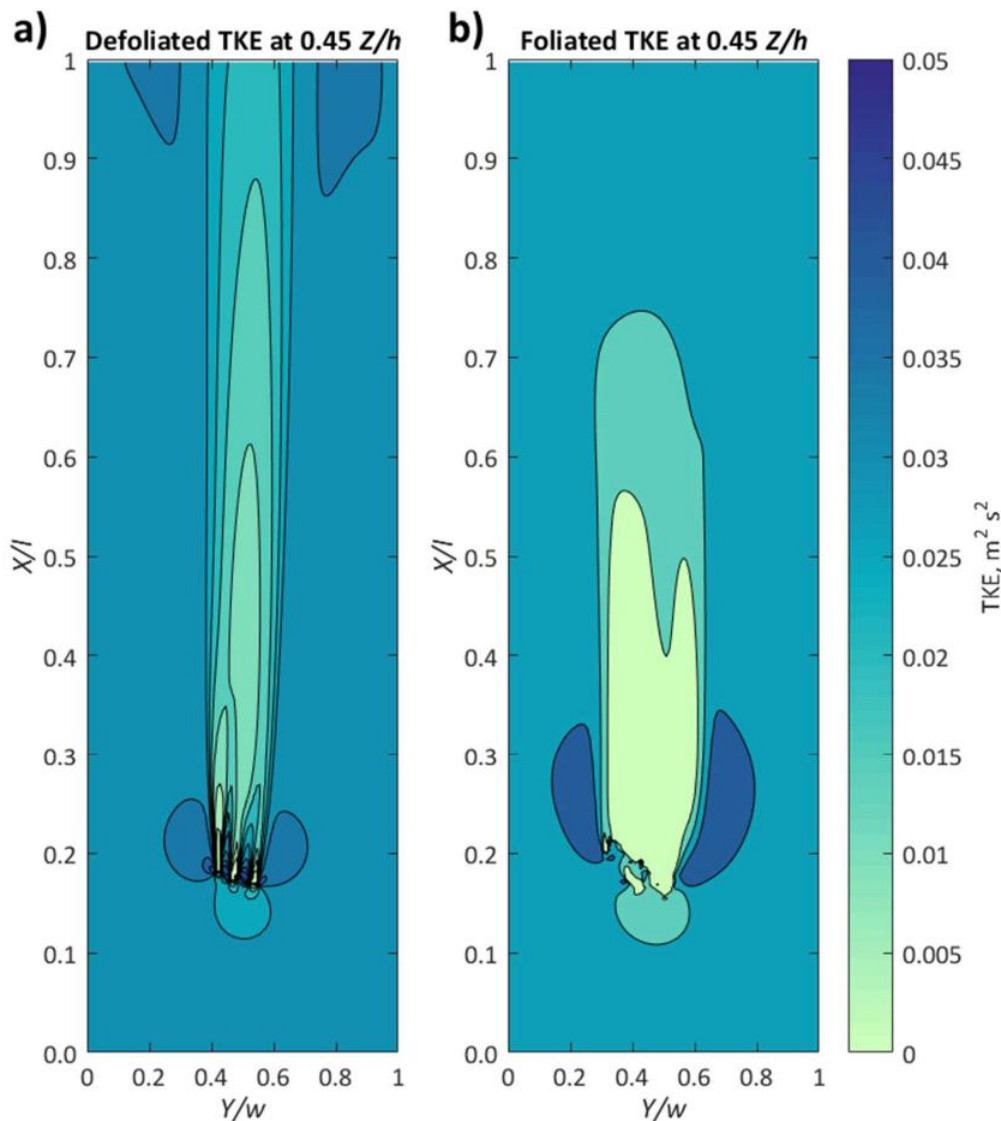


**Figure 6.19 Turbulent kinetic energy (TKE) field for the (a) defoliated and (b) foliated plants at 0.45 Z/h.**

The downstream relationship of TKE is further highlighted in Figure 6.20, by taking incremental vertical slices immediately downstream of the plant blockage at 0.30, 0.45, 0.60, and 0.75 $X/l$. With distance downstream, the zones of highest TKE proximal to the plant blockages diminish in size, and again are shown to be larger for the foliated plant. The vertical slices confirm the fragmentary nature of the low TKE zone around individual branches for the defoliated plant. For the foliated plant, a single low TKE zone around the foliated body persists. Again, the larger zone of high TKE around the foliated plant is indicative of a greater form drag contribution.
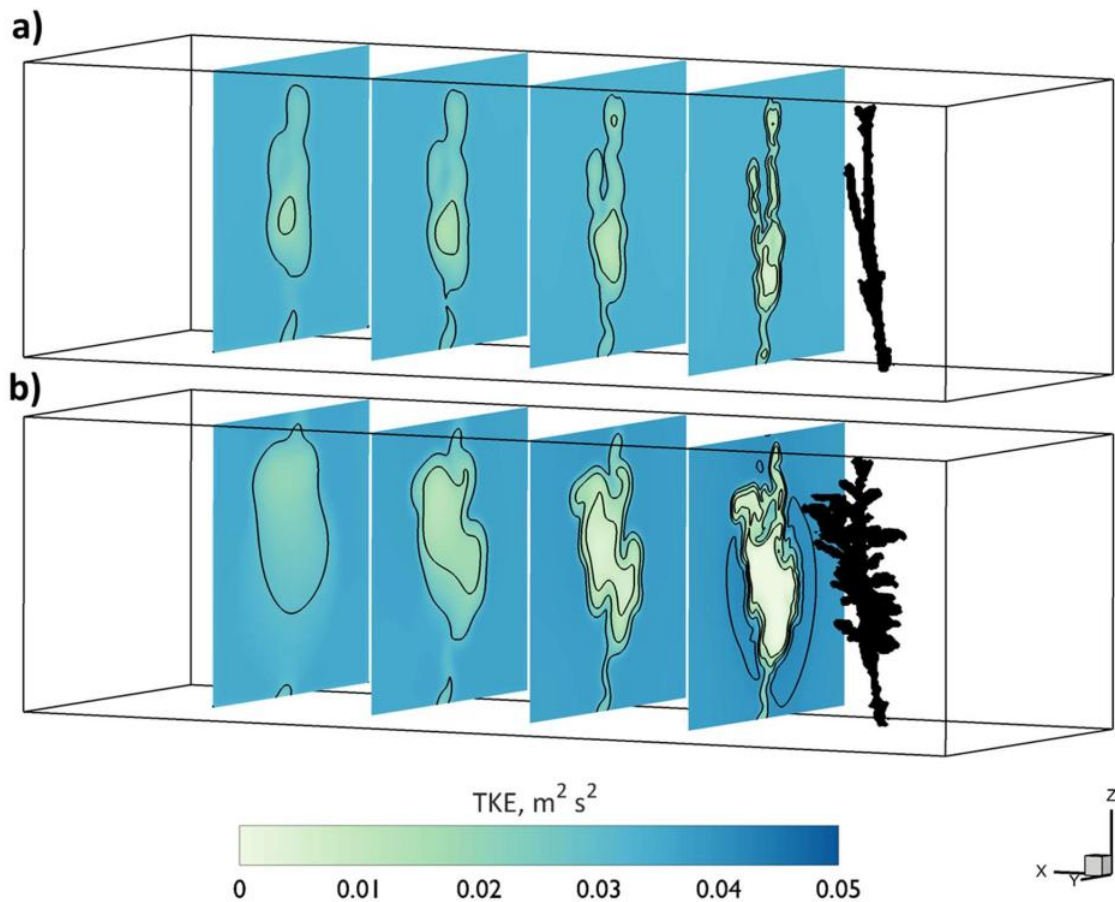


**Figure 6.20 Vertical slices of the turbulent kinetic energy (TKE) field for the (a) defoliated and (b) foliated plants at incremental positions downstream (0.30, 0.45, 0.60 and 0.75 X/l).**

## 6.3.6     Pressure field

Pressure fields are eventually used to calculate the drag response of the plant (Chapter 7). However, the spatial distribution of pressure acting on the defoliated and foliated plants can also help improve the process-understanding of flow-vegetation interactions. Figure 6.21 shows the modelled pressure field at 0.45 $Z/h$. When defoliated, the high-pressure zone located directly upstream of the blockage is small, and isolated about

individual branches. When foliated, however, this zone has coalesced to form a larger, single body that is characterised by higher pressures. Similarly, downstream of the plant, isolated zones of low pressure are associated with individual branches when defoliated, compared with a much more pronounced and extended low pressure zone when the plant is foliated.
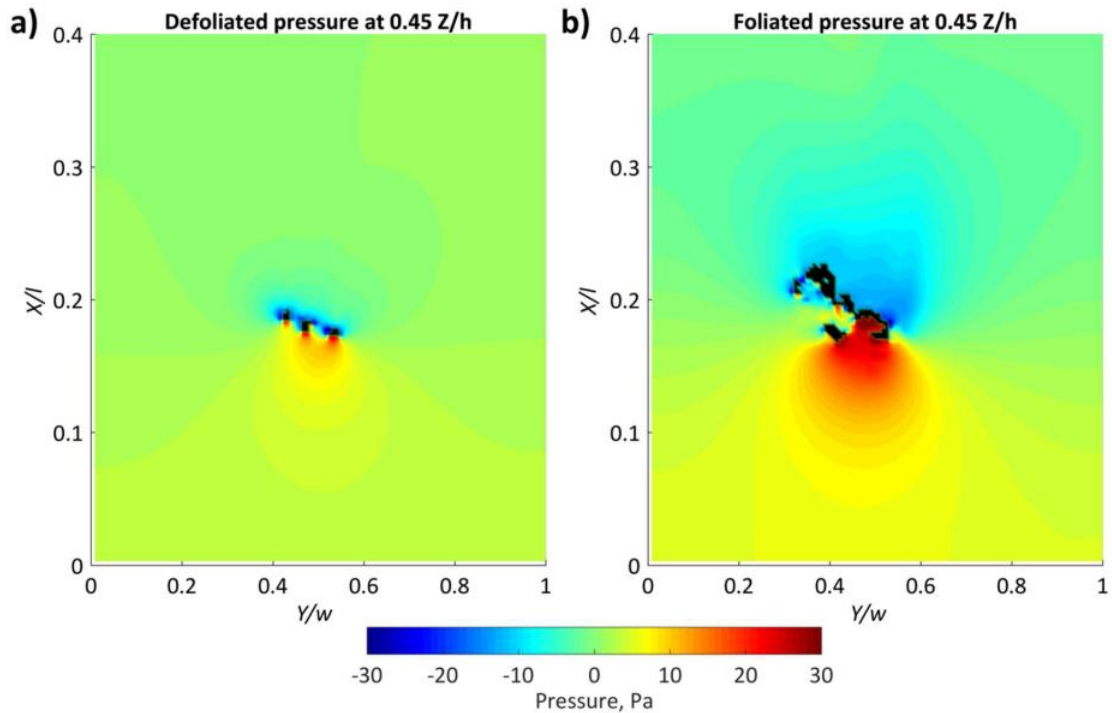


**Figure 6.21 Pressure fields at 0.45 Z/h for the (a) defoliated and (b) foliated plants.**

To further understand the spatial patterns, the spatially heterogeneous distribution of pressure over the surface of the plants are shown in Figure 6.22. For the defoliated plant, highest pressures ($\geq$ 30 Pa) are centred around the initial branching point on the plant front, and the magnitude of the high-pressure regions diminish with distance from this area. More positive pressure values are recorded towards the centre of the branch, and tend towards zero at the outer edge. At the downstream side of the defoliated plant, pressure remains relatively constant ($\sim$-20 Pa) over the plant back.

For the foliated plant, highest pressures ($\geq$ 30 Pa) are centred on the upstream edge of the plant at the base of the foliated body. Again, lower pressure values on the plant front correspond with plant edges. When looking at the back of the blockage, lowest pressures ($\leq$ -30 Pa) are distributed towards the base of the foliated body, although extend further down the main branch. Lowest pressures are distributed more towards

the base of the plant body, than at the front of the blockage where highest pressures were distributed higher on the plant body.

These spatial heterogeneities in the pressure field translate into differences in the pressure gradient over the entire lateral extent of the plant (Figure 6.22c). Overall, the total pressure gradient for the foliated plant is more than twice as great as the total pressure gradient for the defoliated plant. When defoliated, the most adverse pressure gradient exists in the region 0.25-0.40 *Z/h*, corresponding with the main branching point of the plant. When foliated, the most adverse pressure extends from 0.35-0.75 *Z/h*, and is more adverse than for the defoliated plant, with the position corresponding with the bulk of the foliated body. Foliage is therefore responsible for the modelled differences in the pressure regime.
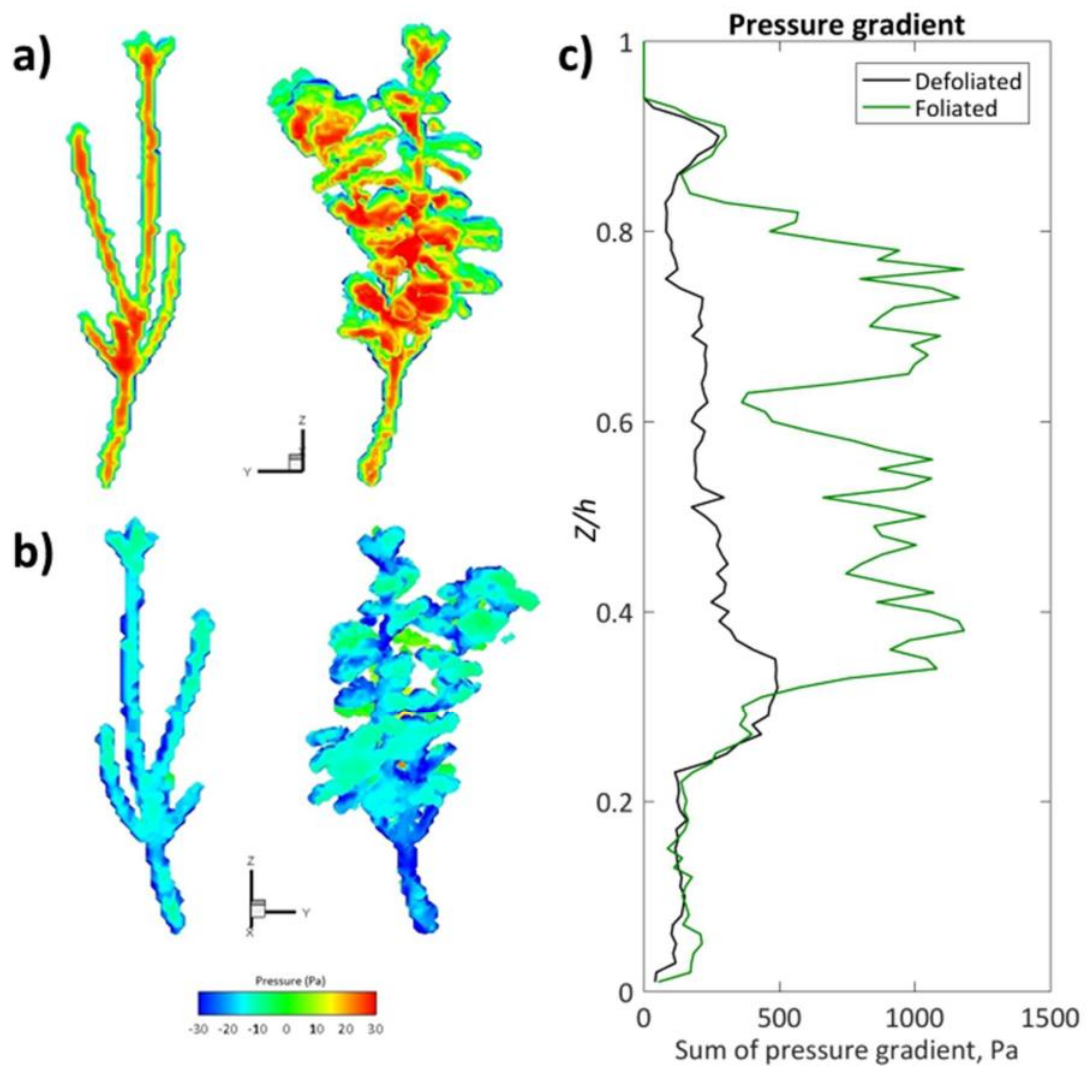


*Figure 6.22 (a) Pressure distributions over the plant front and (b) the plant back for the defoliated and foliated plants. This illustrates the spatially heterogeneous distribution of pressure, and (c) the resulting pressure gradients across the entire lateral plant extent.*

# 6.4      The importance of plant posture and plant aspect on flow field dynamics

Following identification of the influence of foliage on flow field dynamics, the simulated effects of further factors that contribute towards the plant volumetric canopy morphology are presented. Firstly, changes in plant posture will be simulated, followed by changes in the plant aspect. In both cases, changes in the plant volumetric canopy morphology and 'how the plant looks to flow' are hypothesised to influence the flow field dynamics.

## 6.4.1      Simulating changes in plant posture

To investigate the shifts in plant posture that can occur to a plant under hydrodynamic loading, the foliated plant representation from the previous section is rotated at 10° intervals about the horizontal (Figure 6.23a). The plant is therefore rotated from a fully upright posture (as was initially scanned), to a fully rotated posture (rotated through 80°). Although an 80° rotation may appear extreme, Section 2.3.4.1.3 showed that a plant may become fully prone prior to uprooting. In each case the plant is hinged to the same position on the bed (0.14 $X/l$), and the volume of the plant is conserved throughout. The incremental changes in posture complements and extends the analysis completed in Chapter 5, which considered smaller shifts in the time-averaged plant posture. In this section, the overall plant volumetric canopy morphology differs, with the *Prunus laurocerasus* plant having a markedly different form and structure than the *Hebe odora* plant (Section 3.5) investigated in Chapter 5.

The shifts in posture are shown by plotting the position of the plant centroid, shown for the *x*- and *z*- coordinates in Figure 6.23b (*y*-coordinate plant centroid remains the same throughout). By applying the rotation, the plant centroid is predominately shifted in the vertical direction, meaning that with increasing rotation the plant centroid occupies a lower portion of the flow depth. At rotations of 70 and 80° (darkest points in Figure 6.23b), plant centroids are similar because of interactions with the bed of the domain, meaning that the plant can be rotated no further.
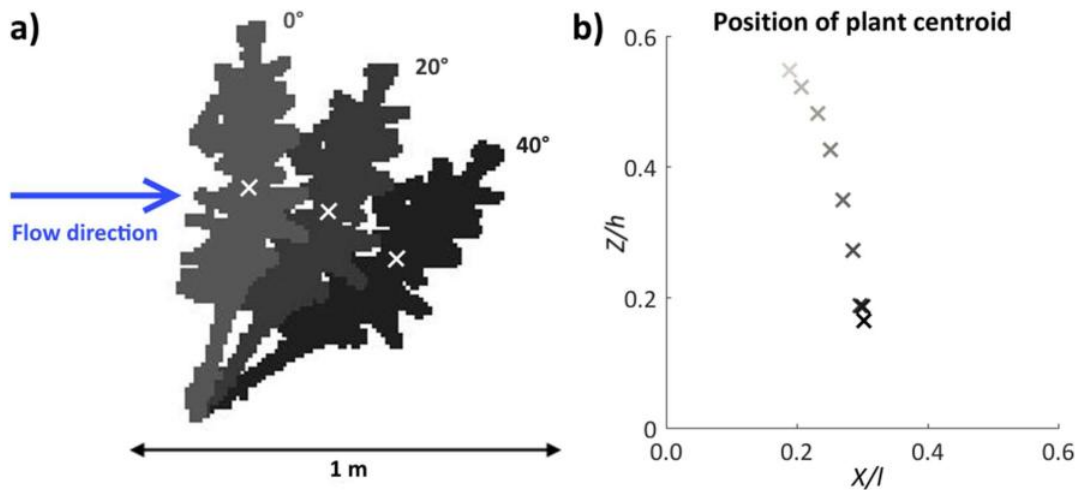
**Figure 6.23 (a) Examples of the shifts in plant posture, with the plant hinged to the bed and rotated over the horizontal. Centroids are shown by white crosses. (b) Shifts in plant posture change the position of the plant centroid.**

Firstly, by focusing on rotations of 0, 20, 40, and 60°, differences in the downstream velocity field are visualised (Figure 6.24a) and delineated according to wake or flow acceleration zones (< 0.5 and > 1.1 inlet velocity, Figure 6.24b). As discussed previously, the upright case is characterised by a double-layered wake structure, with the more pronounced upper wake extending ~4.8 plant lengths downstream. As the plant shifts lower in the flow depth, however, there is a progressive change in the wake structure, moving towards a single wake, and becoming more conical in shape. This occurs when the plant centroid, and therefore the foliated body, is positioned lower in the flow depth (Figure 6.23b). With changes in the wake, the zone of flow acceleration above the foliated body appears to reduce in size (Figure 6.24).

Changes in volume of the wake and flow acceleration zones with shifts in plant posture are shown in Figure 6.25a. The volume of the wake zone is relatively consistent with changes in plant posture, in the range 0.08 to 0.11 m³. In contrast, the volume of the flow acceleration zone decreases markedly between 0 – 20°, but thereafter remains negligible (< 0.005 m³). Further differences emerge when normalising the downstream extent of the zones against the plant length (Figure 6.25b). In the wake zone, upright postures are associated with longer wake lengths (~4.5 plant lengths), compared with the shorter wake lengths when more prone (~2.5 plant lengths). The length of the flow acceleration zone shows a similar shortening trend, from ~2 plant lengths when upright, to ~0.5 plant lengths when fully prone. Flow disturbance is therefore greatest when the plant is upright.
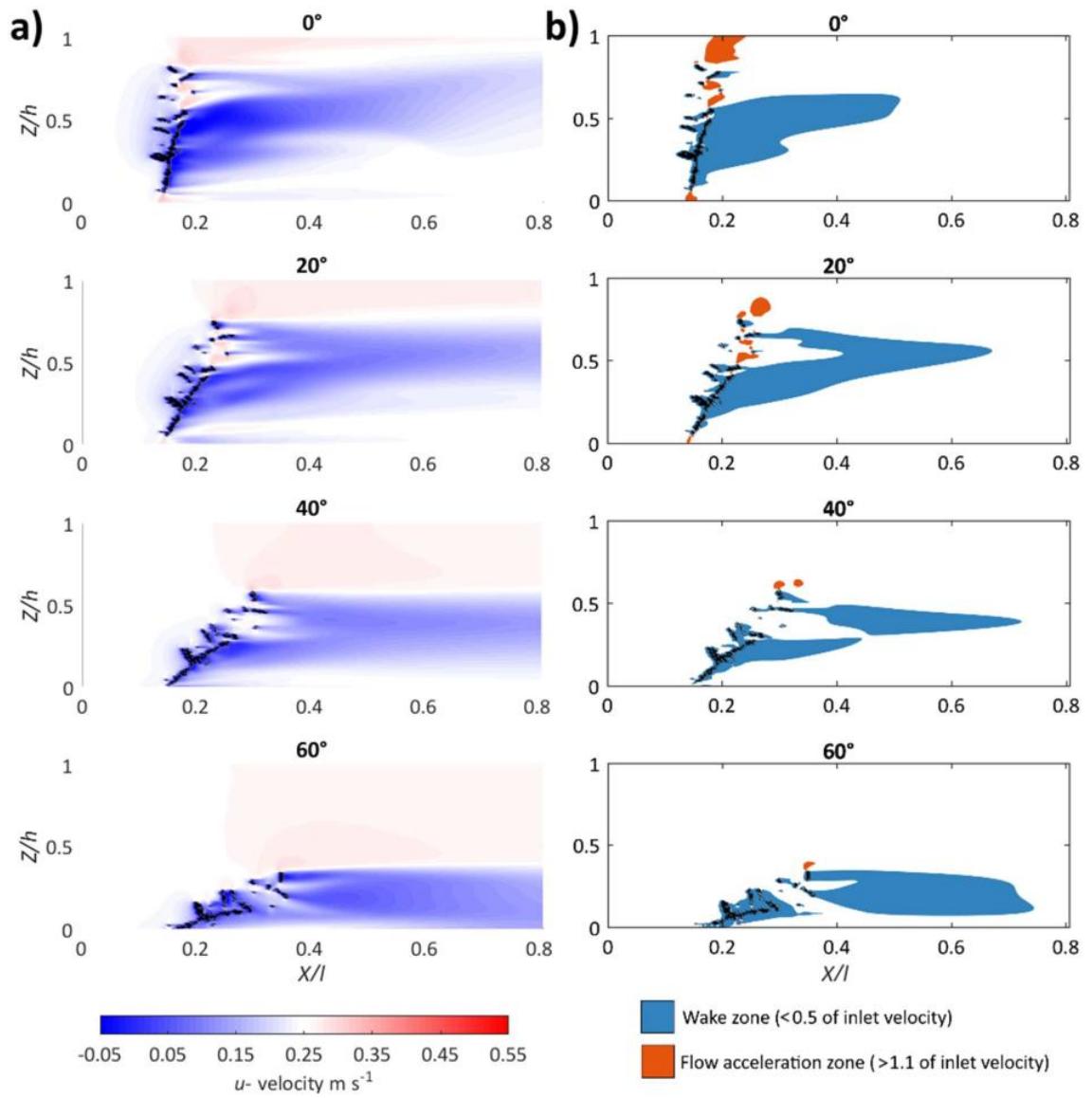
**Figure 6.24 (a) Downstream velocity field data around the foliated plant representation at 0.5 Y/w with changes in posture. (b) Delineation of the wake and flow acceleration zones.**
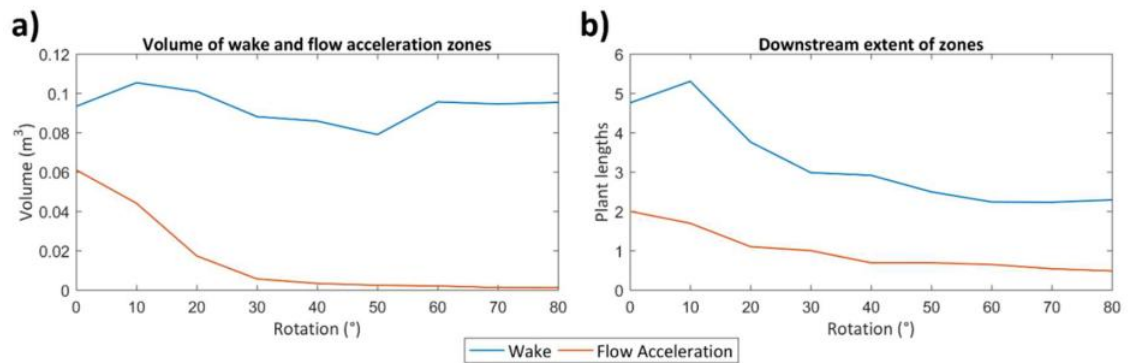


**Figure 6.25 (a) Volume of the wake and flow acceleration zones under changing plant posture and (b) the extent of these zones when normalised against plant length.**

273

The effect of changes in posture on the flow disturbance is further investigated by comparing velocity profiles at 0.5 *X/l*, 0.5 *Y/w* (Figure 6.26). The velocity profiles provide evidence for the downwards deflection of the reduced velocity zone as shown in Figure 6.24, associated with the progressive downwards shift of the plant centroid (Figure 6.23b). In addition to this lowering of position in the flow depth, the reduced velocity zone becomes vertically compressed and changes shape. In the more upright cases, several kinks in the velocity profile are present, and these have previously been shown to be associated with peaks in the plant blockage. As the posture of the plant is shifted, occupying the same volume but a smaller fraction of flow depth, the subtle volumetric peaks corresponding with individual velocity minima are no longer present. Instead, as the plant becomes more prone, a single reduced velocity zone with even lower velocity minima are found.
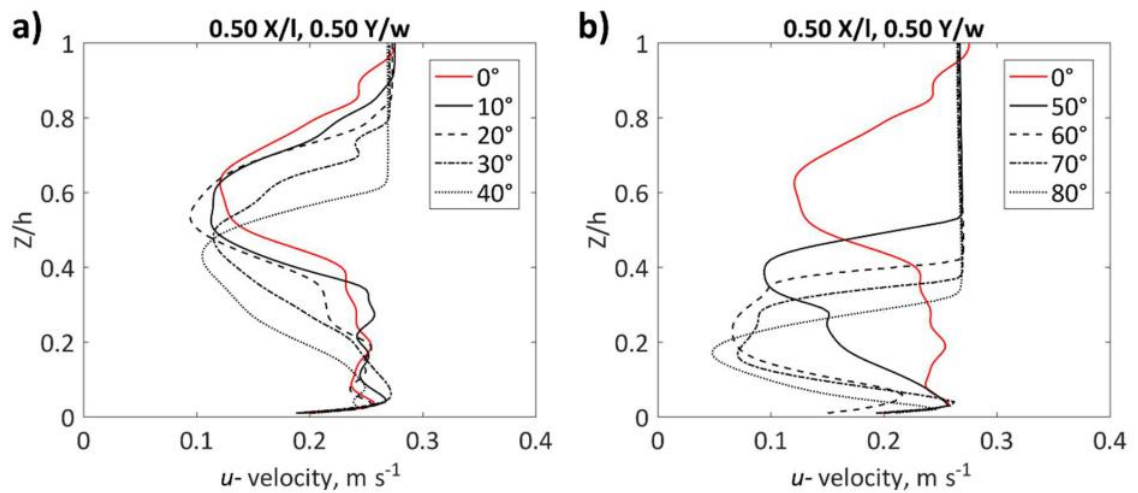


*Figure 6.26 Downstream velocity profiles extracted from 0.5 X/l, 0.5 Y/w with shifts in plant posture from (a) 0-40°, and (b) 50-80°.*

As first introduced in Figure 6.4, by calculating the area under the curve for the velocity profiles at 0.4, 0.5, and 0.6 *X/l* (all at the midline, 0.5 *Y/w*), the effects of posture on the flow disturbance are further quantified (Figure 6.27). In all cases, the area under the curve decreases with increasing distance downstream, as the separated flow recovers. In general, the area under the curve decreases as the plant becomes more prone. Again, this suggests that the magnitude of the flow disturbance reduces as the plant becomes more prone. With the volume of the plant conserved with shifts in posture, changes in the flow disturbance must result from differences in the plant volumetric canopy morphology, and how the plant is presented to flow.
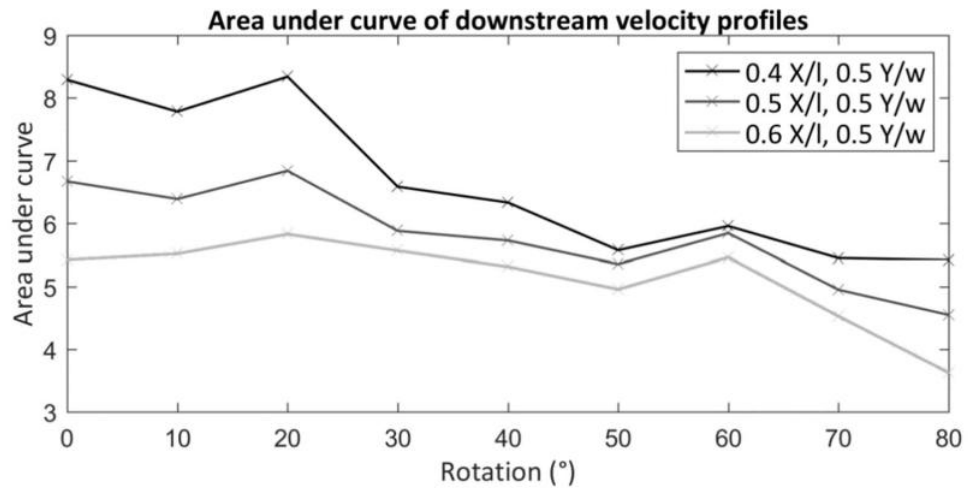
***Figure 6.27 Area under the curve for downstream velocity profiles at 0.4, 0.5 and 0.6 X/l (0.5 Y/w).***

In addition to investigating the effect of plant posture on the downstream velocity field, a consideration of the pressure field is also required. Figure 6.28 demonstrates that the spatial distribution of high pressure (20 - 35 Pa) on the upstream edge of the plant body varies with shifts in plant posture. As the plant becomes more prone, the total area occupied by high pressure decreases, with a progressive shift in the spatial distribution of the zone downwards towards the main stem, away from the main foliated body.

In the upright position, the incident flow would encounter most of the plant blockage at the same position (in terms of *X/l*). However, as the plant becomes more prone, the incident flow would encounter the surface of the plant in a more spatially staggered manner. This will have implications for the pressure gradient. Pressure is highest on the surface of the plant at the first point of contact with the flow. With characteristically higher pressure on the upstream sides of the upright plant, and this will produce a more adverse pressure gradient than when the plant is more prone to flow. Flow field dynamics associated with shifts in plant posture will therefore have direct implications for the drag response (Chapter 7).
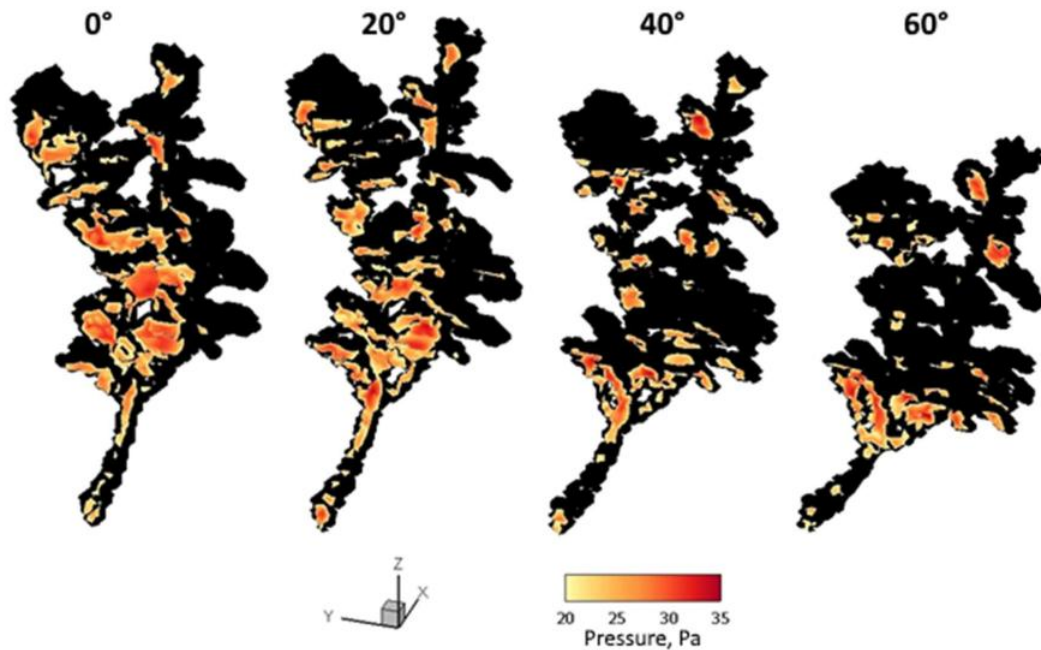
***Figure 6.28 Spatial distribution of high pressures (in the range 20-35 Pa) over the upstream edge of the foliated plant for 0, 20°, 40°, and 60°.***

## 6.4.2 Simulating changes in plant aspect

To further simulate how small changes in 'how the plant looks to flow' can result in modifications to flow field dynamics, the plant aspect to the incident flow is altered. Previously, the orientation of the plant to flow (the plant aspect) has remained the same. This was selected when collecting the first scan using TLS. Here, however, plant aspect is altered at 15° intervals (24 orientations), by rotating the defoliated and foliated plant representations about the vertical axis, thereby altering the position of the plant to the primary flow direction (Figure 6.29). In doing so, although the plant volumetric canopy morphology remains the same, the exposure of the plant to flow is changed. In a natural setting, parallels are drawn with the orientation of plants on a gravel bar, with different orientations resulting in different flow field dynamics.

***Figure 6.29 Example of altering plant aspect, modifying 'how the plant looks to flow'.***

Comparisons of downstream velocity profiles at 0.30 *X/l*, 0.5 *Y/w* for the defoliated and foliated plants (Figure 6.30) reveal considerable differences in velocity profile shape with changes in plant aspect. Although some similarities are noted, such as presence of the sub-canopy region when the plant is foliated, a number of differences emerge.

The position and magnitude of the velocity minima varies with plant aspect. Notable velocity differences between opposite plant aspects of 120 and 300° are shown, therefore although the plant remains similar in structure, the velocity profiles can be dissimilar. This is somewhat surprising for the defoliated plant, given the relatively lack of complexity associated with the leafless branches, but more understandable for the more complex foliated body. Small changes in plant aspect can therefore introduce significant changes to the downstream velocity field.
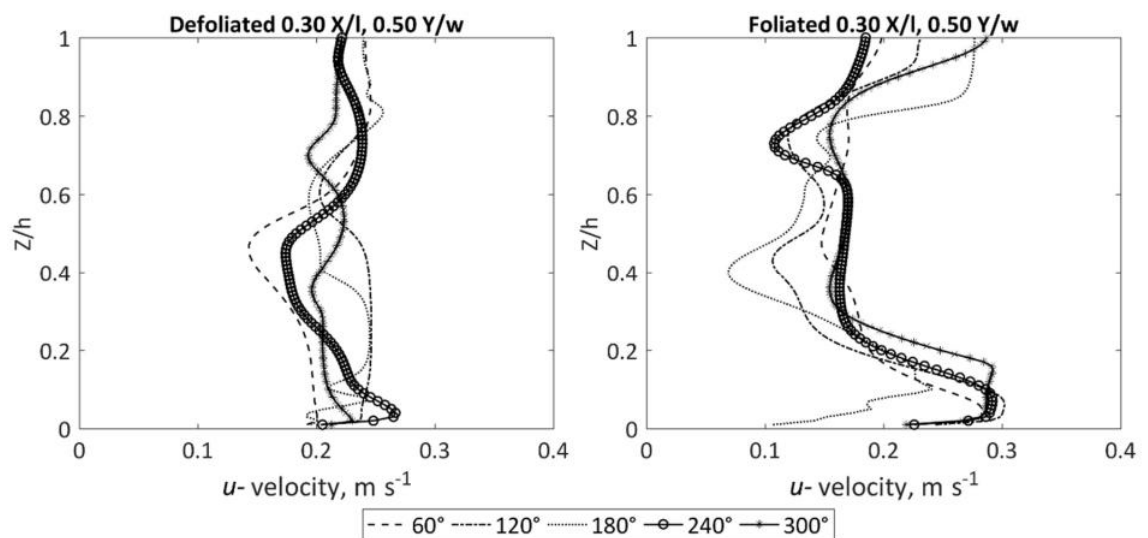


***Figure 6.30 Effect of changing plant aspect on the downstream velocity profile at 0.3 X/l, 0.5 Y/w for the defoliated (left), and foliated (right) states.***

To further understand how changes in plant aspect influences the downstream velocity field, the volume of the wake zone (< 0.5 of inlet velocity) is quantified (Figure 6.31). For the defoliated and foliated plants, the wake volume remains relatively similar across the range of plant aspects, especially for the defoliated plant. When defoliated, the wake volume varies by as much as 26% across all plant aspects, but when foliated this increases to 45%. For the foliated plant, volumetrically greatest wake volumes are found at plant aspects around 0 and 180°, with wake volumes smaller around 90 and 270°. This suggests some form of directional influence on the flow disturbance effects. Around plant aspects of 0 and 180°, the blockage is positioned most perpendicular to the incident flow (as demonstrated in Figure 6.22). At 90 and 270°, the blockage is positioned more parallel to the incident flow, thereby reducing the flow disturbance, and accounting for smaller wake volumes. Although in general the wake volume remains relatively similar with changes in plant aspect, the incremental changes influence the local flow field dynamics. This corresponds with the relatively small changes in total wake volume associated with shifts in plant posture (Figure 6.25a), and demonstrates the underlying importance of the volume of the plant blockage in controlling flow field dynamics.
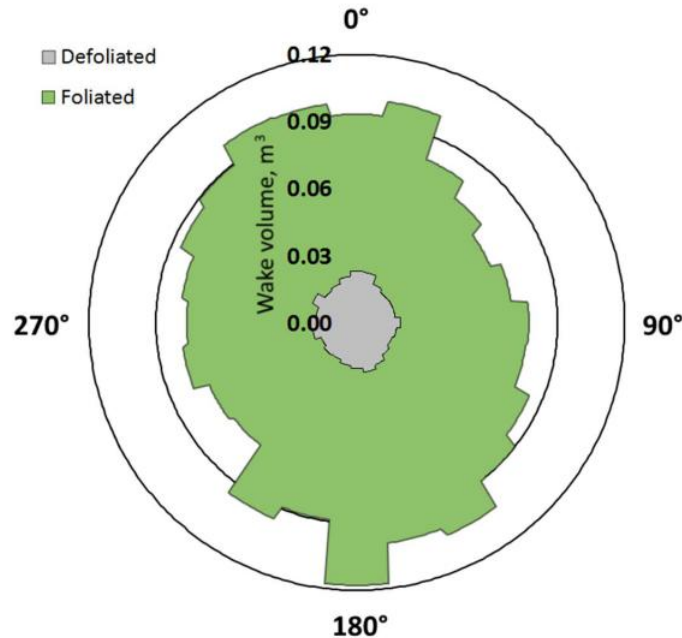


*Figure 6.31 Effect of changing plant aspect on the wake volume for defoliated and foliated plants.*

Simulated changes in plant aspect, and specifically whether the plant is orientated perpendicular or parallel to flow, influences not only the downstream velocity field, but also the TKE field. For the defoliated plant, Figure 6.32 demonstrates that incremental

45° changes in plant aspect result in a highly modified TKE response. Although the magnitude of the TKE response appears to be similar throughout, the spatial patterns of TKE vary. This is especially true where the width of the zone of lowest TKE ($0 - 0.015$ m$^2$ s$^2$) varies markedly with plant aspect. Even where the branches are almost aligned parallel to flow, at plant aspects of 90 and 270°, the spatial patterns of TKE differ greatly between these similar morphologies, with the zone of low TKE at 270° approximatively half the width of the mirrored representation at 90°. Furthermore, discrepancies exist in the spatial patterns of highest TKE. At a plant aspect of 45°, a prominent zone of high TKE is present ($> 0.05$ m$^2$ s$^2$), and this is not replicated by the mirrored representation at 225°. For the defoliated plant, incremental changes in plant aspect result in significant changes to the spatial patterns of TKE.

For the foliated plant, Figure 6.33 demonstrates how changes in plant aspect results in different spatial patterns of TKE. Again, the magnitude of the TKE response remains relatively similar throughout, but the spatial patterns of TKE vary less markedly than for the defoliated plant. TKE patterns for the foliated plant tend to be more symmetrical about the blockage centre, and therefore are more similar throughout the plant aspects shown. Compared with the defoliated plant, zones of highest TKE tend to be larger and persist further in the downstream direction when foliated, illustrating the greater form drag contribution. Moreover, patterns of TKE around mirrored plant representations (90 and 270°) appear more similar than for the defoliated plant. However, when comparing the perpendicular plant aspect (0°) to a more parallel plant aspect (90°), differences begin to emerge, with the zones of highest TKE ($> 0.05$ m$^2$ s$^2$) larger when the plant is orientated perpendicular to flow. In both perpendicular and parallel states, the zone of lowest TKE ($0-0.015$ m$^2$ s$^2$) is constrained by the outer extent of the plant width, however, when the plant aspect falls between perpendicular-parallel (45 and 135°), the zone of lowest TKE extends beyond this outer limit. This displaces laterally the zone of highest TKE outwards from the plant edge, and again reiterates that although the overall TKE response is similar between different plant aspects, the localised patterns differ.

Together the differences in the spatial patterns of TKE with changing plant aspect for the defoliated and foliated plants reveal the importance of plant orientation to the incident flow; and how perpendicular or parallel plant aspects can influence energy conversion. This is further investigated by quantifying the drag response with changes in plant aspect in Chapter 7.
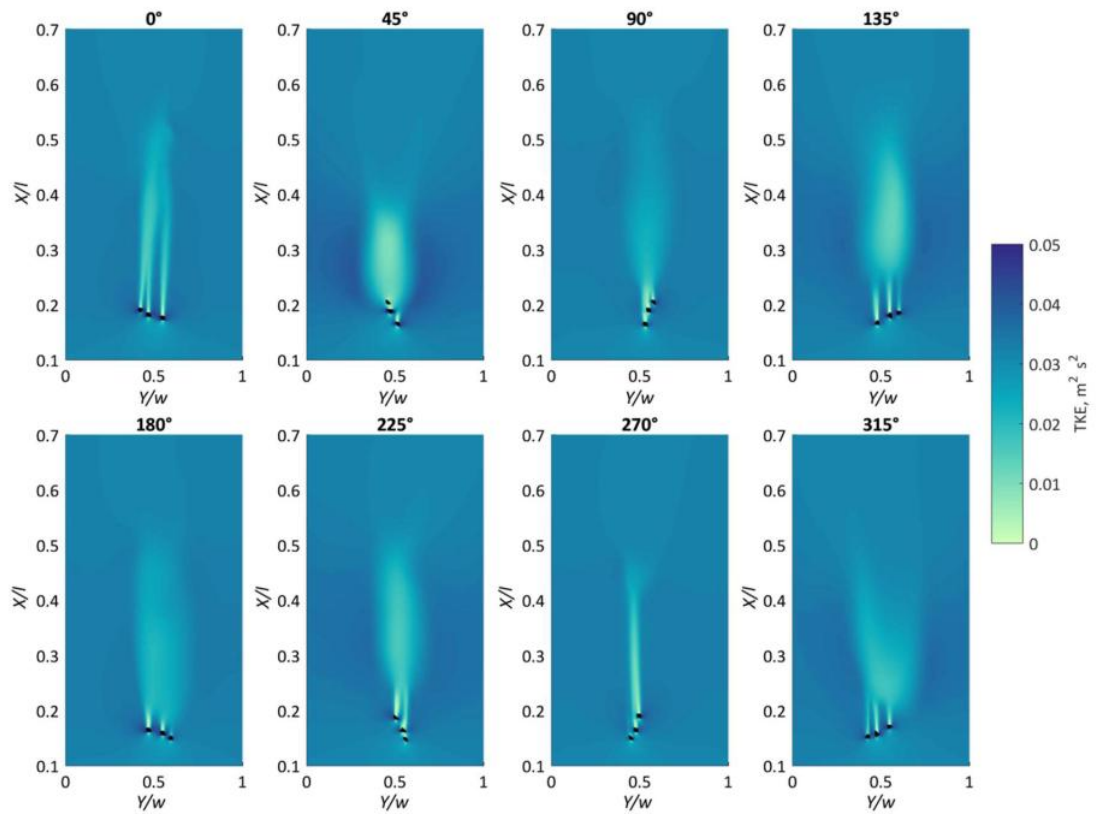
*Figure 6.32 Defoliated plant turbulent kinetic energy field at 0.5 Z/h with changing plant aspect.*
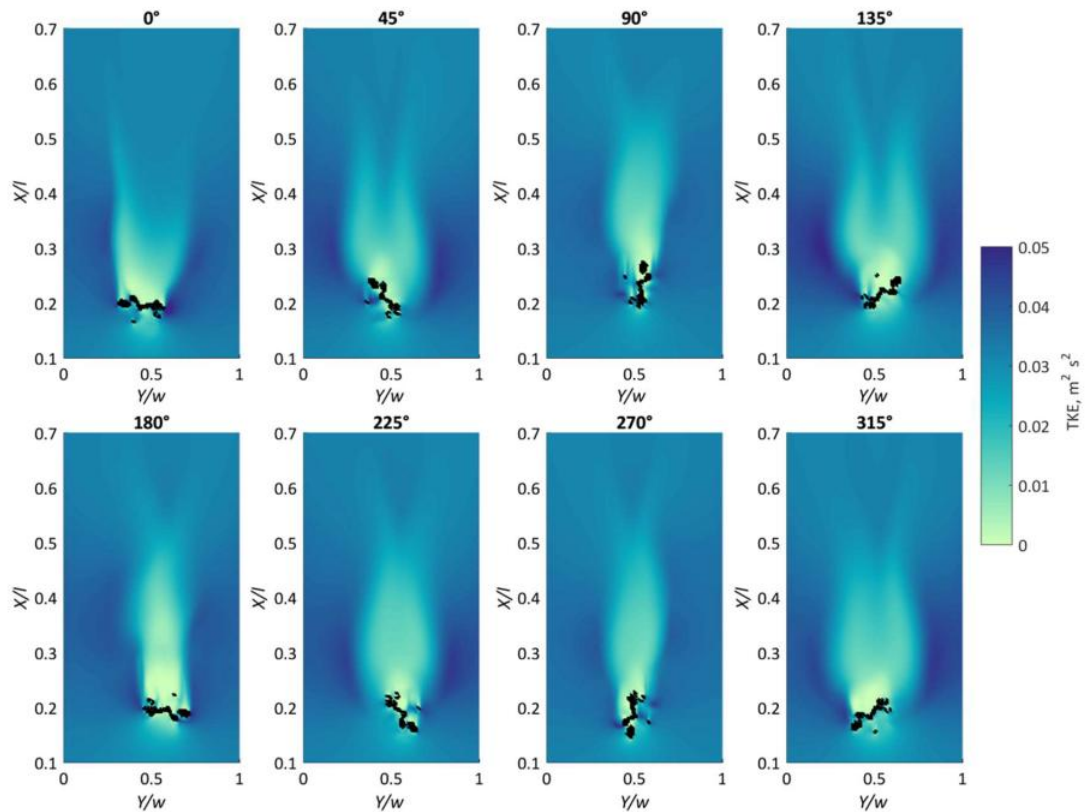


*Figure 6.33 Foliated plant turbulent kinetic energy field at 0.5 Z/h with changing plant aspect.*

## 6.5　　　　Modelling flow around different plants of the same species

To further analyse how natural variation in plant volumetric canopy morphology influences flow field dynamics, the flow around three different specimens of *Prunus laurocerasus* are simulated. The three plants are defined as $Pl_1$, $Pl_2$, and $Pl_3$. Flow around each plant is simulated in isolation, and the three specimens were selected for their similarity in size and foliage density (Figure 6.34), but natural variation in plant form and structure. Each specimen was scanned and voxelised using a 0.01 m voxel size (Figure 6.34c), with inlet boundary conditions held the same as the previous sections.

Plant structure and form is quantified for each of the specimens using the voxelised representations (Figure 6.35), applying the techniques detailed in Section 3.4. Because plant heights differ (ranging from 0.73 – 0.81 m), plant heights are normalised between 0 and 1, so the geometric characteristics can be readily compared. In terms of crown width, $Pl_1$ shows a different vertical distribution than $Pl_2$ and $Pl_3$ (Figure 6.35a). The maximum plant width of $Pl_1$ is 0.83 m, compared with 0.68 and 0.64 m for $Pl_2$ and $Pl_3$, with the maximum crown width positioned higher in the vertical dimension for these narrower plants. $Pl_3$ has the largest frontal area, ~20% larger than $Pl_1$, and ~30% larger than $Pl_2$, and the vertical distribution of the frontal area differs between the three plants (Figure 6.35b). When the frontal area is used to calculate the hypsometry for each of the plants, hypsometric curves are very similar in shape (Figure 6.35c). For the vertical distribution of plant volume (Figure 6.35d), the greatest degree of similarity is shown between $Pl_1$ and $Pl_3$, although $Pl_1$ is volumetrically greatest, ~35% larger than $Pl_2$, and ~10% larger than $Pl_3$. The plant structure and form of $Pl_1$ and $Pl_3$ therefore appear most similar.

The spatially distributed plant solid volume fraction for each specimen is also shown (Figure 6.36). $Pl_1$ and $Pl_3$ show the most similar porosity distributions, with higher solid volume fractions corresponding with a wide band associated with the leaf body. For $Pl_1$, the solid volume fraction is distributed approximately uniformly throughout this region, whereas for $Pl_3$ the highest values are positioned lower in the flow depth. For $Pl_2$, however, the region of highest solid volume fraction is far narrower, meaning that the greatest blockage is confined to a smaller region of $Z/h$ than for $Pl_1$ and $Pl_3$. Differences in plant volumetric canopy morphology between the three plants, resulting from

differences in plant structure and form, are hypothesised to influence flow field dynamics.
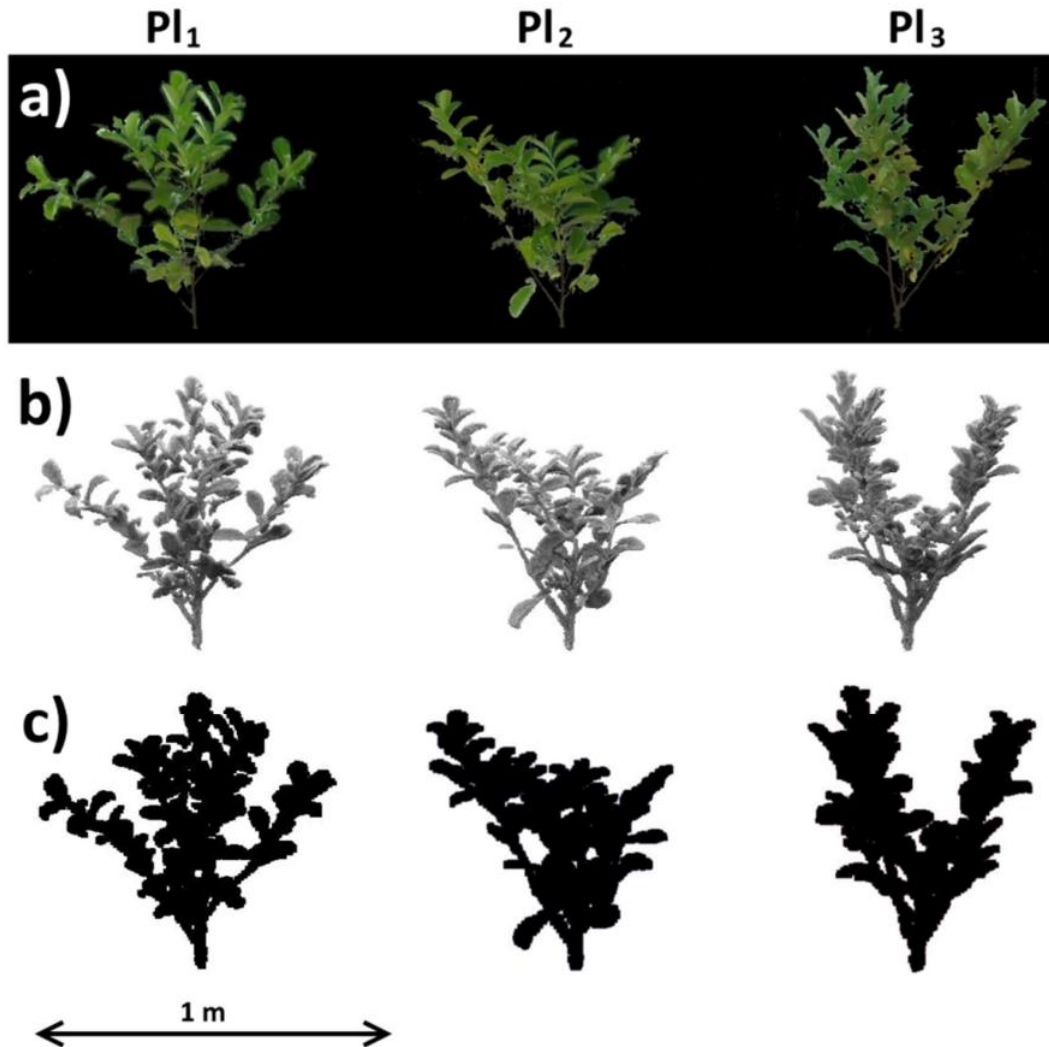


*Figure 6.34 (a) Three Prunus laurocerasus specimens, labelled $Pl_1$, $Pl_2$, and $Pl_3$, with the photographs masked to remove the background, (b) post-processed point clouds, and (c) voxelised representations with a 0.01 m voxel size.*
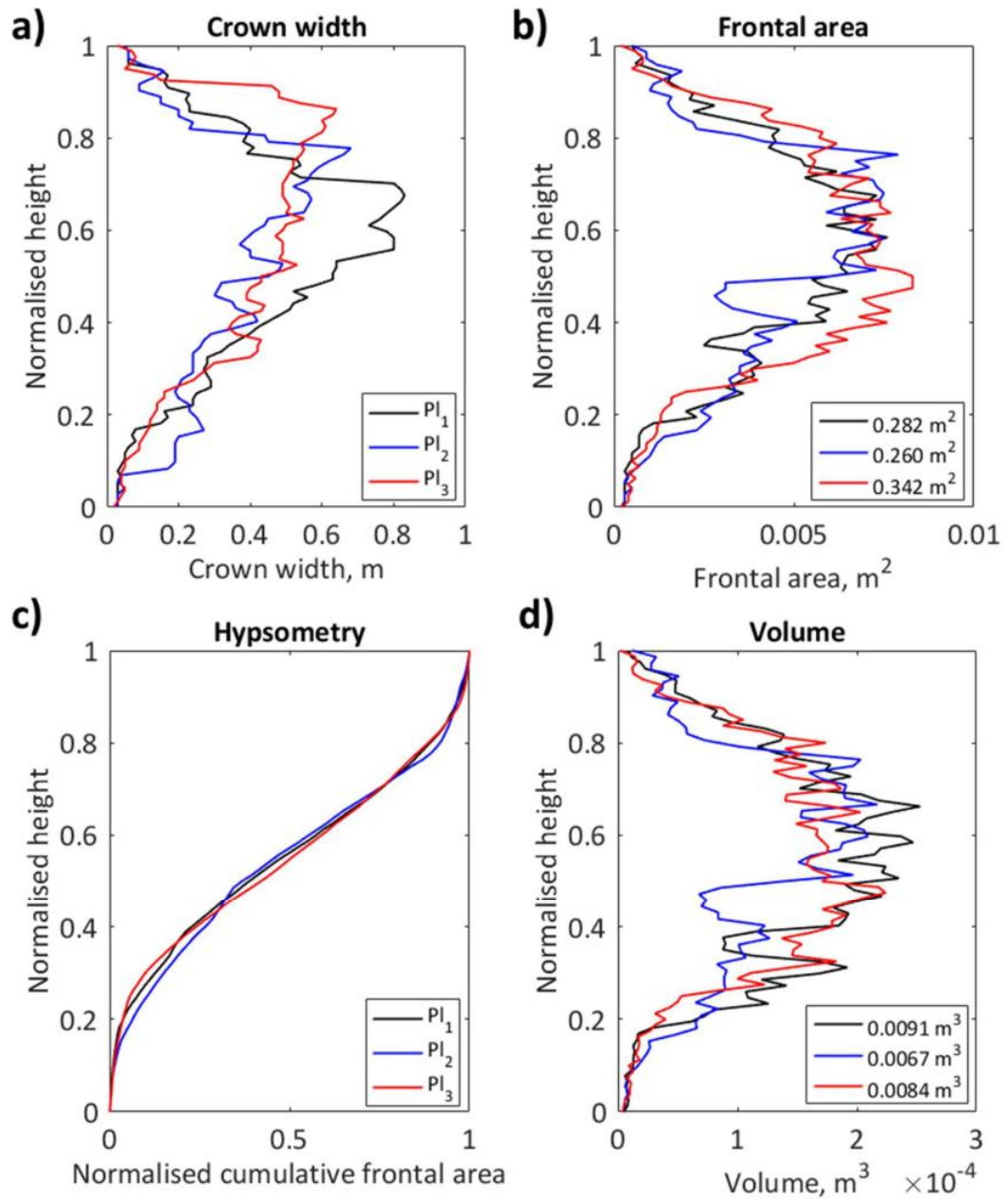
***Figure 6.35 Plant structure and form characteristics for the voxelised** Prunus laurocerasus **specimens:
(a) crown width, (b) frontal area, (c) normalised cumulative frontal area, and (d) volume. Total frontal
areas and total plant volumes are noted in the legends of (b) and (d).*
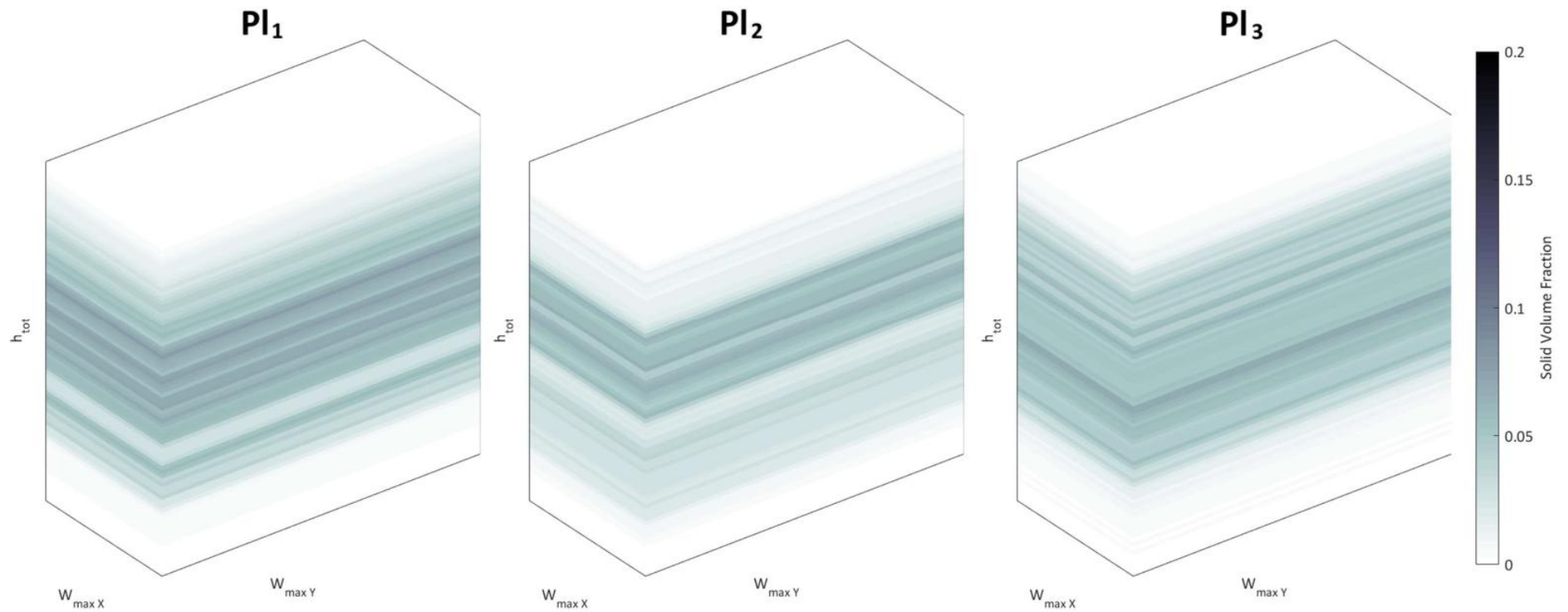
***Figure 6.36** Spatially distributed plant solid volume fraction for the three **Prunus laurocerasus** specimens.  Same reference volume used throughout.  Greatest similarities noted between Pl₁ and Pl₃, where a wider zone of higher solid volume fraction is associated with the leaf body.  For Pl₂, the zone of highest solid volume fraction is confined to a smaller region in Z/h.*

Downstream velocity fields are most similar for $Pl_1$ and $Pl_3$ (Figure 6.37a and b), characterised by an almost symmetrical low velocity zone about the plant blockages, that extend a similar distance downstream. Flow separation and reattachment occurs around the individual clusters of foliated branches (three main clusters in $Pl_1$, two main clusters in $Pl_3$), and these are responsible for forcing the flow patterns, especially at higher $Z/h$. The most notable difference between $Pl_1$ and $Pl_3$ emerges around 0.75 $Z/h$, where a localised region of faster moving flow is modelled between the branch clusters in $Pl_3$. For $Pl_2$, the branch clusters are less clearly defined, with flow separation and reattachment about a single foliated body, rather than the isolated foliated clusters. The overall flow disturbance effect from $Pl_2$ appears smaller than $Pl_1$ and $Pl_3$, and this is not surprising given the smaller frontal area and total volume associated with this plant, imparting a smaller blockage to the flow.

As before, plant wake and flow acceleration zones are identified and quantified, and the three-dimensional extent illustrated (Figure 6.38). Characteristics of the wake and acceleration zones are displayed in Table 6.4.

$Pl_3$ has the volumetrically greatest wake zone, 16% larger than $Pl_1$, and 45% larger than $Pl_2$. For each plant, a complex and highly three-dimensional wake structure is evident (Figure 6.38). The downstream-most extent of the wake is positioned higher in the flow depth for $Pl_2$ than $Pl_3$, and this appears to be associated with the vertical distribution of the plant frontal area (Figure 6.35b). For $Pl_1$, however, the downstream-most extent of the wake appears almost uniformly positioned throughout the entire flow depth. In terms of the maximum length of the wakes, similarity is found between all three plants, with maximum wake lengths in the range 1.27 – 1.37 m. When normalised by plant length, this corresponds to 2.53, 2.44, and 2.54 plant lengths respectively (~2.5 plant lengths), indicating that wake length remains similar throughout the plants. In relation to the spatially distributed plant solid volume fractions previously identified (Figure 6.36), it is noticeable how the reduced velocity zones in the wakes of $Pl_1$ and $Pl_3$ approximately correspond with the distribution of the blockage observed. The wide bands of highest solid volume fraction therefore appear to be associated with the wake patterns observed, especially the lengths of wakes. Furthermore, for $Pl_2$ the wake length is greatest around 0.75 $Z/h$ (Figure 6.37c), and this corresponds with the narrow band of highest solid volume fraction shown in Figure 6.36. Plant volumetric canopy morphology, here quantified through the solid volume fraction, therefore influences flow field dynamics, and introduces heterogeneity to the downstream velocity field.

In terms of the zone of flow acceleration Figure 6.38 and Table 6.4 show that $Pl_3$ has a significantly larger zone than any other plant (> ~400% larger than $Pl_1$ and ~250% larger than $Pl_2$). Looking at Figure 6.38, two main zones of flow acceleration are simulated. The first is common to all specimens, with flow acceleration around the outer-edge of the main branch clusters, with the bulk of this flow acceleration positioned in the near-bed region. For $Pl_3$, this zone is substantially larger than for the other plants. In addition, for $Pl_2$ and $Pl_3$ a second zone of flow acceleration is simulated between the two main branch clusters. This zone is larger and more spatially coherent for $Pl_3$, again contributing to the larger component of flow acceleration shown in $Pl_3$.

Considering the total volumes and characteristics of both the plant wake and flow acceleration zones, the total flow disturbance introduced by $Pl_3$ appears greatest, followed by $Pl_1$ and then $Pl_2$.
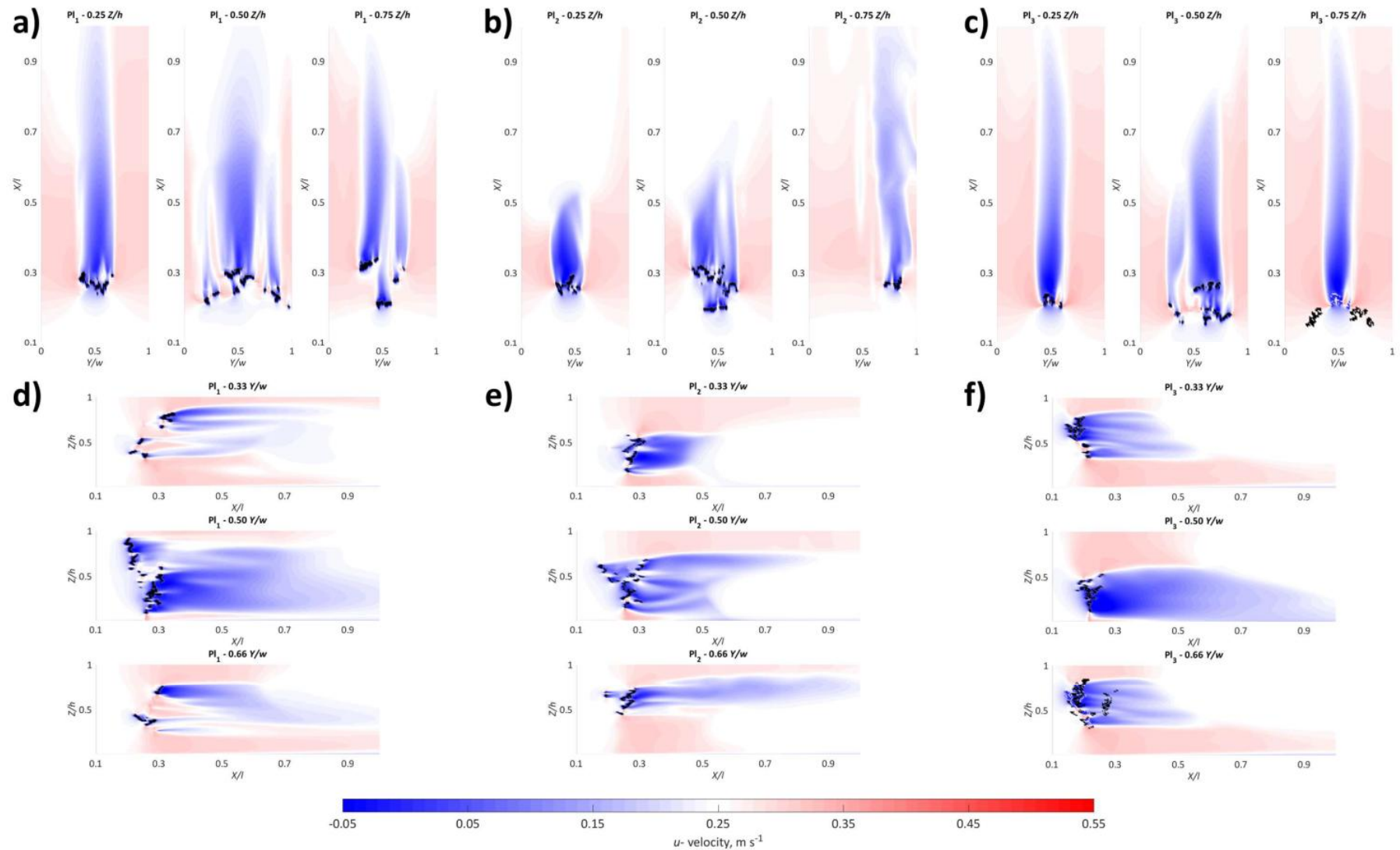
*Figure 6.37 Downstream velocity fields in horizontal (0.25, 0.50, 0.75 Z/h) and vertical (0.33, 0.50, 0.66 Y/w) planes for: (a and b) Pl₁, (c and d) Pl₂, and (e and f) Pl₃.*
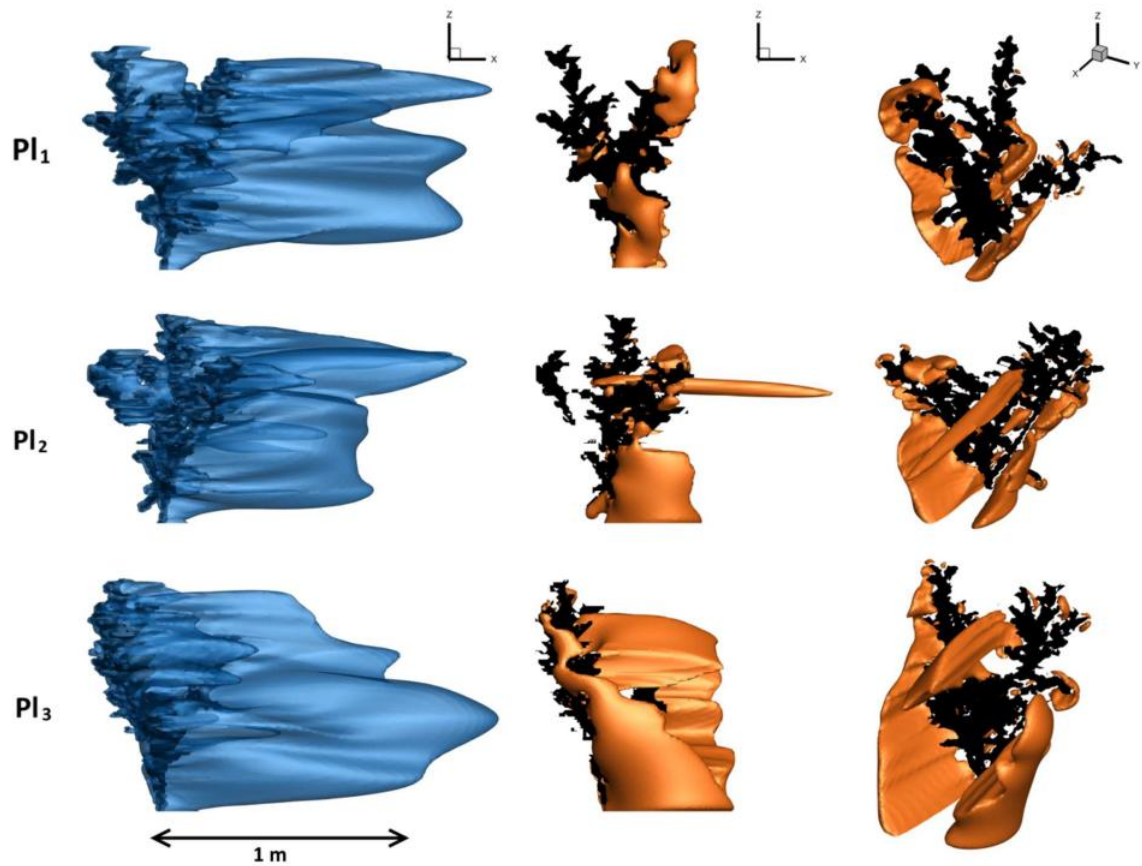
*Figure 6.38 Three-dimensional extent of the wake (< 0.5 of inlet velocity, blue) and flow acceleration (> 1.1 of inlet velocity, orange) zones shown from 2 different perspectives, same scale throughout.*

*Table 6.4 Wake and flow acceleration characteristics around the three* Prunus laurocerasus *specimens.*

| Plant | Wake volume (m³) | Maximum wake length (m) | Flow acceleration volume (m³) | Maximum flow acceleration length (m) |
|-------|------------------|--------------------------|-------------------------------|--------------------------------------|
| $Pl_1$ | 0.092 | 1.37 | 0.008 | 0.43 |
| $Pl_2$ | 0.073 | 1.27 | 0.012 | 0.65 |
| $Pl_3$ | 0.106 | 1.37 | 0.041 | 0.83 |

Three-dimensional streamlines are also used to investigate differences in the patterns of flow between the three plants. Streamlines originate from 0.01 $X/l$, 0.5 $Y/w$ at 10 incremental positions in the flow depth (0.1 – 0.9 $Z/h$), and for each plant these are shown in Figure 6.39. By tracking the positions of each streamline through the modelling domain, their displacements from the origin and deviations from the inlet are also quantified (Figure 6.40).

For $Pl_1$, most of the streamlines are laterally displaced to the left of the plant blockage. Vertical displacements are comparably the greatest of the three plants, with up to 0.28 m of vertical displacement at ~0.3 $Z/h$ (Figure 6.40e). Streamlines tend to move away from

the bed at lower values of $Z/h$ (Figure 6.40b). In contrast, at higher values of $Z/h$, streamlines tend to be deflected downwards towards the bed (Figure 6.40b). The streamlines of $Pl_1$ are associated with the greatest velocity reductions (Figure 6.40c), with large velocity ranges even at higher values of $Z/h$ (Figure 6.40f), indicating that unlike the other plants, flow is still disturbed in this upper region.

For $Pl_2$, again streamlines are mainly displaced to the left of the plant blockage, where with the spikes at ~0.6 $Z/h$ in Figure 6.40a and Figure 6.40d showing lateral displacement by as much as 0.20 m. Vertical displacement is characterised by an upward motion for all but one of the streamlines. The upwards deflection of streamlines is again notable in the near-bed region, and is associated with reductions in the downstream velocity (Figure 6.39 and Figure 6.40f). However, at higher values of $Z/h$, the consistently positive velocity deviations indicate flow acceleration, as shown previously in Figure 6.38.

For $Pl_3$, all but one of the streamlines are laterally displaced to the right of the plant blockage. Lateral displacements are comparably smaller than the other two plants (< 0.10 m, Figure 6.40d). Furthermore, in the near-bed region, streamlines are deflected towards the bed, unlike for $Pl_1$ and $Pl_2$. The largest range in downstream velocity along a single streamline is found at ~0.3 $Z/h$, and is of a similar magnitude to the ranges observed for $Pl_1$ and $Pl_2$ (Figure 6.40f).

Streamlines therefore show different lateral and vertical displacements and deviations for the three plants from the same species, with notable differences in the deflections of flow either towards or away from the bed. These findings have implications for sediment transport processes, as discussed in Chapter 7.
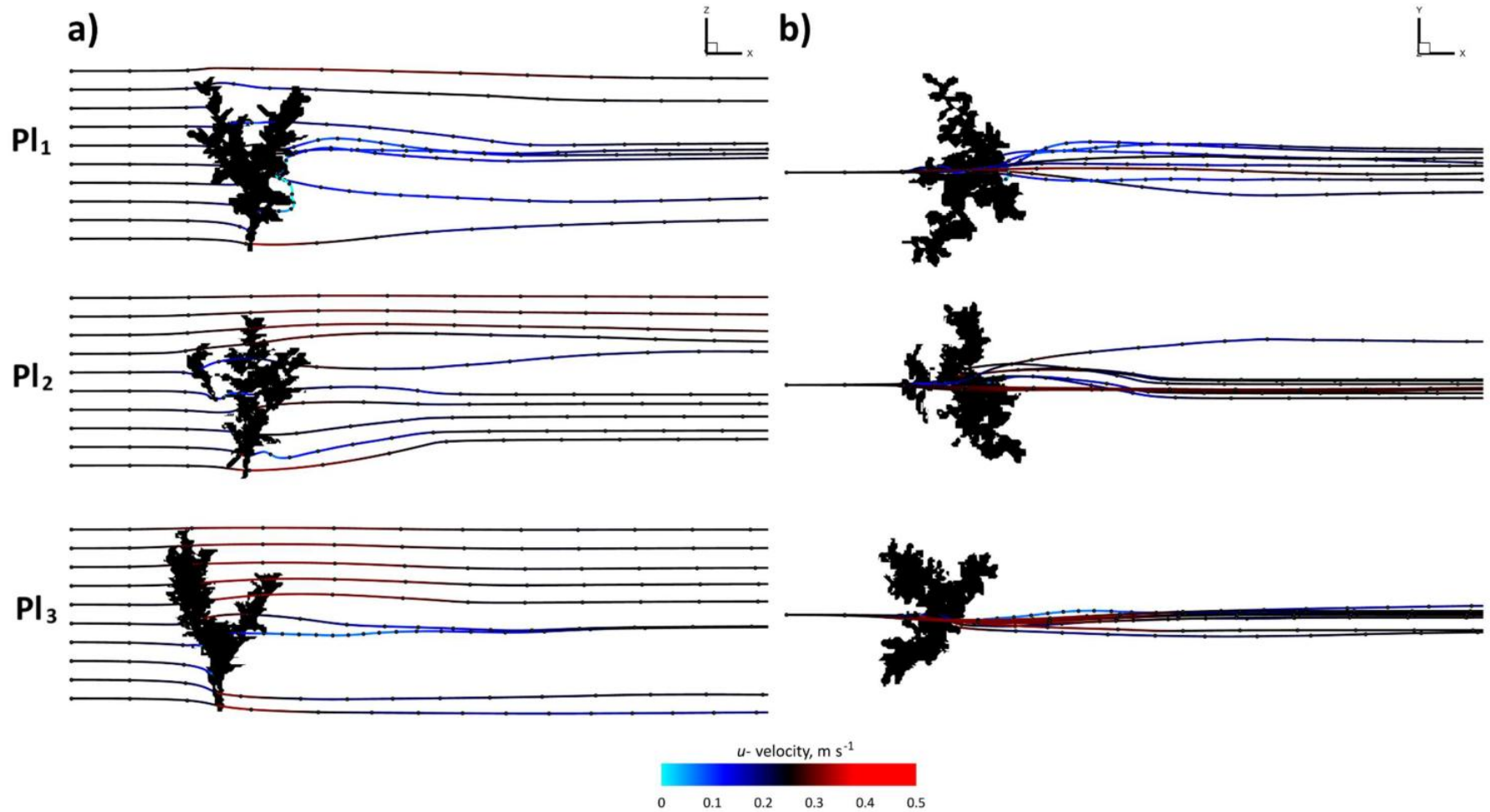
*Figure 6.39 Streamlines from the domain centreline, at incremental positions in flow depth (originating from 0.01 X/l, 0.5 Y/w, 0.1 – 0.9 Z/h) around the three* Prunus laurocerasus *specimens.  Colour change from black indicates a velocity deviation away from inlet velocity.  View is (a) horizontal in flow depth and (b) from above.*
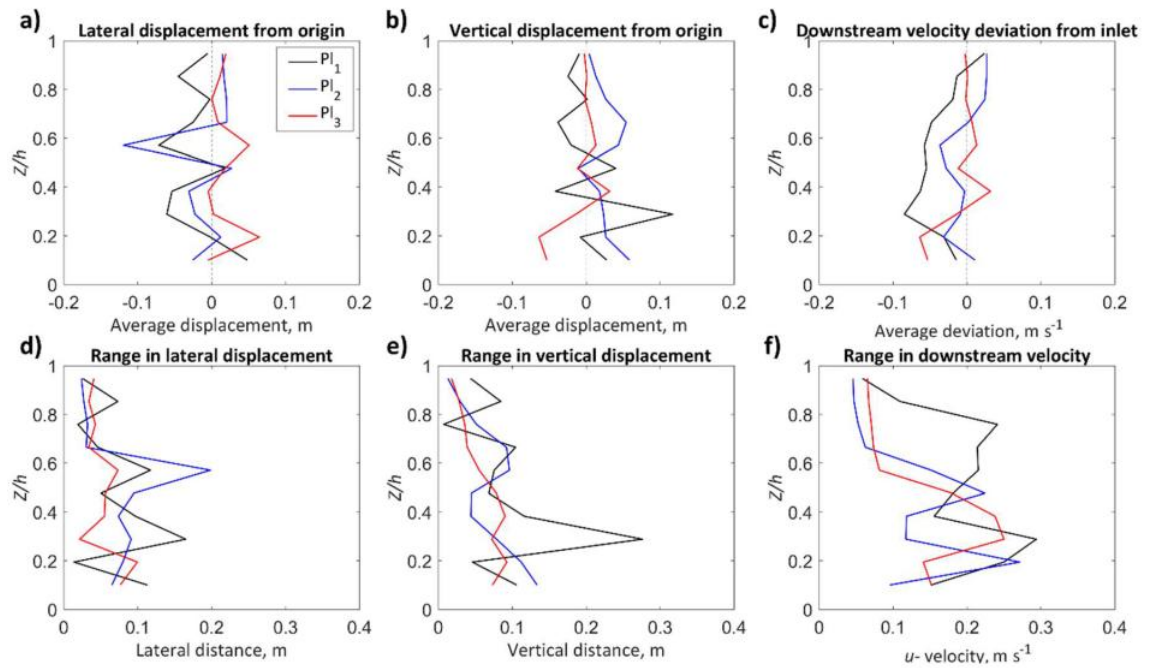
*Figure 6.40 Average lateral (a), and vertical (b) displacements from the streamline origin, downstream velocity deviation from the inlet velocity (c), range in lateral (d,) and vertical displacements (e) from the streamline origin, and the range in downstream velocity (f).*

To further investigate the differences in flow field dynamics between the three plants, the vorticity field is investigated. The mean absolute vorticity magnitudes for $Pl_1$ and $Pl_3$ (0.79 and 0.75 Hz) are slightly higher than $Pl_2$ (0.66 Hz). However, the maximum values for vorticity magnitude are highest for $Pl_2$ (216 Hz), than $Pl_1$ and $Pl_3$ (46 Hz and 59 Hz). It is expected that the spatial patterns of vorticity will also vary between plants.

To investigate these spatial patterns of vorticity, first the *uw-* vorticity for a horizontal plane at 0.5 *Y/w* is shown in Figure 6.41, with two-dimensional *uw-* flowlines overlain. For $Pl_1$, numerous thin regions of positive and negative vorticity are associated with the complex internal plant structure, and extend throughout the bulk of the flow depth. At the bed, a zone of inclined downwards, negative vorticity extends the greatest distance downstream of any plant. For $Pl_2$, a more clearly defined and spatially coherent zone of positive vorticity exists at the upper extent of the plant body, extending the greatest distance of any plant. This is arched in shape, and follows the flowlines over the top of the plant body. The flow structure is therefore indicative of shearing flow. At the bed, the zone of negative vorticity follows a similar arched shape, with flowlines deflected away from the bed. Between these, a region of high positive and negative vorticity is found, similar in structure to $Pl_2$. Finally, $Pl_3$ lacks the internal structure shown in $Pl_1$ and $Pl_2$. The region of positive vorticity at the top of the plant body is again arched, but extends the shortest distance downstream of any plant. At the bed, the region of

negative vorticity and flowlines indicate the most prominent downwards inclination towards the bed, as previously noted in Figure 6.39.
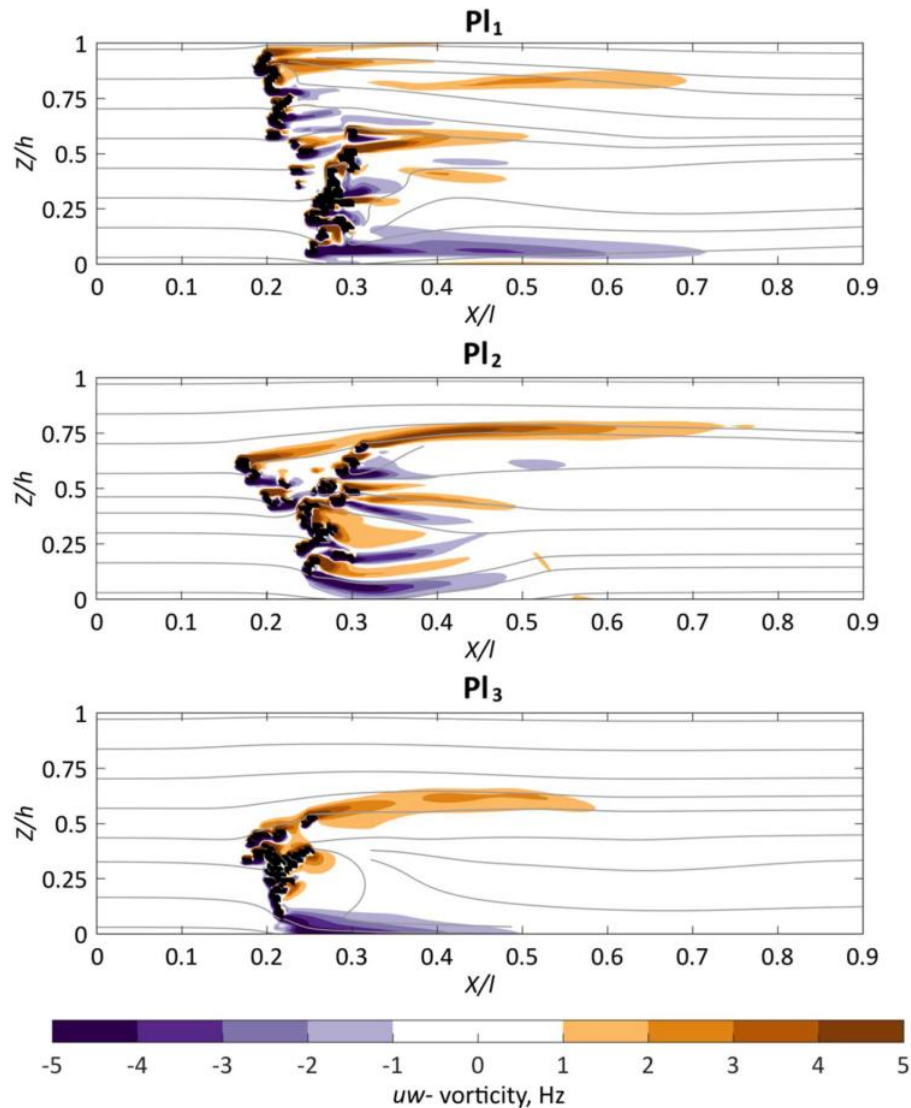


**Figure 6.41 Distribution of uw- vorticity along a horizontal plane at 0.5 Y/w. Two-dimensional uw-flowlines overlain. Flow from left to right. Orange indicate positive regions of vorticity, purple indicate negative regions of vorticity.**

Next, the *uv-* vorticity for a vertical plane at 0.5 *Z/h* is shown in Figure 6.42, with two-dimensional *uv-* flowlines overlain. For each plant, positive and negative regions of vorticity occur, with the development of largest region of vorticity at the outer edge of the plant boundary, whose position correspond with deflections to flowlines. The flow structure is indicative of flow in a junction vortex system (Simpson, 2001), as discussed in Chapter 7. For $Pl_1$, an almost symmetrical distribution of vorticity across *Y/w* is seen. This contrasts with $Pl_3$, where the region of negative vorticity associated with the left edge of the plant boundary extends ~50% further downstream than the region of

positive vorticity from the right edge. For Pl$_2$, *uv*- vorticity appears to play a smaller role than *uw*- vorticity in the generation of vortical flow structures.
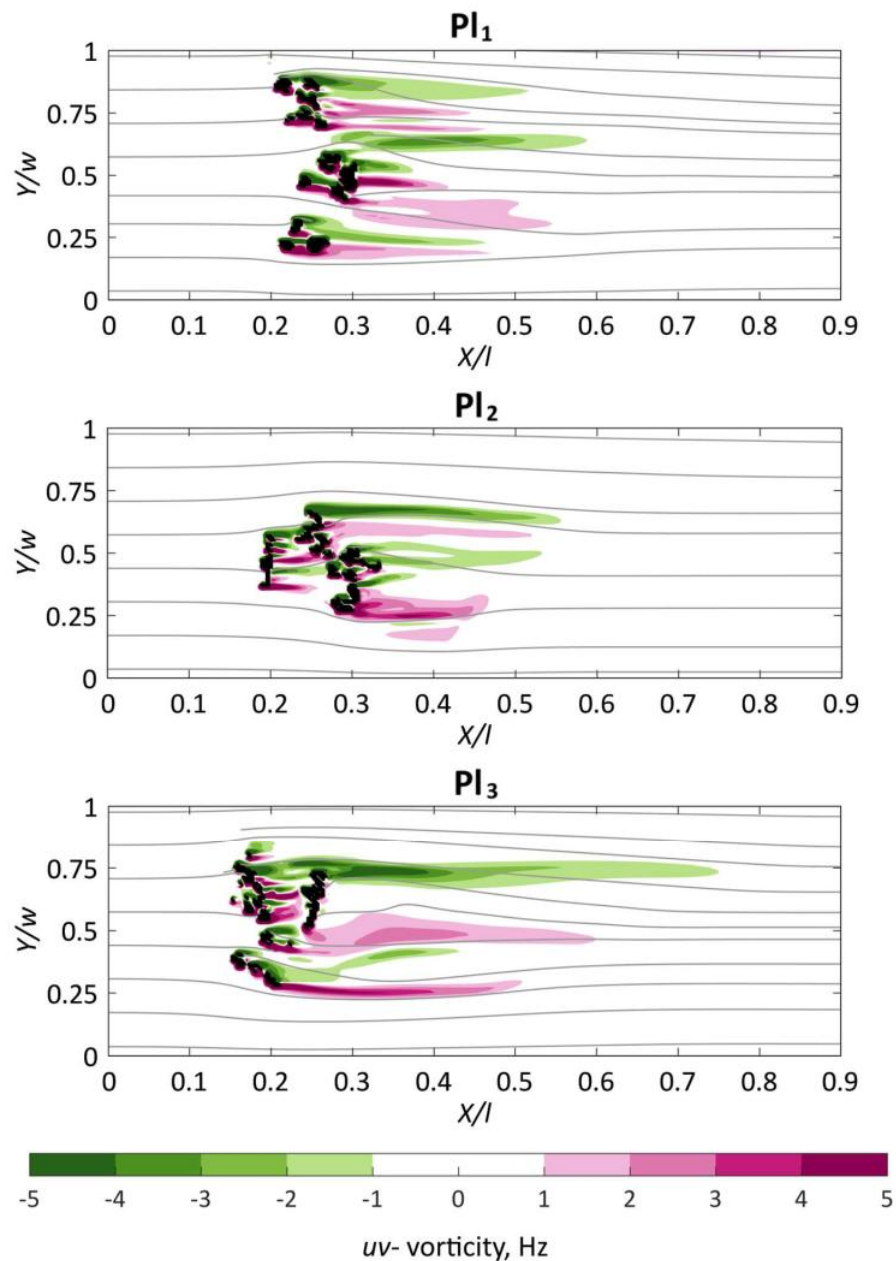


**Figure 6.42 Distribution of uv- vorticity along a vertical plane at 0.5 Z/h. Two-dimensional uv-flowlines overlain. Flow from left to right. Pink indicates regions of positive (clockwise) vorticity, green indicates regions of negative (anti-clockwise) vorticity.**

An impression of the three-dimensional turbulent structures forming around each of the plants are visualised by plotting isosurfaces of the Q criterion, again thresholded at 3.5 (Hunt *et al.*, 1988) (Figure 6.43). Volumetrically, the turbulent structures of the three plants are similar (0.110, 0.110, and 0.102 m$^3$), although the spatial distribution of the

structures differ. Like the defoliated and foliated plants (Figure 6.18), several scales of turbulence are present.

Most notable is the kölk vortex associated with the vortex tail of $Pl_2$, formed as a horseshoe vortex that has wrapped around the plant blockage, lengthened, and stretched downstream. The highly three-dimensional vortex tail is associated with the strong *uw*-vorticity at the top of the plant, and could help explain the significantly higher values of maximum vorticity recorded for this plant. In this region of the flow a strong gradient in downstream velocity is present. This results in a stronger shear layer instability forming between the low velocity wake zones and the free-stream zone above the plant body, helping explain the vortex shape. It is suggested that this plant shear layer turbulence is dominated by Kelvin–Helmholtz and Görtler-type vortices generated through shear instability (Ghisalberti and Nepf, 2002). More details of the turbulent flow structures, and the type of vortex system forming at the plant-scale, are provided in Chapter 7. For $Pl_1$ and $Pl_3$, the three-dimensional turbulent structures around the plants appear similar in shape and length, and this is to be expected given the similarities in plant volume, and the spatial distribution of solid volume fraction that have been linked to patterns of downstream velocity, *uw-* vorticity, and *uv-* vorticity.

Together, the results presented in this section outline how variation in the plant canopy morphology of natural plants can have significant implications for the three-dimensional mean flow and turbulent flow structures. The distribution of vegetal elements, which can be characterised using the spatially distributed plant solid fraction volume, act as a dominant control on flow field dynamics.
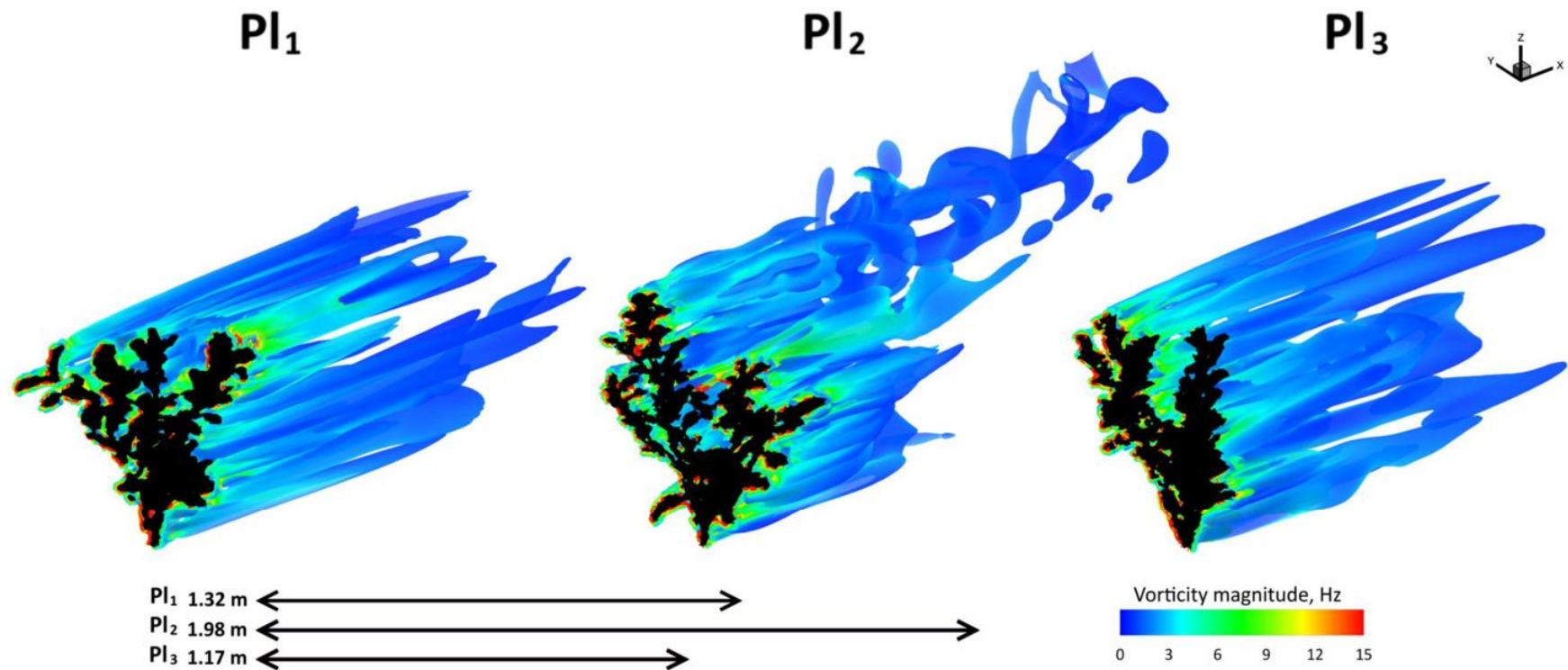
Figure 6.43 Comparison of three-dimensional structure of turbulence using the Q criterion, thresholded at 3.5, with the isosurface coloured by vorticity magnitude. Arrows compare maximum length of the mapped flow structures.

## 6.6　　　Chapter conclusions

In support of RQ4 and RQ5, this chapter has investigated the influence of plant volumetric canopy morphology on flow field dynamics. This contributes to the process-understanding of flow-vegetation interactions at the plant-scale. Key findings include:

- The 'completeness' of the plant representation influences flow field dynamics. When using TLS to capture plant volumetric canopy morphology and applying the workflow developed in Section 3.3; a single scan position represents only 54% of the plant volume represented when four scan positions were applied. The differences in the distribution of the blockage influences local flow field dynamics and the magnitude of the flow disturbance. An 'incomplete' plant representation therefore under-predicts three-dimensional mean flow (Figure 6.6 and Figure 6.7).

- Foliage is a key control on the plant volumetric canopy morphology, thereby influencing three-dimensional mean and turbulent flow. The additional volume posed by the leaf body introduces flow heterogeneity (Figure 6.9) and flow recirculation (Figure 6.15), causing downstream velocity profiles to deviate from the idealised inflected profiles that are associated with canopy flows. Rapid transition between the high velocity free-stream zone and the zone of reduced velocity in the plant wake indicates shearing of flow, with the point of reattachment ~4.5 plant lengths downstream for defoliated and foliated plants.

- Plant postural changes were simulated with the plant volume conserved. As the plant became more prone, the flow disturbance was reduced (Figure 6.24), and when fully prone the wake length was shortened (~2.5 plant lengths, Figure 6.25). Changes in plant posture influenced the spatial distribution of pressure and the pressure gradient acting on the plant surface (Figure 6.28), and this is expected to have implications for the drag response (Chapter 7).

- Plant aspect changes were simulated with the plant volume conserved. Incremental 15° changes in plant aspect influenced the shape of downstream velocity profiles (Figure 6.30), and considerably influenced the spatial distribution of TKE and therefore energy conversion (Figure 6.32 and Figure 6.33). Again, this will have implications for the drag response.

- Comparison of three *Prunus laurocerasus plants* revealed the control of plant structure and form on flow field dynamics, especially relevant to *uw-* and *uv-*vorticity (Figure 6.41 and Figure 6.42) and three-dimensional turbulent flow structures (Figure 6.43).

# Chapter 7

# Discussion: flow-vegetation interactions at the plant-scale, and implications for vegetative resistance

## 7.1    Introduction

This chapter discusses the substantive research contributions made in the thesis. For this, each of the Research Questions outlined in Section 1.3 (and repeated below) are addressed:

***RQ1 – How can plant volumetric canopy morphology be represented in a high resolution numerical model used to predict river flow?***

***RQ2 – How well does the numerical model predict measured three-dimensional mean flow?***

***RQ3 – What are the feedbacks between flow and plant motion dynamics?***

***RQ4 – How important are changes in plant posture and porosity on the three-dimensional mean and turbulent flow?***

***RQ5 – How important is plant morphology and 'how the plant looks to flow' on the three-dimensional mean and turbulent flow?***

***RQ6 – What is the dominant factor controlling the drag exerted on submerged natural plants?***

***RQ7 – What are the implications for vegetative resistance?***

First, the novel methodological developments necessary for understanding flow-vegetation interactions at the plant-scale are discussed (Section 7.2), in support of RQ1 and RQ2. The next section discusses the findings of plant motion dynamics (Section 7.3), relevant to floodplain and riparian species under river flow, in support of RQ3. Following this, a conceptual understanding of flow-vegetation interactions is presented (Section 7.4), with specific reference to the significant controls on flow field dynamics, answering RQ4 and RQ5. Flow features at the plant-scale are identified, including spatially heterogeneous velocity profiles with a sub-canopy component of flow, and the development of plant-scale shear layers. Next, the dominant factors controlling the drag response are discussed (Section 7.5), in support of RQ6. Following this, the implications for vegetative resistance are considered (RQ7), by back-calculating physically-determined Manning's *n* values (Section 7.6).

In the final section of this chapter (Section 7.7), further developments and potential applications for the research are discussed, highlighting the ways in which the research can be used. It is suggested that the novel research developed in this thesis has major implications for the modelling of flow field dynamics, sediment transport processes, and the evolution of vegetated and partially-vegetated near surface landscapes. This includes incorporating multiple plants into the CFD model, as well as dynamic plant representations that reconfigure using a biomechanical model in a time-dependent solution, and the inclusion of bed topography and sediment transport processes in the modelling framework.

## 7.2 Discussion of the methodological developments

With reference to RQ1, Chapter 3 has shown the development of the workflow used to capture the full three-dimensionality of the plant volumetric canopy morphology (Figure 3.23); using Terrestrial Laser Scanning (TLS) to capture a plant point cloud at the millimetre scale spatial resolution; post-processing the point cloud to remove erroneous data points (Figure 3.16), and applying a voxelisation procedure to retain morphological detail, but reduce the number of points (Figure 3.20). The plant volumetric canopy morphology is therefore described by regularly structured, binary occupied/unoccupied cells in the voxel space, that are readily incorporated into the CFD model. From the voxelised representation, plant structure and form has been assessed (Section 3.4), highlighting the complex spatial distribution of plant volume in floodplain and riparian plants, quantified by the spatially distributed plant solid volume fraction (Figure 3.28).

Chapter 4 described how vegetation was conceptualised in the CFD model, as a dynamically moving porous blockage (Lane and Hardy, 2002). A finite-volume solution of the Reynolds-averaged Navier-Stokes equations, using the two-equation $k - \varepsilon$ turbulence model, modified using Renormalized Group Theory (RNG), was selected as the most suitable representation of open channel flow (Section 4.2.5). This was because the time-averaged flow field was of primary interest to this thesis, providing a first step in understanding flow-vegetation interactions at the plant-scale, reducing stability issues relative to Large Eddy Simulation (LES), and allowing many simulations to be run. The RNG $k - \varepsilon$ model has been shown to outperform the standard $k - \varepsilon$ model in regions of high strain (Yakhot and Orszag, 1986), as in the shearing of flow through vegetation. A Mass Flux Scaling Algorithm (MFSA) was used to discretise the plant in the CFD model, having successfully been used to represent complex topography in previous geomorphological CFD applications. The plant was therefore represented as a grid-scale blockage in the computational domain, and treated using numerical porosity; this offered significant advantages over alternative discretisation methods, better resolving plant morphology (Figure 4.5), and providing a more stable numerical treatment (Lane *et al.*, 2002). For the first time, therefore, accurate representations of natural floodplain and riparian vegetation can be incorporated into a high resolution numerical model, used to predict river flow.

Following good practice in numerical modelling, grid independence was comprehensively addressed (Section 4.3.7.2), an essential step in showing that solutions

from the numerical model were credible. With reference to RQ2, however, model validation was also necessary. The flume experiments detailed in Chapter 5 therefore provide the requisite spatially distributed velocity validation data. Evaluation of CFD model predictions against acoustic Doppler velocimeter (aDv) measurements showed very good general agreement. The magnitude of differences between measured and modelled points on the velocity profiles were quantified using reduced major axis (RMA) regression (Figure 5.18), with *u*- velocity correlation coefficients > 0.8 (Figure 5.21). These compared favourably with previous applications of CFD to velocity profiles in open channel flows (Ferguson *et al.*, 2003; Lane *et al.*, 2004; Hardy *et al.*, 2005; Hardy *et al.*, 2011b; Sandbach *et al.*, 2012). Furthermore, to assess in detail the agreement between measured and modelled data, a shape-based similarity statistic, first proposed by Marron and Tsybakov (1995), was used to calculate the visual distance ($d_V$) between velocity profiles. The model was shown to reproduce the shape of measured velocity profiles, suggesting good process representation (Figure 5.23). By comparing the shape of measured and modelled velocity profiles, a more complete evaluation of numerical predictions were made possible. It is suggested that approach is of interest to many geomorphological applications that deal with the comparison of curves/profiles.

## 7.3        Describing plant motion dynamics

Chapter 2 introduced reconfiguration and the modes of plant motion in response to hydrodynamic loading. Traditionally, the spectrum of vegetation canopy motion in response to increasing flow speeds can be categorised into four distinct and main regimes (Section 2.3.4.1.3); erect, gently swaying, strong coherent swaying (monami, or vortex-induced vibrations for the case of a single plant), and prone (Nepf and Vivoni, 2000). To investigate the motion regime, plant motion was subdivided into a time-averaged component that is associated with shifts of the general plant posture, associated with static reconfiguration and streamlining to the mean flow (Sand-Jensen, 2003; Siniscalchi and Nikora, 2013), and a time-dynamic component that is associated with dynamic reconfiguration. The latter is thought to be related to smaller scale oscillations of the plant, associated with the instantaneous flow and correlated with drag fluctuations and upstream turbulence (Siniscalchi and Nikora, 2013). However, the current understanding of plant motion dynamics tends to be gained from idealised canopies of morphologically simple, tensile plants (Nepf and Vivoni, 2000).

Results from the experimental measurements shown in Section 5.3 demonstrate the complexity in the response of a bending type, riparian plant under flow. When tracking individual plant tips to show time-dynamic plant motion, a combination of motion regimes occurs simultaneously for a constant flow speed (Figure 5.15). This is because of the range of biomechanical properties in the plant, and the influence of the plant on the local flow (Hurd, 2000). There will be different stem widths, lengths, thicknesses, and flexural rigidities throughout the plant, all of which vary as a function of age, and therefore the drag force will affect each component differently. This will result in a range of responses to the flow, as the plant is not a single homogeneous unit (Hurd, 2000). Different parts of the plant therefore move differently under flow, but this is not a random process with respect to time and space. Some parts of the plant will respond to the flow first, while other parts of the plant will take longer to readjust and reconfigure. The ability to reconfigure to the changing flow stress therefore varies over the plant body, as shown between Tip 1 and Tip 2 at *Re* 110 000 (Figure 5.15).

Relating to the time-averaged plant motion, there is a shift in the general posture as the plant reconfigures to the mean flow. In doing so, the volumetric canopy morphology is vertically compressed and therefore the volume available for flow to pass through the plant (i.e. porosity of the plant) is reduced (Figure 5.16, Table 5.2). When time-dynamic

motion is analysed, the oscillatory motion is *Re* and location dependent. This results in up to an 18% reduction in plant height, a 14% increase in plant length, and a doubling of the lead and lee angles of the plant body.

If plant motion dynamics for bending type, riparian plants were similar to tensile type, in-channel plants, the plant would demonstrate coherence of plant motions, coupled to strong oscillations in flow velocity as is shown for large scale canopy flow processes (Ghisalberti and Nepf, 2006; Okamoto and Nezu, 2009; Okamoto *et al.*, 2016) where instantaneous motion is closely related to the passage of large scale eddies that interact with the plant (Siniscalchi and Nikora, 2012). This would make the plant motion predictable. In the *Re* range 89 000 – 110 000, an inverse harmonic relationship between plant height and plant length was shown (Figure 5.14), indicating some coherence in the plant response. However, because floodplain and riparian plants are not single homogenous units (Hurd, 2000), the overall plant motion dynamics were more complex, and shown to vary across the single plant body (Figure 5.15 and Figure 5.16). Locally, some parts of the plant move more than others. This is because a range of vegetal elements contribute towards plant volumetric canopy morphology (branches, stems, and leaves), each with different properties relating to age (e.g. thicknesses, lengths, flexural rigidities), each exposed differently to the flow, and influencing flow locally. These findings highlight the difficulty in predicting motion dynamics for floodplain and riparian plants, as exemplified by Weissteiner *et al.* (2015) who show that plant structural properties can control the extent of plant compression during reconfiguration.

## 7.4 Conceptualising flow-vegetation interactions at the plant-scale

### 7.4.1 The importance of plant porosity

Results from Chapter 5 and 6 have shown the importance of the plant volumetric canopy morphology in controlling flow field dynamics. Throughout this thesis, the plant has been conceptualised as a porous blockage, allowing the passage of flow through gaps or conduits in the canopy. This porosity is especially important when considering plant motion dynamics, as shifts in the time-averaged plant posture towards a dynamic equilibrium position results in a vertical compression of the plant volumetric canopy morphology, reducing the plant porosity as vegetal elements such as stems and leaves are forced closer together under hydrodynamic loading.

For the *Hebe odora* plant shown in Chapter 5, as hydrodynamic loading increased (and so plant porosity was reduced), the wake length decreased from ~3.9 plant lengths at *Re* 65 000, to ~3.1 plant lengths at *Re* 110 000 (Figure 5.26), but modelled vortices migrated further downstream as the shear instability grew stronger (Figure 5.29 - Figure 5.31). Analysis of the three-dimensional mean flow explained this, showing that the plant does not behave as a classic bluff body (Schnauder *et al.*, 2007), instead tending towards porous media flow (Yagci *et al.*, 2010), with penetration of fluid through gaps in the canopy resembling bleed-flow (Raine and Stevenson, 1977). For a porous object, de Lima *et al.* (2015) define bleed-flow as the flow that penetrates through the body into the wake, delaying the onset of the von Karman vortex street. Wake behaviour in porous obstacles depends on the body shape and void space (Huang and Keffer, 1996).

To quantify the effect of porosity further, in this section the three-dimensional mean and turbulent flow around porous plant representations are compared against fully impermeable plant representations, where gaps and conduits in the canopy have been closed. This is undertaken for the *Hebe odora* and *Prunus laurocerasus* plants from previous chapters.

Fully impermeable plant representations are produced by application of the slice-wise convex hull algorithm (Fernández-Sarría *et al.*, 2013), as introduced in Section 3.2.2.2. This closes all gaps and conduits in the canopy interior, providing a plant representation that is fully impermeable. The same process is repeated for the *Prunus laurocerasus*

plant. Porous and impermeable plant representations are incorporated and co-located in the CFD model, allowing the three-dimensional mean and turbulent flow to be exactly compared.
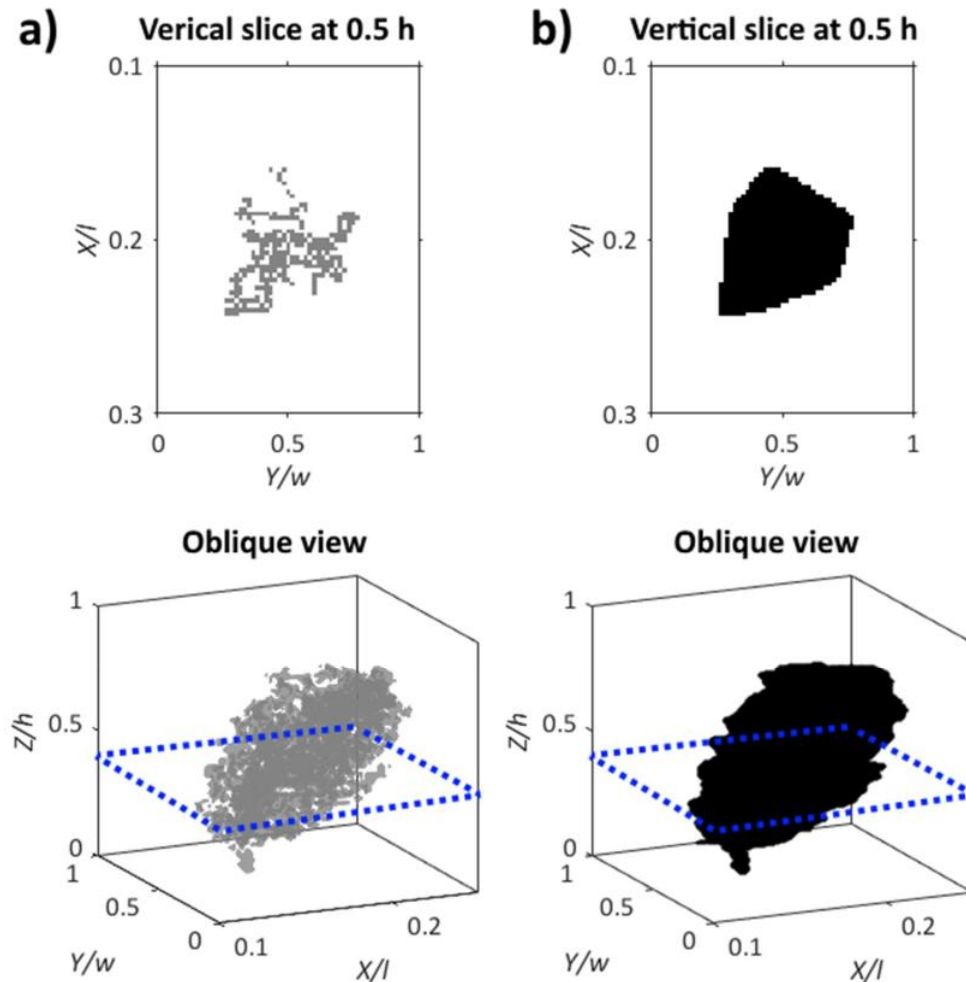


*Figure 7.1 Comparison of the (a) porous and (b) impermeable Hebe odora plant representations following application of the slice-wise convex hull algorithm, shown at 0.5 h and obliquely. The blue dashed box indicates the slice from which the 0.5 h view was taken.*

For the porous and impermeable *Hebe odora* representations, differences in three-dimensional mean flow are shown in Figure 7.2 at 0.5 *Y/w*, and calculated over the entire model domain in Table 7.1. The wake zone, defined as < 0.5 of inlet velocity (as previously used in Section 6.3.2), is larger and extends further downstream when the plant is porous. At 0.5 *Y/w*, maximum wake length is ~10% greater and wake area is ~25% greater than when the plant is impermeable. When considering the entire model domain, the porous wake volume is ~20% greater than the impermeable wake volume. However, close to the plant blockage, the magnitude of the velocity reduction in the wake is locally greater when the plant is impermeable (Figure 7.2b, 0.25 *X/l*). The

structure and magnitude of the wake has important implications for the shape of velocity profiles shown in Figure 7.2b. For the impermeable representation, the wake zone is positioned higher in the flow depth, with a considerable zone of flow acceleration (defined as > 1.1 of inlet velocity, as previously used in Section 6.3.2) in the sub-canopy region beneath the wake. The zone of flow acceleration is ~35% greater in volume when the plant is impermeable, indicating that more flow is being forced around and beneath the plant blockage, and this will have implications for reattachment, vorticity, and the von Karman vortex street.

The structure of *uw-* streamlines in Figure 7.2a differ between porosities. When the plant is impermeable, sub-canopy flow streamlines are initially directed towards the bed in the near-plant region, and then inclined upwards away from the bed further downstream. This modifies the shape of the wake, inclining the wake upwards towards the surface. When the plant is porous, forcing of flow through gaps and conduits in the plant blockage becomes more important, with disturbances to the streamlines indicating the internal flow dynamics. Maximum and minimum spanwise (*v-*) and vertical (*w-*) velocities are greater when porous, and combined with the greater spatial heterogeneity in velocity profiles, this results in greater complexity of the three-dimensional mean flow for the porous *Hebe odora* plant.
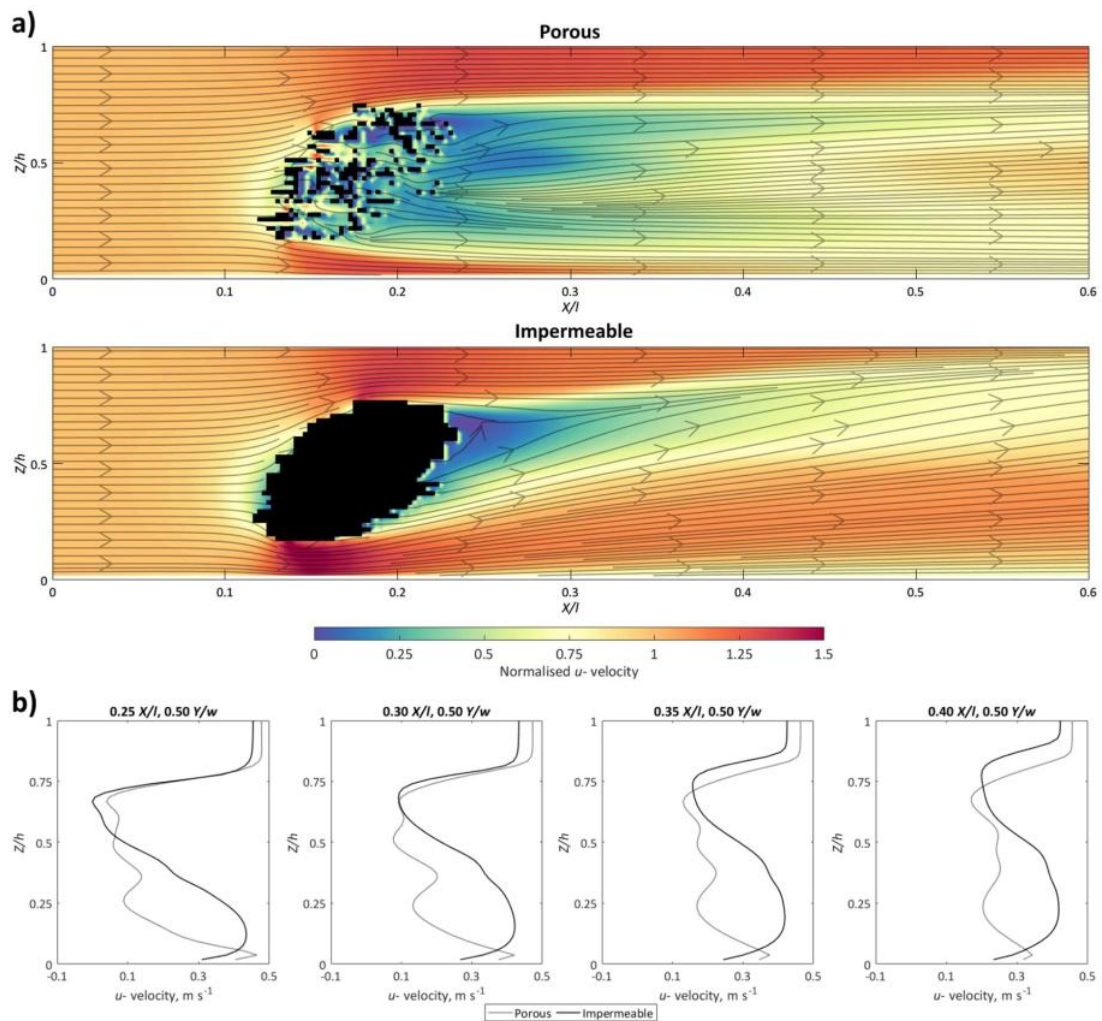
*Figure 7.2 (a) Comparison of normalised u- velocity with uw- streamlines overlain at 0.03 Z/h intervals for the porous and impermeable Hebe odora plant at 0.5 Y/w and (b) u- velocity profiles to show the shape and magnitude of the downstream velocity field with distance from the plant (0.2 – 0.4 X/l). The inlet velocity is set to 0.37 m s⁻¹.*

For the porous and impermeable *Prunus laurocerasus* plant representations, differences in three-dimensional mean flow are shown in Figure 7.3 at 0.5 *Y/w*, and over the entire model domain in Table 7.1. Several similarities are shown with the porous and impermeable *Hebe odora* plant representations. Again, wake length, wake area, and wake volume are greater when the *Prunus laurocerasus* is porous; with the wake positioned higher in the flow depth when the plant is impermeable. The zone of flow acceleration is substantially larger when impermeable, ~150% greater in volume than when the plant is porous, and again this indicates that a greater portion of the flow is being forced around and beneath the impermeable plant blockage. Again, flow complexity is greater when the plant is porous, with substantial flow recirculation in the wake shown by the *uw-* streamlines in Figure 7.3a, and overall a greater spatial heterogeneity in the velocity profiles are introduced (Figure 7.3b). For both plant porosities, rapid gradation between the free-stream zone and the wake zone results in

the formation of a shear layer, although this is positioned higher in the flow depth when the plant is impermeable.



*Figure 7.3 (a) Comparison of normalised u- velocity with uw- streamlines overlain at 0.03 Z/h intervals for the porous and impermeable Prunus laurocerasus plant and (b) u- velocity profiles to show the shape and magnitude of the downstream velocity field with distance from the plant (0.25 – 0.4 X/l). The inlet velocity is set to 0.25 m s⁻¹.*
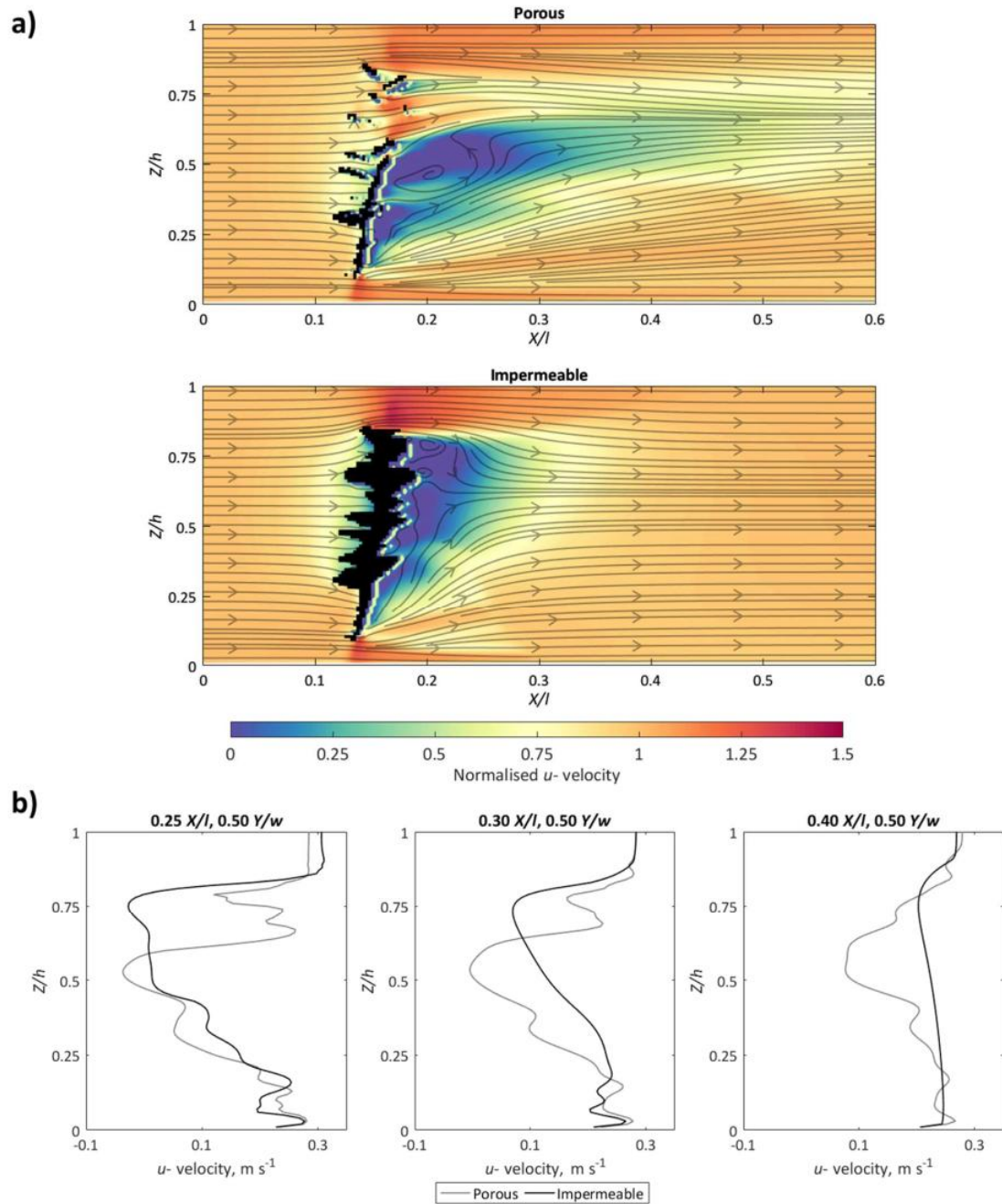
*Table 7.1 Comparison of three-dimensional mean flow between porous and impermeable plants.*

| | *Hebe odora* (inlet velocity = 0.37 m s⁻¹; *Re* 110 000) | | | *Prunus laurocerasus* (inlet velocity = 0.25 m s⁻¹; *Re* 88 000) | | |
|---|---|---|---|---|---|---|
| | Porous | Impermeable | % Change | Porous | Impermeable | % Change |
| Maximum *u*- velocity (m s⁻¹) | 0.639 | 0.655 | -3 | 0.443 | 0.444 | 0 |
| Minimum *u*- velocity (m s⁻¹) | -0.212 | -0.119 | 44 | -0.145 | -0.098 | 32 |
| Maximum *v*- velocity (m s⁻¹) | 0.536 | 0.524 | 2 | 0.310 | 0.366 | -18 |
| Minimum *v*- velocity (m s⁻¹) | -0.484 | -0.422 | 13 | -0.360 | -0.354 | 1 |
| Maximum *w*- velocity (m s⁻¹) | 0.695 | 0.362 | 48 | 0.433 | 0.351 | 19 |
| Minimum *w*- velocity (m s⁻¹) | -0.753 | -0.350 | 54 | -0.264 | -0.249 | 5 |
| Wake length at 0.5 *Y/w* (m) | 0.570 | 0.520 | 9 | 1.280 | 0.650 | 49 |
| Wake area at 0.5 *Y/w* (m²) | 0.061 | 0.046 | 24 | 0.335 | 0.286 | 15 |
| Wake volume (m³) | 0.007 | 0.006 | 21 | 0.093 | 0.074 | 21 |
| Flow acceleration volume (m³) | 0.040 | 0.054 | -36 | 0.061 | 0.150 | -146 |

*Table 7.2 Comparison of turbulent flow between porous and impermeable plants.*

| | *Hebe odora* (inlet velocity = 0.37 m s⁻¹; *Re* 110 000) | | | *Prunus laurocerasus* (inlet velocity = 0.25 m s⁻¹; *Re* 88 000) | | |
|---|---|---|---|---|---|---|
| | Porous | Impermeable | % Change | Porous | Impermeable | % Change |
| Mean turbulent kinetic energy (m² s²) | 0.073 | 0.072 | 1 | 0.032 | 0.032 | 1 |
| Maximum turbulent kinetic energy (m² s²) | 0.402 | 0.234 | 42 | 0.164 | 0.117 | 29 |
| Mean positive *uv*- vorticity (Hz) | 2.259 | 2.172 | 4 | 0.268 | 0.143 | 46 |
| Mean negative *uv*- vorticity (Hz) | -0.922 | -0.697 | 24 | -0.157 | -0.119 | 24 |
| Maximum *uv*- vorticity (Hz) | 87.212 | 119.669 | -37 | 38.936 | 32.734 | 16 |
| Minimum *uv*- vorticity (Hz) | -131.835 | -132.786 | -1 | -42.332 | -43.957 | -4 |
| Mean positive *uw*- vorticity (Hz) | 2.163 | 1.676 | 23 | 0.309 | 0.174 | 44 |
| Mean negative *uw*- vorticity (Hz) | -2.267 | -2.032 | 10 | -0.310 | -0.268 | 13 |
| Maximum *uw*- vorticity (Hz) | 94.397 | 96.967 | -3 | 31.655 | 35.052 | -11 |
| Minimum *uw*- vorticity (Hz) | -95.168 | -97.310 | -2 | -34.065 | -36.160 | -6 |
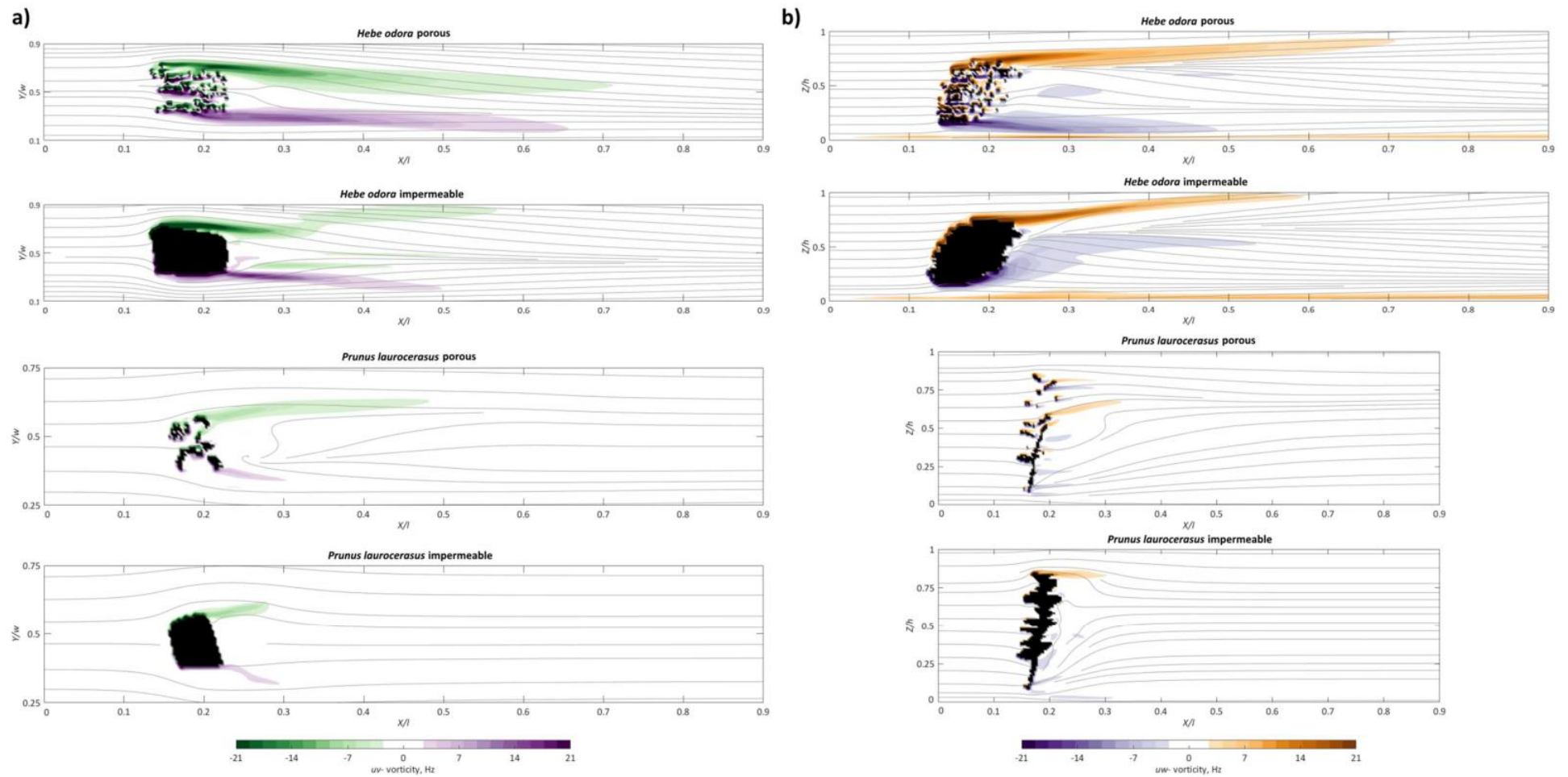
***Figure 7.4 (a) Comparison of uv- vorticity at 0.5 Z/h with uv- streamlines at 0.08 Y/w intervals and (b) uw- vorticity at 0.5 Y/w with uw- streamlines at 0.08 Z/h intervals, for the porous and impermeable representations of both plants.***

Summary statistics of turbulent flow through and around the porous and impermeable plant representations are shown in Table 7.2, with *uv*- vorticity at 0.5 *Z/h* shown in Figure 7.4a, and *uw*- vorticity at 0.5 *Y/w* shown in Figure 7.4b. The figures demonstrate the presence of vortex sheets attached to the outside of the plant blockages, both porous and impermeable. Mean turbulent kinetic energy (TKE) is comparable between the porous and impermeable plants; however, maximum TKE is considerably higher (~40 and ~30%) when the plants are porous. For both *uv*- and *uw*- vorticity, mean positive and negative values are greater when porous, although the maximum and minimum vorticity values tend to be greater when the plants are impermeable, indicating a greater intensity of the vortices. Figure 7.4 shows that for the impermeable plant, the regions of highest vorticity are smaller in size, and distributed more proximal to the plant, whereas for the porous plant these regions of highest vorticity are larger in size, and extend further downstream. Combined, Table 7.2 and Figure 7.4 suggest that the magnitude of *uv*- and *uw*- vorticity is greater close to the impermeable plant, but the region of high vorticity extends further downstream when the plant is porous.

These findings support Schnauder *et al.* (2007), who measured flow around an emergent *cupressus macrocarpa* plant under porous and impermeable states. The *cupressus macrocarpa* plant was selected by Schnauder *et al.* (2007) to represent solitary bush-like floodplain vegetation, but differed from the species' investigated in this thesis as it had fine needle-like branches, rather than leaf dominated branches/stems. Flume experiments were first carried out on the *cupressus macrocarpa* plant when it was fully porous, and then when it was fully impermeable having wrapped the plant in cling-film to retain the morphology, but modify the porosity. Schnauder *et al.* (2007) showed the wake length increased when the plant was porous, and reported stronger shear instabilities when the plant was impermeable. However, unlike results shown in this section, the TKE was significantly lower for the porous plant. This difference is explained by the emergent conditions under which the experiments of Schnauder *et al.* (2007) took place. When the plant is submerged, as in this thesis, an additional vertical interface exists between the free-stream zone and the low velocity wake zone, as well as the horizontal interfaces at the outside of the plant, and this contributes further towards the TKE response.

Similarities are also drawn with results from numerical models around regularly arranged arrays of rigid cylinders, used to resemble obstacles of different porosity (Figure 7.5). Nicolle and Eames (2011) showed that a stable wake formed behind cylindrical

obstacles with moderate porosities, stabilised by bleed-flow, with the formation of vortex sheets on the outside of the array that eventually rolled up to form a von Karman vortex street (labelled, Figure 7.5b). The critical distance downstream where the vortex sheets became unstable, forming the von Karman street, depended on the strength of the bleed-flow. As the array became more impermeable, the strength of bleed-flow was reduced, thereby reducing the critical distance. Wake length therefore decreases when the array becomes more impermeable (Figure 7.5c), meaning that flow patterns become typical of those shown by a single bluff cylinder (Figure 7.5d). Zong and Nepf (2012) also reported a strengthening of the von Karman vortex street as the array became more impermeable. However, such examples consider only geometrically simple, regular arrays. Given that wake behaviour depends on the body shape and void space (Huang and Keffer, 1996), the response in natural plants with additional morphological complexity and non-regular gaps and conduits will be further complicated.
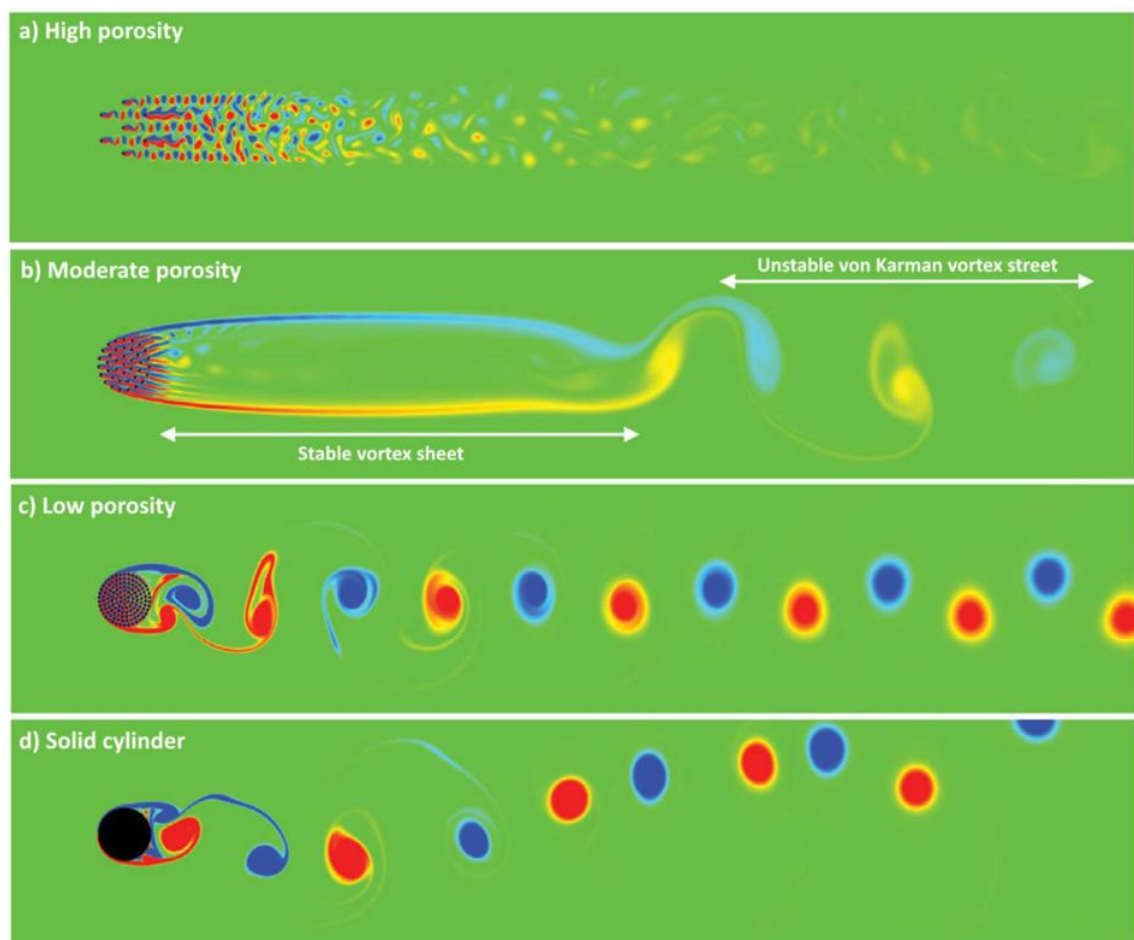


*Figure 7.5 (a-d) Comparison of uv- vorticity around arrays of rigid cylinders (black circles) with decreasing porosity, red and blue areas are positive and negative vorticities, green is irrotational fluid. The stable vortex sheet and the unstable von Karman vortex street are labelled for the moderate porosity (b), from Nicolle and Eames (2011).*

By explicitly representing plant volumetric canopy morphology in a CFD model, and extending analysis to consider fully impermeable plant representations, the influence of porosity on the three-dimensional mean and turbulent flow has been quantified (Figure 7.2 and Figure 7.3). Results support those obtained from flume experiments using real vegetation, and numerical experiments using rigid arrays of cylinders; bleed-flow through the porous plant blockages imparts a substantial control on mean and turbulent flow structure. Bleed-flow is responsible for the lengthening of the wake, thereby extending the shear instability that forms at the vertical and horizontal interfaces of the plant blockage. This causes a lengthening of turbulent flow structures, namely the vortex sheet, and results in higher values in the TKE response for the plant morphologies investigated here. Although the shear instability is stronger when the plant is impermeable, a smaller wake is formed, with the shear instability and turbulent structures unable to extend as far downstream.

Overall, key differences emerge in the three-dimensional mean and turbulent flow between porous and impermeable plant representations, with bleed-flow through gaps and conduits in the canopy responsible for lengthening the wake, and modifying shear interactions at the vertical and horizontal interfaces of the submerged porous plant blockage. Similarities are drawn with previous flume experiments around natural plants and numerical models that used rigid arrays of cylinders to resemble porous obstacles. However, it is important to note that flow through and around natural plants differs from geometrically simple blockages because of the additional complexity introduced by the plant volumetric canopy morphology, due to the spatial distribution of vegetal elements. Quantitative differences in plant volumetric canopy morphology therefore impart a control on flow field dynamics, and it is likely that even within a particular species differences in porosity would lead to differences in the flow field response. Furthermore, natural plants are highly complex and three-dimensional, and 'how the plant looks to flow' will introduce additional spatial heterogeneity into the flow field, as discussed in the next section.

## 7.4.2      The importance of foliage, plant aspect, and plant posture

The influence of foliage was quantified for the *Prunus laurocerasus* plant following the removal of leaves, with the volume of the blockage approximately four times greater when the plant was foliated (Figure 3.25). The presence of foliage influences the volumetric canopy morphology, but also influences 'how the plant looks to flow'.

Section 3.4 quantified the differences in the plant structure between the defoliated and foliated plants. When defoliated, a peak in volume was seen around the main branching point of the plant, but when foliated, much of the volume was distributed beyond this branching point, associated with the leaf body (Figure 3.26). Section 6.3 quantified the effect of these structural differences on the three-dimensional mean and turbulent flow field.

For defoliated and foliated plants, spatially heterogeneous velocity profiles were modelled (Figure 6.10), with the wake region closely associated with peaks in the plant volumetric canopy morphology, extending between ~4.4 and ~4.8 plant lengths downstream (Figure 6.11). Downstream velocity reductions were greatest when the plant was foliated, associated with the greater momentum absorbing area of the vegetal elements (Wilson *et al.*, 2003). Furthermore, when foliated the volume of the wake zone was four times greater, and the volume of the flow acceleration zone an order of magnitude greater, indicating a greater flow disturbance introduced by the larger volume of the foliated blockage. The presence of foliage was shown to influence modelled streamlines, introducing streamline deflection and recirculation around the leaf body (Figure 6.13). Beyond the branching point, the presence of foliation had major implications for turbulent flow structures, with a lengthening, widening, and thickening of regions of the vortex sheets (Figure 6.17). Furthermore, a larger zone of high TKE around the foliated plant was indicative of a greater form drag contribution (Wilson *et al.*, 2008). Turbulent flow structures therefore scale with the thickness of the vegetal elements. With the explicit representation of foliage, represented as a grid-scale blockage in the CFD model, an improved process-understanding has therefore been derived. In doing so, this improves upon previous modelling approaches that have attempted to represent foliage as a porous sub-domain around defoliated branches (e.g. Endalew *et al.*, 2011).

These findings have important implications for the flow field dynamics with seasonal changes in foliage. However, these changes are not limited to floodplain and riparian plants, as the form and volume of in-channel vegetation also varies over seasonal cycles (Thomas *et al.*, 2016), with temporal development of vegetation cover and the vegetative blockage factor influential for local flow velocity and channel resistance (Green, 2005a). Furthermore, foliage has implications for plant motion dynamics, where the level of plant bending moderately increases with the level of foliage (Jalonen and Järvelä, 2014). This additional flow-vegetation interaction further increases the complexity in response

of floodplain and riparian plants under flow, linking together plant structure and the flow response.

In the experiment where the plant was rotated in the flow at 15° increments, Section 6.4.2 showed the significance of plant aspect on flow field dynamics. With each rotation the plant volume remained constant, changing only how the plant was presented to flow. With incremental changes in plant aspect, the shape of velocity profiles differed, specifically the position and magnitude of the velocity minima (Figure 6.30). This is explained by changes in the exposure of vegetal elements to the flow (Hurd, 2000), with upstream elements extracting energy from the flow (Marjoribanks *et al.*, 2014a), and thereby providing a localised sheltering effect. Over the full range of plant aspects investigated, the wake volume ranged by ~25% when defoliated, and ~50% when foliated, with wake volumes greatest when the plant was aligned most perpendicular to flow (Figure 6.31). The effect of alignment was also reflected in the TKE field, with regions of highest TKE displaced laterally away from the plant blockage when the plant was aligned perpendicular to the incident flow (Figure 6.32 and Figure 6.33). When aligned more parallel, regions of highest TKE were constrained by the outer extent of the plant blockage. Changes in how the plant was presented to the flow therefore influenced the flow field dynamics. To the author's knowledge, this has not yet been investigated in the field, but plant orientation could have important implications for flow-vegetation interactions on gravel bar structures.

Similarities are drawn with flow around impermeable, surface-mounted cuboidal blockages, positioned either face-on or edge-on to the incident flow. When face-on, a large portion of the kinetic energy in the incident flow is extracted through form drag. However, when the cube is edge-on, much of this kinetic energy is retained, with streamlines compressed and flow accelerated around the outside of the blockage (Lee and Soliman, 1977). The perpendicular alignment of the plant is therefore analogous to the edge-on orientation of the cube. When an impermeable, surface-mounted cuboidal blockage is rotated from face-on to edge-on, the spatial patterns of erosion substantially change (Figure 7.6). In aeolian flows, McKenna-Neuman *et al.* (2013) show that when the cube is rotated to edge-on, fluid momentum increasingly spills around the blockage edges. This substantially extends and stretches vortex tails in the leeward direction, resulting in substantial erosion from the vortices that have formed (Sutton and McKenna-Neuman, 2008; Bauer *et al.*, 2013). When face-on, however, the spatial extent of erosion is smaller, with very limited erosion in the lee of the blockage. Significant

variation in sediment removal has therefore been reported with changes in obstacle orientation. Although the flow processes do not transfer directly from impermeable blockages to permeable blockages (Section 7.4.1), plant aspect does exert a primary control on flow field dynamics, will have considerable implications for flow resistance (Section 7.5.1.4), and is expected to exert an influence on sediment transport processes.
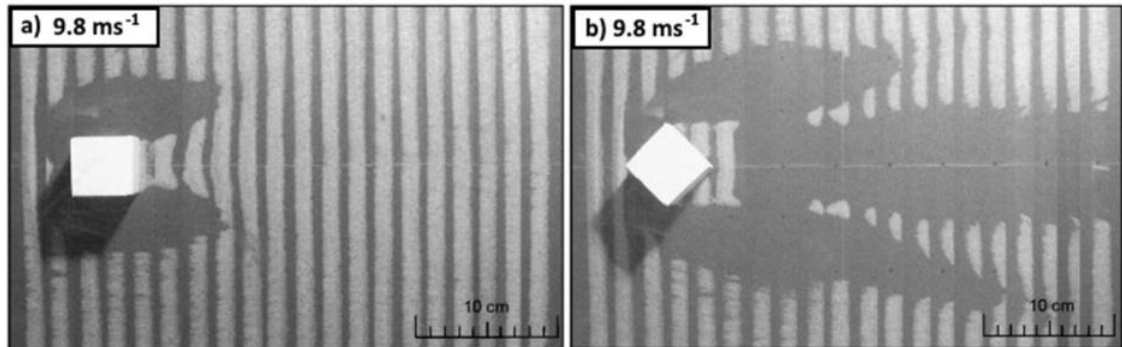


*Figure 7.6 Patterns of sand strip erosion around (a) a face-on cube and (b) an edge-on cube; with the cube volume held constant, inlet airflow velocity held constant to 9.8 m s⁻¹, and flow from left to right, from McKenna-Neuman et al. (2013).*

Plant posture exerts a further control on flow field dynamics. For the *Hebe odora* plant in Chapter 5, measurements show that as the plant is shifted lower in the flow depth with increasing $Re$, so is the trailing edge of the wake (Figure 5.25). Model predictions where the *Prunus laurocerasus* plant was hinged to the bed in Section 6.4.1 further support this finding. The difference in wake structure with changes in plant posture has previously been shown when representing *Salix spp.* stands either as vertical obstacles to flow, or as obstacles in bending, where Wilson *et al.* (2005) showed velocity profiles substantially change as modelled riparian plant stands diverge from the upright.

The range of plant postures simulated in this thesis represent the transition of a plant from upright towards a fully prone posture, as would be expected immediately before uprooting (Nepf and Vivoni, 2000). For the *Prunus laurocerasus* plant, the wake volume varies by ~33% over the range of postures modelled (Figure 6.25), and when wake length is normalised by plant length, as the plant becomes more prone the maximum wake length decreases from ~4.5 to ~2.5 plant lengths. Furthermore, as the plant becomes more prone, the shear layer that forms between the wake zone and sub-canopy flow region becomes flatter, losing the inclined shape that characterised the upright plant posture (Figure 6.24). The flow field is therefore modified with changes in plant posture. Similarities are noted with results from Marjoribanks *et al.* (2017), who modelled a dynamically moving, geometrically simple plant canopy in which individual vegetation

elements moved independently, and compared this to a semi-rigid canopy where the individual elements remained mainly upright. When the canopy is highly flexible, the individual elements shift into a prone position; and it is this plant motion that results in the shear layer becoming less clearly defined, adding greater complexity to the turbulent flow structures.

Changes in plant posture are also shown to influence the spatial distribution of pressure acting on the upstream end of the plant (Figure 6.28). Pressure is highest at the first point of contact with the plant, with energy dissipation preferentially occurring in this zone. As the plant becomes more prone, the zone where energy dissipation takes place is positioned lower in the flow depth. Postural changes therefore strongly influence the pressure distribution, with the implications for drag examined in Section 7.5.1.3.

The plant structure and form exerts a primary influence on the three-dimensional mean and turbulent flow. This is shown in Section 6.5, with the flow field modelled around three plants of the same species, resulting in broadly similar three-dimensional mean flow (Figure 6.37 and Figure 6.38), but considerable differences in vorticity characteristics and turbulent flow structures (Figure 6.43). The volumetric canopy morphology and porosity of the blockage is crucial in influencing the flow field dynamics. It is the combination of these factors that influences the three-dimensional mean and turbulent flow at the plant-scale.

### 7.4.3      Flow features at the plant-scale

Several flow features have been consistently identified across the *Hebe odora* and *Prunus laurocerasus* plants. These interlinked flow features are categorised into the spatial heterogeneity of velocity profiles, in addition to plant-scale shear layers and turbulent flow structures.

#### 7.4.3.1      Spatially heterogeneous velocity profiles: the significance of the sub-canopy flow component

Flume measurements and numerical model predictions around both plant species show spatially heterogeneous velocity profiles (in the vertical direction), deviating from the inflected profiles that have been used to characterise flows through vegetation. A region of sub-canopy flow acceleration beneath the bulk of the plant blockage has been highlighted, and this is responsible for interacting with, and inclining upward, the low

velocity wake zone; resulting in a spatially complex and three-dimensional wake structure. This feature is a key source of heterogeneity in the velocity profiles behind floodplain and riparian plants. The sub-canopy flow component is present even when the plant is defoliated, although the magnitude of sub-canopy flow increases when the plant is foliated, as the leaf body effectively forces more flow towards the bed, and is further exemplified by the impermeable plant blockage (Figure 7.2 and Figure 7.3), which results in a stronger sub-canopy flow component.

Although consistently identified as a key flow feature throughout this thesis, sub-canopy flow has rarely been identified in the literature, and has yet to be modelled in high resolution. For shrubs with an open area beneath the primary leaf mass, Freeman *et al.* (2000) and Schnauder and Moggridge (2009) hypothesise flow to be significantly diverted beneath the canopy (Figure 7.7). However, very few data exist to describe these velocity profiles (Horn and Richards, 2008).
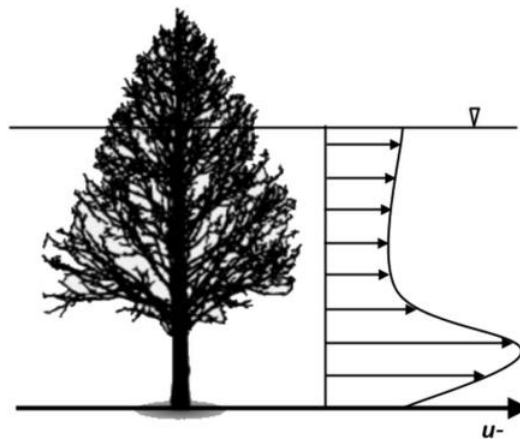


*Figure 7.7 Hypothetical velocity profile through an emergent tree (redrawn from Freeman et al., 2000).*

In the field, Bölscher *et al.* (2005) used an upward-pointing acoustic Doppler current profiler (aDcp) to measure flow velocities around a *Salix spp.* dominated floodplain on the Upper River Rhine between 2000 and 2002. The floodplain frequently flooded, with floodplain inundation recorded for 43 days in 2000, 142 days in 2001, and 91 days in 2002. Velocity profiles were collected through time, recording for the duration of individual flood events (Figure 7.8 shows a typical event between 11/08/2002 – 13/08/2002, maximum water level 2.75 m). At these water levels, the tree canopy became inundated and so retarded flow in the region > 1.5 m above the bed (> 0.55 $Z/h$), and it is below this that the sub-canopy flow component is most substantial.

Throughout the flood event, peak velocity was distributed ~0.9 – 1.2 m above the ground (0.33 – 0.44 $Z/h$), in the sub-canopy region. For the area dominated by *Salix spp.,* mean surface velocities were always less than the mean velocity recorded in the sub-canopy region. The sub-canopy region introduces considerable spatial heterogeneity into the velocity profiles, and so velocity profiles substantially deviate from the logarithmic velocity profiles measured in grassed areas during the same flood event. The field data of Bölscher *et al.* (2005) also allows seasonal changes in vegetation to be detected in the flow field response, with up to a 9% change in mean velocity between August 2002 and November 2002 measured for the flood events with the same peak in maximum water level. This difference in mean velocity is explained by changes in the amount and density of vegetal elements. The spatial heterogeneity of velocity profiles, and specifically the sub-canopy component of flow has been reproduced well by the flume measurements and numerical model predictions made in this thesis.
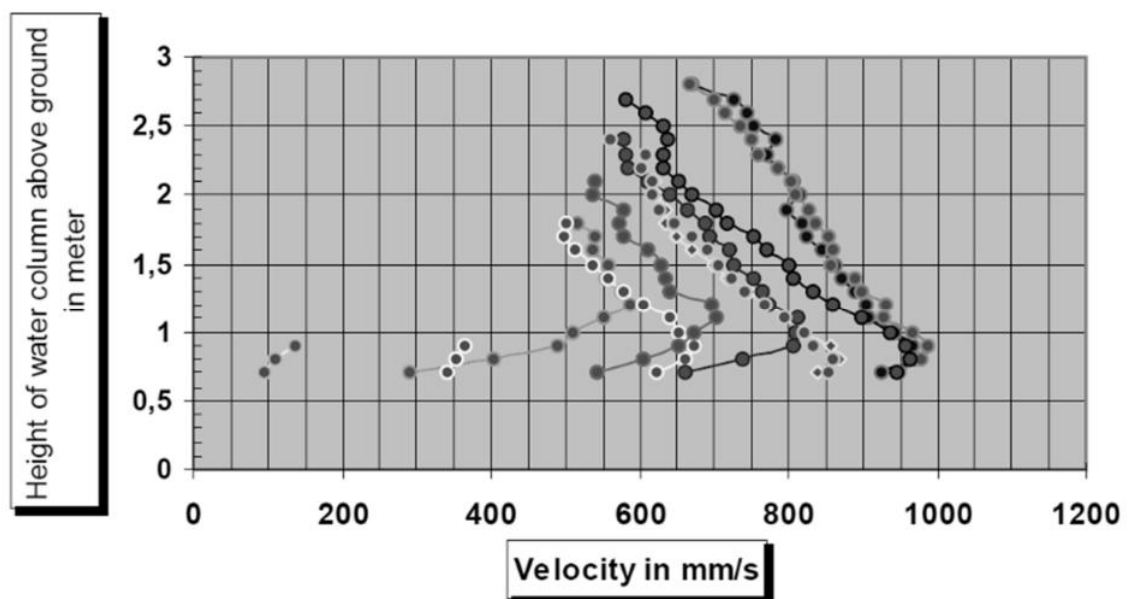


*Figure 7.8 Acoustic Doppler current profiler (aDcp) measured velocity profiles taken during a flood event between 11/08/2002 – 13/08/2002 on a Salix spp. dominated floodplain in the Upper River Rhine. The maximum discharge was ~1600 m³s⁻¹, with a maximum flow depth of ~2.75 m. Maximum tree height was ~8 m. The temporal development in velocity profile shape over the floodplain is shown by the different coloured makers (lightest shade to darkest shade with progression of the flood). As flow depth increases, the sub-canopy flow component becomes more substantial, from Bölscher et al. (2005).*

At the individual plant-scale, Yagci and Kabdasli (2008) and Yagci *et al.* (2010) observe spatially heterogeneous velocity profiles with a sub-canopy flow component in flume experiments around three emergent plants (*Pinus spp., Thuja spp.,* and *Cupressus spp.*; all tree saplings, but different cumulative volume over height for each species).

However, measurements were limited only to the flume midline; so do not provide the spatial coverage necessary to develop a full process-understanding. Furthermore, differences in flow are expected between emergent and submerged plants. When emergent, the interaction of the free-water surface with the dynamic vegetation can add to the flow complexity. When submerged, however, an additional flow-vegetation interface forms at the top of the submerged plant blockage, further complicating the flow structure. The validated numerical model developed in this thesis allows for flow field predictions to be made for submerged plants at a spatial coverage and resolution that would otherwise be unobtainable, thereby improving the process-understanding of flow-vegetation interactions.

The sub-canopy flow component has direct implications for elevated bed shear stresses around plants, and for surface scour. Yagci *et al.* (2016) report differences in the scour patterns behind individual natural vegetation elements compared against isolated or hexagonal arrays of circular cylinders. Natural vegetation is shown to produce two elongated scour holes at the downstream end of the plant, with a well-defined longitudinal ridge. How this interacts with plant orientation is not quantified, but would be expected to follow a similar pattern as that shown in Figure 7.6. In contrast, the solid cylinder is shown to generate wider and deeper scour holes; spatial patterns of scour are therefore different between the solid cylinder and the natural plant. However, although the vertical diameter of the natural vegetation is five times smaller than solid cylinder, the scour volumes are of a similar magnitude, and Yagci *et al.* (2016) attribute this to the substantial effect of the sub-canopy flow component. An additional complication that is not discussed in the above experiments would arise with the eventual exposure of plant roots, which would not scour; instead diverting flow and altering flow field dynamics. In addition, Bölscher *et al.* (2005) show that plants will trap sediment, although this is not accounted for in the scour experiments. The role of roots and sediment trapping are yet to be investigated in detail.

Järvelä *et al.* (2006) specify that for predicting erosion and sediment transport around vegetation, a three-dimensional modelling solution that can adequately predict the turbulent flow field is needed. This thesis has developed the numerical modelling solution necessary; whereby an accurate representation of the plant volumetric canopy morphology is crucial. Simplified plant representations would fail to adequately capture the spatial heterogeneity introduced into the flow field, omitting key features such as the sub-canopy flow component, and this will be influential for modelling patterns of

sediment erosion and transport. However, more research is needed to address the role of roots and the capacity of plants to trap sediment, influencing sediment erosion and transport.

### 7.4.3.2          Plant-scale shear layers and turbulent flow structures

As part of the spatially heterogeneous velocity profiles, sharp transitions are evident between reduced velocity zones in the plant wake, and relatively faster zones above and below the wake. These sharp transitions represent vegetated shear layers, and are most clearly defined for foliated plants where the plant thickness was greatest, suggesting that the shear instability scales positively with the plant blockage (Figure 6.16 and Figure 6.17). Shear layer turbulence is suggested to be dominated by Kelvin–Helmholtz and Görtler-type vortices generated through shear instability (Ghisalberti and Nepf, 2002). With plants submerged, shear instabilities develop at both the horizontal and vertical interfaces of the blockage (at the two outer edges, and at the top and bottom of the plant canopy), and this results in additional complexity for the turbulent flow structures produced. Furthermore, with the plant blockages porous, bleed-flow through the canopy extends the shear instabilities further downstream, and as discussed in Section 7.4.1, this inhibits the roll up of the vortex sheet to form a von Karman vortex street until further downstream. Vortex growth stops when turbulent energy production is equal to dissipation (Ghisalberti and Nepf, 2004). However, vortices associated with shear instabilities are not the only form of turbulent flow structures associated with the plant-scale. To begin to understand the additional turbulent flow structures, flow around an impermeable obstruction mounted on a planar surface is first considered.

Acceleration of flow around an impermeable obstruction, for instance a single, emergent cylinder (analogous to a plant stem, or morphologically simple plant), results in wake vortices associated with shear instability in the downstream region, but also the formation of a horseshoe vortex proximal to the blockage in the near bed region (Graf and Yulistiyanto, 1998; Richardson and Davis, 2001). Horseshoe vortices form due to three-dimensional boundary layer separation (Stoesser, 2013), as schematised in Figure 7.9, with the incident flow decelerated immediately upstream of the blockage (in the junction region), with the strong downflow along the adverse pressure gradient forming horseshoe vortices at the base (labelled HV). The horseshoe vortices wrap around the obstruction, extending downstream.
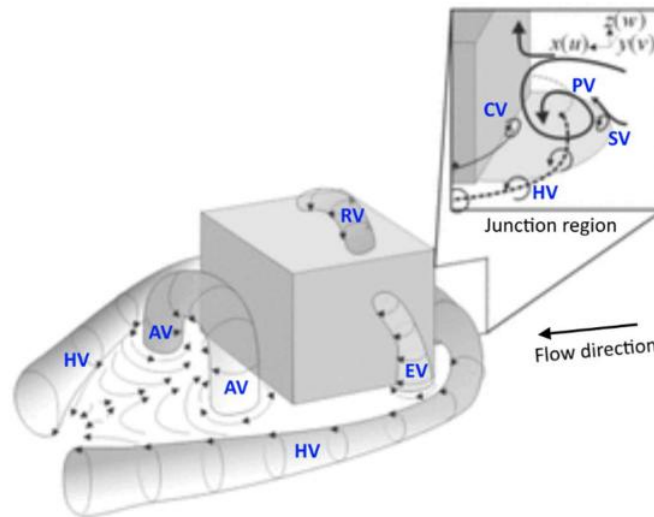
*Figure 7.9 Classic flow structures that develop around a surface mounted obstruction, including the horseshoe vortex (HV) that wraps around the obstruction.  Other labelled vortices include: arch vortex (AV), cavity vortex (CV), edge vortex (EV), primary vortex (PV), reattachment vortex (RV), and saddle point vortex (SV).  From Lawless et al. (2004).*

For flow past a submerged plant represented by a rigid array of porous cylinders, however, additional levels of complexity are added.  Chang *et al.* (2014) model necklace vortices at the plant blockage edge.  As the plant becomes less porous, the coherence of the necklace vortices increases (Chang and Constantinescu, 2015).  Necklace vortices have a similar structure to horseshoe vortices, both of which have a dominant outward motion, although necklace vortices are generally thinner and attached to the base, whereas as shown in Figure 7.9, horseshoe vortices wrap further around the blockage (Piquet, 1999).  In addition to the presence of necklace/horseshoe vortices, the LES simulations of Chang *et al.* (2014) demonstrate shear layer formation at the two horizontal interfaces (at the outside edges of the plant).  However, penetration of down flow from over the top of submerged plants suppresses the interactions between the horizontal shear layers.  It is these interactions that would normally result in the formation of successive vortices with opposite directions of rotation in a von Karman vortex street.  Instead, with the down flow over the top of the submerged plant supressing these interactions, vortices are shed symmetrically and this lowers the levels of turbulent kinetic energy (Chang *et al.*, 2014).  Porosity and the effects of submergence therefore influence the turbulent flow structures present.  For the above-mentioned examples (e.g. Figure 7.9), the geometry of the blockages remains simple, and the porosity is constant over the obstacle.  With complex turbulent flow structures already triggered by relatively simple geometries, the added differences in morphology and

porosity over plant height, and potential for sub-canopy flow, further complicates the turbulent flow structures associated with natural plants (Valyrakis *et al.*, 2015).

For the plants modelled in this thesis, in addition to the vortices associated with shear instabilities, horseshoe vortices have been shown to wrap around the edges of the plant and stretch downstream (Figure 7.10). Horseshoe vortices are convected downstream before eventually diffusing, or can rise to the surface forming kölk-boil vortices (Stoesser, 2013). These vortices provide a transport mechanism for redistributing downstream the low velocity fluid from the separated region (Rizzetta, 1994). Each leg of the vortex is shown by opposing positive and negative regions of high vorticity (Simpson, 2001). The turbulent flow structures identified around the porous plant blockages resemble some of the main elements of a junction vortex system (Simpson, 2001), previously labelled in Figure 7.9. In theory, a junction vortex system will develop around any three-dimensional obstacle attached to a surface and exposed to a boundary layer, and is theoretically independent of wake vortices (Dargahi, 1989), although in reality these can interact. The presence of a junction vortex system at the plant-scale is supported by sedimentation patterns around trees on deformable beds, termed vegetation-induced obstacle marks (Nakayama *et al.*, 2002). Horseshoe vortices in junction vortex systems allow sediment movement at velocities below the threshold of motion, and this results in scour and locally coarse sediment within sparse stands of vegetation (Fonseca and Koehl, 2006; Lefebvre *et al.*, 2010; Paul *et al.*, 2014).

However, because of the plant volumetric canopy morphology and changes in porosity over plant height, with a complex spatial distribution of vegetal elements, not all features of the junction vortex system are identified or can develop. In the junction region immediately upstream of the blockage (labelled in Figure 7.9), a primary vortex which flow rolls down the upstream face towards the bed would be expected to have been observed. However, this is not clearly identified, or has not developed. One reason for this is the lack of plant blockage in the near bed region, and this substantially differs from the constant distribution of the blockage in geometrically simple objects, such as cubes, for which the junction vortex system was initially identified. In addition, the upstream face of the plant blockage has a complex morphology, and is intrinsically three-dimensional. Again, this differs from the planar surface that characterise geometrically simple shapes. Because of these differences, the primary vortex is likely formed higher in the flow depth, and this would shift the position of the horseshoe vortex higher, as shown in Figure 7.10. To further quantify and understand the turbulent

flow structures at the plant-scale, application of Large Eddy Simulation (LES) would be the next step to allow further investigation of the instantaneous and time-averaged flow field, helping further elucidate turbulent flow structures.
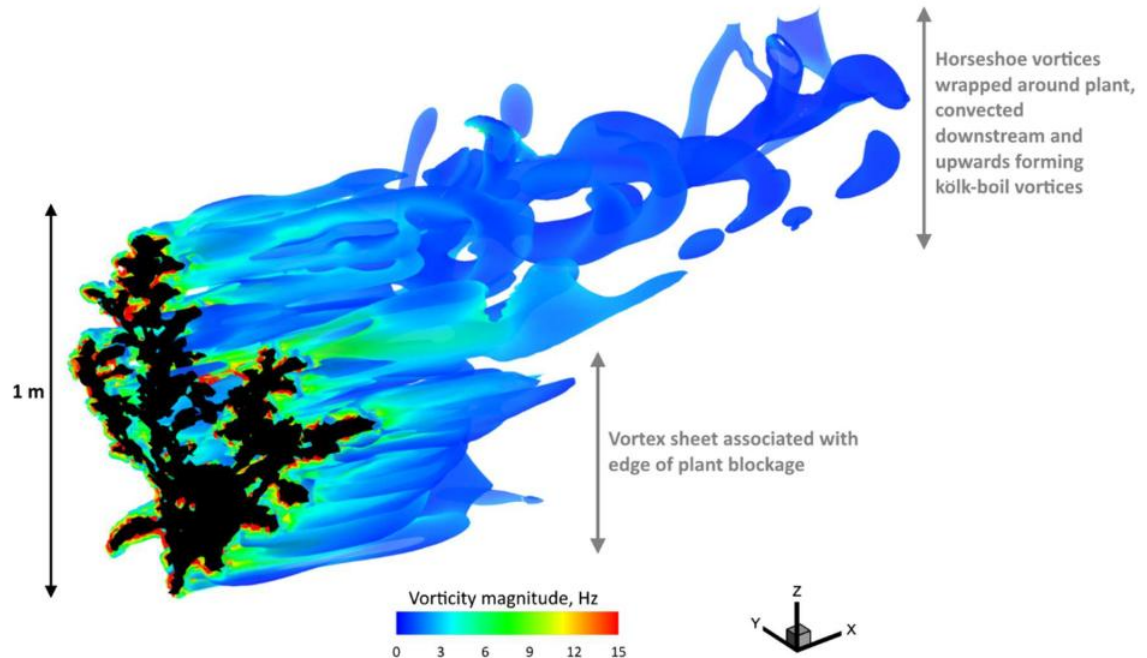


*Figure 7.10 Three-dimensional structure of turbulence around a Prunus laurocerasus plant using the Q criterion, applying a Q threshold of 3.5, with the isosurface coloured by vorticity magnitude. Notable is the extension of horseshoe vortices downstream and upwards towards the free surface, forming kölk-boil vortices. The elements present suggest flow in a junction vortex system.*

### 7.4.4      A conceptual model of flow through and around floodplain and riparian plants

With reference to RQ3 – RQ5, the previous sections have improved the process-understanding of flow-vegetation interactions at the plant-scale. It has been shown that the feedbacks between plant motion dynamics, plant volumetric canopy morphology, and 'how the plant looks to flow' all play an important role in controlling the three-dimensional mean and turbulent flow.

By taking three hypothetical plant states: defoliated (porous), foliated (porous), and foliated (impermeable); conceptual models of flow through and around natural floodplain and riparian plants are produced (Figure 7.11). The plant states are not intended to definitively represent every factor discussed in the previous chapters, but instead reflect the key controls. For instance, the difference between the foliated (porous) and foliated (impermeable) plants could reflect how plant porosity is modified

under increasing hydrodynamic loading, with vegetal elements forced closer together thereby reducing plant porosity.  Likewise, the transition could reflect a marked increase in foliation due to seasonal changes, from foliated (porous) to foliated (impermeable). Figure 7.11 therefore summarises the key flow features identified throughout the previous sections, with the descriptions provided below:

- Defoliated (porous) – an asymmetrical wake forms about peaks in the defoliated plant volume, individual wakes may form around individual branches, but these can coalesce depending on the size and proximity of branches.  The sub-canopy component of flow is small, resulting in only a minor disturbance to the downstream velocity profile.  The shear instability is weakest of the three hypothetical plant states, and the overall disturbance on the flow field is smallest.

- Foliated (porous) – a pronounced wake forms downstream of the porous blockage, extending the greatest distance downstream as the strongest bleed-flow sustains the wake, and this can introduce flow recirculation in the region.  The wake is not necessarily symmetrical, and depends on the distribution of vegetal elements.  Sub-canopy flow is considerably stronger than when defoliated (porous), but weaker than when foliated (impermeable), and therefore points of inflection in the velocity are present.  Because wake length extends further downstream, this inhibits development of the von Karman vortex street until further downstream; before this, regions of high vorticity remain attached to the horizontal shear layers as vortex sheets are constrained by the width of the plant blockage.

- Foliated (impermeable) – the magnitude of the velocity reduction in the wake is greatest, however, the wake does not extend as far downstream as when foliated (porous) because no bleed-flow is present.  The strongest sub-canopy component of flow is shown, and this will have important implications for sediment transport processes, especially with a deformable bed.  Furthermore, the sub-canopy flow component inclines upwards the wake, modifying the shape.  Shear instabilities are strongest of any plant state, but because wake length is limited, the shear instabilities do not extend as far downstream as previously.  A von Karman vortex street will form closer to the foliated plant blockage when impermeable, than when porous.
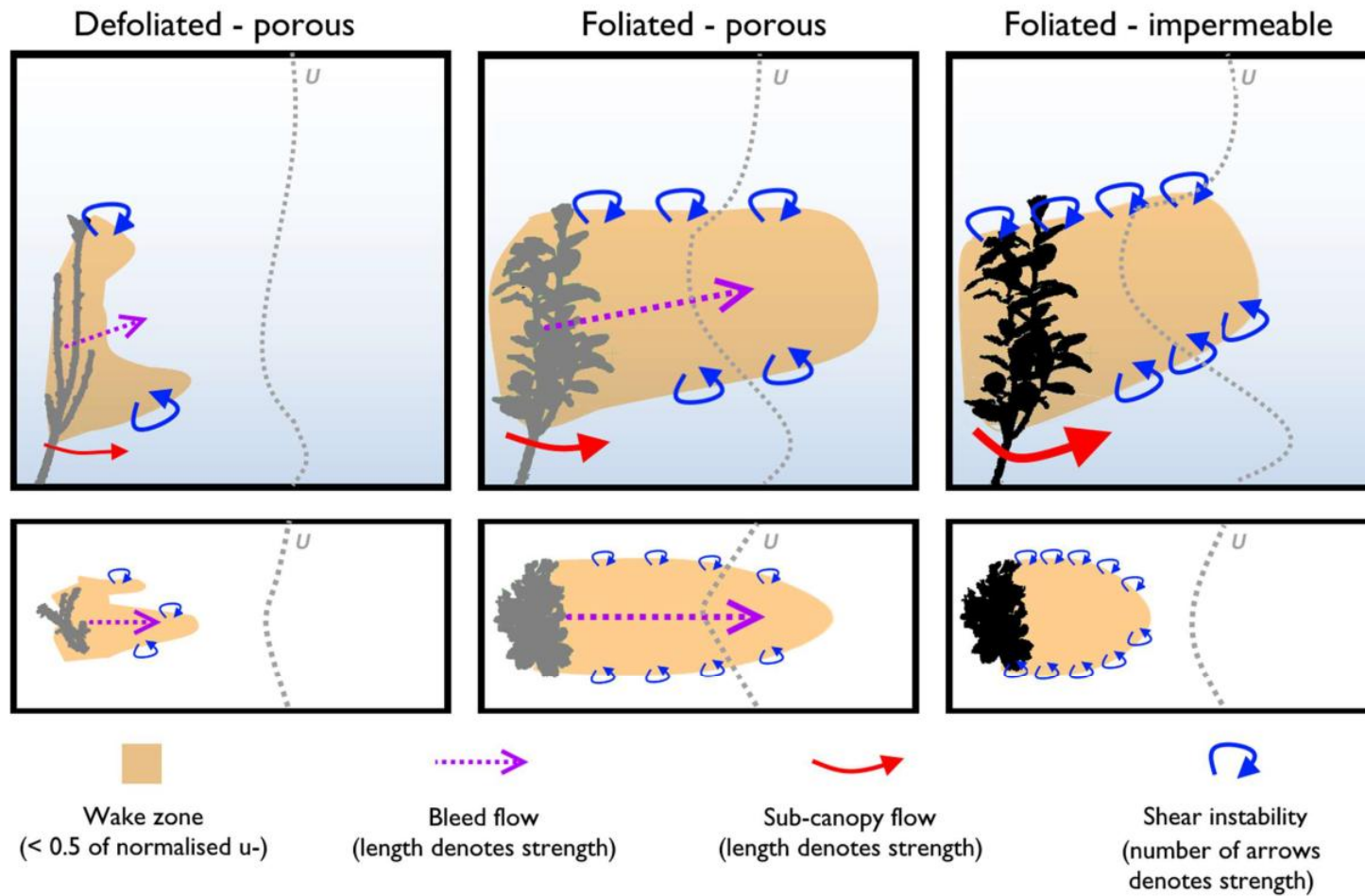
*Figure 7.11 Conceptual model of flow through and around defoliated and foliated plants of different porosities. The main flow features of each plant state are described on the previous page.*

325

## 7.4.5      Summary

This section has demonstrated that the three-dimensional mean and turbulent flow around a porous plant blockage substantially differs from an impermeable plant blockage with the same morphology. Additionally, how the plant is presented to flow poses a further control, as demonstrated by differences in flow field dynamics with simulated changes in plant aspect and posture. It is the combined effects of, and feedbacks between, plant motion dynamics and plant volumetric canopy morphology (RQ3 – RQ5) that influence the three-dimensional mean and turbulent flow at the plant-scale. Findings throughout this thesis question the extent to which natural plants can be conceptualised as simple bluff body objects, and instead suggests that submerged plants should be conceptualised as porous bluff objects. The object is bluff, given the flow separation and reattachment about the blockage. However, the body is also porous given the passage of flow through gaps and conduits in the plant canopy, termed the bleed-flow, which extends the wake zone downstream, and lengthens shear instabilities that form at the vertical and horizontal interfaces of the blockage. In the next section, the implications for the drag response and vegetative resistance are quantified.

## 7.5　Implications for the drag response

### 7.5.1　What are the controls influencing the drag of natural submerged plants?

The high resolution process understanding of flow-vegetation interactions gained in the previous chapters are extended to consider the drag response (RQ6). Application of CFD modelling offers the advantage of providing full flow field predictions, including the pressure field, which are used to quantify the drag response. This offers a significant step forwards when quantifying and defining plant-scale drag coefficients, which are poorly understood for the complex geometries that characterise natural vegetation (Marjoribanks *et al.*, 2014a).

As described in Section 2.2.2 and Section 4.5, the drag force of a plant is calculated by integrating the difference in the pressure field acting normal to the plant surface, over the entire lateral extent of the plant. The drag force is used to calculate the drag coefficient. The equations for calculating the drag force, $F_d$, and drag coefficient $C_d$, are both repeated below:

$$F_d = \int_A \left(p_f - p_b\right)dA_p \tag{7.1}$$

$$C_d = \frac{F_d}{\frac{1}{2}\rho u^2 A_p} \tag{7.2}$$

where $F_d$ is the drag force (N m$^2$), $p_f$ is the pressure at the blockage front (Pa), $p_b$ is the pressure at the blockage back (Pa), $A_p$ is the frontal area (m$^2$), $\rho$ is the density (kg m$^{-3}$), and $u$ is the characteristic velocity (m s$^{-1}$). For the plants investigated in this thesis, the factors that contribute towards the drag response are now discussed.

#### 7.5.1.1　Influence of porosity

For both the *Hebe odora* and *Prunus laurocerasus* plants analysed in Section 7.4.1, the calculated drag forces and drag coefficients are greater when the plant is impermeable (Table 7.3). When the plant is impermeable, drag forces are calculated to be ~20 and ~30% greater than when porous, and drag coefficients ~105 and 65% greater. The greater drag force when impermeable is associated changes in the plant volumetric

canopy morphology that influences the local flow field dynamics and the local pressure gradient. Differences in the drag coefficient between the porous and impermeable plants are attributed to changes in how the plant is presented to the flow, considering the different exposures of vegetal elements. When porous, the surface exposed to flow is highly irregular and three-dimensional, whereas when impermeable, the surface becomes more regular and planar (as shown in Figure 7.1). The overall shape of the plant representation therefore changes, and it is these changes in shape or geometry that substantially alters the drag coefficient (Douglas *et al.*, 2005). The control of porosity is therefore particularly important in modifying the drag coefficient, with porous plant representations having substantially smaller drag coefficients than impermeable plant representations.

*Table 7.3 The drag force ($F_d$) and drag coefficient ($C_d$) using the i) porous plant representation and ii) impermeable plant representations from Section 7.4.1.*

| Plant species | Drag Force (N m$^2$) | | | Drag Coefficient | | |
|---|---|---|---|---|---|---|
| | i) Porous | ii) Impermeable | % Change (i – ii) | i) Porous | ii) Impermeable | % Change (i – ii) |
| Hebe odora | 1.541 | 1.822 | 18.2 | 1.372 | 2.826 | 106.0 |
| Prunus laurocerasus | 1.742 | 2.244 | 28.8 | 1.243 | 2.042 | 64.3 |

### 7.5.1.2 Influence of foliation

Drag forces of 0.15 and 1.74 N m$^2$ are calculated for the defoliated and foliated *Prunus laurocerasus* plants, respectively. This order of magnitude difference is attributed to the increase in plant frontal area, previously shown as a four-fold increase from defoliated to foliated, but also the additional volume introduced by the leaf body (again approximately a four-fold increase), which results in a greater flow field disturbance. The increased plant frontal area is crucial to this, as form drag is roughly proportional to the frontal area of an object (Vogel, 1994). With a greater plant frontal area exposed to flow, it follows that the drag force will be greater. Drag therefore increases with foliage density (Wilson *et al.*, 2003). This corresponds with the more pronounced TKE patterns observed when foliated (Section 6.3.5), indicating a greater form drag contribution when the plant is foliated. The drag forces are of a similar magnitude to the direct measurements of drag force for small natural woody trees, undertaken by Jalonen and Järvelä (2014).

Drag forces are used to calculate the drag coefficient, with a drag coefficient of 1.54 when the plant is defoliated and 1.24 when the plant is foliated. Both calculated values significantly exceed the typically assumed value of unity that used to describe vegetation in hydraulic applications (gained from studies of flow around cylinders), and agree with several studies that have reported a drag coefficient value of 1.5 as physically-acceptable for defoliated trees (Klaassen and Van Der Zwaard, 1974; Mertens, 1989; Järvelä, 2002a).

An inverse trend between drag force and drag coefficient is somewhat surprising given the drag coefficient in the defoliated plant is higher, though the drag force is an order of magnitude lower than the foliated plant. This discrepancy is again explained by differences in 'how the plant looks' to flow. Namely, the dominance of individual branches when defoliated, compared with the dominance of a single leaf body when foliated. Furthermore, the effect of sheltering and different exposures to flow across the plant further reduces the drag coefficient when foliated. In drag force experiments on defoliated and foliated *Salix spp.* branches, Wunder *et al.* (2011) also reported greater drag coefficients when branches were defoliated.

However, Järvelä (2002a) show that additional complexity arises when calculating the drag coefficient for multiple defoliated and foliated *Salix spp.* plants; with the drag coefficient three to seven times greater in foliated plant stands. With multiple plants present, Järvelä (2002a) show that the number of plants in the stand control the drag coefficient response, with a doubling of the number of plants approximately doubling the drag coefficient. However, multiple plants represent a very different case than what has been investigated here. For multiple plants, the incident flow depends on the structure of the upstream plant, whereas the conceptual model here only applies to uniform flow approaching a single plant. The control on the drag response for multiple plants will therefore be more complex, as upstream plants will modify the pressure and velocity field of downstream plants. However, the methodology developed in this thesis would allow for these effects to be investigated (see Section 7.7.2), as the lateral pressure gradient is calculated about individual vegetal elements (e.g. branches, stems, or leaves), regardless of the number of plants.

In summary, it has been shown that drag forces are substantially greater for a single foliated plant than a single defoliated plant, but the drag coefficient is smaller in the foliated plant than in the defoliated plant. The newly quantified, physically-determined drag coefficients are significantly higher than the typically assumed value of unity. This

is shown to be controlled by the plant volumetric canopy morphology, that influences the drag response at the plant-scale.

### 7.5.1.3　　Influence of plant posture

For the *Hebe odora* plant, the drag force and drag coefficients are compared between the unstressed and stressed plant representations, to analyse how differences in the time-averaged plant posture influence the drag response. As before, the unstressed model relates to the upright plant representation, whereas the stressed model captures changes in the time-averaged plant posture under hydrodynamic loading. For unstressed and stressed plant representations, drag force increases almost linearly with *Re* (Table 7.4). However, the modelled drag force is consistently lower in the stressed plant representation, by as much as 27.1%. By capturing and incorporating shifts in the time-averaged plant posture, the drag force is reduced relative to the unstressed plant representation, where the plant remained fully upright to flow. This is explained by the reduction in the plant frontal area and compression of the volumetric canopy morphology, which in turn reduces the drag force, as the plant reconfigures to the mean flow.

For the drag coefficient, similar patterns emerge. The drag coefficient is consistently lower for the stressed plant representations, which incorporate shifts in the time-averaged plant posture, representing the streamlining of the plant under hydrodynamic loading. Such changes emphasise the dynamic nature of the drag coefficient, and the overall sensitivity of the drag response to changes in plant posture. A single drag coefficient value is therefore unlikely to accurately reflect the drag response of a riparian plant under hydrodynamic loading. This drag response is further quantified through the Vogel exponent, to consider the drag implications of reconfiguration over the *Re* range.

*Table 7.4 The drag force (Fd) and drag coefficient (Cd) using the i) unstressed plant posture and ii) stressed plant posture.*

| *Re* | Drag Force (N m$^2$) | | | Drag Coefficient | | |
|---|---|---|---|---|---|---|
| | i) Unstressed | ii) Stressed | % Change (i – ii) | i) Unstressed | ii) Stressed | % Change (i – ii) |
| 65 000 | 0.765 | 0.667 | -12.9 | 1.605 | 1.451 | -9.6 |
| 89 000 | 1.373 | 1.081 | -21.3 | 1.548 | 1.339 | -13.5 |
| 110 000 | 2.111 | 1.541 | -27.1 | 1.564 | 1.372 | -12.3 |

The Vogel exponent, $\psi$, quantifies the drag reduction by reconfiguration of a flexible body through a power law dependence with velocity (Vogel, 1984), as discussed in Section 2.3.4.1.3. Applying the $F_d$ – U relationship from Equation 2.9, $\psi$ = -0.37 for the *Hebe odora* specimen investigated in this thesis. Considering reconfiguration and the drag response, this suggests that the plant falls at the flexible end of the stiffer range. It is important to remember that the $F_d$ – U relationship is representative of only the relatively low velocity range investigated (< 0.37 m s$^{-1}$), and therefore could be modified at higher velocities. However, the marked plant deflection and considerable motion detected suggest the plant has moved beyond the trans-flexing zone where deflection is negligible, and into the flexing zone where the plant streamlines and the plant frontal area reduces with velocity (Xavier *et al.*, 2010).

Because the Vogel exponent is not dimensionally correct, it cannot be used to calculate the drag force and subsequent energy loss within vegetated rivers (Marjoribanks *et al.*, 2014a). However, it does allow for the broader quantification of flexibility in plants (Dittrich *et al.*, 2012), as has been demonstrated here. Furthermore, using the Vogel exponent approach, a number of authors have characterised bulk vegetative resistance terms including parameterisation of plant biomechanical and plant geometry components, with inclusion of separate foliage and stem contributions (Västilä and Järvelä, 2014), and species-dependent drag coefficients (Järvelä, 2002b; Järvelä, 2004; Aberle and Järvelä, 2013) to improve process representation in such equations (Marjoribanks *et al.*, 2014a).

To further investigate the effect of plant posture on the drag response, analysis is extended to the foliated *Prunus laurocerasus* plant, with results shown in Figure 7.12. With inlet velocity held constant at 0.25 m s$^{-1}$, as the plant posture is shifted from fully upright (0°) to fully prone (80°), the drag force increases non-linearly. Unlike the *Hebe odora* plant, where the vertical compression of the plant representation led to a reduction in the volumetric canopy morphology and plant frontal area, for the *Prunus laurocerasus* hinged to the bed, changes in volumetric canopy morphology and plant frontal area are only negligible, and the volume is conserved. Changes in the drag response are therefore caused by differences in how the plant is presented to flow.

Again, it is noted that calculated drag coefficients remain above the commonly assigned value of unity, although the response of the drag coefficient does not follow the same pattern as the drag force. From 0° to 30°, the drag coefficient initially decreases, which

is to be expected given the greater streamlining of the plant representation as the plant is tilted in the flow. Beyond this point, however, as the plant becomes more prone in the flow, the drag coefficient increases non-linearly, with the greatest increase between 70° and 80°. It is suggested that this increase in drag coefficient with further shifts in posture is caused by the protrusion of the leaf body and individual branches into the flow, and for the static plant representation modelled here, would result in greater hydrodynamic drag.
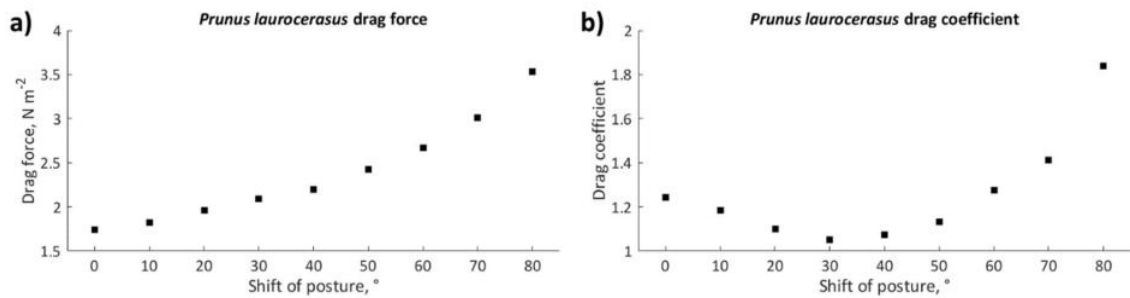


***Figure 7.12 (a) Drag force and (b) drag coefficient with shifts in Prunus laurocerasus plant posture. Note different units and scaling of axes.***

In nature, however, the fully prone plant posture represented in the model for the *Prunus laurocerasus* plant is unlikely to be realised. Substantial increases in the flow velocity would be required for such a posture to be achieved, and at these high velocities streamlining of all vegetal elements would occur (Oplatka, 1998; Vollsinger *et al.*, 2005; Järvelä *et al.*, 2016). Complexity is added where the streamlining response is not constant over the different vegetal elements at the plant-scale. Järvelä *et al.* (2016) demonstrate piece-wise behaviour of the streamlining response for riparian trees in towing tank experiments, with leaves and small twigs shown to streamline first at lower velocities, followed by the main branches and trunks at higher velocities. It is the contribution of the main branches and trunks that have the greatest effect on modifying the plant posture, and therefore it is these vegetal elements than contribute most towards the drag response. In the past, simplified beam elasticity equations have been used to quantify the deflections of riparian vegetation under flow when modelling the drag response (Manners *et al.*, 2013). Whether such equations account for the full range of plant motion dynamics remains unclear, especially as it has been highlighted here that plant motion varies spatially over the plant body across different scales. Too simplistic a representation of reconfiguration would not adequately represent the processes that contribute towards the drag response in floodplain and riparian plants.

This section has demonstrated the importance of changes in plant posture on the drag response. For the *Hebe odora* plant, by explicitly representing changes in the time-averaged plant posture, volumetric canopy morphology, and porosity, the drag force is 12.9 – 27.1% lower than that of the fully upright plant representation for the same *Re*. This highlights the significance of plant postural changes in reducing flow separation through streamlining and reconfiguration (Vollsinger *et al.*, 2005), leading to a subsequent reduction in form drag (Nikora, 2010), which accounts for 90-97% of the total drag for turbulent flows (Lilly, 1967; Vogel, 1994; Stoesser *et al.*, 2010). Furthermore, as the plant becomes more streamlined with increasing *Re* from 65 000 to 110 000, the drag coefficient decreases (Table 7.4). By providing an understanding of plant motion dynamics during reconfiguration, the drag response has been successfully quantified.

However, the drag response was less simple for the *Prunus laurocerasus* plant, where changes in plant posture were modelled by tilting the foliated plant representation that was hinged to the bed (Figure 7.12). As the plant becomes more prone, drag forces increase, while the drag coefficient responds non-linearly. This is because the plant is represented as a static porous blockage, with changes of how the plant is presented to the flow resulting in changes to the local flow field dynamics, specifically the pressure gradient. In the model, the plant was simply tilted, with the volume conserved. However, recent laboratory work using full-scale riparian plants has shown that the reconfiguration and streamlining response is more nuanced than this, and instead is a non-linear process with respect to the different vegetal elements at the plant-scale (Järvelä *et al.*, 2016). As such, these findings question the extent to which simple bending models can be applied to study the drag response of riparian plants under hydrodynamic loading. It is suggested that a more complete process-understanding of plant motion dynamics is therefore required when quantifying the drag response.

### 7.5.1.4    Influence of plant aspect

The influence of small changes in plant aspect for both the defoliated and foliated *Prunus laurocerasus* plants were discussed in relation to the flow field disturbance in Section 7.4.2. Calculated drag forces for these plants are shown in Figure 7.13a, with drag coefficients shown in Figure 7.13b. In the defoliated state, calculated drag forces vary by up to ~350%, ranging between 0.08 and 0.37 N m². In the foliated state, drag forces are around an order of magnitude greater, varying by up ~130% across the plant aspects modelled, ranging between 1.02 and 2.32 N m². In the defoliated state, drag coefficients

range from 0.95 to 2.92 (varying by up to ~210%), and when foliated over a smaller range from 0.76 to 1.36 (varying by up to ~80%). In Figure 7.13b it is shown that for both plant states, the drag coefficient tends to be greater than unity (shown by the red circle). Overall, the sensitivity of the drag response to plant aspect is greater when the plant is defoliated.

With changes in plant aspect, the volumetric canopy morphology and plant volume are conserved, however, the plant is presented differently to the flow, with differences in drag explained by the various exposures of vegetal elements to flow (Hurd, 2000). It is suggested that sensitivity is greater for the defoliated plant because of the dominance of individual branches, and these are 'seen' differently by the flow depending on plant aspect, resulting in a wider range of drag coefficients. This contrasts with the foliated plant, where the slightly more streamlined, single leaf body appears somewhat similar to flow regardless of plant aspect, accounting for the smaller range of drag coefficients.

For the foliated plant, small differences in the drag response emerge depending on the alignment of the plant relative to flow. This was previously noted for the downstream velocity field, with larger wake volumes indicative of a greater flow disturbance when the plant was orientated more perpendicular to flow, and was also shown in the TKE response (Figure 6.33). This effect extends into the drag response, where the drag force for the foliated plant is greater around 150° and 330°, when the plant is aligned more perpendicular to the flow. When perpendicular, this is analogous to the face-on cube in Figure 7.6, where the drag coefficient is greater than for the same cube positioned edge-on (face-on drag coefficient = 1.10; edge-on cube drag coefficient = 0.80, Streeter (1998)). This does not extend to the defoliated plant because of the large spikes in drag response (15° and 75°) caused by branch configurations that are particularly blunt to flow, thereby promoting flow separation and resulting in additional form drag at specific plant aspects. Clearly, therefore, plant aspect exerts an additional control on the modelled drag response.
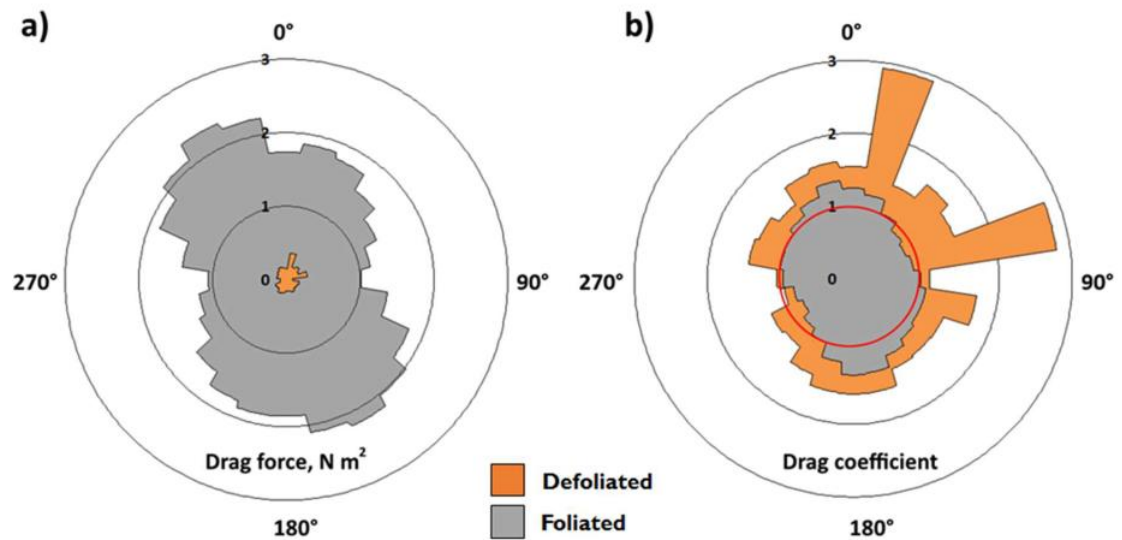
*Figure 7.13 Effect of plant aspect on (a) drag force and (b) drag coefficient. Note the order of magnitude difference in drag force between defoliated (orange) and foliated (grey) plants. Maximum drag for the foliated plant runs from 150° and 330°, whereas discrete spikes around 15° and 75° are noted for the defoliated plant. The red circle represents a drag coefficient value of unity, commonly assigned to represent vegetation in hydraulic applications.*

### 7.5.1.5        Summary

This section has shown that the drag acting on floodplain and riparian plant depends on the combined effect of multiple influences that contribute towards the volumetric canopy morphology. In answer to RQ6, there is not one single dominant factor controlling the drag response; instead, it is the combined effect of multiple contributing factors. Because of this, a range of drag coefficients have been calculated for each plant species. Practical applications dealing with vegetation often assume a predefined, constant drag coefficient of 1.0 or 1.2 (Dittrich *et al.*, 2012). However, for the plants investigated here, the calculated drag coefficients tend to be substantially higher, but considerably vary with the above-mentioned factors.

It has been shown that the factors controlling the drag response include plant porosity, foliation, plant posture, and plant aspect. Relevant to the control of porosity, porous plant representations have substantially smaller drag coefficients than impermeable plant representations. Furthermore, at the plant-scale, drag forces increase with the presence of the foliage, although the drag coefficient for the defoliated plant is greater than for the foliated plant, due to the dominance of individual branches rather than a single leaf body. However, the drag response is sensitive to changes in time-averaged plant posture, and a single drag coefficient value is unlikely to fully represent the drag response of a reconfiguring plant. It is suggested that for a reconfiguring plant, the drag

coefficient is dynamic, and a drag coefficient range is more appropriate. A more complete process-understanding of plant motion dynamics during reconfiguration is necessary when quantifying the drag response. In addition to this, plant aspect exerts a further control on the drag response. Whether the plant is positioned parallel or perpendicular to flow is shown to influence the drag response, with a perpendicular plant aspect shown to result in higher drag forces and drag coefficients. It is acknowledged that only form drag is directly modelled using the current approach, although for floodplain and riparian plant species, form drag is shown to dominate over viscous drag (Nikora, 2010; Västilä and Järvelä, 2014). In the next section, the newly quantified drag coefficients (Table 7.4) that are physically-determined and based on an improved process-understanding, are used to describe the implications for vegetative resistance, in support of RQ7.

## 7.6　Implications for vegetative resistance, and upscaling findings to the reach-scale

The physically-determined drag coefficients quantified in this thesis are now used to quantify vegetative resistance. First, Manning's *n* is back-calculated, before the implications for vegetative resistance at the reach-scale are discussed.

### 7.6.1　Implications for vegetative resistance through the back-calculation of Manning's n

Focusing on the *Hebe odora* plant, for which a high resolution process-understanding and physically-determined drag response has been quantified, the implications for vegetative resistance through back-calculation of Manning's *n* are presented. In submerged cases, the presence of a turbulent mixing layer between the vegetated low velocity and free-stream zones adds complexity to derivations of vegetative resistance (Shucksmith *et al.*, 2011), and therefore an equation applicable to submerged vegetation is required. For submerged grasses, Wilson and Horritt (2002) consider the plant frontal area for the calculation of Manning's *n* ($m^{1/3}$ $s^{-1}$), following:

$$n = \left( \frac{1}{2g} R^{1/3} C_d \frac{A_p}{CSA} \right)^{1/2} \tag{7.3}$$

where $g$ is gravitational acceleration (m $s^{-2}$), $R$ is the hydraulic radius (m), $A_p$ is the plant frontal area ($m^2$) calculated from the TLS, and $CSA$ is the cross-sectional flow area ($m^2$). Manning's *n* values of 0.086, 0.080, and 0.078 are calculated for the single *Hebe odora* plant in the stressed state at *Re* 65 000, 89 000, and 110 000 respectively. It is the reconfiguration of the plant through the quantified reduction in drag coefficient and frontal area that results in this decrease of Manning's *n* over the *Re* range.

For *Re* 110 000, for which the drag response was previously compared between porous and impermeable *Hebe odora* representations (Section 7.4.1), back-calculation of the Manning's *n* value is extended to consider the impermeable plant representation. When porous, a Manning's *n* value of 0.078 was quantified, however, when impermeable this increases by ~125% to 0.176. This significant increase in the Manning's *n* value is attributed to the increase in drag coefficient, and differences in the plant frontal area

between the porous and impermeable plant representations. Such differences highlight the necessity to account for the plant volumetric canopy morphology and porosity when quantifying vegetative resistance. Had porosity not been considered, a significantly greater Manning's *n* value would be quantified, and this has implications for vegetative resistance at the reach-scale.

It is the *Re* dependent drag coefficient that exerts a major control on the back-calculation of bulk vegetative resistance, and demonstrates the necessity to account for the factors discussed in Section 7.5.1 when quantifying vegetative resistance, instead of relying on predefined drag coefficient parameterisations. The Manning's *n* values calculated here for the porous plant representations are greater than those suggested by established texts, with Chow (1959) suggesting a Manning's *n* value of 0.035 – 0.070 for floodplains with scattered brush and heavy weeds. Furthermore, the values back-calculated fall within a narrow range (0.008) compared the wider ranges from which Manning's *n* values are normally selected. For the impermeable plant representation, the calculated value is in the range comparable to dense, foliated trees (Manning's *n* values of 0.11 – 0.20, Chow (1959)). The look-up table values, however, represent the resistance to flows over large spatial areas in channel and floodplains, whereas the calculated values presented here are reflective of a single vegetation element in a flume. The values for the single plant could be higher because the width of the flume is less than the normal packing density of the plants. More work is therefore needed to assess the sensitivity of back-calculated Manning's *n* for a range of packing densities.

## 7.6.2 Implications for upscaling findings to the reach-scale

Once sensitivity analysis for a range of packing densities has been completed, the physically-determined, Manning's *n* values calculated in this thesis could be applied to conveyance estimators either applying a one-dimensional hydrodynamic model or using a Conveyance Estimation System (Wallingford, 2004). These are typically based upon the Manning's equation which parameterises and/or calibrates all frictional resistance and is applied to produce the correct relationship between flow and water level (Section 2.2.1). The same is true for industry-standard two-dimensional hydraulic models, which are shown to be particularly sensitive to the floodplain roughness values selected (Straatsma and Baptist, 2008). For example, Abu-Aly *et al.* (2014) report a maximum Manning's *n* value of 0.343 for woody vegetation patches (which is far higher than established texts), and find that application of spatially distributed vegetation roughness

values cause a 7.4% increase in mean depth, and a 17.5% decrease in mean velocity relative to an unvegetated roughness scenario. Changes in the Manning's *n* values associated with the vegetation component of resistance will therefore alter hydraulic model outputs.

In practice, however, the roughness term in these models are used as a calibration parameter (e.g. Mason *et al.,* 2003), and may no longer reflect the intended process representation. The Manning's *n* value therefore becomes effective as it represents several processes that contribute to energy loss (e.g. momentum loss, dispersion associated with secondary circulation, and diffusion). Applications of these models therefore tend to be run for a matrix of effective Manning's *n* values over a parameter range to ensure an optimum value is identified, meaning the values used may differ significantly from their measured or estimated values (Lane, 2005). This potentially undermines the predictive ability of the model as it introduces uncertainty into the application of the model when it is used beyond the range of conditions for the optimisation, or where it has to be applied to other situations. However, by deriving Manning's *n* for a single species following the approach developed in this thesis, which considers the momentum loss, dispersion associated with secondary circulation, and diffusion, the Manning's *n* value has greater physical basis. This is because the drag coefficient is physically-determined and calculated using a full process-understanding of flow-vegetation interactions at the plant-scale. The magnitude of the discrepancy could then be quantified, comparing Manning's *n* values derived following the new approach against those calculated through calibration in hydraulic modelling applications.

Because of this improved process-understanding, the approach developed in this thesis goes well beyond previous attempts to parameterise vegetative resistance based only on TLS derived point clouds (e.g. Antonarakis *et al.* (2009); Antonarakis *et al.* (2010), focusing on full-scale trees), or ALS derived point clouds (e.g. Straatsma and Baptist (2008), focusing on the reach-scale). By measuring and modelling flow-vegetation interactions at high-spatial resolutions, and capturing and representing the full three-dimensionality of the plant volumetric canopy morphology and porosity, the approach developed here improves upon vegetative resistance parameterisations that are based only on plant frontal areas and predefined drag terms. The quantification of flow field dynamics using a CFD model, and subsequent recalculation of physically-determined drag terms, is what makes this possible.

Furthermore, the substantial differences in drag coefficients and Manning's *n* values between plant representations, for instance between porous and impermeable plant representations, raises questions over the extent to which vegetative resistance could be estimated from point clouds with lower spatial resolutions. Unmanned Aerial Vehicles (UAVs) have recently been used for mapping in-channel, floodplain and riparian vegetation (Visser *et al.*, 2013; Flynn and Chapra, 2014), and it has been suggested that vegetation point clouds could be derived from these platforms (Jalonen *et al.*, 2015). However, UAV derived point clouds have lower spatial resolutions than TLS derived point clouds (TLS having approximately five times higher spatial resolution, Table 3.1). They would therefore be unlikely to accurately represent the plant volumetric canopy morphology necessary to quantify flow field dynamics using the approach developed in this thesis.

Instead it is suggested that UAV derived vegetation maps at high-spatial resolutions to be combined with the physically-determined drag terms and vegetative resistance values. Upscaling from the plant-scale to the reach-scale would be made possible by combining these approaches, and producing spatially distributed roughness maps (Kouwen and Fathi-Moghadam, 2000). This offers an exciting opportunity to progress the research and develop future practical outputs.

## 7.7 Further developments and potential applications

Having successfully demonstrated the development of a numerical representation of vegetation in response to river flow at the plant-scale, the final section of the chapter presents further developments and potential applications of the research. First, a discussion of whether it is necessary to move beyond a binary plant representation is provided (Section 7.7.1). This considers whether it is feasible, or necessary, to explicitly represent porosity at the scale of individual voxels. Having addressed this issue, the potential to incorporate multiple plants is discussed (Section 7.7.2), because in-channel vegetation, but also floodplain and riparian plants, are not always found in isolation. Finally, preliminary results are shown for two potential applications, including:

i. The incorporation of a dynamically moving plant representation. This goes beyond application of the Reynolds-averaged Navier Stokes equations that have been used to this point in the thesis, moving towards explicitly representing plant motion in a time-dynamic solution. How this can be achieved is discussed in Section 7.7.3.

ii. The inclusion of bed topography and the modelling of sediment transport processes are discussed (Section 7.7.4), with specific examples given of where this research could be applied.

## 7.7.1 Beyond a binary plant representation – should porosity be explicitly represented at the voxel scale?

With reference to Section 4.3.4, in order to represent a plant in the CFD model, cells were either completely blocked ($P = 0$), or completely unblocked ($P = 1$), following the binary occupied/unoccupied treatment in the voxelisation procedure. This means that no interface or partly blocked cells are present. However, the fraction of each voxel occupied by vegetal elements will fall somewhere between 0 and 1, with a completely blocked cell only realised for voxels at the interior of main branches. Elsewhere, in the leaf body for example, the fraction of the voxel occupied by vegetal elements will be greater than 0, and vary considerably based on the presence and density of foliage; therefore the potential exists to attach a porosity value to each voxel.

Although on first appearance omission of porosity at the voxel scale may appear a limitation of the methodology, there is strong justification for selecting a binary classification. Firstly, an important consideration for the magnitude of spatial errors recorded in the TLS scans is necessary. Riegl (2015a) report that at a distance of 10 m, the VZ-1000 scanner has a range accuracy of 0.008 m, and a precision of 0.005 m. For the VZ-4000 scanner, at a distance of 150 m a range accuracy of 0.01 m and a precision of 0.015 m is reported (Riegl, 2015b). In practice, when using the Riegl VZ-1000 scanner at 5 m, the mean distance between points is 0.0026 m when the *Prunus laurocerasus* was defoliated, and 0.0023 m when foliated. When using the Riegl VZ-4000 scanner at 5 m, the mean distance between neighbouring points for the *Hebe odora* point cloud was 0.0024 m. To ensure an adequate representation of the plant, especially of the internal plant canopy structure where returns are fewer and the mean distance between points is higher, the voxel size must be larger than the scan resolution. A minimum voxel size of ~0.005 m must therefore be used to represent the plant, which is approximately double the scan resolution, and this directly maps onto the grid resolution necessary to resolve flow field dynamics (in the range 0.005 – 0.01 m).

However, because of the uncertainty associated with the accuracy and precision of measurement points relative to the voxel size, it cannot be said with certainty that any one point falls exactly within any one single voxel. This means that considerable uncertainty would be associated with assigning porosities based on the number of returns at the voxel sizes required to accurately represent plant morphology. Furthermore, additional uncertainty arises because points are non-equally distributed over the full three-dimensional extent of the plant, due to the effects of occlusion and fewer returns penetrating the plant canopy interior. This non-equal distribution was shown by the relative point density, used as a means of assessing the quality of the scan (Section 3.5). Although this information is useful to analyse the distribution of returns, it does not accurately inform the porosity for each voxel, as the number of potential returns differs for each voxel, and when used to calculate porosity at the voxel scale, this would result in an underrepresentation of vegetal elements where returns are fewest.

Unless these uncertainties can be addressed, the relative point density should not be used to inform porosity at the voxel scale. This is because of issues relating to the magnitude of spatial errors in the point data relative to the voxel size, and challenges associated with the non-equal distribution of points over the full three-dimensional structure of the plant. Currently, therefore, a binary porosity treatment is preferred;

although this does not explicitly account for porosity at the voxel scale, it does accurately represent plant volumetric canopy morphology and explicitly represents the gaps and conduits in plant structure that influence flow field dynamics.

## 7.7.2    Incorporating multiple plants

Individual plants isolated in floodplain and riparian zones have been the focus of this thesis. However, in-channel vegetation is seldom found in isolation (Sand-Jensen and Madsen, 1992), and as such the forces on individual plants can be reduced due to sheltering and through the reduced velocities in wakes from upstream plants. This also extends to floodplain and riparian plants, as for pioneer species such as *Populus nigra* that are involved with colonisation of gravel bars, existing plants facilitate succession by trapping sediment and providing sheltered conditions for further plant establishment (Edwards *et al.*, 1999). The interactions between individual plants therefore drives biogeomorphic succession (Corenblit *et al.*, 2009). Because of this, engineer species such as *Populus nigra* act as 'autogenic ecosystem engineers' that are capable of modulating the riparian ecosystem structure and function (Edwards *et al.*, 1999; Gurnell and Petts, 2006), with positive feedbacks developing as the species establishes and constructs landforms and functional biogeomorphic units (Corenblit *et al.*, 2014; Corenblit *et al.*, 2016).

Recent experimental work has shown how the interaction of neighbouring emergent vegetation patches can influence deposition dynamics (Meire *et al.*, 2014). This has been extended into a numerical scheme, where de Lima *et al.* (2015) used CFD to show that geometrically simple patch distributions and interactions may be responsible for the feedbacks that influence the evolution of vegetated landscapes at the channel scale. However, in both examples plants were represented by cylinders of varying densities, neglecting the volumetric canopy morphology that has been shown influential for flow field dynamics around natural plants. Extending the approach developed in this thesis to include multiple, realistic plant representations will allow flow field dynamics to be quantified in the zones where establishment and biogeomorphic succession takes place. The effects of multiple plants could easily be tested by applying cyclic boundary conditions (Section 4.3.6), and the process-understanding of flow-vegetation interactions between plants is necessary when upscaling results from the plant-scale to the reach-scale (Section 7.6.2).

### 7.7.3 Incorporating dynamic plant representations

Plant reconfiguration influences flow field dynamics and the drag response at the plant-scale. In this thesis, plant motion has been represented through changes in the time-averaged plant posture, with the flow field modelled using a finite volume solution of the full three-dimensional Navier-Stokes equations, using the Reynolds-averaged Navier Stokes equations with a RNG k-ε turbulence model. Moving forwards, the next step would involve explicitly representing plant motion in a time-dynamic solution. To achieve this, the following steps could be taken:

1. For a time-dynamic solution, Large Eddy Simulation (LES) could be used to simulate the flow field around a stationary plant. This would help to further elucidate turbulent flow structures, as discussed in Section 7.4.3.2.

2. To explicitly account for plant motion, unsteady Reynolds-averaged Navier-Stokes equations could be coupled with a biomechanical model used to describe plant motion. Marjoribanks *et al.* (2015) and Marjoribanks *et al.* (2017) have developed a suitable biomechanical model, used to dynamically reconfigure vegetation under hydrodynamic forcing.

3. A combination of steps 1 and 2, coupling LES with a biomechanical model to provide a time-dynamic solution that explicitly represents plant motion.

Work has been underway to develop step 3. The numerical scheme applies LES at each time-step in a sequentially staggered manner. The Navier-Stokes equations are solved using the SIMPLEST algorithm (Patankar and Spalding, 1972). A standard Smagorinsky sub-grid model with $C_s$ = 0.17 is used to simulate flow within the LES. For each time-step the flow is iteratively solved, with the convergence criterion set so that mass and momentum flux residuals were reduced to 0.1% of inlet flux. The plant is represented by applying a time-dynamic MFSA, so that the plant representation can evolve through time in a stable numerical framework (Lane and Hardy, 2002; Lane *et al.*, 2002). This effectively removes the need to remesh the modelling domain for each time-step, improving computational efficiency and avoiding stability issues. Appropriate to floodplain or riparian species which have high rigidity, plant motion is controlled by the bending forces that act on the plant (Li and Xie, 2011). For this, a dynamic version of the Euler-Bernoulli beam equation is used to represent plant biomechanics (Marjoribanks *et al.*, 2014c). Using this biomechanical model, the flexural rigidity is the key property responsible for controlling plant motion, with a flexural rigidity value of 0.7 N m²

preliminarily assigned based on a review of literature studies covering rigid vegetation types (Erduran and Kutija, 2003). However, the biomechanical model is sensitive to the flexural rigidity value used, and it is difficult to select a representative value for an entire plant given the challenges identified in Section 2.3.4.1.3.

A hypothetical domain 150 cells long, 100 cells wide, and 100 cells high (1 500 000 cells) was created at a spatial resolution of 0.01 m. The inlet velocity was set to 0.50 m s$^{-1}$, so that the plant would experience substantial motion and reconfigure in the flow. Preliminary results for the downstream velocity field around the dynamically moving *Prunus laurocerasus* plant at 0.5 *Y/w* are shown in Figure 7.14.

Significant changes in plant posture are observed within this 5.5 second time-period, with reconfiguration achieved through plant bending. As a result, the foliated blockage is displaced lower in the flow depth, with a downward shift in the position of the wake zone. In addition to this gradual displacement caused by plant bending, a rapid rebound between 1.5 and 3.5 seconds is noted, with this motion exaggerated at the plant tip. The 'whip-like' movement has a significant influence on the downstream velocity field, forcing flow over and around the branch whilst moving in the opposing direction to the flow, thereby producing a turbulent and highly localised wake zone. It is believed that these preliminary results are the first instance of dynamically treating a realistic riparian plant in a LES framework, coupled with a biomechanical plant model, and this will act as a first step for future model development.
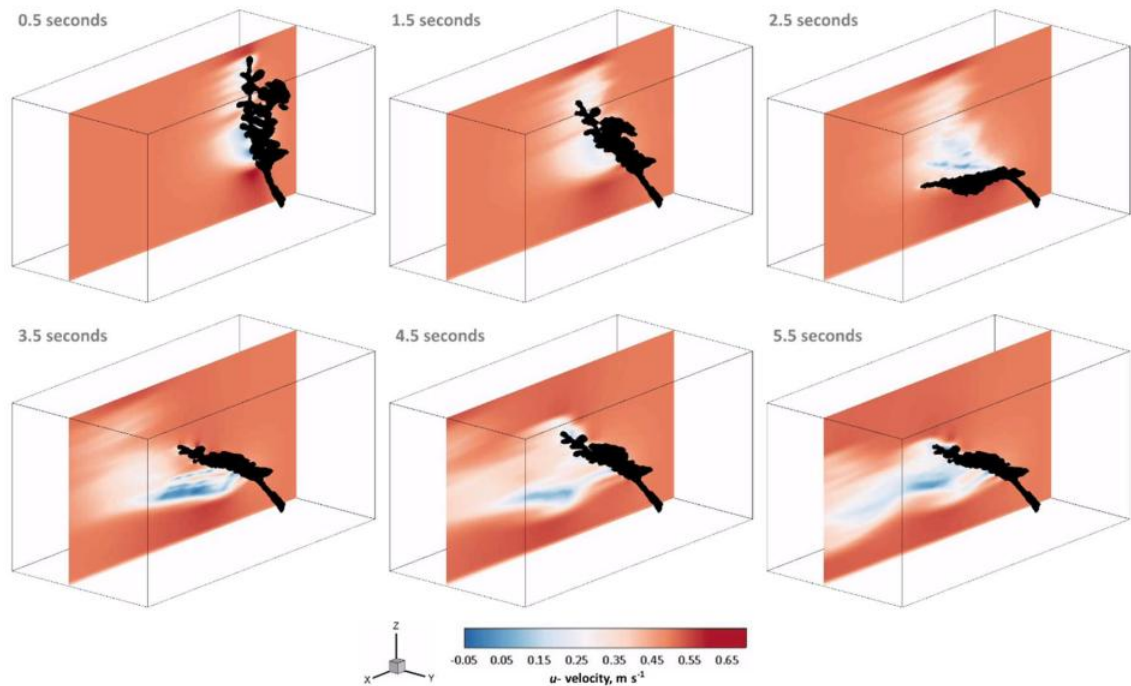
*Figure 7.14 Example of the downstream velocity field at 0.5 Y/w for a dynamically moving Prunus laurocerasus plant applying a Euler-Bernoulli beam equation biomechanical model, in a LES coupled with a dynamic MFSA. Time steps are shown in grey, with flow from right to left.*

### 7.7.4    Incorporating bed topography and modelling sediment transport processes

To minimise bed-generated turbulence, and focus only on flow-vegetation interactions, this thesis has treated the bed as a simple flat boundary. In natural settings, however, the bed will have topography, and this topography will modify the turbulence and drag response where vegetation is present. Figure 7.15 shows an example of this, demonstrating the topographic control of saltmarsh vegetation for a section of the estuary in Mont Saint-Michel Bay, France, captured by a TLS derived point cloud. The data shows that underneath and immediately downstream of the vegetation patch, a topographic ridge exists. In these estuary environments, landform evolution processes including sediment erosion, entrainment, transport pathways, and deposition are influenced by flow-vegetation interactions (Tempest *et al.*, 2015).

The CFD model developed in this thesis has the capacity to represent bed topography in addition to the plant blockage, and therefore offers a unique opportunity to model flow-vegetation-topography interactions. A digital elevation model of the bed topography is incorporated into the CFD model using the MFSA (Lane and Hardy, 2002; Lane *et al.*, 2002; Hardy *et al.*, 2007), in the same way that the voxelised plant blockage was

previously incorporated.  Future work will investigate flow field dynamics around realistic vegetation, with the bed topography explicitly represented.  This will allow the influence of bed topography to be isolated from the influence of vegetation, and will improve the process-understanding of flow-vegetation-topography interactions, especially relevant to estuarine environments where bedforms are present.  Potential applications are not limited to fluvial and estuarine environments, however, with the CFD model highly relevant to aeolian research; with Smyth (2016) highlighting the need to model wind flows over vegetated aeolian landforms.
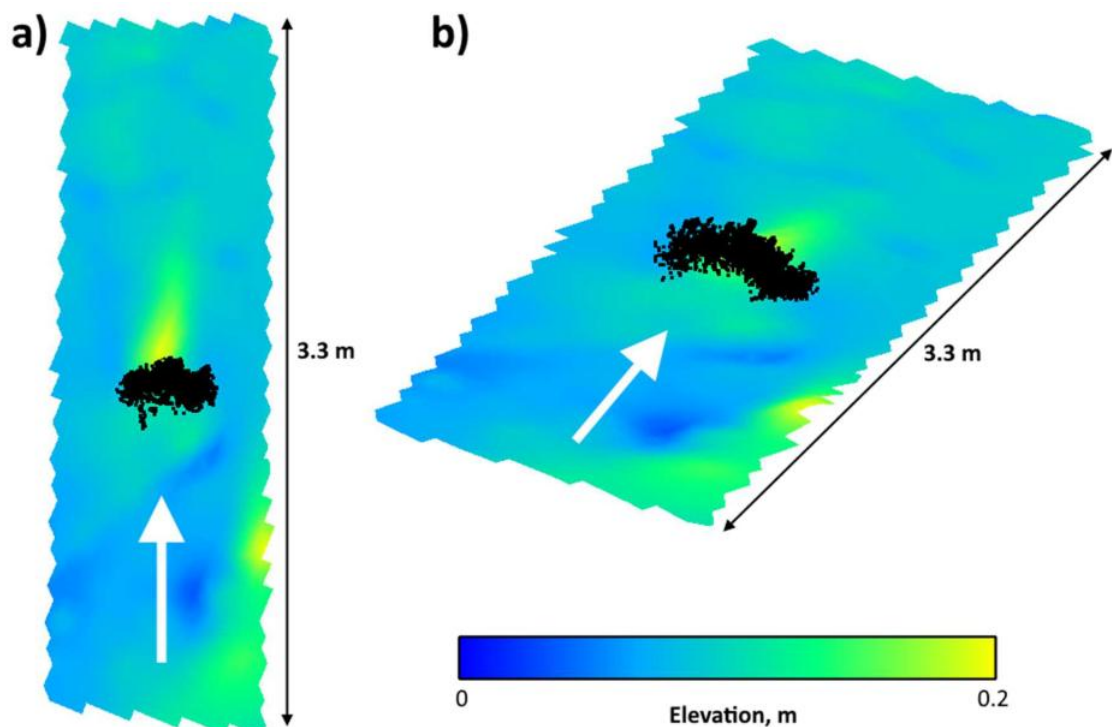


*Figure 7.15 Visualisation of voxelised saltmarsh vegetation and topography at Mont Saint-Michel Bay, France.  Point cloud visualised from (a) above and (b) obliquely.  White arrow indicates flow direction. Data collected by Jerome Leroux and Dimitri Lague.*

The next logical step after incorporating bed topography is to begin to represent sediment transport processes in the CFD model.  Järvelä *et al.* (2006) specify that for predicting erosion and sediment transport, a three-dimensional modelling solution that can adequately predict the turbulent flow field is needed.  The approach developed in this thesis meets these demands, and offers the potential for modelling sediment transport dynamics.  The CFD model will be coupled to a sediment routing model, thereby modelling flow-vegetation-sediment interactions simultaneously.  This development will allow sediment particles to be tracked around vegetation, and the patterns of local scour and deposition to be mapped.

In summary, the potential to incorporate bed topography and sediment processes into the numerical scheme, as well as dynamically moving plant representations, has major implications for the modelling of flow field dynamics, sediment transport processes, and the evolution of vegetated and partially-vegetated near surface landscapes. Alongside upscaling results to the reach-scale, these will be the next challenges of future research.

# Chapter 8

# Conclusions

## 8.1        Introduction

This thesis has developed a numerical representation of floodplain and riparian vegetation response to river flow, improving the process-understanding of flow-vegetation interactions at the plant-scale.  A novel methodology has been developed that captures and explicitly represents the volumetric canopy morphology of natural plants in a high resolution Computational Fluid Dynamics (CFD) model.  This has been extended to consider plant motion dynamics under hydrodynamic loading.   Results have demonstrated how these factors interact and influence flow field dynamics and the drag response, with the implications for vegetative resistance at the reach-scale discussed. The findings are significant given the importance of floodplain and riparian vegetation in river corridor management practices.

In this chapter, the thesis aim and Research Questions identified in Chapter 1 are revisited

***The aim of this research was to investigate how plant volumetric canopy morphology influences three-dimensional mean and turbulent flow, drag, and vegetative resistance at the plant-scale.***

To address this aim, a series of Research Questions were devised, and specific thesis objectives developed having identified knowledge gaps in the literature (Section 2.5).

## 8.2      Research Questions and key findings

Throughout this thesis it has been shown that floodplain and riparian vegetation has a significant effect on flow field dynamics. Results have demonstrated that the interplay between plant motion and plant volumetric canopy morphology, with implications for the plant drag response and vegetative resistance. In this section, each of the Research Questions from Chapter 1 are revisited, with the key findings shown.

*RQ1 – How can plant volumetric canopy morphology be represented in a high resolution numerical model used to predict river flow?*

This thesis has developed a novel method to incorporate plant volumetric canopy morphology into a high resolution CFD model. Realistic representations of natural floodplain and riparian plants were incorporated into the CFD model, made possible by the workflow developed in Section 3.3.

Terrestrial Laser Scanning (TLS) was deemed the most appropriate remote sensing technique to capture plant volumetric canopy morphology (Table 3.1), as this technique met the assessment criteria detailed in Section 3.2, providing a fully three-dimensional plant representation at a millimetre scale spatial resolution, in a format that could be readily incorporated into the CFD model. A comprehensive workflow was developed to collect and process TLS derived point clouds (Figure 3.23), including application of a voxelisation procedure to reduce the number of points, but retain the three-dimensional morphological detail required in the plant representations (Boothroyd *et al.*, 2016a). Using the voxelised plant representations, details of plant structure and form were identified, including the spatially distributed plant solid volume fraction, that quantifies the spatial distribution of porosity over the plant body (Figure 3.28).

As described in Chapter 4, the voxelised plant representations were incorporated into the CFD model by application of a mass flux scaling algorithm (MFSA). In CFD applications, the MFSA has previously been applied to represent various scales of topography (Lane and Hardy, 2002; Hardy *et al.*, 2005; Hardy *et al.*, 2007; Sandbach *et al.*, 2012), and geometrically simple, in-channel vegetation (Marjoribanks *et al.*, 2014c; Marjoribanks *et al.*, 2016). Here, with the numerical grid defined as having vertices that are exactly collocated with the voxelised plant representation, the plant maps directly onto the grid cells, and a binary numerical porosity treatment follows (Lane *et al.*, 2004). This means that the plant was represented as a grid-scale blockage in the computational

domain, with gaps and conduits in the plant canopy explicitly represented (Figure 4.5). The plant was therefore conceptualised as a porous blockage to flow (Lane and Hardy, 2002), and to the author's knowledge, is the first instance of incorporating realistic plant representations into a numerical model used to predict river flow (or any Newtonian flow). This improves upon previous attempts that have only represented plants as morphologically simple elements, and have not adequately resolved the complexity of natural plant structure and form.

### RQ2 – *How well does the numerical model predict measured three-dimensional mean flow?*

Chapter 5 showed results from the combined flume and numerical model study of depth-limited flow around a submerged *Hebe odora* plant at three different flow Reynolds (*Re*) numbers; enabling an evaluation of how well the CFD model predicted the three-dimensional mean flow. With the time-averaged plant posture used as boundary conditions to discretise the plant in the CFD model, analysis showed the modelling system able to accurately reproduce velocity measurements (Boothroyd *et al.*, 2017) collected as velocity profiles using an acoustic Doppler velocimeter (aDv), whereby:

- General agreement between aDv velocity measurements and CFD model predictions was quantified using reduced major axis (RMA) regression, with *u*- velocity correlation coefficients > 0.8 (Figure 5.18). The correlation coefficients compared favourably with previous applications of CFD to velocity profiles in open channel flows (Ferguson *et al.*, 2003; Lane *et al.*, 2004; Hardy *et al.*, 2005; Hardy *et al.*, 2011b; Sandbach *et al.*, 2012), and demonstrated a very good general agreement. This is further shown in Figure 5.26, with the normalised *u*- velocity compared across the measurement region for each *Re*.
- Root-mean-square and mean absolute errors were consistently small (maximum errors < 0.06 m s$^{-1}$ for *u*-, < 0.02 m s$^{-1}$ for *v*-, and < 0.02 m s$^{-1}$ for *w*- velocity), indicating minor differences between measured and modelled velocity profiles.
- Spatially heterogeneous velocity profiles were well reproduced by the CFD model, quantified using the visual distance statistic (Marron and Tsybakov, 1995), and this demonstrated the similarity between the shapes of measured and modelled velocity profiles (Figure 5.23), indicating the correct process capture by the numerical model.
- When investigating the spatial patterns of *u*- velocity difference (Figure 5.25), the CFD model under-predicted flow in the sub-canopy region. This was attributed to

potentially under-representing the plant blockage in the CFD model, suggesting that the modelled plant representations were more porous than the plants in the flume, thought to arise because the spanwise plant motion dynamics were not quantified.

▪ Similarities in the characteristics of the measured and modelled wakes were shown (Figure 5.26), with wake length reducing from 3.9 plant lengths at *Re* 65 000 (both measured and modelled), to 3.1 plant lengths when measured, and 3.3 plant lengths when modelled (*Re* 110 000). The overall wake shape, and downstream reductions in thickness were well reproduced by the CFD model.

### RQ3 – *What are the feedbacks between flow and plant motion dynamics?*

The flume experiments in Chapter 5 showed the complexity in the response of a riparian plant under hydrodynamic loading. Plant motion was separated into time-dynamic and time-averaged components, each of which resulted in feedbacks with the flow.

▪ Time-dynamic plant motions were investigated by tracking the motion of plant tips, and showed a transition from horizontally dominated to vertically dominated movement, and increased movement extents, as *Re* increased. Plant tip motion varied across the plant body in reaction to the local flow, and showed a dependence with *Re* (Figure 5.15). This is because a riparian plant is not a single homogenous unit (Hurd, 2000), with different parts of the plant exposed differently, and therefore moving differently under flow. Locally, some parts of the plant move more than others. This is not a random process with respect to time and space, as some parts of the plant will respond to the flow first, while other parts of the plant will take longer to readjust and reconfigure. Time-dynamic motion will introduce additional turbulence into the flow, but it is shown that plant motion dynamics are accompanied by considerable spatial and temporal complexity.

▪ Time-averaged plant motion is associated with shifts in the general plant posture with reconfiguration to the mean flow. In the *Re* range 89 000 – 110 000, an inverse harmonic relationship between plant height and plant length was shown (Figure 5.14). Over the entire *Re* range, this resulted in up to an 18% reduction in plant height, a 14% increase in plant length, and a doubling of the lead and lee angles of the plant body (Figure 5.16). These motions were responsible for vertically compressing the plant in the flow, thereby reducing the volumetric canopy morphology and plant porosity. Feedbacks with flow are associated with these changes, with the forcing of more flow around the outside of the plant blockage, and

the positioning of the plant wake lower in the flow depth. Time-averaged plant motion therefore influences local flow field dynamics.

***RQ4 – How important are changes in plant posture and porosity on the three-dimensional mean and turbulent flow?***

*and*

***RQ5 – How important is plant morphology and 'how the plant looks' to flow on the three-dimensional mean and turbulent flow?***

Chapters 5, 6, and 7 demonstrated substantial links and overlap between RQ4 and RQ5, it is therefore useful to pair the Research Questions, rather than revisit them individually. The key findings include:

- With changes in plant posture, the wake volume remained similar as the plant volume was conserved, although local flow field dynamics differed (e.g. the spatial heterogeneity in downstream velocity profiles, Figure 6.26). Furthermore, the spatial distribution of pressure acting on the plant changed (Figure 6.28), and this had implications for the pressure gradient and the drag response.
- With changes in plant porosity, the strength of bleed-flow through gaps or conduits in the plant canopy is modified (Figure 7.2 and Figure 7.3). Comparing porous and impermeable plant representations, bleed-flow lengthened the plant wake and influenced the turbulence response. Porosity therefore controlled the extent to which a plant can be conceptualised as a porous bluff object.
- Plant morphology factors such as foliage posed a significant control on local flow field dynamics. For the *Prunus laurocerasus* plant modelled when defoliated and foliated, Section 6.3 demonstrated considerably more flow disturbance when the leaf body was present, and this influenced the streamline and turbulent kinetic energy (TKE) response. Differences in plant form and structure also influenced flow field dynamics, shown when modelling flow around three different plants of the same species (Section 6.5).
- With changes in how the plant is presented to flow, resulting in different exposures of vegetal elements and therefore different local sheltering effects, the turbulent kinetic energy response varied considerably (Figure 6.32 and Figure 6.33). Whether

a plant was aligned parallel or perpendicular to the incident flow therefore influenced energy conversion.

- It is the combined effect of the above factors that influenced flow field dynamics. Flow features that were consistently identified included spatially heterogeneous velocity profiles with a component of sub-canopy flow in the near-bed region, and the development of vegetated shear layers at the horizontal and vertical interfaces of the plant blockage. These have implications for sediment transport processes. It is suggested that shear layer turbulence was dominated by Kelvin–Helmholtz and Görtler-type vortices generated through shear instability (Ghisalberti and Nepf, 2002). Furthermore, the presence of horseshoe vortices that wrap around the plant blockages (Figure 7.10) resembled flow in a junction vortex system (Simpson, 2001). Further work is needed to fully resolve the turbulent flow structures present at the plant-scale, and application of Large Eddy Simulation (LES) would help elucidate these.

- The improved process-understanding gained throughout this thesis has led to development of a new conceptualisation of flow-vegetation interactions for floodplain and riparian plants (Figure 7.11).

### RQ6 – *What is the dominant factor controlling the drag exerted on submerged natural plants?*

Chapter 7 showed that a range of factors influenced the drag response for submerged floodplain and riparian plants. The effect of the plant frontal area is central to this, as form drag is roughly proportional to the frontal area of an object (Vogel, 1994). Drag force increased with plant frontal area, with drag force increasing from 0.15 to 1.74 N m$^2$ between defoliated and foliated *Prunus laurocerasus* plants (Section 7.5.1.2). Furthermore, the drag coefficient decreased as the *Hebe odora* plant reconfigured and became more streamlined to the flow (Section 7.5.1.3).

However, additional complexities emerged when considering the other factors that contributed towards the drag response. The combined effects of the plant volumetric canopy morphology and porosity, and 'how the plant looks to flow' that influenced the local flow field dynamics, in turn influenced the pressure gradient acting on the plant. The drag coefficient was over 100% greater for impermeable plant representations than porous plant representations, and this demonstrated the considerable control of porosity on drag. Furthermore, with the plant volumetric canopy morphology conserved, and only plant aspect incrementally changed, Figure 7.12 demonstrated the substantial range

of drag responses possible for the same plant; as drag coefficients varied by up to ~210%. This substantial variation was attributed to the different exposures and sheltering effects of the plant in flow, and was analogous to differences in the drag response of face-on and edge-on cubes mounted on a planar surface (Streeter, 1998).

A reoccurring theme throughout this thesis is that the newly quantified, physically-determined drag coefficients deviated substantially from the commonly assigned value of unity, or the typical drag coefficient value range from 1.0 – 1.2 that has been used to represent vegetation in hydraulic modelling applications (Dittrich *et al.*, 2012). Results from this thesis showed that drag coefficients for floodplain and riparian plants are generally greater than the previously established values, and should be considered dynamic. A single drag coefficient value is unlikely to reflect the full range of the plant motion in response to hydrodynamic loading; shown by changes in the drag coefficient with changes in the time-averaged plant posture during reconfiguration. Over longer timescales, with seasonal changes in foliage density the drag coefficient would also vary; shown by the differences in drag response between defoliated and foliated plants. For any one plant species, therefore, a range of drag coefficients are more representative than a single value, given the improved process-understanding developed in this thesis.

### RQ7 – *What are the implications for vegetative resistance?*

The physically-determined drag coefficients and high resolution plant frontal area measurements were used to back-calculate Manning's *n*. The back-calculated values remained considerably higher than traditional bulk vegetative resistance terms for comparable vegetation types, selected from classical look-up tables (e.g. Chow, 1959). This was highlighted for the impermeable *Hebe odora* plant, with the back-calculated Manning's *n* value of 0.176 within the range of dense, foliated trees (Manning's n values of 0.11 – 0.20), rather than the expected range of scattered brush and heavy weeds (Manning's n values of 0.035 – 0.070, (Chow, 1959)). The dynamic nature of the drag coefficient was reflected in the back-calculated Manning's *n* values, falling from 0.086 to 0.078 for the porous *Hebe odora* plant due to plant reconfiguration.

The newly quantified Manning's *n* values can be applied to conveyance estimators or to represent vegetative resistance in industry standard, two-dimensional hydraulic models. Changes in the Manning's n values associated with the vegetation component of resistance alter hydraulic model outputs (e.g. Abu-Aly *et al.,* 2014). Often, however, the Manning's *n* value is applied as either an effective parameter (Lane, 2005), or as a

calibration parameter (e.g. Mason *et al.,* 2003), therefore lacking in physical basis. Derivation of Manning's *n* values for a single plant species following the approach developed in this thesis has a greater physical basis, and can be upscaled to the reach-scale following the recommendations in Section 7.6. This is because the drag coefficient is physically-determined and has been calculated using an improved process-understanding of flow-vegetation interactions at the plant-scale. Given the importance of vegetation in river corridor management, the approach developed here demonstrates the necessity to account for plant volumetric canopy morphology when calculating vegetative resistance.

# References

Abdelrhman MA. 2007. Modeling coupling between eelgrass Zostera marina and water flow. *Marine Ecology Progress Series* **338**: 81-96.

Aberle J, Dittrich A. 2012. An experimental study of drag forces acting on flexible plants. In *River Flow 2012*, Murillo Muñoz RE (ed). Taylor & Francis: San José, Costa Rica.

Aberle J, Järvelä J. 2013. Flow resistance of emergent rigid and flexible floodplain vegetation. *Journal of Hydraulic Research* **51**: 33-45.

Aberle J, Järvelä J. 2015. Hydrodynamics of Vegetated Channels. In *Rivers – Physical, Fluvial and Environmental Processes*, Rowiński P, Radecki-Pawlik A (eds). Springer International Publishing: Berlin; 519-541.

Abu-Aly TR, Pasternack GB, Wyrick JR, Barker R, Massa D, Johnson T. 2014. Effects of LiDAR-derived, spatially distributed vegetation roughness on two-dimensional hydraulics in a gravel-cobble river at flows of 0.2 to 20 times bankfull. *Geomorphology* **206**: 468-482.

Ackerman JD, Okubo A. 1993. Reduced Mixing in a Marine Macrophyte Canopy. *Functional Ecology* **7**: 305-309.

Acrement GR, Schneider VR. 1989. Guide for selecting Manning's roughness coefficients for natural channels and flood plains. Water supply paper 2339. U.S. Geological Survey Washington, USA.

Albayrak I, Nikora V, Miler O, O'Hare M. 2012. Flow-plant interactions at a leaf scale: effects of leaf shape, serration, roughness and flexural rigidity. *Aquatic Sciences* **74**: 267-286.

Alben S, Shelley M, Zhang J. 2002. Drag reduction through self-similar bending of a flexible body. *Nature* **420**: 479-481.

Anderson JD. 1984. Fundamentals of aerodynamics. McGraw-Hill: New York, USA.

Anderson JD. 1995. Computational Fluid Dynamics. McGraw-Hill: New York, USA.

Anderson K, Hancock S, Disney M, Gaston KJ. 2016. Is waveform worth it? A comparison of LiDAR approaches for vegetation and landscape characterization. *Remote Sensing in Ecology and Conservation* **2**: 5-15.

Anderson SM, Charters AC. 1982. A fluid dynamics study of seawater flow through Gelidium nudifrons1. *Limnology and oceanography* **27**: 399-412.

Andersson AG, Leonardsson K, Lindberg D, Lundström TS, Hellström JGI, Lundqvist H. 2016. Describing fish passage in a river confluence with telemetry and CFD. In *Proceedings of the 11th International Symposium on Ecohydraulics*, Webb JAC, J.F., Casas-Mulet R, Lyon JP, Stewardson MJ (eds). The University of Melbourne: Melbourne, Australia.

Antonarakis AS. 2010. Evaluating forest biometrics obtained from ground lidar in complex riparian forests. *Remote Sensing Letters* **2**: 61-70.

Antonarakis AS, Richards KS, Brasington J, Bithell M. 2009. Leafless roughness of complex tree morphology using terrestrial lidar. *Water Resources Research* **45**: W10401.

Antonarakis AS, Richards KS, Brasington J, Muller E. 2010. Determining leaf area index and leafy tree roughness using terrestrial laser scanning. *Water Resources Research* **46**: W06510.

Argyropoulos CD, Markatos NC. 2014. Recent advances on the numerical modelling of turbulent flows. *Applied Mathematical Modelling*.

ASME. 1993. Statement on the Control of Numerical Accuracy. *American Society of Mechanical Engineers, Journal of Fluid Engineering*.

Baker CJ. 1980. The turbulent horseshoe vortex. *Journal of Wind Engineering and Industrial Aerodynamics* **6**: 9-23.

Bakker A. 2008. Lecture 10 - Turbulence Models. http://www.bakker.org/dartmouth06/engs150/10-rans.pdf.

Bakry MF, Gates TK, Khattab AF. 1992. Field-Measured Hydraulic Resistance Characteristics in Vegetation-Infested Canals. *Journal of Irrigation and Drainage Engineering* **118**: 256-274.

Barber C, Dobkin D, Huhdanpaa H. 1996. The quickhull algorithm for convex hulls. *ACM Trans. Math. Softw.* **22**: 469-483.

Bardina J, Ferziger J, Reynolds W. 1980. Improved subgrid-scale models for large-eddy simulation. In *13th Fluid and Plasma Dynamics Conference*. American Institute of Aeronautics and Astronautics: Standford, USA.

Barnes H. 1967. Roughness characteristics of natural channels. Water supply paper 1849. U.S. Geological Survey: Washington, USA.

Bates PD. 2014. Flood crisis: dredging is a simplistic response to a complex problem. In *The Guardian*, 12th February 2014.

Bathurst JC. 1978. Flow resistance of large-scale roughness. *Journal of the Hydraulics Division* **104**: 1587-1603.

Battiato I, Rubol S. 2014. Single-parameter model of vegetated aquatic flows. *Water Resources Research* **50**: 6358-6369.

Bauer BO, Walker IJ, Baas ACW, Jackson DWT, McKenna-Neuman C, Wiggs GFS, Hesp PA. 2013. Critical Reflections on the Coherent Flow Structures Paradigm in Aeolian Geomorphology. In *Coherent Flow Structures at Earth's Surface*, Venditti JG, Best JL, Church M, Hardy RJ (eds). John Wiley & Sons, Ltd: Chichester, UK; 111-134.

Béland M, Baldocchi DD, Widlowski J-L, Fournier RA, Verstraete MM. 2014a. On seeing the wood from the leaves and the role of voxel size in determining leaf area distribution of forests with terrestrial LiDAR. *Agricultural and Forest Meteorology* **184**: 82-97.

Béland M, Widlowski J-L, Fournier RA. 2014b. A model for deriving voxel-level tree leaf area density estimates from ground-based LiDAR. *Environmental Modelling & Software* **51**: 184-189.

Béland M, Widlowski J-L, Fournier RA, Côté J-F, Verstraete MM. 2011. Estimating leaf area distribution in savanna trees from terrestrial LiDAR measurements. *Agricultural and Forest Meteorology* **151**: 1252-1266.

Beraldin J-A, Blais F, Lohr U. 2010. Laser Scanning Technology. In *Airborne and terrestrial laser scanning*, Vosselman G, Maas H-G (eds). Whittles Publishing: Dunbeath, Scotland; 318.

Bergeron NE, Carbonneau P. 1999. The effect of sediment concentration on bedload roughness. *Hydrological Processes* **13**: 2583-2589.

Bernard PS, Wallace JM. 2002. Turbulent flow: analysis, measurement, and prediction. Wiley: Hoboken, USA.

Best J. 2005. The fluid dynamics of river dunes: A review and some future research directions. *Journal of Geophysical Research: Earth Surface* **110**: F04S02.

Bienert A, Hess C, Maas HG, von Oheimb G. 2014. A voxel-based technique to estimate the volume of trees from terrestrial laser scanner data. *Int. Arch. Photogramm. Remote Sens. Spatial Inf. Sci.* **XL-5**: 101-106.

Bienert A, Scheller S, Keane E, Mullooly G, Mohan F. 2006. Application of terrestrial laser scanners for the determination of forest inventory parameters. In *Proceedings of the ISPRS Commission V Symposium 'Image Engineering and Vision Metrology'* Dresden, Germany.

Blazek J. 2005. Computational Fluid Dynamics: Principles and Applications. Elsevier Science: Oxford, UK.

Bölscher J, Ergenzinger P, Obenauf PJ. 2005. Hydraulic, sedimentological and eco-logical problems of multifunctional riparian forest management - RIPFOR the scientific. Heft 65 report. Berliner Geographische Abhandlungen: Berlin, Germany.

Boothroyd RJ, Hardy RJ, Warburton J, Marjoribanks TI. 2016a. The importance of accurately representing submerged vegetation morphology in the numerical prediction of complex river flow. *Earth Surface Processes and Landforms* **41**: 567-576.

Boothroyd RJ, Hardy RJ, Warburton J, Marjoribanks TI. 2016b. Modelling vegetation-flow interactions: the importance of accurately representing plant morphology. In *11th International Symposium on Ecohydraulics* Melbourne, Australia.

Boothroyd RJ, Hardy RJ, Warburton J, Marjoribanks TI. 2017. Modeling complex flow structures and drag around a submerged plant of varied posture. *Water Resources Research* **53**: 2877-2901.

Borazjani I, Sotiropoulos F. 2009. Numerical investigation of the hydrodynamics of anguilliform swimming in the transitional and inertial flow regimes. *Journal of Experimental Biology* **212**: 576-592.

Boussinesq J. 1877. Essai sur la théorie des eaux courantes. Imprimerie Nationale: Paris.

Bradbrook KF. 2000. Numerical, field and laboratory studies of three-dimensional flow structures at river channel confluences. University of Cambridge: Cambridge, UK.

Bradbrook KF, Biron PM, Lane SN, Richards KS, Roy AG. 1998. Investigation of controls on secondary circulation in a simple confluence geometry using a three-dimensional numerical model. *Hydrological Processes* **12**: 1371-1396.

Bradbrook KF, Lane SN, Richards KS. 2000. Numerical simulation of three-dimensional, time-averaged flow structure at river channel confluences. *Water Resources Research* **36**: 2731-2746.

Brand A, Noss C, Dinkel C, Holzner M. 2016. High-Resolution Measurements of Turbulent Flow Close to the Sediment–Water Interface Using a Bistatic Acoustic Profiler. *Journal of Atmospheric and Oceanic Technology* **33**: 769-788.

Brasington J, Vericat D, Rychkov I. 2012. Modeling river bed morphology, roughness, and surface sedimentology using high resolution terrestrial laser scanning. *Water Resources Research* **48**: W11519.

Braza M, Chassaing P, Minh HH. 1986. Numerical study and physical analysis of the pressure and velocity fields in the near wake of a circular cylinder. *Journal of Fluid Mechanics* **165**: 79-130.

Braza M, Chassaing P, Minh HH. 1990. Prediction of large-scale transition features in the wake of a circular cylinder. *Physics of Fluids A: Fluid Dynamics (1989-1993)* **2**: 1461-1471.

Breusers HNC, Nicollet G, Shen HW. 1977. Local Scour Around Cylindrical Piers. *Journal of Hydraulic Research* **15**: 211-252.

Bridge JS, Demicco RV. 2008. Earth surface processes, landforms and sediment deposits. Cambridge University Press: Cambridge, UK.

Brodu N, Lague D. 2012. 3D terrestrial lidar data classification of complex natural scenes using a multi-scale dimensionality criterion: Applications in geomorphology. *ISPRS Journal of Photogrammetry and Remote Sensing* **68**: 121-134.

Buffington JM, Montgomery DR. 1999. Effects of hydraulic roughness on surface textures of gravel-bed rivers. *Water Resources Research* **35**: 3507-3521.

Cameron SM, Nikora VI, Albayrak I, Miler O, Stewart M, Siniscalchi F. 2013. Interactions between aquatic plants and turbulent flow: a field study using stereoscopic PIV. *Journal of Fluid Mechanics* **732**: 345-372.

Carpenter SR, Lodge DM. 1986. Effects of submersed macrophytes on ecosystem processes. *Aquatic Botany* **26**: 341-370.

Carrivick JL, Smith MW, Quincey DJ. 2016. Structure from Motion in the Geosciences. John Wiley & Sons: London, UK.

CHAM. 2005. CHAM Technical Report: TR 001, PHOENICS Overview. http://www.cham.co.uk/phoenics/d_polis/d_docs/tr001/tr001.htm.

CHAM. 2007. PHOENICS Encyclopaedia. http://www.cham.co.uk/phoenics/d_polis/d_enc/encindex.htm.

CHAM. 2013. PHOENICS. Private License.

Chambers PA, Kaiff J. 1985. Depth Distribution and Biomass of Submersed Aquatic Macrophyte Communities in Relation to Secchi Depth. *Canadian Journal of Fisheries and Aquatic Sciences* **42**: 701-709.

Champion PD, Tanner CC. 2000. Seasonality of macrophytes and interaction with flow in a New Zealand lowland stream. *Hydrobiologia* **441**: 1-12.

Chandler J, Buckley S. 2016. Structure from motion (SFM) photogrammetry vs terrestrial laser scanning. In *Geoscience Handbook 2016: AGI Data Sheets*, Carpenter MB, Keane CM (eds). American Geosciences Institute: Alexandria, USA.

Chang K, Constantinescu G. 2015. Numerical investigation of flow and turbulence structure through and around a circular array of rigid cylinders. *Journal of Fluid Mechanics* **776**: 161-199.

Chang S, Iaccarino G, Ham F, Elkins C, Monismith S. 2014. Local shear and mass transfer on individual coral colonies: Computations in unidirectional and wave-driven flows. *Journal of Geophysical Research: Oceans* **119**: 2599-2619.

Chapman JA, Wilson BN, Gulliver JS. 2015. Drag force parameters of rigid and flexible vegetal elements. *Water Resources Research* **51**: 3292-3302.

Chen L, Chen X. 2016. Comments on "An improved Cauchy number approach for predicting the drag and reconfiguration of flexible vegetation" By Peter Whittaker, Catherine A.M.E. Wilson, and Jochen Aberle. *Advances in Water Resources* **106**: 223-235.

Cheng N-S. 2013. Calculation of Drag Coefficient for Arrays of Emergent Circular Cylinders with Pseudofluid Model. *Journal of Hydraulic Engineering* **139**: 602-611.

Chow V. 1959. Open Channel Hydraulics. McGraw-Hill: New York, USA.

Chartered Institution of Water and Environmental Management. 2014. Floods and Dredging: A Reality Check. London: Chartered Institution of Water and Environmental Management. Chartered Institution of Water and Environmental Management: London.

Clarke SJ. 2002. Vegetation growth in rivers: influences upon sediment and nutrient dynamics. *Progress in Physical Geography* **26**: 159-172.

CloudCompare. 2017. CloudCompare. Retrieved from http://www.cloudcompare.org/; GPL Software.

Cockayne L. 1958. The vegetation of New Zealand. Engelmann: Weinheim, W. Germany.

Colombini M. 1993. Turbulence-driven secondary flows and formation of sand ridges. *Journal of Fluid Mechanics* **254**: 701-719.

Connell BSH, Yue DKP. 2007. Flapping dynamics of a flag in a uniform stream. *Journal of Fluid Mechanics* **581**: 33-67.

Constantinescu G, Miyawaki S, Liao Q. 2013. Flow and Turbulence Structure past a Cluster of Freshwater Mussels. *Journal of Hydraulic Engineering* **139**: 347–358.

Coon WF. 1998. Estimation of roughness coefficients for natural stream channels with vegetated banks. Water supply paper 2441. U.S. Geological Survey: Washington, USA.

Cooper GG, Callaghan FM, Nikora VI, Lamouroux N, Statzner B, Sagnes P. 2007. Effects of flume characteristics on the assessment of drag on flexible macrophytes and a rigid cylinder. *New Zealand Journal of Marine and Freshwater Research* **41**: 129-135.

Corenblit D, Steiger J, Charrier G, Darrozes J, Garófano-Gómez V, Garreau A, González E, Gurnell AM, Hortobágyi B, Julien F, Lambs L, Larrue S, Otto T, Roussel E, Vautier F, Voldoire O. 2016. Populus nigra L. establishment and fluvial landform construction: biogeomorphic dynamics within a channelized river. *Earth Surface Processes and Landforms* **41**: 1276-1292.

Corenblit D, Steiger J, González E, Gurnell AM, Charrier G, Darrozes J, Dousseau J, Julien F, Lambs L, Larrue S, Roussel E, Vautier F, Voldoire O. 2014. The biogeomorphological life cycle of poplars during the fluvial biogeomorphological succession: a special focus on Populus nigra L. *Earth Surface Processes and Landforms* **39**: 546-563.

Corenblit D, Steiger J, Gurnell AM, Tabacchi E, Roques L. 2009. Control of sediment dynamics by vegetation as a key function driving biogeomorphic succession within fluvial corridors. *Earth Surface Processes and Landforms* **34**: 1790-1810.

Cowan W. 1956. Estimating hydraulic roughness coefficients. *Agricultural Engineering* **37**: 473-475.

Crouzy B, Edmaier K, Pasquale N, Perona P. 2013. Impact of floods on the statistical distribution of riverbed vegetation. *Geomorphology* **202**: 51-58.

Cucitore R, Quadrio M, Baron A. 1999. On the effectiveness and limitations of local criteria for the identification of a vortex. *European Journal of Mechanics* **18**: 261-282.

Cullen S. 2005. Trees and wind: a practical consideration of the drag equation velocity exponent for urban tree risk management. *Journal of Arboriculture* **31**: 101-113.

Curran JC, Hession CW. 2013. Vegetative Impacts on Hydraulics and Sediment Processes across the Fluvial System. *Journal of Hydrology* **505**: 364-376.

Dandois JP, Ellis EC. 2013. High spatial resolution three-dimensional mapping of vegetation spectral dynamics using computer vision. *Remote Sensing of Environment* **136**: 259-276.

Daniels MD, Rhoads BL. 2003. Influence of a large woody debris obstruction on three-dimensional flow structure in a meander bend. *Geomorphology* **51**: 159-173.

Danson FM, Gaulton R, Armitage RP, Disney M, Gunawan O, Lewis P, Pearson G, Ramirez AF. 2014. Developing a dual-wavelength full-waveform terrestrial laser scanner to characterize forest canopy structure. *Agricultural and Forest Meteorology* **198–199**: 7-14.

Dargahi B. 1989. The turbulent flow field around a circular cylinder. *Experiments in Fluids* **8**: 1-12.

Davies P, Morvan C, Sire O, Baley C. 2007. Structure and properties of fibres from sea-grass (Zostera marina). *Journal of Materials Science* **42**: 4850-4857.

de Langre E. 2008. Effects of Wind on Plants. *Annual Review of Fluid Mechanics* **40**: 141-168.

de Langre E, Gutierrez A, Cossé J. 2012. On the scaling of drag reduction by reconfiguration in plants. *Comptes Rendus Mécanique* **340**: 35-40.

de Lima PHS, Janzen JG, Nepf HM. 2015. Flow patterns around two neighboring patches of emergent vegetation and possible implications for deposition and vegetation growth. *Environmental Fluid Mechanics* **15**: 881-898.

Deck S, Duveau P, d'Espiney P, Guillen P. 2002. Development and application of Spalart–Allmaras one equation turbulence model to three-dimensional supersonic complex configurations. *Aerospace Science and Technology* **6**: 171-183.

Defina A, Bixio AC. 2005. Mean flow and turbulence in vegetated open channel flow. *Water Resources Research* **41**: W07006.

Denny M, Gaylord B. 2002. The mechanics of wave-swept algae. *Journal of Experimental Biology* **205**: 1355-1362.

Denny M, Gaylord B, Helmuth B, Daniel T. 1998. The menace of momentum: Dynamic forces on flexible organisms. *Limnology and oceanography* **43**: 955-968.

Devaney RL. 1989. An introduction to chaotic dynamical systems. Addison-Wesley Reading, UK.

Diehl S, Kornijów R. 1998. Influence of Submerged Macrophytes on Trophic Interactions Among Fish and Macroinvertebrates. In *The Structuring Role of Submerged Macrophytes in Lakes*, Jeppesen E, Søndergaard M, Søndergaard M, Christoffersen K (eds). Springer: New York, UK; 24-46.

Dijkstra JT. 2012. Macrophytes in Estuarine Gradients: Flow Through Flexible Vegetation. In *Civil Engineering and Geosciences*. Delft University of Technology: Delft; 135.

Dijkstra JT, Uittenbogaard RE. 2010. Modeling the interaction between flow and highly flexible aquatic vegetation. *Water Resources Research* **46**: W12547.

Dittrich A, Aberle J, Schoneboom T. 2012. Drag forces and flow resistance of flexible riparian vegetation. In *Environmental Fluid Mechanics*, Rodi W, Uhlmann M (eds). CRC Press: Oxford, UK; 195-215.

Douglas JF, Gasoriek JM, Swaffield J, Jack L. 2005. Fluid mechanics. Pearson Prentice Hall: Harlow, UK.

Duarte CM. 1991. Seagrass depth limits. *Aquatic Botany* **40**: 363-377.

Edwards PJ, Kollmann J, Gurnell AM, Petts GE, Tockner K, Ward JV. 1999. A conceptual model of vegetation dynamics on gravel bars of a large Alpine river. *Wetlands Ecology and Management* **7**: 141-153.

Einstein HA, Banks RB. 1950. Fluid resistance of composite roughness. *Eos, Transactions American Geophysical Union* **31**: 603-610.

Eitel JUH, Magney TS, Vierling LA, Dittmar G. 2014. Assessment of crop foliar nitrogen using a novel dual-wavelength laser system and implications for conducting laser-based plant physiology. *ISPRS Journal of Photogrammetry and Remote Sensing* **97**: 229-240.

Eitel JUH, Vierling LA, Magney TS. 2013. A lightweight, low cost autonomously operating terrestrial laser scanner for quantifying and monitoring ecosystem structural dynamics. *Agricultural and Forest Meteorology* **180**: 86-96.

Endalew AM, Debaer C, Rutten N, Vercammen J, Delele MA, Ramon H, Nicolaï BM, Verboven P. 2011. Modelling the Effect of Tree Foliage on Sprayer Airflow in Orchards. *Boundary-Layer Meteorology* **138**: 139-162.

Endalew AM, Hertog M, Delele MA, Baetens K, Persoons T, Baelmans M, Ramon H, Nicolaï BM, Verboven P. 2009. CFD modelling and wind tunnel validation of airflow through plant canopies using 3D canopy architecture. *International Journal of Heat and Fluid Flow* **30**: 356-368.

Endalew AM, Hertog M, Verboven P, Baetens K, Delele MA, Ramon H, Nicolaï BM. 2006. Modelling airflow through 3D canopy structure of orchards. In *International Advances in Pesticide Application 2006*. Association of Applied Biologists: Cambridge; 465-472.

Environment Agency. 2009a. Fluvial Design Guide. Environment Agency: Bristol, UK.

Environment Agency. 2009b. Investing for the Future: Flood and Coastal Risk Management in England, A Long-Term Investment Strategy. Environment Agency: Bristol, UK.

Environment Agency. 2014. Aquatic and riparian plant management: controls for vegetation in watercourses. Environment Agency: Bristol, UK.

Erduran K, Kutija V. 2003. Quasi-three-dimensional numerical model for flow through flexible, rigid, submerged and non-submerged vegetation. *Journal of Hydroinformatics* **5**: 189-202.

Evangelinos C, Karniadakis G. 1999. Dynamics and flow structures in the turbulent wake of rigid and flexible cylinders subject to vortex-induced vibrations. *Journal of Fluid Mechanics* **400**: 91-124.

Evans EP, Simm JD, Thorne CR, Arnell NW, Ashley RM, Hess TM, Lane SN, Morris J, Nicholls RJ, Penning-Rowsell EC, Reynard NS, Saul AJ, Tapsell SM, Watkinson AR, Wheater HS. 2009. An update of the Foresight Future Flooding 2004 qualitative risk analysis. Cabinet Office: London, UK.

Eyquem J. 2007. Using fluvial geomorphology to inform integrated river basin management. *Water and Environment Journal* **21**: 54-60.

Ferguson RI, Parsons DR, Lane SN, Hardy RJ. 2003. Flow in meander bends with recirculation at the inner bank. *Water Resources Research* **39**: 1322-1333.

Fernández-Sarría A, Martínez L, Velázquez-Martí B, Sajdak M, Estornell J, Recio JA. 2013. Different methodologies for calculating crown volumes of Platanus hispanica trees using terrestrial laser scanner and a comparison with classical dendrometric measurements. *Computers and Electronics in Agriculture* **90**: 176-185.

Ferreira E, Chandler J, Wackrow R, Shiono K. 2017. Automated extraction of free surface topography using SfM-MVS photogrammetry. *Flow Measurement and Instrumentation* **54**: 243-249.

Ferreira E, Yonekura S, Giles R, Shiono K, Chandler J, Wackrow R, Ishigaki T. 2015. Drag forces of submerged shrubs and trees in open-channel flows. In *IAHR 36th Congress* The Hague, The Netherlands.

Ferziger JH, Perić M. 2002. Turbulent Flows. Springer Berlin Heidelberg, USA.

Feurich R, Boubée J, Olsen NRB. 2012. Improvement of fish passage in culverts using CFD. *Ecological Engineering* **47**: 1-8.

Finnigan JJ. 2000. Turbulence in plant canopies. *Annual Review of Fluid Mechanics* **32**: 519-571.

Fischer-Antze T, Stoesser T, Bates P, Olsen NRB. 2001. 3D numerical modelling of open-channel flow with submerged vegetation. *Journal of Hydraulic Research* **39**: 303-310.

Fisher K. 1992. The Hydraulic Roughness of Vegetated Channels. Report SR 305. Hydraulics Research Ltd: Wallingford, UK.

Flynn K, Chapra S. 2014. Remote Sensing of Submerged Aquatic Vegetation in a Shallow Non-Turbid River Using an Unmanned Aerial Vehicle. *Remote Sensing* **6**: 12815-12836.

Folkard AM. 2005. Hydrodynamics of model Posidonia oceanica patches in shallow water. *Limnology and oceanography* **50**: 1592-1600.

Folkard AM. 2011. Flow regimes in gaps within stands of flexible vegetation: laboratory flume simulations. *Environmental Fluid Mechanics* **11**: 289-306.

Folkard AM. 2016. Creating patches of comprehension and filling gaps in knowledge: physical modelling contributions to joined-up understanding of heterogeneous eco-scapes. In *11th International Symposium on Ecohydraulics*: Melbourne, Australia.

Fonseca MS, Koehl MAR. 2006. Flow in seagrass canopies: The influence of patch width. *Estuarine, Coastal and Shelf Science* **67**: 1-9.

Fonstad MA, Dietrich JT, Courville BC, Jensen JL, Carbonneau PE. 2013. Topographic structure from motion: a new development in photogrammetric measurement. *Earth Surface Processes and Landforms* **38**: 421-430.

Franceschi M, Teza G, Preto N, Pesci A, Galgaro A, Girardi S. 2009. Discrimination between marls and limestones using intensity data from terrestrial laser scanner. *ISPRS Journal of Photogrammetry and Remote Sensing* **64**: 522-528.

Franklin P, Dunbar M, Whitehead P. 2008. Flow controls on lowland river macrophytes: A review. *Science of The Total Environment* **400**: 369-378.

Freeman GE, Rahmeyer WH, Copeland RR. 2000. Determination of resistance due to shrubs and woody vegetation. Report ERDC/CHL TR-00-25. U.S. Army Corps of Engineers, Coastal and Hydraulics Laboratory: Vicksburg, USA.

Frostick LE, McLelland SJ, Mercer TG. 2011. Users Guide to Physical Modelling and Experimentation: Experience of the HYDRALAB Network. CRC Press: Leiden, The Netherlands.

Furbish D. 1987. Conditions for geometric similarity of coarse stream-bed roughness. *Mathematical Geology* **19**: 291-307.

Garbrecht J, Brown G. 1991. Calculation of Total Conveyance in Natural Channels. *Journal of Hydraulic Engineering* **117**: 788-798.

Gatski TB, Rumsey CL. 2002. Linear and Nonlinear Eddy Viscosity Models. In *Closure Strategies for Turbulent and Transitional Flows*, Launder BE, Sandham ND (eds). Cambridge University Press: UK; 9-46.

Ghisalberti M, Nepf HM. 2002. Mixing layers and coherent structures in vegetated aquatic flows. *Journal of Geophysical Research: Oceans* **107**: 3-1-3-11.

Ghisalberti M, Nepf HM. 2004. The limited growth of vegetated shear layers. *Water Resources Research* **40**: W07502.

Ghisalberti M, Nepf HM. 2005. Mass Transport in Vegetated Shear Flows. *Environmental Fluid Mechanics* **5**: 527-551.

Ghisalberti M, Nepf HM. 2006. The structure of the shear layer in flows over rigid and flexible canopies. *Environmental Fluid Mechanics* **6**: 277-301.

Ghisalberti M, Nepf HM. 2009. Shallow Flows Over a Permeable Medium: The Hydrodynamics of Submerged Aquatic Canopies. *Transport in Porous Media* **78**: 309-326.

Gienko GA, Terry JP. 2014. Three-dimensional modeling of coastal boulders using multi-view image measurements. *Earth Surface Processes and Landforms* **39**: 853-864.

Godin C, Caraglio Y. 1998. A Multiscale Model of Plant Topological Structures. *Journal of Theoretical Biology* **191**: 1-46.

Godin C, Costes E, Sinoquet H. 1999. A Method for Describing Plant Architecture which Integrates Topology and Geometry. *Annals of Botany* **84**: 343-357.

Gorte B, Winterhalder D. 2004. Reconstruction of laser-scanned trees using filter operations in the 3D raster domain. *International Archives of Photogrammetry, Remote Sensing and Spatial Information Sciences* **36**: 39-44.

Gourlay MR. 1970. Discussion of: Flow resistance in vegetated channels, by Kouwen N, Unny TE and Hill HM. *Journal of the Irrigation and Drainage Division of the American Society of Civil Engineers* **96**: 351-357.

Graf WH, Yulistiyanto B. 1998. Experiments on flow around a cylinder; the velocity and vorticity fields. *Journal of Hydraulic Research* **36**: 637-654.

Graham RL. 1972. An efficient algorith for determining the convex hull of a finite planar set. *Information processing letters* **1**: 132-133.

Green JC. 2005a. Comparison of blockage factors in modelling the resistance of channels containing submerged macrophytes. *River Research and Applications* **21**: 671-686.

Green JC. 2005b. Further comment on drag and reconfiguration of macrophytes. *Freshwater Biology* **50**: 2162-2166.

Green JC. 2005c. Modelling flow resistance in vegetated streams: review and development of new theory. *Hydrological Processes* **19**: 1245-1259.

Green JC. 2006. Effect of macrophyte spatial variability on channel resistance. *Advances in Water Resources* **29**: 426-438.

Gross G. 1987. A numerical study of the air flow within and around a single tree. *Boundary-Layer Meteorology* **40**: 311-327.

Gurnell A. 2014. Plants as river system engineers. *Earth Surface Processes and Landforms* **39**: 4-25.

Gurnell AM, Petts G. 2006. Trees as riparian engineers: the Tagliamento river, Italy. *Earth Surface Processes and Landforms* **31**: 1558-1574.

Hackenberg J, Spiecker H, Calders K, Disney M, Raumonen P. 2015. SimpleTree —An Efficient Open Source Tool to Build Tree Models from TLS Clouds. *Forests* **6**: 4245.

Hanjalić K. 1994. Advanced turbulence closure models: a view of current status and future prospects. *International Journal of Heat and Fluid Flow* **15**: 178-203.

Hanjalić K. 2004. Closure models for incompressible turbulent flows (lecture series). In *Introduction to turbulence modeling*, Beeck JPvBC (ed). Von Karman Institute for Fluid Dynamics: Rhode Saint Genese.

Hankin BG, Hardy R, Kettle H, Beven KJ. 2001. Using CFD in a GLUE framework to model the flow and dispersion characteristics of a natural fluvial dead zone. *Earth Surface Processes and Landforms* **26**: 667-687.

Harder D, Speck O, Hurd C, Speck T. 2004. Reconfiguration as a Prerequisite for Survival in Highly Unstable Flow-Dominated Habitats. *Journal of Plant Growth Regulation* **23**: 98-107.

Hardy RJ, Best JL, Parsons DR, Keevil GM. 2011a. On determining the geometric and kinematic characteristics of coherent flow structures over a gravel bed: a new approach using combined PLIF-PIV. *Earth Surface Processes and Landforms* **36**: 279-284.

Hardy RJ, Lane SN, Ferguson RI, Parsons DR. 2003. Assessing the credibility of a series of computational fluid dynamic simulations of open channel flow. *Hydrological Processes* **17**: 1539-1560.

Hardy RJ, Lane SN, Ferguson RI, Parsons DR. 2007. Emergence of coherent flow structures over a gravel surface: A numerical experiment. *Water Resources Research* **43**: W03422.

Hardy RJ, Lane SN, Lawless MR, Best JL, Elliott L, Ingham DB. 2005. Development and testing of a numerical code for treatment of complex river channel topography in three-dimensional CFD models with structured grids. *Journal of Hydraulic Research* **43**: 468-480.

Hardy RJ, Lane SN, Yu D. 2011b. Flow structures at an idealized bifurcation: a numerical experiment. *Earth Surface Processes and Landforms* **36**: 2083-2096.

Hardy RJ, Marjoribanks TI, Parson DR, Reesink AJ, Murphy B, Ashworth PJ, Best JL. 2014. Modelling time dependent flow fields over three dimensional dunes. In *River flow 2014 : proceedings of the International Conference on Fluvial Hydraulics, (River Flow 2014), Lausanne, Switzerland, 3-5 September 2014.*, Schleiss AJ, De Cesare G, Franca MJ, Pfister M (eds). CRC Press, Taylor & Francis Group: London; 1045-1052.

Hargeby A, Andersson G, Blindow I, Johansson S. 1994. Trophic web structure in a shallow eutrophic lake during a dominance shift from phytoplankton to submerged macrophytes. *Hydrobiologia* **279**: 83-90.

Haslam SM. 1978. River plants: the macrophytic vegetation of watercourses. Cambridge University Press: Cambridge, UK.

Heritage G, Hetherington D. 2007. Towards a protocol for laser scanning in fluvial geomorphology. *Earth Surface Processes and Landforms* **32**: 66-74.

Hess C, Bienert A, Härdtle W, von Oheimb G. 2015. Does Tree Architectural Complexity Influence the Accuracy of Wood Volume Estimates of Single Young Trees by Terrestrial Laser Scanning? *Forests* **6**: 3847.

Hicks DM, Mason PD. 1991. A handbook for assigning hydraulic roughness coefficients to river reaches by the "visual comparison" approach. Water Resources Survey, DSIR Marine and Freshwater: Wellington, NZ.

Ho C, Huerre P. 1984. Perturbed free shear layers. *Annual Review of Fluid Mechanics* **16**: 365-422.

Hodge R, Brasington J, Richards K. 2009. In situ characterization of grain-scale fluvial morphology using Terrestrial Laser Scanning. *Earth Surface Processes and Landforms* **34**: 954-968.

Hodskinson A, Ferguson RI. 1998. Numerical modelling of separated flow in river bends: model testing and experimental investigation of geometric controls on the extent of flow separation at the concave bank. *Hydrological Processes* **12**: 1323-1338.

Hopkinson C, Chasmer L, Young-Pow C, Treitz P. 2004. Assessing forest metrics with a ground-based scanning lidar. *Canadian Journal of Forest Research* **34**: 573-583.

Horn R, Richards K. 2008. Flow–Vegetation Interactions in Restored Floodplain Environments. In *Hydroecology and Ecohydrology*, Wood PJ, Hannah DM, Sadler JP (eds). John Wiley & Sons, Ltd: Chichester, UK; 269-294.

Hosoi F, Nakai Y, Omasa K. 2013. 3-D voxel-based solid modeling of a broad-leaved tree for accurate volume estimation using portable scanning lidar. *ISPRS Journal of Photogrammetry and Remote Sensing* **82**: 41-48.

Hosoi F, Omasa K. 2006. Voxel-Based 3-D Modeling of Individual Trees for Estimating Leaf Area Density Using High-Resolution Portable Scanning Lidar. *IEEE Transactions on Geoscience and Remote Sensing* **44**: 3610-3618.

Hoyas S, Jiménez J. 2006. Scaling of the velocity fluctuations in turbulent channels up to Reτ=2003. *Physics of Fluids* **18**: 011702.

Huang Z, Keffer JF. 1996. Development of structure within the turbulent wake of a porous body. Part 1. The initial formation region. *Journal of Fluid Mechanics* **329**: 103-115.

Hui E, Hu X, Jiang C, Ma F, Zhu Z. 2010. A study of drag coefficient related with vegetation based on the flume experiment. *Journal of Hydrodynamics, Ser. B* **22**: 329-337.

Hunt JCR, Wray AA, Moin P. 1988. Eddies Stream, and Convergence Zones in Turbulent Flows. In *Center for Turbulence Research, Report CTR-S88, 193*.

Hurd CL. 2000. Water motion, marine macroalgal physiology, and production. *Journal of Phycology* **36**: 453-472.

Hurd CL, Pilditch CA. 2011. Flow-induced morphological variations affect diffusion boundary-layer thickness of Macrocystis pyrifera. *Journal of Phycology* **47**: 341-351.

Hyyppä J, Holopainen M, Olsson H. 2012. Laser Scanning in Forests. *Remote Sensing* **4**: 2919-2922.

Hyyppä J, Hyyppä H, Litkey P, Yu X, Haggrén H, Rönnholm P, Pyysalo U, Pitkänen J, Maltamo M. 2004. Algorithms and methods of airborne laser scanning for forest measurements. *International Archives of Photogrammetry, Remote Sensing and Spatial Information Sciences* **36.8**: 82-89.

Ikeda S, Kanazawa M. 1996. Three-Dimensional Organized Vortices above Flexible Water Plants. *Journal of Hydraulic Engineering* **122**: 634-640.

Ingham DB, Ma L. 2005. Fundamental Equations for CFD in River Flow Simulations. In *Computational Fluid Dynamics*, Bates P, Lane SN, Ferguson RI (eds). John Wiley & Sons, Ltd: Chichester, UK; 17-49.

Jaboyedoff M, Oppikofer T, Abellán A, Derron M-H, Loye A, Metzger R, Pedrazzini A. 2012. Use of LIDAR in landslide investigations: a review. *Natural Hazards* **61**: 5-28.

Jalonen J, Järvelä J. 2014. Estimation of drag forces caused by natural woody vegetation of different scales. *Journal of Hydrodynamics, Ser. B* **26**: 608-623.

Jalonen J, Järvelä J, Aberle J. 2012. Vegetated flows: Drag force and velocity profiles for foliated plant stands. In *River Flow 2012*, R.E MM (ed). CRC Press: San José, Costa Rica; 233-239.

Jalonen J, Järvelä J, Aberle J. 2013. Leaf Area Index as Vegetation Density Measure for Hydraulic Analyses. *Journal of Hydraulic Engineering* **139**: 461-469.

Jalonen J, Järvelä J, Koivusalo H, Hyyppä H. 2014. Deriving Floodplain Topography and Vegetation Characteristics for Hydraulic Engineering Applications by Means of Terrestrial Laser Scanning. *Journal of Hydraulic Engineering* **140**: 04014056.

Jalonen J, Järvelä J, Virtanen J-P, Vaaja M, Kurkela M, Hyyppä H. 2015. Determining Characteristic Vegetation Areas by Terrestrial Laser Scanning for Floodplain Flow Modeling. *Water* **7**: 420-437.

Järvelä J. 2002a. Determination of flow resistance of vegetated channel banks and floodplains. In *River Flow 2002*, Bousmar D, Zech Y (eds). CRC Press Louvain-La-Neuve, Belgium; 311-318.

Järvelä J. 2002b. Flow resistance of flexible and stiff vegetation: a flume study with natural plants. *Journal of Hydrology* **269**: 44-54.

Järvelä J. 2004. Determination of flow resistance caused by non-submerged woody vegetation. *International Journal of River Basin Management* **2**: 61-70.

Järvelä J, Aberle J, Dittrich A, Rauch HP, Schnauder I. 2006. Flow-vegetation-sediment interaction: Research challenges. In *River Flow 2006*. Taylor & Francis: Lisbon, Portugal; 2017-2026.

Järvelä J, Aberle J, Jalonen J. 2016. Dynamic reconfiguration of riparian trees in towing tank experiments. In *River Flow 2016*, Constantinescu G, Garcia M, Hanes D (eds). CRC Press: St. Louis, USA; 2182-2187.

Kaasalainen S, Jaakkola A, Kaasalainen M, Krooks A, Kukko A. 2011. Analysis of Incidence Angle and Distance Effects on Terrestrial Laser Scanner Intensity: Search for Correction Methods. *Remote Sensing* **3**: 2207-2221.

Kadlec R. 1990. Overland Flow in Wetlands: Vegetation Resistance. *Journal of Hydraulic Engineering* **116**: 691-706.

Kaimal JC, Finnigan JJ. 1994. Atmospheric boundary layer flows: their structure and measurement. Oxford University Press: New York, USA.

Kankare V, Holopainen M, Vastaranta M, Puttonen E, Yu X, Hyyppä J, Vaaja M, Hyyppä H, Alho P. 2013. Individual tree biomass estimation using terrestrial laser scanning. *ISPRS Journal of Photogrammetry and Remote Sensing* **75**: 64-75.

Keylock CJ, Constantinescu G, Hardy RJ. 2012. The application of computational fluid dynamics to natural river channels: Eddy resolving versus mean flow approaches. *Geomorphology* **179**: 1-20.

Keylock CJ, Hardy RJ, Parsons DR, Ferguson RI, Lane SN, Richards KS. 2005. The theoretical foundations and potential for large-eddy simulation (LES) in fluvial geomorphic and sedimentological research. *Earth-Science Reviews* **71**: 271-304.

Kim J, Moin P, Moser R. 1987. Turbulence statistics in fully developed channel flow at low Reynolds number. *Journal of Fluid Mechanics* **177**: 133-166.

Kim SJ, Stoesser T. 2011. Closure modeling and direct simulation of vegetation drag in flow through emergent vegetation. *Water Resources Research* **47**: W10511.

Klaassen GJ, Van Der Zwaard JJ. 1974. Roughness Coefficients Of Vegetated Flood Plains. *Journal of Hydraulic Research* **12**: 43-63.

Knight D, Shiono K. 1996. River channel and floodplain hydraulics. In *Floodplain processes*, Anderson M, Walling D, Bates P (eds). John Wiley & Sons: Chichester; 139-181.

Knight DW, Shiono K. 1990. Turbulence measurements in a shear layer region of a compound channel. *Journal of Hydraulic Research* **28**: 175-196.

Knutson PL, Brochu RA, Seelig WN, Inskeep M. 1982. Wave damping in Spartina alterniflora marshes. *Wetlands* **2**: 87-104.

Koch EW. 2001. Beyond light: Physical, geological, and geochemical parameters as possible submersed aquatic vegetation habitat requirements. *Estuaries* **24**: 1-17.

Koenig K, Höfle B. 2016. Full-Waveform Airborne Laser Scanning in Vegetation Studies—A Review of Point Cloud and Waveform Features for Tree Species Classification. *Forests* **7**: 198.

Koeser AK, Roberts JW, Miesbauer JW, Lopes AB, Kling GJ, Lo M, Morgenroth J. 2016. Testing the accuracy of imaging software for measuring tree root volumes. *Urban Forestry & Urban Greening* **18**: 95-99.

Koken M, Constantinescu G. 2016. On the spatial development of the mixing layer at the interface between open water and a region containing emerged vegetation. In *River Flow 2016*, Constantinescu G, Garcia M, Hanes D (eds). Taylor & Francis: London: Iowa City; 79-84.

Kolmogorov AN. 1942. Equations of turbulent motion of an incompressible fluid. *Izv. Akad. Nauk SSSR, Ser. Fiz* **6**.

Kouwen N, Fathi-Moghadam M. 2000. Friction Factors for Coniferous Trees along Rivers. *Journal of Hydraulic Engineering* **126**: 732-740.

Kouwen N, Unny TE. 1973. Flexible Roughness in Open Channels. *Journal of the Hydraulics Division* **99**: 713-728.

Kouwen N, Unny TE, Hill H. 1969. Flow retardance in vegetated channels. *Journal of Irrigation and Drainage Division* **95**: 329-342.

Kumar KL. 2008. Engineering fluid mechanics. S. Chand Publishing: New Delhi, India.

Kumar P, Cai J, Miklavcic S. 2012. High-throughput 3D modelling of plants for phenotypic analysis. In *Proceedings of the 27th Conference on Image and Vision Computing New Zealand*. ACM: Dunedin, New Zealand; 301-306.

Lacey RWJ, Roy AG. 2007. A comparative study of the turbulent flow field with and without a pebble cluster in a gravel bed river. *Water Resources Research* **43**: W05502.

Lane SN. 1998. Hydraulic modelling in hydrology and geomorphology: a review of high resolution approaches. *Hydrological Processes* **12**: 1131-1150.

Lane SN. 2005. Roughness – time for a re-evaluation? *Earth Surface Processes and Landforms* **30**: 251-253.

Lane SN. 2008. Climate change and the summer 2007 floods in the UK. *Geography* **93**: 91-97.

Lane SN, Bradbrook KF, Richards KS, Biron PA, Roy AG. 1999. The application of computational fluid dynamics to natural river channels: three-dimensional versus two-dimensional approaches. *Geomorphology* **29**: 1-20.

Lane SN, Hardy RJ. 2002. Porous Rivers: a New Way of Conceptualising and Modelling River and Floodplain Flows? In *Transport Phenomena in Porous Media II*, Ingham DB, Pop I (eds). Pergamon: Oxford, UK; 425-449.

Lane SN, Hardy RJ, Elliott L, Ingham DB. 2002. High-resolution numerical modelling of three-dimensional flows over complex river bed topography. *Hydrological Processes* **16**: 2261-2272.

Lane SN, Hardy RJ, Elliott L, Ingham DB. 2004. Numerical modeling of flow processes over gravelly surfaces using structured grids and a numerical porosity treatment. *Water Resources Research* **40**: W01302.

Lane SN, Hardy RJ, Ferguson RI, Parsons DR. 2005. A Framework for Model Verification and Validation of CFD Schemes in Natural Open Channel Flows. In *Computational Fluid Dynamics*, Bates P, Lane SN, Ferguson RI (eds). John Wiley & Sons, Ltd: Chichester, UK; 169-192.

Lane SN, Richards KS. 2001. The 'validation' of hydrodynamic models: Some critical perspectives. In *Model Validation for Hydrological and Hydraulic Research*, Anderson MG, Bates PD (eds). Wiley: Chichester, UK; 413-438.

Large ARG, Prach K. 1999. Plants and water in streams and rivers. In *Eco-hydrology. Plants and water in terrestrial and aquatic environments*, Baird AJ, Wilby RL (eds). Routledge: London; 402.

Launder BE, Reece GJ, Rodi W. 1975. Progress in the development of a Reynolds-stress turbulence closure. *Journal of Fluid Mechanics* **68**: 537-566.

Launder BE, Spaulding DB. 1972. Mathematical Models of Turbulence. Academic Press: London, UK.

Launder BE, Spaulding DB. 1974. The numerical computation of turbulent flows. *Computer Methods in Applied Mechanics and Engineering* **3**: 269-289.

Lawless MR, Lane SN, Best JL. 2004. The junction vortex system: time-mean and instantaneous flow fields. In *Shallow Flows: Research Presented at the International Symposium on Shallow Flows*, Jirka GH, Uijttewaal WSJ (eds). Taylor & Francis: Delft, Netherlands; 117-126.

Lee BE, Soliman BF. 1977. An Investigation of the Forces on Three Dimensional Bluff Bodies in Rough Wall Turbulent Boundary Layers. *Journal of Fluids Engineering* **99**: 503-509.

Lee JP, Lee SJ. 2012. PIV analysis on the shelter effect of a bank of real fir trees. *Journal of Wind Engineering and Industrial Aerodynamics* **110**: 40-49.

Lefebvre A, Thompson CEL, Amos CL. 2010. Influence of Zostera marina canopies on unidirectional flow, hydraulic roughness and sediment movement. *Continental Shelf Research* **30**: 1783-1794.

Leonard LA, Luther ME. 1995. Flow hydrodynamics in tidal marsh canopies. *Limnology and oceanography* **40**: 1474-1484.

Leopold LB, Bagnold RA, Wolman MG. 1960. Flow resistance in sinuous or irregular channels. Professional Paper, 282D. US Geological Survey Washington, USA.

Leschziner MA. 1990. Modelling engineering flows with Reynolds stress turbulence closure. *Journal of Wind Engineering and Industrial Aerodynamics* **35**: 21-47.

Leschziner MA, Rodi W. 1979. Calculation of strongly curved open channel flow. *Journal of Hydraulics Division* **105**: 1297-1314.

Leyland J, Darby SE, Teruggi L, Rinaldi M, Ostuni D. 2015. A self-limiting bank erosion mechanism? inferring temporal variations in bank form and skin drag from high resolution topographic data. *Earth Surface Processes and Landforms* **40**: 1600-1615.

Li CW, Xie JF. 2011. Numerical modeling of free surface flow over submerged and highly flexible vegetation. *Advances in Water Resources* **34**: 468-477.

Liang X, Hyyppä J. 2013. Automatic Stem Mapping by Merging Several Terrestrial Laser Scans at the Feature and Decision Levels. *Sensors* **13**: 1614-1634.

Liang X, Kankare V, Hyyppä J, Wang Y, Kukko A, Haggrén H, Yu X, Kaartinen H, Jaakkola A, Guan F, Holopainen M, Vastaranta M. 2016. Terrestrial laser scanning in forest inventories. *ISPRS Journal of Photogrammetry and Remote Sensing* **115**: 63-77.

Lichti DD. 2005. Spectral Filtering and Classification of Terrestrial Laser Scanner Point Clouds. *The Photogrammetric Record* **20**: 218-240.

Lien FS, Leschziner MA. 1994. Assessment of turbulence-transport models including non-linear rng eddy-viscosity formulation and second-moment closure for flow over a backward-facing step. *Computers & Fluids* **23**: 983-1004.

Liénard J, Lynn K, Strigul N, Norris BK, Gatziolis D, Mullarney JC, Bryan KR, Henderson SM. 2016. Efficient three-dimensional reconstruction of aquatic vegetation geometry: Estimating morphological parameters influencing hydrodynamic drag. *Estuarine, Coastal and Shelf Science* **178**: 77-85.

Lightbody AF, Nepf HM. 2006. Prediction of velocity profiles and longitudinal dispersion in salt marsh vegetation. *Limnology and oceanography* **51**: 218-228.

Lilly DK. 1967. The representation of small scale turbulence in numerical simulation experiments. In *IBM Scientific Computing Symposium on Environmental Sciences*, Goldstine HH (ed). Watson Research Centre: New York; 195-210.

López F, García M. 1998. Open-channel flow through simulated vegetation: Suspended sediment transport modeling. *Water Resources Research* **34**: 2341-2352.

López F, García M. 2001. Mean Flow and Turbulence Structure of Open-Channel Flow through Non-Emergent Vegetation. *Journal of Hydraulic Engineering* **127**: 392-402.

Lübcke H, Schmidt S, Rung T, Thiele F. 2001. Comparison of LES and RANS in bluff-body flows. *Journal of Wind Engineering and Industrial Aerodynamics* **89**: 1471-1485.

Luhar M, Nepf HM. 2011. Flow induced reconfiguration of buoyant and flexible aquatic vegetation. *Limnology and oceanography* **56**: 2003-2017.

Luhar M, Nepf HM. 2013. From the blade scale to the reach scale: A characterization of aquatic vegetative drag. *Advances in Water Resources* **51**: 305-316.

Ma L, Ashworth PJ, Best JL, Elliott L, Ingham DB, Whitcombe LJ. 2002. Computational fluid dynamics and the physical modelling of an upland urban river. *Geomorphology* **44**: 375-391.

Ma L, Zheng G, Eitel JUH, Moskal LM, He W, Huang H. 2016. Improved Salient Feature-Based Approach for Automatically Separating Photosynthetic and Nonphotosynthetic Components Within Terrestrial Lidar Point Cloud Data of Forest Canopies. *IEEE Transactions on Geoscience and Remote Sensing* **54**: 679-696.

Ma X, Karamanos GS, Karniadakis GE. 2000. Dynamics and low-dimensionality of a turbulent near wake. *Journal of Fluid Mechanics* **410**: 29-65.

MacVicar BJ, Dilling S, Lacey RWJ, Hipel K. 2014. A quality analysis of the Vectrino II instrument using a new open-source MATLAB toolbox and 2D ARMA models to detect and replace spikes. In *River Flow 2014*, Schleiss AJ, De Cesare G, Franca MJ, Pfister M (eds). CRC Press: London, UK; 1951-1959.

Manga M, Kirchner JW. 2000. Stress partitioning in streams by large woody debris. *Water Resources Research* **36**: 2373-2379.

Manners R, Schmidt J, Wheaton JM. 2013. Multiscalar model for the determination of spatially explicit riparian vegetation roughness. *Journal of Geophysical Research: Earth Surface* **118**: 65-83.

Manning R. 1891. On the flow of water in open channels and pipes. *Transactions of the Institution of Civil Engineers of Ireland* **20**: 161-207.

Marion A, Nikora V, Puijalon S, Bouma T, Koll K, Ballio F, Tait S, Zaramella M, Sukhodolov A, O'Hare M, Wharton G, Aberle J, Tregnaghi M, Davies P, Nepf H, Parker G, Statzner B. 2014. Aquatic interfaces: a hydrodynamic and ecological perspective. *Journal of Hydraulic Research* **52**: 744-758.

Marjoribanks TI, Hardy RJ, Lane SN. 2014a. The hydraulic description of vegetated river channels: the weaknesses of existing formulations and emerging alternatives. *Wiley Interdisciplinary Reviews: Water* **1**: 549-560.

Marjoribanks TI, Hardy RJ, Lane SN, Parsons DR. 2014b. Dynamic drag modeling of submerged aquatic vegetation canopy flows. In *River Flow 2014*, Schleiss AJ, De Cesare G, Franca MJ, Pfister M (eds). CRC Press: London, UK; 517-524.

Marjoribanks TI, Hardy RJ, Lane SN, Parsons DR. 2014c. High-resolution numerical modelling of flow—vegetation interactions. *Journal of Hydraulic Research* **52**: 775-793.

Marjoribanks TI, Hardy RJ, Lane SN, Parsons DR. 2017. Does the canopy mixing layer model apply to highly flexible aquatic vegetation? Insights from numerical modelling. *Environmental Fluid Mechanics* **17**: 277-301.

Marjoribanks TI, Hardy RJ, Lane SN, Tancock MJ. 2016. Patch-scale representation of vegetation within hydraulic models. *Earth Surface Processes and Landforms* **42**: 699-710.

Marjoribanks TI, Hardy RJ, Parsons DR. 2015. On validating predictions of plant motion in coupled biomechanical-flow models. *Journal of Hydraulic Research* **53**: 808-813.

Markatos NC. 1986. The mathematical modelling of turbulent flows. *Applied Mathematical Modelling* **10**: 190-220.

Marron JS, Tsybakov AB. 1995. Visual Error Criteria for Qualitative Smoothing. *Journal of the American Statistical Association* **90**: 499-507.

Massey BS. 2006. Mechanics of fluids. Taylor & Francis: London, UK.

Mazda Y, Wolanski E, King B, Sase A, Ohtsuka D, Magi M. 1997. Drag force due to vegetation in mangrove swamps. *Mangroves and Salt Marshes* **1**: 193-199.

McBride M, Hession WC, Rizzo DM, Thompson DM. 2007. The influence of riparian vegetation on near-bank turbulence: a flume experiment. *Earth Surface Processes and Landforms* **32**: 2019-2037.

McKenna-Neuman C, Sanderson RS, Sutton SLF. 2013. Vortex shedding and morphodynamic response of bed surfaces containing non-erodible roughness elements. *Geomorphology* **198**: 45-56.

McLelland SJ, Nicholas AP. 2000. A new method for evaluating errors in high-frequency ADV measurements. *Hydrological Processes* **14**: 351-366.

Meire DWSA, Kondziolka JM, Nepf HM. 2014. Interaction between neighboring vegetation patches: Impact on flow and deposition. *Water Resources Research* **50**: 3809–3825.

Mendez FJ, Losada IJ. 2004. An empirical model to estimate the propagation of random breaking and nonbreaking waves over vegetation fields. *Coastal Engineering* **51**: 103-118.

Mertens W. 1989. Zur Frage hydraulischer Berechnungen naturnaher Fließgewässer. *Wasserwirtschaft* **79**: 170-179.

Meselhe EA, Odgaard AJ. 1998. 3D Numerical Flow Model for Fish Diversion Studies at Wanapum Dam. *Journal of Hydraulic Engineering* **124**: 1203-1214.

Middleton GV, Southard JB. 1984. Mechanics of Sediment Movement. In *SEPM Short Course Notes*; 11.

Miler O, Albayrak I, Nikora V, O'Hare M. 2012. Biomechanical properties of aquatic plants and their effects on plant–flow interactions in streams and rivers. *Aquatic Sciences* **74**: 31-44.

Miller J, Morgenroth J, Gomez C. 2015. 3D modelling of individual trees using a handheld camera: Accuracy of height, diameter and volume estimates. *Urban Forestry & Urban Greening* **14**: 932-940.

Minas C, Waddell SJ, Montana G. 2011. Distance-based differential analysis of gene curves. *Bioinformatics* **27**: 3135-3141.

Mittal S, Tezduyar TE. 1992. A finite element study of incompressible flows past oscillating cylinders and aerofoils. *International Journal for Numerical Methods in Fluids* **15**: 1073-1118.

Moorthy I, Miller JR, Berni JAJ, Zarco-Tejada P, Hu B, Chen J. 2011. Field characterization of olive (Olea europaea L.) tree crown architecture using terrestrial laser scanning data. *Agricultural and Forest Meteorology* **151**: 204-214.

Moorthy I, Miller JR, Hu B, Chen J, Li Q. 2008. Retrieving crown leaf area index from an individual tree using ground-based lidar data. *Canadian Journal of Remote Sensing* **34**: 320-332.

Morris HM. 1955. A new concept of flow in rough conduits. *Trans Am Soc Civ Eng* **120**: 373–398.

Moser RD, Kim J, Mansour NN. 1999. Direct numerical simulation of turbulent channel flow up to Reτ=590. *Physics of Fluids (1994-present)* **11**: 943-945.

Naden P, Rameshwaran P, Mountford O, Robertson C. 2006. The influence of macrophyte growth, typical of eutrophic conditions, on river flow velocities and turbulence production. *Hydrological Processes* **20**: 3915-3938.

Næsset E. 2002. Predicting forest stand characteristics with airborne scanning laser using a practical two-stage procedure and field data. *Remote Sensing of Environment* **80**: 88-99.

Næsset E, Gobakken T. 2008. Estimation of above- and below-ground biomass across regions of the boreal forest zone using airborne laser. *Remote Sensing of Environment* **112**: 3079-3090.

Nakayama K, Fielding CR, Alexander J. 2002. Variations in character and preservation potential of vegetation-induced obstacle marks in the variable discharge Burdekin River of north Queensland, Australia. *Sedimentary Geology* **149**: 199-218.

Nallasamy M. 1987. Turbulence models and their applications to the prediction of internal flows: A review. *Computers & Fluids* **15**: 151-194.

Nepf HM. 1999. Drag, turbulence, and diffusion in flow through emergent vegetation. *Water Resources Research* **35**: 479-489.

Nepf HM. 2012a. Flow and Transport in Regions with Aquatic Vegetation. *Annual Review of Fluid Mechanics* **44**: 123-142.

Nepf HM. 2012b. Hydrodynamics of vegetated channels. *Journal of Hydraulic Research* **50**: 262-279.

Nepf HM, Ghisalberti M. 2008. Flow and transport in channels with submerged vegetation. *Acta Geophysica* **56**: 753-777.

Nepf HM, Ghisalberti M, White B, Murphy E. 2007a. Retention time and dispersion associated with submerged aquatic canopies. *Water Resources Research* **43**: W04422.

Nepf HM, Sullivan JA, Zavistoski RA. 1997. A model for diffusion within emergent vegetation. *Limnology and oceanography* **42**: 1735-1745.

Nepf HM, Vivoni ER. 2000. Flow structure in depth-limited, vegetated flow. *Journal of Geophysical Research: Oceans* **105**: 28547-28557.

Nepf HM, White B, Lightbody A, Ghisalberti M. 2007b. Transport in aquatic canopies. In *Flow and Transport Processes with Complex Obstructions: Applications to Cities, Vegetative Canopies, and Industry*, Gayev YA, Hunt JCR (eds). Springer Netherlands: Dordrecht; 221-250.

Neumeier U. 2007. Velocity and turbulence variations at the edge of saltmarshes. *Continental Shelf Research* **27**: 1046-1059.

Nezu I, Onitsuka K. 2001. Turbulent structures in partly vegetated open-channel flows with LDA and PI V measurements. *Journal of Hydraulic Research* **39**: 629-642.

Nezu I, Sanjou M. 2008. Turburence structure and coherent motion in vegetated canopy open-channel flows. *Journal of Hydro-environment Research* **2**: 62-90.

Nicolle A, Eames I. 2011. Numerical study of flow through and around a circular array of cylinders. *Journal of Fluid Mechanics* **679**: 1-31.

Nicoud F, Ducros F. 1999. Subgrid-Scale Stress Modelling Based on the Square of the Velocity Gradient Tensor. *Flow, Turbulence and Combustion* **62**: 183-200.

Nield JM, Wiggs GFS, Squirrell RS. 2011. Aeolian sand strip mobility and protodune development on a drying beach: examining surface moisture and surface roughness patterns measured by terrestrial laser scanning. *Earth Surface Processes and Landforms* **36**: 513-522.

Niklas KJ. 1992. Plant biomechanics: an engineering approach to plant form and function. University of Chicago Press: London, UK.

Niklas KJ, Spatz HC. 2012. Plant Physics. University of Chicago Press: Chicago, USA.

Nikora V. 2010. Hydrodynamics of aquatic ecosystems: An interface between ecology, biomechanics and environmental fluid mechanics. *River Research and Applications* **26**: 367-384.

Nikora V, Cameron S, Albayrak I, Miler O, Nikora N, Siniscalchi F, Stewart M, O' Hare M. 2012. Flow-biota interactions in aquatic systems. In *Environmental Fluid Mechanics*. CRC Press; 217-235.

Nikuradse J. 1933. Stromungsgesetze in rauhen Rohren (Laws of flow in rough pipes). NACA-TM-1292. Germany.

Nortek. 2012. Vectrino Profiler: User Guide. Nortek Scientific Acoustic Development Group Inc. User Manual

O'Hare MT, Mountford JO, Maroto J, Gunn IDM. 2016. Plant Traits Relevant To Fluvial Geomorphology and Hydrological Interactions. *River Research and Applications* **32**: 179-189.

O'Hare MT, Hutchinson KA, Clarke RT. 2007. The drag and reconfiguration experienced by five macrophytes from a lowland river. *Aquatic Botany* **86**: 253-259.

O'Hare MT, McGahey C, Bissett N, Cailes C, Henville P, Scarlett P. 2010. Variability in roughness measurements for vegetated rivers near base flow, in England and Scotland. *Journal of Hydrology* **385**: 361-370.

Oberkampf WL, Trucano TG. 2002. Verification and validation in computational fluid dynamics. *Progress in Aerospace Sciences* **38**: 209-272.

Okamoto T, Nezu I. 2009. Turbulence structure and "Monami" phenomena in flexible vegetated open-channel flows. *Journal of Hydraulic Research* **47**: 798-810.

Okamoto T, Nezu I, Sanjou M. 2016. Flow–vegetation interactions: length-scale of the "monami" phenomenon. *Journal of Hydraulic Research* **54**: 251-262.

Olsen NRB, Stokseth S. 1995. Three-dimensional numerical modelling of water flow in a river with large bed roughness. *Journal of Hydraulic Research* **33**: 571-581.

Olson RM, Wright SJ. 1990. Essentials of engineering fluid mechanics. Harper and Row: New York, USA.

Olsoy PJ, Glenn NF, Clark PE, Derryberry DR. 2014. Aboveground total and green biomass of dryland shrub derived from terrestrial laser scanning. *ISPRS Journal of Photogrammetry and Remote Sensing* **88**: 166-173.

Oplatka M. 1998. Stabilität von Weidenverbauungen an Flussufern. Eidgenössische Technische Hochschule Zürich, Switzerland.

Ortiz AC, Ashton A, Nepf HM. 2013. Mean and turbulent velocity fields near rigid and flexible plants and the implications for deposition. *Journal of Geophysical Research: Earth Surface* **118**: 2585-2599.

Otsu N. 1979. A Threshold Selection Method from Gray-Level Histograms. *IEEE Transactions on Systems, Man, and Cybernetics* **9**: 62-66.

Panton RL. 1984. Incompressible Flow. John Wiley & Sons: New York, USA.

Papaioannou G, Yue D, Triantafyllou M, Karniadakis G. 2006. Three-dimensionality effects in flow around two tandem cylinders. *Journal of Fluid Mechanics* **558**: 387-413.

Papke A, Battiato I. 2013. A reduced complexity model for dynamic similarity in obstructed shear flows. *Geophysical Research Letters* **40**: 3888-3892.

Parker C, Clifford NJ, Thorne CR. 2012. Automatic delineation of functional river reach boundaries for river research and applications. *River Research and Applications* **28**: 1708-1725.

Parkhurst J, Price G, Sharrock P, Moore C. 2011. Phase unwrapping algorithms for use in a true real-time optical body sensor system for use during radiotherapy. *Appl Opt* **50**: 6430-6439.

Patankar SV, Spalding DB. 1972. A calculation procedure for heat, mass and momentum transfer in three-dimensional parabolic flows. *International Journal of Heat and Mass Transfer* **15**: 1787-1806.

Patterson MR, Harwell MC, Orth LM, Orth RJ. 2001. Biomechanical properties of the reproductive shoots of eelgrass. *Aquatic Botany* **69**: 27-40.

Pattison I, Lane SN. 2012. The relationship between Lamb weather types and long-term changes in flood frequency, River Eden, UK. *International Journal of Climatology* **32**: 1971-1989.

Paul M, Thomas RE, Dijkstra JT, Penning WE, Vousdoukas MI. 2014. Plants, hydraulics and sediment dynamics. In *Users Guide to Ecohydraulic Modelling and Experimentation*, Frostick LE, Thomas RE, Johnson MF, Rice SP, McLelland SJ (eds). CRC Press: Boca Raton, USA; 91-116.

Peerless SJ. 1967. Basic fluid mechanics. Pergamon Press: Oxford, UK.

Petr T. 2000. Interactions between fish and aquatic macrophytes in inland waters. A review. Fisheries Technical Paper 396. UN Food and Agriculture Organisation: Rome, Italy.

Petrie G, Toth CK. 2008. Introduction to Laser Ranging, Profiling, and Scanning. In *Topographic Laser Ranging and Scanning*, Shan J, Toth CK (eds). CRC Press: Boca Raton, USA; 1-28.

Petryk S, Bosmajian G. 1975. Analysis of Flow through Vegetation. *Journal of the Hydraulics Division* **101**: 871-884.

Piquet J. 1999. Turbulent flows: models and physics. Springer-Verlag Berlin: Heidelberg, USA.

Pirotti F, Guarnieri A, Vettore A. 2013. Ground filtering and vegetation mapping using multi-return terrestrial laser scanning. *ISPRS Journal of Photogrammetry and Remote Sensing* **76**: 56-63.

Pitlo RH, Dawson FH. 1990. Flow resistance of aquatic weeds. In *Aquatic Weeds: The Ecology and Management of Nuisance Aquatic Vegetation*, Pieterse AH, Murphy KJ (eds). Oxford University Press: Oxford, UK; 74-84.

Pitt M. 2008. The Pitt review: learning lessons from the 2007 floods: London, UK.

Polunin O, Everard B. 1969. Flowers of Europe: A Field Guide. Oxford University Press: Oxford, UK.

Pope SB. 2000. Turbulent Flows. Cambridge University Press: Cambridge, UK.

Powell KEC. 1978. Weed growth a factor of channel roughness. In *Hydrometry: Principles and Practices*, Herschy RW (ed). John Wiles & Sons Ltd: Chichester; 327-352.

Prandtl L. 1925. Bericht über Untersuchungen zur ausgebildeten Turbulenz. *Zeitschrift fuer Angewandte Mathematik und Mechanik* **5**: 136-139.

Prandtl L. 1945. Uber ein neues Formelsystem für die ausgebildete Turbulenz. Vandenhoeck & Ruprecht: Göttingen.

Preston CD, Croft JM. 2001. Aquatic Plants in Britain and Ireland. Harley Books: Colchester, UK.

Pritchard PJ, Fox RW, McDonald AT, Leylegian JC. 2010. Introduction to fluid mechanics. Wiley: Chichester, UK.

Pueschel P, Newnham G, Rock G, Udelhoven T, Werner W, Hill J. 2013. The influence of scan mode and circle fitting on tree stem detection, stem diameter and volume extraction from terrestrial laser scans. *ISPRS Journal of Photogrammetry and Remote Sensing* **77**: 44-56.

Quan L, Ping T, Gang Z, Lu Y, Jingdong W, Sing BK. 2006. Image-based plant modeling. *ACM Trans. Graph.* **25**: 599-604.

Raine JK, Stevenson DC. 1977. Wind protection by model fences in a simulated atmospheric boundary layer. *Journal of Wind Engineering and Industrial Aerodynamics* **2**: 159-180.

Raumonen P, Kaasalainen M, Åkerblom M, Kaasalainen S, Kaartinen H, Vastaranta M, Holopainen M, Disney M, Lewis P. 2013. Fast Automatic Precision Tree Models from Terrestrial Laser Scanner Data. *Remote Sensing* **5**: 491-520.

Raupach M, Shaw R. 1982. Averaging procedures for flow within vegetation canopies. *Boundary-Layer Meteorology* **22**: 79-90.

Raupach MR, Finnigan JJ, Brunei Y. 1996. Coherent eddies and turbulence in vegetation canopies: The mixing-layer analogy. *Boundary-Layer Meteorology* **78**: 351-382.

Reynolds O. 1895. On the Dynamical Theory of Incompressible Viscous Fluids and the Determination of the Criterion. *Philosophical Transactions of the Royal Society of London. A* **186**: 123-164.

Richardson E, Davis S. 2001. Evaluating Scour at Bridges. NHI 01-001 HEC-18. US Department of Transportation Federal Highway Administration Colorado, USA.

Riegl. 2015a. Riegl Laser Measurement Systems; Riegl VZ-1000 datasheet. www.riegl.com/.

Riegl. 2015b. Riegl Laser Measurement Systems; Riegl VZ-4000 datasheet. www.riegl.com/.

Riegl. 2017. RiScan Pro. Processing License.

Righetti M. 2008. Flow analysis in a channel with flexible vegetation using double-averaging method. *Acta Geophysica* **56**: 801-823.

Rizzetta DP. 1994. Numerical simulation of turbulent cylinder juncture flowfields. *AIAA Journal* **32**: 1113-1119.

Roache PJ. 1994. Perspective: A Method for Uniform Reporting of Grid Refinement Studies. *Journal of Fluids Engineering* **116**: 405-413.

Roache PJ. 1997. Quantification of uncertainty in computational fluid dynamics. *Annual Review of Fluid Mechanics* **29**: 123-160.

Roache PJ. 1998. Verification and validation in computational science and engineering. Hermosa: Albuquerque, USA.

Rodi W. 1993. Turbulence Models and Their Application in Hydraulics - A State of the Art Review. CRC Press: Delft, The Netherlands.

Rodi W. 1997. Comparison of LES and RANS calculations of the flow around bluff bodies. *Journal of Wind Engineering and Industrial Aerodynamics* **69–71**: 55-75.

Rodi W. 2017. Turbulence Modeling and Simulation in Hydraulics: A Historical Review. *Journal of Hydraulic Engineering*: 03117001.

Rodi W, Ferziger JH, Breuer M, Pourquiée M. 1997. Status of Large Eddy Simulation: Results of a Workshop. *Journal of Fluids Engineering* **119**: 248-262.

Rogallo RS, Moin P. 1984. Numerical Simulation of Turbulent Flows. *Annual Review of Fluid Mechanics* **16**: 99-137.

Rominger JT, Nepf HM. 2011. Flow adjustment and interior flow associated with a rectangular porous obstruction. *Journal of Fluid Mechanics* **680**: 636-659.

Rominger JT, Nepf HM. 2014. Effects of blade flexural rigidity on drag force and mass transfer rates in model blades. *Limnology and oceanography* **59**: 2028-2041.

Rosell JR, Llorens J, Sanz R, Arnó J, Ribes-Dasi M, Masip J, Escolà A, Camp F, Solanelles F, Gràcia F, Gil E, Val L, Planas S, Palacín J. 2009. Obtaining the three-dimensional structure of tree orchards from remote 2D terrestrial LIDAR scanning. *Agricultural and Forest Meteorology* **149**: 1505-1515.

Rosser NJ, Petley DN, Lim M, Dunning SA, Allison RJ. 2005. Terrestrial laser scanning for monitoring the process of hard rock coastal cliff erosion. *Quarterly Journal of Engineering Geology and Hydrogeology* **38**: 363-375.

Rouse H. 1965. Critical analysis of open-channel resistance. *Journal of the Hydraulics Division* **91**: 1-23.

Rubol S, Battiato I, de Barros FPJ. 2016. Vertical dispersion in vegetated shear flows. *Water Resources Research* **52**: 8066–8080.

Rusu RB, Marton ZC, Blodow N, Dolha M, Beetz M. 2008. Towards 3D Point cloud based object maps for household environments. *Robotics and Autonomous Systems* **56**: 927-941.

Rutzinger M, Höfle B, Hollaus M, Pfeifer N. 2008. Object-Based Point Cloud Analysis of Full-Waveform Airborne Laser Scanning Data for Urban Vegetation Classification. *Sensors* **8**: 4505.

Ryding J, Williams E, Smith M, Eichhorn M. 2015. Assessing Handheld Mobile Laser Scanners for Forest Surveys. *Remote Sensing* **7**: 1095.

Saarinen N, Vastaranta M, Vaaja M, Lotsari E, Jaakkola A, Kukko A, Kaartinen H, Holopainen M, Hyyppä H, Alho P. 2013. Area-Based Approach for Mapping and Monitoring Riverine Vegetation Using Mobile Laser Scanning. *Remote Sensing* **5**: 5285-5303.

Sagnes P. 2010. Using multiple scales to estimate the projected frontal surface area of complex three-dimensional shapes such as flexible freshwater macrophytes at different flow conditions. *Limnology and Oceanography: Methods* **8**: 474-483.

Sand-Jensen KAJ. 2003. Drag and reconfiguration of freshwater macrophytes. *Freshwater Biology* **48**: 271-283.

Sand-Jensen KAJ, Jeppesen E, Nielsen K, Van Der Bijl L, Hjermind L, Nielsen LW, Ivlrsln TM. 1989. Growth of macrophytes and ecosystem consequences in a lowland Danish stream. *Freshwater Biology* **22**: 15-32.

Sand-Jensen KAJ, Madsen T. 1992. Patch dynamics of the stream macrophyte, Callitriche cophocarpa. *Freshwater Biology* **27**: 277-282.

Sandbach SD, Lane SN, Hardy RJ, Amsler ML, Ashworth PJ, Best JL, Nicholas AP, Orfeo O, Parsons DR, Reesink AJH, Szupiany RN. 2012. Application of a roughness-length representation to parameterize energy loss in 3-D numerical simulations of large rivers. *Water Resources Research* **48**: W12501.

Schlatter P, Örlü R. 2010. Assessment of direct numerical simulation data of turbulent boundary layers. *Journal of Fluid Mechanics* **659**: 116-126.

Schlichting H. 1955. Turbulent Boundary Theory. McGraw-Hill: New York, USA.

Schnauder I, Moggridge HL. 2009. Vegetation and hydraulic-morphological interactions at the individual plant, patch and channel scale. *Aquatic Sciences* **71**: 318-330.

Schnauder I, Yagci O, Kabdasli S. 2007. The effect of permeability of natural emergent vegetation on flow velocities and turbulence. In *32nd Congress of IAHR*: Venice, Italy.

Schoelynck J, Meire D, Bal K, Buis K, Troch P, Bouma T, Meire P, Temmerman S. 2013. Submerged macrophytes avoiding a negative feedback in reaction to hydrodynamic stress. *Limnologica - Ecology and Management of Inland Waters* **43**: 371-380.

Schoelynck J, Puijalon S, Meire P, Struyf E. 2015. Thigmomorphogenetic responses of an aquatic macrophyte to hydrodynamic stress. *Frontiers in Plant Science* **6**: 43.

Schoneboom T, Aberle J, Dittrich A. 2010. Hydraulic resistance of vegetated flows: Contribution of bed shear stress and vegetative drag to total hydraulic resistance. In *River Flow*: Braunschweig, Germany; 269-276.

Sellin R. 1964. A laboratory investigation into the interaction between the flow in the channel of a river and that over its flood plain. *La Houille Blanche*: 793-802.

Shaw CT. 1992. Using Computational Fluid Dynamics. Prentice Hall: New York, USA.

Shields FD, Coulton KG, Nepf HM. 2017. Representation of Vegetation in Two-Dimensional Hydrodynamic Models. *Journal of Hydraulic Engineering* **143**: 1-9.

Shucksmith J, Boxall J, Guymer I. 2011. Bulk Flow Resistance in Vegetated Channels: Analysis of Momentum Balance Approaches Based on Data Obtained in Aging Live Vegetation. *Journal of Hydraulic Engineering* **137**: 1624-1635.

Sillero J, Jiménez J, Moser R, Malaya N. 2011. Direct simulation of a zero-pressure-gradient turbulent boundary layer up to Re θ = 6650. *Journal of Physics: Conference Series* **318**: 022023.

Simpson RL. 1989. Turbulent boundary-layer separation. *Annual Review of Fluid Mechanics* **21**: 205-232.

Simpson RL. 2001. Junction Flows. *Annual Review of Fluid Mechanics* **33**: 415-443.

Siniscalchi F, Nikora V. 2012. Flow-plant interactions in open-channel flows: A comparative analysis of five freshwater plant species. *Water Resources Research* **48**: W05503.

Siniscalchi F, Nikora V. 2013. Dynamic reconfiguration of aquatic plants and its interrelations with upstream turbulence and drag forces. *Journal of Hydraulic Research* **51**: 46-55.

Sinoquet H, Rivet P, Godin C. 1997. Assessment of the three-dimensional architecture of walnut trees using digitising. *Silva Fennica* **31**: 265-273.

Smagorinsky J. 1963. General circulation experiments with the primitive equations. *Monthly Weather Review* **91**: 99-164.

Smith A, Porter JJ, Upham P. 2016a. "We cannot let this happen again": reversing UK flood policy in response to the Somerset Levels floods, 2014. *Journal of Environmental Planning and Management* **60**: 351-369.

Smith MW. 2015. Section 2.1.5: Direct acquisition of elevation data: Terrestrial Laser Scanning. In *Geomorphological Techniques*, Cook SJ, Clarke LE, Nield JM (eds). British Society for Geomorphology: London.

Smith MW, Carrivick JL, Quincey DJ. 2016b. Structure from motion photogrammetry in physical geography. *Progress in Physical Geography* **40**: 247-275.

Smith MW, Vericat D. 2015. From experimental plots to experimental landscapes: topography, erosion and deposition in sub-humid badlands from Structure-from-Motion photogrammetry. *Earth Surface Processes and Landforms* **40**: 1656-1671.

Smith MW, Vericat D, Gibbins C. 2012. Through-water terrestrial laser scanning of gravel beds at the patch scale. *Earth Surface Processes and Landforms* **37**: 411-421.

Smyth TAG. 2016. A review of Computational Fluid Dynamics (CFD) airflow modelling over aeolian landforms. *Aeolian Research* **22**: 153-164.

Snavely N, Seitz SM, Szeliski R. 2008. Modeling the World from Internet Photo Collections. *International Journal of Computer Vision* **80**: 189-210.

Sontek. 1999. SonTek ADV Acoustic Doppler Velocimeters. SonTec Inc: San Diego, USA.

Sotiropoulos F. 2005. Introduction to Statistical Turbulence Modelling for Hydraulic Engineering Flows. In *Computational Fluid Dynamics*, Bates P, Lane SN, Ferguson RI (eds). John Wiley & Sons, Ltd; 91-120.

Spalart PR. 1988. Direct simulation of a turbulent boundary layer up to Rθ = 1410. *Journal of Fluid Mechanics* **187**: 61-98.

Spalart PR, Allmaras SR. 1994. A one-equation turbulence model for aerodynamic flows. *AIAA-Paper 92-0439*.

Spalding DB. 1980. Mathematical Modelling of Fluid Mechanics, Heat Transfer and Mass Transfer Processes. In *Mechanical Engineering Department, Imperial College of Science, Technology and Medicine*: London, UK.

Spalding DB. 1985. The Computation of Flow Around Ships with Allowance for Free-Surface and Density-Gradient Effects. In *Maritime Simulation: Proceedings of the First Intercontinental Symposium, Munich, June 1985*, Heller MR (ed). Springer Berlin Heidelberg: Berlin, Heidelberg; 101-113.

Stace CA. 2010. New flora of the British Isles. Cambridge University Press: Cambridge, UK.

Stevens CL, Hurd CL. 1997. Boundary-layers around bladed aquatic macrophytes. *Hydrobiologia* **346**: 119-128.

Stoesser T. 2013. Calculation and Eduction of Coherent Flow Structures in Open-Channel Flow Using Large-Eddy Simulations. In *Coherent Flow Structures at Earth's Surface*, Venditti JG, Best JL, Church M, Hardy RJ (eds). John Wiley & Sons, Ltd: Chichester, UK; 175-197.

Stoesser T, Kim SJ, Diplas J. 2010. Turbulent Flow through Idealized Emergent Vegetation. *Journal of Hydraulic Engineering* **136**: 1003-1017.

Stoesser T, Salvador GP, Rodi W, Diplas P. 2009. Large Eddy Simulation of Turbulent Flow Through Submerged Vegetation. *Transport in Porous Media* **78**: 347-365.

Stone MC, Chen L, Kyle McKay S, Goreham J, Acharya K, Fischenich C, Stone AB. 2013. Bending of submerged woody riparian vegetation as a function of hydraulic flow conditions. *River Research and Applications* **29**: 195-205.

Straatsma MW, Baptist MJ. 2008. Floodplain roughness parameterization using airborne laser scanning and spectral remote sensing. *Remote Sensing of Environment* **112**: 1062-1080.

Straatsma MW, Warmink JJ, Middelkoop H. 2008. Two novel methods for field measurements of hydrodynamic density of floodplain vegetation using terrestrial laser scanning and digital parallel photography. *International Journal of Remote Sensing* **29**: 1595-1617.

Strahler AN. 1957. Quantitative analysis of watershed geomorphology. *Eos, Transactions American Geophysical Union* **38**: 913-920.

Streeter VL. 1998. Fluid mechanics. McGraw-Hill: New York, USA.

Sukhodolov A, Sukhodolova T. 2010a. Case Study: Effect of Submerged Aquatic Plants on Turbulence Structure in a Lowland River. *Journal of Hydraulic Engineering* **136**: 434-446.

Sukhodolov A, Sukhodolova T. 2010b. Case study: Effect of submerged aquatic plants on turbulence structure in a lowland river. *Journal of Hydraulic Engineering* **137**: 434-446.

Sukhodolov A, Sukhodolova T. 2014. Shallow wake behind exposed wood-induced bar in a gravel-bed river. *Environmental Fluid Mechanics* **14**: 1071-1083.

Sukhodolov AN, Rhoads BL. 2001. Field investigation of three-dimensional flow structure at stream confluences: 2. Turbulence. *Water Resources Research* **37**: 2411-2424.

Sutton SLF, McKenna-Neuman C. 2008. Sediment entrainment to the lee of roughness elements: Effects of vortical structures. *Journal of Geophysical Research: Earth Surface* **113**: F02S09.

Takemura T, Tanaka N. 2007. Flow structures and drag characteristics of a colony-type emergent roughness model mounted on a flat plate in uniform flow. *Fluid Dynamics Research* **39**: 694-710.

Tanaka N, Yagisawa J. 2010. Flow structures and sedimentation characteristics around clump-type vegetation. *Journal of Hydro-environment Research* **4**: 15-25.

Tanino Y, Nepf H. 2008. Laboratory Investigation of Mean Drag in a Random Array of Rigid, Emergent Cylinders. *Journal of Hydraulic Engineering* **134**: 34-41.

Tempest JA, Möller I, Spencer T. 2015. A review of plant-flow interactions on salt marshes: the importance of vegetation structure and plant mechanical characteristics. *Wiley Interdisciplinary Reviews: Water* **2**: 669–681.

Thomas RE, Jordan DN, Keevil GM, Parsons DR. 2016. Monitoring seasonal changes to macrophyte patch form with infrared photography. In *11th International Symposium on Ecohydraulics* Melbourne, Australia.

Thomas RE, McLelland SJ. 2015. The impact of macroalgae on mean and turbulent flow fields. *Journal of Hydrodynamics, Ser.B* **27**: 427-435.

Thomas RE, Schindfessel L, McLelland SJ, Creelle S, Mulder TD. 2017. Bias in mean velocities and noise in variances and covariances measured using a multistatic acoustic profiler: The Nortek Vectrino Profiler. *Measurement Science and Technology* **28**: 075302.

Thorne C. 2014. Geographies of UK flooding in 2013/4. *The Geographical Journal* **180**: 297-309.

Trepel M, Holsten B, Kieckbush J, Otten I, Pieper F. 2003. Influence of macrophytes on water level and flood dynamics in a riverine wetland in Northern Germany. In *Proceedings of the International Conference "EcoFlood—Towards Natural Flood Reduction Strategies"*. Institute for Land Reclamation and Grassland Farming: Raszyn, Poland.

Tritton DJ. 1988. Physical Fluid Dynamics. Clarendon Press: Oxford, UK.

Usherwood JR, Ennos AR, Ball DJ. 1997. Mechanical and anatomical adaptations in terrestrial and aquatic buttercups to their respective environments. *Journal of Experimental Botany* **48**: 1469-1475.

Vaaja MT, Virtanen JP, Kurkela M, Lehtola V, Hyyppä J, Hyyppä H. 2016. The effect of wind on tree stem parameter estimation using terrestrial laser scanning. *ISPRS Ann. Photogramm. Remote Sens. Spatial Inf. Sci.* **III-8**: 117-122.

Valiela I, Teal JM, Deuser WG. 1978. The Nature of Growth Forms in the Salt Marsh Grass Spartina alterniflora. *The American Naturalist* **112**: 461-470.

Valyrakis M, Kitsikoudis V, Yagci O, Kirca VSO, Koursari E. 2015. Experimental investigation of the modification of the flow field, past emergent aquatic vegetation elements. In *36th IAHR World Congress*: The Hague, Netherlands.

Västilä K, Järvelä J. 2014. Modeling the flow resistance of woody vegetation using physically based properties of the foliage and stem. *Water Resources Research* **50**: 229-245.

Västilä K, Järvelä J, Aberle J. 2013. Characteristic reference areas for estimating flow resistance of natural foliated vegetation. *Journal of Hydrology* **492**: 49-60.

Vauhkonen J, Holopainen M, Kankare V, Vastaranta M, Viitala R. 2016. Geometrically explicit description of forest canopy based on 3D triangulations of airborne laser scanning data. *Remote Sensing of Environment* **173**: 248-257.

Versteeg HK, Malalasekera W. 1995. An Introduction to Computational Fluid Dynamics. Longman: Harlow, UK.

Vetter M, Höfle B, Hollaus M, Gschöpf C, Mandlburger G, Pfeifer N, Wagner W. 2012. Vertical vegetation structure analysis and hydraulic roughness determination using dense als point cloud data - a voxel based approach. *Int. Arch. Photogramm. Remote Sens. Spatial Inf. Sci.* **XXXVIII-5/W12**: 265-270.

Vierling KT, Vierling LA, Gould WA, Martinuzzi S, Clawges RM. 2008. Lidar: shedding new light on habitat characterization and modeling. *Frontiers in Ecology and the Environment* **6**: 90-98.

Visser F, Buis K, Verschoren V, Meire P. 2015. Depth Estimation of Submerged Aquatic Vegetation in Clear Water Streams Using Low-Altitude Optical Remote Sensing. *Sensors* **15**: 25287.

Visser F, Wallis C, Sinnott AM. 2013. Optical remote sensing of submerged aquatic vegetation: Opportunities for shallow clearwater streams. *Limnologica* **43**: 388-398.

Vogel S. 1984. Drag and Flexibility in Sessile Organisms. *American Zoologist* **24**: 37-44.

Vogel S. 1989. Drag and Reconfiguration of Broad Leaves in High Winds. *Journal of Experimental Botany* **40**: 941-948.

Vogel S. 1994. Life in moving fluids: the physical biology of flow. Princeton University Press: Chichester, UK.

Vogel S. 2009. Leaves in the lowest and highest winds: temperature, force and shape. *New Phytologist* **183**: 13-26.

Vollsinger S, Mitchell SJ, Byrne KE, Novak MD, Rudnicki M. 2005. Wind tunnel measurements of crown streamlining and drag relationships for several hardwood species. *Canadian Journal of Forest Research* **35**: 1238-1249.

Wackrow R, Ferreira E, Chandler J, Shiono K. 2015. Camera Calibration for Water-Biota Research: The Projected Area of Vegetation. *Sensors* **15**: 30261-30269.

Wahl TL. 2003. Discussion of "Despiking Acoustic Doppler Velocimeter Data" by Derek G. Goring and Vladimir I. Nikora. *Journal of Hydraulic Engineering* **129**: 484-487.

Wallingford H. 2004. Reducing uncertainty in river flood conveyance, Phase 2 conveyance manual. Report to DEFRA, Project W5A/057/PR/1.

Wardle P. 1991. Vegetation of New Zealand. Cambridge University Press: Cambridge, UK.

Watt PJ, Donoghue DNM. 2005. Measuring forest structure with terrestrial laser scanning. *International Journal of Remote Sensing* **26**: 1437-1446.

Watts JFW, G.D. 1990. Seasonal change in aquatic vegetation and its effect on channel flow. In *Vegetation and Erosion*, Thornes JB (ed). Wiley: Chichester; 518.

Weerakoon SB, Tamai N. 1989. Three-dimensional calculation of flow in river confluences using boundary-fitted coordinate. *Journal of Hydroscience and Hydraulic Engineering* **7**: 51 - 62.

Wehr A. 2008. LiDAR Systems and Calibration. In *Topographic Laser Ranging and Scanning*, Shan J, Toth C (eds). Taylor and Francis: Boca Raton, USA; 129-172.

Wehr A, Lohr U. 1999. Airborne laser scanning—an introduction and overview. *ISPRS Journal of Photogrammetry and Remote Sensing* **54**: 68-82.

Wei T, Smith CR. 1986. Secondary vortices in the wake of circular cylinders. *Journal of Fluid Mechanics* **169**: 513-533.

Weissteiner C, Jalonen J, Järvelä J, Rauch HP. 2015. Spatial–structural properties of woody riparian vegetation with a view to reconfiguration under hydrodynamic loading. *Ecological Engineering* **85**: 85-94.

Weissteiner C, Rauch HP, Jalonen J, Järvelä J. 2013. Spatial-structural analysis of leafless woody riparian vegetation for hydraulic considerations. In *Proc. 35th IAHR World Congress*. Tsinghua University Press: Chengdu, China.

Westoby MJ, Brasington J, Glasser NF, Hambrey MJ, Reynolds JM. 2012. 'Structure-from-Motion' photogrammetry: A low-cost, effective tool for geoscience applications. *Geomorphology* **179**: 300-314.

Wheater HS. 2006. Flood hazard and management: a UK perspective. *Philosophical Transactions of the Royal Society A: Mathematical, Physical and Engineering Sciences* **364**: 2135-2145.

White BL, Nepf HM. 2007. Shear instability and coherent structures in shallow flow adjacent to a porous layer. *Journal of Fluid Mechanics* **593**: 1-32.

Whittaker P, Wilson C, Aberle J, Rauch HP, Xavier P. 2013. A drag force model to incorporate the reconfiguration of full-scale riparian trees under hydrodynamic loading. *Journal of Hydraulic Research* **51**: 569-580.

Wilcox AC, Wohl EE. 2006. Flow resistance dynamics in step-pool stream channels: 1. Large woody debris and controls on total resistance. *Water Resources Research* **42**: W05418.

Wilcox DC. 2006. Turbulence modeling for CFD. DCW Industries: La Canada, USA.

Williams RD, Brasington J, Vericat D, Hicks DM. 2014. Hyperscale terrain modelling of braided rivers: fusing mobile terrestrial laser scanning and optical bathymetric mapping. *Earth Surface Processes and Landforms* **39**: 167-183.

Williamson CHK. 1996. Vortex Dynamics in the Cylinder Wake. *Annual Review of Fluid Mechanics* **28**: 477-539.

Williamson CHK, Wu J, Sheridan J. 1995. Scaling of streamwise vortices in wakes. *Physics of Fluids* **7**: 2307-2309.

Wilson CA, Horritt MS. 2002. Measuring the flow resistance of submerged grass. *Hydrological Processes* **16**: 2589-2598.

Wilson CAME, Hoyt J, Schnauder I. 2008. Impact of Foliage on the Drag Force of Vegetation in Aquatic Flows. *Journal of Hydraulic Engineering* **134**: 885-891.

Wilson CAME, Stoesser T, Bates P, Pinzen A. 2003. Open Channel Flow through Different Forms of Submerged Flexible Vegetation. *Journal of Hydraulic Engineering* **129**: 847-853.

Wilson CAME, Stoesser T, Bates PD. 2005. Modelling of Open Channel Flow through Vegetation. In *Computational Fluid Dynamics: Applications in Environmental Hydraulics*, Bates PD, Lane SN, Ferguson RI (eds). John Wiley & Sons, Ltd: Chichester, UK; 395-428.

Wilson CAME, Yagci O, Rauch HP, Stoesser T. 2006. Application of the drag force approach to model the flow-interaction of natural vegetation. *International Journal of River Basin Management* **4**: 137-146.

Wilson NR, Shaw RH. 1977. A Higher Order Closure Model for Canopy Flow. *Journal of Applied Meteorology* **16**: 1197-1205.

Wooding RA, Bradley EF, Marshall JK. 1973. Drag due to regular arrays of roughness elements of varying geometry. *Boundary-Layer Meteorology* **5**: 285-308.

Wunder S, Lehmann B, Nestmann F. 2011. Determination of the drag coefficients of emergent and just submerged willows. *International Journal of River Basin Management* **9**: 231-236.

Xavier P, Wilson CAME, Aberle J, Rauch HP, Schoneboom T, Lammeranner W, Thomas H. 2010. Drag force of flexible submerged trees. In *Hydralab III Joint User Meeting*: Hannover, Germany.

Yagci O, Celik MF, Kitsikoudis V, Ozgur Kirca VS, Hodoglu C, Valyrakis M, Duran Z, Kaya S. 2016. Scour patterns around isolated vegetation elements. *Advances in Water Resources* **97**: 251-265.

Yagci O, Kabdasli MS. 2008. The impact of single natural vegetation elements on flow characteristics. *Hydrological Processes* **22**: 4310-4321.

Yagci O, Tschiesche U, Kabdasli MS. 2010. The role of different forms of natural riparian vegetation on turbulence and kinetic energy characteristics. *Advances in Water Resources* **33**: 601-614.

Yakhot V, Orszag S. 1986. Renormalization group analysis of turbulence. I. Basic theory. *Journal of Scientific Computing* **1**: 3-51.

Yakhot V, Smith L. 1992. The renormalization group, the ε-expansion and derivation of turbulence models. *Journal of Scientific Computing* **7**: 35-61.

Yang K, Cao S, Knight D. 2007. Flow Patterns in Compound Channels with Vegetated Floodplains. *Journal of Hydraulic Engineering* **133**: 148-159.

Yen BC. 1992. Channel flow resistance: centennial of Manning's formula. Water Resources Publication: Colorado, USA.

Yen BC. 2002. Open Channel Flow Resistance. *Journal of Hydraulic Engineering* **128**: 20-39.

Zedel L, Hay AE. 2010. Resolving Velocity Ambiguity in Multifrequency, Pulse-to-Pulse Coherent Doppler Sonar. *IEEE Journal of Oceanic Engineering* **35**: 847-851.

Zheleznyakov G. 1965. Relative Deficit of Mean Flow of Instable River Flow, Kinematic Effect in River Beds with Floodplains. In *Proc. 11th International Congress of the International Association for Hydraulic Research*: Leningrad.

Zheleznyakov G. 1971. Interaction of Channel and Floodplain Streams. In *Proc. 14th International Congress of the International Association for Hydraulic Research*: Paris.

Zong L, Nepf HM. 2010. Flow and deposition in and around a finite patch of vegetation. *Geomorphology* **116**: 363-372.

Zong L, Nepf HM. 2012. Vortex development behind a finite porous obstruction in a channel. *Journal of Fluid Mechanics* **691**: 368-391.